The University of Sheffield

Multiscale experimentation & modeling of fatigue crack development in aluminium alloy 2024

A dissertation submitted in partial satisfaction
of the requirements for the degree
Doctor of Philosophy in Mechanical Engineering

by

Panos Efthymiadis

2014

Table of Contents

Abstract of the Dissertation

Multiscale experimentation & modeling of fatigue crack development in aluminium alloy 2024

A dissertation submitted in partial satisfaction

of the requirements for the degree

Doctor of Philosophy in Mechanical Engineering

by

Panos Efthymiadis

The objective of this research project is to be able to understand the role of various microstructural features on Fatigue Crack Initiation (FCI) of metallic alloys. By employing a novel experimental set-up, mechanical testing was performed in situ within an SEM chamber, and the deformation of the individual grains was observed real time. A physically-based Crystal Plasticity (CP) model was then developed that accurately predicts the macro and micro mechanical behaviour for Al2024 T3. An experimentally informed FCI criterion was developed that accounts for the effect of local slip bands and the applied local strains. While 'precious' insights were given on the small crack growth regime observing the occurring microscale phenomena.

FCI is a multiscale process and thus evaluating the microscale does not cover fully the understanding of local deformation and damage. Thus a multiscale DIC process was employed to better understand the macro and mesoscale as well. 3D Digital Image Correlation (DIC) was employed and the strain distributions (at the sample scale) were obtained for various loading conditions. High magnification camera based 2D DIC was then used and the strain measurements were also extracted at clusters of grains. Useful observations were given for the different strain components (ε_{xx}, ε_{yy}, ε_{xy}). Finally the total fatigue lifetime of the component was compared to the modeled FCI for various loading conditions.

Abbreviations and Acronyms

EBSD   *Electron Back-Scattered Diffraction*

CTOD   *Crack Tip Opening Displacement*

CTSD   *Crack Tip Sliding Displacement*

CP   *Crystal Plasticity*

CPFEM   *Crystal Plasticity Finite Element Method*

DIC   *Digital Image Correlation*

FEM   *Finite Element Method*

FCI   *Fatigue Crack Initiation*

FCP   *Fatigue Crack Propagation*

FIP   *Fatigue Indicator Parameters*

OOF   *Object Oriented Finite element analysis developed at NIST*

SEM   *Scanning Electron Microscopy*

TEM   *Transmission Electron Microscopy*

IPF   *Inverse Pole Figure*

<div style="text-align: right">

1

</div>

Introduction

Current developments in industry are targeting the minimisation of production costs, service lifetime expenses, as well as a reduction of environmental pollution. In the aerospace industry, the production of light weight structures with adequate strength and endurance is of primary concern. Light weight airplanes reduce the consumption of gasoline and become more 'environmentally - friendly' for the modern society.

As a result aerospace companies are using thinner, stronger materials, and use more sophisticated designs and models in order to understand better and design more efficiently the airplanes of the future.

It is well known that the production and lifetime approach for such structures is based on damage tolerant designs. Imperfections, such as cracks, occur in different parts of an airplane, such as the ones observed recently at the ribs of Airbus A380 (see figure 1.1) [1]. Crack occurrence is frequently monitored to determine the tolerance of the structure and the required time for service, repair or even replacement. Minimising the sections of such structures makes the design much more critical.
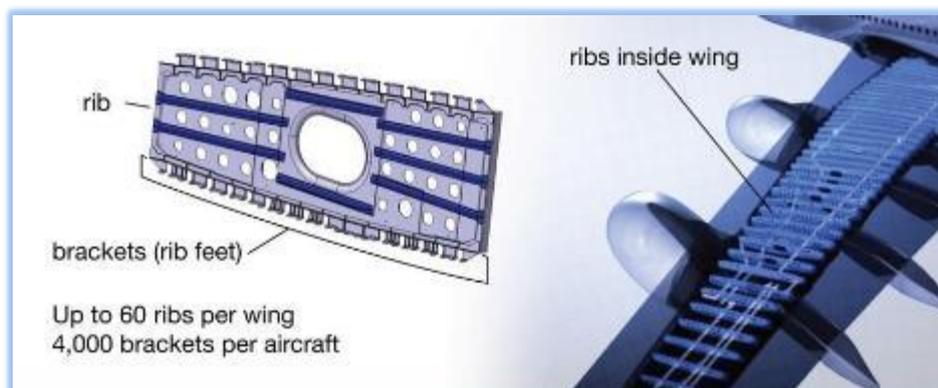
Figure 1-1. Cracks observed at the rib structures of Airbus A380 [1].

Cracks tend to develop within small regions of the material and grow very slowly. During the initiation period of a crack the microstructure plays a crucial role and the cracks during this stage are called Stage I cracks (see figure 1.2). For a large part of their lifetime, cracks remain undetected and stay in

the Stage I region. Some of them though may reach a certain size and enter the Stage II region; where they can be detected by means of Non-Destructive Techniques. The famous Paris-Law relation is used to represent the propagation of cracks whose size is large with respect to the grain size and are named Stage II cracks. The Paris law relation correlates the crack growth rate (da/dN) with the range of stress intensity factor (ΔK) via a linear relationship in a logarithmic scale (see figure 1.2). Periodic measurements are taken over the different parts of a structure to evaluate the existence of various crack sizes; thorough investigation of the loading system and geometry lead to critical decisions, such as repair, replacement or the structure is determined to be safe. It is obvious that this process is time consuming and costly. Being able to understand the material behavior and physically model fatigue crack propagation, especially during the early stages at the microstructure level, becomes more and more important. After Stage II, cracks tend to grow with very high speeds, leading to catastrophic failures. Stage III cracks is a region that should always be avoided during a structure's lifetime.

A lot of knowledge has been obtained on the behavior of stage II cracks and, as explained before, their evolution can be easily monitored with well-established techniques. However what happens in the stage I region is not well understood yet, and is the focus area of this research project. The formation of cracks, the transition-period between stage I and II are still areas that need further developments and investigations.
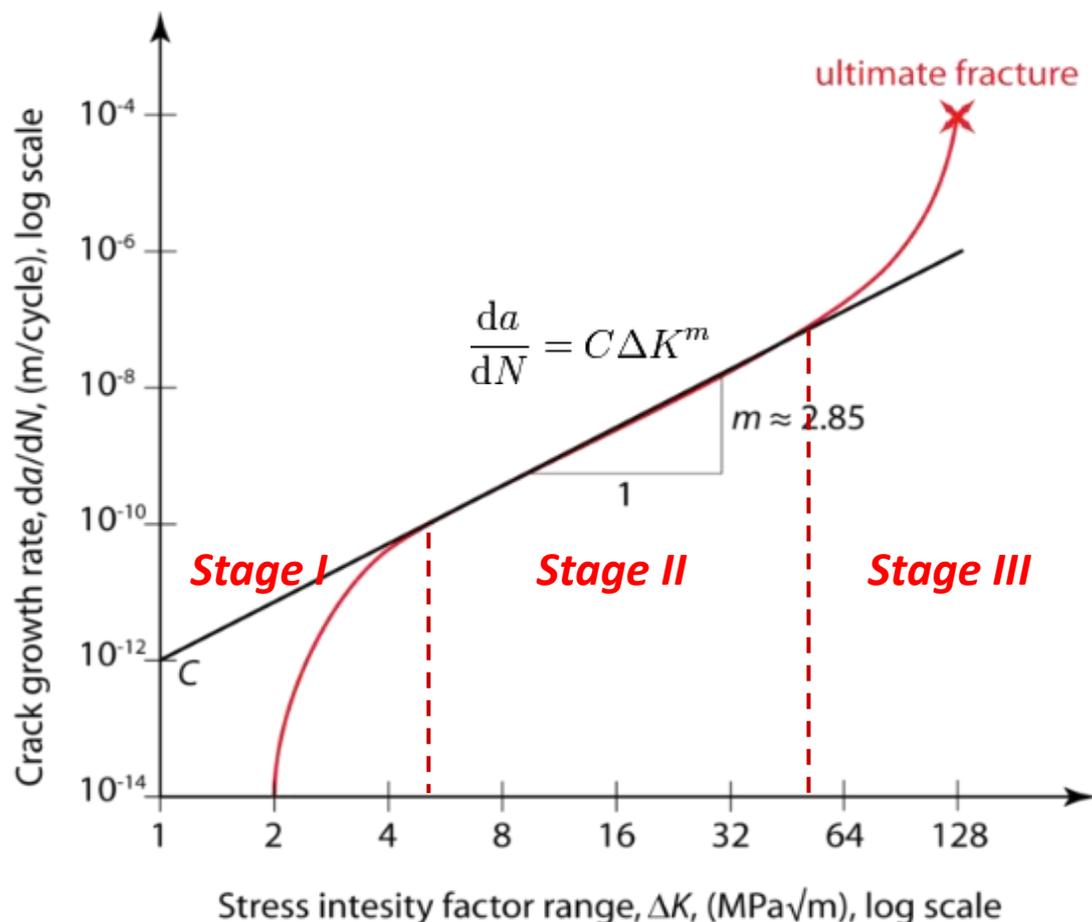
Figure 1-2. Fatigue lifetime: the 3 fatigue lifetime regimes-stages and the Paris law relation describing stage II cracks.

Normally Stage I cracks tend to initiate at Persistent Slip bands; bands within a grain where shear deformation occurs along specific orientations with respect to the principal loading direction. Crystal imperfections such as inclusions, particles or pores may also act as crack initiation points by leading to high local stresses concentration, decohesion and/or crack initiation at the very first cycles of the lifetime of a component. In all cases, cracks form within grains and stop upon reaching a grain boundary. Therefore the behaviour of grain boundaries and crystal matrix is of great importance in understanding fatigue crack propagation. The adjacent grains to the cracked grain determine the Fatigue Crack Initiation Period and the resistance to small crack growth.

1.1. Experimental outline

The material investigated is Al2024 T3, which is extensively used in the aerospace sector. The metallurgy of the material was revealed in terms of optical microscopy. Scanning Electron Microscopy (SEM) analysis was used to further reveal the microstructural details, and Electron BackScattered Diffraction (EBSD) technique to acquire the orientation of the grains. 3D Digital Image Correlation (DIC) was employed during tensile testing to evaluate the macroscopic mechanical properties of the material. Fatigue testing on tensile specimens was employed, coupled to 2D DIC to observe any localised deformations, and damage accumulation within grain clusters. In situ micro-mechanical testing was then employed within a SEM chamber, coupled with EBSD and Digital Image Correlation (DIC) measurements to relate the orientation of the grains to the occurring localised deformation and damage. The orientation of cracks was related to the formation of strong slip bands, which strongly depends on the local crystal orientation and on the applied local displacements due to the BCs and sample geometry. By employing such a novel procedure it was possible to introduce a new criterion for FCI. Furthermore, the above explained multiscale image correlation process yielded very useful results about the connection between the different scales. What is happening at the macroscale clearly affects the meso and microscale.

1.2. Modelling outline

A CP model was used that can model effectively the macroscopic stress strain behaviour. The behaviour of the material at the microscale is of great importance as well and thus grains and particles were explicitly modeled to account for their micromechanical behaviour. Figure 1.3 shows a chart with the CP model developed to evaluate the mechanical behaviour of the grains. A new FCI criterion was established based on the insight gained from the experimental results. Particles were explicitly modeled to evaluate the influence of particles on FCI for the case of low amplitude fatigue loading. Then a Multiscale technique was used to move from the microscale to a larger scale to enable the modelling of larger components.
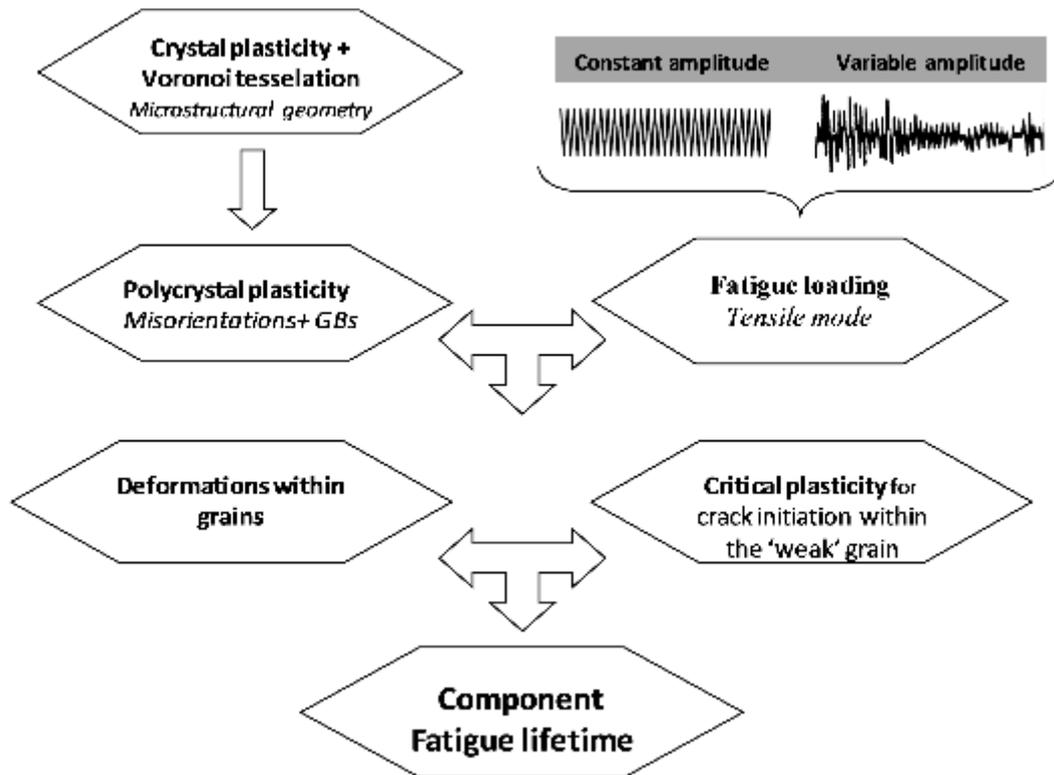
Figure 1-3. Modelling Scheme for Fatigue.

1.3. Thesis structure

Chapter 2 presents the published work on FCI modelling, concentrating mostly on crystal plasticity approaches. In Chapter 3 the experimental procedures are presented including the mechanical testing equipments, the in-situ tester, the DIC and the SEM equipments. Chapter 4 presents the basic concepts of plastic deformation with a particular focus on crystal plasticity. The rules of continuum mechanics are outlined, followed by the corresponding yielding criteria and hardening rules. Afterwards, the basic metallic crystal structures are introduced and the concepts of crystal plasticity are discussed. The second part of Chapter 4 discusses the Voronoi RVE method and its application to FCI, while formulations of crystal misorientation are presented in the 2nd section of this chapter.

In Chapter 5 the experimental results are presented: microstructure of Al2024, tensile properties, fatigue testing coupled with DIC imaging, followed by a macro- and meso-scopic characterisation of the strain dictributions. Chapter 6 presents the experimental results at the microscale using in-situ fatigue testing.

Finally Chapter 7 presents and discusses the modelling results with respect to the experimental observations. And the last Chapter, i.e. Chapter 8, reports the main conclusions drawn from the new insight gained from the combined multi-scale experimental/modelling approach developed in this work as regards initiation and development of fatigue cracks in the investigated aluminium alloy, as well as future recommendations.

<div style="text-align: right;">

2

</div>

Fatigue

Fatigue is the progressive and localised structural damage that occurs to a material subjected to cyclic loading. The stress values are always less than the ultimate tensile stress limit, and in many cases below the yield stress limit of the material. Upon repeated loading and unloading of the structure, microscopic cracks form; usually cracks occur preferentially at triple points, at particle - matrix interfaces due to decohesion, at pores due to high stress concentrations, and at the so called 'weak' grains. In the beginning cracks are confined within grains but at some stage reach a critical length and propagate from grain to grain, 'ignoring' the microstructural features. At a certain point a crack will reach a critical size, and will start propagating progressively fast and the structure will suddenly fracture. For the case of high cyclic loading crack tend to occur at the free surface, at a preferential 45 degrees orientation with respect to the principal loading direction. In this chapter a brief description of the current modelling techniques used for fatigue and fatigue crack initiation is presented.

2.1. General Overview of Fatigue Crack Initiation and Small Crack Growth

In this section an overview on the theory of fracture and fatigue is presented based on the work of Stroh, Miller, Polak et al and Holdsworth [2-6]. Stroh presented an overview on the transcrystalline fracture of polycrystalline materials [4]. Two types of fracture are mainly observed: brittle and ductile. The strength of the ideal lattice was then calculated and compared with the observed fracture strength of polycrystalline materials. For a substance with perfect crystalline lattice, the maximum stress (σ_m) is:

$$\sigma_m = \sqrt{\frac{2E\gamma}{b}} \qquad\qquad (2.1)$$

Substituting the material constants E, b and γ in equation (2.1) gives a value 20 to 1000 times the observed. The calculations were also confirmed from other authors, Zwicky (1923), Born and Furth (1940), by calculations on the interatomic forces. To account for the discrepancy, Griffith in (1920) assumed that a real material contains preexisting small cracks which act as stress concentrators. Yet the experiments were performed in glass samples, and such approach cannot be realistic of metals. To account for the observed strength, the cracks would need to be macroscopic extending several

millimeters within the samples. Brittle fracture at the microscale was discussed in the context of piled up dislocations at a grain boundary. If a critical number of edge dislocations are piled up on a grain boundary, they may produce a stress that can cause local failure; micro-cracking. The normal stress to the slip line of the piled-up dislocations is:

$$\sigma = \sigma_s \sqrt{\frac{L}{r}}\, f(\vartheta) \qquad\qquad (2.2)$$

Where L is the length of aligned dislocations, σ_s is the resolved shear stress on the slip plane, and $f(\vartheta)$ is a factor depending on the orientation of the grain. Eshelby et al (1951) stated that the number of dislocations (n) to initiate a crack is given by:

$$n\sigma_s b = \frac{3}{8}\pi^2 \gamma \qquad\qquad (2.3)$$

Rough calculations indicate that 100 dislocations producing a 200 Å height are necessary. Most observations made in FCC metals showed that 30 dislocations are sufficient to produce a crack. Yet in coarse iron, slip lines of the order of 800 Å (300 dislocations) have been observed.

Dislocations are necessary to produce a crack. Therefore plastic flow is always necessary to produce a crack. The amount needed is small and confined within the large elastic body. Brittle fractures are usually preceded by small plastic strains. Crussard (1956) found that the plastic strain near the notch of steel specimens broken in brittle manner was approximately equal to an elongation of at least 3%. Low (1954) found that fracture cannot occur until the yield stress has been exceeded. Let's consider an edge dislocation. By forcing more dislocations adjacent to each other, a wider wedge can be produced, till the neighbouring planes are so far apart that a crack forms. Once the crack forms the stresses are relieved, so it becomes easier for dislocations to glide towards the proximity of the crack. This in turn widens the wedge and causes the crack to propagate further. The normal stress to the crack becomes more important the greater the crack length. Once the crack reaches a critical length, the normal stress alone will be sufficient to spread the crack to the rest of the material. Therefore when the crack is small, crack growth is controlled by the slip line, when it is large, by the applied tensile stress.

Plastic flow can be generated by: existing Franck-Read sources which generate new dislocations, or when the stresses in the perfect lattice are sufficient to initiate slip. If slip could occur within the perfect lattice, deformation then would spread throughout the rest of the material, and it would be possible to identify the process with the spread of a Lüders band. Therefore the possibility of generating plasticity in ideal lattice is rejected. Plastic flow can only be due to dislocations from Frank-Read sources. If the material is brittle, plastic flow does not occur via the piled-up dislocations, and the sources are blocked. The dislocation sources can be blocked by segregation of impurities (Cottrell locking), or due to some slip systems being difficult to generate slip (non-basal slip in hexagonal closed packed structures). In brittle fractures, the growth of a crack occurs when:

$$\sigma = \sqrt{\frac{Ep}{c}} \qquad\qquad (2.4)$$

The stress here is inversely proportional to the square root of the initial crack length.

Miller discusses the main issues of metal fatigue, concentrating on fatigue crack initiation and short crack growth [2, 3]. The behaviour of a crack depends largely on its size and on the mechanical conditions applied. For defects (cracks, pores etc) larger than 1mm, Linear Elastic Fracture Mechanics may be applied in all cases.

Figure 2.1a is an overview of a crack life. Three different zones may be seen: Zone A-B, the so-called microstructural short crack growth regime, the B-C zone known as physically small crack growth regime and C-D zone where the crack is large enough for LEFM to be applied. In the B-C zone Elasto-Plastic Fracture Mechanics concepts should be used. In zone A-B crack initiation and growth depends on material microstructure at the grain level. In zone A-B, precipitates, inclusions, triple point boundaries act as stress concentration points and therefore facilitate fatigue crack initiation. The b_3, b_4 and b_5 barriers are of increasing strength opposing early crack growth. As example b_3 can be a twin boundary, the intermediate barrier a grain boundary, and the strongest a phase boundary with high misorientation. It should be noted that during cyclic loading, hundreds of individual slip bands may be generated in a polycrystalline metal, but only one crack and its associated plasticity will cause ultimate failure.
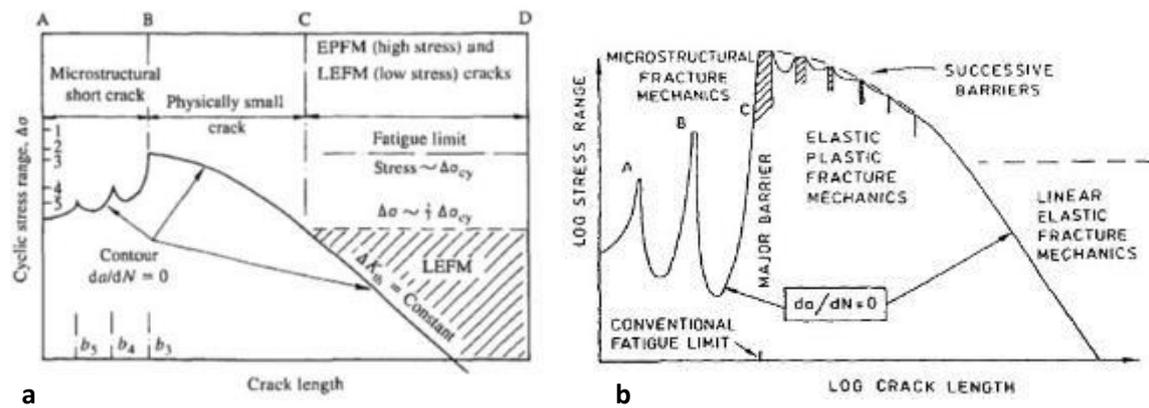
Figure 2-1. a) Regimes of fatigue life during crack formation and growth, b) highlighting the effect of grain boundaries upon crack growth [2].

Miller extended the Microstructurally Short Crack (MSC) region of figure 2.1a, revealing that the microstructure effects have an important role also in the physically short crack region. But figure 2.1b shows that the effect of the grains and grain boundaries becomes smaller and smaller as the crack grows. Crack growth in the microstructurally short crack growth regime involves both retardation when the crack approaches a barrier and acceleration after penetrating the barrier. The equations for the three different regimes are as follows. For the microstructurally short crack growth regime:

$$\frac{da}{dN} = A\Delta\gamma_p^\alpha \left(d - A \right) \tag{2.5}$$

where A and α are material constants, $\Delta\gamma_p^\alpha$ is the plastic shear strain range, d is the distance to the strongest barrier and a is the crack length. It may be seen that increasing the grain size, increases d value which in turn increases crack speed. For the physically small crack growth regime:

$$\frac{da}{dN} = B\Delta\gamma_p^{\beta}\alpha - C \qquad\qquad (2.6)$$

where B and $\Delta\gamma_p^{\beta}$ are material constants and C is the crack threshold condition. Finally, for the LEFM regime:

$$\frac{da}{dN} = D\Delta K^n \qquad\qquad (2.7)$$

where ΔK is the range of the stress intensity factor, and D and n are material constants. Thus fracture mechanics equations are already available for all the spectrum of crack lengths. The important zone in figure 2.1 is the microstructurally short crack growth regime where crack lengths and crack growth speeds are very low, governing the overall fatigue life. Figure 2.1 also shows why surface finish is important: if surface scratches are deeper than b_3, then the fatigue strength is reduced significantly. In figure 2.2a the S-N curves are shown for four different types of specimen: from plain to deeply cracked specimen. The fatigue limit of type A specimen can be increased by decreasing grain size; while for type D specimen the inverse is true. It follows that the threshold conditions relating the two specimens are fundamentally different. Figure 2.2b shows two boundary conditions between failure and non failure of notched specimens. These two conditions are called: material threshold applicable to plain specimens and mechanical threshold, ΔK_{th}, applicable to deeply notched specimens.
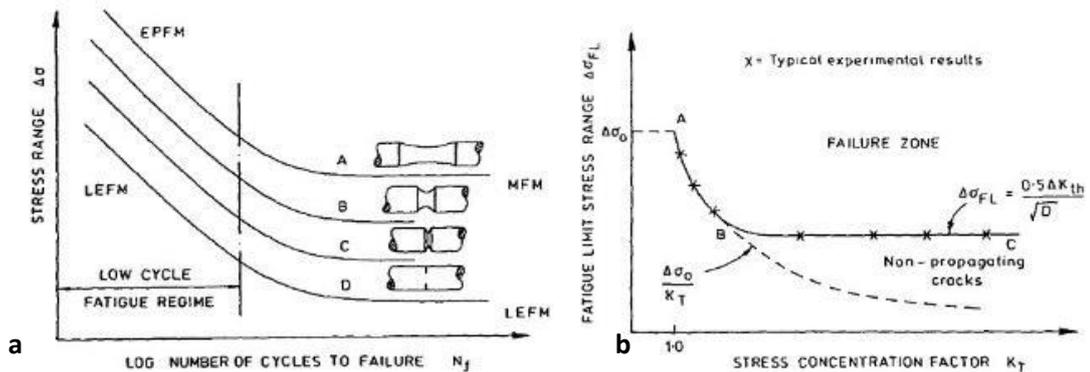
Figure 2-2. a) S-N curves for the same ferrous material but four different geometries of specimen, b) The boundary conditions between failure and non-failure of variously notched specimens A-B: the material threshold condition. B-C: the mechanical threshold condition. B-C: the mechanical threshold condition [2].

15
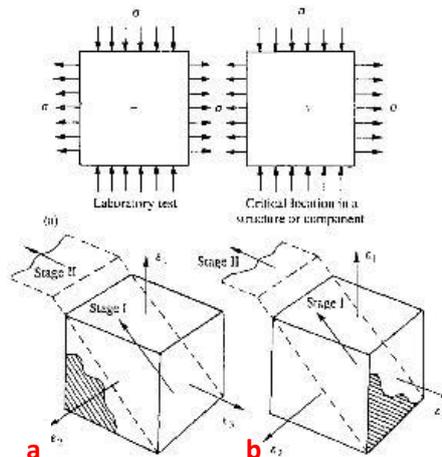
Figure 2-3. The importance of orientation of the applied stress-strain field with respect a) to the defect and b) the surface plane [2].

It has already been said that in order to improve the fatigue resistance, a decrease in grain size is required for zone A-B in figure 2.1a, while for C-D zone in figure 2.1a an increase in grain size is needed. At the LEFM regime increasing the grain size increases the mismatch of fatigue crack faces, reducing the cyclic crack opening distance and crack propagation rate. But this effect is eliminated when the applied mean stress increases simply because the crack faces remain open throughout the whole cycle.

In uniaxial fatigue it has been observed that cracks follow the Stage I and Stage II directions upon crack growth (see figure 2.3). In some cases classical fracture mechanics fail to predict crack growth and failure. In figure 2.3a the stress system is identical in both the experimental specimen and for the component of the structure. Thus the equivalent stress strain response should be identical, but failure occurs differently. The result is that the laboratory specimen does not fail while the component fails from crack growth. In figure 2.3b the three dimensional stress-strain response is similar, as is the orientation of the crack growth planes (for the stage I cracks). But one cracking system is far more dangerous since it is propagating the crack further away from the surface.

Figure 2.4 shows how it is possible to double the fatigue life of a specimen by previously subjecting the material to another stress state.
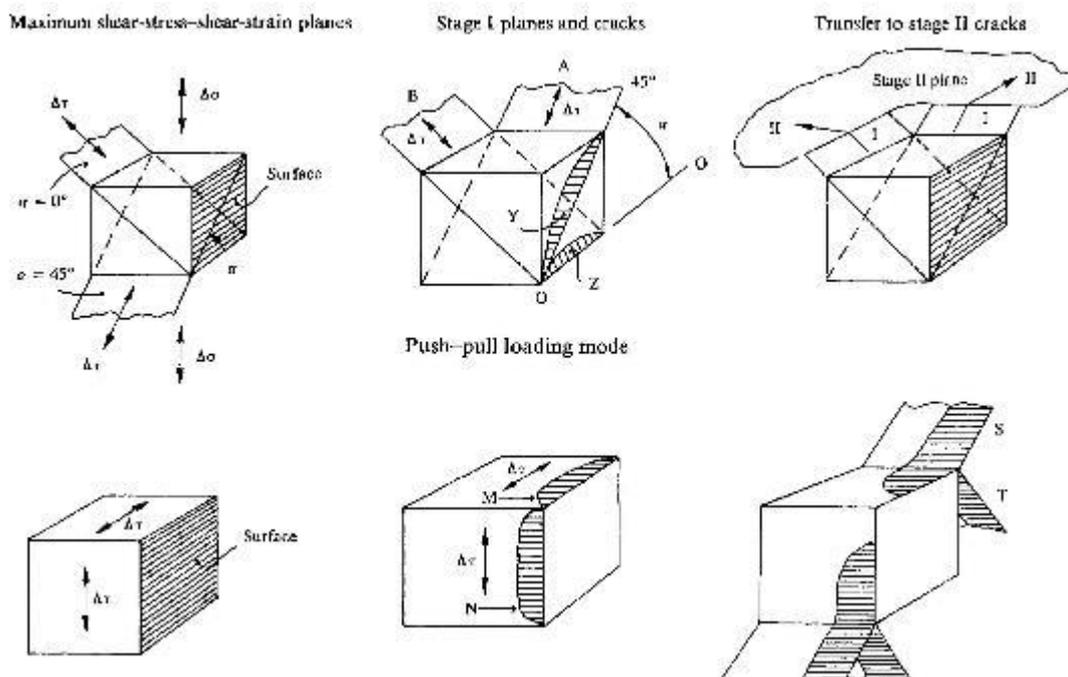
Figure 2-4. The effects of loading mode on the development of stage I and II cracks. Y, Z, M and N are stage I cracks while S and T are stage II cracks [2].

Figure 2.4 shows two stress states: the application of push-pull loading prior to torsional loading can lead to Stage I cracks incompatible with the load direction (torsional loading). Moreover the former cracks act as barriers to the evolution of the latter cracks.

Figure 2.5 shows the difficulty of an initially stage I crack on becoming stage II crack. In the transition region the crack has to grow in both tangential and radial direction across several grains of various sizes and crystallographic orientations; and therefore has a three dimensional character. It is this transition phase that determines the fatigue resistance of the material and represents the dominant period of fatigue lifetime. An inclusion in this region may provide an easy bridge between Stage I and Stage II crack growth. Thus the size of inclusions is critical with respect to the grain size.
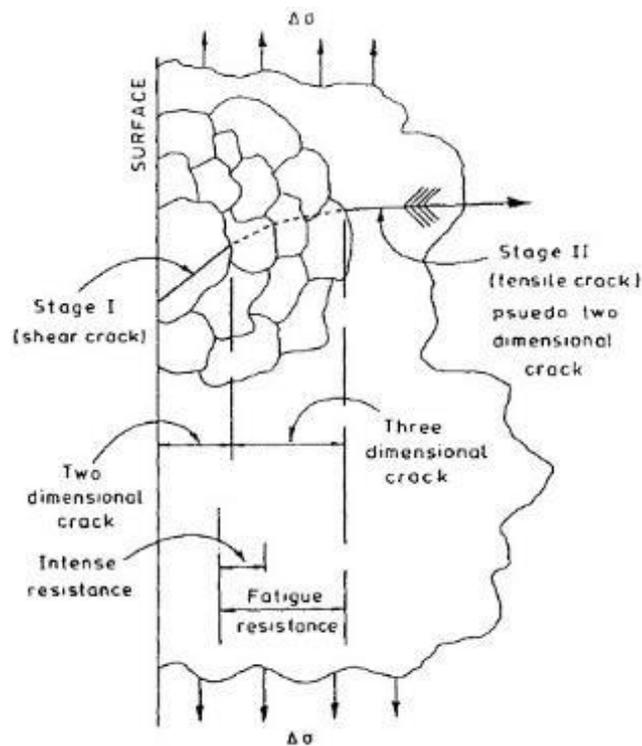
Figure 2-5. Fatigue resistance indicated in terms of the difficulty of an initial Stage I shear crack becoming a Stage II tensile crack [3].

The morphology and profile of the persistent slip bands was evaluated by atom force microscopy in the study of Polak et al [5]. Surface relief in the neighbourhood of persistent slip bands (PSBs) in polycrystalline 316L stainless steel cyclically loaded (constant plastic strain amplitude) up to 60% of total fatigue lifetime was studied using atomic force microscopy. The morphology of the PSB formed surface relief was later related respect to the crystallographic orientation (determined by EBSD) and the size of individual grains. It was found that the occurring surface relief is formed mostly by ribbon-like extrusions whose height within each grain is proportional to the thickness of the corresponding PSB. The extrusions grow predominantly in the direction of the active Burgers vector and the height of the extrusion in the direction of the active Burgers vector is proportional to the grain size. Figure 2-6 shows the occurring surface relief in two neighbouring grains (namely grain nr 21 and 22). The surface relief consists of parallel approximately equidistantly-spaced extrusions, separated by regions of flat non-deformed surface. The width of the corresponding extrusions and the separating distance were 0.5 and 1.3μm, 1 and 4μm for grain 21 and 22 respectively.
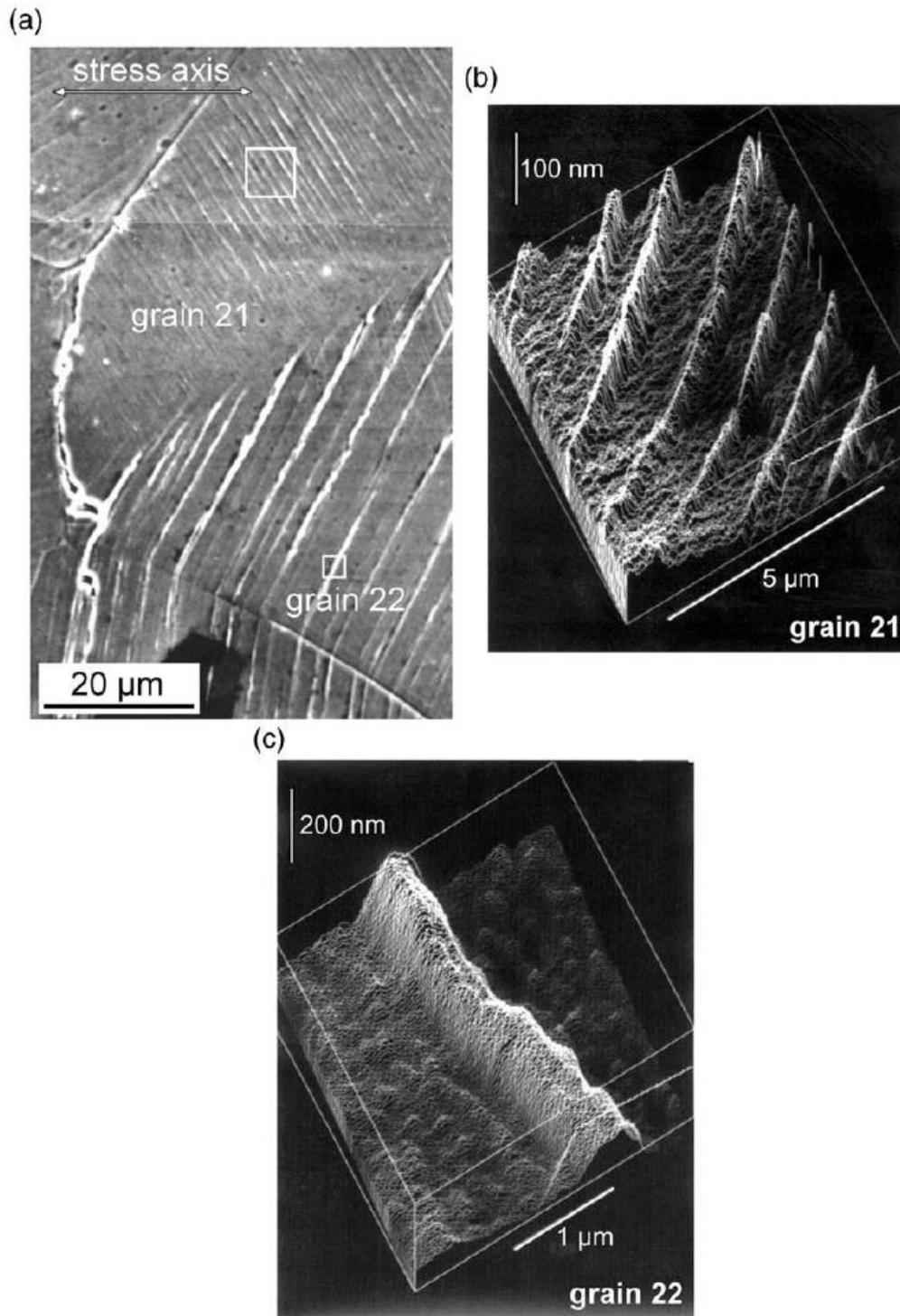
Figure 2-6. Surface relief within the grains nr 21 and 22 of 316L stainless steel cycled with constant plastic strain amplitude of 1×10^{-3} for 30.000 cycles. a) SEM micrograph at the area of the two grains at low magnification. b-c) Three-dimensional AFM images showing the detail of the occurring surface relief within grain nr 21 and 22 respectively. The areas scanned by atom force microscopy are marked in (a) with white boxes [5].

The main objective in the study of Holdsworth was to develop, optimise and validate effective and economic methods for predicting crack initiation and small crack growth in components subject to complex cyclic loading conditions [6]. Many engineering components operating at low and high

18

temperatures are subject to complex creep-fatigue loading conditions. Strain based methodologies have proven to be more accurate in predicting endurances. Yet the effectiveness of such approaches has not been fully validated for complex loading conditions. Especially in situations where primary and secondary loading systems are acting on components which already contain metallurgical and geometrical discontinuities (such as weldments, drilled holes and sharp corners), creep-fatigue assessments are less certain. Therefore large safety factors are generally applied. The project was divided into six tasks, shown in Diagram 2-1. The loading conditions were identified by nuclear plant manufacturers in order to represent real service conditions (Task 1). The effectiveness of the assessment methods was tested using results from five categories of specimens, which modelled a range of engineering components by incorporating geometrical stress concentrations and weldments. The five categories of specimen geometries are shown in Diagram 2-2.

STRUCTURE OF THE C-FAT PROJECT

1 TARGET COMPONENTS
1.1 1CrMoV TURBINE Castings
1.2 1CrMoV PIPEWORK
1.3 1CrMoV ROTOR FORGINGS
1.4 9CrMoVNb HEADERS
1.5 18Cr11Ni FF3R STRUCTURES

5 CREEP-FATIGUE ASSESSMENT
•METHOD DEVELOPMENT
• APPLICATION
• VALIDATION
•SENSITIVITY TO ANALYSIS ROUTE & MATERIAL PROPERTY INPUT DATA

2 MATERIAL PROPERTY INPUT DATA
• HEAT SPECIFIC DATA
•ALLOY SCATTERBAND DATA
•INTER-LAB VARIABILITY
. CONSTITUTIVE EQUATIONS
•COMPLEX CYCLE DATA (UNIAXIAL/BIAXIAL)
•NEW TEST MACHINE

4 INSPECTION
•ON-LINE MONITORING
•OFF-LINE MONITORING
•INITIATION CRITERION
•DAMAGE MECHANISM

3 FEATURE SPECIMEN TESTS
3.1 LARGE SENB TESTPIECE, CAST 1CrMoV, 550°C, COMPLEX LOADING CYCLE
3.2 LARGE RATCHETTING TESTPIECE, CAST 1CrMoV, 550°C, COMPLEX LOADING CYCLE
3.3 LARGE CNRT TESTPIECE, 1CrMoV ROTOR, 525°C, COMPLEX LOADING
3.4 MODEL WELDED HEADER GEOMETRY, 9CrMoVNb, 585°C, CYCLIC CREEP LOADING
3.5 LARGE WELDED WIDE PLATE TESTPIECE, 18Cr11Ni, 570°C, COMPLEX LOADING CYCLE

6 KNOWLEDGE BASED SYSTEM
•DOCUMENT REFERENCE BASE
•MULTI-LEVEL MATERIAL PROPERTY DATABASE
•DYNAMIC WORKED EXAMPLE CASE STUDY BASE

Diagram 2.1. Structure of the C-FAT project [6].

FEATURE SPECIMEN TESTS

3.1- LARGE SENB SPECIMEN TEST
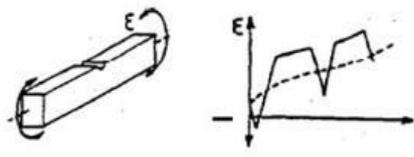
Material: Cast 1CrMoV
Section: 75x100mm
Notch root radius: 6mm
Temperature: 550°C
Monitor: HTSG, DCPD

LCF with $\sigma_s + \sigma_p$ creep

3.2- LARGE RATCHETING SPECIMEN TEST
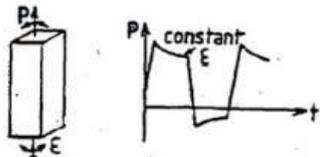
Material: Cast 1CrMoV
Section: 45x45mm
Temperature: 550°C
Monitor: HTSGs, visual

LCF with $\sigma_s + \sigma_p$ creep

3.3 - LARGE CNRT SPECIMEN TEST
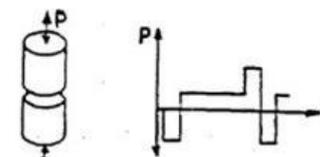
Material: 1CrMoV rotor
Net diameter: *90mm*
Notch root radius: 10mm
Temperature: 525°C
Monitor: HTSG, ACPD

LCF with $\sigma_s + \sigma_p$ creep

3.4 - WELDED HEADER GEOMETRY TEST
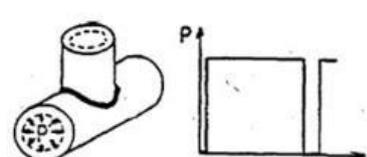
Material: 9CrMoVNb pipe
Section: 225 OD x 23mm
Temperature: 585°C
Monitor: HTSGs, ACPD, US, replica
Loading: cyclic pressure

3.5 - WELDED WIDE PLATE SPECIMEN TEST
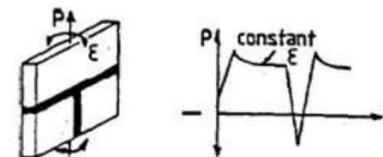
Material: 18Cr11Ni plate
Section: 40x460mm
Temperature: 570°C
Monitor: HTSGs, replica

LCF with $\sigma_s + \sigma_p$ creep

Diagram 2.2. Specimen geometries [6].

The components are fully assessed in terms of applied forces imposed during the lifetime (Diagram 2-3), and by assigning the appropriate material constitutive equations, the distribution of stresses and strains can be obtained throughout the structure by using non-linear finite element analysis. The risk of cracking is then evaluated by predicting cyclic deformation behaviour and damage accumulation. A range of modelling approaches have been applied: steady state cyclic deformation and creep with plasticity and creep being clearly distinguished, state-variable models to predict damage evolution (with separate sets of equations employed for plastic and creep deformation) and the fully unified Chaboche and Interatom approaches. The two visco-plastic models are fully unified with no distinction between plastic and creep strain. Having established the total strain range $(\Delta\varepsilon)_i$, the primary stress $(\sigma_p)_i$, and the secondary stress $(\sigma_s)_i$ for each cycle, damage due to cyclic and creep loading is determined and summed. The cyclic damage fraction is expressed via:

20

$$D_F = \sum_i \left(\frac{n_i}{(N_{XC})_i} \right)$$ 2.8

Where n_i is the number of cycles of type i and N_{XC} the endurance to crack initiation.
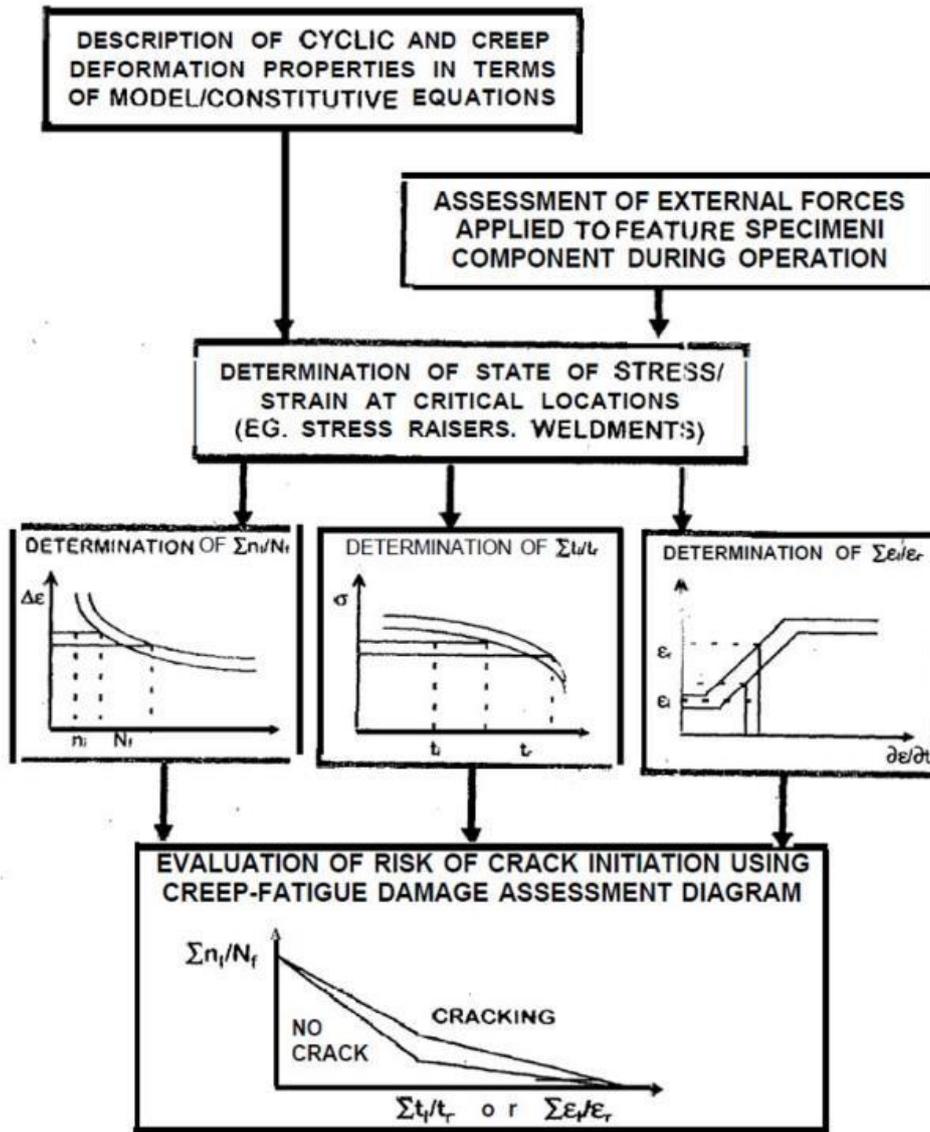
Diagram 2.3. Creep-Fatigue assessment [6].

2.2. Some specialised models on Fatigue Crack Initiation and Small Crack Growth

In this section specialised models on Fatigue Crack Initiation (FCI) are reviewed. The models available are quite versatile, extending from Tanaka-Mura based models to crystal plasticity modeling and extreme value statistics.

2.2.1. Discrete dislocation dynamics for fatigue crack initiation

A computational framework was introduced by Brinckmann et al that incorporates dislocation dynamics, the fields due to crystallographic surface steps and the cohesive surfaces, in order to model near-atomic separation leading to fracture [7] . Cyclic tension-compression simulations were carried out for a single plastically deformed grain next to the free surface surrounded by elastic material. While initially, the cycle-by-cycle maximum cohesive opening increased slowly, the growth rate at some instant increased rapidly, leading to FCI at the free surface and subsequent growth.

A plane strain specimen was modeled with an initially flat traction-free surface and the rest of its boundary subjected to either a prescribed displacement u_0 or traction t_0. The model accounts for a) plastic deformation by the motion of discrete dislocations, b) the presence of cohesive surfaces and c) the development of surface roughness caused by dislocations exiting the material through the free surface (elastic solution of a wedge). These three ingredients were integrated by using the superposition principle. As shown in figure 2.7, the response of a 2 μm × 2 μm grain at the free surface was modelled. A rectangular grain with three slip systems at 60° from each other (2-D FCC crystal), one being favourably oriented for slip (primary slip system) at 45° from the remote tensile direction is shown in figure 2.7.
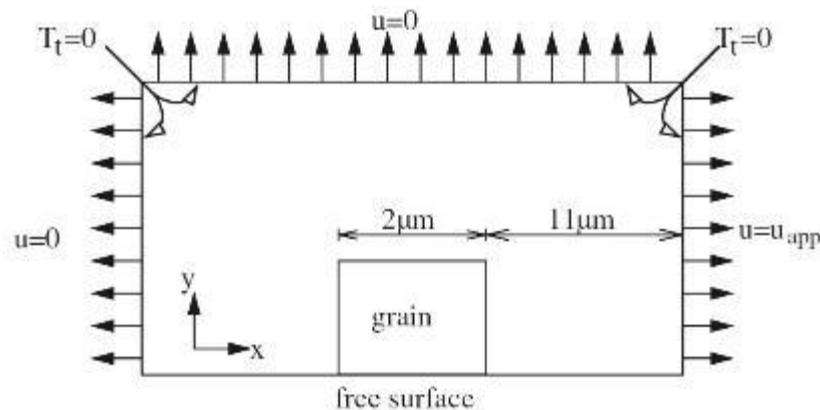
Figure 2.7. a)Boundary conditions and model, b) The single grain inside of which dislocation dynamics is applied; the surrounding material is elastic. The grain has three slip systems [7].

All dislocations are of edge character with respect to the Burgers vector in the plane of the model and of length b. Dislocations are treated as singularities in a linear-elastic, isotropic continuum medium. The Peach-Koehler force [8] on each dislocation is calculated at each time step of the incremental calculation. This force governs the evolution of the dislocation structure through a number of constitutive rules. Dislocation motion is confined to be by glide. Climb or cross-slip are not modelled. The nucleation of new dislocations is incorporated through two-dimensional Frank-Read sources [9].

These are randomly positioned and generate a dipole when the resolved shear stress exceeds the source strength or a sufficiently long time. Dislocation annihilation occurs when the distance between two dislocations of opposite sign is less than a critical distance of 6b. Furthermore, dislocations can escape from the grain at the free surface, leaving behind crystallographic surface steps. Finally, dislocations can get pinned at point obstacles (small precipitates or forest dislocations). If the Peach-Koehler force exceeds the strength of the obstacle, the dislocation is released. Grain boundaries are assumed, for simplicity, to be impenetrable by dislocations. The isolated single grain is close to elastic-perfectly plastic. The surface roughness is included in the analysis by incorporating the accumulation of crystallographic surface steps that are left when dislocations leave the crystal. The interaction between surface steps is neglected.

The applied strain rate is 50,000/s, which is an unrealistically high value, but was chosen from a computation point of view. The grain is initially dislocation free, and dislocation sources and obstacles are randomly distributed. The highest dislocation activity intersects the free surface leading to localized high stresses. One of the dislocations pair moved out of the crystal through this section, and the sister dislocation remained inside. While dislocation motion relaxes stresses, on average, the long-range interaction of the internally stored dislocations tends to produce a high stress field at the end of the slip plane. In this area the surface roughness was highest due to the high dislocation activity on the long primary slip planes. Crack initiation is hypothesised to take place and two cohesive elements were employed (normal and shear opening). In Fig. 2.8a the normal opening of the first cohesive element at the free surface is shown as a function of time. For the first realization of dislocation sources the opening increased slowly for roughly 120 cycles, after which the growth rate increased in every cycle. During the 166th cycle, the opening reaches the critical opening, i.e. $\Delta_n/\delta_n = 1$; referred to as FCI and the simulation was terminated. The opening response found with the second realization of source strengths is initially similar to that for the first realization, but then features two 'jumps'. After 38.7 cycles the opening increases rapidly. After this jump the rate of increase gradually rised until the second rapid increase at 53.9 cycles. From that moment, the opening increased even more rapidly and reached the critical value shortly afterwards. Both jumps start during the compressive loading phase and finished during the subsequent tensile phase.
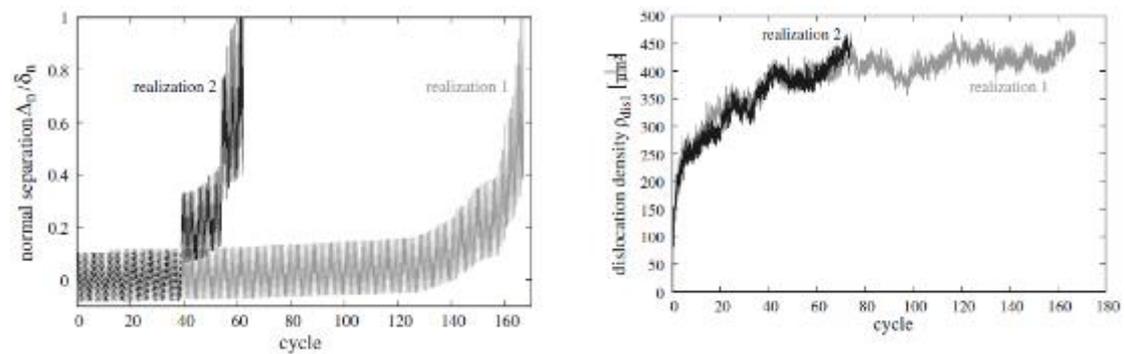
Figure 2-8. a) The normal opening of the first cohesive element at the free surface for two realizations of dislocation sources, b) Dislocation density evolution for the two realizations [7].

The first rapid increase is the origin for the premature failure. At almost maximum compressive loading the 'jump' occurs. Prior to the 'jump' the dislocations move chaotically back and forth in the changing potential energy valleys caused by neighbouring dislocations and the external boundary conditions. Exactly before crack initiation and upon compression a significant amount of strain energy is stored in the crack process zone. Therefore, during this compression cycle the dislocations move to a neighbouring valley of the potential which is energetically favorable, changing the landscape of the potential. This rapid increase in material separation is observed as a jump. The cohesive law induces an exponential traction–separation curve, which leads to the absolute stresses being lower during the tensile phase than during compression. This difference leads to a significantly lower stored strain energy during the tensile phase, which makes reversal of the jump events during the subsequent tensile phase highly unlikely. The 'jumps' in the opening of the cohesive surface are a local event and do not have a strong effect on the overall response (evolution of the overall dislocation density), as demonstrated in figure 2.14b. The dislocation density increases rapidly initially, but the average growth rate decreases in later cycles and approaches a slow but steady average growth rate. However, during a few tens of cycles just prior to fracture initiation, an increase in the dislocation density is observed for both realizations. It should be noted that in the first cohesive element, the tangential opening was smaller than the normal opening. Therefore, this framework predicts that fatigue initiation is associated with mode I crack opening. Furthermore, the crack opening is maximum at the free surface, i.e. the crack initiates at the free surface and grows into the grain. To study whether surface roughness is a necessary contribution for FCI, one simulation (using the first realization of sources) is repeated but without taking surface roughness into account. Figure 2.9 shows the effect of the presence of surface roughness on the evolution of the fatigue crack and dislocation density. Figure 2.9 revealed crack initiation within the first 167 cycles, the computation without including surface roughness does not lead to any accumulation of the normal opening at the free surface over the same period. Therefore, the surface roughness is a significant contribution to FCI. Removal of the surface roughness leads to a significant delay in FCI. The evolution of dislocation density, shown in Fig. 2.9b, appears not to depend on surface roughness. Thus, the dislocation density depends on the initial conditions (dislocation source and obstacle distribution, grain geometry) and on the applied loading. The dislocations that glide to the surface and produce surface roughness, have virtually no effect on the dislocation density evolution, but surface roughness is necessary for the initiation of a fatigue crack.
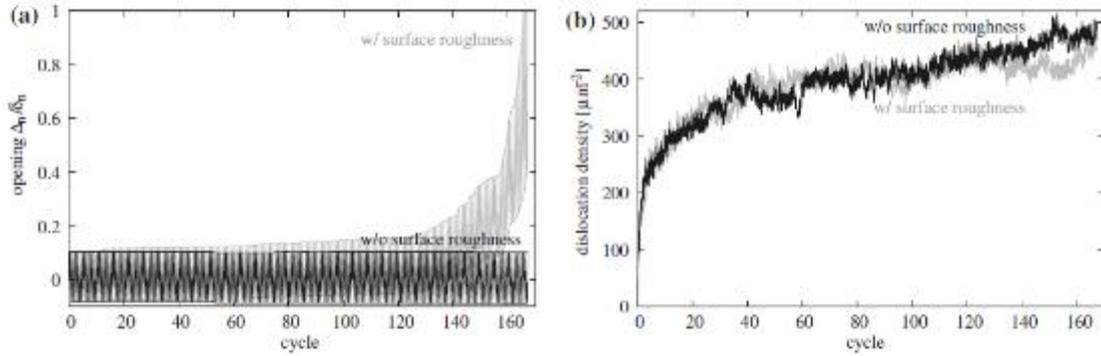
Figure 2-9. The effect of surface roughness a) on the normal opening of the first cohesive element for the first realization of dislocation sources, b) on dislocation density evolution [7].

The current study yields very fruitful results about the physical mechanisms of FCI, as well as the influence of surface roughness, however, the computationally expensive method employed; i.e. dislocation dynamics limits the application of the current method to over simplified geometries such as the one in figure 2.6. For complex geometries involving several hundreds of grains, as well as real engineering structures the current technique would not be able to be applied due to the computational times needed.

2.2.2. *Monte-Carlo Finite Element Calculations on polycrystals*

The effect of crystalline elasticity anisotropy on the stress state of individual (well-oriented) grains was studied numerically by Sauzay et al. Four metals with varying crystalline elasticity anisotropy were considered: aluminium, ferrite, copper and austenite. Three elastic parameters were employed: the C_{11}, C_{12} and C_{44}. One main grain is considered located at the free surface, and its orientation is kept constant, favouring type A or type B type of slip as shown in Figure 2-10. The neighbouring grains have random orientation. The geometry and mesh is shown in figure 2-11 and consists of a small aggregate of seven grains represented by seven cylinders with hexagonal base. The central grain has a certain orientation for type A or B slip, while the neighbouring grains have random orientations. 60 sets of orientations are employed, yielding 60 finite element computations for each case (metal, crystallographic orientation for the middle grain, loading condition).
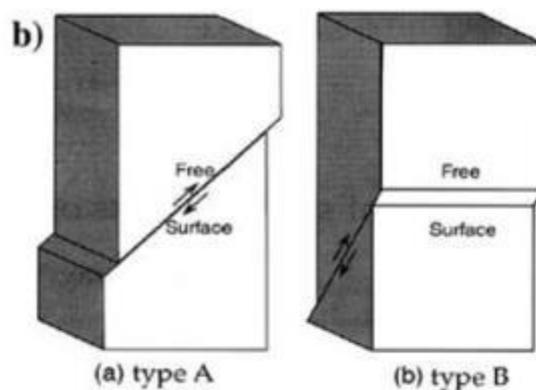
Figure 2-10. Type A and B facets.

25
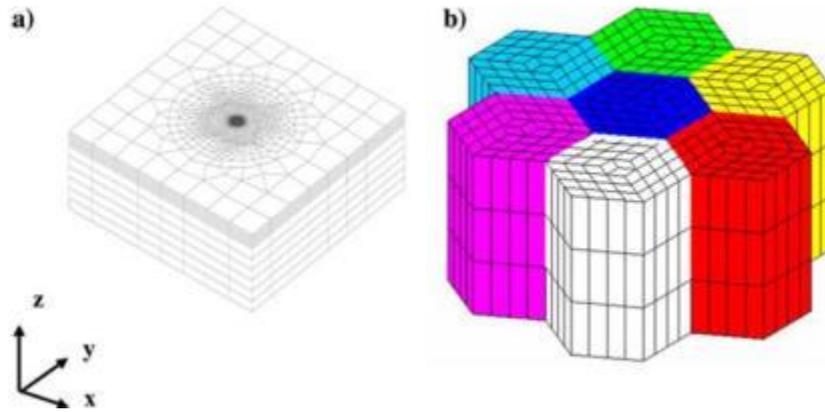
Figure 2-11. a) The global mesh and b) the mesh of the surface aggregate containing seven prismatic grains.

For copper and austenite subject to tension-compression, the average resolved shear stress and normal stress is well different from the corresponding macroscopic values (a ratio of 0.81 and 1.04 was calculated). The modified Schmid factor, defined as the ratio between the local resolved shear stress and macroscopic tensile stress is just 0.41, smaller than the classical 0.5 value. The scatter on the resolved shear stress is approximately $\pm$22%, while the scatter in the normal stress is even higher, roughly $\pm$38%. These scatters calculated for small applied loads can explain the large scatter in FCI and small crack growth.

2.2.3. *Fatigue crack initiation based on the Tanaka-Mura model*

The following published work discusses FCI modelling based on the Tanaka-Mura model. Foit et al. discuss the initiation of small cracks in martensitic steel under low cycle fatigue loading [10, 11]. The Tanaka Mura relation postulates that crack initiation occurs due to slip bands, and micro-cracks are initiated by irreversible pile-ups in slip bands. The relationship is:

$$N = \frac{8GWc}{\pi(1-\nu)d(\Delta\tau_{res} - 2\tau_c)^2}$$

(2.9)

Fatigue loading was applied with R=-1 and ε=8x10^{-4}/sec. Several scans were performed on the specimen surface at predefined cycles using a camera (triggered at maximum strain). Scans showed that parallel slip bands were distributed along the whole surface and micro-cracks formed parallel to the slip bands and parallel to the martensitic laths. After continuous loading the micro-cracks coalesced.

The average size for the grains containing a crack was larger than the average grain size; therefore it was assumed that large grains are more likely to develop micro-cracks. The distribution of the orientation angle was non uniform with a peak at 45°; aggreeing with Tanaka-Mura model which suggested that crack initiation is shear-controlled. The number of cracks increased linearly with fatigue life at the early stages of fatigue initiation.

Simulation was performed using a 2-D RVE generated by the Voronoi tessellation process, with a random number representing the grain orientation (see figure 2.12a). The RVE contained up to 100 grains and represented a 0.25 mm^2 surface area. The stress evolution was calculated using a FEM code at ABAQUS. Orthotropic linear elastic behavior was assumed in each grain. The stress distribution in the RVE was calculated from a quasi static FEM analysis; cyclic effects do not play any role in the linear elastic behaviour and the Tanaka Mura model does not take into account cyclic hardening effects.

It was found that grains with high resolved shear stress will develop cracks in the early stages of fatigue. Potential crack paths were defined along the longest paths within a grain and assumed that once a crack is formed it will immediately grow until it reaches the GB (grain growth within a grain was not modeled). No crack coalesence criterion was used since only crack initiation was modelled.
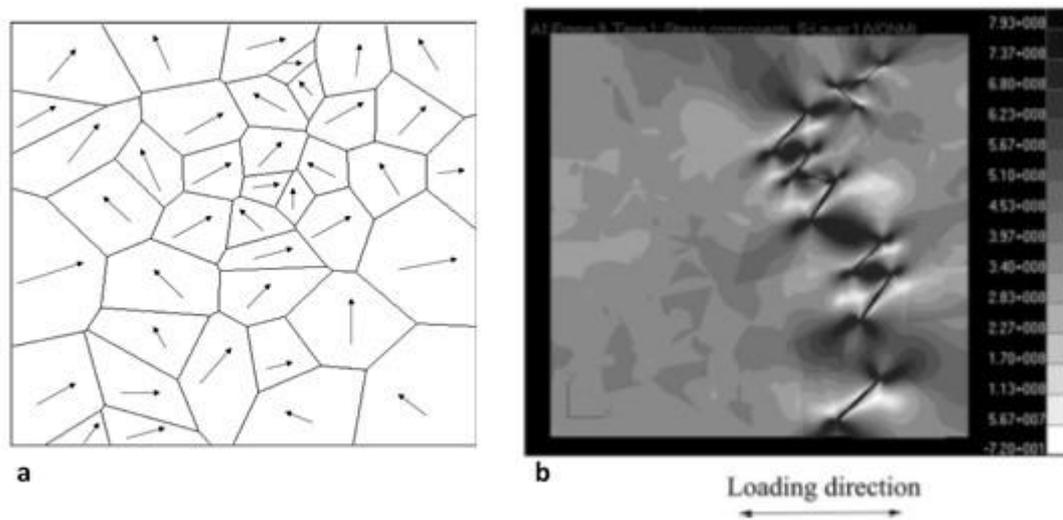
Figure 2-12. a) Voronoi tessellation, arrows show grain orientations, b) damage accumulation containing nine cracks, for high strain range (Δε=0.9%) [10].

Cracks close to the boundaries were excluded for stability reasons. The effect of the existence of a crack (or more) on the stress distribution was also simulated at each calculation step. Displacement boundary conditions were applied to the x direction whereas the other boundary was traction-free. The simulation stopped after 20% of the total fatigue lifetime observed (so the total fatigue lifetime was not explicitly modeled) or when the RVE structure was unstable. It was observed that there were regions with cracks and undamaged regions. Cracks tended to arrange themselves in parallel stacks. High plastic strains were observed between the cracks (crack interaction; see figure 2.12b). This indicated that cracks would coalesce and form zig-zag cracks. The crack density was calculated; and showed quite good agreement for medium values of strain amplitude.

Foit et al. later extended their work by developing a 3-D model with 80 grains (extending the 2-D model to the 3rd direction); the thickness was 0.4 compared to the length [11] . It was identified that for the 3-D case cracks form more perpendicular to the loading direction due to fact that one more slip direction is available, and cracks accumulate in a small volume of material tending to lead to coalescence. Therefore 3-D modelling predicted earlier crack bridging.

Kramberger et al. based on the Tanaka-Mura relation tried to improve the model by Foit et al. to model FCI [12] . Their work was based on thermally cut martensitic steels. They defined that the main deficiencies of the previous model is that it deals with crack nucleation in separate grains - whereas it does not deal with micro-crack coalescence and the model uses an average shear stress to determine crack nucleation. It was observed that with the previous model, an existing crack significantly raised the stresses at a neighboring grain; but yet no crack nucleation occurred. The problem became more pronounced for high cycle fatigue.
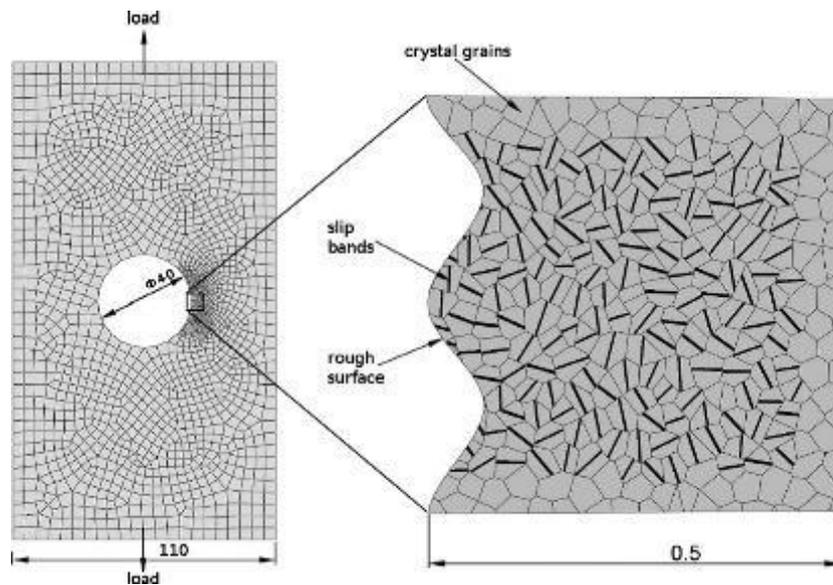
Figure 2-13. Global model and submodel [12] .

In this model, multiple slip systems were used in each grain as opposed to the one slip system of Foit et al [10, 11]; therefore handling both crack nucleation and coalescence. A sub-model to simulate fatigue cracking at the region of an inner hole was used (figure 2.13) to study a specific specimen portion where high stresses are present. Moreover surface roughness and residual stresses were also simulated. The Voronoi tessellation technique was used with orthotropic material properties and an average grain size of 20 μm with 400 grains in total. In this model it was found that micro-crack coalescence occured at earlier stages compared to the case of slip only along the centre of the grains (longest path). Figure 2.14a shows that once a crack is formed at the centre of the left grain, stress concentrations at the right grain lead to the formation of a crack at that particular grain far from the centre of the grain. Crack coalescence occurred when the average stresses along the line connecting the two cracks exceeded the yield stress; and significant stress relaxation was observed. Crack coalescence was simulated to be instantaneous so that the sum of cycles for fatigue initiation was attributed only to micro-crack nucleation. Segmented micro-crack paths were used in order to better visualise stress concentration at smaller areas compared to a grain (see figure 2.18). Therefore crack extension inside a grain was segmented, which is more realistic. Crack nucleation goes through multiple iterations; therefore dislocation pile up was taken into account by accounting for the damage accumulated in previous steps. It was observed that cracks form in large grains, favorably oriented

and then start to coalesce. When this crack grew to a given length (0.3 mm), crack initiation was determined as terminated.
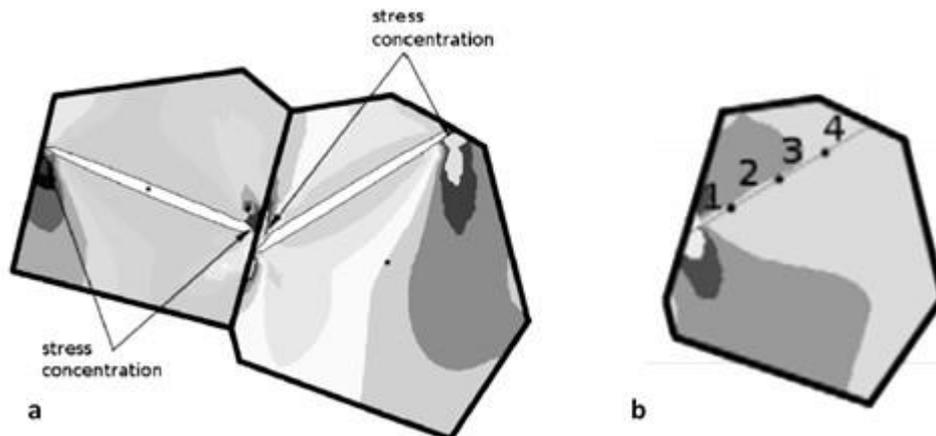
Figure 2-14. a) Nucleated crack in two grains, b) Segmented crack inside a grain **[12]**.

The papers discussed above, present a very efficient way to model FCI, however the models are over-simplified, ignoring the presence of various slip systems within each grain, and therefore potential cracking locations and orientations. Furthermore, the most critical point for FCI cannot be obtained within this context. Strain gradients are also ignored.

2.2.4. *Crystal plasticity based models for fatigue crack initiation (FCI)*

a. *Image-based micromechanical modeling, elastic anisotropy & polycystal plasticity of FCI*

- *Predicting fatigue crack initiation through image based micromechanical modelling*

Cheong et al studied the influence of grain orientation on FCI in a four-point bending fatigue test both numerically and experimentally [13]. The experiments were performed on 99.99% aluminium samples subjected to high cycle fatigue (HCF); while a small part of the top surface was characterized by using EBSD analysis (figure 2.15). On the top surface, the tensile stresses are highest and uniform across the width. An alternating tension– tension load cycle (with a stress ratio of 0.20, maximum stress 0.95% r_y and frequency of 143Hz) was applied. Measurements for crack detection were carried out every 10^5 cycles until fatigue cracking was observed.

Applying FEM modelling, the microstructure was digitally reconstructed and refined studies were carried out in three regions of interest. The constitutive behavior of aluminium was described by a crystal plasticity model which considers the evolution of dislocations and the accumulation of edge dislocation dipoles. Using an energy-based approach to quantify fatigue damage, the model correctly predicts regions in grains where early fatigue crack initiation was observed. The tendency for fatigue cracks to initiate in these grains appears to be strongly linked to the orientations of the grains relative to the direction of loading. Limitations of this modelling approach were found, as some grains predicted to initiate cracks did not show any visible signs of fatigue cracking.

The average grain diameter by means of EBSD analysis was measured to be 84 μm. Fatigue cracking occurred after 5×10^5 cycles. DIC images revealed the presence of slip bands and lines, as well as micro-cracks. Cracks were typical of Stage I cracking, initiated at grain boundaries, triple points and slip bands. Crack growth occurred along slip bands signifying the orientation importance; cracks were confined within individual grains (arrested at GBs). Fatigue cracks were predominantly found in grains above the average grain size. Both intergranular and transgranular cracking were observed. The equations used in the crystal plasticity model together with the corresponding material parameters may be seen in Table 2.1.
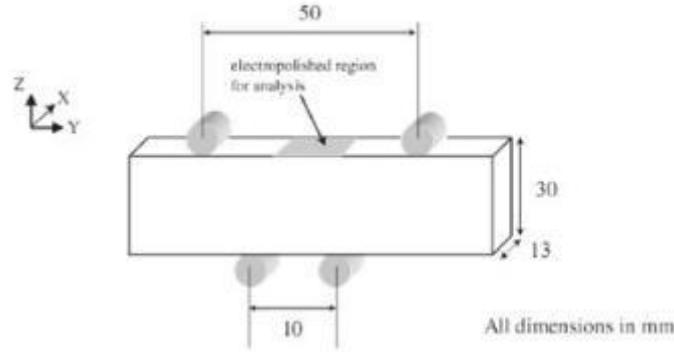
Figure 2-15. Schematic representation of the four-point bend test specimen geometry for high cycle fatigue testing [13].

Kinematics-Hardening laws: deformation tensor (decomposed to elastic and plastic part), spatial gradient of F^P, flow rule, resistance to dislocation motion & latent hardening modulus, resolved shear stress & second Piola–Kirchoff stress tensor	$F = F^e F^p$ $\dot{F}^p = \left(\sum_{a=1}^{N} \dot{\gamma}^{\alpha} P^a \right) F^p \quad , \qquad P^a = m^a \otimes n^a$ $\dot{\gamma}^{\alpha} = \dot{\gamma}_0 \cdot \exp\left[-\frac{F_0}{\kappa\theta} \left\{ 1 - \left\langle \frac{\left| \tau^a \right| - S^a}{\hat{\tau}} \right\rangle^p \right\}^q \right] sgn(\tau^a)$ $S^a = \mu b \sqrt{\sum_{\beta=1}^{N} h_{\alpha\beta} \rho_{\mathrm{T}}^{\beta}}, \quad h_{\alpha\beta} = \omega_1 + (1 - \omega_2)\delta_{\alpha\beta}$ $\tau^{\alpha} = \mathrm{T} : P^{\alpha} \quad , \quad \mathrm{T} = (\det F^e) F^{e-1} \sigma F^{e-\mathrm{T}}$
Dislocation density: discretized into screw and edge density components	$\dot{\rho}_e^{\alpha} = \frac{C_e}{b} \left[K_e \sqrt{\sum_{\beta=1}^{N} \rho_{\mathrm{T}}^{\beta}} - 2(Y_e + Y_d)\rho_e^{\alpha} \right] \left| \dot{\gamma}^{\alpha} \right|$ $\dot{\rho}_s^{\alpha} = \frac{C_s}{b} \left[K_s \sqrt{\sum_{\beta=1}^{N} \rho_{\mathrm{T}}^{\beta}} - 2Y_s \rho_s^{\alpha} \right] \left| \dot{\gamma}^{\alpha} \right|.$

Material parameters for Aluminium:	F_{o} (J) 3×10^{-19}	$\dot{\gamma}_0$ (s^{-1}) 1×10^{6}	p 0.141	q 1.10
	C_{e}, C_{s} 0.5	C_{d} 0.01	K_{e} 3.7×10^{-3}	K_{s} 7.4×10^{-3}
	Y_{e} (nm) 2.0	Y_{s} (nm) 10.0	Y_{d} (nm) 20.0	ω_1 0.45
	C_{11} (GPa) 113	C_{12} (GPa) 66	C_{44} (GPa) 28	
Density clusters of edge dislocation dipoles	$$\dot{\rho}_g^{\alpha} = \frac{C_d}{b}\left[Y_d \rho_e^{a} \right]\left| \dot{\gamma}^{\alpha} \right|$$			
Local energy dissipation	$$\mathrm{E}_p = \int \sigma : L^p \, dt \ , \ L^p = \dot{F}^p F^{p-1}$$			

Table 2-1. Equations used for the crystal plasticity model [13].

The dislocation density was discretised into screw and edge density components. As a material cyclically deforms, its dislocation structure evolves to cell-type structures. The accumulation of trapped edge dislocation dipoles go on to form clusters or groups, resulting in dislocation substructures observed in metal fatigue. These dislocation ''rich'' regions were quantified by calculating the density clusters of edge dislocations; i.e. ρ_g^{α} (see Table 2.1). The constitutive model was implemented into an ABAQUS finite-element code, employing a fully implicit time-integration scheme. The mobility of edge dislocations was set to be twice as that of screw dislocations. Comparisons were made at two different strain amplitudes after the same number of applied cycles and the comparison showed good agreement. Prominent slip band and micro-cracking was observed only in a small proportion of grains. In this regard, a sub FEM model was employed for refined studies. A coarse model was used to reconstruct the microstructure, therefore reducing the computational costs and the resolution of the reconstructed images while selected parts of the microstructure were analysed with mesh refinement. For the sub-model three regions were selected (see figure 2.16) and reconstructed using exactly the EBSD microstructural image.
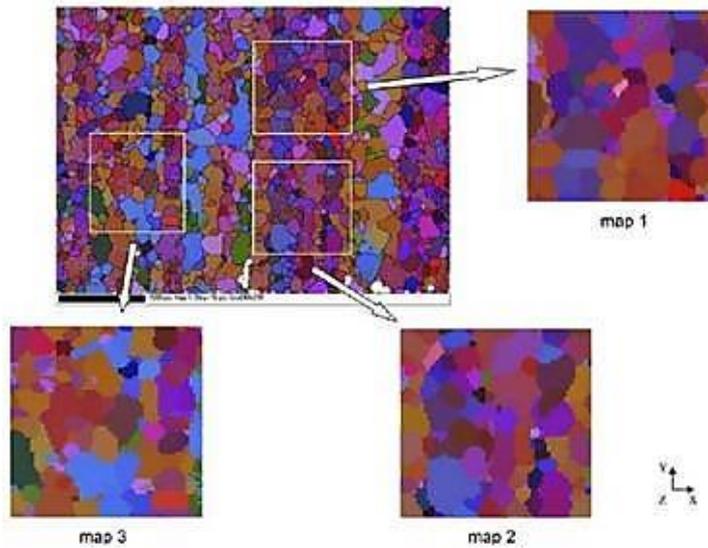
Figure 2-16. Digitally constructed microstructures, labelled Maps 1, 2 and 3, using 100x100 finite-elements for sub-modelling, based on the experimentally derived EBSD image [13].
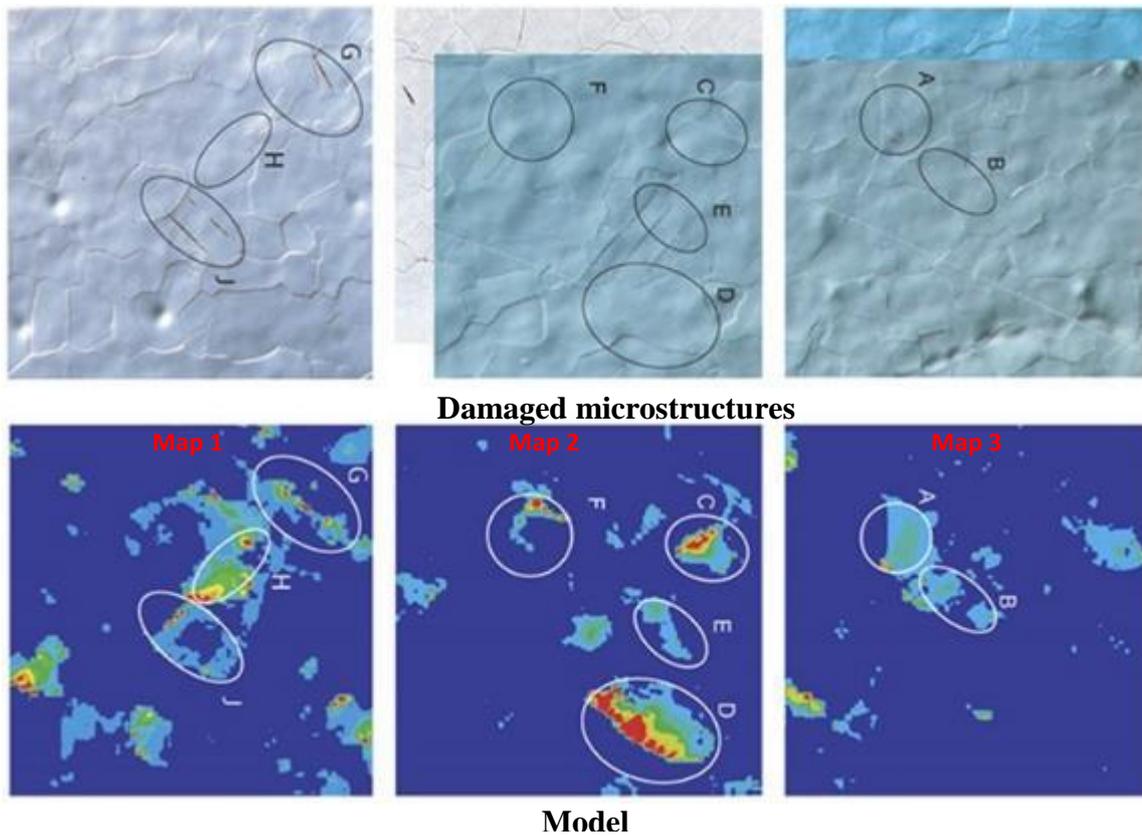
Figure 2-17. Contour plots of local energy dissipation E_p predicted in Maps 1, 2 and 3 after 143 cycles, compared with corresponding images taken after 5 x10^5 load cycles [13].

143 simulated load cycles were applied to the surface microstructure. To evaluate the predictive capability of the model, an energy-based approach was used, based on the local energy dissipation (E_p) in terms of plastic work (see Table 2.1). E_p was used as an indicator of fatigue crack initiation. Contour plots of accumulated plastic slip and plastic work for Maps 1, 2 and 3 were obtained and

compared with experimental results, showing identical trends. High E_p values indicated potential fatigue crack initiation sites (figure 2.17).

These plots were superimposed onto the microstructural images of the same location after $5x10^{-5}$ cycles. Map 1 and 3 correctly predict the grains in which early crack initiation is likely to occur. The predictions in Map 2 are less agreeable with microstructural image (regions C and D have higher predicted E_p values while E and F regions are more agreeable). It is apparent that the model generated several ''false positives'' – predicting fatigue cracking in grains which have not been experimentally observed. However, the ability of this modelling approach to correctly locate grains that develop early fatigue cracks based on the orientation data from the EBSD analysis clearly shows that the orientation of each grain is a major contributing factor; grains, based on their orientation, can be classified as 'hard' or 'soft', identifying the orientations of grains more susceptible to fatigue cracking. It was found that grain size and character (hard-soft) played a critical role on FCI as well as the character of the neighbouring grains.

The current model seems to predict quite well the FCI sites. However the material used; i.e. 99% pure aluminium, is over-simplified. In engineering materials, much more complex microstructures are created and used, such as multiphase alloys, and alloys with precipitates and inclusions. Furthermore, the model already predicts some false locations for FCI where no damage is observed. Finally the strain plots could not be obtained experimentally to yield a more comprehensive comparison between the model and the experiment.

- *High and low cycle fatigue crack initiation using polycrystal plasticity*

A polycrystal plasticity finite-element model has been developed for fatigue lifetime modelling in nickel-base alloy C263 [14]. An RVE with 60 grains was created and FCI was modeled with just a single material property; the critical resolved shear stress. The model was found to be capable of predicting correctly the fatigue behavior of the material.

A FCI criterion was proposed, based simply on critical accumulated slip. The model predicts that crack initiation occurs preferentially at grain triple points under both low- (LCF) and high-cycle fatigue (HCF). For the case of HCF, this corresponds to the free surface. The polycrystal plasticity model combined with the fatigue crack initiation criterion are shown to predict correctly the standard Basquin and Goodman correlations in HCF, and the Coffin–Manson correlation in LCF. The model predictions are based on just two material properties: the critical resolved shear stress and the critical accumulated slip. Good agreement with experiments is achieved, despite the simplicity of the proposed 'two-parameter' model. The equations used for the crystal plasticity model are listed in Table 2.2.

Deformation gradient F	$F = F^e F^p$
Velocity gradient L	$L = \dot{F}F^{-1} = \dot{F}^e \left(F^e \right)^{-1} + F^e \dot{F}^p \left(F^p \right)^{-1} \left(F^e \right)^{-1}$
Velocity gradient L	$L = D + W$

Deformation rate D	$$D = \frac{1}{2}\left(L + L^T\right)$$
Spin tensor W	$$W = \frac{1}{2}\left(L - L^T\right)$$
Plastic velocity gradient	$$L^p = \sum_{a=1}^{n} \dot{\gamma}^a s^a n^{aT}$$ Defined as the sum of the shearing rates on all slip systems
Plastic deformation rate D_p and plastic spin tensor W_p	$$\left\{\begin{array}{l} D^p = \sum_{a=1}^{n} P^a \dot{\gamma}^a \\ W^p = \sum_{a=1}^{n} \Omega^a \dot{\gamma}^a \end{array}\right\} \text{ with } \left\{\begin{array}{l} P^a = \frac{1}{2}\left(s^a n^{aT} + n^a s^{aT}\right) \\ \Omega^a = \frac{1}{2}\left(s^a n^{aT} - n^a s^{aT}\right) \end{array}\right\}$$
Elastic deformation rate and elastic spin tensor	$$D^e = D - \sum_{a=1}^{n} P^a \dot{\gamma}^\alpha$$ $$W^e = W - \sum_{a=1}^{n} \Omega^a \dot{\gamma}^\alpha$$
Cauchy stress rate	$$\dot{\sigma} = C:D - \sigma \cdot tr(D) - W\sigma + \sigma W - \sum_{\alpha=1}^{n}\left(C:P^a + \beta^a\right)\dot{\gamma}^a$$ $$\beta^a = \Omega^a \sigma - \sigma \Omega^a$$
Shear rate at the αth slip system	$$\dot{\tau}_c^a = \sum_{\alpha=1}^{n} h_{\alpha\beta} \dot{\gamma}^\alpha$$
Resolved shear stress, or Schmid stress	$$\tau^\alpha = s^\alpha\left(\sigma n^\alpha\right) = P^\alpha : \sigma$$
System of equations to be solved	$$\sum_{a=1}^{n} A_{\alpha\beta} \dot{\gamma}^\alpha = b^\alpha$$ $$A_{\alpha\beta} = h_{\alpha\beta} + P^\alpha : C : P^\alpha + \beta^\alpha : P^\alpha$$ $$b^\alpha = P^\alpha : \left[C:D - \sigma tr(D)\right] + \beta^\alpha : D$$

Table 2-1. Equations used for the crystal plasticity model [14].

An αth slip system is considered to slip, or flow plastically, when the resolved shear stress on the slip system τ^α exceeds a critical resolved shear stress, τ_c^α. The critical resolved shear stress τ_c^α was determined by the current dislocation density and substructure. Figure 2.18*a* shows a typical microstructure of a standard heat-treated nickel-base alloy C263, with a mean grain size of 104 μm, and with a small portion of γ' and M23C6 carbide precipitates at grain boundaries. Because of the size of precipitates their influence is very small; and they have not been modeled explicitly. Both strain controlled and stress controlled fatigue have been used for the simulations. The equations were applied into an ABAQUS nonlinear solver. Random crystallographic orientations for each grain were

generated. Yielding was highly localised, depending upon the local slip direction and how quickly the resolved shear stress reaches its critical value.
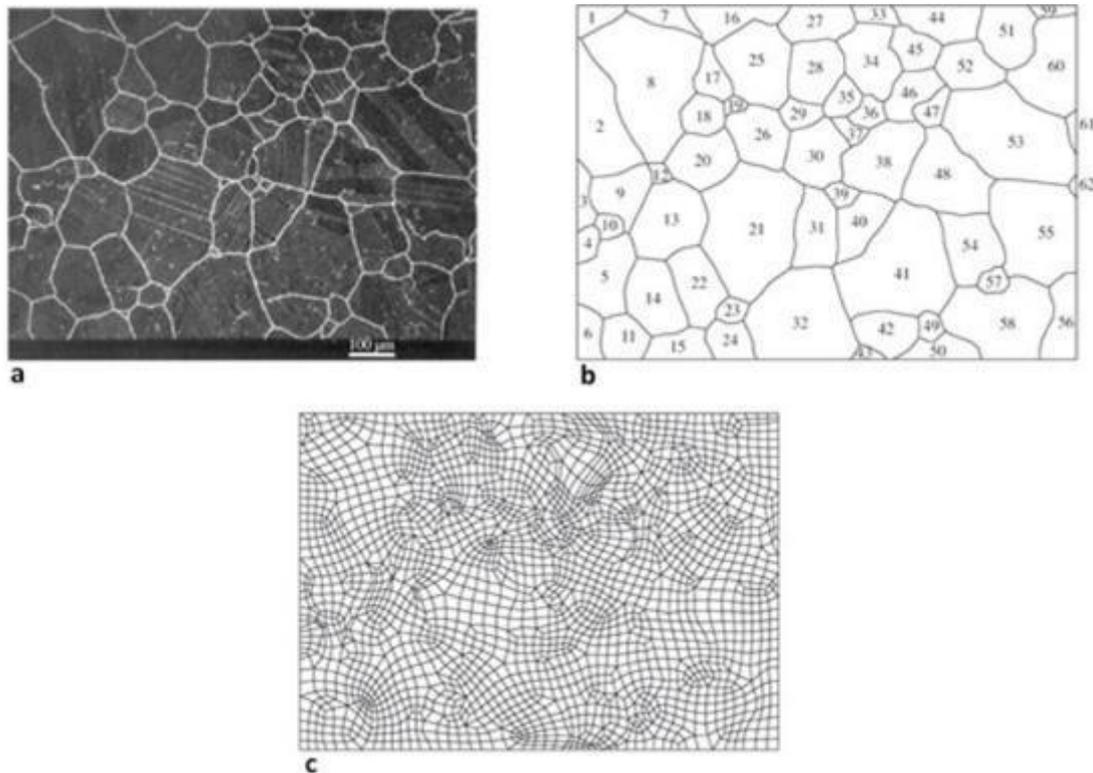
Figure 2-18 (a) A typical microstructure of the standard heat-treated C263; (b) the grain boundaries simulated; (c) a finite-element mesh for the corresponding microstructure [14].

It was argued that strain-based and energy-based fatigue crack initiation criteria are likely to lead to the same result. However, a general initiation criterion is proposed in the study of Manonukul et al, applicable to both HCF and LCF, based on (plastic) slip [14].

There exists a critical accumulated slip, p_{crit}, at the micro-level, which once reached, leads to crack initiation. The accumulated slip, p, is calculated at all material points. Figure 2.19 shows the field variation of p after two cycles of fully reversed LCF at 300 ^{o}C with strain amplitude 0.5%. It can be seen how localised this quantity is, with the peak values occurring at just one or two grain boundaries. The higher values follow the grain boundaries, but the highest values occur at, or close to, grain triple points. The accumulated slip is localised even within individual grains, leading to the formation of intense persistent-slip bands.

The determination of the critical accumulated slip, p_{crit}, requires experimental knowledge of when crack *initiation* occurs. In general, it is easy to determine the number of cycles to *failure*. Since in this material, the number of cycles to crack initiation is significantly larger than that for propagation, the critical accumulated slip for crack initiation can be assumed to be equal to the accumulated slip to cause failure. Hence, in this way, p_{crit} can be determined by a single experiment. So a single LCF test was used to determine the critical accumulated slip.
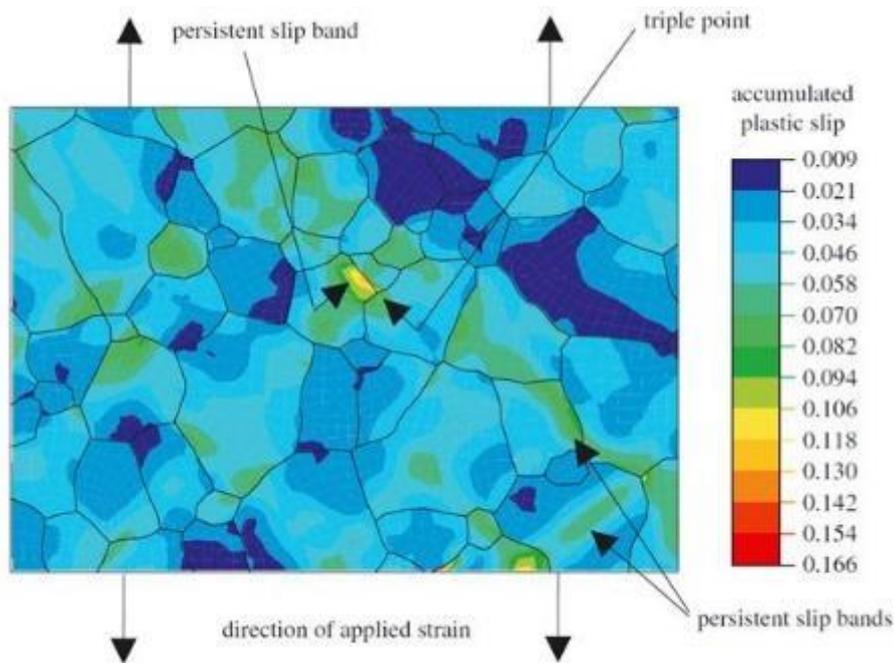
Figure 2-19. Accumulated plastic slip after two fully reversed cycles in LCF at 300 o C and strain amplitude 0,5% [14].

***S–N curve for nickel alloy* C263**

An *S–N* curve for nickel alloy C263 has been obtained at 20°C using rotating-bend tests carried out on circular-section test specimens [14]. The experimental results are shown in figure 2.20 as circular symbols. The plasticity model together with the crack initiation criterion has been used to simulate HCF tests, and the predicted results are shown in figure 2.20 by the cross symbols. Good agreement can be seen between predicted and experimental results, at higher stress amplitudes. As the stress amplitude is reduced, the resolved stress on the critical slip planes will fall below the critical resolved shear stress, and all the deformation will become elastic. At this point, there is no further accumulation of plastic slip, and hence the critical accumulated slip will never be achieved. The model will therefore predict infinite life. As shown in figure 2.20, at a stress amplitude of *ca*. 450 MPa and below, no further plastic slip is predicted to occur and the fatigue limit is reached. This is considerably higher compared to the experiments. In order to solve this problem, a simple three dimensional model was developed; an 'extrusion' of the 2-D elements along the out-of-plane direction. Free-surfaces were introduced. The *S–N* curve predictions for the three-dimensional model are shown by the broken lines in figure 2.20. The comparison of the predicted fatigue limit with the experimental points can be seen to be significantly improved. But both tend to over-predict the fatigue limit.
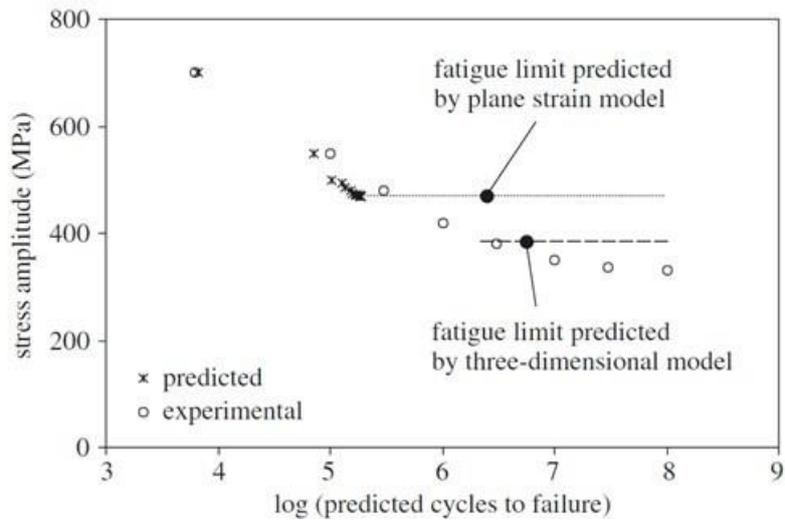
Figure 2-20. Predicted and experimental S-N curves [14].

This paper presented a simplified method to qualtify FCI. The model quantified FCI based on a single parameter, which significantly boosts the applicability of the current model. However, no direct comparison was provided between the model and the experiment. The total number of cycles was also wrongly predicted.

- *The role of elastic anisotropy, length scale and crystallographic slip in fatigue crack nucleation*

FCI in ferritic steel is investigated both experimentally and via simulations. Several large-grained, notched, four-point bending tests were performed and coupled to explicit microstructural modeling using crystal plasticity FEM, in order to assess FCI, the role of elastic anisotropy and the presence of length scale effects [15].

Elastic anisotropy plays an important role in polycrystal slip, and to the potency of FCI with respect to the presence of constrained cyclic microplasticity. However, length scale effects did not seem to alter substantially the distributions or magnitudes of slip with respect to the FCI site. Detailed analyses in one experiment showed that the location of highest magnitude of geometrically necessary dislocations (GNDs: dislocations incorporated to model strain gradient effects) coincided precisely with the position of predicted maximum plasticity and the experimentally observed FCI site.

The distributions of microplasticity within a oligocrystal changed significantly between the first yield and after multiple cycles. Therefore, it was found that the effective plastic strain per cycle was a better FCI indicator than the peak effective plastic strain. In nine independently tested and analysed samples, the cyclic effective plastic strain and crystallographic system peak accumulated slip were observed to be good indicators for the FCI sites.

A more detailed description of the development of a similar CP constitutive model (incorporating strain-gradient plasticity, but without isotropic hardening) can be found in Dunne et al. [16]. The technique employed is described in Dunne et al. [16]. The ρ_{GND} (density of geometrically necessary dislocations) depends on the spatial gradients of the plastic deformation gradient, and therefore introduces length scale effects into CP-FEM. Eight-noded, reduced integration elements are used,

defined within UEL (User-defined ELement facility). Out-of-plane crystallographic slip is allowed, but within an overall constraint of generalised plane strain conditions.

The material is a SUS 430LX ferritic steel, provided by Nippon Steel Corporation, with a BCC crystal structure and 48 slip systems in total. Yet, the 24 {123} <111> slip systems do not operate extensively at room temperature [15] and therefore only 24 slip systems are used in that model: the 12 {110} <111> and the 12 {112} <111> slip systems.

Simple shear tests were carried out on two SUS 430LX steel specimens to calibrate the CP modeling constants: the critical resolved shear stress, τ_c, and the isotropic hardening evolution, h. The model geometry consisted of a 2D oligocrystal with 27 arbitrarily oriented grains, with average grain size equal to experimentally obtained (1856 μm). The shear tests were simulated using the specified RVE geometry. For one specimen, analyses were carried out for both isotropic and anisotropic elasticity. A Young's modulus of 206 GPa and Poisson's ratio of 0.3 are used to represent isotropic elasticity. For anisotropic elasticity, the cubic constants were C_{11}=277 GPa, C_{12}=119 GPa and C_{44}=168 GPa and the length scale effects were excluded from the analysis.

Four-point bending fatigue tests were carried out on nine specimens. Each specimen had significantly different microstructure. The specimen geometry and the four-point bending equipment are shown in figure 2.21. A 500N cyclic load was applied at the two central lower supports with R=0; as shown in figure 2.21. Specimens were tested till failure or up to 2.5×10^6 cycles. The FCI sites and subsequent crack propagation paths were obtained by employing SEM imaging. The grain orientations at the notched region were obtained by EBSD technique. The assumption of large prismatic grains is reasonable, as a relatively large grain size was found in all cases (as shown in the inset of figure 2.21).
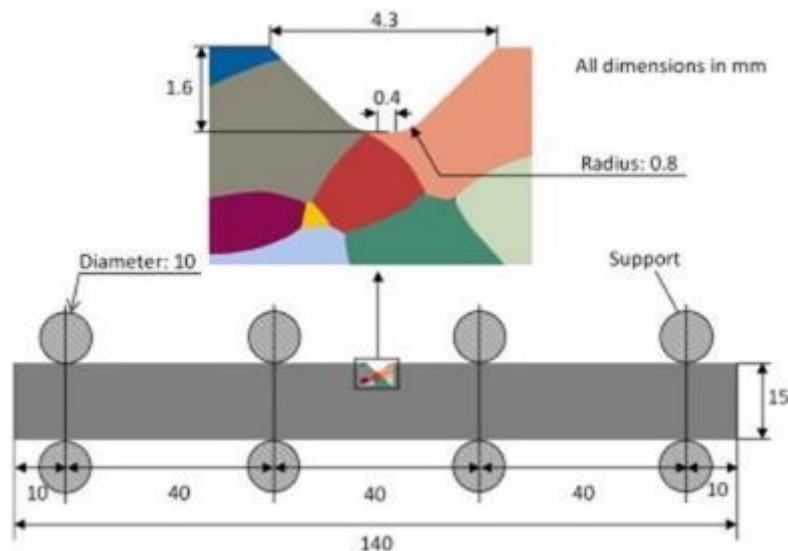
Figure 2-21. 4 point bending set-up and the grain geometry at the edge of the notch [15].

Separate FE models were developed for each of the nine specimens and crystal plasticity analyses were employed. An average of 35,000 elements was used in each model, with an average of 661 elements per grain. An example of the meshed geometry is shown in figure 2.22. The loading

corresponds to HCF and it is expected that the bulk material remains within the elasticity region. Crystal plasticity is therefore employed only within the notched region, where plasticity occurs. Outside of this region, the material is expected to deform elastically only. The BCs and loading applied can be seen in figure 2.22. Nodes A and D are fixed in the *x*- and *y*-directions and cyclic loads of 500 N are applied in the *y*-direction at nodes B and C. 5.5 cycles are applied for each simulation, except for one additional case with more cycles.
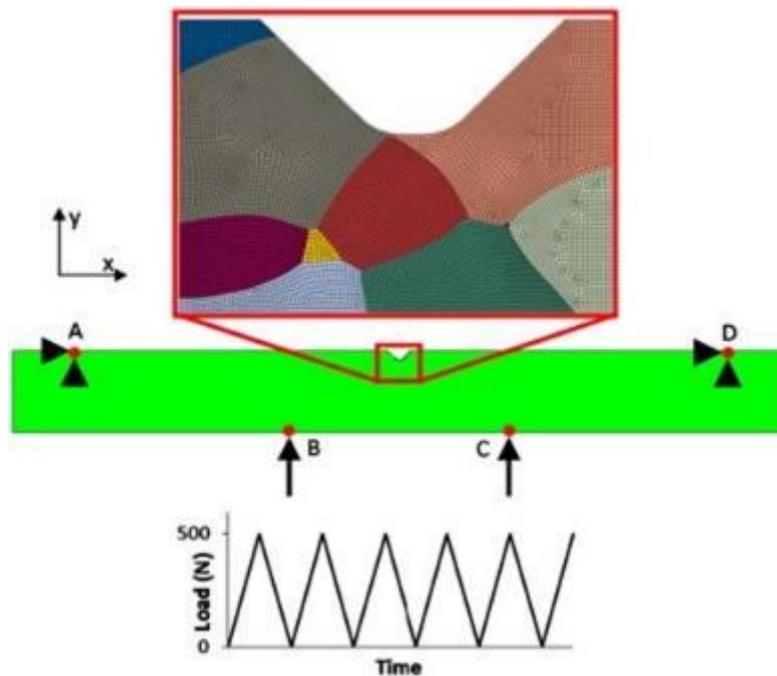
Figure 2-22. The BCs are shown on the sample, the loading conditions, and the meshed geometry at the edge of the notch [15].

Two fatigue indicator parameters are used for analysing the results: a) the effective plastic strain, *p*, and b) the effective plastic strain accumulated over a single cycle of the analysis. Figure 2.23 shows the accumulated plastic strain fields after monotonic (to peak cycle load) and cyclic loading conditions. The FCI site and the crack growth path in the notched region of specimen 1 are shown in figure 2.23(a), along with the FE mesh. In this specimen, the key microstructural feature appears to be the GB terminating at the root of the notch.

Figure 2.23(b) shows the strain fields for the effective plastic strain, *p*, after monotonic (to peak cycle load) and cyclic loading conditions (after 5.5 cycles). Figure 2.23(a) shows that FCI does not match the locations of maximum predicted effective plastic strain in figure 2.23(b) for the case of monotonic loading. However, for the case of cyclic loading the the peak for the effective plastic strain clearly matches the observed FCI site.

Changes occur for the accumulated slip distributions on dominant slip systems during cyclic loading and these directly affect the distribution for the effective plastic strain and therefore the predicted FCI sites. This necessitates the usage of cyclcic loading in fatigue simulations.
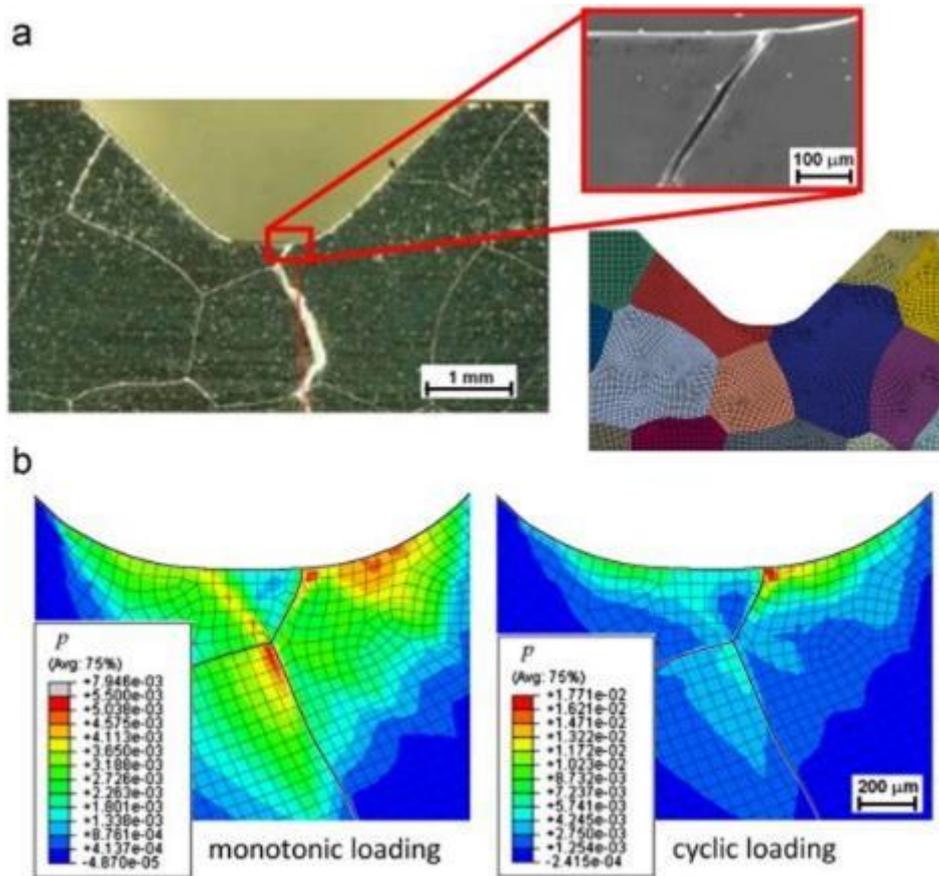
Figure 2-23. (a) Images of crack path for specimen 1 along with the FE mesh in the notch region, together with predicted field variations for specimen 1 of (b) effective plastic strain, *p*. Plots are provided for full load after monotonic loading and full load after cyclic loading as indicated [15].

The strain distributions for the effective plastic strain for the case of isotropic and anisotropic elasticity are much different in figure 2.24, for the after yielding condition. The peak in effective plastic strain occurs to the right of the notch in isotropic elasticity, while in the anisotropic-elasticity model, the peak occurs to the left of the notch which matches with the experimentally observed FCI site. The peak value for the effective plastic strain in isotropic elasticity is much higher than that for the anisotropic elasticity model. After cyclic loading in figure 2.24, the plastic strain distributions for the two models are still much different. The highest strain for the isotropic elasticity model is at the opposite side of the notch compared to the experimentally observed FCI site, whereas for the anisotropic model appears to predict correctly the FCI site with a peak well localized at the corresponding location. Different slip systems were found to exhibit the highest peak slip for the two models. Figure 2.24(c) shows the slip distributions for these two dominant slip systems, for each model, after cyclic loading. An image of the experimental crack path has been superimposed for correlation in figure 2.24c. It can be seen that the dominant slip system for the anisotropic elasticity model correctly predicts the FCI site, whilst this does not occur for the isotropic elasticity model.

The introduction of length scale effects tends to increase the highest peak of effective plastic strain, *p*, at the notch surface, but leaves the strain distributions at the rest of the region largely unaffected.

The development of GND is highly localised and that the initial distribution of GND density corresponds precisely with the FCI site. FIPs should therefore include the effective plastic strain and density of GNDs, as it is stated that it is most likely that FCI occurs where the peaks in both quantities coincide.
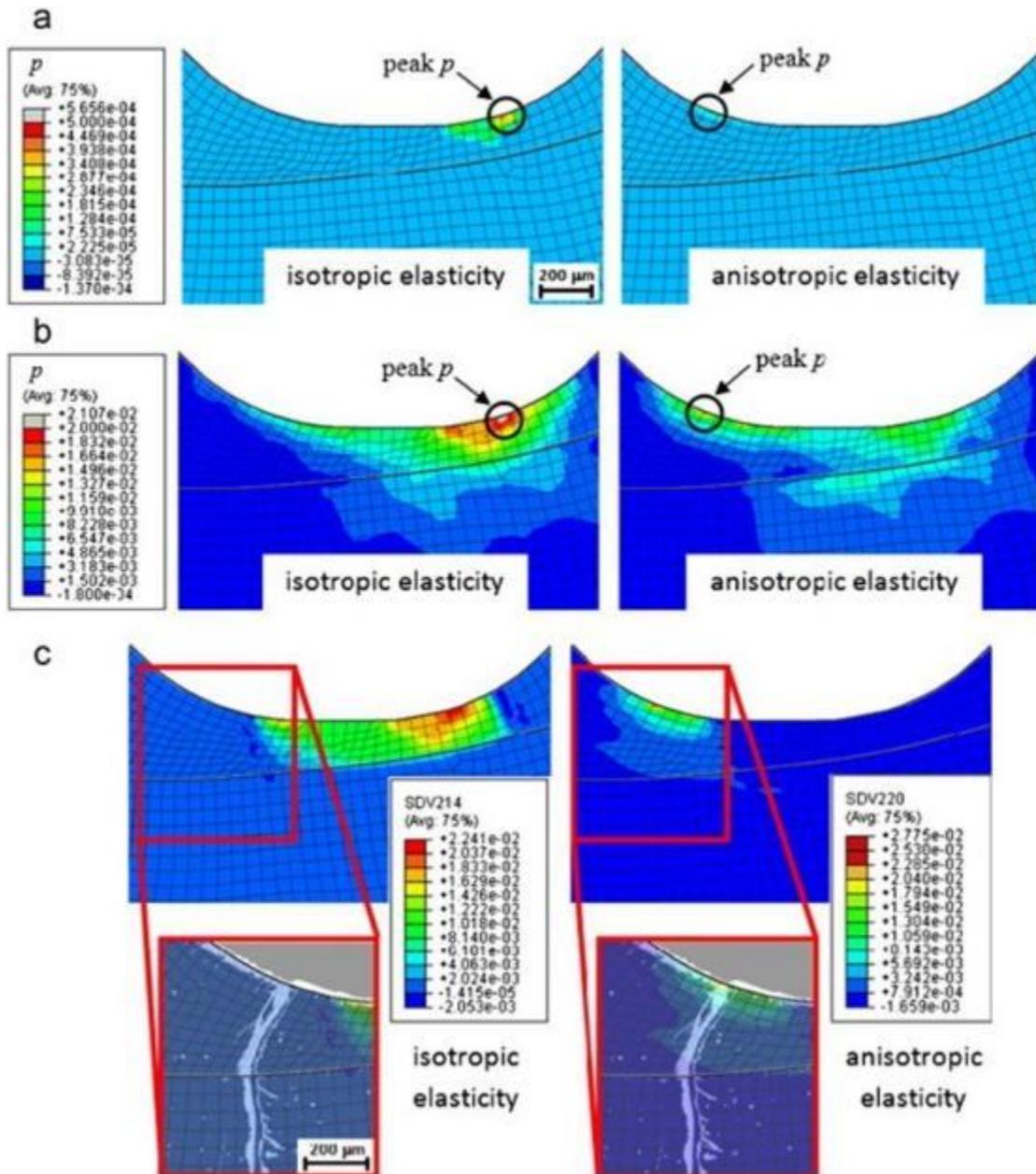
Figure 2-24. Field variations for specimen 2 from crystal FE models with isotropic and anisotropic elasticity of (a) effective plastic strain, p, initially after yielding, (b) effective plastic strain, p, at full load after cyclic loading and (c) accumulated plastic slip, $\gamma\alpha$, on the slip system with the highest slip for each model at full load after cyclic loading [15] .

The distribution of effective plastic strain, p, for specimens for which the FCI site is a) correctly predicted, b) predicted slightly to one side and c) predicted at the opposite side of the notch are shown in figure 2.25a-c, respectively. The experimentally observed FCI sistes and small crack growth

paths are also superimposed. For specimen 6 in figure 2.25c, one of the two localised zones of effective plastic strain coincides precisely with the observed FCI site. However, the use of cyclic accumulation of effective plastic strain more accurately predicts the crack nucleation site for specimen 6, as shown in figure 2.26b. Figure 2.26a shows the accumulation of effective plastic strain, at two points A and B at the notch surface for specimen 6. Point A corresponds to the FCI site predicted using p and B corresponds to the experimentally observed nucleation site. It can be seen that the rate of accumulation of p is higher at point B than at point A. Therefore, if more cycles were used in the simulation, the peak for the effective plastic strain distribution would correspond to point B. An extended simulation was performed and shows this effect in the inset of figure 2.26a. The effective plastic strain at point B exceeds that at point A after seven loading cycles and therefore a different predicted FCI site can result by using the effective plastic strain *and not the* cyclic *effective* plastic strain.
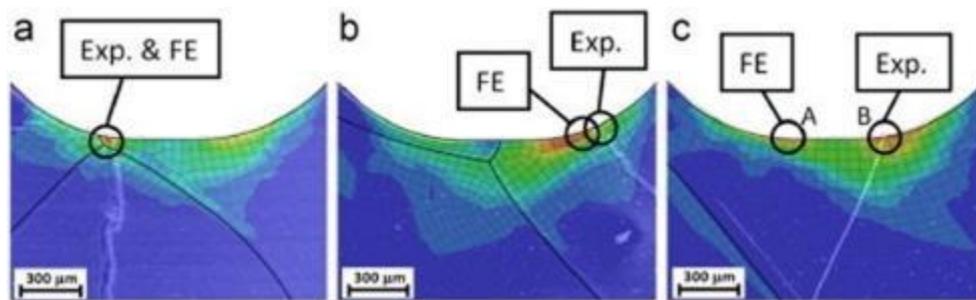
Figure 2-25. Field variations of effective plastic strain, p, with superimposed images of experimentally observed crack nucleation and growth for (a) specimen 7, (b) specimen 8 and (c) specimen 6. Experimental and crystal FE predicted sites of fatigue crack nucleation are highlighted [17].
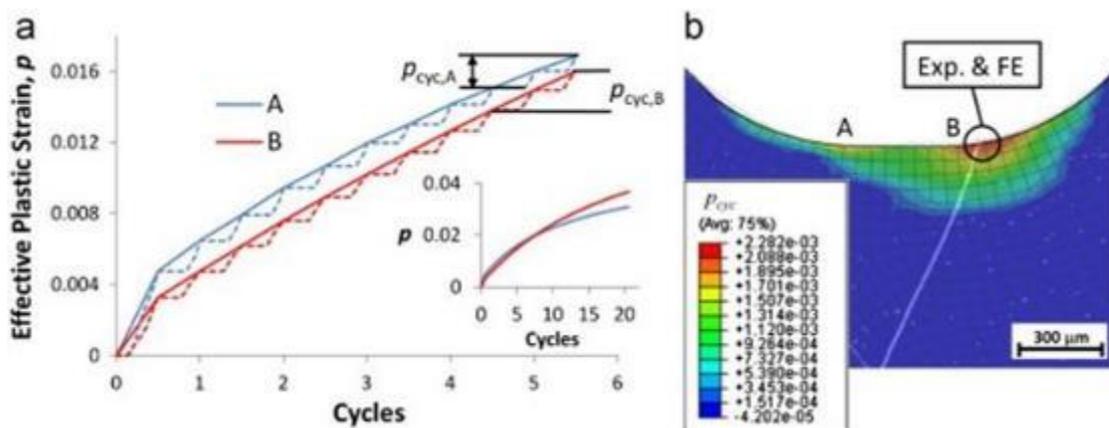
Figure 2-26. (a) Plot of effective plastic strain, p, against number of cycles for two points at the notch surface for specimen 6 and (b) distribution of cyclic effective plastic strain, $pcyc$, for crystal FE simulation of specimen 6, with the experimental and predicted sites of fatigue crack nucleation indicated [15].

Each of the five slip systems was found to contribute to different regions of the effective plastic strain distribution. The most dominant slip system was identified, due to a peak accumulated slip

significantly higher than for other slip systems. This dominant slip system was found to match with the experimentally observed crack nucleation site. Therefore, it is important to take into incorporate the accumulated slip on dominant slip systems as a possible FIP.

Comparing with the experimental images, the predicted crack propagation path was found to correlate well with the experimentally observed. It is noted though that the initial crack directions are not aligned (or parallel) with the predicted dominant slip directions. It is stated that high plastic slip on dominant slip systems facilitates crack growth, but there is no evidence that a crack will propagate along a slip system. Yet grain rotations were not included into CP FEM simulations.

The model appears to predict accurately the position of highest accumulated slip as well as the position and orientation of cracking. The model is coupled with data from 9 experiments, verifying further the validity of the model. Yet, the geometry created, with the notch, highly localises the strains within one, maximum three grains, for the current experimental set-up and the material provided. It is unclear whether the same model, simulating several hundreds of grains can accurately predict the right locations for FCI.

- *Prediction of fatigue crack initial stage based on a multiscale damage criterion*

Reference [18] presents a multiscale FCI damage criterion. A damage evolution relationship is obtained, related to the strain energy density and modified to incorporate crystal plasticity. A damage tensor was introduced to indicate the local damage state. Damage information is passed from local to grain level, bridging microscale and mesoscale. Finally, the damage evolution rule for a RVE with several grains is calculated via the Kreisselmeier–Steinhauser (KS) function. The weighted averaging method is employed to obtain the corresponding damage evolution direction at the meso-scale. A critical value is obtained in order to assess the total fatigue lifetime.

Damage evolution was estimated by employing two steps: calculate the stress–strain distribution for the multiscale model and apply a multiscale damage criterion based on the stress–strain distributions obtained from the first step in order to estimate the failure of a meso RVE and the potential crack growth directions in the RVE. In that study, the developed multiscale damage criterion predicts FCI, damage evolution and small crack growth direction simultaneously. The modeling equations are shown in Table 2.3.

Flow Rule	$\dot{\gamma}^{(\alpha)} = \dot{\gamma}_0^{(\alpha)} \left\lvert \dfrac{\tau^{(\alpha)} - \chi^{(\alpha)}}{g^{(\alpha)}} \right\rvert^n sign(\tau^{(\alpha)} - \chi^{(\alpha)})$
Isotropic hardening	$\dot{g}^{(\alpha)} = \sum_\beta h_{\alpha\beta} \dot{\gamma}^\beta$
Kinematic hardening	$\dot{\chi}^{(\alpha)} = b\dot{\gamma}^{(\alpha)} - r\chi^{(\alpha)} \lvert \dot{\gamma}^{(\alpha)} \rvert$
Self and latent hardening moduli	$\begin{cases} h(\gamma) = h_0 sech^2 \left\lvert \frac{h_0\gamma}{\tau_s - \tau_0} \right\rvert, & \alpha = \beta \\ qh(\gamma), & \alpha \neq \beta \end{cases}$

| Cumulative shear strain on all slip systems | $\gamma = \sum_\alpha \int_0^t |\dot{\gamma}^{(\alpha)}| dt$ |

Table 2.3. Relations used for the crystal plasticity model [18].

In that study [18], ABAQUS was employed and single crystal plasticity was employed within a user-defined material subroutine (UMAT), based on the work of Huang [19]. In previous publications by the same authors [20, 21] a modified UMAT code was developed, able to model fatigue hardening and saturation.

Jiang et al. [22-24] further extended the application of the model developed in [20, 21] to model successfully both multiaxial and non-proportional loading. In reference [21], Luo et al. introduced a the critical material plane upon which the maximum accumulated fatigue damage reaches a critical value and therefore small crack growth will occur upon that critical material plane. In that study [18], single crystal plasticity was incorporated within damage evolution so instead of calculating accumulated fatigue damage along all directions, calculation was limited only between the active slip systems.

Modeling was on a polycrystal of FCC crystal structure comprising of 12 slip systems, four slip planes, each with three slip directions. In their previous work [21], a critical parameter for damage evolution is presented for a aluminium single grain within a meso RVE, with 12 active slip systems, under uniaxial cyclic loading. A damage tensor, $D^{(\alpha)}$ was introduced and calculated at each point for all the active slip systems, to indicate the damage status at that particular point. The damage tensor was also used to model and predict crack propagation; by calculating crack growth rate and cracking direction simultaneously. The modeling geometry is shown in figure 2.27.

Since damage occurs after plastic deformation, in that paper [18], the effects of elasticity were not considered. Optimisation methods and averaging techniques were employed to obtain the local damage information and be able to transfer it into a global damage variable. A procedure based on Kreisselmeier–Steinhauser (KS) function was employed to take into account the effect of all grains in the RVE to the total damage accumulation at the meso-scale. Thus that model was more of a statistical tool rather than a progressive damage model. The KS function allows the contribution from the most critical grains to be accounted in damage calculation. The KS function is an envelope function (for a set of objective functions) with the multiple objective functions being the damage growth of all the grains in a meso RVE as a function of time.

The procedure for creating the meso RVE mesh comprised of two steps: a EBSD scan was used to obtain the grain orientations and the OOF (Object Oriented Finite element analysis by NIST) software was used to assign the material properties within the individual grains and mesh it. So the real microstructure is modeled in the FE simulation. Each grain in the RVE (figure 2.24) is treated as a single unit in order to calculate the damage parameter and direction. The output of each grain is a damage vector obtained by using an averaging technique.

The magnitude of the damage vector, D, in each grain is a function of time. The model calculates the number of grains that reach the critical damage value, D_c. This critical value is used to determine FCI in the meso-scale RVE. The damage direction is obtained by normalizing the sum of all damage vectors for all grains. When the maximum damage parameter of each grain within a meso RVE reaches the critical damage threshold, the corresponding grain is regarded as cracked. The goal is to determine whether failure has occurred for the RVE by checking whether D_{meso} has reached the critical value 1. The failure crack length of the meso RVE is taken as 1 mm, with respect to the RVE size and considering the resolution of the digital image acquisition system employed. The meso RVE size is approximately 1 mm × 1 mm and failure of the meso-scale RVE is validated by experimental observations.

The surface energy density for aluminium, ω, is 865.18 MJ/m^2 [25]. Thus the critical damage value is reached when the cumulative damage due to plastic deformation in the RVE is greater than the minimum energy for creating the two free surfaces for the crack. So the critical damage value is only a function of the average grain size l, the meso RVE size A and the surface energy density ω:

$$D_c = \frac{2 \times \omega \times l}{A} \tag{2.10}$$

The lug joint is a structural component where FCI occurs and leads to structural performance problems [18]. Fatigue testing was done on lug joint samples of Al 2024 T351. An Instron 1331 hydraulic load frame was employed. A digital image acquisition system was used to monitor the occurrence of FCI and measuring crack length. A cyclic loading of 490 N (110 lbs) to 4900 N (1100 lbs) with a frequency of 20 Hz in sinusoidal waveform was employed through the bottom clevis. From the images taken, the crack length versus the number of cycles curve is plotted. The experimental results for 1 mm crack were compared with the estimations of the 1 mm × 1 mm meso-scale RVE. Image acquisition also captured the initial crack direction on the specimen and were subsequently compared with the potential crack growth directions from the simulations.
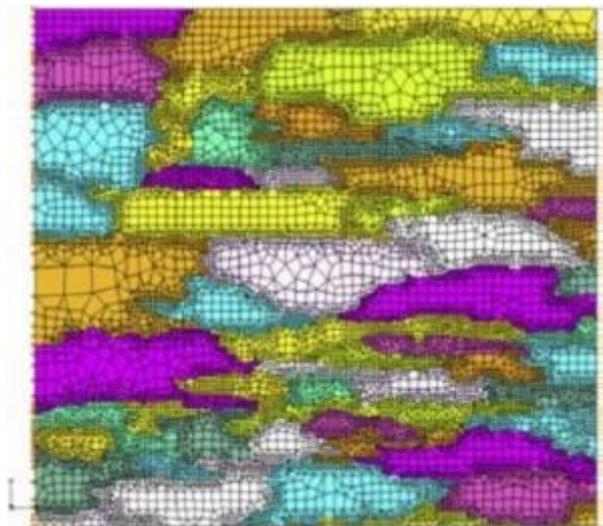
Figure 2-27. Meso RVE containing different oriented grains [18].

A two-scale mesh was used, a mesh generated using the software OOF creating a RVE at the hotspot of the lug joint [OOF], and a large mesh employed for the rest of the lug joint described as homogenous material. Figure 2.28 shows the two-scale mesh, generated by using the commercial software Altair Hypermesh. The constitutive relation of the homogeneous material was obtained by homogenising the stress–strain fields for the meso-scale RVE. A force was applied at the right edge of the RVE with plane stress elements employed. CPS3 and CPS4 elements are used in order to investigate the surface of the specimen. The displacement of each node at the edge was calculated. Symmetric BCs were used for that simulation, so only half of the lug joint was analysed. The load condition is the same as for the experiment; i.e. cyclic loading between 490 N and 4900 N with a frequency of 20 Hz (sinusoidal waveform). Figure 2.29 shows the non-uniform von Mises stress distribution at the lug joint due to the different grain orientations.
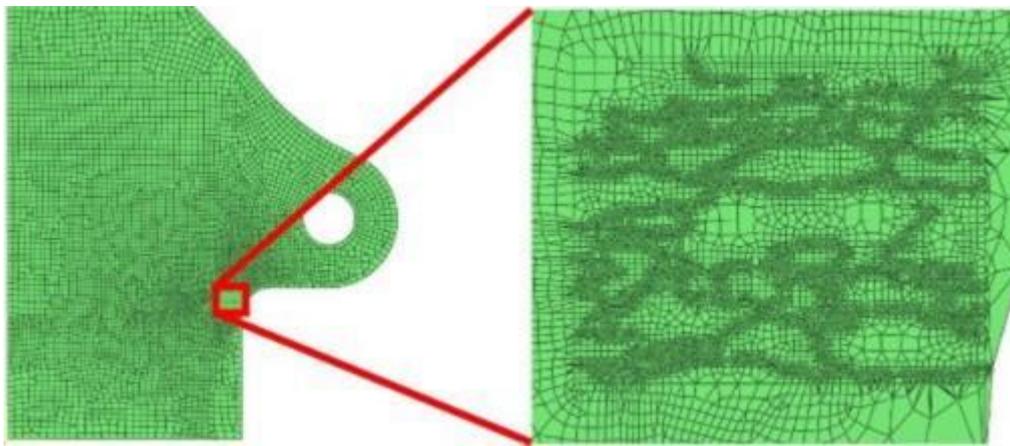
Figure 2-28. Finite element mesh of lug joint [18].
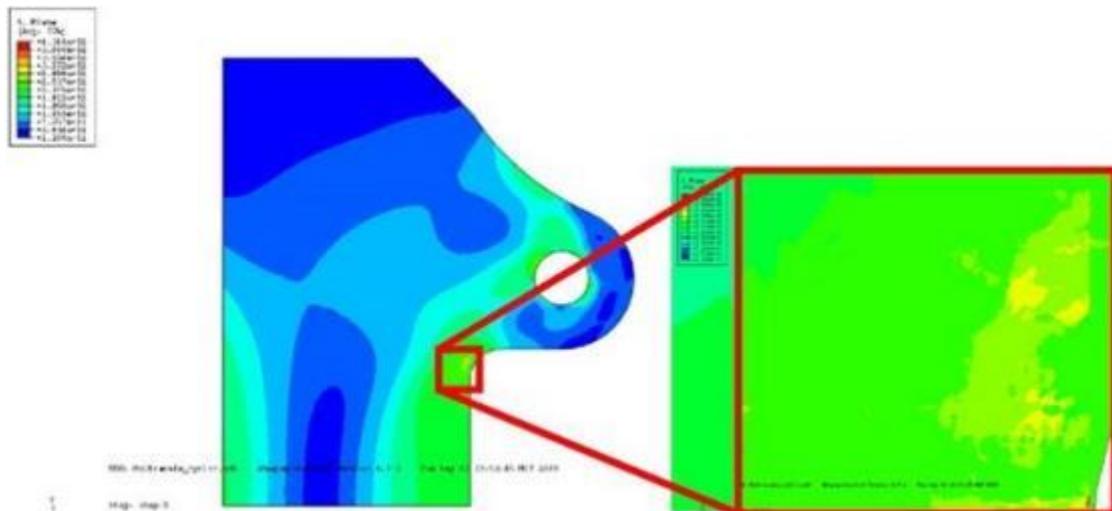
Figure 2-29. Mises stress distribution of lug joint [18].

The damage tensor was implemented in the UMAT and therefore the damage state was obtained within individual grains. Figure 2.30 shows the damage evolution for all the grains within the RVE of figure 2.30 for the first 20 cycles. The damage evolution in each grain stabilises after the tenth cycle which suggest that a linear fit can be used to extrapolate damage evolution within each grain. All

simulations were under constant cyclic loading. Therefore, damage evolution within each grain becomes approximately linear after 10 cycles.
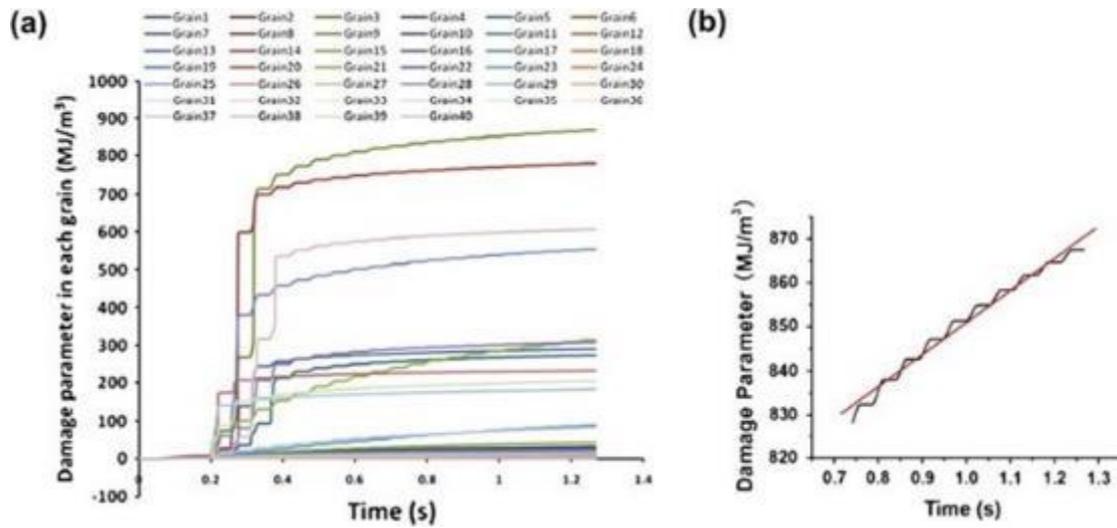
Figure 2-30. (a) Damage evolution in each grain for 20 cycles, and (b) an example shows that damage grows linearly after 10 cycles in each individual grain [18].

Figure 2.31 shows a histogram with the 'appearance frequency' of the corresponding eigenvector angle with respect to the horizontal axis-direction. The figure shows that the directions of maximum damage in the RVE are approximately −30° and 52°, while the experimental crack directions from lug joint fatigue tests are −34°, −29°, 0°and -30° (Figure 2.31). The comparison is therefore partly successful.
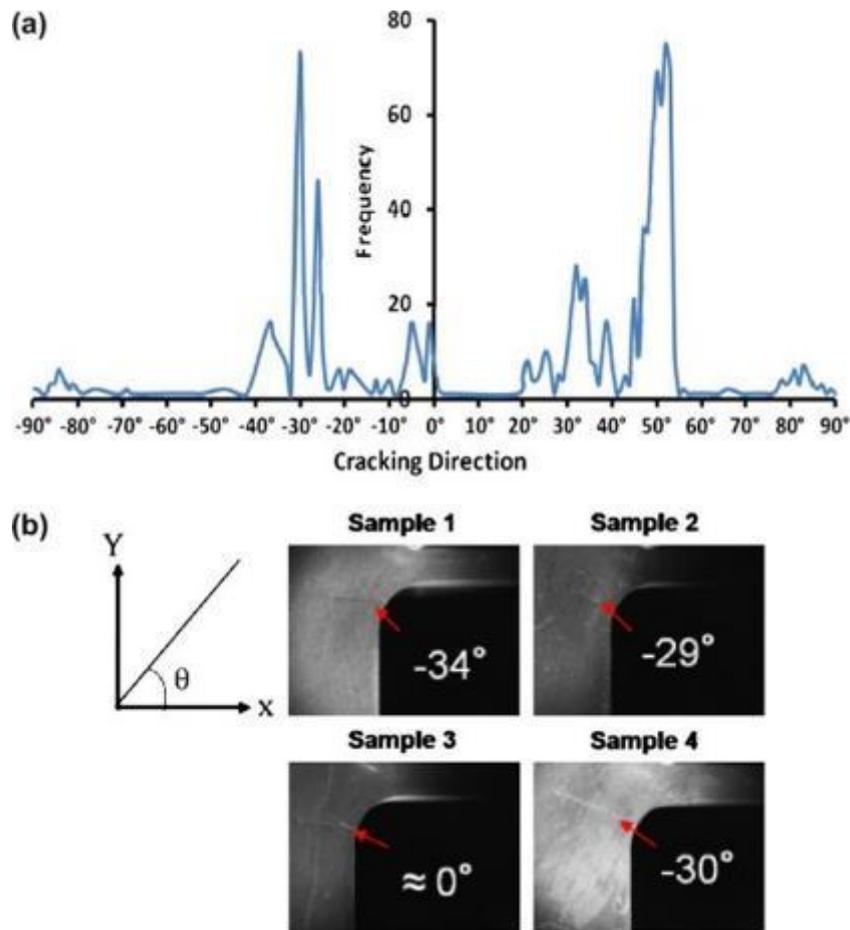
Figure 2-31. (a) Histogram of damage direction in RVE, and (b) cracking directions from fatigue tests

[18].

Five independent simulations yielded different fatigue lifetimes for the different microstructures, suggesting that the microstructure plays a vital role in the failure of the RVE. However, the EBSD obtained RVEs are not directly acquired from the lug joint samples, which therefore leads to variabilities in the results. To prevent this variability for the input data, an EBSD scan was performed directly on the lug joint and is shown in figure 2.32. EBSD scans were obtained from both shoulders of the lug joint on both sides and fatigue tests were afterwards conducted. The EBSD scans were imported into OOF for FEM modeling. As shown in figure 2.32c, the experimentally obtained number of cycles for a 1.5 mm crack was 33000 cycles. The simulation result for the same RVE failure was 12400 cycles. Taking into account the number of cycles needed for the crack to grow to a total length of 1.5 mm, the authors suggest that the simulation result is acceptable. The crack growth direction (in figure 2.32c) is approximately −53° with respect to the horizontal direction. Simulation results showed that two major crack growth directions exist: one between −58° and −43° and another one between 60° and 85°. Experimental observations showed that the crack propagated along one of the (simulation obtained) potential crack direction ranges, indicating that the model can predict the potential crack growth directions.
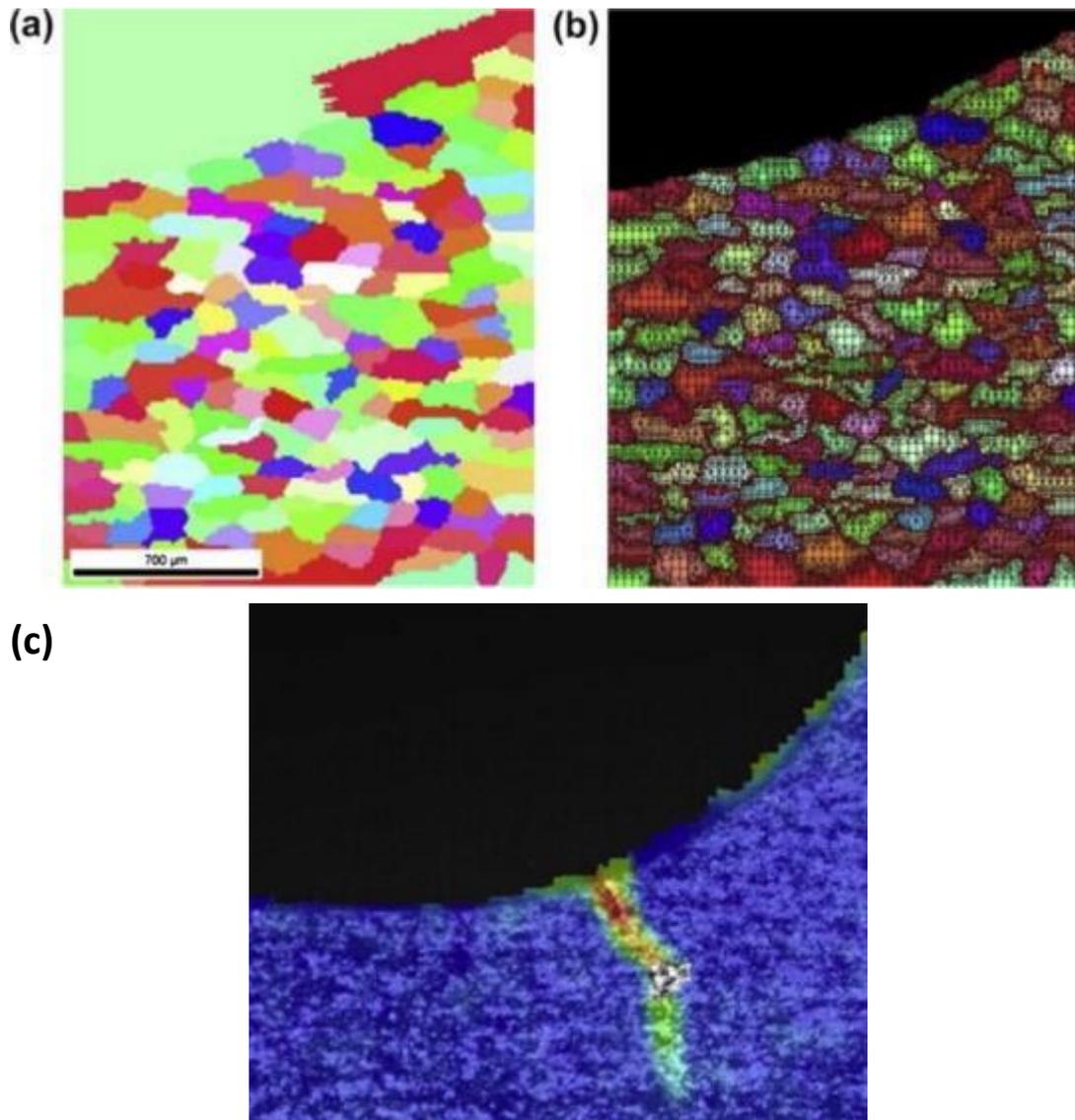
Figure 2-32. a) EBSD scan directly at the lug joint, b) Meshed geometry, and c) experimentally observed crack propagation for the same geometry as in a and b [18].

The reported model appears quite versatile, and proves its purpose as a multiscale model. However the exact location for FCI cannot be extracted from the current model. Being able to accurately predict the exact location for FCI can be quite important as different results for the number of cycles can be obtained if different FCI locations are used.

b. *Fatigue sensitivity & Extreme value statistics for Ni-base superalloys*

A computational study is conducted to determine the influence of microstructure attributes on driving forces for fatigue crack formation and microstructurally small crack growth in a polycrystalline Ni-base superalloy, IN100 [26]. A microstructure-sensitive crystal plasticity model is used to explicitly model individual grains and explore the effects of: (a) grain size distribution, (b) secondary and tertiary coherent γ' precipitate size distributions and volume fractions. Multiple statistical volume elements (SVEs) are used to build up statistically significant measures of distributions of cyclic

microplasticity. Multiaxial fatigue criteria with critical plane approaches are used to estimate the crack initiation life.

Two types of dislocation slip systems are considered for this FCC material; 12 octahedral and 6 cube slip systems. A series of IN100 microstructures with various precipitate size distributions and volume fractions obtained by different thermomechanical processing were considered.

Fatigue parameters and modelling

Fatigue Indicator parameters were introduced to study the influence of microstructure and micro-mechanical conditions on fatigue crack initiation potency. Mononukul and Dunne postulated that the cumulative plastic strain per cycle (P_{cyc}) in a representative volume element is given by [14]:

$$P_{cyc} = \int_{cyc} \sqrt{\frac{2}{3}}\, p \; \mathrm{d}t = \int_{cyc} \sqrt{\frac{2}{3} \mathbf{D}^p : \mathbf{D}^p} \; \mathrm{d}t \tag{2.11}$$

While the crack incubation life (N_{inc}) is:

$$P_{cyc} N_{inc} = p_{crit} \tag{2.12}$$

Impingement of slip on grain boundaries could also be a possible mechanism for fatigue crack formation. This is correlated to the build-up of dislocations (i.e. pile-ups), reflected on the continuum level by the cumulative net plastic shear strain measure:

$$P_r = \max\left(\int_{cycle} \dot{\varepsilon}_{ij}^p \, n_i \, t_j \; \mathrm{d}t \right) \tag{2.13}$$

where **t** is the direction along any given plane with normal **n**. The maximum value of this parameter is obtained along all possible slip directions and planes for one cycle. Crack incubation associated with slip band cracking and shear-dominated microstructurally small crack growth is correlated to the Fatemi–Socie parameter, P_{FS} :

$$P_{FS} = \frac{\Delta \gamma_{max}^p}{2} \left[1 + k^* \frac{\sigma_n^{max}}{\sigma_y} \right] \tag{2.14}$$

where $\Delta\gamma^p{}_{max}$ is the maximum range of cyclic plastic shear strain, $\sigma_n{}^{max}$ is the peak tensile stress normal to the plane associated with this maximum shear range and σ_y is the cyclic yield strength. The peak normal stress term in above equation for reflecting the effect on the opening process of small cracks, has been shown to be related well to the growth of microstructurally small cracks. If the incubation life is completely controlled by the irreversible motion of dislocations with no assistance of normal stress, then $k^* = 0$, and the related maximum range of cyclic plastic shear strain parameter P_{mps} is given by:

$$P_{mps} = \frac{\Delta \gamma_{max}^p}{2} \tag{2.15}$$

The approach was used to study the distribution of the FIPs, i.e., P_{cyc}, P_r, P_{mps} and P_{FS}, in an IN100 polycrystal. In this study, 216 (i.e. $6 \times 6 \times 6$) grains were used. This was not a representative volume element (RVE); but different realisations of statistical volume elements (SVEs); multiple realisations of SVEs are necessary to build up statistics over representative volumes for the fatigue parameter distribution. For any selected microstructure, three realisations are constructed and analysed; by modifying the mean grain size ($<d_{gr}>$).

Experimental data were available for a similar Ni-base superalloy (Rene88). In Rene88, the majority of the fatigue cracks form at slip bands while the others form at grain or twin boundaries. The evolution of the crack size distribution as a function of the number of cycles (normalised by fatigue life N_f) is shown in figure 2.33. Small cracks were observed to dominate for up to 70% of the specimen failure life.

The FIPs exhibited log normal distributions; an initial peak was observed due to the number of grains that have a low value of FIP. The peak shifted to the right as the strain amplitude increased since plasticity was more uniformly distributed, which is consistent with the large number of cracks observed at high strain amplitudes. The effect of grain size distribution on the FIP distribution was examined. The influence of the grain size on the FIPs is studied for three average grain sizes: 8, 16 and 32 μm. All the FIPs showed similar grain size dependence. Both max $P_{FS, max}$ and max $P_{r,max}$ increased as a function of the average grain size; however max $P_{FS, max}$ displayed a much weaker dependence on the grain size than max $P_{r,max}$.
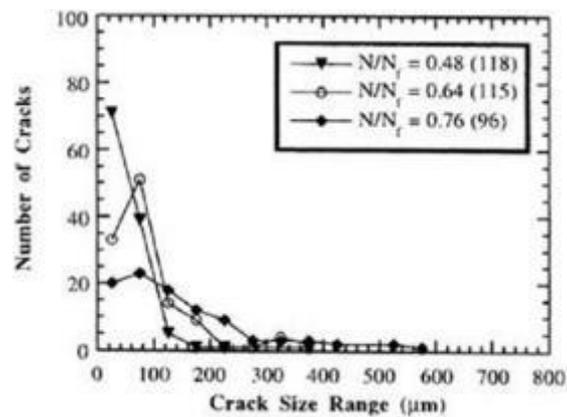
Figure 2-33. Microcrack size distributions in a Rene88 as a function of the nr of cycles (normalized by total fatigue life N_f), with $R_\varepsilon = -1$, room temperature, $\sigma_a = 0.9\sigma_y$, and cycle frequency 1 Hz [26].

The fatigue life is composed of the following stages in a polycrystalline Ni-based superalloy: a) crack incubation at favorably oriented grains, b) microstructurally small crack growth, and c) crack coalescence and long crack growth until failure. Here only the first two stages were considered in defining the fatigue crack initiation life via the FIPs; moreover crack coalescence is neglected.

Crack incubation

The model was based on the dislocation theory proposed by Tanaka and Mura. Incubation life for a Stage I crack is related to the macroscopic plastic strain range according to:

$$N_{inc}(\Delta\varepsilon^p)^2 = \frac{a_p}{d_{gr}}$$ (2.16)

where α_p is a constant.

Microstructurally small crack growth

The grain scale averaged Fatemi–Socie parameter ($P_{FS,av}$) gives an indication of the microstructurally small crack (MSC) growth rate, once the crack is incubated. Here, a modified form of the MSC growth law is used with $P_{FS,av}$ as the driving force:

$$\left.\frac{da}{dN}\right|_{msc} = A_{FS}\tau_y \left(P_{FS,av}\right)\alpha$$ (2.17)

where A_{FS} is a constant and τ_y is the resolved shear stress (Taylor factor , M = 3.06). The incubated cracks are assumed to grow from one grain to the neighbouring grains with the highest values of $P_{FS,av}$.

The MSC life is defined as the number of cycles for the incubated crack to grow to $3d_{gr}$(or 40μm). The initiation life (N_I) for a crack length = $3d_{gr}$ is given by:

N_I = N_{inc} + N_{msc} (2.18)

The distribution of the number density of cracks (*fraction of cracks*), defined as the number of grains with incubated cracks that have grown to $3d_{gr}$ divided by the total number of grains in a SVE, is plotted as a function of the total life in figure 2.34. The fraction of grains with cracks increases with the applied strain amplitude, as seen in Figure 2.34. A higher variability for the lower strain amplitudes (≤$0.6\varepsilon_y$) was obtained. This is expected since the plastic strain is distributed more uniformly at higher strain amplitudes. Although crack coalescence has not been accounted for in this analysis, it is noted that the probability of coalescence increases with increasing strain amplitude.

Microstructure optimisation for fatigue resistance

Once the microstructure influence on fatigue crack initiation life is characterised, a computational material design framework using neural network analysis may be used for fatigue resistant microstructures. A computational exercise is carried out for a fatigue resistant microstructure that maximises the fatigue crack initiation life (**N_{inc} + N_{msc}**).

Design variables include (i) secondary γ' precipitate size (d_2), (ii) secondary γ' precipitate volume fraction (f_{p2}), (iii) tertiary γ' precipitate size (d_3) and (iv) tertiary γ' precipitate volume fraction (f_{p3}). Forty microstructures are generated with different values of d_2, f_{p2}, d_3, f_{p3} within the experimentally observed ranges. The average grain size was fixed at 16 μm. The microstructure parameters are used as the input parameters and the crack initiation life is used as the output variable. The forty microstructures were used to assess microstructures that maximise fatigue life for a given applied strain amplitude.

The microstructure with the maximum fatigue crack initiation life corresponded to design variables hitting the upper or lower boundaries of their specified ranges. The threshold stress increased with

increasing tertiary precipitate size (d_3) and volume fractions (f_{p3}), decreasing secondary precipitate size (d_2), and by minimising volume fraction of the secondary precipitates (f_{p2}).
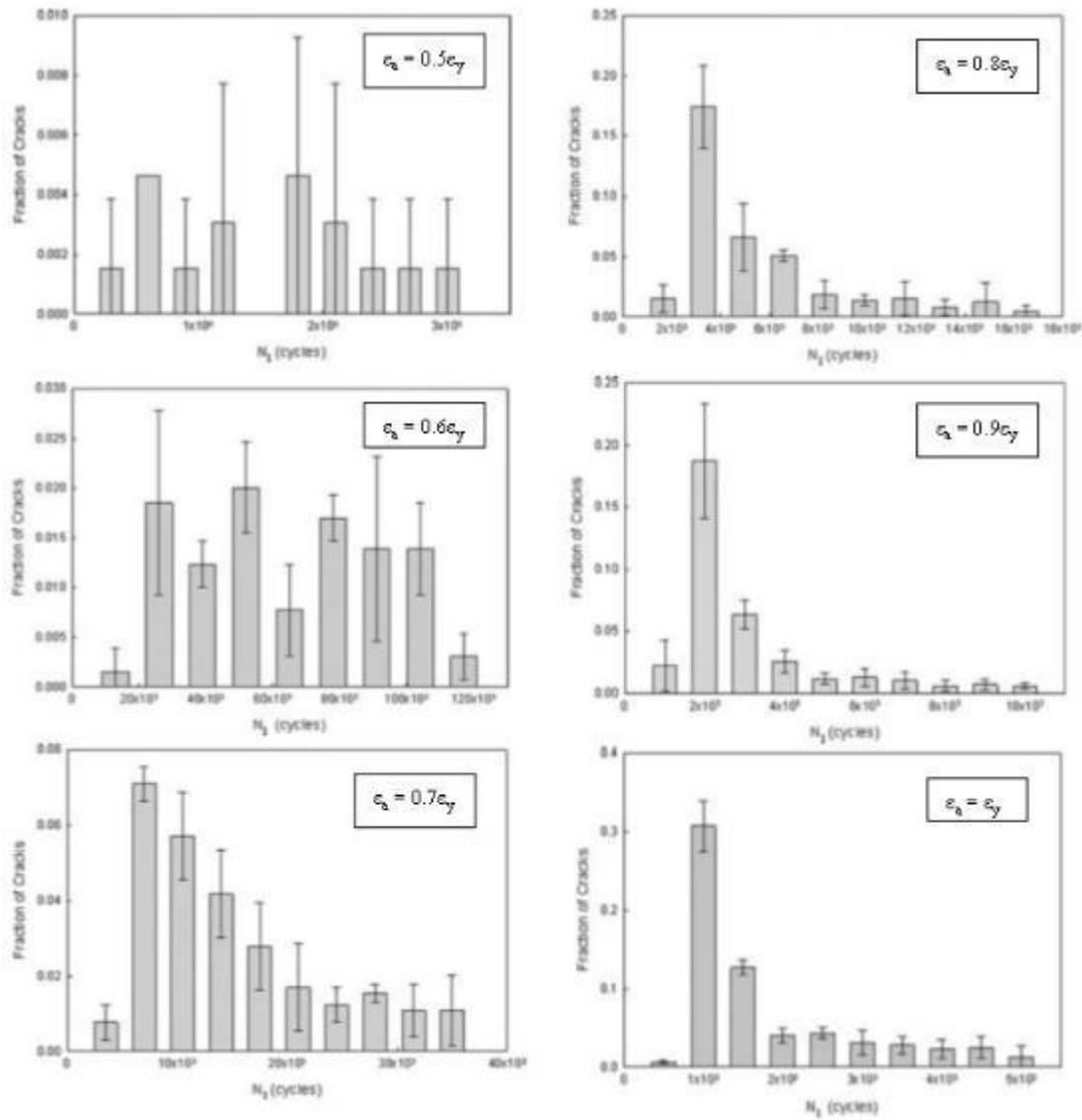
Figure 2-34. Distribution of fraction of cracked grains corresponding to a range of fatigue crack initiation lives IN100 for T = 650 $^{\circ}$C, Rε =−1 and $\dot{\varepsilon}$ = 10^{-3} s^{-1} [26].

- *Extreme value statistics*

To quantify the effects of interactions between various microstructure attributes on high cycle fatigue (HCF) life, a new microstructure-sensitive extreme value statistical framework was proposed by Przybyla et al [27]. This framework couples the extreme value distributions of certain fatigue indicator parameters (FIPs) to the correlated microstructure attributes, to investigate the fatigue response of a PM Ni-base superalloy IN100. Statistical volume elements (SVEs) were used to compute the local response, for 200 generated models. These SVEs were constructed and simulated via a finite element method coupled with crystal plasticity constitutive relations; based on the previous work outlined above.

Scatter in the High Cycle Fatigue (HCF) life of specimens depends on the extreme value probabilities of having existing *hot spots* or regions with increased local driving forces for fatigue damage formation. Specifically, the probability of fatigue damage formation in a particular volume of material is established by the extreme value (i.e., rare event) probability of a particular existing combination of microstructure attributes that couple with the applied stress state.

In multiphase material systems, multiple interacting microstructure features couple and interact to increase the local driving forces for fatigue damage formation. This dependence cannot merely be deduced from direct quantitative image analysis of various microstructure attributes. A combination of experiments, computational simulation along with extreme value statistics is necessary for the assessment of the coupling of microstructure attributes.

In general, fatigue damage formation in polycrystalline metallic materials is primarily driven by irreversible slip. Interacting microstructure attributes (e.g., grains, phases, inclusions, and voids) can increase local slip. In HCF, cyclic plasticity is quite heterogeneous and fatigue lives are dominated by fatigue damage formation rather than by physically small or large crack propagation.

This work is primarily concerned with how the crystallographic attributes of a polycrystalline microstructure (e.g., grain orientation, disorientation, size, and shape distributions) affect the local driving forces for fatigue crack formation and early growth in HCF. In general, plastic strain inhomogeneity at the grain level is directly linked to crystallographic texture; plasticity occurs preferentially in grains having slip systems with high Schmid factors. High plastic heterogeneity is directly related to complex interactions between grains of differing orientations.

Fatigue damage formation in polycrystalline Ni-base superalloys has been linked to the existence of large pores or nonmetallic inclusions introduced during processing. However, as processing techniques improve, cleaner superalloys are being developed that have lower number density of inclusions/pores; consequently, fatigue cracks are increasingly observed to form along crystallographic planes. Cracks form predominantly in larger grains or at inclusions near large grains. These grains were associated with higher Schmid factors (favorably oriented for slip). It is known that fatigue damage formation is more common in coarser grained superalloys, while deformation in the smaller grains has been observed to be more homogeneous.

Significant variability in the overall fatigue lives in IN100 may be observed, for a range of applied stress magnitudes. The variability of fatigue life is assessed by extensive experimentation to obtain a statistically significant sample. The problem is complicated as multiple mechanisms of damage formation occurred; making it difficult to accurately predict fatigue life.

Processes of HCF crack formation and early growth depend on a few key attributes such as the largest inclusion or void within a population of such features. There is significant scatter in experimentally measured HCF life because attributes that govern failure lie within the tails of distributions, necessitating consideration of extreme value statistics; for example the largest inclusion size.

Different models exist that predict the fatigue resistance based on the largest inclusion size. All of these methods, however, assume failure based on a single attribute (e.g., inclusion size) and do not consider how interacting attributes affect the damage processes of interest.

The objective is to develop a statistical framework that is able to quantify the coupling of the extreme values of certain FIPs to the key microstructure attributes that are associated with these extreme value response parameters.

The main approach was based on the extreme value marked radial correlation function, $R^{max(\alpha)}$ (β, β'/r, Ω), which was associated with the probability of finding of a sphere with the microstructure attribute β at its center, with maximum response parameter α, and a microstructure attribute β' at a distance within r and $r + dr$ from β in any direction. This component captures both the extreme value response of the microstructure as represented by the response parameter α and the biased correlations of microstructure attributes between β and β' in the extreme value neighborhood. The method requires multiple instantiations of Ω, facilitating comparison among multiple microstructures which can support materials design. The method requires a significant number of simulations/experiments if they are to be considered statistically meaningful; and therefore extensive processing time.

Sometimes a particular response of a RVE of reasonable size is unattainable. This is particularly true when trying to capture extreme value distributions of microstructure response that affect rare event damage formation and growth. This implies that complete characterisation of the tail of the probability distribution function (PDF) for fatigue response requires a very large RVE.

The same relations of Coffin Manson power law and Fatemi-Socie were used to model crack incubation and small crack growth. To understand how the local microstructure influences the extreme value fatigue response, the microstructure attributes were calculated in the neighbourhoods where the extreme value FIPs were recorded.

In these two presented works, the authors used sophisticated models to predict FCI potency. Several FCI parameters were employed and estimated at hot spots. However a critical single parameter for FCI modeling has not been obtained. Furthermore no parameters for the small crack growth regime have been introduced in order to understand the physical mechanisms of both processes: FCI and small crack growth.

2.2.5. *Modeling short fatigue cracks*

Crack-growth paths for a polycrystalline nickel-based superalloy modeled by crystal plasticity

Crystal plasticity FEM simulations were employed to model the cyclic constitutive behaviour of a polycrystalline nickel-based superalloy at elevated temperature. Alloy RR1000 is a FCC polycrystal with a fine grain microstructure [28]. A RVE with 150 randomly oriented grains was considered with periodic BCs. Figure 2.35 shows that there is only one circle in the pole figure of a 150-grain RVE (figure 2.35a and c) and a line in the inverse pole figure (figure 2.35e) when only one Euler angle is employed for the grain orientation. If random grain orientations with three Euler angles are

employed, the pole and inverse pole figures of figure 2.35b, d and f can be considered. The equations used in the model are shown in Table 2.4 [28].

Strain-controlled cyclic test data at 650 °C were used to determine the modeling parameters. Simulation results were in good agreement with the experimental ones for the stress–strain loops, cyclic hardening behaviour and stress relaxation behaviour. Using the FE submodelling technique, the crystal plasticity model was able to be applied to study explicitly the effect of local microstructure on the stress-strain fields at the neighbourhood of the crack-tip of a notched sample. The accumulated shear deformation was calculated within individual slip systems near the crack tip and utilised to predict the influence of grain orientation on the crack path.

The grain microstructure is shown to have a strong influence on the von Mises stress distribution near the crack tip, and the grain texture heterogeneity modifies the well-known butterfly shape for the plastic zone. The stress–strain response near the crack tip, as well as the accumulated shear deformation, is strongly influenced by the orientation of the grain at the crack tip, which influences the subsequent crack growth through grains. Individual slip systems near the crack tip accumulate different amounts of shear deformation, which was utilised as a criterion for the crack growth path.

Flow Rule	$\dot{\gamma}_\alpha = \dot{\gamma}_0 \exp\left[\dfrac{-F_0}{\kappa\theta}\left\langle 1 - \left\langle\dfrac{|\tau^\alpha - B^\alpha| - S^\alpha \mu/\mu_0}{\hat{\tau}_0 \mu/\mu_0}\right\rangle^p\right\rangle^q\right]\mathrm{sgn}(\tau^\alpha - B^\alpha),$
Slip resistance on a generic slip system	$\dot{S}^\alpha = \left[h_S - d_D(S^\alpha - S_0^\alpha)\right]|\dot{\gamma}^\alpha|,$
Backstresses	$\dot{B}^\alpha = h_B\dot{\gamma}^\alpha - r_D B^\alpha |\dot{\gamma}_\alpha|$
Dynamic recovery function	$r_D = \dfrac{h_B \mu_0}{S^\alpha}\left\{\dfrac{\mu_0'}{f_c \lambda} - \mu\right\}^{-1}$

Table 2-4. Relations used for the crystal plasticity model [28].
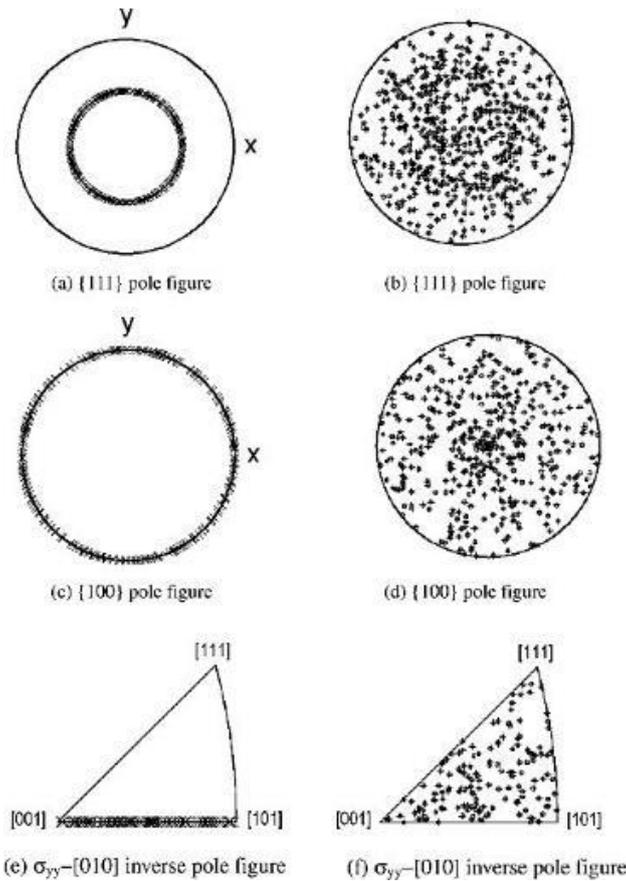
Figure 2-35. Pole and inverse pole figures for a 150-grain RVE with one Euler angle (a, c and e) and three Euler angles (b, d and f) [28].

Two slip system families were required to describe consistently the inelastic behaviour of f.c.c. Ni-base superalloys at high temperature, the octahedral ({1 1 1} <1 1 0>) and the cubic ({1 0 0} <1 1 0>) slip. The RVE was meshed into first-order four-node plane strain elements with full integration. Due to the large strains in plasticity analyses, first-order elements are usually recommended [17]. To obtain the global response of the material, homogenization techniques over the RVE area were employed [29]. A mesh-sensitivity study showed that the stress–strain curves reached a good convergence for 1450 elements.

A standard CT specimen (width W = 26 mm and height H = 15.6 mm) was considered for the crack tip deformation analyses. The meshed part is shown in figure 2.36. Cyclic load, with ΔK = 25 MPa m$^{1/2}$ and R = 0.1, was applied to a rigid pin fitted into the hole of the specimen. FE submodelling was adopted to study the influence of grain orientation on crack tip deformation. 150 grains were used in the sub-model, with randomly assigned orientations, where the loading was prescribed by the displacement of its boundaries from the global model analyses. A transgranular crack across a couple of grains was introduced in the submodel.

The deformation of the submodel follows the crystal plasticity formulation, while the global model was described by a viscoplastic constitutive formulation [9], as adopted for RR1000 [30], where both isotropic and kinematic hardening are considered for the transient and saturated stages of cyclic

57

responses. The viscoplasticity model used a user-defined material subroutine (UMAT), with fully implicit integration and Euler backward iteration algorithm [31], implemented in ABAQUS.

The submodelling analyses only satisfied the displacement continuity at the interface between the submodel and global model. Traction continuity was not ensured at the interface and the results near the interface are therefore approximate. Yet, the crack tip is reasonably away from the interface and the influence of the crack is limited, which was confirmed by the same ΔK values obtained from the submodelling analyses. The modeling results agreed very well with the test data. The stress response and the shape of hysteresis loops were both well captured. For the cyclic hardening behaviour a good match was demonstrated.

Figure 2.37a shows the contour plot of the von Mises stress distribution. The stress concentrations near the crack tip follow the well-known butterfly shape for the viscoplastic material. However, for the case of crystal plasticity, the grain orientation influences the Von Mises stress contour zone which does not have a butterfly shape (figure 2.37b). The stress concentration zone obtained from crystal plasticity analysis has an arbitrary shape. The shape and size of the stress contour zone seem to be clearly affected by the heterogeneity at the microstructural level.
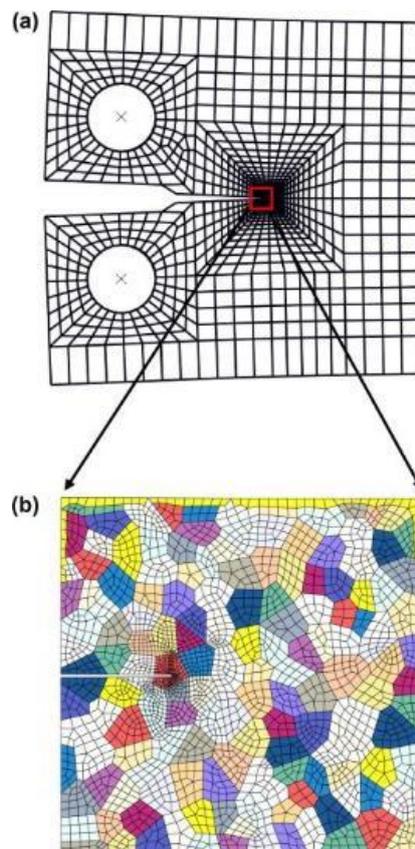
Figure 2-36. Global finite element model for the CT specimen; (b) a 150-grain submodel with crack introduced across a couple of grains (mesh size near the crack tip is ~0.20 μm) [28].
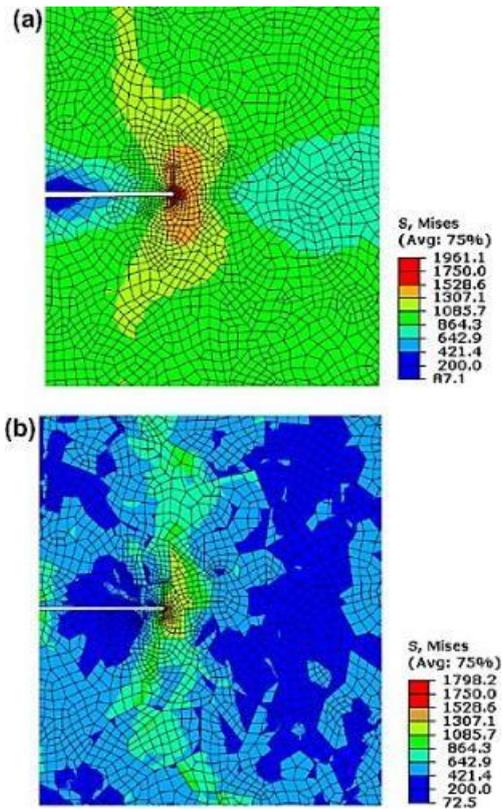
Figure 2-37. Contour plots of the von Mises stress obtained from the FE analyses using (a) crystal plasticity and (b) viscoplasticity model [28].

The shear deformation along individual slip systems has been obtained near the crack tip and was found to vary along each slip system. Four slip systems appeared to have the highest amount of accumulated shear deformation after four cycles and corresponded to three octahedral slip systems (1 1 1)[1 −1 0], (1 −1 1)[−1 0 1] and (1 −1 1)[1 1 0] and one cubic slip system (1 0 0)[0 −1 1]. The 2D in-plane traces of these four slip systems are shown in figure 2.38a, and the corresponding accumulated shear strains are plotted in figure 2.38b.
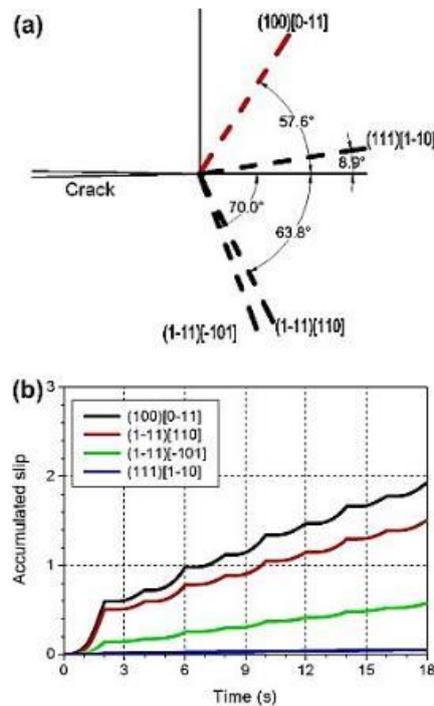
Figure 2-38. (a) The 2D in-plane traces of the four slip systems with the most notable amount of accumulated shear deformation in four cycles; (b) accumulated slip, averaged over a distance of 0.40 μ m ahead of the crack tip, as a function of the time for the four slip systems [28].

After four cycles, the cubic slip system (1 0 0) [0 −1 1] accumulated the largest shear deformation. In that study it was proposed that crack growth in the grain interior follows the direction of the slip trace with the maximum accumulated slip. Once the slip trace was calculated, the crack length was immediately increased to the GB along the slip system, representing a series of stationary cracks. When the crack met the GB, the model was re-meshed to evaluate the crack growth path into the next grain. The size for the crack tip mesh near the grain boundary was about 0.6 µm and mesh sensitivity results showed that the maximum amount of shear deformation remained unchanged with mesh refinement. Two submodels with different sets of random orientation were considered and the predicted crack growth paths are shown in figure 2.39. The loading condition was the same, the stress intensity factor range is ΔK = 25 MPa m$^{1/2}$, load ratio R = 0.1 and frequency f = 0.25 Hz. The level of ΔK is well below the fracture toughness for alloy RR1000. A closer look at the zig-zag path, predicted from the maximum shear deformation criterion, seems to suggest that the overall crack path tends to follow the major growth direction which is perpendicular to the external load.

(a)

1: (100)[0-11]
2: (-111)[101]
3: (010)[-101]
4: (001)[-110]
5: (111)[1-10]
6: (1-11)[-101]
7: (111)[1-10]
8: (-111)[01-1]
9: (-1-11)[-110]

(b)

1: (100)[0-11]
2: (100)[0-11]
3: (001)[-110]
4: (1-11)[-101]
5: (-111)[-1-10]
6: (1-11)[110]
7: (100)[011]
8: (100)[011]
9: (-1-11)[101]
10: (1-11)[110]
11: (1-11)[110]
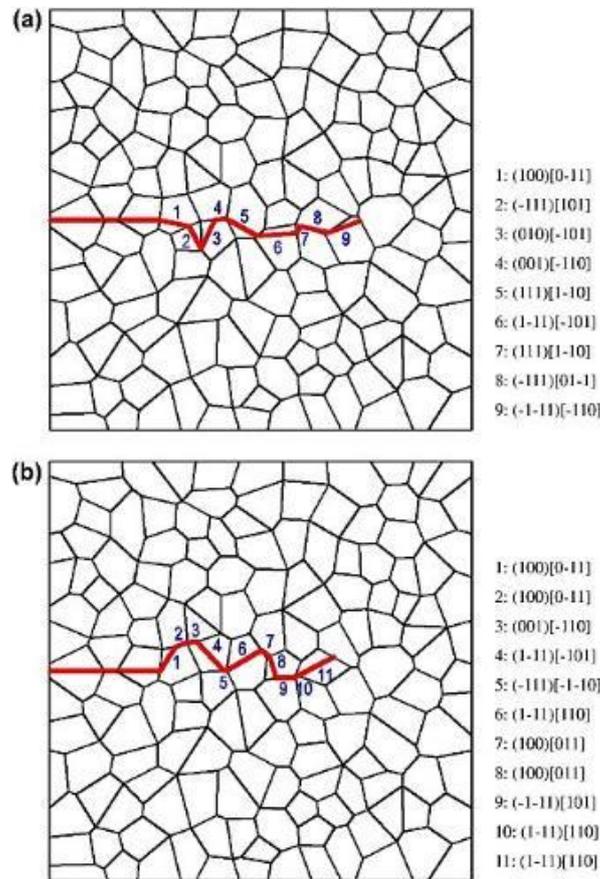
Figure 2-39. Predicted crack growth paths for two submodels with different sets of random grain orientation [28].

This model assumes crack growth only along (specific) slip planes. The effect of GBs has been ignored. Strain gradients close to GBs have also been ignored. Furthermore, the cracks seem to follow during the whole process up to final failure the slip planes. While it is widely known that after 2-3 grains the crack becomes macroscopic and the influence of the microstructure decreases. Therefore modelling the crack paths in figure 2.39 is not practical and reasonably important. However the insights given in figure 2.39 about the strain fields around a crack tip are very insightful about what is happening at the tip of the crack, and at the grains within its neighbourhood. Also, while continuum mechanics predicts butterfly stress fields, crystal plasticity shows highly non-homogeneous stress fields within the grains.

The influence of crystallographic orientation on crack tip displacements

Microstructurally short cracks were modeled by using a CPFEM in [32]. A short crack was introduced along a slip plane in one of the grains at the top boundary and extended along one of the available slip planes of the neighbouring grain for monotonic loading conditions. Crack tip opening (CTOD) and sliding (CTSD) displacements were then calculated for various crystal orientations and crack lengths. It was found that the orientation of the neighbouring grain can change the crack tip displacements by up to 26%. However, the displacements changed by up to a factor of 10, once the crack was extended beyond the GB into the next grain. Significant CTSD values were observed in all the analysed cases pointing to mixed mode loading (Mode I + Mode II). Another important observation is that the

random crystallographic orientations of grains beyond the first two crack-containing grains affect the CTOD by a factor of up to 4.4. This effect decreases with increased crack length.

The model was a rectangular 2D RVE with 212 randomly sized and shaped grains. The aggregate was generated by using the VorTESS code [33]. The model resulted in an average grain size of about 53 μm which is in agreement with published values for 316L steel. 316L steel has a relatively weak morphological texture, with elongated grains along the rolling direction (about 20% elongation along the rolling direction) [34]. This effect was, however, not accounted for in the model. 316L is an austenitic steel with a FCC crystal structure.

A simulation containing a crack is shown in figure 2.40. Each grain is subdivided into 8-noded, reduced-integration, plane strain elements. The mesh is composed of inner, middle and outer layers. The inner layer has an average element size of 0.125 μm, the middle layer 2.5 μm and the outer layer 13 μm. The finite element meshing of the grains in these layers was automatically done according to reference [35].

The number of grains included in the model was not sufficient to result in a size-independent macroscopic response of the aggregate (RVE). However, the error was around 5% [36]. A short inclined surface crack was introduced in the model. Crack is placed along a slip plane to mimic Stage I fatigue crack. This is achieved by first setting the angle between the crystallographic [1 0 0] direction (crack orientation) and the macroscopic X-axis to 135°. Each crystal is rotated around the global Z-axis by an angle α, obtained by a random generator with uniform distribution. We will refer to this angle as crystallographic orientation.

Crystallographic orientation of the grain 38 (the first crack-containing grain, see figure 2.38) is set to 9.375° so that the crack falls along the 2nd slip plane, P2. The crystallographic orientation of grain 124 (second crack-containing grain) was such that the crack was either along the P2 or the P4 slip plane. The crack tip opening (CTOD) and sliding (CTSD) displacements were calculated at a distance of 2.5% of the average grain size behind the crack tip (i.e. $0.025 \times 52.9 = 1.3$ μm). This is consistent with the literature [37, 38].

A thorough study on mesh sensitivity study was performed in [37] resulting in the optimal mesh shown in figure 2.40. The applied mesh underestimated the CTOD and CTSD values by about 4.6% and 8.4% [39], respectively, which is sufficient for this analysis. The applied macroscopic loading and boundary conditions are illustrated in figure 2.40. The left and right edges were loaded in macroscopic monotonic uniaxial tension up to a maximum load of $0.96R_{p_{0.2}}$ (240 MPa) with zero shear traction. The upper and lower edges were traction free.
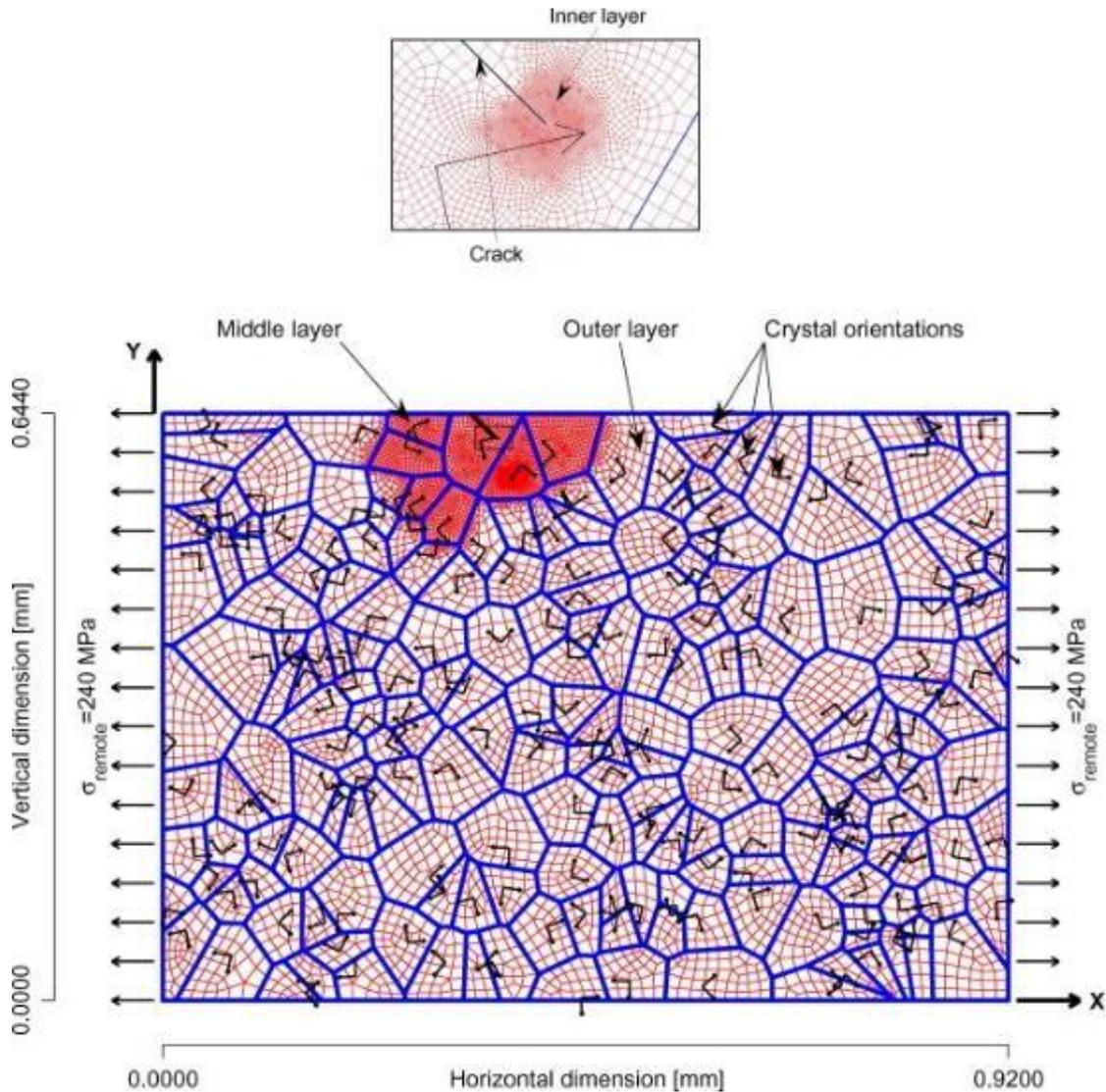
Figure 2-40. The finite element model. Details of the crack tip mesh are shown in the insert [32].

The elastic constants and crystal plasticity parameters for AISI 316L single crystal were taken from the literature [40]: C_{iiii} = 163,680 MPa, C_{iijj} = 110,160 MPa, C_{ijij} = 100,960 Mpa, h_0 = 330 MPa, τ_s = 270 MPa, τ_0 = 90 MPa, n = 55, q = 1.0, and $\dot{a}^{(\alpha)}$ = 0.001. The crack tip displacements and accumulated slip around the crack tip were examined as the crack was extended from the first into the second grain. The sizes of these two grains can influence the crack tip displacements. A larger grain with a favourable orientation will tend to increase the crack tip displacements compared to a smaller grain with the same orientation [41]. In all cases Stage I cracking can be assumed to propagate only along slip planes. The crystallographic orientation of the grain 38 is rotated in anti-clockwise direction by an angle α = 9.735° so that the crack at an angle of ϑ_{38} = 135° falls onto the P2 slip plane. Once the crack extends across the grain boundary (into the grain 124) its length is up to $0.5D_{124}$. D_{124} = 60.78 μm is the size of the grain 124, estimated as a square root of its area. Several crystallographic orientations of the grain 124 were used while placing the crack in either slip plane P2 or P4. Figure 2.41 shows the CTOD and CTSD displacements for crack in grain 124 placed in the slip plane P2. Different crystallographic orientations of grain 124 change the CTOD values by 26% for the

case of the shortest crack. As the crack is extended into the grain 124 this effect becomes much more pronounced. This is to be expected since the crack has to change its direction at the grain boundary. Up to 10 times smaller crack tip displacements were found as the crack crosses the GB. Another important observation is that in all analyzed cases significant CTSD values were observed. Cracks were therefore of mixed mode type.
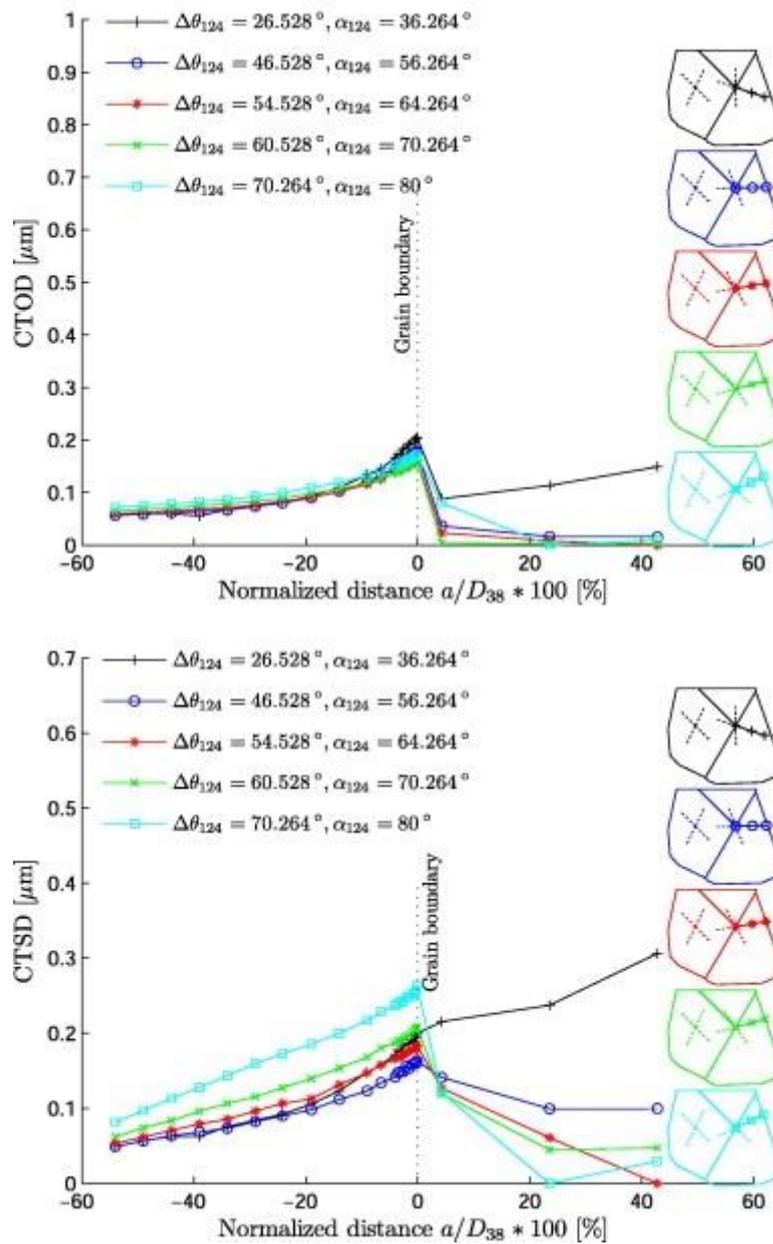
Figure 2-41. The influence of different crystallographic orientations of grain 124 on the crack tip displacements. Crack in grain 124 is placed in slip plane P2 [32].

The crack tip displacements were also calculated for the crack placed along the slip plane P4 in grain 124. It was observed that the crack in grain 124 could propagate almost perpendicular to the external load in this case. Therefore, the CTOD values were larger and the CTSD values lower. It was suggested that the crack would propagate through the slip plane that is more perpendicular to the external load; i.e. P4 and not P2.

The crack propagation rate was measured via the amount of accumulated plastic displacement along the slip system in front of the crack tip [42]. The cumulative slip was calculated upon placing the crack tip in grain 124 and either along slip plane P2 or P4. The accumulated slip steadily increased until the crack reached the GB. For a crack along P2 slip plane, the accumulated slip decreased since the crack turns away from being perpendicular to the applied load, and increased for the crack along P4 slip plane.

To evaluate the influence of random crystallographic orientations on the CTOD 100 cases were generated where for each fixed orientation of grains 38 (9.735°) and 124 (36.264°, 56.264°, 64.264°, 70.264° and 80°) all other grains were randomly oriented. This was done for two different crack lengths: (a) crack located entirely in the grain 38 with crack length $0.5D_{38}$ and (b) crack extended up to half grain 124 size ($0.5D_{124}$). Crack in grain 124 was placed in slip plane P4. For each case a cumulative probability (distribution) function was calculated. For a crack located entirely in grain 38 we see that different lines are very close to each other. This suggests that the orientation of the grain 124 has a relatively small effect on the CTOD values when the crack is contained in the first cracked grain (grain 38). However, the scatter of the results showed that the orientations of grains beyond grains 38 and 124 have a significant impact. Changing the orientations of these grains resulted in a scatter of CTOD values by a factor of 4.4.

The impact of '124' grain orientation increased once the crack is extended into grain '124'. On the other hand, the impact of the orientations of grains beyond grains 38 and 124 on CTOD values decreased- 3.3 compared to 4.4. The ratio between maximal and minimal CTOD is 4.4 if the crack is contained in the first grain. When the crack is extended into the second grain this ratio is reduced to a still significant value of 3.3. With further increase of the crack length the crack would become less and less depended upon the local microstructural features and therefore the ratio would continue to decrease. Two interlinked factors should also be mentioned once the crack is extended into the grain 124. The first is crack deflection. Larger CTODs are obtained when the crack extension in grain 124 is more perpendicular to the external load. Additionally, the crystallographic orientation also affects the stiffness of grain 124. At α_{124} = 36.264° grain '124' has the lowest Schmid factors among the analysed configurations. However, since the crack in this case is more perpendicular to the external load, the CTODs are the highest. As we increase the α_{124}, the Schmid factor increases, but the CTODs decrease. The crack extension direction in this case seems to be the main factor influencing the CTOD.

A thorough study of the small crack growth regime was presented, which gives new insights about the CTOD and CTSD values at the neighbourhood of a small crack. However, strain gradient effects should be incorporated, and real time experiments should be made to further calibrate the model.

2.2.6. *Modeling FCI at particles and inclusion sites*

- *Modeling of subsurface FCI at primary inclusions in heat treated and shot peened martensitic gear steels*

A computational strategy is applied for FCI at subsurface primary inclusions in carburized and shot peened C61 martensitic gear steels [43]. Experimental investigation revealed that fatigue is controlled by subsurface crack nucleation at inclusion clusters under cyclic bending. An algorithm is presented to simulate residual stress distribution induced through the shot peening process following carburization and tempering. Rate- independent 3D finite element analyses were developed to evaluate plastic deformation during processing and service; and to analyze the potency of FCI at subsurface inclusions. Idealised inclusion geometries (ellipsoidal) were considered to study the fatigue crack nucleation potency at various subsurface depths. Three distinct types of second-phase particles were analysed: perfectly bonded, partially debonded, and cracked ones. Parametric studies quantified the effects of inclusion size, orientation and clustering in the high cycle fatigue (HCF) or very high cycle fatigue (VHCF) regimes. The nonlocal average values of maximum plastic shear strain amplitude, $\Delta\gamma^p_{max}$, and Fatemi-Socie (FS) parameter were calculated in the proximity of the inclusions and considered to be the primary driving force parameters for FCI and microstructurally small crack growth. The simulations indicate a strong propensity for crack nucleation at subsurface depths in agreement with experiments in which fatigue cracks nucleated at inclusion clusters, still in the compressive residual stress field. The residual stress distribution, bending stress, and carburized material properties play a vital role in fatigue crack nucleation and small crack growth at subsurface primary inclusions. The fatigue potency of inclusion clusters is greatly increased by prior interfacial damage during processing. Experimental observations were made in a case hardened steel. This is a martensitic steel with predominantly tempered lath martensite microstructure. Increasing the depth from the surface, the carbon content and the microhardness decreased due to the prior heat treatment and shot peening process. Compressive residual stresses exist after shot peening within a thickness of 0.5 mm from the surface and reach a maximum value -1400 MPa, at a depth of 75-100 μm. Fatigue cracks formed at a depth of approximately 200-270 μm below the surface. Analysis indicated that the cracks are formed at clusters of inclusions. Debonding of particles was observed. Inclusion clustering indicates a potential role for inclusion interaction.

Three-dimensional FE analyses were performed to understand the mechanisms of fatigue crack nucleation. The inclusions were assumed to be isotropic, linear-elastic with Young's modulus E = 400GPa and Poisson's ratio m = 0.2. The matrix was modeled as a rate-independent elastic-plastic material with a nonlinear kinematic hardening law. Carbon content has a significant influence on local mechanical properties of the material. Elastic modulus, yield strength and work hardening rate depend strongly on carbon content. Therefore the simulated monotonic tension stress-strain curves varied at various depths in the model for the material considered. The residual stresses introduced by carburization and tempering are much less than those introduced through the shot peening process.

FE simulations for FCI were performed at depths ranging from 75 μm to 300 μm below the surface. Ellipsoidal shapes of inclusions were employed. Figure 2.42 shows a 3D FE mesh with two closely spaced inclusions. A fine mesh is employed close to the inclusion(s) for detailed investigation. All simulations were performed using 4-node 3D tetrahedral elements. The inclusion sizes are small enough so that the gradient of applied stress and residual stress over the scale of an inclusion is negligible. The stress state is imposed at discrete depths within the subsurface inclusion- matrix volume element. The driving forces for crack nucleation were calculated.
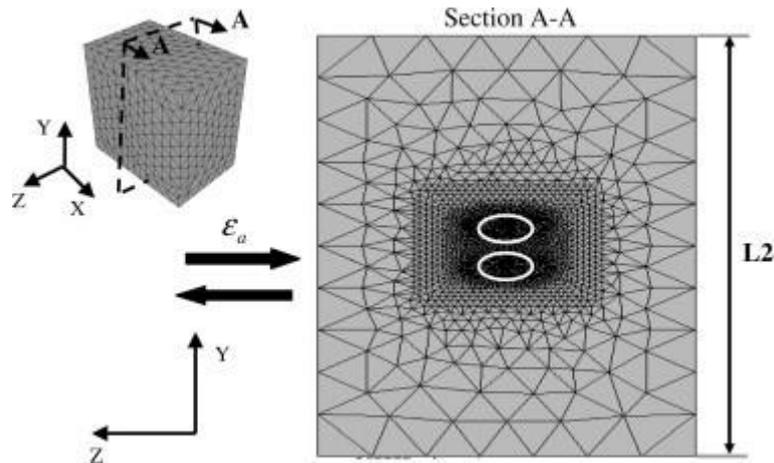
Figure 2-42. Cross-section of FE mesh through the center of inclusion with refinement close to the inclusion [43].

Two parameters, namely the nonlocal average maximum plastic shear strain range, $\Delta\gamma^{p}_{max}{}^{*}$, and the Fatemi–Socie (FS) parameter, were considered as the main driving force parameters. The maximum plastic shear strain amplitude was averaged over 1 μm^3, which corresponds to 10% of the volume of an inclusion size; this particular volume corresponds to the notch root that maximizes the nonlocal plastic shear strain amplitude; to evaluate the probability to form a crack. Within the nonlocal averaging region, the nonlocal average plastic shear strain and non-local maximum cyclic plastic shear strain range are calculated. A volume average was performed in the nonlocal region in order to calculate the nonlocal FS parameter. Coffin-Manson law was used to correlate the number of cycles for nucleation of fatigue cracks.

Simulations on intact ellipsoidal inclusions were performed and results showed negligibly small driving force. Plastic strain intensification was observed to depend on the size of the inclusion and inclusion spacing. The maximum values correspond to a depth of about 250 μm below the surface, observed also in experiments. Note that this depth is still within the regime of initial compressive residual stress. The driving forces were negligibly small at depths between 75 and 150 μm even though the applied strain amplitude was high. The shot peening process suppresses the fatigue crack nucleation at the surface and shifts the crack nucleation site further in the interior. The nonlocal maximum plastic shear strain amplitude, $\Delta\gamma^{p}_{max}$, and FS parameters were also calculated for cases with two cracked inclusions closely spaced (for two different geometrical configurations). The trends

were similar but the values were an order of magnitude higher depending on the size and interaction of inclusions. The potency of fatigue crack was most pronounced at lower stress levels than at stress levels above macroscopic yielding.

Analyses were performed involving partially debonded inclusions. Variations for $\Delta\gamma^p_{max}$ and nonlocal FS parameter were observed with depth. Comparing with the case of intact interfaces, the driving force for FCI was higher for the case of partially debonded inclusions. The debonded inclusions showed greater crack initiation potencies also from the cracked inclusions. Again it was observed that the size and spacing of partially debonded inclusions played a significant role in fatigue crack nucleation potency. The presence of large inclusions had more detrimental effect upon fatigue.

This study is rather specialised to a specific material made by specific processing route, and studies the effect of subsurface inclusions and therefore cannot be applied for a range of crystalline material where FCI occurs within the matrix or for materials subject to high loads during cyclic fatigue which favours damage within the matrix rather than at inclusion sites.

- *Modelling microstructurally small fatigue crack formation in AA 7075-T651*

Hochhalter et al studied the fatigue crack nucleation process in an AA 7075 T651 aluminium alloy [44-46]. AA 7075 T651 is an age-hardened alloy, strengthened by non-shearable - Al_7Cu_2Fe- precipitates. The sample dimensions may be seen in figure 2.43. Damage initiation was observed to occur at the interface between particles and matrix. Particles were found to be already broken from the manufacturing process or usually cracked within the first fatigue cycles. Therefore the resistance of the crystalline matrix to crack initiation is crucial. As shown in figure 2.43 microstructurally small fatigue crack (MSFC) growth phase consists of 3 main stages: i) crack incubation where cracking occurs within particles, ii) crack nucleation in the matrix and iii) microstructurally small propagation. These 3 stages have been found to account for 50-70% of the total fatigue lifetime.

Hochhalter et al used a crystal plasticity approach to model the matrix deformation and resistance to crack growth. No cracks were modelled explicitly, while damage parameters -Nucleation Metrics- were identified in order to predict the occurence of damage in preferential orientations. 5 Nucleation Metrics were used and were found to correlate well with damage initiation potency and crack orientation preference (Table 2.5). D1 represents the maximum accumulated slip Γ^α over each slip system, D2 is the maximum accumulated slip Γ^α over each slip plane, D3 is the maximum accumulated slip Γ^α over all slip systems, D4 is the maximum energy dissipated on a given slip plane over a cycle and D5 is a modified Fatemi-socie parameter ($\langle - \rangle$ are Macaulay brackets defined such that only tensile stress has an effect on crack propagation).
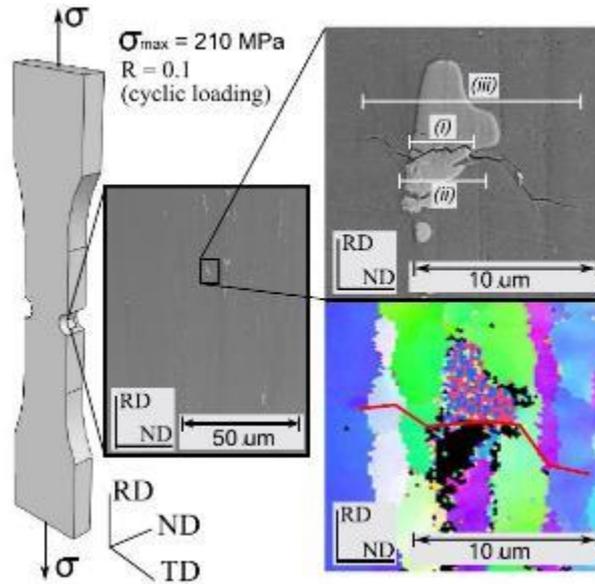
Figure 2-43. The geometry of the samples, showing also the 3 stages of MSFC phase [45].

Nucleation Metrics

$$\Gamma^\alpha = \int_0^t |\dot{\gamma}^\alpha| \, dt$$

$$D_1 = \max_\alpha \Gamma^\alpha$$

$$D_2 = \max_p \Gamma^p$$

$$D_3 = \Gamma = \sum_{\alpha=0}^{N_s} \Gamma^\alpha$$

$$D_4 = \max_p \int_0^t \sum_{\alpha=0}^{N_d} \left| \dot{\gamma}_p^\alpha \tau_p^\alpha \right| \, dt$$

$$D_5 = \max_p \int_0^t \sum_{\alpha=0}^{N_d} |\dot{\gamma}_p^\alpha| \left(1 + k \frac{\langle \sigma_n^p \rangle}{g_o} \right) \, dt$$

Table 2-5. Nucleation Metrics used for the MSFC stage [45].

The model geometry may be seen in figure 2.44. A 3D cube representing a single grain was employed with an ellipsoid particle embedded in order to represent correctly the early stages of fatigue damage. Different mesh sizes were used in order to quantify the effect of mesh size, the particles already had a crack in the middle, and a non-local arc was used at the crack front to avoid mesh dependencies at the crack tip. A mesh sensitivity study was performed to use the appropriate value for the arc radius; which was related to the crack dimension, a, of the incubated crack (figure 2.45).

Two values were selected for the arc radius: 0.10a and 0.25a; and the results are shown in figure 2.46. By comparing the nucleation metrics for the 4 levels of mesh refinement in figure 2.46, it can be seen that the results for the fine and concentrated refinement meshes produce acceptably similar results. Moreover it was found that all the values for the 5 metrics were qualitatively similar along the non-local arc (figure 2.47).
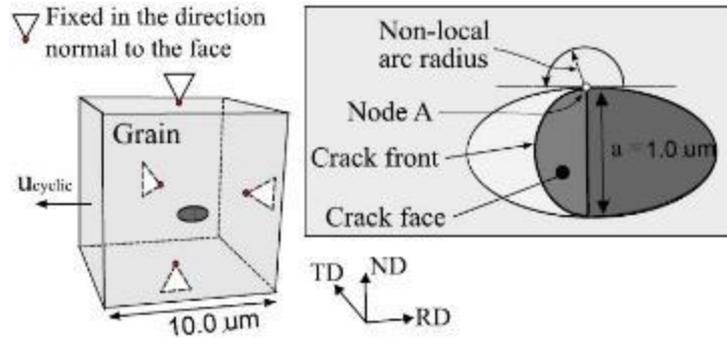
Figure 2-44 Single grain with embedded particle baseline model configuration [45].
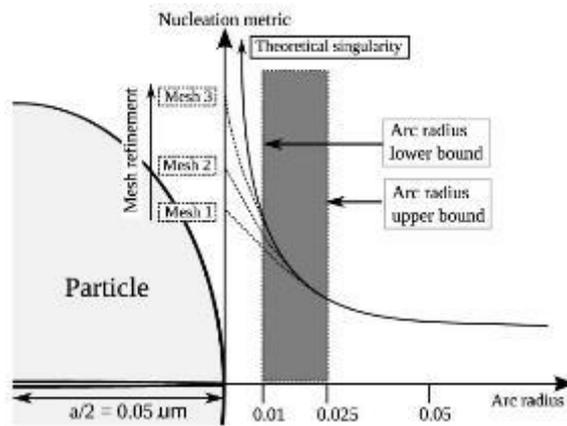
Figure 2-45. Schematic diagram showing the effect of the non-local arc radius on convergence [45].
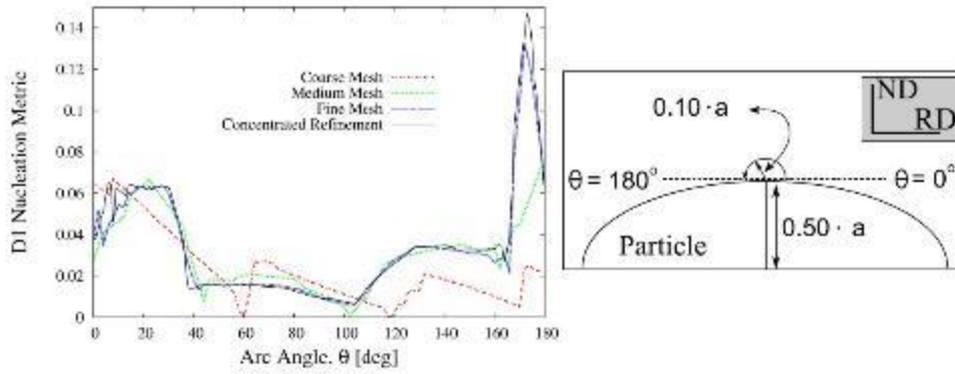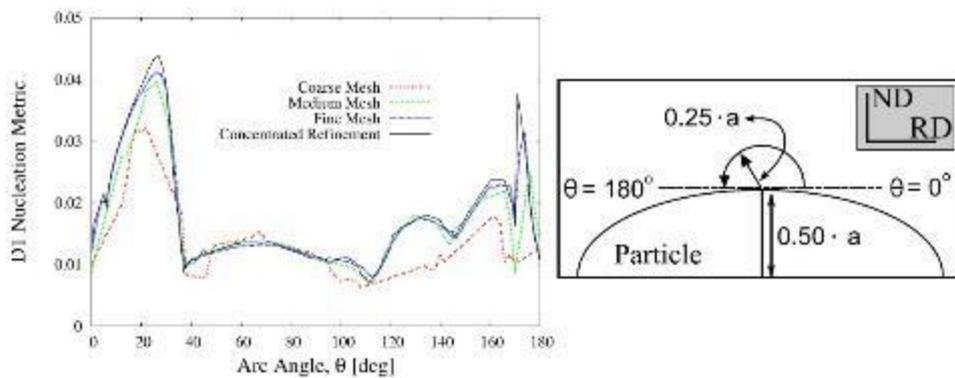
Figure 2-46. D1 Nucleation Metric versus arc angle for 4 levels of mesh refinement; for arc radius a) 10% and b) 25% of the crack dimension a [45].
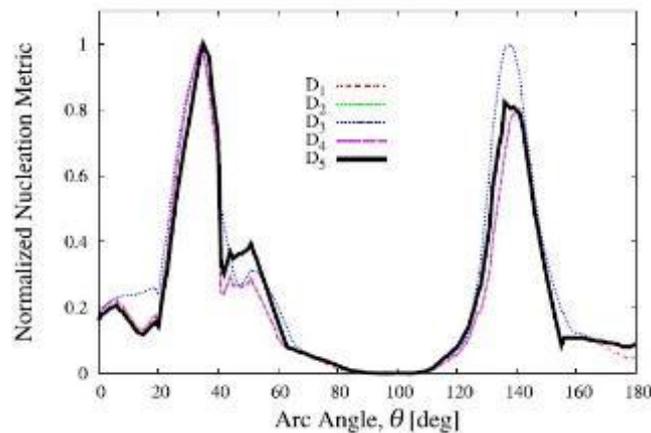
Figure 2-47. A plot of the 5 Nucleation Metrics. Each metric was normalised by its maximum value along the non-local arc (for non-local arc=25% a) [45].

Figure 2.47 highlights the effect of the angle, θ, on the corresponding values for the 5 metrics. While the effect of grain orientation on the localisation of the nucleation metrics, D_1-D_5, is shown in figure 2.47. Figure 2.48(a), (c) and (e) show the D_1 scalar field at the peak of the first cycle. Figure 2.48(b), (d) and (f) display the directions of the two slip systems with the highest Schmid factor. The corresponding values of Schmid factor m are also shown along these slip systems; and it may be seen that the D_1 localisation contours align well with the corresponding slip systems with high Schmid factors.
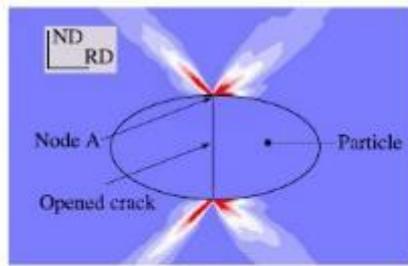
(a) D_1 metric color contour for Orientation A
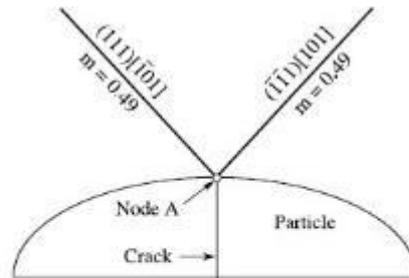
(b) Illustration of the 2 slip systems with the highest Schmid factor, m, in Orientation A.
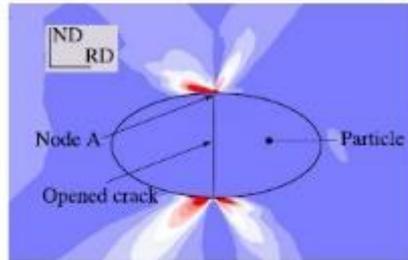
(c) D_1 metric color contour for Orientation B
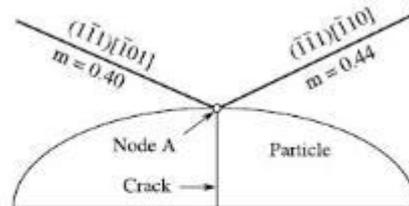
(d) Illustration of the 2 slip systems with the highest Schmid factor, m, in Orientation B
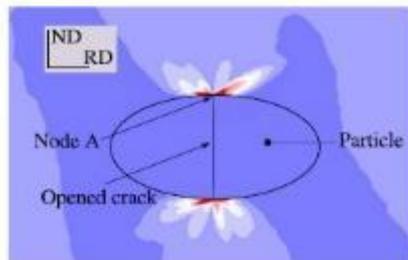
(e) D_1 metric color contour for Orientation C
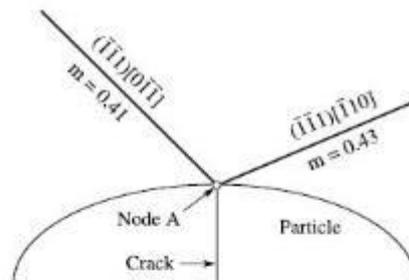
(f) Illustration of the 2 slip systems with the highest Schmid factor, m, in Orientation C
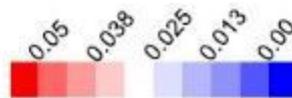
Figure 2-48. D_1 contour plots at the peak of the 1st cycle; showing the effect of grain orientation on localization. The two critical slip systems with the highest schmid factors are also shown [45].

Figure 2.49 shows the accumulation of slip during the course of concecutive fatigue cycles for 3 different grain orientations (a, b and c). It can be seen that the slip localisation field is very different in each case. Finally, EBSD experiments were performed to create a model with the actual geometry of the microstructural features such as grain size, particle size and shape, grain orientation. The results are shown in figure 2.50 and 2.51, and it can easily be seen that the proposed Nulceation metrics and the critical slip systems identify efficiently the occurence of cracking at the experimentally-observed orientations.
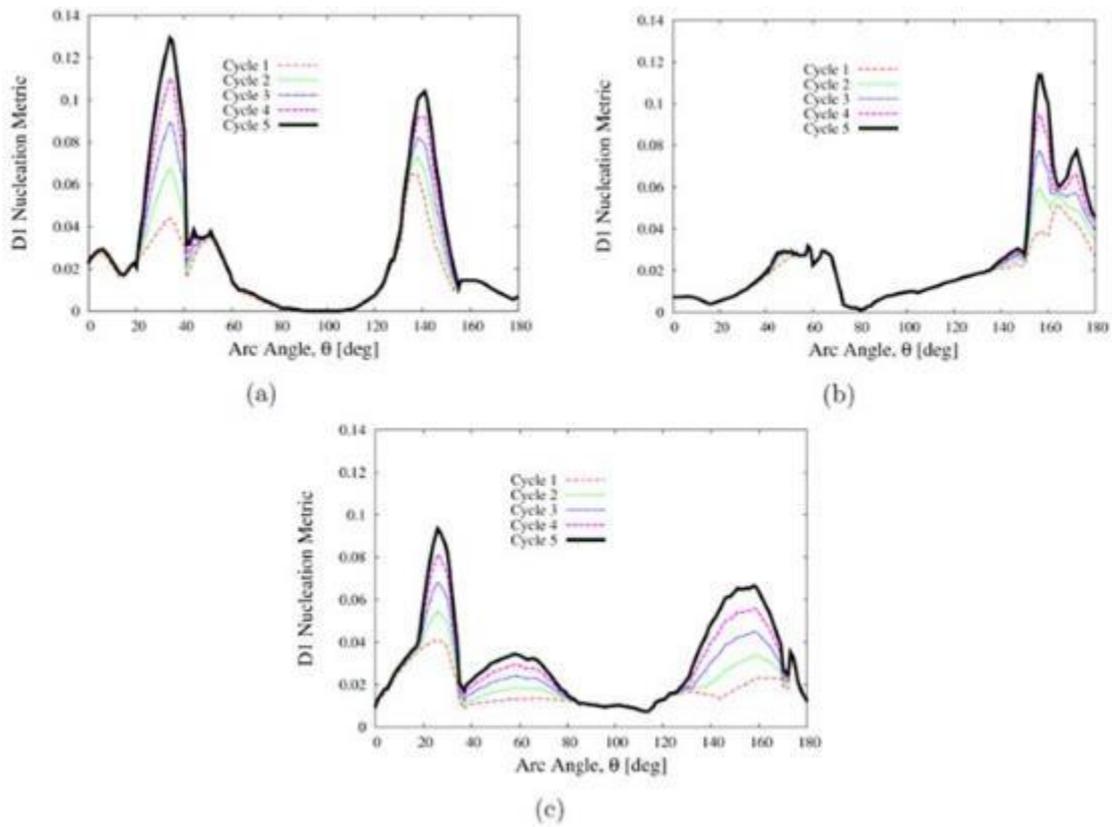
Figure 2-49. D1 localisation and accumulation for 5 concecutive cycles; for 3 different grain orientations [45].
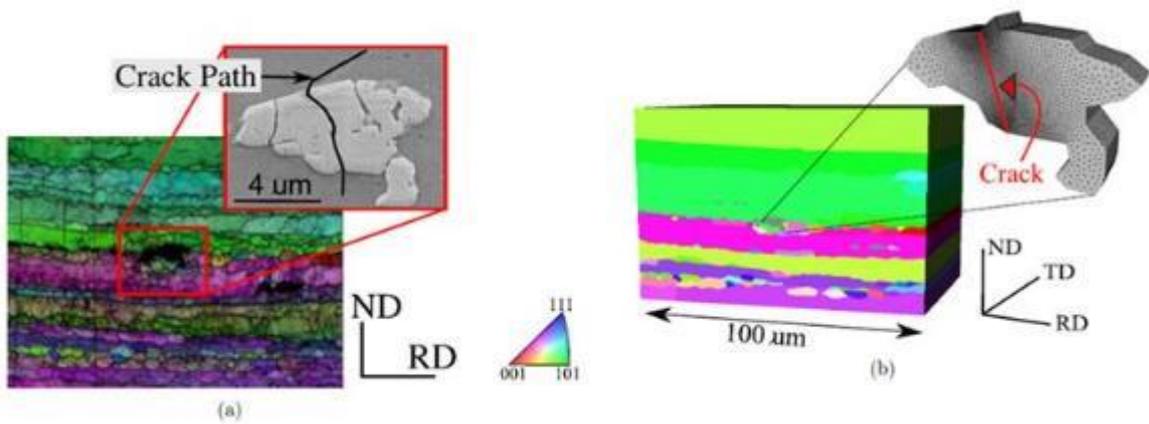
Figure 2-50. Finite Element Model generated from experimental data [45].
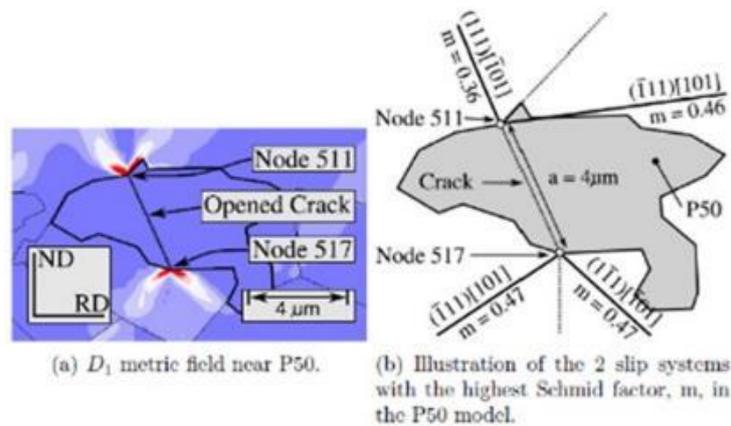
Figure 2-51. D1 localisation fields at the first peak load [45].

This study has focused on FCI at second phase particles, however real time measurements have not been made to compare with and validate the model. Furthermore it does not evaluate the small crack growth regime and the rates of crack growth. However it investigates intensively the stress and strain fields in the neighbourhood of a crack at a particle sites and provides useful insight about mesh sensitivity problems near the tip of the crack.

Summary

A broad spectrum of modeling techniques has been presented in this chapter and is available in the literature. Further modeling methods can also be found in the literature such as ab initio or molecular dynamics but these models are out of the scope of this work which tries to bring light towards the engineering applications of the area of fatigue and specifically of FCI. In this broad spectrum of work, models based on discrete dislocations have been presented, which bring insight into the micro-mechanisms of FCI, but are rather computationally expensive to be applied to real 3-dimensional polycrystal and real structures. On the opposite side of the spectrum, from a computational point of view, lie models based simply on the Tanaka-Mura relationship and the use of specific slip planes where cracks can develop. However it was suggested that these models are over-simplified and are not able to predict the critical locations for FCI. More advanced crystal plasticity models have then been presented even though they currently remain rather computationally expensive. Yet they are able to predict critical locations where damage should be expected in a polycrystalline material. Furthermore by employing dislocation based crystal plasticity (using dislocation densities) it was possible to obtain the exact location where FCI occurs in several case studies employing a 4-point bending test with a sample containing a notch. Specifically the material contained rather large grains, and an oligocrystal was modeled only at the edge of the notch. It was shown that dislocation based crystal plasticity can be advantageous in some cases over traditional crystal plasticity for modeling FCI. In section 2.2.4 the small crack growth regime was modeled, and the crack potency along specific slip planes was evaluated. Furthermore the CTOD and CTSD values were obtained to further understand the mechanisms of small crack growth. However real time experimental measurement

were not obtained to validate the modeling parameters. In the last section modeling FCI at particle and inclusion sites was presented. It was shown that the meshing techniques in the neighbourhood of a particle can be quite difficult. The stress-strain values obtained can also be rather inaccurate depending on the distance that those are measured from the crack tip of a cracked particle. Real time measurements are also needed in this case to further validate these models and understand the underlying physics.

The main focus of this work was therefore to try to fill the gaps that have been identified above within the literature. With respect to FCI, several 'FIP' have been used widely [8-10, 13-14, 21-23], yet it is not clear which of these parameter is the most reliable, and can serve as a criterion for FCI. Moreover in reference [15] the model predicted FCI only within a small region of 1-3 grains.

Multi-scale experimental fatigue testing including cyclic bending tests in a SEM combined with modern characterisation techniques such as DIC and EBSD to analyse fatigue crack initiation and propagation in the microstructure of a commercial aerospace grade alumimium alloy in relation to local orientations and strain distributions have been carried out in this work and will be presented in the following chapters. Analysis of the effect of microstructural features such as inclusions/particles, grain orientation and distributions, slip band and shear band formation as well as mechanical fields such as strain distributions on fatigue crack initiation and propagation can then be used to understand FCI in this material. Physical insight gained from this analysis can then be used to inform a CPFE model, aiming to predict FCI and therefore the total life time of the specimens more accurately.

Experimental Procedures & Materials

In this study, the fatigue crack initiation behavior of alluminium alloys was investigated experimentally and theoretically (from a modelling perspective). Particularly, the mechanical behavior of Al2024 T3 alloy was investigated across different length scales. In this chapter, all the experimental equipments and techniques employed in this work are presented.

3.1. Material codes, specimen geometries and tensile testing equipment

The material investigated is the aluminium alloy Al2024 T3. Three types of specimen geometries were used in this study. A tensile specimen geometry for obtaining the macroscopic mechanical properties of the Al2024 T3, and for investigating the FCI behavior of Al2024 T3 under (tension-tension) fatigue loading. The same sample geometry was employed also for macro- and meso-scale characterisation and is shown in figure 3.1a. The specimens were designed according to ASTM E8 standards. A 4-point bending sample geometry was employed for microscale investigation in order to facilitate crack initiation at the sample top surface (figure 3.1b). A 1mm hole was drilled throughout the full thickness of the sample at the centre of the top surface (AB surface) in 2 of the 4 point bending samples in order to facilitate FCI. Finally, a specimen geometry for fully reversed fatigue loading was designed and is shown in figure 3.1c.
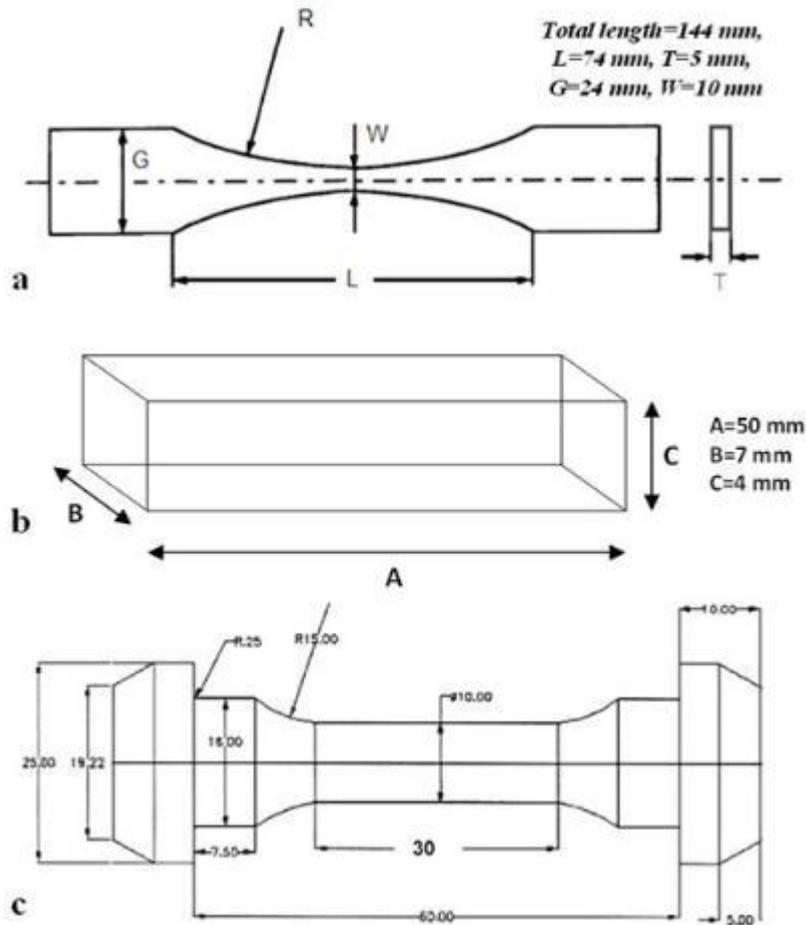
Figure 3-1. a) Specimen geometry for tensile and fatigue (tension-tension) experiments, b) for 4-point bending, and c) for fully reversed fatigue loading.

3.2. Sample Preparation and scanning electron microscopy

Prior to microstructural inspection, the samples were mechanically ground and polished down to 0.06μm (with Silico). A fine finish surface quality was necessary to remove any surface scratches prior to EBSD measurements. Electropolishing was then performed in a solution containing 30% Nitric acid and 70% Methanol, for 13 seconds, at -16° C, 15V and 10mA. EBSD measurements were carried out using a FEI-Sirion SEM, at 20kV and spot size 5 as operating conditions. The step size varied depending on the observed grain size in each case. After the EBSD measurements, the specimens were re-polished with Silico for 4 minutes, to remove any Hydrocarbon (HC) deposition during EBSD-measurement acquisition. Initial experiments revealed that a considerable amount of HC deposition occurs on the surface of the sample at the scanned area (EBSD map-region), which causes SEM imaging problems. Figures of HC deposition are shown in Appendix B. Mechanical polishing with Silico for only 4 minutes was sufficient to remove the HC deposition. The samples were then etched with Keller's reagent (95ml water, 2.5ml Nitric acid, 1.0ml Hydrochloric Acid and 1.5ml Hydrofluoric acid) for approximately 4-5 seconds, to reveal microstructural features such as GBs, particles and inclusions. Not in all the samples EBSD measurements were obtained, and in the specified samples only polishing and etching was performed. An etched microstructure is shown in figure 3.2. The GBs

have been successfully revealed while the particles and inclusions appear black as they have been over-etched due to their chemical composition.

Images of the Electron Microscopy equipments used in the present work are shown in figure 3.3a-d. 4 different microscopy equipments were employed for different purposes described in Table 3.1. For in situ studies CamScan S2 was employed due to the large vacuum chamber facilitating the ease of importing mechanical testing equipment into the chamber. The CamScan S2 system can be seen in figure 3.3a. A Voltage of 15 kV with a spot size of 3nm, and a working distance of 40 were employed in all tests. The magnification varied depending on the purpose of each study, while brightness and contrast were kept constant throughout each test to facilitate accurate DIC measurements. During the consecutive images upon a mechanical test in the SEM chamber, focusing needs to be adjusted, especially if high magnifications are employed. This is due to the fact that the material is displaced out of the focusing plane, resulting in out of focus images. Furthermore for the vertical bending equipment the sample moves vertically, so the focusing plane shifts significantly. The errors related to this process were minimised by using as small as possible working distance. The closer the sample is located with respect to the beam head, the more parallel the electron beam, and therefore the imaging errors from refocusing are reduced.

For the EBSD measurements a FEI Sirion FEG-SEM system was employed and is shown in figure 3.3b. The Voltage and spot size were always set at 20kV and 5nm respectively. The working distance was 14 mm, at which the EBSD detector was calibrated. The hitting rate was always above 92% for the samples included in this work. Channel 5 software was used for the post-processing of the orientation data: for grain orientations, minimising the zero solutions (areas where no indexing was obtained), obtaining the inverse pole figures and the overall texture. An example image of the Euler map for Al2024 is shown in figure 3.5.

Finally, for high resolution metallurgical inspections an Inspect-F FEG-SEM was employed which can acquire images at high magnification with the highest sharpness and contrast (figure 3.3d). Finally, for quantitative chemical analysis (EDS) a JEOL JSM 6400 SEM was employed which is calibrated to yield very accurate quantitative measurements for the composition present within the matrix or at particle and inclusion sites.
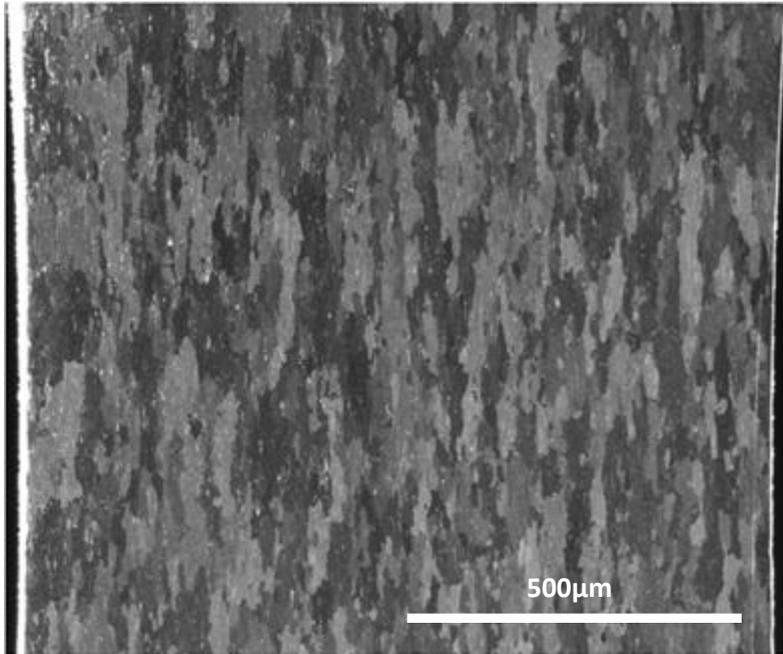
Figure 3-2. Etched microstructure of Al2024.

Table 3-1. SEM equipments used with respect to the purpose of the investigation.

SEM equipment	Purpose
CamScan S2	Micromechanical testing
FEI Sirion FEG	EBSD measurements
Inspect-F FEG	High-resolution imaging
JEOL JSM 6400	EDS analysis

Figure 3-3. SEM equipments used: a) Inspect-F FEG, b) JEOL JSM 6400, c) CamScan S2 and d) FEI Sirion FEG.
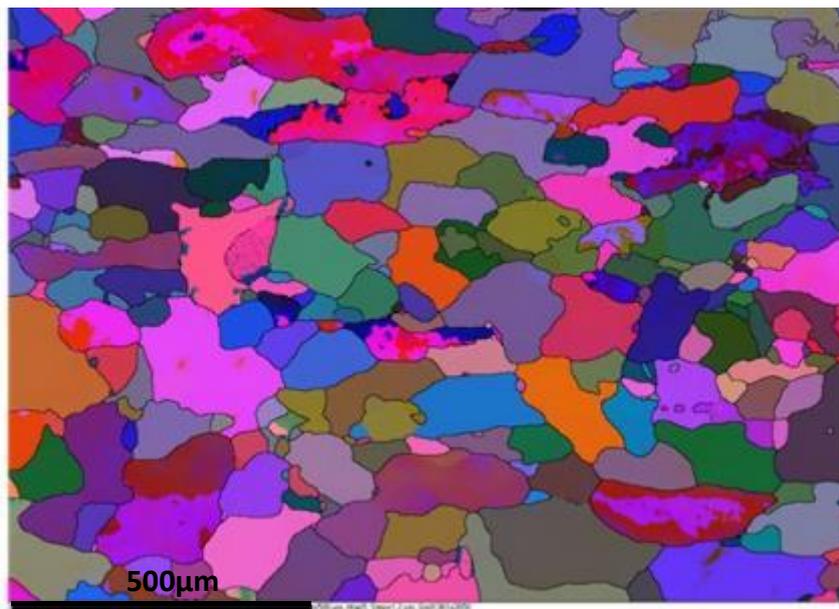
Figure 3-4. Euler map of Al2024.

3.3. Multiscale Mechanical testing

Tensile testing was performed with an electromechanical Mayes DM 100 machine (see figure 3.4) and in situ DIC and strain gauge measurements were obtained to accurately acquire the mechanical behaviour of Al2024 T3. For fatigue testing, a hydro-mechanical Instron 8501 was employed (figure 3.6). Fatigue testing under load controlled conditions was used. In situ DIC measurements were taken with a specially designed set-up particularly for this purpose. A stereo microscopy light was used at a small distance from the sample (just 10-14mm) in order to provide adequate light for the microstructure, and reveal the microstructural features. In this case the microstructural features act as the tracking particles in the DIC. More details on the DIC procedure can be found in the next section 3.4.

Figure 3-5. Electromechanical Mayes DM 100 tensile testing equipment.

Figure 3-6. Instron 8501 hydraulic machine.

3.3.1.   In situ micromechanical bending test

A 2kN Deben vertical bending equipment was employed for the in situ studies and is shown in Figure 3.7. It is a 3-point and 4-point bending equipment, but for this study the 4-point bending configuration was employed for the samples shown in figure 3.1b. The micro-mechanical tester was inserted into the SEM chamber of CamScan S2, and in situ imaging was employed during 4-point bending fatigue testing. The mechanical tester was initially calibrated in house with standard specimens provided by TATA steel. The Deben software was employed but modified and calibrated for the specific set-up (importing the micro-bending tester in the CamScan chamber). Importing such a large component into a SEM chamber requires a lof of time to reach proper vacuum conditions; i.e. below 5×10^{-5} Torr. Therefore the equipment was imported into the chamber and left overnight to reach high vacuum conditions. Prior to that the micro-bending equipment was checked outside the chamber, the sample was placed central conditions. Prior to that the micro-bending equipment was checked outside the chamber, the sample was put centrally and a small load was placed on the sample to avoid any slippage between the sample and the clamp. The equipment was slidden onto the stage. It is necessary to place the micro-bending equipment onto the stage in order to be able to move it freely into the chamber. During testing the sample moves vertically, but also slight movements occur horizontally as the sample deforms and the microstructure is stretched and laterally contracted along the perpendicular direction.

There are several parameters that need to be set during the test. Initially the parameters for a static test are introduced, in order to deform the sample to the maximum displacement. The displacement rate (2mm/min), maximum displacement (5.5mm), data recording data rate (0.5/sec), and the time or displacement increments upon which correlation images will be acquired (20 seconds interval) have to be determined by the user. Subsequently, once the specimen has travelled to the maximum displacement, a cyclic test is set up. The static test represents the first quarter of the first cycle. At this stage the user has to set the frequency (0.5 Hz), the minimum displacement (4mm), the total number of cycles (500 or 700 cycles) and the cycles upon which the test will be stopped at maximum displacement (1st cycle, 10th, 100th, 200th, 300th, 400th, 500th, 600th and 700th) and SEM images will be acquired for image correlation.
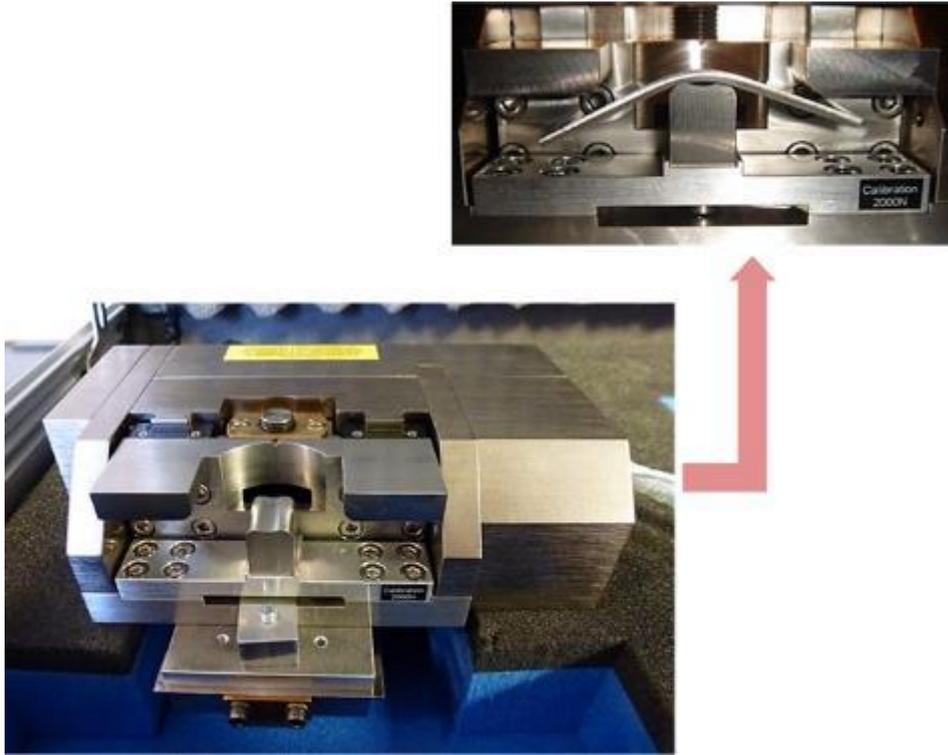
Figure 3-7. Deben vertical bending equipment

3.4. Digital Image Correlation

Digital Image Correlation (DIC) is an optical method that acquires consecutive images of the surface of the sample and then calculates the displacements at any given point. It is mainly used to measure displacements, deformations and strains on the surface of a specimen at different length scales in 2D and 3D space. This chapter is based on references [47, 48] and only key principles will be presented in the following sections, further information on DIC theory and applicabilities may be found in [47, 48].

DIC techniques have recently found increased popularity, being employed across all length scales from macroscale down to the nano-scale. The displacement fields have been obtain for various complicated testing geometries, due to the robustness, high accuracy and easiness of the technique. Furthermore, advances in computer technology and digital cameras have enabled the rapid development of the technique. DIC has now been extended to almost any imaging technology (SEM, TEM etc) [49-52].

3.4.1. Theoretical background

DIC is based on maximising the correlation coefficient, which is defined by examining the pixel intensity array subsets of two or more corresponding images and obtaining the deformation mapping function that relates the corresponding images (figure 3.8). Iterative techniques (nonlinear optimisation techniques) are used to minimise the 2D correlation coefficient. The cross correlation coefficient **r$_{ij}$** is defined as:

$$r_{ij}\left(u, v, \frac{\partial u}{\partial x}, \frac{\partial u}{\partial y}, \frac{\partial v}{\partial x}, \frac{\partial v}{\partial y}\right) = 1 - \frac{\sum_i \sum_j [F(x_i, y_j) - \bar{F}][G(x_i^\star, y_j^\star) - \bar{G}]}{\sqrt{\sum_i \sum_j [F(x_i, y_j) - \bar{F}]^2 \sum_i \sum_j [G(x_i^\star, y_j^\star) - \bar{G}]^2}} \qquad (3.1)$$

where F(x_i,y_j) is the pixel intensity at a point (x_i,y_j) in the undeformed image. G(x_i^*,y_j^*) is the pixel intensity at a point (x_i^*,y_j^*) in the deformed image, $\overline{F}$ and $\overline{G}$ are the mean values of the corresponding intensity matrices F and G. Similar to the cross correlation coefficient, the least squares correlation coefficient could be used; further details on the DIC theoretical background can be found in reference [47]. The coordinates of the points (x_i,y_j) and (x_i^*,y_j^*) are given by the deformation that occurs between the two images. If the motion is perpendicular to the optical axis of the camera, then the relation between (x_i,y_j) and (x_i^*,y_j^*) can be approximated by:

$$x^\star = x + u + \frac{\partial u}{\partial x}\Delta x + \frac{\partial u}{\partial y}\Delta y$$
$$y^\star = y + v + \frac{\partial v}{\partial x}\Delta x + \frac{\partial v}{\partial y}\Delta y$$

(3.2)

where u and v are the corresponding translations of the centre of the sub-image in the X and Y directions, and Δx and Δy are the distances from the center of the sub-image to the point (x, y), respectively. Thus, the correlation coefficient r_{ij} is a function of the displacement components (u, v) and gradients:

$$\frac{\partial u}{\partial x}, \frac{\partial u}{\partial y}, \frac{\partial v}{\partial x}, \frac{\partial v}{\partial y}$$

(3.3)

The same principles can be applied to 3D DIC. In this case two or more cameras are employed to capture the three-dimensional surface of the sample (figure 3.8). Subsequently the three-dimensional deformations on the surface of the sample (such as sample necking) can be captured quite accurately. The whole procedure is based on calibrating the images obtained by all cameras and correlating them with the initial ones (reference images).
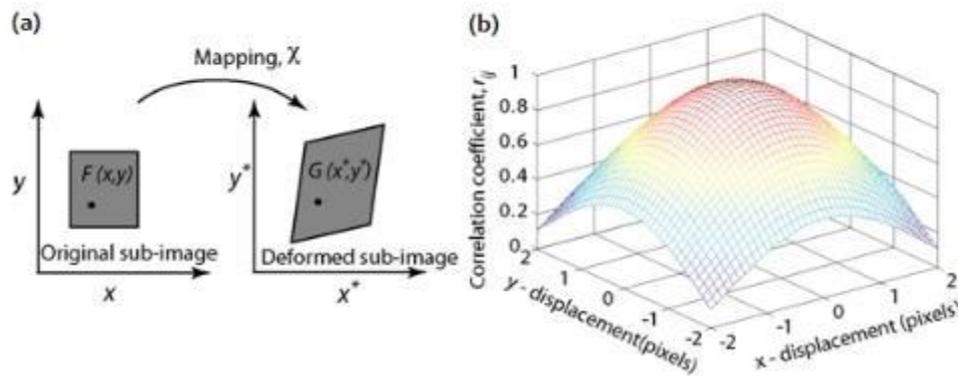
Figure 3-8. Basic concept of DIC [48].

3.4.2. System Set-up and technical details

In general a DIC system comprises of a camera, two light sources on the sides of the specimen and a computer for storing and processing further the images (figure 3.9). The camera with the CCD (small

photosensitive cells for high pixel count) array records the intensity of the light falling on a pixel. The array in the high resolution camera is rectangular with thousand or more pixels per line and a thousand or more lines per image. In figure 3.10 a 3x3 pixel is shown. The signal from the CCD array is digitised and gives a reading of the light intensity for each pixel. Intensity readings are shown as 0 for black pixels and 100 for white pixel (on a grey scale). The storage of the image into pixels and combination of pixels is called convolution.

To locate the target from intensity data on pixel array, DIC uses an intensity pattern matching method called correlation. This is done by defining the subset of pixels that surround the key feature of the target. Matching two similar patterns in two successive images before and after a deformation step establishes the desired target displacement (see figure 3.11). The surface of the sample needs to be sprayed in order to introduce unique patterns on the surface and facilitate the acquisition of the displacement fields during the test. If a target with a uniform colour was used, then it would be impossible to obtain the displacement plots. A unique shape for each point is necessary; and this is achieved with the so-called "speckles". Each speckle should cover at least a 3x3 pixel area [47, 48]. If the speckle is very small for example, and completely dark or white, it would be impossible to locate its position after deformation. The speckles can be introduced by spraying the surface of the sample with a white primer spray, and by lightly spraying on top of this layer a second layer of black paint; see figure 3.12. A picture was taken and is shown in figure 3.13 from a sprayed specimen to obtain a more realistic view of the speckle patterns.
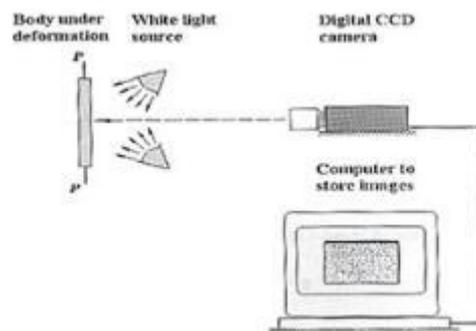
Figure 3-9. DIC set-up system for one camera.
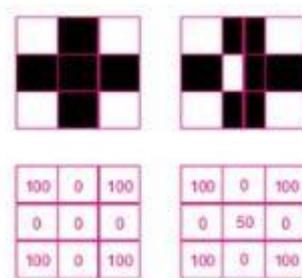
Figure 3-10. A 3x3 pixel with the dark and light pixels assigned to the corresponding numbers (0-50-100) for DIC analysis.
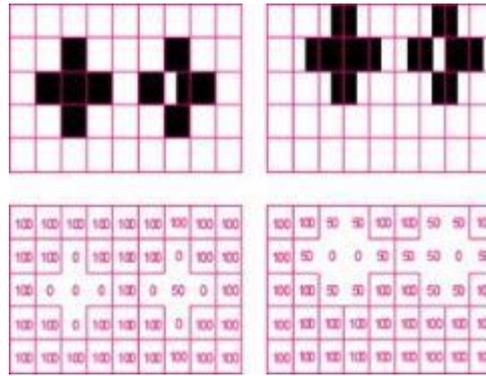
Figure 3-11. Obtaining the displacements by locating and matching the corresponding patterns.
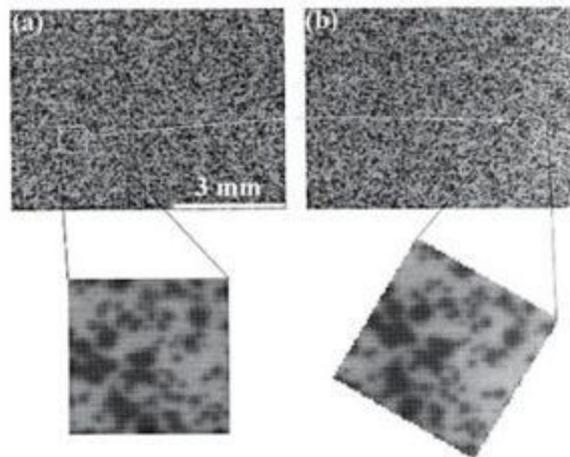
Figure 3-12. Speckle patterns for DIC image processing.

Figure 3-13. The sample after spraying with white and black paints.

A last point to be discussed about the theory and application of DIC, is the set-up for performing a 3-dimensional Image processing. Sometimes the specimens are not flat, or even when they are flat, out-of plane displacements occur during testing, so 3-dimensional analysis is needed. In order to do this, instead of using one camera, two cameras are used with a certain distance between them, creating a certain angle with the axis perpendicular to the specimen (figure 3.14). Images from the surface of the sample are simultaneously obtained from different angles, gaining a 3-D view of the deformation. The user can even employ more cameras and cover the 360^0 area and obtain the displacements of the whole surface around the sample. Both 2-D and 3-D DIC set-ups were used in this project.
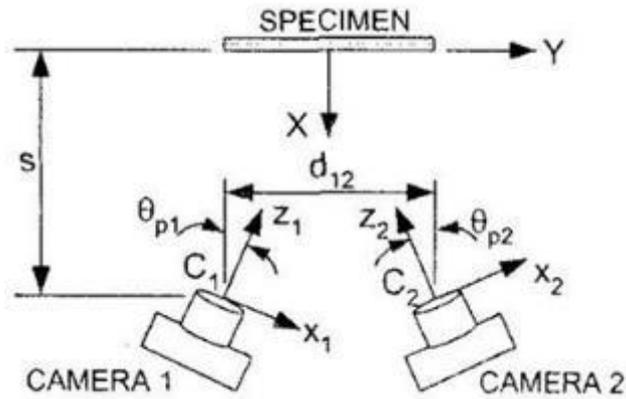
Figure 3-14. System set-up for 3D DIC.

Figure 3-15. 3D DIC set-up with 2 cameras.

3.4.3. **Microstructural-level DIC**

Multiscale DIC experiments were pursued in this study. Apart from the macroscopic DIC set-up shown in figure 3-15, microstructural-level DIC configurations were employed to reveal the role of the microstructure on strain localisation and damage nucleation. Micromechanical testing equipments were imported into the SEM chamber as explained in section 3.3.1 and a series of high magnification SEM images were taken at the same microstructural location during straining in order to capture the microscopic deformations and local strains. The surfaces of the samples were polished down to 0.05 micron and then etched prior to mechanical testing. In this case the microstructure, such as grain boundaries, inclusions, particles and precipitates were employed as the tracking patterns for the image correlations. So the paint speckle patterns showin in figures 3-12 and 3-13 were not employed here. In order to validate the technique an IF steel sample was polished and etched, and then a gold grid with 5 micron pitch was layed over the surface as explained in [53]. Tensile testing up to failure was performed and the test was regurarly interrupted to capture SEM images in order to capture the evolution of the microstructure upon consecutive straining. Strain maps were then obtained by employing the displacement of the nodes of the grids and by using the LaVision software with 32x32 multiscale interrogation windows and the results are shown in figure 3-16 [50, 53]. The strain maps

obtained from the two techniques yield similar results, demonstrating the reliability of using the DIC technique at the level of the microstructure.
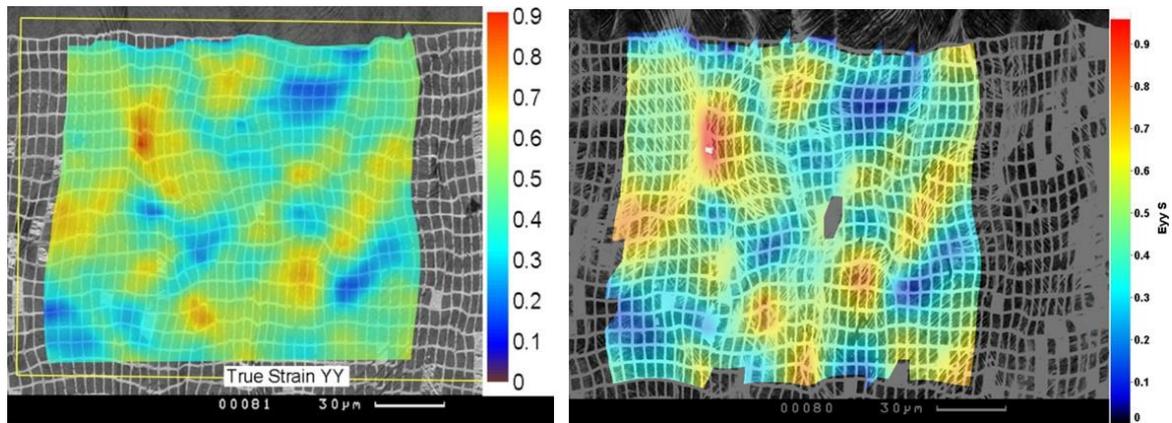
Figure 3-16. DIC Strain map obtained: a) with the microgrid technique, b) with LaVision software [53].

Modeling Procedure

In order to model deformation and fatigue, a thorough understanding of the principles of continuum mechanics is essential. A brief description of linear elasticity, plasticity and hardening laws is outlined in section 4.1; which provides the foundations for the more specialised models used in fatigue modeling, while the crystal plasticity theory, the creation of geometrical polycrystals with the Voronoi technique, and polycrystal modelling are presented in section 4.2.

4.1. Stress-Strain, Yield Criteria & Hardening laws

In general, stress is not uniformly distributed over the cross section of a material body, and consequently the stress at a point in a given region is different from the average stress over the entire area. Therefore it is necessary to define the stress not over a given area but at a specific point in the body. So the stress at any point in a continuum object is defined by nine components (2nd order tensor components) σ_{ij}, known as the Cauchy stress tensor σ:

$$\sigma = \begin{pmatrix} \sigma_{11} & \sigma_{12} & \sigma_{13} \\ \sigma_{21} & \sigma_{22} & \sigma_{23} \\ \sigma_{31} & \sigma_{32} & \sigma_{33} \end{pmatrix} \equiv \begin{pmatrix} \sigma_{xx} & \sigma_{xy} & \sigma_{xz} \\ \sigma_{yx} & \sigma_{yy} & \sigma_{yz} \\ \sigma_{zx} & \sigma_{zy} & \sigma_{zz} \end{pmatrix} \equiv \begin{pmatrix} \sigma_x & \tau_{xy} & \tau_{xz} \\ \tau_{yx} & \sigma_y & \tau_{yz} \\ \tau_{zx} & \tau_{zy} & \sigma_z \end{pmatrix} \quad (4.1)$$

where i, j=1,2,3. For an infinitesimal element of volume within a stressed solid, the stress components may be seen in figure 4.1.
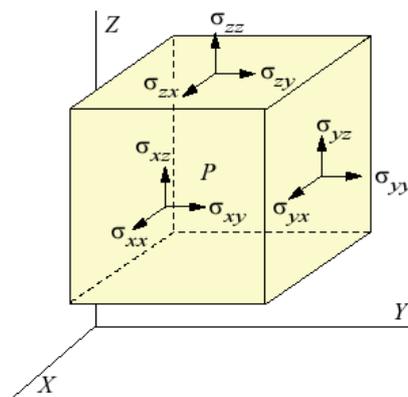
Figure 4-1. Definition of stress components on an infinitesimal volume element.

the σ_{11}, σ_{22}, and σ_{33} are called normal stresses, and the remaining shear stresses. For every stress state there is one set of coordinate axes where the shear stresses vanish. The corresponding normal stresses along these axes are called principal stresses: σ_1, σ_2, σ_3. The principal stresses can be calculated from the 3 roots of:

$$\sigma_p^3 - I_1 \cdot \sigma_p^2 - I_2 \cdot \sigma_p - I_3 = 0 \qquad (4.2)$$

$$where:$$

$$I_1 = \sigma_1 + \sigma_2 + \sigma_3 \qquad (4.3)$$

$$I_2 = \left(\sigma_1 \cdot \sigma_2 + \sigma_2 \cdot \sigma_3 + \sigma_3 \cdot \sigma_1\right) \qquad (4.4)$$

$$I_3 = \sigma_1 \cdot \sigma_2 \cdot \sigma_3 \qquad (4.5)$$

where I_1, I_2, I_3 are called stress invariants. Upon applying a force onto a material body, the material deforms, reacting to the imposed load. Figure 4.2 shows 3 basic cases of strain. In the first 2 cases the load is applied perpendicular to the surfaces, while in the 3rd case the load is of shear type.
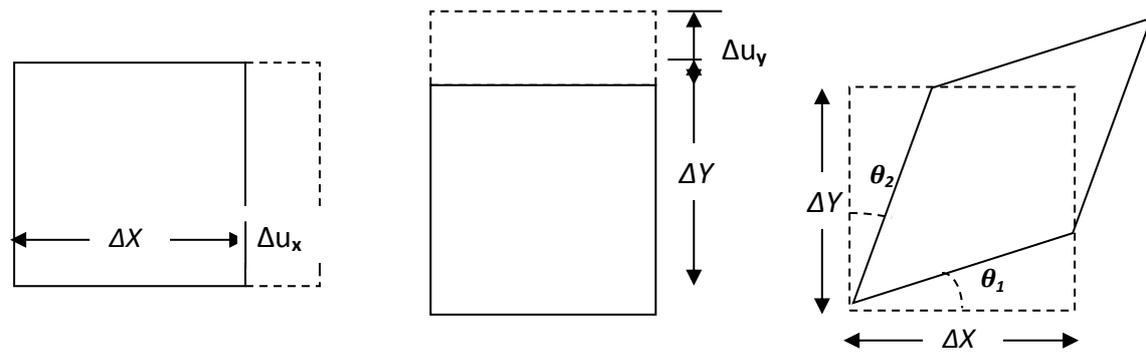
Figure 4-2. a) Uniaxial extension in the x-direction, b) Uniaxial extension in the y-direction and c) Pure shear without rotation ($\theta_1=\theta_2$).

By applying different displacements to the initial rectangular, different deformed shapes are obtained, as shown in figure 4.2. The corresponding relations for the extensions in the x- and y-direction and for the shear mechanism may be seen below:

$$\varepsilon_{xx} \approx \frac{\Delta u_x}{\Delta X}, \quad \varepsilon_{yy} \approx \frac{\Delta u_y}{\Delta Y} \qquad (4.6)$$

$$and$$

$$\gamma_{xy} = \theta_1 + \theta_2, \quad \varepsilon_{xy} = \frac{1}{2} \cdot \gamma_{xy} \approx \frac{1}{2} \cdot \left(\frac{\Delta u_x}{\Delta X} + \frac{\Delta u_y}{\Delta Y}\right) \qquad (4.7)$$

The relation between stresses and strains is obtained by the so-called Constitutive equations. In the case of Linear Elasticity, the material obeys Hooke's law:

$$\sigma_{ij} = C_{ijkl}\, \varepsilon_{kl} \qquad (4.8)$$

where C is the elasticity tensor. In the case the tensor is constant along every direction the relation becomes:

$$\sigma = E \cdot \varepsilon \qquad (4.9)$$

where E is Young modulus. For uniaxial tension: $\sigma_1>0$ and $\sigma_2=\sigma_3=0$. So $\sigma_1 = E \cdot \varepsilon_1$, while:

$\varepsilon_2=\varepsilon_3=-v\,\varepsilon_1$, where v is the Poisson's ratio. For $\sigma_1,\sigma_2,\sigma_3\neq0$: Hooke's law becomes:

$$\varepsilon_{11} = \frac{1}{E}\left[\sigma_{11} - v(\sigma_{22} + \sigma_{33})\right] \qquad (4.10)$$

$$\varepsilon_{22} = \frac{1}{E}\left[\sigma_{22} - v(\sigma_{11} + \sigma_{33})\right] \qquad (4.11)$$

$$\varepsilon_{33} = \frac{1}{E}\left[\sigma_{33} - v(\sigma_{11} + \sigma_{22})\right] \qquad (4.12)$$

$$\varepsilon_{12} = \frac{1}{2G}\sigma_{12}, \quad \varepsilon_{13} = \frac{1}{2G}\sigma_{13}, \quad \varepsilon_{23} = \frac{1}{2G}\sigma_{23} \qquad (4.13)$$

where G is the shear modulus. In most engineering cases, loads exceed the elastic region, and the material deforms plastically, under large deformations. The extent of deformation in the plastic region is considerably higher compared to the elastic strain for the case of metallic materials. A typical stress-strain curve obtained from a tensile test may be seen in figure 4.3.
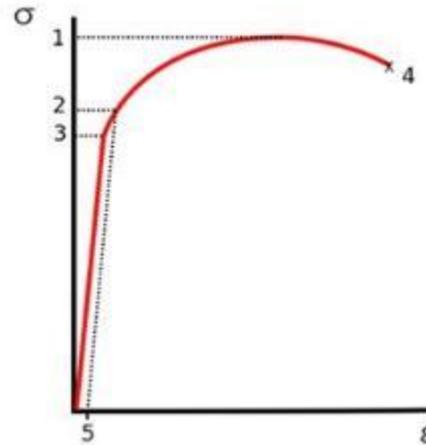
Figure 4-3. Stress-strain curve obtain from a typical tensile experiment.

Upon loading, the specimen is loaded elastically up to the point (σ_2, ε_5). Further increase in the stress/ strain (load/displacement) leads to plastic deformation (onset of plastic flow). At point 1, the specimen reaches its highest strength and further loading to point 4 leads to its final fracture. For strains above point 1, the deformation is non uniform as necking takes place.

The total strain imposed on an elastic-plastic solid ε, can be written as the sum of the elastic and plastic strains: $\varepsilon=\varepsilon_e+\varepsilon_p$. Any general plasticity theory has the following major components:

1. A yield criterion, specifying the onset of plastic deformation for different loading conditions/stress components. The Von Mises and Tresca yield conditions are the most widely used yield criteria for isotropic materials (see figure 4.5).

2. A hardening rule, which relates work hardening and the updated yield condition with the current state of plastic deformation.

3. A flow rule, describing the relation between the increments of plastic deformation or rate of plastic deformation with stress components.
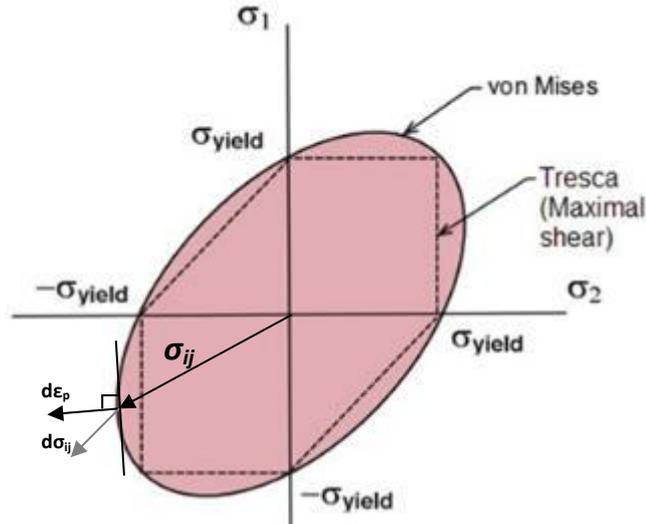
Figure 4-4. Von Mises and Tresca criteria for a 2-D stress state.

The yield criterion postulates that the onset of plastic deformation will initiate once the stress state reaches the yield surface (see figure 4.5). So any given combination of stress states on the corresponding yield surface implies that the material is under plasticity conditions. For an isotropic material, the general relation is as follows:

$$f\left(\sigma_{xx},\sigma_{yy},\sigma_{zz},\tau_{xy},\tau_{yz},\tau_{zx}\right)=C \ , with \quad C=constant \qquad (4.14)$$

Rewritten for principal stresses:

$$f\left(\sigma_1,\sigma_2,\sigma_3\right)=C \qquad (4.15)$$

The mean hydrostatic stress does not influence yielding and is given by:

$$\sigma_m=\frac{\sigma_1+\sigma_2+\sigma_3}{3} \qquad (4.16)$$

The Tresca criterion corresponds to the trapezoid in figure 3.5 and is given by:

$$\sigma_{max}-\sigma_{min}=C=2k \ , \quad k=constant \qquad (4.17)$$

The Von Mises criterion corresponds to the ellipse in figure 3.5 and is given by:

$$\left(\sigma_1-\sigma_2\right)^2+\left(\sigma_2-\sigma_3\right)^2+\left(\sigma_3-\sigma_1\right)^2=6k^2=C \qquad (4.18)$$

As may be seen in figure 4.5 the Tresca criterion is more conservative with respect to the Von Mises criterion. For 3-D stress states the corresponding yield surfaces may be seen in figure 4.5. The coordinate axes are given by the values of principal stresses. The Von Mises surface corresponds to a circular cylinder, while the Tresca criterion to an hexagonal prism; the surfaces parallel to the π-plane. The π-plane corresponds to the condition: $\sigma_1 + \sigma_2 + \sigma_3$=0. The axis perpendicular to the π-plane corresponds to the magnitude of the hydrostatic stress.

During plastic deformation, the rate of energy dissipation is non-negative, given by:

$$\sigma_{ij}\cdot d\varepsilon_{ij}^p \geq 0 \qquad (4.19)$$

This condition implies that for a stress point at the yield surface, the incremental strain component should be directed outward of the yield surface (see figure 4.4), and perpendicular to the respective surface, while the incremental rate of stress component should also have a certain angle with the strain vector. For the Tresca criterion, at a corner point, the above criterion must be applied separately to the 2 surfaces intersecting the corner.
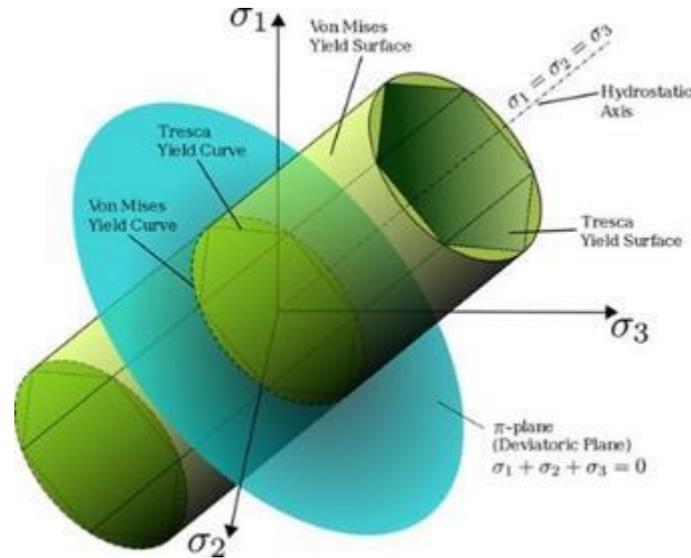
Figure 4-5. 3-D image of the yield surface for a 3-D stress state.

This normality is reflected by the flow rule:

$$d\varepsilon_{ij}^p = d\lambda \cdot \frac{\partial f}{\partial \sigma_{ij}}$$ (4.20)

dλ is a positive scalar and f is the plastic potential.

It is important to clarify the effect of plastic deformation onto the shape and position of the yield surface. The simplest model is the so-called isotropic hardening model, which implies that the yield surface expands uniformly and has a fixed shape expanding outwards keeping its center fixed (see figure 4.6a). The relation between deformation and the size of yield surface is given by:

$$\sigma_e = h\left(\int d\overline{\varepsilon}^p\right)$$ (4.21)

Where h is a function between the 2 scalars. Using the Von Mises criterion leads to:

$$\sigma_e = \sqrt{\frac{3}{2} s_{ij} \cdot s_{ij}}$$ (4.22)

While the effective plastic strain is:

$$d\overline{\varepsilon}^p = \sqrt{\frac{3}{2} d\overline{\varepsilon}_{ij}^p \cdot d\overline{\varepsilon}_{ij}^p}$$ (4.23)

An alternative equation for isotropic hardening may be given by using the total plastic work along the actual strain path:

$$w_p = \int \sigma_{ij} \cdot d\overline{\varepsilon}_{ij}^{\ p}$$

<div align="right">(4.24)</div>

But the use of isotropic hardening leads to limitations, as in reality for a typical tension-compression deformation, there are differences observed for the elastic limit between forward and reverse loading. In an attempt to account for this effect, Bauschinger effect, the kinematic hardening rule has been proposed [54]. For kinematic hardening, the yield surface does not change its shape or size, but simply translates in stress space in the direction of its normal (see figure 4.6b).
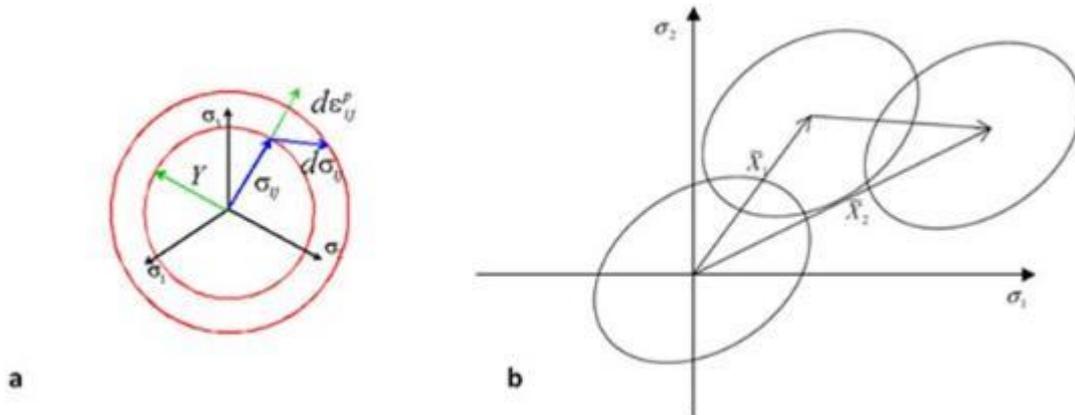
Figure 4-6. a) Isotropic hardening behaviour: Yield surface outward expansion, b) Kinematic hardening (same shape-same size).

4.2. Crystal Plasticity

In this section the basic concepts of crystallography are introduced. The crystal structure of metallic materials is outlined, followed by the physics of deformation of single crystals. Afterwards, the basic phenomenological formulas are presented, which shape the modern theory of single crystal and polycrystal plasticity.

4.2.1. Crystal structure

Crystallography is the scientific branch that reveals the arrangement of atoms within a solid material. Metals have crystalline structure, which means that the atoms are situated in a repeating array over a long range. To describe crystalline structures, atoms are imaged as hard spheres sitting next to each other with different patterns. The minimum repeating pattern is defined as a unit cell. The 3 basic crystal structures - Face-Centered (FCC), Hexagonal Closed-Packed (HCP) and Body-Centered Cubic (BCC) crystalline structures - are shown in figure 4.7. Copper, aluminium, and nickel alloys have FCC crystal structures, while iron has a bcc crystalline structure. Some other metals, like zinc, titanium, magnesium, have HCP crystal structures.

The mechanical properties of metals depend largely on their crystalline structures and defects such as dislocations. In early studies large discrepancies were found between the theoretical strength of metals and the actual measured values for strength [8]. In 1930s, this discrepancy was attributed to the existence of special features, named dislocations. A dislocation is a crystallographic defect, or

irregularity within a crystal structure. There are two types of dislocations: edge dislocations and screw dislocations; but there can also be mixed dislocations which are a combination of the above two types. In figure 4.8 the 2 basic types of dislocations can be seen. The direction and magnitude of the corresponding lattice distortion due to the presence of a dislocation is given by the Burgers vector, denoted by vector b.

Dislocations may be observed by using transmission electronic microscopes. The variations in the density of dislocations for engineering materials vary a lot: from 10^3 m^{-2} to 10^{10} - 10^{15} m^{-2} for heavily deformed metals. To understand how large the above numbers are, a 1 cm^3 of metallic material may have more than 10^{10} cm length of dislocations, which means that in 1 cubic centimetre there are approximately 100.000 km of dislocations. Planet earth has equatorial circumference just above 40.000 km.

When the material is subjected to loads higher than the yield point, plastic deformation initiates and dislocations start to glide on slip planes along certain slip directions; this process is called slip. Dislocations glide on certain crystallographic planes along certain slip directions causing plastic deformation. A combination of slip plane and direction forms the so called slip system. Different crystal structures have different numbers of slip systems. FCC crystalline structure has 12 slip systems, which are the combination of the {111} slip plane family and the (110) slip direction family; the notations here follow the Miller index notations, which is a widely established tool for crystallographic representations. For the BCC crystalline structure, there are 48 slip systems. In general, the gliding resistance for an FCC structure is much lower than that for a bcc structure as the spheres are closer together (FCC is a denser crystal with respect to BCC) [8]. This means that the dislocations within a FCC crystal structure are easier to slide than dislocations in a BCC crystal. So FCC materials can undergo plastic deformation more easily than BCC materials.
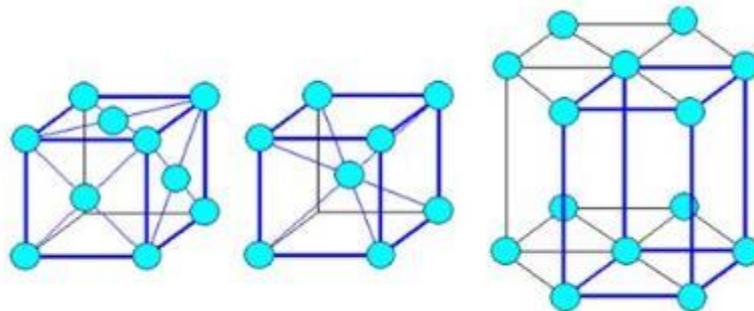
Figure 4-7. Three basic crystal structures; FCC, BCC, HCP.
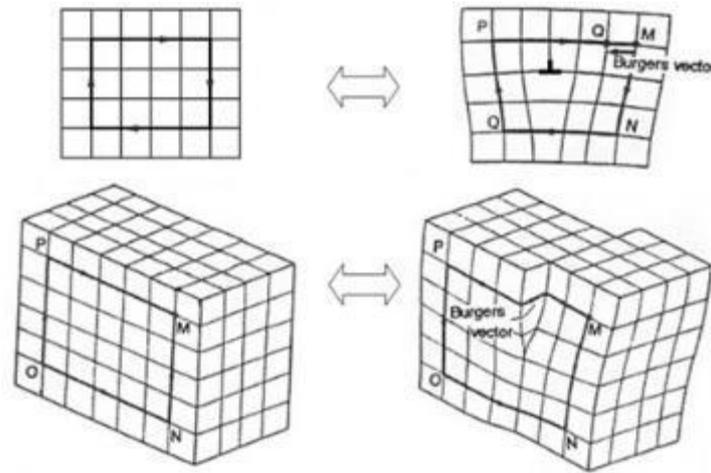
Figure 4-8. The two basic types of dislocation within a lattice: edge and screw dislocation.

The theory of plastic deformation within single crystals is called single crystal plasticity theory; but most materials consist of more than one crystal. Many crystals joined together make the metallic matrix; these crystals have different orientations and in many cases different chemical compositions and different mechanical behaviours. Therefore in the real microstructure of a metal, we may see many grains-crystals, separated by grain boundaries (figure 4.9). The size and shape of grains varies significantly. In order to be able to model the behaviour of such polycrystals, understanding the mechanical behaviour of single crystals is quite essential.

Figure 4-9. Metallic microstructure.

4.2.2. Deformation of single crystals

Single crystals are highly anisotropic, slip and deformation occurs along specific crystallographic planes. The physical parameters that determine the deformation of a single crystal are: the resolved shear stress and the critical resolved shear stress, which represents the difficulty for a dislocation to glide along a specific slip plane and direction [8]. In figure 4.10a, a cylindrical single crystal specimen loaded in uniaxial tension under a traction force P can be seen.

The n and b are defined as the unit vectors normal to the slip plane and along the slip direction respectively, and ϕ_0 and λ_0 the corresponding angles between the n and b vectors and the loading

axes. Resolving the force T along the slip direction and dividing by the area of the slip plane leads to the following expression for the initial resolved shear stress:

$$\tau_{R_0} = \frac{P}{A} \cos \varphi_0 \cos \lambda_0 = \sigma \cos \varphi_0 \cos \lambda_0 \qquad (4.25)$$

The onset of plastic deformation occurs when the resolved shear stress acting along the slip direction on the slip plane reaches a critical value, τ_c:

$$\sigma \cos \varphi_0 \cos \lambda_0 = M\sigma = \tau_c \qquad (4.26)$$

The above relation is named Schmid law, and M the Schmid factor. M has a maximum value for $\varphi_0=\lambda_0=45^0$. Upon slip, the single crystal deforms and changes its shape (figure 4.10b). The initial gauge length vector changes both direction and magnitude, from ℓ_0 to ℓ (initial and instantaneous gauge length). So the resolved shear strain can be written as:

$$\gamma_R = \frac{1}{\cos \varphi_0} \left[\sqrt{\left(\frac{l}{l_0}\right)^2 - \sin^2 \lambda_0} - \cos \lambda_0 \right] \qquad (4.27)$$

In an actual tensile experiment, the two vectors ℓ_0 to ℓ are confined to remain parallel and along the loading axis. Consequently, a rotation of the slip plane and slip direction occurs towards the loading direction, decreasing the initial φ_0-λ_0 angles. The instantaneous value of the resolved shear stress may be expressed by:

$$\tau_R = \frac{P}{A} \cos \varphi_0 \sqrt{1 - \left(\frac{l_0 \sin \lambda_0}{l}\right)^2} \qquad (4.28)$$
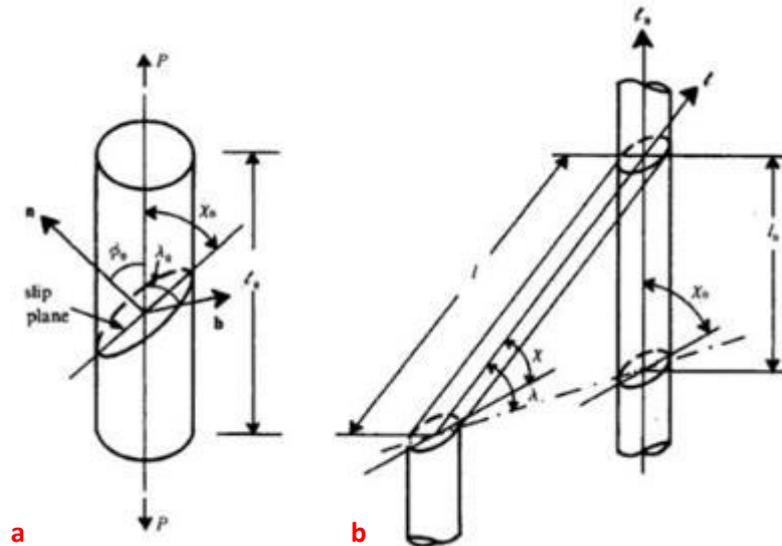
Figure 4-10. a) A single crystal with the associated slip plane and direction. b) Change of the shape of the single crystal due to slip [8].

τ_R increases monotonically with increasing the elongation of the crystal; this phenomenon is called geometrical softening. It is stated that rotation of the slip plane and direction occurs only under monotonic loads; for reversed loads (fatigue loading) no orientation changes occur [8].
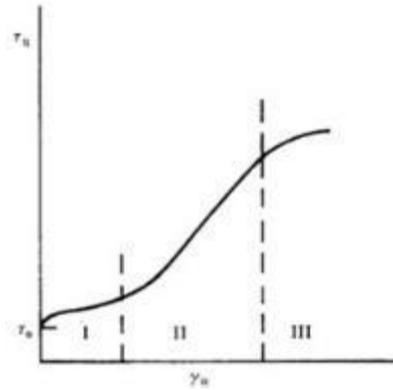
Figure 4-11. A stress - strain curve for an FCC single-crystal, and the 3 regimes of deformation [8].

In figure 4.11, a typical stress-strain curve for an FCC single- crystal, under uniaxial tension can be seen. There are 3 distinct regimes in figure 4.11. Stage I initiates at τ_o (limit of elastic deformation), and it is characterised by easy glide. Primary slip occurs and the slip lines appear straight and uniformly spaced. As the crystal deforms further and the slip systems rotate, secondary slip is activated. The decrease in the mean slip distance initiates Stage II regime, where the crystal undergoes significant work hardening. In the later stages of Regime II, the formation of cell structures is promoted (networks of dislocations at grain boundaries). A further increase in the load, gives the dislocation enough energy to overcome-circumvent the barriers by cross slip (process by which a screw dislocation can move from one slip plane to another). Therefore all the microstructural barriers formed in the previous stages become redundant. So the onset of cross slip in Stage III leads to a reduction in work hardening. Materials with high stacking fault energies (materials with increased mobility of dislocations, such as Aluminium) have high propensity for cross slip, and exhibit pronounced Stage III deformation even at low load conditions.

4.2.3. Single Crystal Plasticity

Crystal plasticity is a very complex subject due to the scale of the phenomena occurring, the geometry and imperfections of the crystal structure, the deformation of the metallic crystal structure that occur in a highly anisotropic manner, favouring specific slip systems, and the mathematical laws that are capable of describing such complicated phenomena. The initial studies forming the basis of the theory go back to Taylor's work [55], while modern single crystal formulations are based mainly on the work of Hill, Rice and Asaro [56-60].

The most important problems related to crystal plasticity modelling are described in this paragraph. Kinematics and constitutive relations have been built and developed over the last 30 years; but three main problems are still encountered in crystal plasticity theory. How can we determine which slip systems are active and how the increments of plastic strain in each active slip system can be determined as these were described in the work of Pierce et al in 1982 [61]. A 3rd problem arises from the multiplicity of slip systems in crystals which leads to solutions that are not necessarily unique. When the constitutive equations are numerically solved on boundary value problems, these three features in rate-independent plasticity lead to numerical problems. The first numerical

calculations for a rate-independent single crystal were performed by Peirce et al in 1982 [62]. The absence of a strategy to determine the active slip systems and the amount of respective slip, resulted into singular stiffness matrices and subsequent numerical instabilities. To overcome the limitations of the rate-independent crystal plasticity, Asaro and Needleman developed a rate-dependent crystal plasticity model, which uniquely predicts the constitutive response for an arbitrary deformation history [63, 64].

In the formulation of Asaro et al, all slip systems are always active and slip occurs at a rate which depends on the resolved shear stress and slip resistance [57]. For a certain external force, the resolved stress may be obtained, and so the plastic increments on all slip systems are uniquely determined. In their model, no restriction in the form of the $h_{\alpha\beta}$ hardening matrix is required. The $h_{\alpha\beta}$ hardening matrix determines the effect on the hardening rate on slip system α due to a plastic increment on another slip system, namely β (the diagonal terms, $h_{\alpha\alpha}$, account for the self-hardening effect and the off-diagonal terms, $h_{\alpha\beta}$, for latent-hardening or the interaction between the slip systems). All the terms in the matrix are deformation history-dependent.

There has been considerable recent progress in the extension of Asaro et al's model to solve the important boundary value problems, however the rate-dependent formulation leads sometimes to calculations that are very time consuming. Currently, research is concentrated into developing a robust calculation scheme to determine the active slip systems, the corresponding plastic increments and the unique solutions for rate-independent theory of crystal plasticity [63, 65].

Several authors have made great contributions on formulating a numerical algorithm to solve rate-independent crystal plasticity and these have been described also in the PhD thesis of Luo [63]. During the last decade, these solution methods have been further developed and extended to study crystallographic texture and lattice rotation for single and poly-crystals during uniaxial monotonic or cyclic loading. The last 20 years concentration has been given on the concept of strain gradient plasticity [63]. But still the research of Asaro et al provides the main framework of the kinematics and constitutive relations for finite strain crystal plasticity [19].

Huang in 1991 [19] based on the work of Asaro et al [57], wrote a user-material subroutine that incorporates single crystal plasticity formulations into a finite element code. This led to a fast growth of the research field; it brought the interest of the industry and it was extended into many emerging fields: fatigue, creep, fracture, thermomechanical processing and many others which are overviewed in reference [65]. This research project is based on the work of Huang; with some minor modifications that were necessary to accurately predict the behaviour of the alloy during cyclic loading.

Kinematics, Constitutive & Hardening laws

In this section the kinematics, the constitutive laws, the hardening laws of rate dependent crystalline materials, and the incrementation scheme are discussed.

The displacements in a crystalline solid are caused and can be calculated via the so called deformation gradient F. The total deformation of a crystalline material is decomposed into an elastic and a plastic part (see figure 4.12):

$$F = F^e F^p = F^e F^*$$

(4.29)

where F_p denotes plastic deformation due to slip - no shape change of the crystal lattice occurs by shear, while F_e is responsible for lattice stretching and rotation caused by elastic deformations; lattice becomes distorted. The elastic deformation, F_e, shows the reversible response of the lattice to external loads and displacements, while the plastic deformation, F_p, is the irreversible permanent deformation that appears even after unloading of the system.
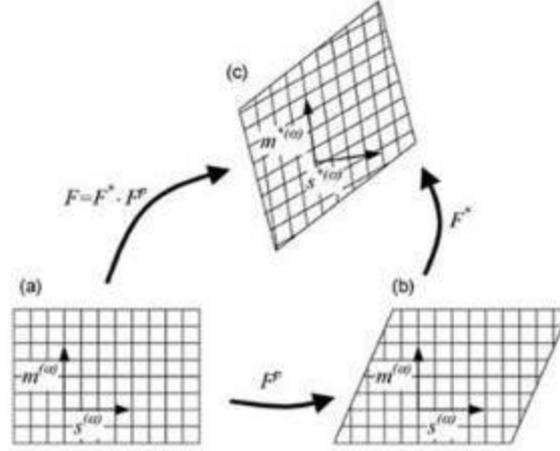
Figure 4-12. Decomposition of tensor F.

Proper analysis of the kinematics of finite deformations requires knowledge of the rate of change for F. The spatial gradient for F, velocity L, is given by the following expression:

$$L = \dot{F} \cdot F^{-1}$$

(4.30)

$$L = \dot{F} \cdot F^{-1}$$

With: $\dot{F} = \dot{F}^e F^p + F^e \dot{F}^p$

(4.31)

The rate of change of F_p is related to the slip rate $\dot{\gamma}^{(\alpha)}$ of the active slip system α according to:

$$L^p = \dot{F}^P \cdot F^{P-1} = \sum_\alpha \dot{\gamma}^{(\alpha)} \cdot s^{(\alpha)} \otimes m^{(\alpha)}$$

(4.32)

where the sum represents all the activated slip systems, and s, m the slip direction and the normal to the slip plane, respectively. The resolved shear stress is derived from the Cauchy stress tensor:

$$\tau^{(\alpha)} = \sigma : \left(s^{(\alpha)} \otimes m^{(\alpha)} \right)_{sym}$$

(4.33)

The slip direction and the vector normal to the slip plane are defined here for the deformed state and not for the reference configuration. The velocity gradient in the current state can be decomposed into a symmetric rate of stretching tensor D and an antisymmetric spin tensor Ω:

$$L = \dot{F} \cdot F^{-1} = D + \Omega$$

(4.34)

with: $D = D^e + D^p \ and \ \Omega = \Omega^e + \Omega^p$

(4.35)

So the following expression may be obtained:

$$\begin{cases} \boldsymbol{D}^e + \Omega^e = \dot{\boldsymbol{F}}^e \cdot \boldsymbol{F}^{e-1} \\ \boldsymbol{D}^P + \Omega^P = \sum_\alpha \dot{\gamma}^{(\alpha)} \cdot \boldsymbol{s}^{(\alpha)} \otimes \boldsymbol{m}^{(\alpha)} \end{cases} \tag{4.36}$$

Based on Hill and Rice's work [60], the stretching tensor and the Jaumann rate of Cauchy stress may be written as:

$$\tilde{\sigma} + \sigma\left(\mathrm{I} : \boldsymbol{D}^e\right) = \boldsymbol{L} : \boldsymbol{D}^e \tag{4.37}$$

The main difference from Huang's work [19] is that the power-law used in this work includes the kinematic term reflected in the backstresses. For the strain rate, two different relations may be used; depending on whether monotonic or cyclic loading conditions are applied. For monotonic loading conditions, - based on the Schmid law - the slip rate $\dot{\gamma}^{(\alpha)}$ is related to the corresponding resolved shear stress τ_α as follows:

$$\dot{\gamma}^{(\alpha)} = \dot{\gamma}_o^{(\alpha)} \cdot \left| \frac{\tau^{(\alpha)}}{g^{(a)}} \right|^n sign\left(\tau^{(\alpha)}\right) \tag{4.38}$$

Where $\dot{\gamma}^{(\alpha)}$ is the reference strain rate on the slip system α, n is the strain rate exponent and g_α determines the current strength of the αth slip system. While for cyclic loading conditions a power law relationship is used for the flow rule [5, 6]:

$$\dot{\gamma}^{(\alpha)} = \dot{\gamma}_o^{(\alpha)} \cdot \left| \frac{\tau^{(\alpha)} - \chi^{(\alpha)}}{g^{(a)}} \right|^n sign\left(\tau^{(\alpha)} - \chi^{(\alpha)}\right) \tag{4.39}$$

where g^α and χ^α represent the isotropic and kinematic hardening, respectively. The hardening law for g^α and χ^α may be written as:

$$\dot{g}^{(\alpha)} = \sum_\beta h_{\alpha\beta} \cdot \dot{\gamma}^{(\beta)} \tag{4.40}$$

$$\dot{\chi}^{(\alpha)} = b\dot{\gamma}^{(a)} - r\chi^{(\alpha)} \left| \dot{\gamma}^{(a)} \right| \tag{4.41}$$

where the self and latent hardening moduli are given by:

$$h_{\alpha\alpha} = h(\gamma) = h_o \cdot sec\, h^2 \left| \frac{h_o}{\tau_s - \tau_o} \right|, \ \alpha = \beta \tag{4.42}$$

$$h_{\alpha\beta} = q \cdot h(\gamma), \ \alpha \neq \beta \tag{4.43}$$

where b and r and q are material constants, h_0 is the initial hardening modulus, τ_s is the stage I stress and τ_0 is the yield stress, while the cumulative shear strain on all slip systems can be obtained by:

$$\gamma = \sum_a \int_0^t \left| \dot{\gamma}^{(\alpha)} \right| dt \tag{4.44}$$

Forward Gradient Integration Scheme and Incremental Formulation

At this part of the section the integration schemes and incremental formulations within the UMAT subroutine are outlined. The linear interpolation within a time increment Δt is as follows:

$$\Delta\gamma^{(\alpha)} = \Delta t \left[(1-\theta)\dot{\gamma}_t^{(\alpha)} + \theta\dot{\gamma}_{t+\Delta t}^{(\alpha)} \right] \qquad (4.45)$$

The parameter θ is controlling the interpolation scheme and ranges from 0 to 1. When θ=0, the above equation is simplified to the basic Euler time integration scheme and when θ=1, it becomes fully implicit integration scheme. A value of θ=0.5 was selected for this research topic following the recommendation from Peirce's work [64].

The slipping rate may be written as a form of Taylor expansion:

$$\dot{\gamma}_{t+\Delta t}^{(\alpha)} = \dot{\gamma}_t^{(\alpha)} + \frac{\partial\dot{\gamma}^{(\alpha)}}{\partial\tau^{(\alpha)}}\Delta\tau^{(\alpha)} + \frac{\partial\dot{\gamma}^{(\alpha)}}{\partial g^{(\alpha)}}\Delta g^{(\alpha)} \qquad (4.46)$$

Equation (4.45) becomes:

$$\Delta\gamma^{(\alpha)} = \Delta t \left[\dot{\gamma}_t^{(\alpha)} + \theta\frac{\partial\dot{\gamma}^{(\alpha)}}{\partial\tau^{(\alpha)}}\Delta\tau^{(\alpha)} + \theta\frac{\partial\dot{\gamma}^{(\alpha)}}{\partial g^{(\alpha)}}\Delta g^{(\alpha)} \right] \qquad (4.47)$$

Where $\Delta\tau_\alpha$ and Δg_α are the corresponding increments of resolved shear stress and current strength for the αth slip system within the time increment Δt. Equation (4.46) may be rewritten as:

$$\Delta\gamma^{(\alpha)} = \Delta t \left[\dot{\gamma}_t^{(\alpha)} + \theta\frac{\partial\dot{\gamma}^{(\alpha)}}{\partial\tau^{(\alpha)}}\Delta\tau^{(\alpha)} + \theta\frac{\partial\dot{\gamma}^{(\alpha)}}{\partial g^{(\alpha)}}\Delta g^{(\alpha)} \right] \qquad (4.48)$$

At this stage, the Schmid factor μ and tensor **ω** are introduced, given by:

$$\mu_{ij}^{(\alpha)} = \frac{1}{2}\left[s_i^{(a)} \cdot m_j^{(a)} + s_j^{(a)} \cdot m_i^{(a)} \right] \qquad (4.49)$$

$$\omega_{ij}^{(\alpha)} = \frac{1}{2}\left[s_i^{(a)} \cdot m_j^{(a)} - s_j^{(a)} \cdot m_i^{(a)} \right] \qquad (4.50)$$

Similarly to equation (4.40), the increments of current hardening function, Δg^α, are expressed by:

$$\Delta g^{(\alpha)} = \sum_\beta h_{\alpha\beta} \cdot \Delta\gamma^{(\beta)} \qquad (4.51)$$

The resolved shear stress increment $\Delta\tau_\alpha$ may be obtained, by combining equations (4.33), (4.35), (4.36) and (4.37):

$$\Delta\tau^{(\alpha)} = \left[C_{ijkl}\mu_{kl}^{(\alpha)} + \omega_{ik}^{(\alpha)}\sigma_{jk} + \omega_{jk}^{(\alpha)}\sigma_{ik} \right] \cdot \left[\Delta\varepsilon_{ij} - \sum_\beta \mu_{ij}^{(\beta)}\Delta\gamma^{(\beta)} \right] \qquad (4.52)$$

where **C** is the elastic stiffness tensor. The linear solution of $\Delta\gamma^\alpha$ may be obtained by substituting the incremental relations (4.51 & 4.52) and the flow rule (4.39) into Equation (4.48):

$$\Delta\gamma^{\alpha} - (1-\theta)\Delta t\dot{\gamma}_{t}^{(\alpha)} - \theta\Delta t\dot{\gamma}_{0}^{(\alpha)}\left|\frac{\tau_{t}^{(\alpha)} + \Delta\tau^{(\alpha)} - \chi_{t}^{(\alpha)} - \Delta\chi^{(\alpha)}}{g_{t}^{(a)} + \Delta g^{(a)}}\right|^{n} sign\left(\tau_{t+\Delta t}^{(\alpha)} - \chi_{t+\Delta t}^{(\alpha)}\right) = 0 \quad (4.53)$$

where $\Delta\chi^{\alpha}$ is calculated via Equation (4.41). This nonlinear equation is solved using a Newton-Raphson iterative method, while the linear solution obtained from Equation (4.48) is taken as an initial estimation.

4.2.4. Overall Diagram of UMAT

UMAT subroutines are used in ABAQUS framework, in the case the user is interested to define its own material behaviour via an external subroutine. In such cases, users can define their own constitutive model and execute it once called via Abaqus. Figure 4.2 and Table 4.1 show the flowchart of the UMAT subroutine together with the descriptions of the corresponding subroutines. The UMAT subroutine performs 2 functions: it updates the stresses and the solution dependent state variables to their current values at the end of the increment and it provides the Jacobian matrix, J=θΔσ/θΔε, for the constitutive model. The subroutine provides an option for using either a linearised solution scheme or non-linear incrementation by using Newton-Raphson iterative method. The original formulations are based on the work of Huang et al [19], but modifications are made as described in the previous section 4.2.3.
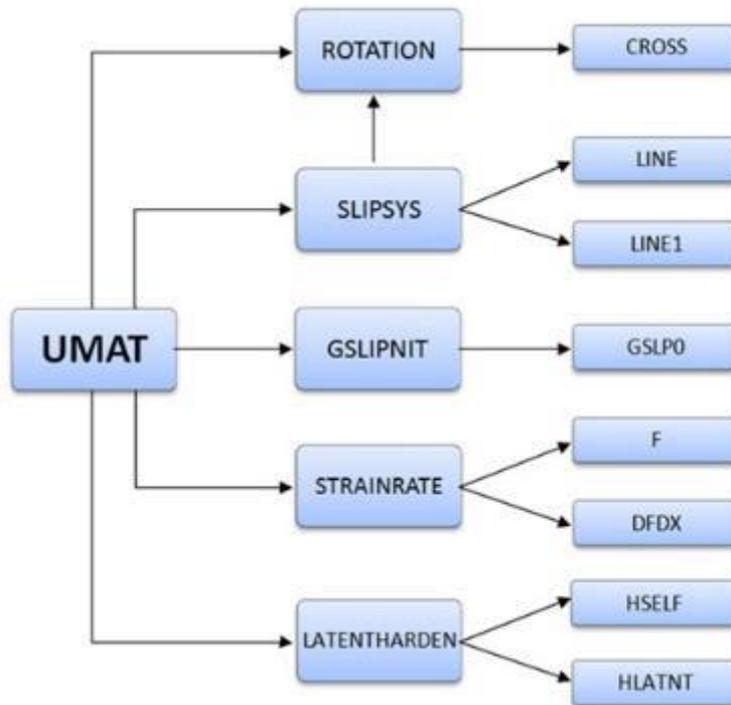
Figure 4-13. Flowchart of UMAT.

UMAT	Main subroutine
ROTATION	Initial orientation of cubic crystal in the global system
CROSS	Cross product of two vectors
SLIPSYS	Generates all slip systems

LINE	*Generates all possible slip directions [lmn]*
LINE1	*Generates all possible slip directions [0mn]*
GSLPINIT	*Initial values of current strength in all slip systems*
GSLP0	*Initial value of current strength in each slip system*
STRAINRATE	*Shear strain-rates in all slip systems*
F	*Shear strain-rate in each slip system*
DFDX	*Derivative of function F*
LATENTHARDEN	*Hardening matrix, i.e. self- and latent-hardening in all slip systems*
HSELF	*Self-hardening moduli; diagonal elements in the hardening matrix*
HLATNT	*Latent-hardening moduli; off-diagonal elements in the hardening matrix*

Table 4-1. Subroutines used within UMAT.

4.3. Polycrystals – Computational techniques

In this section the basic concepts of a Representative Volume Element (RVE) are presented. First of all the geometry needs to be separated in different regions. These separate regions must have a geometry which is representative of the microstructure of the material; for polycrystals the Voronoi technique has been proved to adequately represent metallic polycrystals [10, 28, 66]. At the next stage these regions-crystals must be assigned different mechanical properties; assigning the correct mechanical parameters (such as hardening parameters or elastic moduli) for the polycrystal while giving the appropriate crystal orientation to individual crystals is of crucial importance in crystal plasticity modelling. So polycrystal geometries may be obtained by using the Voronoi algorithm, while the crystal misorientation can be introduced by using texture analysis concepts.

4.3.1. Voronoi algorithm

The Voronoi algorithm splits the space into random polyhedra. The principle that enables the creation of a polyhedral is that each point in every polygon is closer to its centre than any other centre of any other polygon (figure 4.14a). Matlab 2010a version was used to obtain the RVE [67]. The mathematics behind Voronoi algorithms are well established and can be found in reference [66]. Here only the outline of the algorithm will be presented. Initially 20 random points were created between 0 and 1. Then using the Voronoi concept, polyhedra are being created with their centres corresponding to the initial random points, while the vertices are also randomly distributed. The coordinates of the random pointed centres and the vertices of the polyhedra are easily obtained in matrix forms within Matlab. The simple Voronoi algorithm carries some problems (see figure 4.14b); there are some vertices that extent to infinity which cannot be defined, while there are also some polygons missing on one side. To solve these problems a square domain is defined within a larger square domain (figure 4.14c); but again we have a new problem of some polygons having their centres outside the small square (the area of interest) and covering space in the area of interest. These regions remain undefined, so they cannot be assigned the appropriate mechanical properties afterwards. To come up with a solution, we have the number of polygons within the area of interest, while we have a coarser polygon

structure for the large square domain. Therefore we ensure that no polygons are coming into the central domain from the large region (figure 4.15a). Furthermore, circular or ellipsoid particles can be easily introduced into the model as shown in figure 4.15b, following a certain distribution, density etc. The basic rule for the incorporation of particles is that they do not cross the GBs or the boundaries of the RVE.
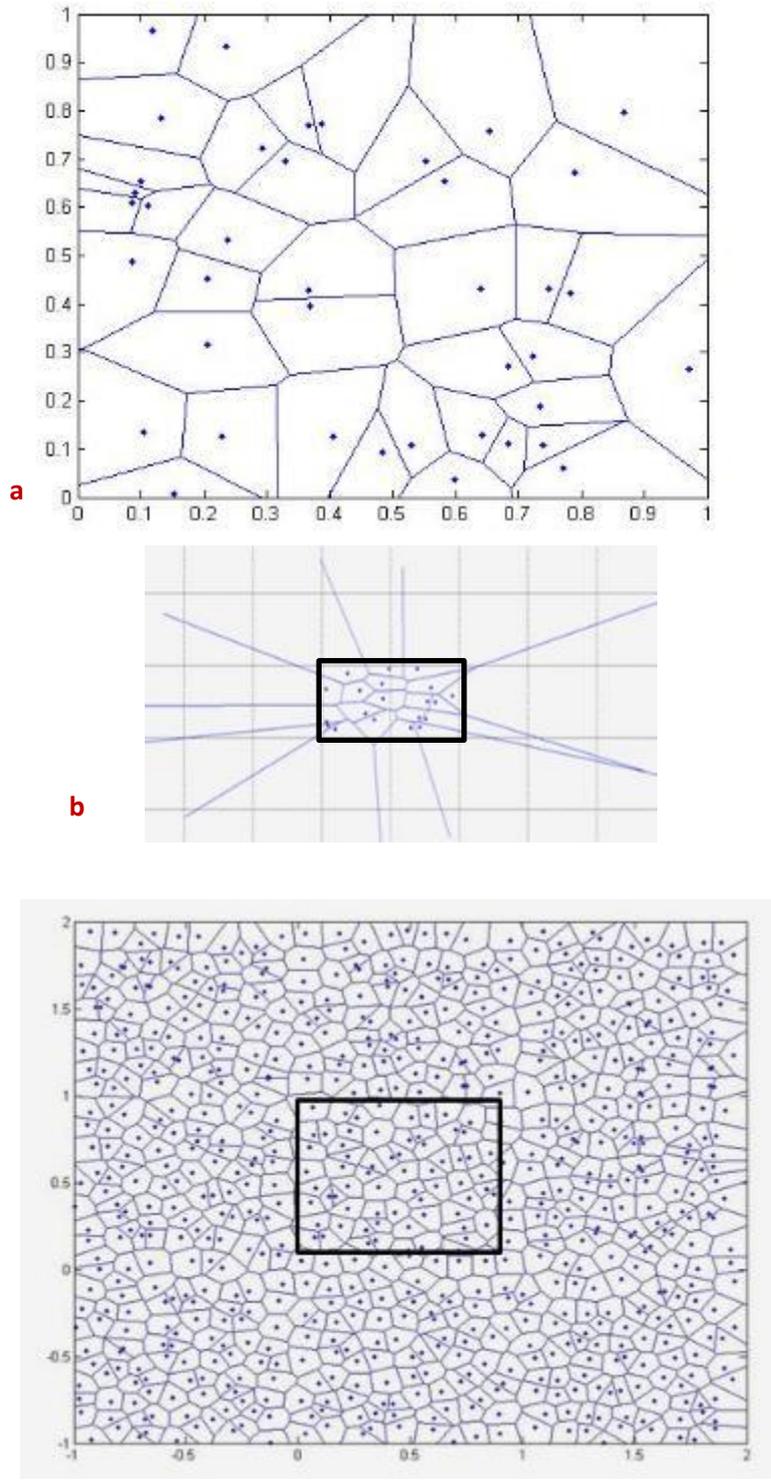
Figure 4-14. a) Simple case of a 2D Voronoi diagram for the case of 20 randomly centred polyhedra, b) clarifying the unclosed polygons and the problem with some vertices extending to infinity, and c) creating a square domain within a region.
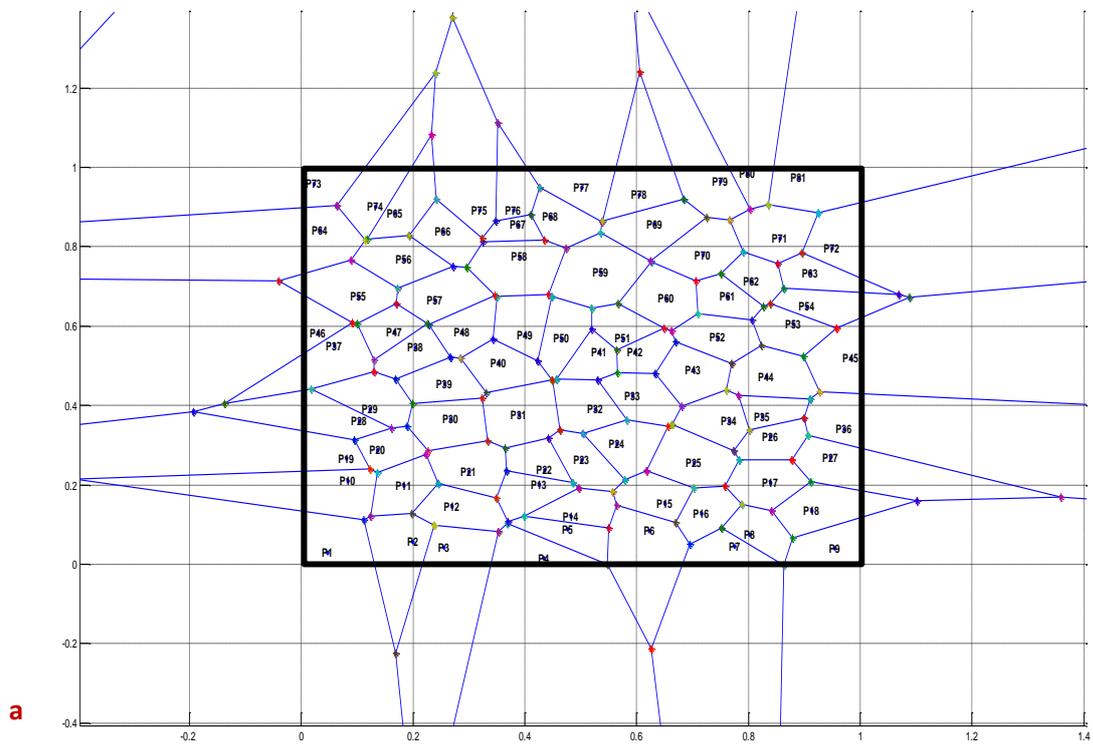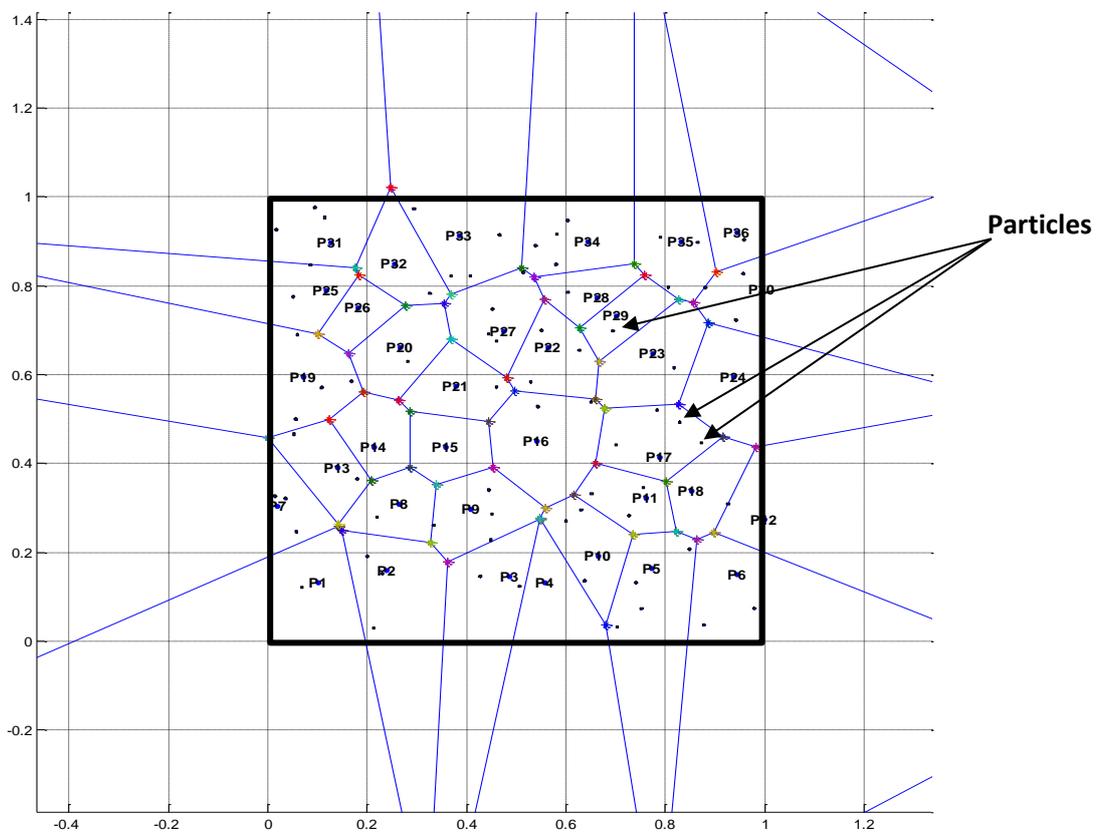
Figure 4-15. a) The geometry of the Voronoi polygons imported into Abaqus, b) Polygons with particles.

The correct vertices and centres of the polygons are then obtained into matrix forms and imported into Abaqus via python scripts developed by the author for the purpose of this PhD thesis. Each grain is assigned a name, an orientation and the corresponding mechanical properties.

4.3.2. Misorientation representation and conversions: Miller indices - Euler angles

In texture analysis, different mathematical representation parameters exist that describe crystal orientation [68]. The commonly used and established crystallographic mathematical tools are: the Rotation or Orientation matrix, the Ideal orientation (Miller indices), the Euler angles, the Axis/angle of rotation, and the Rodriguez space.

All descriptors are employed to process different aspects of orientation measurements. Crystallographic orientation may refer to a crystal (3-D character) and it comprises 3 independent variables; or to a crystallographic plane comprising 2 independent variables. In order to specify a crystal orientation, 2 coordinate systems are required: one corresponding to the whole sample (K_s) and one for the local crystals (K_c) of the specimen (see figure 4.16). Therefore, the 1st coordinate system (sample axes), S= {S1 S2 S3} is often chosen to coincide with the Rolling Direction (RD), Normal direction (ND) and Transverse Direction (TD) directions of the sample. The 2nd coordinate system (crystal coordinate system), C={ C1 C2 C3} is given by the local directions of the crystals. Conventionally the local system is adapted to coincide with the crystal symmetry directions. For an orthogonal symmetry, the 3-Dimensional Cartesian local system corresponds to the: [100], [010] and [001] directions, as shown in figure 4.17. As already explained, Miller indices are a widely used tool in metallurgy. Miller indices represent planes and directions in a crystal unit cell. The planes are represented by brackets, enclosing 3 numbers, i.e. (111) crystallographic plane, while the directions are represented by square brackets, i.e. [110] crystallographic orientation. So far, two coordinate systems have been defined; a relationship may be drawn which relates the two coordinate systems, which is expressed by:

Kc=g · Ks

where g is the so called g matrix, Rotation or Orientation matrix. Due to the 3-dimensionality of the system the Rotation matrix is a 3x3 table:

$$g = \begin{bmatrix} g_{11} & g_{12} & g_{13} \\ g_{21} & g_{22} & g_{23} \\ g_{31} & g_{32} & g_{33} \end{bmatrix} \quad (4.54)$$

The rows are the direction cosines of [100], [010] and [001] in the sample coordinate system, X, Y, Z; while the columns are the direction cosines of RD, TD and ND in the crystal coordinate system:

$$[g] = \begin{bmatrix} g_{11} & g_{12} & g_{13} \\ g_{21} & g_{22} & g_{33} \\ g_{31} & g_{32} & g_{33} \end{bmatrix} \quad \begin{matrix} [100] \text{ direction cosine} \\ [010] \text{ direction cosine} \\ [001] \text{ direction cosine} \end{matrix} \quad (4.55)$$

$$[uvw] \equiv \quad RD \qquad TD \qquad ND \equiv (hkl)$$

$$[g] = \begin{bmatrix} g_{11} & g_{12} & g_{13} \\ g_{21} & g_{22} & g_{33} \\ g_{31} & g_{32} & g_{33} \end{bmatrix} \qquad (4.56)$$

Only the orientation of a plane and direction is required to determine local crystal orientation. Conveniently, (hkl) crystallographic plane is related to the rolling plane, and [uvw] crystallographic direction is related to the rolling direction.

In the g matrix, both rows and columns are unit vectors. The matrix is orthonormal (its inverse is equal to its transpose). The g matrix contains non- independent elements. The cross product of any 2 rows or columns gives the 3rd. For any row or column, the sum of the squares of the 3 elements is equal to unity. The orientation matrix is a mathematical tool for calculating every other orientation descriptor (Rodriguez space, angle/axis pair, Euler angles, pole figure, Miller indices). The notation to obtain the misorientation relationship follows the Bunge's notation. There are two rotations along the Z axis Z_1 and Z_2 and one along the X axis X'. First, a rotation along Z_1 axis (ND) is applied, followed by a rotation along X' axis (RD') and a rotation along Z_2 axis (ND'). So, no rotation is applied along the Y axis (TD) while the corresponding rotations: φ1, Φ, φ2 may be seen in figure 5.4.

a

b
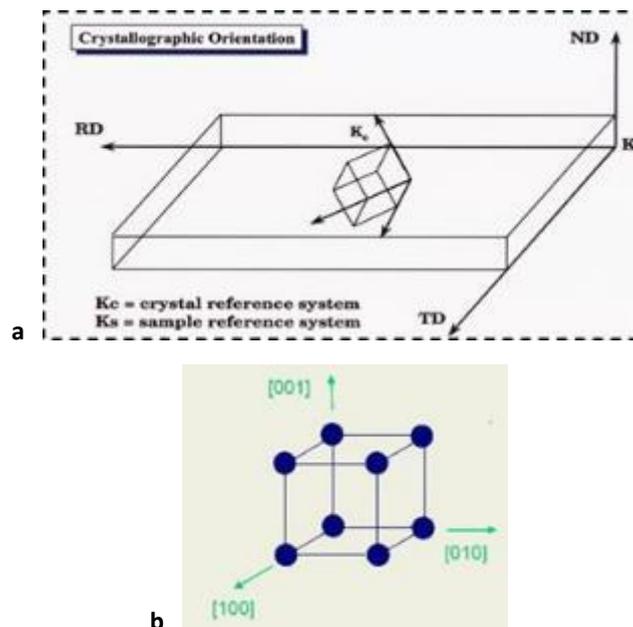
Figure 4-16. a) Reference systems for the representation of crystal orientation in a specimen, and b) the corresponding local coordinate system for orthogonal cubic symmetry.
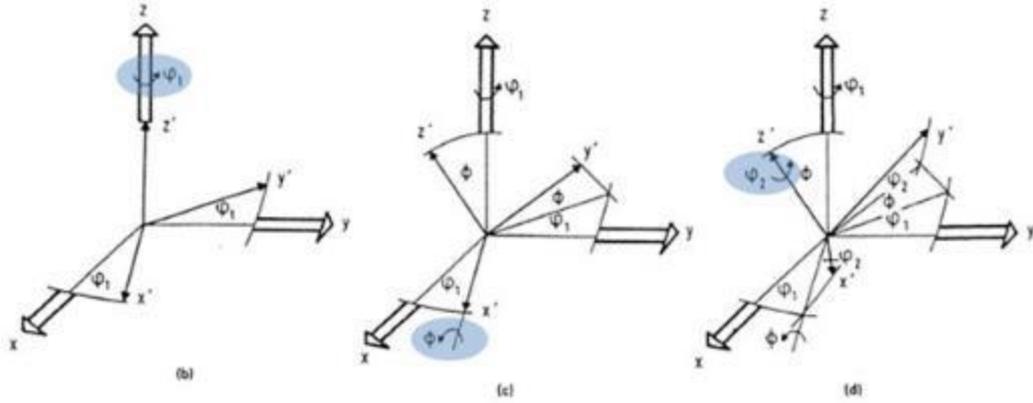
Figure 4-17. Rotation according to Bunge notation.

Analytically, rotation 1 (φ_1) is applied anticlockwise about the sample Z_1 axis, [ND], rotation 2 (Φ) anticlockwise about the rotated X axis, [100] – note that it does not coincide yet with the [100] crystal axis - and rotation 3 (ϕ_2) rotates anticlockwise about the crystal Z_2 axis, [001]. All this process can be mathematically represented by the following expressions:

$$Z_1 = \begin{pmatrix} \cos\phi_1 & \sin\phi_1 & 0 \\ -\sin\phi_1 & \cos\phi_1 & 0 \\ 0 & 0 & 1 \end{pmatrix}, \quad X = \begin{pmatrix} 1 & 0 & 0 \\ 0 & \cos\Phi & \sin\Phi \\ 0 & -\sin\Phi & \cos\Phi \end{pmatrix} \quad and \quad Z_2 = \begin{pmatrix} \cos\phi_2 & \sin\phi_2 & 0 \\ -\sin\phi_2 & \cos\phi_2 & 0 \\ 0 & 0 & 1 \end{pmatrix}$$

$$g = Z_2 \cdot X \cdot Z_1 \qquad\qquad (4.57)$$

which yields:

$$g = Z_2 \cdot X \cdot Z_1 =$$

$$= \begin{pmatrix} \overbrace{\begin{matrix} \cos\varphi_1\cos\varphi_2 - \sin\varphi_1\sin\varphi_2\cos\Phi \\ -\cos\varphi_1\sin\varphi_2 - \sin\varphi_1\cos\varphi_2\cos\Phi \\ \sin\varphi_1\sin\Phi \end{matrix}}^{[uvw]} & \begin{matrix} \sin\varphi_1\cos\varphi_2 + \cos\varphi_1\sin\varphi_2\cos\Phi \\ -\sin\varphi_1\sin\varphi_2 + \cos\varphi_1\cos\varphi_2\cos\Phi \\ -\cos\varphi_1\sin\Phi \end{matrix} & \overbrace{\begin{matrix} \sin\varphi_2\sin\Phi \\ \cos\varphi_2\sin\Phi \\ \cos\Phi \end{matrix}}^{(hkl)} \end{pmatrix}$$

1. *Cubic-Orthorhombic:*
   0≤φ1 ≤90°, 0≤Φ ≤90°, 0≤φ2 ≤90°
2. *Cubic-Monoclinic:*
   0≤φ1 ≤180°, 0≤Φ ≤90°, 0≤φ2 ≤90°
3. *Cubic-Triclinic:*
   0≤φ1 ≤360°, 0≤Φ ≤90°, 0≤φ2 ≤90°

$$(4.58)$$

The conversion of Miller indices to Euler angles is complicated and the result is shown below. According to Rollett [69]:

$$\begin{cases} h = n\sin\Phi\sin\varphi_2 \\ k = n\sin\Phi\cos\varphi_2 \\ l = n\cos\Phi \end{cases}, \qquad \begin{cases} u = n'\left(\cos\varphi_1\cos\varphi_2 - \sin\varphi_1\sin\varphi_2\cos\Phi\right) \\ v = n'\left(-\cos\varphi_1\sin\varphi_2 - \sin\varphi_1\cos\varphi_2\cos\Phi\right) \\ w = n'\sin\Phi\sin\varphi_1 \end{cases} \qquad (4.59)$$

n, n': factors to make integers

According to V. Randle :

$$g_{11} = u/D, \quad g_{21} = v/D, \quad g_{31} = w/D, \quad g_{13} = h/C, \quad g_{23} = k/C \quad and \quad g_{33} = l/C$$

$$where: \quad D = \sqrt{u^2 + v^2 + w^2} \quad and \quad C = \sqrt{h^2 + k^2 + l^2} \qquad (4.60)$$

V. Randle also uses the n, n' factors, but first the vectors are divided by the C and D factors, which are given by the norm of the two 'ideal' Miller indices (hkl) [uvw]. In both cases, an experimentally measured orientation is expressed as the nearest ideal orientation if the deviation is only a few degrees.

To make the opposite conversion, Euler angles from Miller indices, we may invert the previous relations:

$$\cos\Phi = \frac{l}{\sqrt{h^2 + k^2 + l^2}}, \cos\varphi_2 = \frac{k}{\sqrt{h^2 + k^2}} \text{ and } \sin\varphi_1 = \frac{w}{\sqrt{u^2 + v^2 + w^2}}\frac{\sqrt{h^2 + k^2 + l^2}}{\sqrt{h^2 + k^2}} \qquad (4.61)$$

By using the inverse trigonometric functions, the range of results is limited to 0° ≤ cos-1θ ≤ 180°, or -90° ≤ sin-1θ ≤ 90°. It is not possible to access the full 0-360° range of angles. Therefore, it is more reliable to go from Miller indices to orientation matrix, and then calculate the Euler angles. For misorientation calculations between grains, again the g matrix is used. If we know the orientations of two grains, in terms of matrices of direction cosines g_A and g_B, then the misorientation operator Δg_{AB} at the (A→B) Grain Boundary can be written as:

$$g_B = \Delta g_{AB} \cdot g_A$$
$$\Delta g_{AB} = g_B \cdot g_A^{-1} \qquad (4.62)$$

In this way, misorientation has been defined as the successive operation of transforming the first crystal frame (A) back to the sample frame and subsequently to the new crystal frame (B). An example is outlined below in order to understand better the concept of misorientation. If the orientation of 2 grains is given in Euler angles: G1 [90, 35, 45] and G2 [59, 37, 63], the orientation matrix can be obtained:

$$g = \begin{pmatrix} \cos\varphi_1\cos\varphi_2 - \sin\varphi_1\sin\varphi_2\cos\Phi & \sin\varphi_1\cos\varphi_2 + \cos\varphi_1\sin\varphi_2\cos\Phi & \sin\varphi_2\sin\Phi \\ -\cos\varphi_1\sin\varphi_2 - \sin\varphi_1\cos\varphi_2\cos\Phi & -\sin\varphi_1\sin\varphi_2 + \cos\varphi_1\cos\varphi_2\cos\Phi & \cos\varphi_2\sin\Phi \\ \sin\varphi_1\sin\Phi & -\cos\varphi_1\sin\Phi & \cos\Phi \end{pmatrix}$$

Yielding :

$$g_{G1} = \begin{bmatrix} -0.579 & 0.707 & 0.406 \\ -0.579 & -0.707 & 0.406 \\ 0.574 & 0 & 0.819 \end{bmatrix}, \quad g_{G2} = \begin{bmatrix} -0.376 & 0.756 & 0.536 \\ -0.770 & -0.577 & 0.273 \\ 0.516 & -0.310 & 0.799 \end{bmatrix}$$

So the misorientation matrix between the 2 grains is:

$$\Delta g_{12} = g_{G2} \cdot g_{G1}^{-1} = \begin{bmatrix} 0.970 & 0.149 & -0.194 \\ -0.099 & 0.965 & 0.244 \\ 0.224 & -0.218 & 0.950 \end{bmatrix}$$

However, in order to calculate the misorientation angle, crystal symmetry operators need to be employed. Due to the symmetry of the cubic FCC lattice, 24 symmetry operators have to be employed for the conversion, and are shown in Table 4.2, taken from reference [70]. So equation 5.9 becomes:

$$\Delta g'_{AB} = O_c \cdot \Delta g_{AB} \tag{4.63}$$

Where O_c are the symmetry operators given in Table 4.2. So for the example above, 24 solutions exist for the misorientations angles. But only the operator that gives the minimum miorientation angle is correct. The minimum angle is then obtained via [69, 70]:

$$\vartheta = cos^{-1}(trace(\Delta g'_{AB})-1)/2) \tag{4.64}$$

All the above concepts have been introduced into Fortran subroutines developed by the author for the purpose of this PhD thesis, which easily enables the user to use the above conversions. A multiuser environment was created. The experimentally measured values from EBSD (Euler angles) could be easily transformed into vector notation or misorientations at GBs. But also experimentally independent techniques, such as Voronoi polygons were created and employed, with orientations assigned by the user (either random or rolling-textured).

cubic branch

1	0	0	0	0	-1
0	1	0	0	-1	0
0	0	1	-1	0	0
0	0	1	0	0	1
1	0	0	0	-1	0
0	1	0	1	0	0
0	1	0	0	0	1
0	0	1	0	1	0
1	0	0	-1	0	0
0	-1	0	0	0	-1
0	0	1	0	1	0
-1	0	0	1	0	0
0	-1	0	-1	0	0
0	0	-1	0	0	-1
1	0	0	0	-1	0
0	1	0	1	0	0
0	0	-1	0	0	-1
-1	0	0	0	1	0
0	0	-1	1	0	0
1	0	0	0	0	1
0	-1	0	0	-1	0
0	0	-1	-1	0	0
-1	0	0	0	0	1
0	1	0	0	1	0
0	0	1	0	-1	0
-1	0	0	-1	0	0
0	-1	0	0	0	-1

23

-1	0	0	0	1	0
0	1	0	-1	0	0
0	0	-1	0	0	-1
-1	0	0	0	1	0
0	-1	0	1	0	0
0	0	1	0	0	-1
1	0	0	0	-1	0
0	-1	0	1	0	0
0	0	-1	0	0	1

432

Experimental results

In this chapter the microstructure and mechanical properties of Al2024 T3 are presented. Optical microscopy and SEM analysis are used to reveal the microstructural features. Tensile testing, followed by fatigue testing are utilized to obtain the yield strength, UTS, total elongation point and fatigue resistance of Al2024 T3. Image correlation techniques are developed and employed at different length scales in order to link the macroscopic behaviour to the microscale phenomena that occur.

5.1. Al2024 T3 microstructure

The material investigated is Al2024 T3, which has been studied extensively in literature, and its mechanical behavior is well established [71]. It has copper (Cu) additions as the active-strengthening alloy element. The increased yield and tensile strength is due to the formation of Al-Cu particles during the T3 tempering process. The particles act as obstacles for the propagation of dislocations, increasing the strength of the alloy. The material was provided by ALCAN in the form of a 50 mm thick slab, and is shown in figure 5.1.

Figure 5-1. Slab of Al2024 T3, provided by ALCAN.

The (etched) microstructure of the alloy can be seen in figure 5.2a, and consists of irregularly shaped grains with clusters of particles (black spots) embedded within its matrix. An SEM image of the microstructure is shown in figure 5.2b. Not all GBs are revealed which necessitates the use of EBSD for more accurate characterization of grain size and shape. A FEG-SEM Sirion system was used to acquire texture surface measurements. EBSD maps were taken at various locations across the thickness of the aluminium slab and figures 5.32a to 5.3c show the grain size and shape morphology variations that exist. In figure 5.3a the grain size close to the surface of the slab is rather small (44 micron average grain size) with equiaxed shape, but moving towards the center of the slab the grains become large and elongated along the rolling direction as shown in figure 5.3c (average grain size 227 micron).
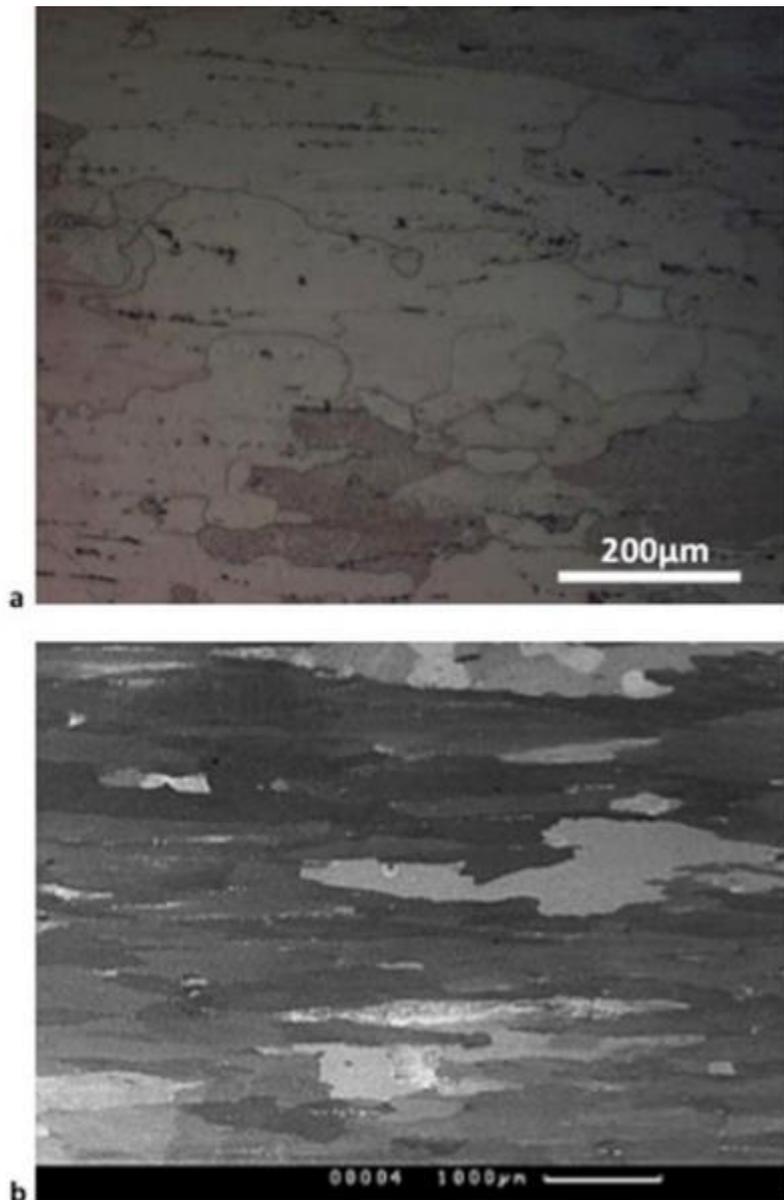
Figure 5-2. a) Optical microscopy image of the microstructure of Al2024 T3 alloy, b) low magnification SEM image for the same alloy (Al2024 T3).
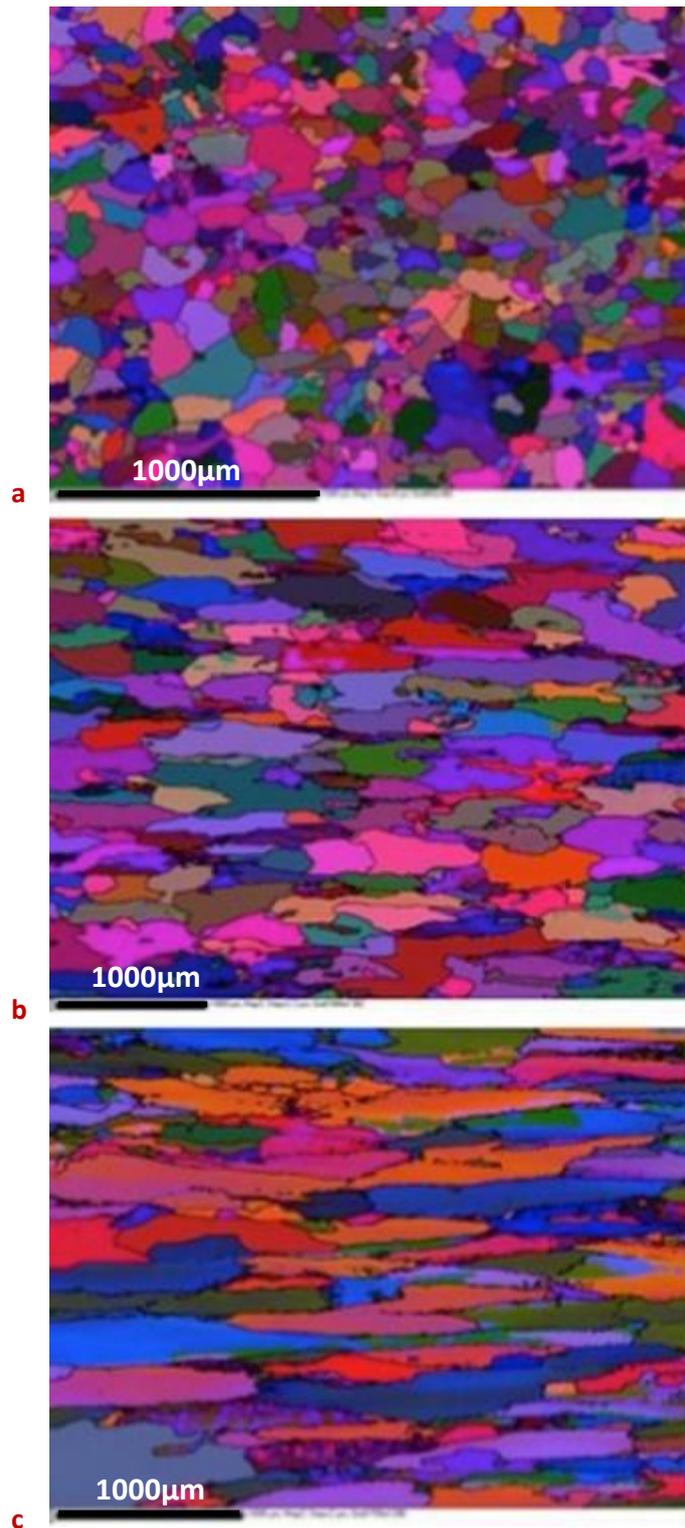
Figure 5-3. EBSD maps at various locations of the aluminium slab. a) From surface (~ 200 micron from the slab surface), b) moving towards the slab centre (approximately 1 cm from the slab surface) and c) at the centre of the slab.

5.2. Particles

The matrix in Al2024 is hardened via precipitation-aging mechanisms. The long heat-treatment of the alloy lead to relatively large grain sizes as well as large sizes for the second phase particles. In many cases the particles were aligned along the RD direction in clusters forms. SEM images were taken with

a CamScan S2 SEM and show this effect in figure 5.4. The brightness of the particles is due to over-etching. During etching, localized accelerated etching occurs at grain boundaries and particles, while the matrix is more resistant to the etching process and therefore the extent of etching is much less. Etching was done using HF agent for approximately 3 seconds.
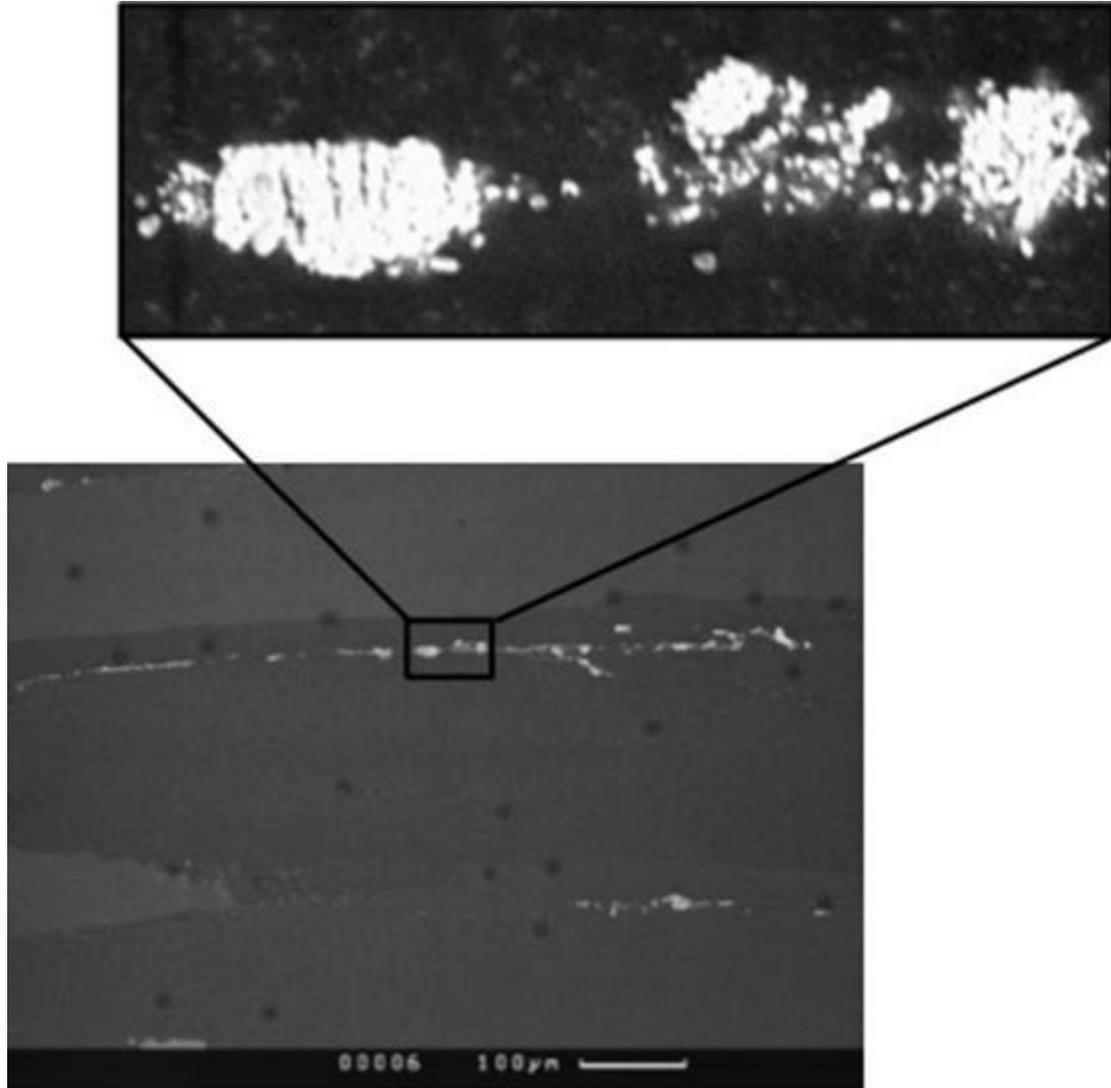
Figure 5-4. Particles in Al2024, in an etched sample.

Samples were inspected for particles in the un-etched condition, in order to better visualise the size, shape and distribution of the particles. Figure 5.5 shows different locations with clusters of particles. The size of the particles varies. Figure 5.6 shows clusters of as large as 20µm particles with clusters of particles of less than 1µm (diameter) in the same sample. EDS analysis was done with a JEOL JSM 6400 SEM to analyse all the elements present in the sample, and showed that the particles were Al-Cu ones. The chemical composition map of figure 5.7 shows the presence of high contents of Cu in the particles, and the low presence of Al with respect to the matrix.

Figure 5-5. Clusters of particles in un-etched Al2024 T3 sample. The length scale in figure 5-5 is 100μm, 100μm and 50μm.
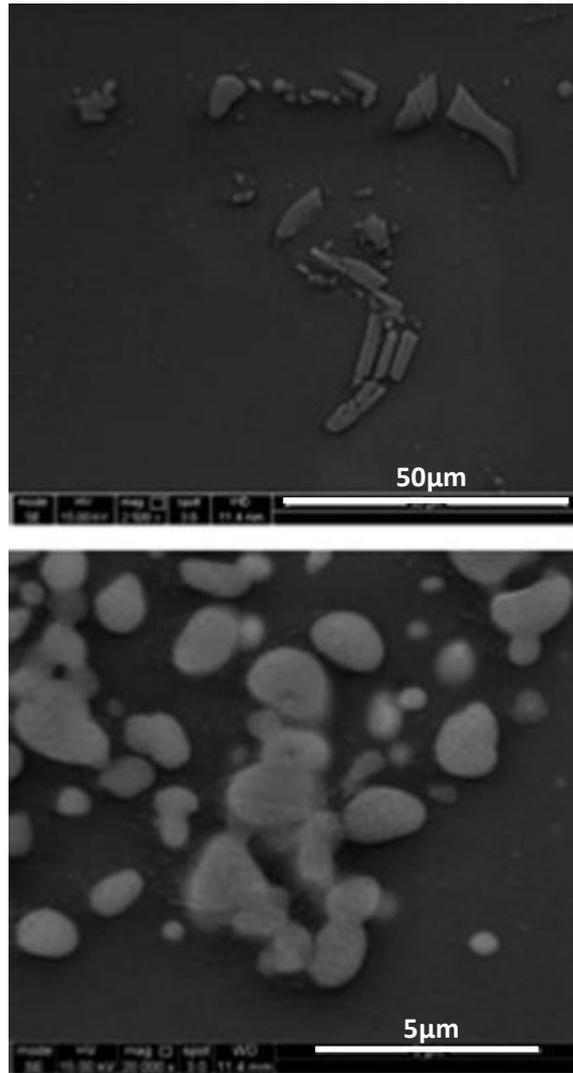
Figure 5-6. Particle size for the same sample.
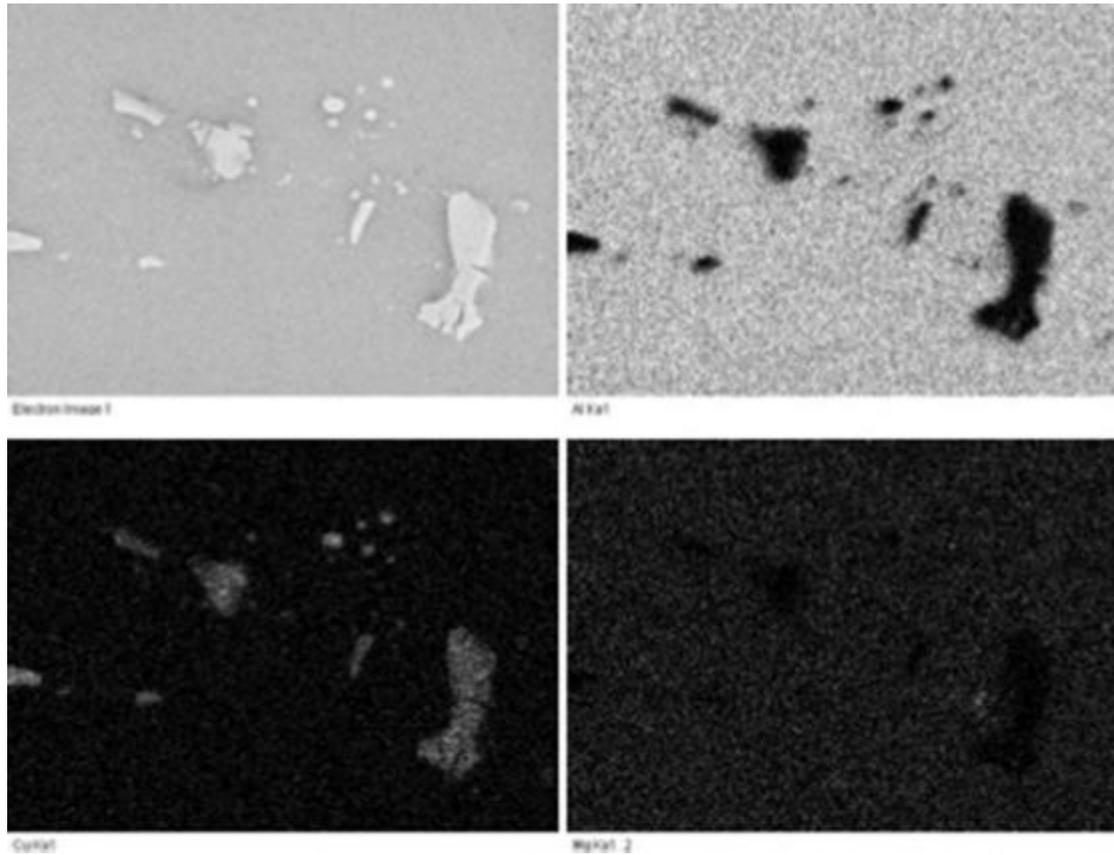
Figure 5-7. Chemical composition map at a location of containing large particles. The spot size was 3nm with the particle size varying from 2 micron up to 50 micron.

Table 5.1 and 5.2 shows that the Al/Cu ratio within the matrix is approximately constant and set at 0.04. The values in Table 5.1 for the matrix were taken from a large area as shown in figure 5.8a for representative measurements. Yet Tables 5.1 and 5.2 show that the Al/Cu ratio for the different Al-Cu particles in figures 5.8b and c varies from 0.15 up to 1.01. Variations in the ratio are found even within the same particles as shown in the yellow pointed particles of figure 5.8b and c. The corresponding Al/Cu ratio values are shown in Table 5.1 and 5.2 (yellow values). The variations can be due to the local cooling conditions and chemical compositions that drive diffusion of elements. In case the sample was in a rolled condition with much smaller thickness , the heat-treatment time would have been much smaller, and therefore the size of the particles would have been smaller, more homogeneous, and with smaller spectrum of chemical compositions.

119
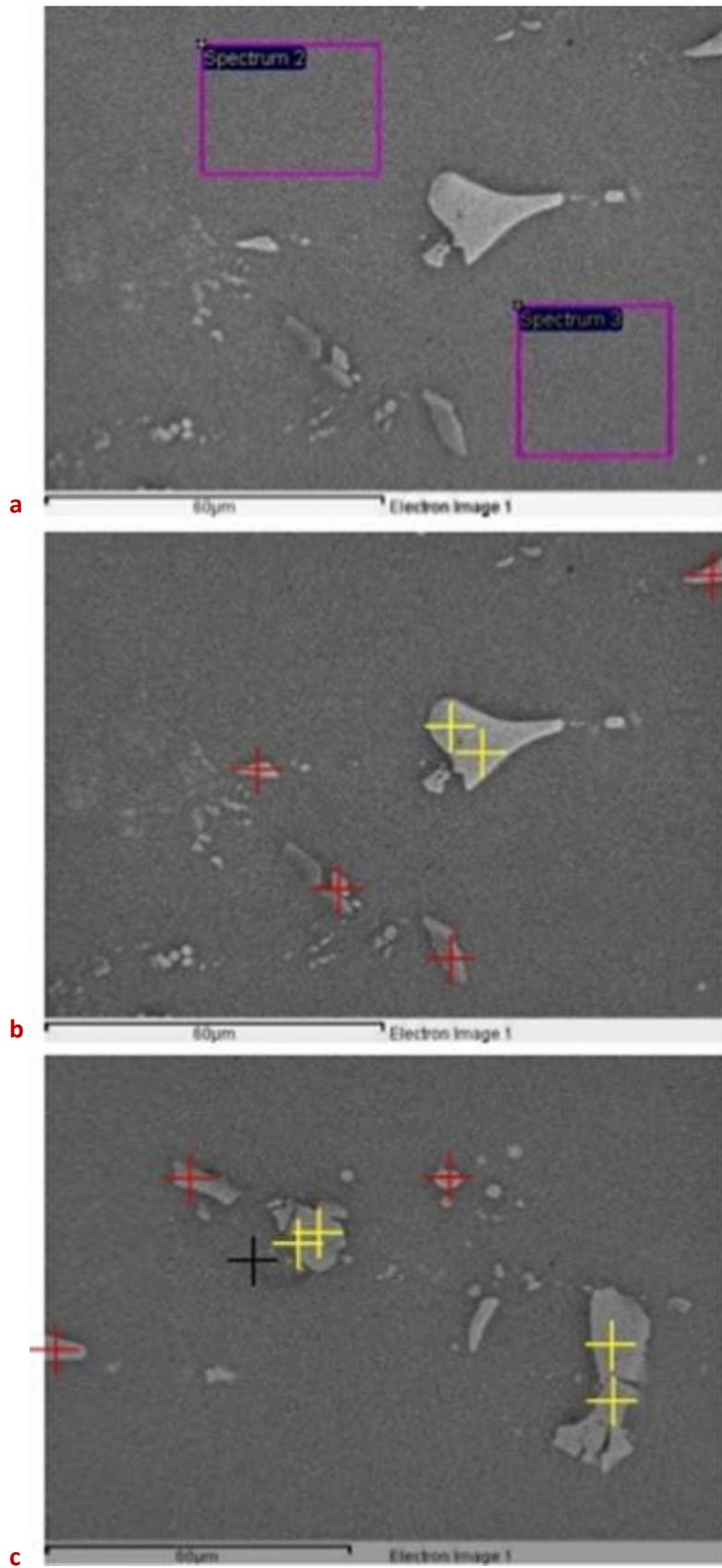
Figure 5-8. a-c) Chemical composition spectrums and spot analysis at various locations highlighted with crosses and boxes.

Table 5.1. Chemical composition spectrums within the matrix and spot analysis at various particles in figure 5.7a and b.

	Spot 1	Spot 2	Spot 3	Spot 4	Spot 5	Spot 6	Matrix	Matrix
Al (%)	62.09	55.43	57.21	67.24	85.46	78.63	94.49	94.33
Cu (%)	34.43	40.9	39.29	29.42	12.67	18.78	4.1	4.14
Cu/Al ratio	0.55	0.74	1.45	0.68	0.15	0.24	0.04	0.04

Table 5.2. Chemical composition spectrums and spot analysis at various locations in figure 5.7c

	Spot 1	Spot 2	Spot 3	Spot 4	Spot 5	Spot 6	Spot 7	Matrix
Al (%)	58.43	69.56	57.32	49.39	71.62	50.81	54.91	94.1
Cu (%)	37.8	27	38.85	50.22	25.51	48.79	40.91	4.44
Cu/Al ratio	0.65	0.39	0.68	1.01	0.35	0.96	0.75	0.04

5.3. Tensile testing

Tensile testing with an electromechanical Mayes DM 100 machine was performed at a displacement rate of 2mm/min. The resulting stress-strain curve is shown in figure 5.9a. The displacement fields were also captured using 3D-DIC. The strain was calculated using the formula: $\delta l/l$, where δl is the displacement of the total gauge length and l is the total gauge length. A second experiment was performed with a strain gauge placed at the back of the sample to accurately obtain the yield point and the slope of the curve in the elastic region (Young modulus), and also to correlate the DIC results with the strain-gauge measurements. The displacement of the machine was set to run up to a strain of 0.025 and the results are shown in figure 5.9b. A Young's modulus value of 72 GPa, yield strength value of 338MPa at 0.48 % elongation and ultimate tensile strength value of 435 MPa are obtained from the curve. The stress-strain curves in figure 5.9a and b were identical, verifying that both techniques (strain gauge and DIC) yield the same results.
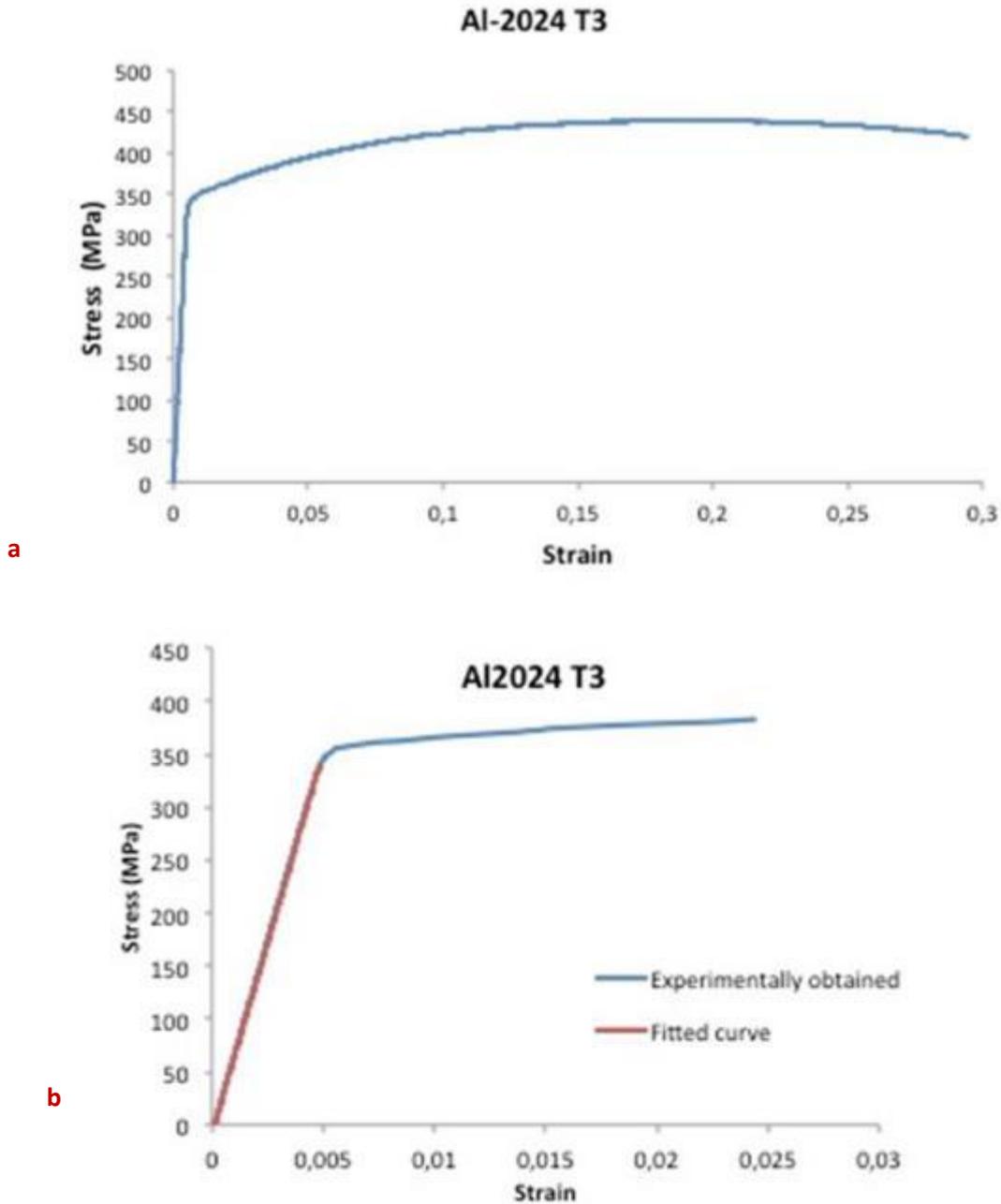
Figure 5-9. a) Tensile curve for Al2024 T3, where the stress is obtained by the formula F/A where F is the machine load and A is the cross section of the sample, and the strain is obtained by using the formula: δl/l, where δl is the displacement of the total gauge length and l is the total gauge length , b) zoom in the elastic region and yield point of the curve (strain gauge), the strains in the blue curve were obtained by a 10mm strain gauge placed at the centre of the sample and the stresses similar to a).

Virtual strain gauges with the DIC-VIC software were utilised to obtain the difference between the global and local displacement at the centre of the sample, and identify the effect of the radius of curvature in the sample. Two virtual extensometers were employed: one for the full sample length (gauge length of 74mm) and one at the centre of the sample (gauge length of 10mm). This is shown in the caption of figure 5.10. Figure 5.10 shows that in the linear elastic region there is no effect of the cross section reduction (radius of curvature), but as soon as the material enters the plasticity region, it work-hardens in different proportions depending on the local cross section, and the two values

become much different. The 74mm extensometer does not increase significantly, and actually the slight increase is due to the increase occurring at the centre of the sample (see figure 5-10). This is also the reason why the machine/global stress-strain graphs were matched with the local stress strain curves, as all the displacements and strains occurred within 1 cm at the centre of the sample as soon as the sample enters the plastic region. Therefore it was decided that the use of strain gauges and virtual extensometers at the center of the sample is critical in order to control the amplitude of strain at the center of the sample, during the experiment. Both strain gauge and virtual extensometer were used in the experiments in order to verify the strains developed. After a few cycles though, the strain gauges were detached. Yet calculations were obtained via the virtual extensometers. So the strain gauges were only used for verification just during the first fatigue cycles.

Influence of cross section to strain localization
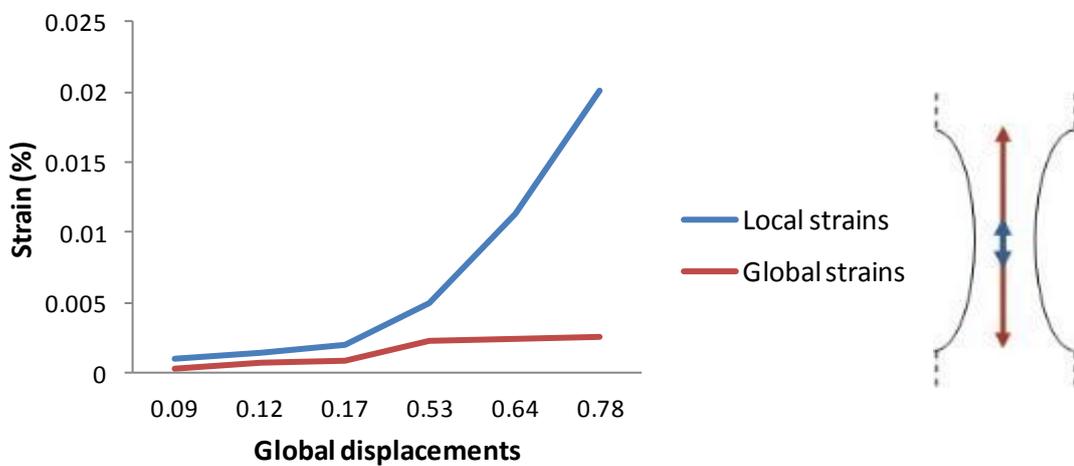
Figure 5-10. Global-local strains during tensile testing. The strains are obtained by using the formula: δl/l, where δl is the displacement of the gauge length and l is the gauge length. The strains in the blue curve were obtained by a 10mm strain gauge placed at the centre of the sample, while the strains in the red curve were obtained from the machine displacements using the total gauge length of 74 mm.

During the tensile test, consecutive pictures were taken with the DIC equipment, in order to quantify the deformation and strain contours at different loading stages. Figure 5.11 shows the strain contours of the ε_{yy} component at increasing displacement values during the tensile test. At the early stages of loading (first 4 pictures) the strain contours are non uniform, different regions in the material are loaded and strained in different proportions, based on the mechanical properties of the corresponding microstructure. In the 5th picture the load is considerably high and the strain is highly localised in the middle of the specimen. Hence the influence of the cross section is critical for high displacement values but not within the elastic region. The highly localized deformation in image 7 close to the end of the experiment led to the fracture of the sample in the centre of the specimen.

Figure 5-11. Strain development for the ε_{yy} during a tensile testing, by using VIC software.
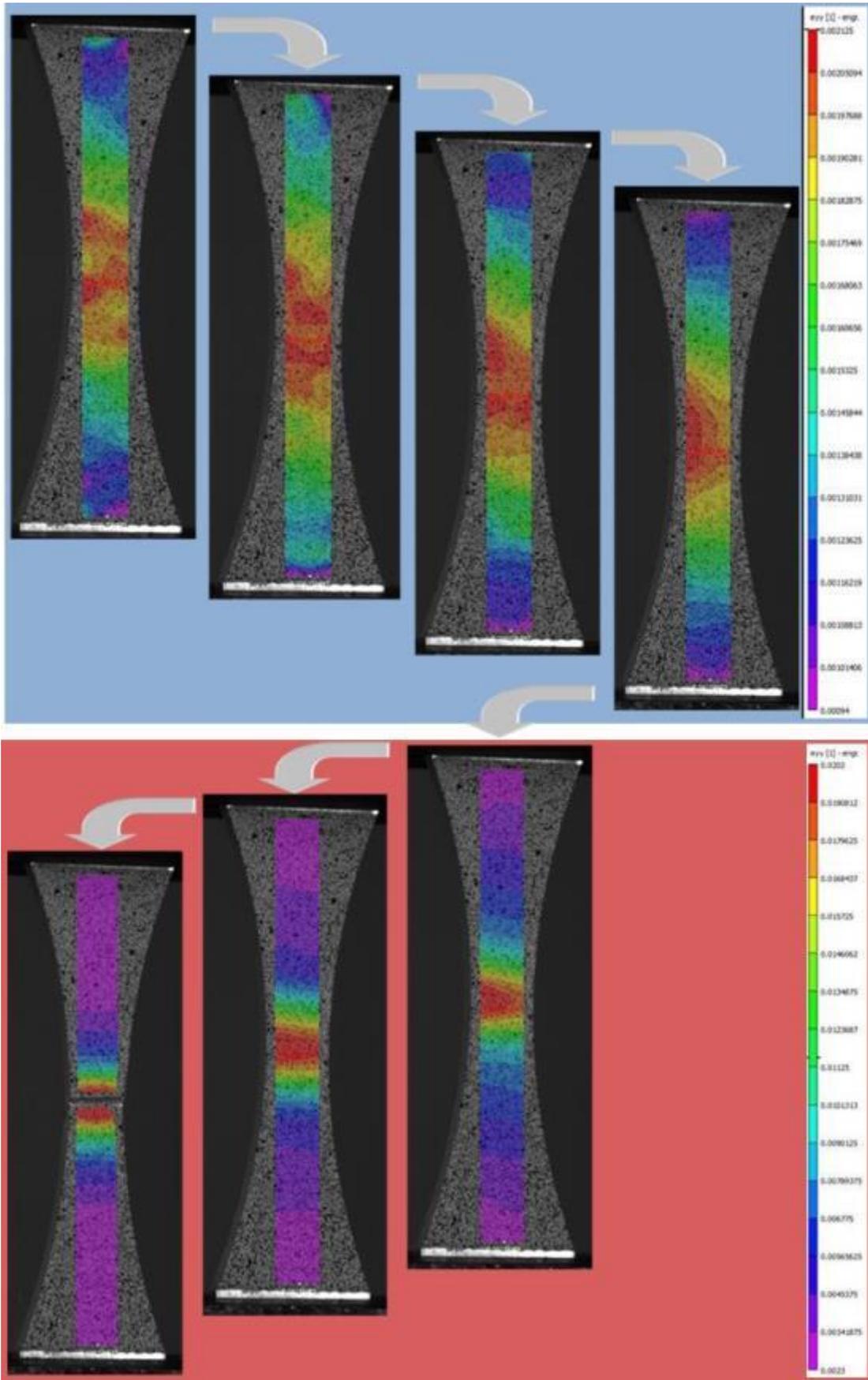
5.4. Fatigue testing & Image Correlation results

In this section the main experimental results from the fatigue tests are presented. Stress controlled experiments were performed to investigate the macroscopic strain development at different stress amplitudes while in next chapter strain controlled experiments were employed in order to investigate strain localization within individual grains, crack initiation and small crack growth. In the first case various regions within the microstructure develop high strains, while in the latter case only a few grains are highly strained, and at some point suddenly crack initiation will occur.

Initially a macroscale characterisation is pursued with 3D DIC, followed by a meso-scale characterization at the microstructural level with 2D DIC. Effects such as necking, distribution and accumulation of the major strain component, lateral contraction, and shear strain distribution are thoroughly described and presented.

5.4.1. Fatigue tests set-up

As discussed already in the literature review (section 2.2), the occurrence of fatigue failures is easier to predict for low cycle fatigue, where the stress-strain amplitudes are considerably higher and therefore considerable amount of plastic deformation occurs prior to component failure. At low stress-strain amplitudes, the influence of the microstructure becomes dominant; crystal size and orientation, strain gradients and dislocation structures determine the occurrence of cracking and local failure; therefore predicting cracking becomes mechanically, metallurgically and statistically more challenging [14, 26, 27]. The target in this project was to evaluate the behaviour of the material at low, medium and high stress amplitudes. The black circles in figure 5.12 correspond to the stress amplitudes used for the fatigue cycles. The stress amplitudes correspond to $0.75\sigma_y$, $1.02\sigma_y$ and $1.11\sigma_y$, with R=0. Therefore the specimens were loaded in the tensile regime; from σ_y=0*amplitude up to σ_y'=2*amplitude, and the loading curve was sinusoidal. The frequency was variable to keep the loading rate constant in all 3 experiments. The relationship between stress amplitude and frequency can be seen in Table 5.4. For the fatigue test a hydraulic Instron 8501 machine was used.
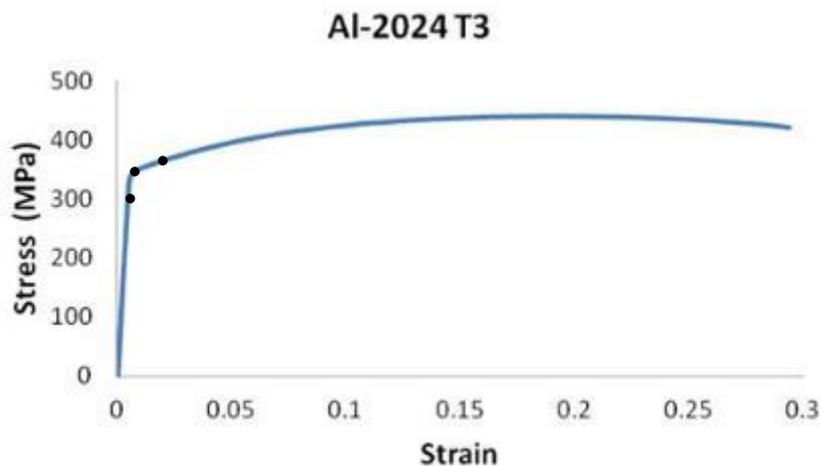
Figure 5-12. The strain amplitudes used for the fatigue cycles.
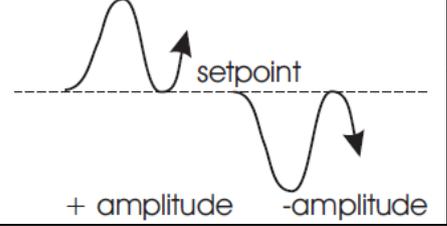
	Time	Total Strain	Stress rate	Stress rate-frequency
	t=T	$4\varepsilon_o$	$\dot{\sigma} = 10^{-2}$/sec	$\dot{\sigma} = d\sigma/dt = 4\sigma_o/T = 4\sigma_o f$

Table 5.3. Relationship between strain rate and frequency for cyclic loading.

Stress (σ_y)	Frequency (f)
$0.75\sigma_y$	0.625
$1.02\sigma_y$	0.35
$1.11\sigma_y$	0.08

Table 5.4. The corresponding frequency values for the specified amplitudes of stress.

The hysteresis loop was recorded in real time during the experiment by placing a strain gauge on the back face of the specimen, and obtaining the load output from the Instron machine. 3D DIC image acquisition was employed during the fatigue test. The camera set-up was capable of correlating the displacements and mapping the corresponding strain distributions. So, deformation patterns were obtained and superimposed over the corresponding microstructure. Not all samples were cyclically loaded till final failure; since the characterization of Fatigue Crack Initiation (FCI) was the main focus of this study.

5.4.2. Macro-scale in situ mechanical testing

Macroscopic 3D-DIC experiments were initially performed in the specimen geometries shown in figure 3.1a. Consecutive images were taken during the experiment with a 3D DIC camera set-up. The images were taken after a specified number of cycles, in this case at: 0 cycles, 1000 cycles, 3000 cycles, 5000 cycles and then every 5000 cycles. At the specified number of cycles, the loading was temporarily stopped, and images were acquired for one cycle from zero load up to the maximum load (and back to zero) and the same procedure was followed in the next cycle were images were taken (0-max-0 then again 0-max-0); therefore the image correlation and the corresponding microstructural displacements were extracted at maximum loading, at the specified number of cycles. Figure 5.13 shows the ε_{yy} strain contours for 3 samples at different stress amplitudes: $0.75\sigma_y$, $1.02\sigma_y$ and $1.11\sigma_y$; after 30000, 5000 and 5000 cycles, respectively. For $0.75\sigma_y$ no strain accumulation was observed after 5000 cycles, and therefore the strained configuration after 30000 cycles is shown where significant strain has accumulated for the sample. For stress amplitude of $1.11\sigma_y$, strain accumulates quickly at the centre of the sample due to the geometry of the specimen, after just 5000 cycles. At lower stress amplitudes, i.e. $0.75\sigma_y$ - $1.02\sigma_y$, the strain fields are heterogeneous at the central region of the sample and the geometry of the sample is not so critical. The microstructure in the latter cases plays a more important role to the occurring local strain values and contours. The cyclic accumulation of strain at

0.75σ_y amplitude is considerably smaller with respect to 1.02σ_y, as the former lies within the elastic part of the stress-strain curve, while the latter, i.e. 1.02σ_y corresponds to the early stages of plastic deformation in the stress-strain curve. An average of 0.45% strain accumulation occurs for a strain amplitude of 0.75σ_y in figure 5.13b, after 30000 cycles, measured via a 10 mm virtual extensometer placed at the centre of the sample, while in figure 5.13c, a strain accumulation of 1.5% occurs at stress amplitude of 1.02σ_y in one sixth of the number of cycles; i.e. 5000 cycles. In figure 5.13d, a 7.1% accumulated strain is measured with a 10 mm virtual extensometer after 5000 cycles.
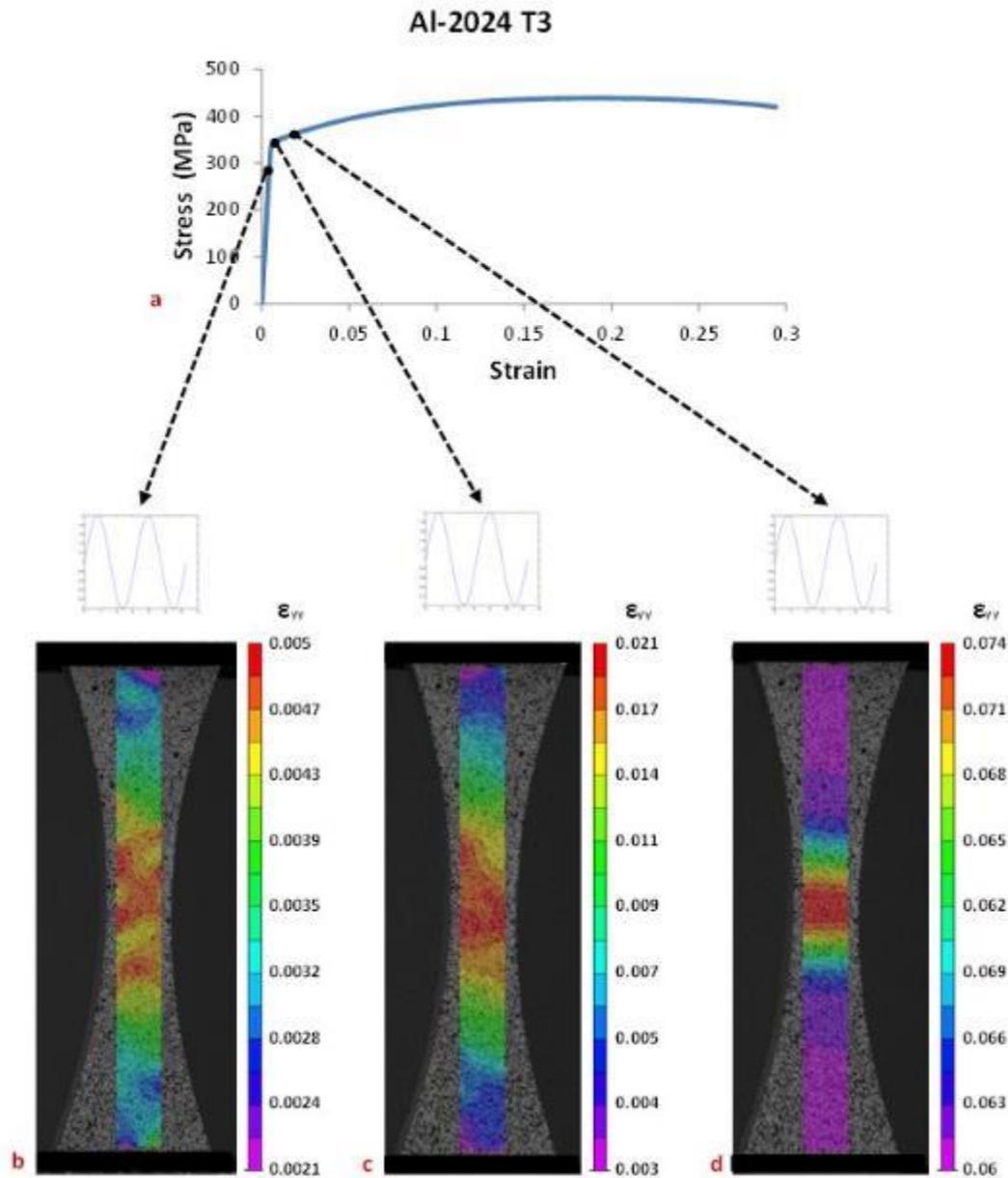
Figure 5-13. a) The stress-strain curve obtained by tensile testing. The ε_{yy} strain distributions for 3 samples cyclically loaded (R=0) at different stress amplitudes: b) 0.75σ_y and after 30000 cycles, c) 1.02σ_y and after 5000 cycles and d) 1.11σ_y and after 5000 cycles. The sinusoidal graphs are shown just schematically.

The amount of necking was also calculated for the 3 cases of figure 5.13 in order to quantify the amount of necking during cyclic loading. The 3 necked surface contours during cyclic loading for a

certain amount of accumulated strain were compared to the amount of necking during monotonic tensile testing for the same applied strains at the centre of the sample. So the accumulated strain during cyclic loading was the same with the applied strain at the centre of the sample both measured with a virtual extensometer. The amount of necking was found not to be the same for the monotonic and the cyclically loaded samples. Thus damage during cyclic loading could be estimated by comparing the observed smaller necking area to the identified larger monotonic tensile testing necking part. The difference between the two values is an estimate of non-homogeneities that occur during cyclic loading. Figure 5.14b shows the strain distribution and amount of necking after 5000 cycles, for an applied strain of 0.065. The z-contraction at the centre of the sample was approximately 0.08 mm, while the total accumulated strain was calculated with a 10mm virtual extensometer to be approximately 0.065. The strain values and amount of necking were also obtained for the same applied strain in the central region (0.065 measured via a virtual extensometer), for the tensile test described in previous section 5.2. For the same accumulated strain, i.e. 0.06, the amount of necking at the centre of the sample was higher in comparison to figure 5.14b. The z-contraction at the centre of the sample was 0.12 mm, i.e 50% higher than for the cyclically loaded specimen. The missing necking component (0.12-0.08=0.04) from the cyclically loaded sample is related to non-homogeneous deformation and damage that occurs during fatigue testing and to the highly localised straining that occurs during fatigue in comparison to the uniform plastic deformation during tensile testing. It has to be pointed out that only one of the sample surfaces was inspected, which means that the total amount of necking was doubled for the whole sample. A total thickness reduction of 0.16 and 0.24 mm out of the 5 mm initial thickness of the sample should be considered in both cases in figure 5.14a and b.

At smaller fatigue loading amplitudes ($1.02\sigma_y$ for figure 5.14c and $0.75\sigma_y$ for figure 5.14d), the influence of cyclic loading on necking is much smaller. The amount of necking in figure 5.14c in the central region of the sample was around 0.04 after 5000 cycles, while in figure 5.14d the z-contraction was only 0.01 after 5000 cycles. The sample in figure 5.14d is loaded elastically, and it is found that after 30000 cycles, the amount of necking is negligible, which signifies the absence of ductility during damage evolution at low amplitude fatigue.
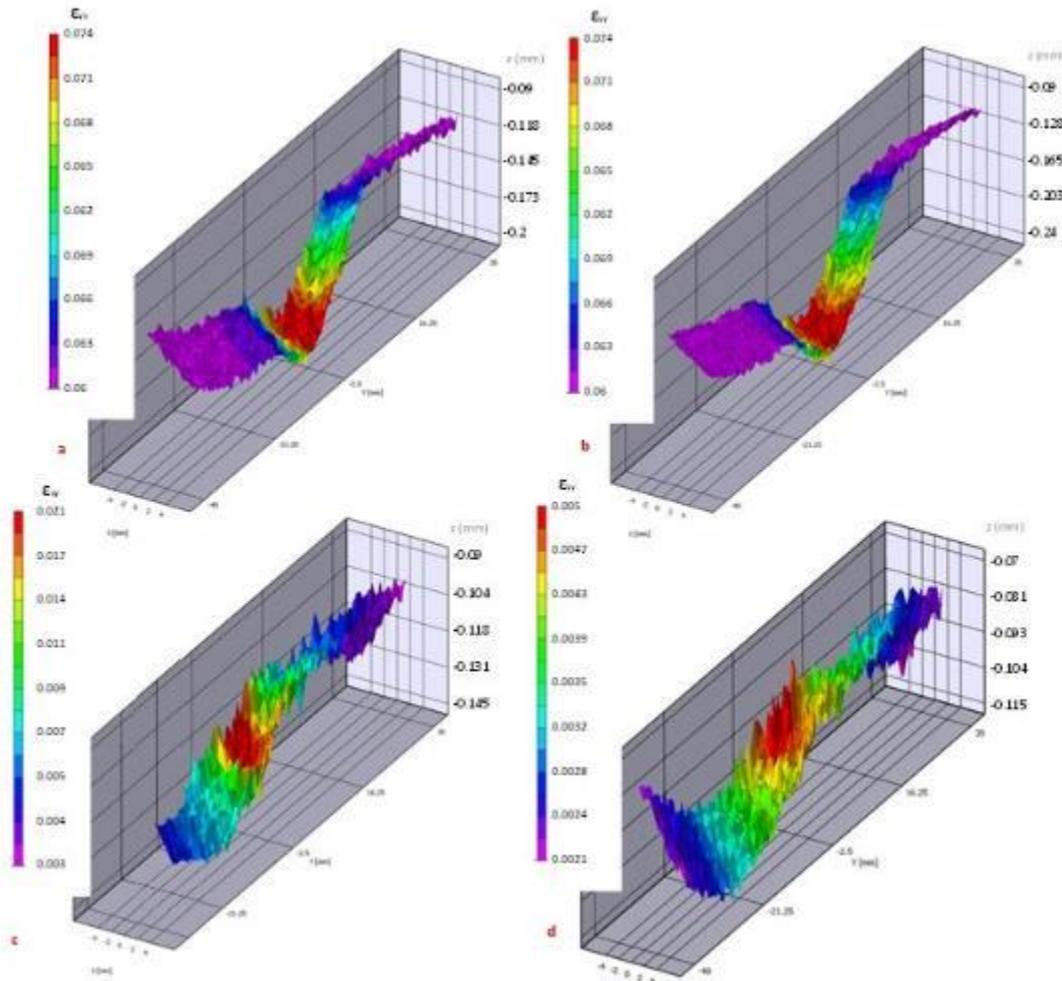
Figure 5-14. ε_{yy} strain contours and surface profile for: a) tensile loading at 0.065 strain, b) the same accumulated strain 0.065 after 5000 cycles and $1.11\sigma_y$ stress amplitude, c) after 5000 cycles and at a stress amplitude $1.02\sigma_y$ and d) after 30000 cycles and at a stress amplitude $0.75\sigma_y$.

5.4.3. Meso-scale in situ mechanical testing

Cyclic loading was performed for the same specimen geometry (figure 3.1a) to investigate strain development at a smaller scale. A modified DIC kit was employed this time to facilitate small scale strain measurements. 150mm Pentax extension tube was attached on a 5MP DIC camera to increase the magnification. The camera was positioned at a relatively small distance from the sample: around 15-20 cm. In this case, spraying on the sample surface was not applied. The samples were mechanically polished and etched to reveal the microstructure. The microstructural features were then used to correlate the images during mechanical testing.

The configuration of the light was different compared to the case of the set-up for macroscopic 3D DIC; a fiber-optic ring light was used in order to enhance the density of light towards the sample surface. Conventional DIC lights (shown in figure 3.13) were not adequate and the sample surface appeared to be very dark. The shiny polished surface of the sample was reflecting the light which resulted in poor lighting configuration for the samples. The contrast was also relatively small, in comparison to samples used in conventional DIC set-up (where the sample surface is sprayed with white and black speckles to increase the contrast). All these observations necessitated the use of high

intensity and homogeneous light configuration. The ring light was located as close as possible to the sample; 10-15 cm in this instance, and the ring light was positioned parallel to the sample surface (the light reaching the sample surface perpendicularly).

Figure 5.15 shows a microstructural image obtained by the 2D DIC camera. The microstructure appears much darker in comparison to the image of the microstructure in figure 5.2, obtained using a conventional microscope; which is due to the light configuration. In the conventional microscopes the light is much closer to the sample surface (0.05 up to 2.5 cm), and the intensity is much higher. The main drawback for the current set-up of the light was the distance of the ring-light from the sample surface. Due to this distance between the ring-light and the sample, a large percentage of the light was reflected from the (shiny) sample surface towards the surrounding environment (in all possible directions). Therefore the grains appeared to be relatively dark (reflecting the light away). In contrast, the particles appear here white instead of black (see figure 5.2). Actually, it is not possible to see individual particles at this scale; but what is observed in the picture are clusters of particles. And these clusters appear to be white instead of black as they absorb the light in contrast (the particles are not shiny, but over-etched in comparison to the surrounding matrix) and thus they become supersaturated in the image (therefore they appear as white). The presence of these clusters was also found by SEM analysis and was shown in figures 5.4 and 5.5. The presence of these clusters of particles is beneficial for the image correlation process as it enables the tracking and movement of these particles by the DIC cameras during mechanical testing. So DIC measurements become more accurate, detailed and reliable.
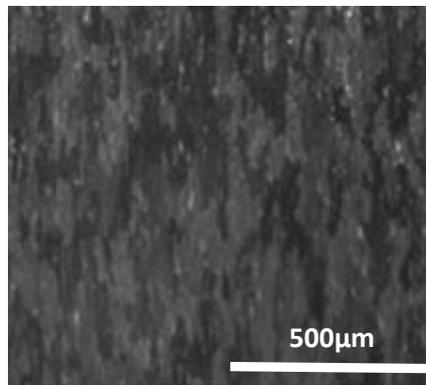
Figure 5-15. Microstructural image at the centre of the sample of figure 3-1a, obtained with the Correlated Solutions camera (5MP), with a special extension tube attached.

Three different fatigue tests were performed for the same stress amplitudes as for section 5.4.2, a low amplitude within the elastic part of the stress-strain curve, a mid-amplitude for an applied stress corresponding to the very first stages of plastic deformation (in the stress-strain curve), and a relatively high amplitude within the plastic region. Three strain components were evaluated in each case, the major strain component, ε_{yy}, which is parallel to the macroscopic loading direction, the lateral contraction strain component, ε_{xx}, and the shear strain component. Evaluating the shear strain component was important as it is the shear strains that in most cases nucleate slip bands along which crack initiation occurs.

Low-amplitude (0.75σ$_y$)

Fatigue testing within the elastic part of the stress-strain curve was initially pursued. The test was stopped every 5000 cycles to acquire images from 0 up to maximum amplitude (0.75σ$_y$), to obtain the corresponding strain distributions for the ε$_{xx}$, ε$_{yy}$, and ε$_{xy}$ components. Figure 5.16a shows the ε$_{yy}$ strain distribution after the 1st cycle for the fully loaded condition of the sample. Large areas of relatively high local strains, mid-range and low strain values are highlighted with red, white and blue broken lines. The local strains are observed to be clustered and highly non-homogeneous. Figure 5.16b shows that the evolution of the ε$_{yy}$ strain component is relatively small, and the strain distribution after 30000 cycles seems similar to that in figure 5.16a. The strains appear still non homogeneous, similarly to figure 5.16a. The clusters circled in figure 5.16a which have similar strain values become quite smaller and more irregular. Also the strain scale in figure 5.16b is larger, but this effect is better analysed in figure 5.17b. Figure 5.17a and b shows the stress strain curves (output from the tensting machine) throughout the whole test and the strain distributions (obtained from DIC) after a specified number of cycles. The strain values over the whole DIC area were calculated and the distribution plots were obtained after a specified number of cycles; i.e. 1, 10000, 20000 and 30000 cycles. It is shown that during cyclic loading the distribution widens allowing a broad spectrum for the strain values that occur on the microstructural level. So the non-homogeneous plastic deformation is enhanced during cyclic loading. Furthermore, the distribution curves move towards lower strain values. In general, strain accumulation is expected during cyclic loading, and the distribution curves should move towards the right; at higher strain values during cyclic loading. Yet the opposite occurs in this case. This is due to the local hardening of the material within the grain structure occurring during cyclic loading. It has been reported that material hardening and softening occurs in metals during fatigue testing [8, 54, 72]. In this case, hardening occurs in the central area of the sample, where the highest (elastic) stresses are applied. Material hardening at the central area of the sample (10mm x 10 mm reduced area), leads to decreased strain values in the corresponding region as the material hardens, moving the necessary displacements away from the central region towards the edges of the sample as the material is softer there.
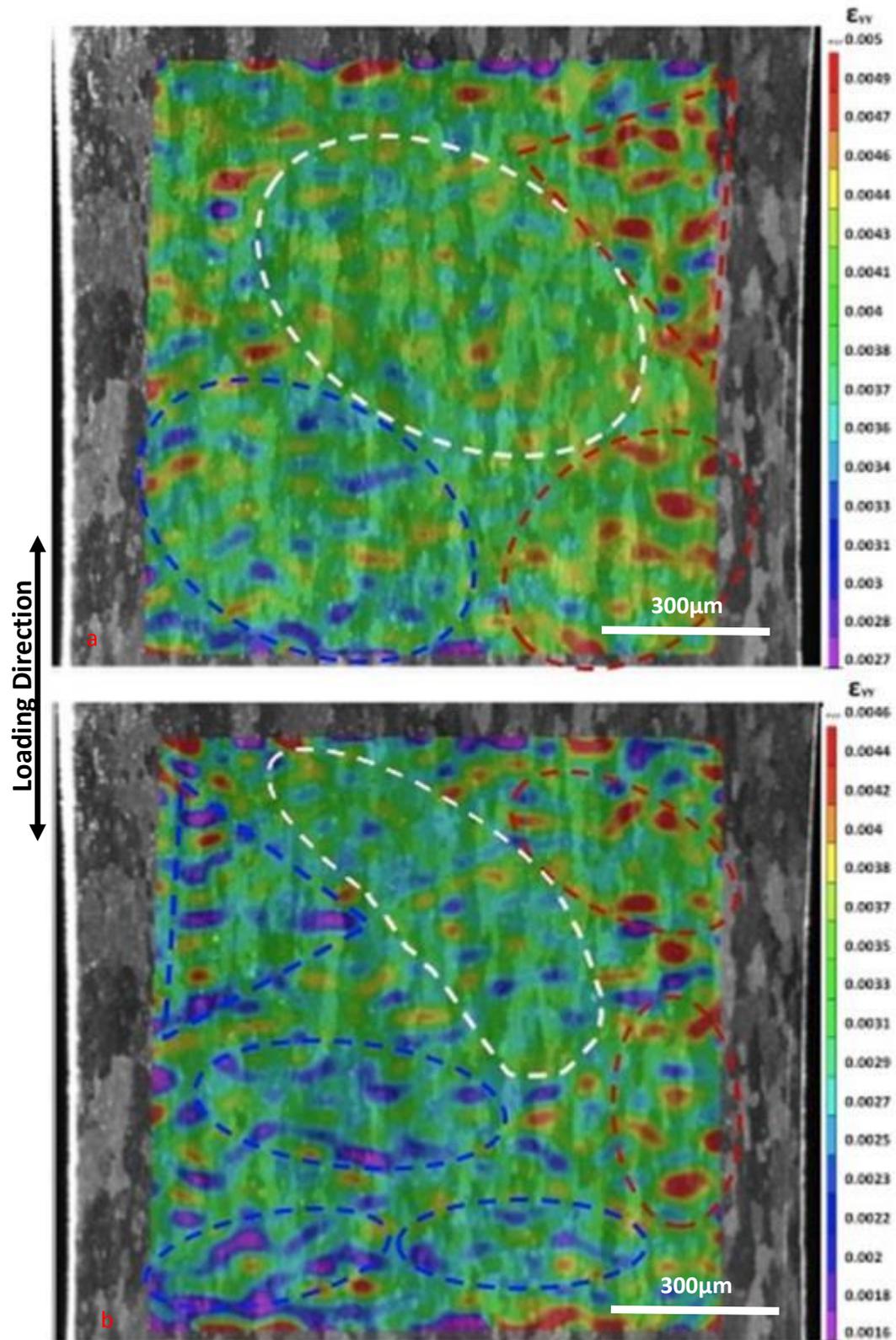
Figure 5-16. Strain distributions (on the principal direction, ε_{yy}) for the fully loaded sample after: a) 1 cycle, and b) 30000 cycles.
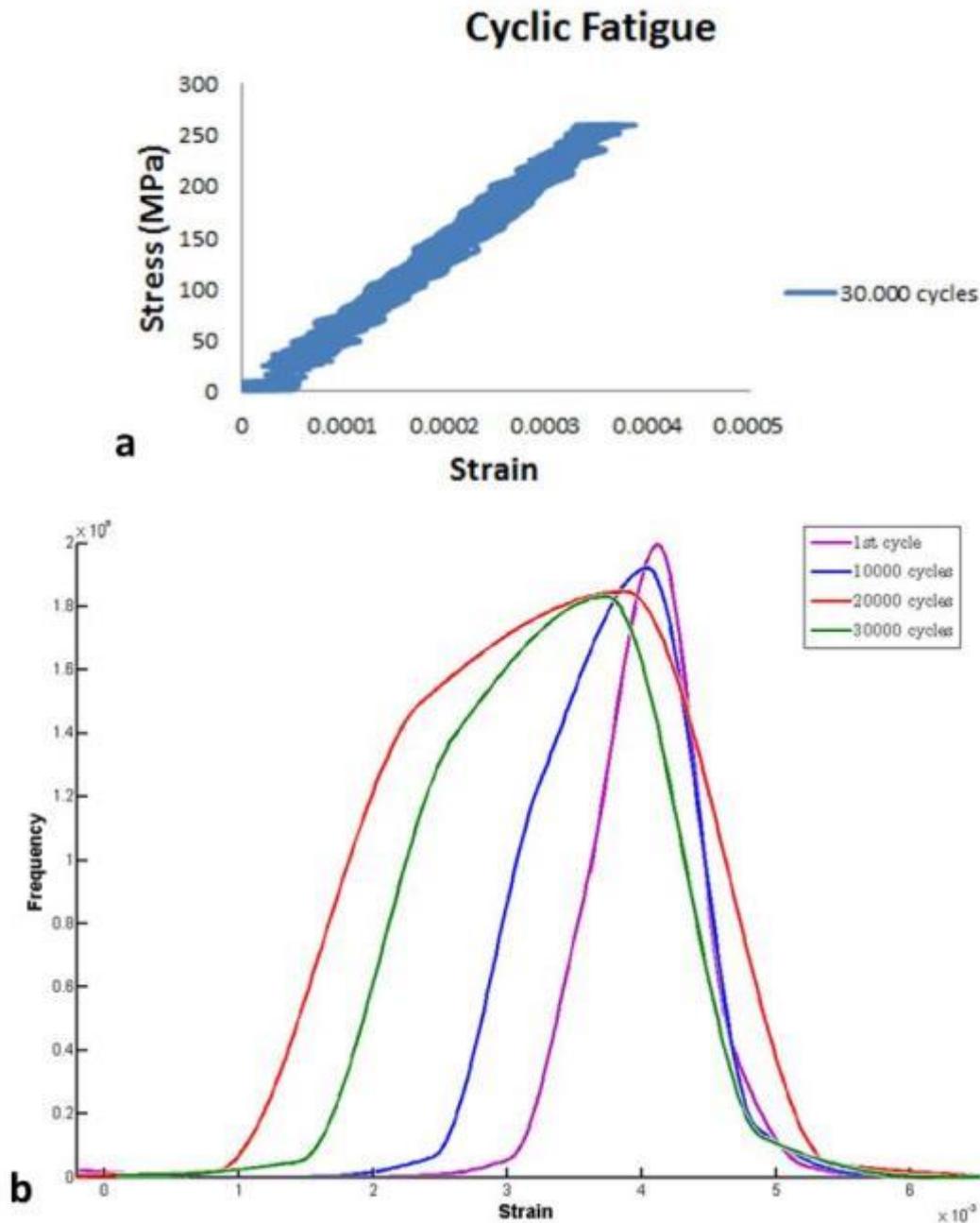
Figure 5-17. a) Stress-strain curves output from the testing machine, b) Strain distributions measured by means of DIC at maximum load (0.75σ_y and initial applied strain 0.004) after 1, 10000, 20000, and 30000 cycles.

Figure 5.16 showed that the ε_{yy} strain component does not follow the microstructural features (grains); this is further explained in section 5.5. Yet, in figure 5.18 it may be seen that the lateral contraction, or ε_{xx} strain component does follow the observed microstructure. The blue arrows in both figure 5.18a and b show that the corresponding grains are compressed in much larger proportions with respect to grains-regions pointed by red arrows. The x-direction strain component is highly non homogeneous with the high compressive strain values lying next to regions with relatively

small (compressive) strains. During cyclic loading the strain heterogeneities are enhanced, and the highly compressed regions shown with blue contours lie just next to low compressed areas in figure 5.18b. The non-homogeneities for the ε_{xx} strain component were increased during cyclic loading and also the strain spectrum increased by 56% between figure 5.18a and b.

The ε_{xy} shear strain component was also evaluated, and the shear strain distribution is shown in figure 5.19. The strain fields were also highly heterogeneous and had similar patterns to the ε_{yy} component. The major ε_{yy} strain component had a direct influence on the distribution of the shear strains. Clusters and groups of strain fields appear in figure 5.19, similarly to figure 5.16a and b. Yet the strain patterns do follow in some cases the grains, like in the locations highlighted by arrows in figure 5.19. However in other locations the shear strains cross several grains, like at the location with the red broken line. So the ε_{xy} component is affected by both the ε_{yy} and the ε_{xx} components. Macroscopically ε_{xy} is affected by the major strain component but locally is influenced by the lateral contraction component, following the microstructural features.
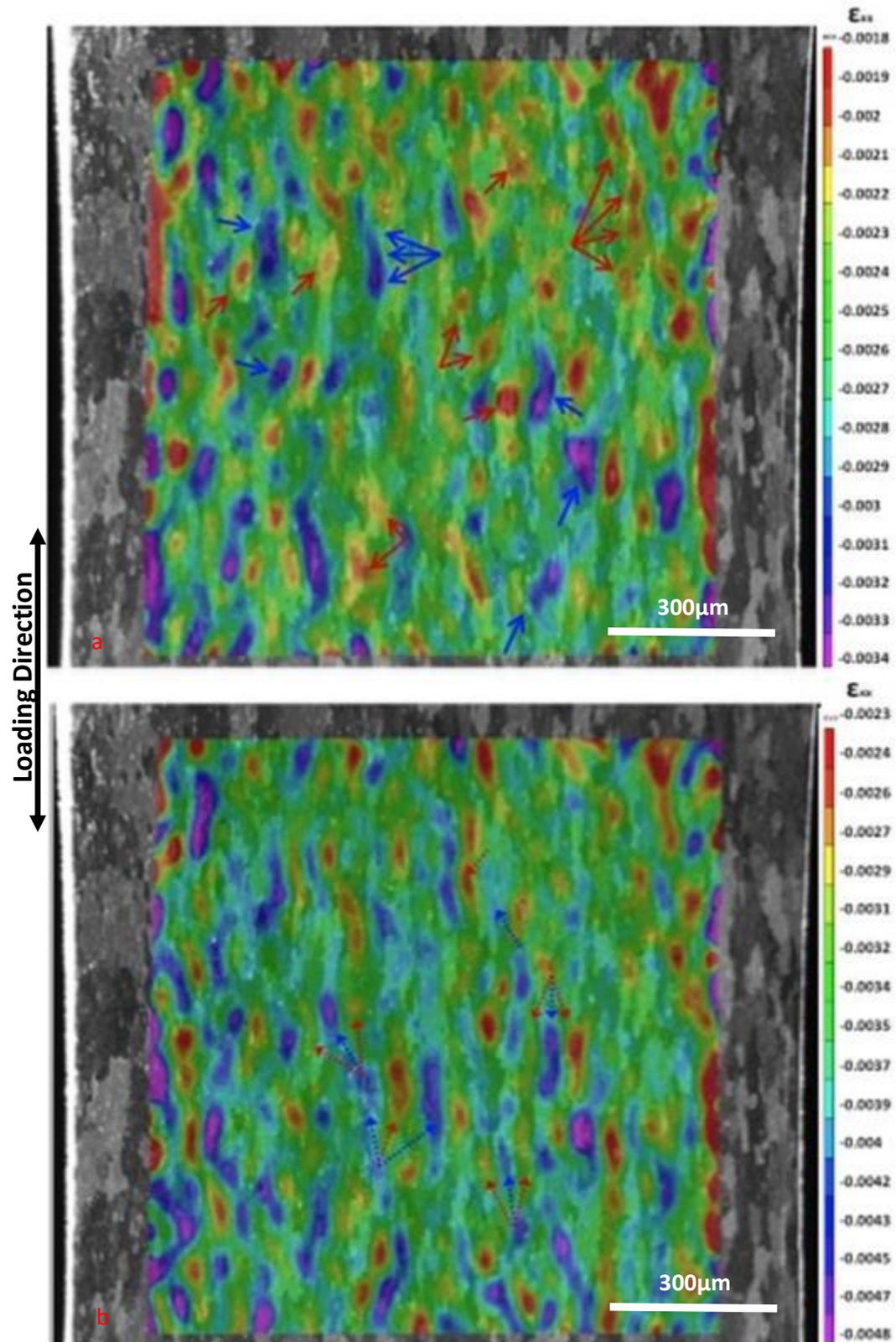
Figure 5-18. Strain distributions on the x-direction for the fully loaded sample after: a) 1 cycle, and b) 30000 cycles.
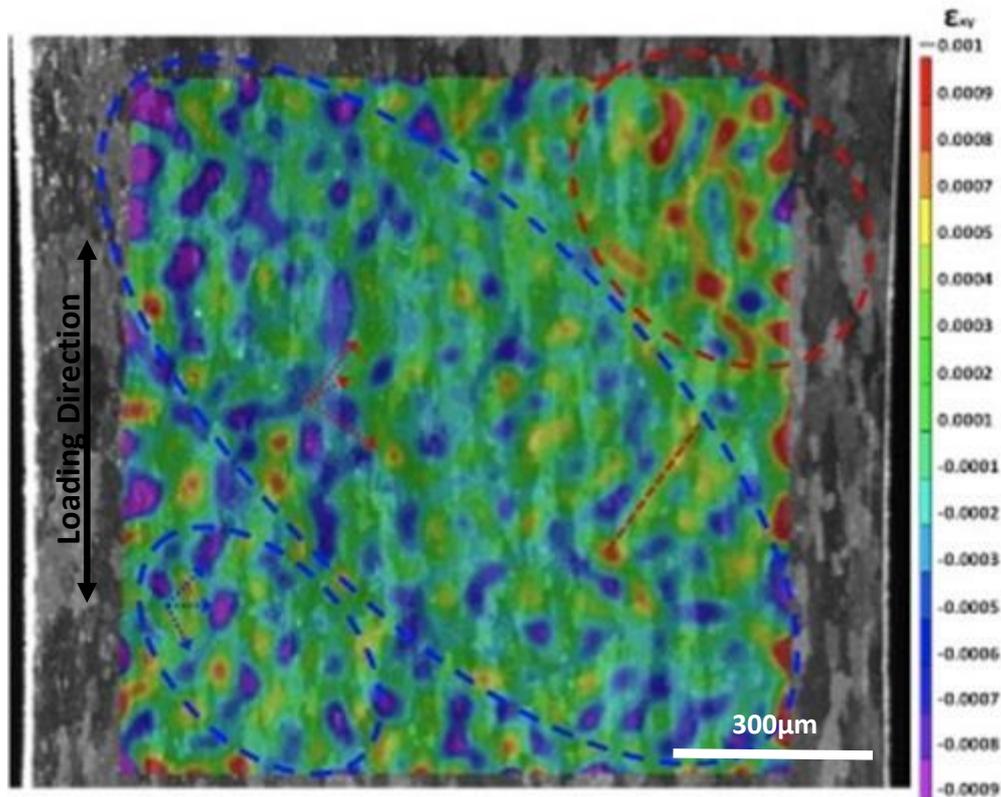
Figure 5-19. Shear strain distribution for the fully loaded sample after 30000 cycles.

Mid-amplitude ($1.02\sigma_y$)

Cyclic loading up to $1.02\sigma_y$ was performed, and the strain development was captured by means of DIC. Figure 5.20a shows the ε_{yy} strain distribution after the first cycle. The strains appear to be separated in 3 distinctive regions: the blue boxed areas which correspond to low strained areas, the white boxed region which has average strain values, and the red boxed area close to the edge of the sample which has relatively large strain values. Figure 5.20b shows the strain distribution after 5000 cycles. The strain fields between figure 5.20a and b are much different. Macroscopic shear bands have formed in the analysed region, approximately 45^0 with respect to the loading direction. Two main shear bands have formed shown with red broken lines. Three more shear bands with smaller strain values are also shown with white broken lines. All bands appear to have formed along the same direction, parallel to each other, approximately 45^0 with respect to the loading direction. Figure 5.21a and b shows the stress strain curves (output from the tensting machine) and the strain distribution (obtained from DIC) in the beginning of the test and after 5000 cycles. It is shown that during cyclic loading the strain distribution spectrum widens, enhancing non-homogeneities in the local strain fields. So the non-homogeneous plastic deformation is enhanced during cyclic loading.
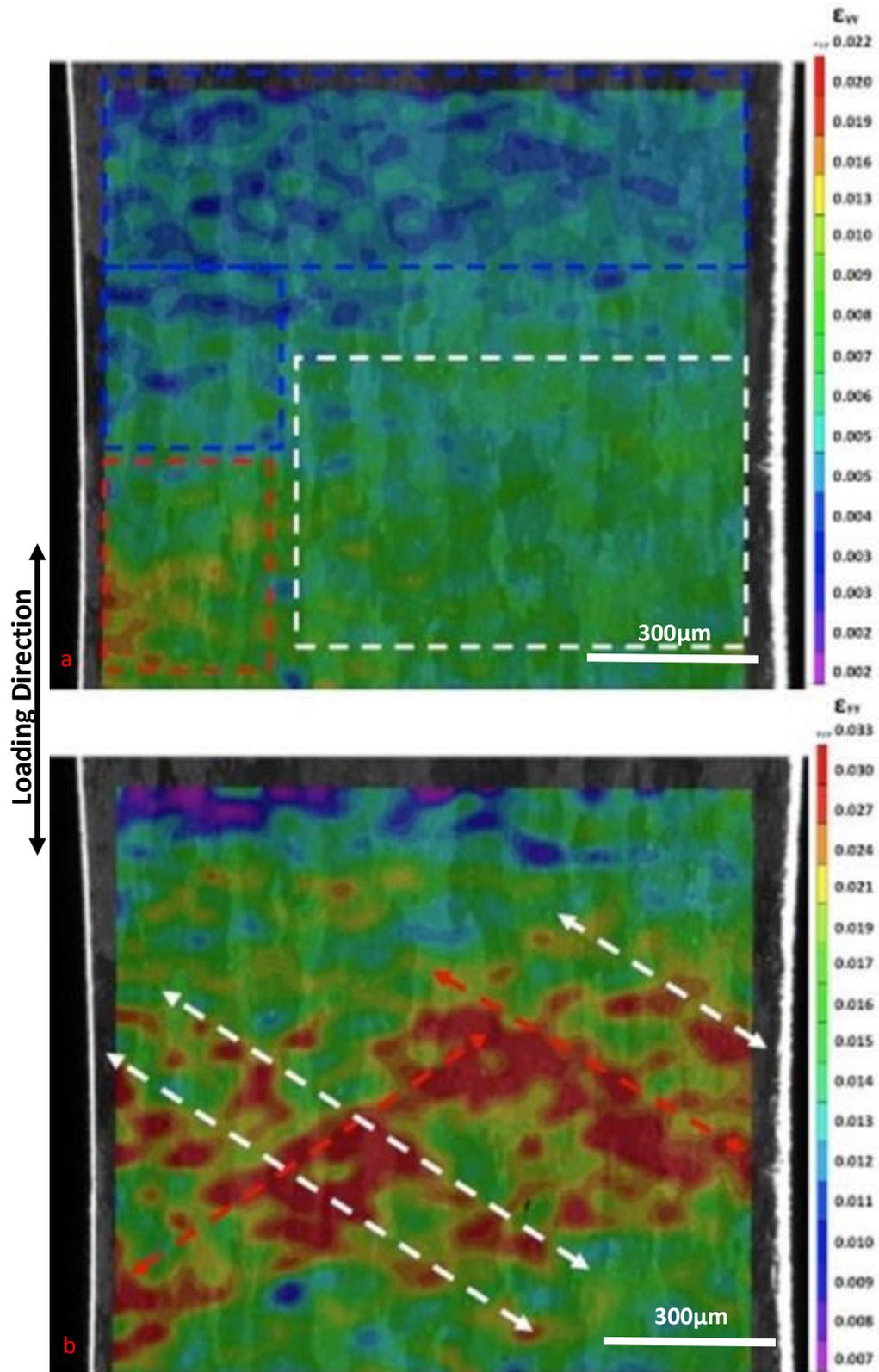
Figure 5-20. Strain distributions (on the principal direction: ε_{yy}) for the fully loaded sample after: a) 1 cycle, and b) 5000 cycles.
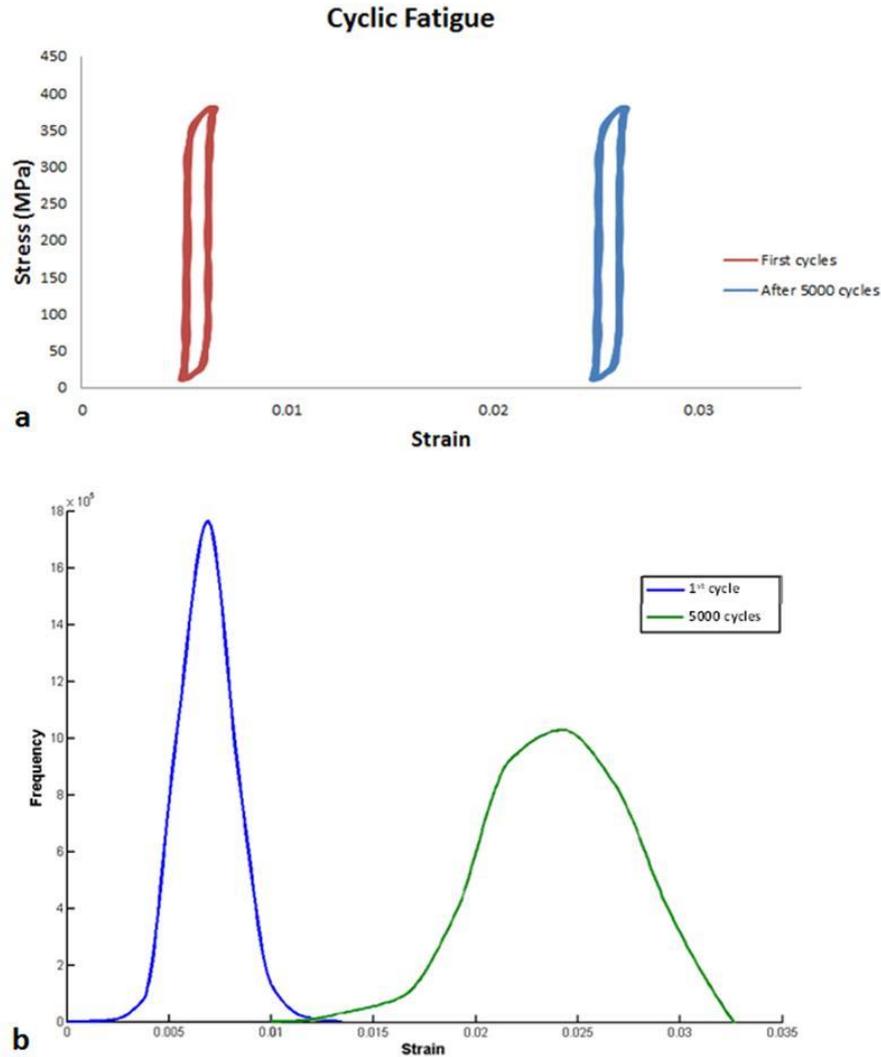
Figure 5-21. a) Stress-strain curves output from the testing machine, b) Strain distributions measured by means of DIC at maximum displacement ($1.02\sigma_y$ and initial applied strain 0.007) after 1, and 5000 cycles.

The ε_{xx} strain component was also evaluated and it is shown in figure 5.22. Figure 5.22a shows the x-direction strain component after 1 cycle. The fields appear highly non homogeneous in half of the area of interest (left side). The highest compressive strains (purple contours) appear in the bottom part of the image. In figure 5.20a, the lower part carried the highest local strains along the y-direction. So it is expected to have higher compressive strains in the lower part of the image. During cyclic loading, the x-direction strain field becomes more non-homogeneous. High compressive strains lie next to regions which have undergone relatively small compression. The strain fields cross the whole microstructural area, and the material has the tendency to form regions of high compressive strains next to regions which do not compress considerably. So during cyclic testing in the plastic region, the material has the tendency to form areas of banded deformation. Highly compressed grains aligned next to grains which barely carry any compressive strains. All strains though for the lateral contraction component are within the elastic region.

The shear strain component was also evaluated and is shown in figure 5.23. Large areas of low, mid and high shear strain distributions can be seen in the blue, white and red circled areas respectively. The strain distribution is highly non-homogeneous with high strain values existing close to low strains. The highest positive and negative shear strain values are aligned approximately 45° with respect to the loading direction. The highest positive shear strains are aligned along the red broken arrow, while the lowest shear strains, or highest negative shear strains (highest in absolute values), are aligned perpendicular to the highest positive shear strain values, also aligned close to 45 with respect to the loading direction. But apart from this macroscopic effect, at the microscale, strong non-homogeneities exist.
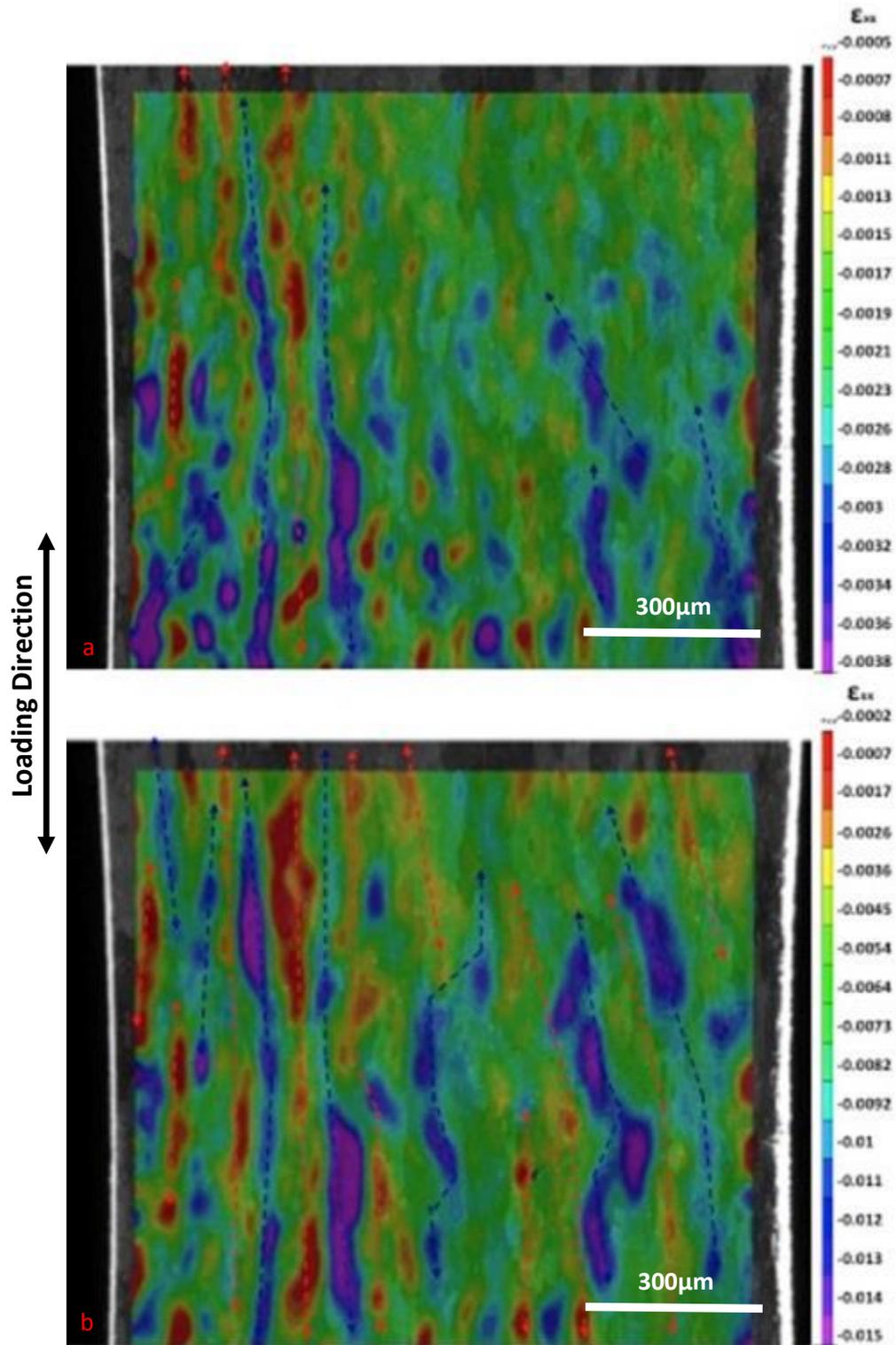
Figure 5-22. Strain distributions on the x-direction for the fully loaded sample after: a) 1 cycle, and b) 5000 cycles.
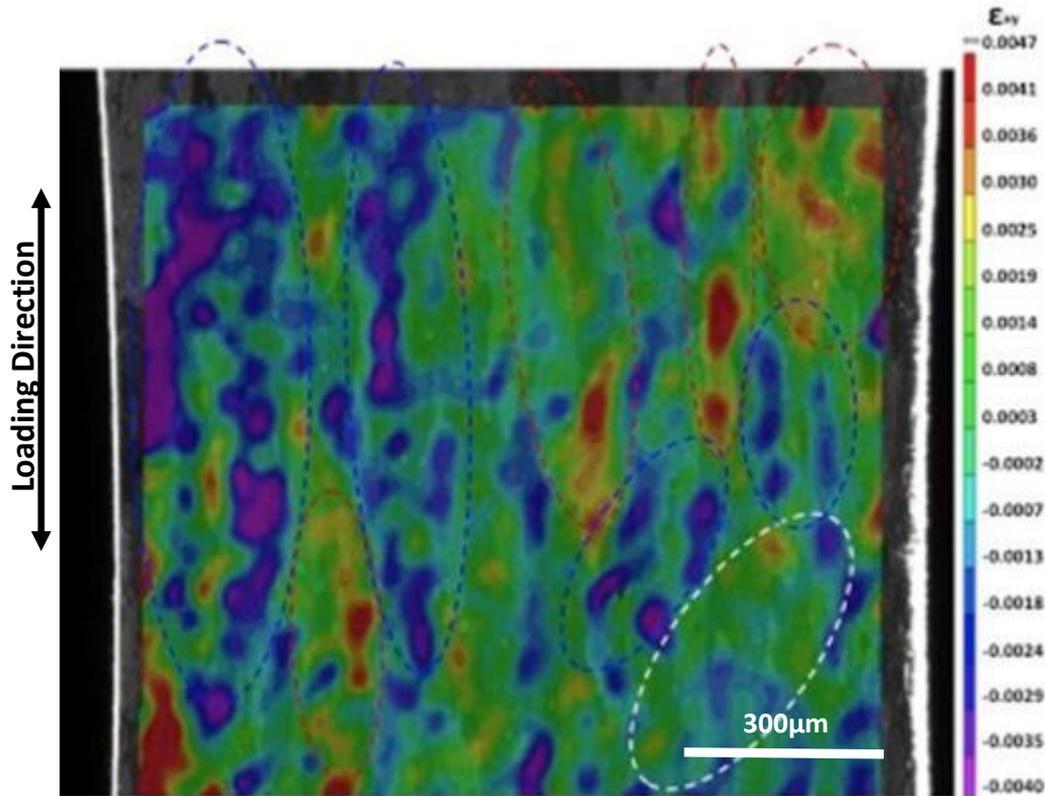
Figure 5-23. Shear strain distribution for the fully loaded sample after 5000 cycles.

High-amplitude ($1.11\sigma_y$)

Cyclic loading up to $1.11\sigma_y$ was performed. Figure 5.24a shows the ε_{yy} strain distribution after the 1st cycle. The highest strains are already localized at the centre of the sample from the first cycle. The highest strains appear to be within a circular region in figure 5.24a, with no evidence of shear banding mechanisms. There is a distinct, circular, highly deformed region in figure 5.24a. During cyclic loading, and after 5000 cycles, the strain distribution does not change, and only strain accumulation occurs at the corresponding region. There is no alteration or shift of the strain patterns. Figure 5.25a and b shows the stress strain curves (output from the tensting machine) and the strain distribution (obtained from DIC) in the beginning of the test and after 5000 cycles. The strain distribution for the latter case is wider, similar to the results found for the two previous cases (low and mid amplitudes). The strain increase though in this case is much higher. The applied strain increases from 0.03 for the 1st cycle to 0.058 after 5000 cycles (calculated via a virtual extensometer). The lateral contraction component was also calculated and is shown in figure 5.26. The distributions similar to the previous results were found to follow the grain structure. There is negligible influence of cyclic loading on the strain patterns and distribution in figure 5.26a and b. Only the strain spectrums were increased in figure 5.26b, which was expected. The shear strain distribution was also evaluated.

The shear strain distribution, shown in figure 5.27, is not influenced by the major strain component (ε_{yy}), as the two plots in figure 5.24b and 5.27 are not similar macro- and microscopically. The distribution of ε_{yy} is much different from the distribution of the shear strain component.

141
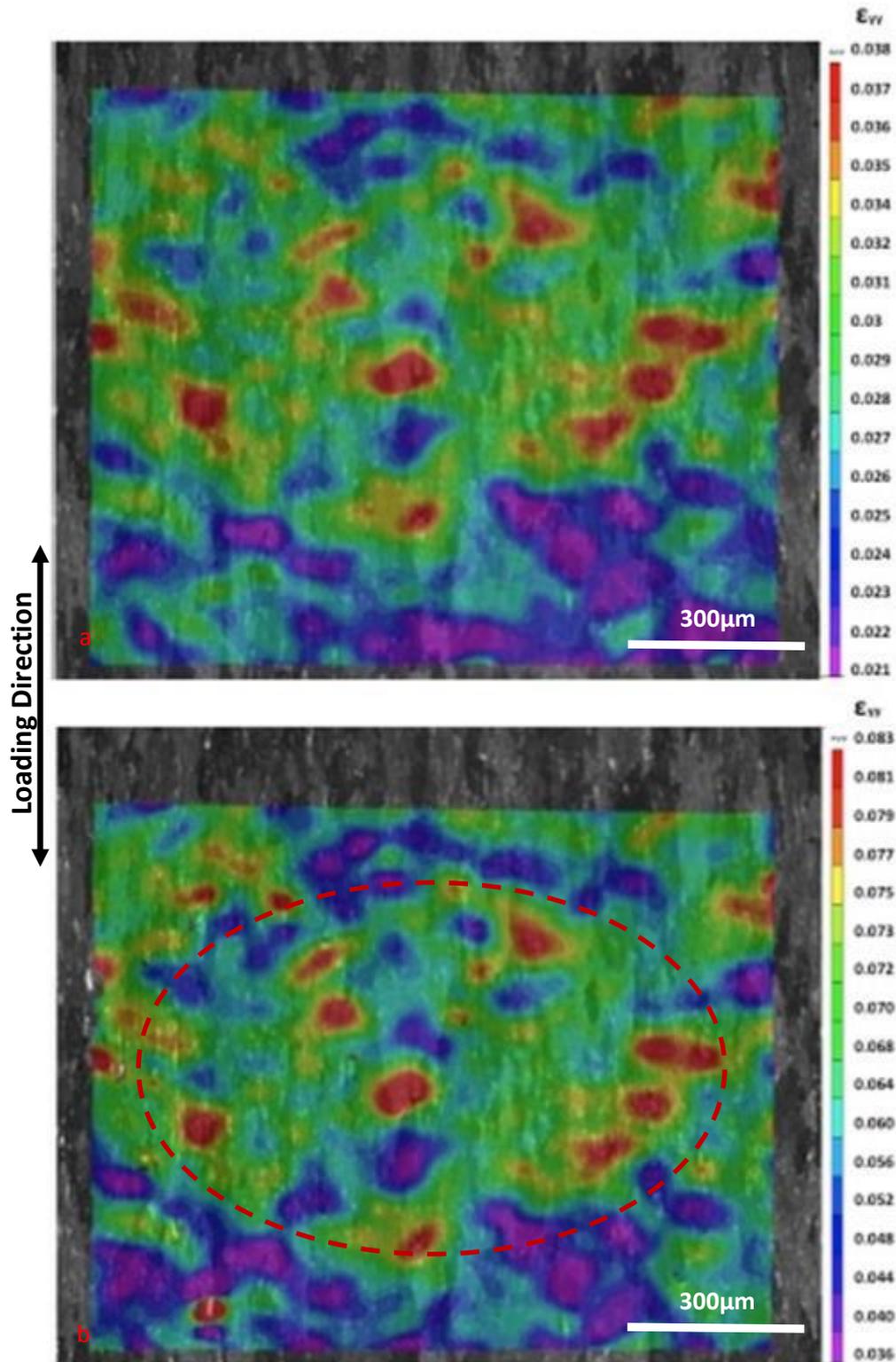
Figure 5-24. Strain distributions (on the principal direction: ε_{yy}) for the fully loaded sample after: a) 1 cycle, and b) 5000 cycles.
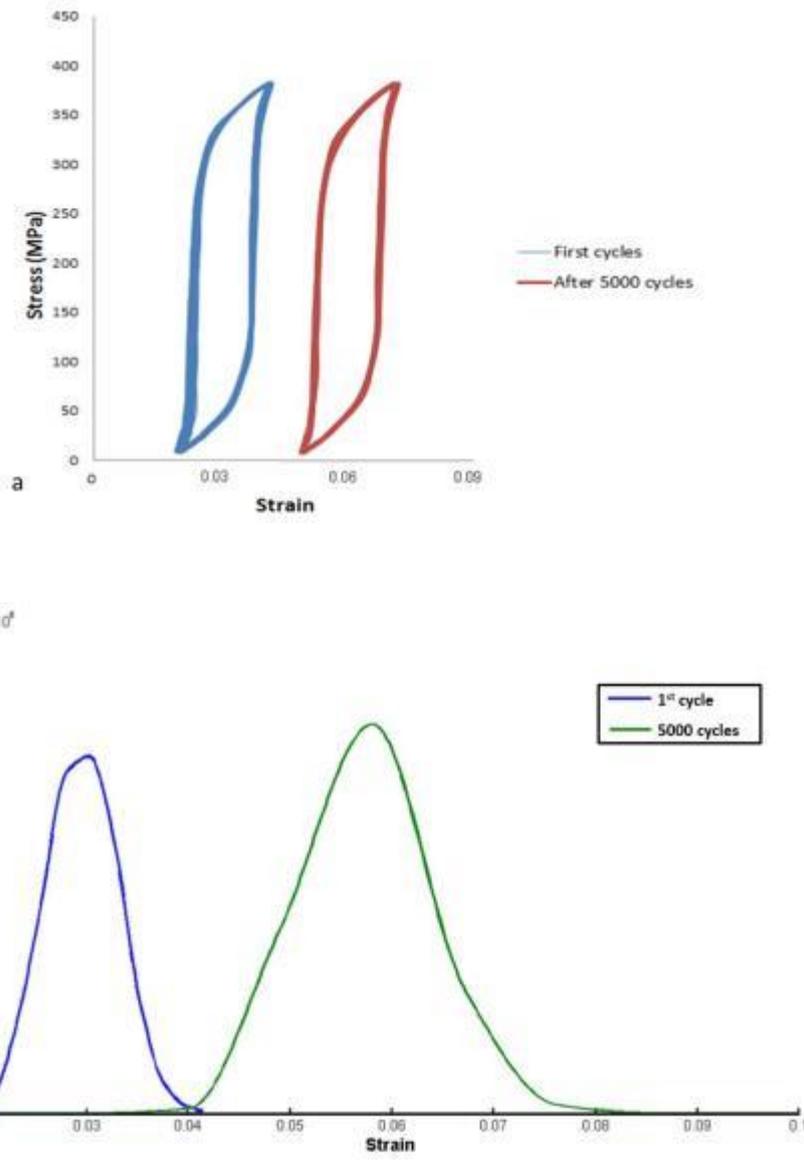
Figure 5-25. a) Stress-strain curves output from the testing machine, b) Strain distributions measured by means of DIC at maximum displacement ($1.11\sigma_y$ and initial applied strain 0.03) after 1 cycle (blue line), and after 5000 cycles (green line).
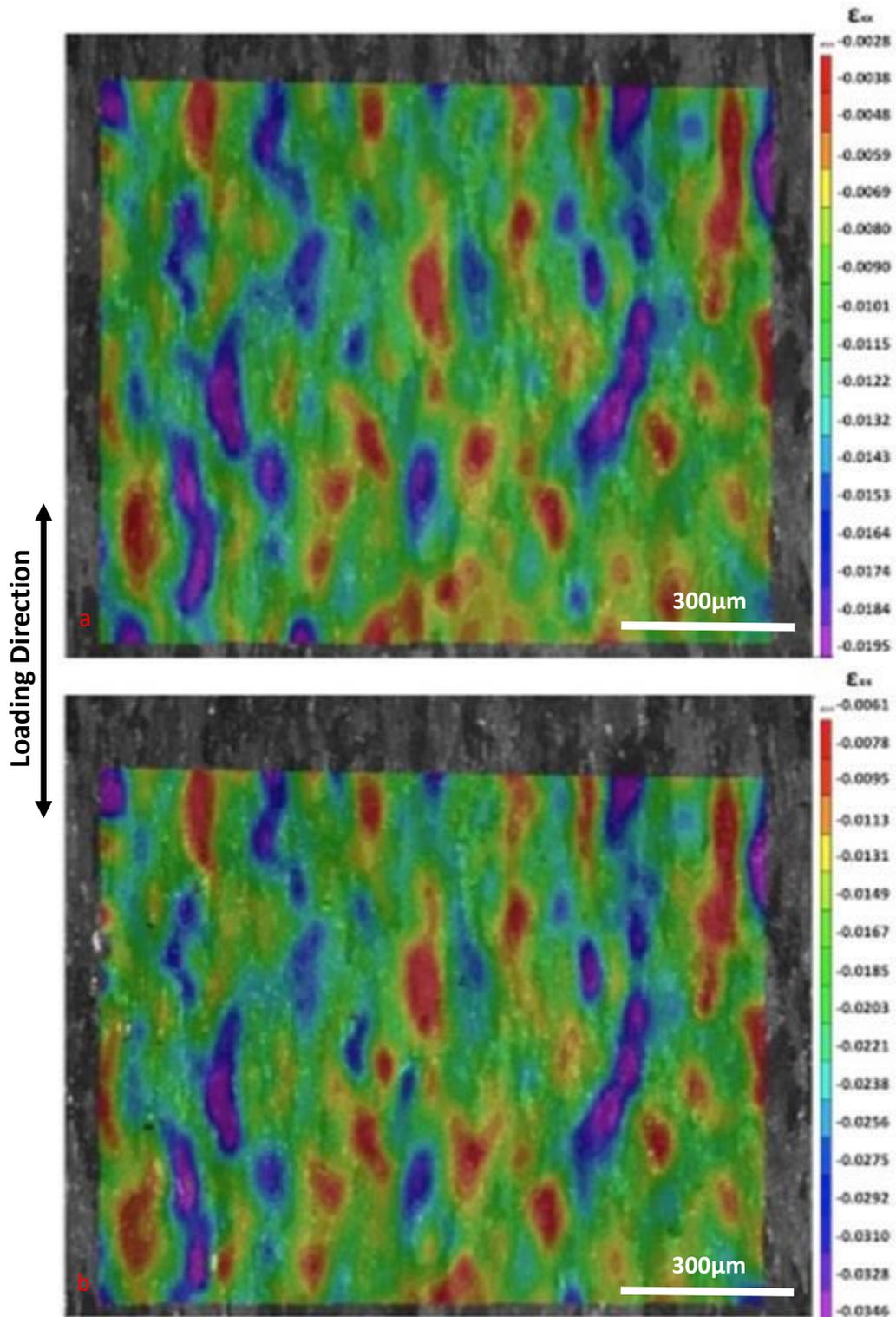
Figure 5-26. Strain distributions on the x-direction for the fully loaded sample after: a) 1 cycle, and b) 5000 cycles.
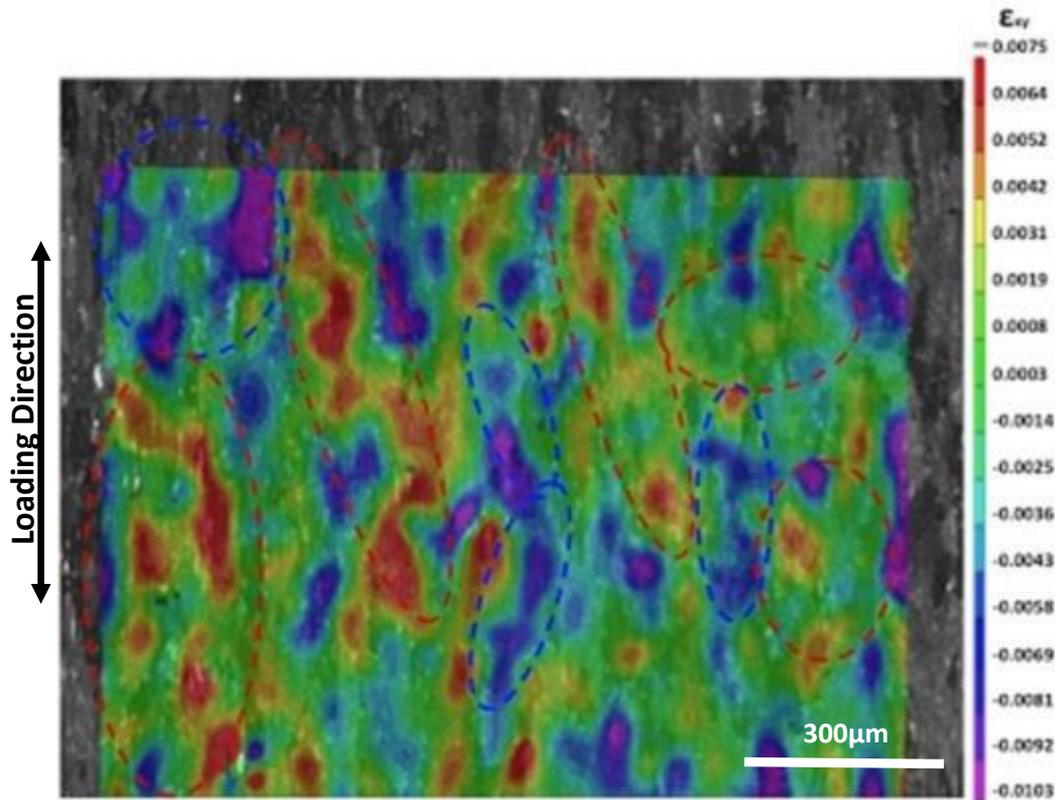
Figure 5-27. Shear strain distribution for the fully loaded sample after 5000 cycles.

5.5. Discussion

The material investigated was Al2024 T3, provided by ALCAN in the form of a 5 cm thick slab. The microstructure was initially revealed by optical microscopy, SEM imaging and EBSD analysis. The shape of the grains varied depending on the corresponding location of the material within the slab. Small equiaxed grains were found close to the slab surface, while the grains appeared to have columnar shape towards the centre of the sample (figure 5.3). The size of the grains is related to the local cooling conditions. Slow cooling rates allow large time intervals for grain growth and the shape of the grains (i.e. columnar) is largely affected by the cooling direction, while fast cooling rates lead to many dispersed nucleation points and thus smaller grains size [73].

The matrix was hardened with Al-Cu particles. Chemical analysis was done to investigate the chemical composition of the particles and it was found that Al and Cu were the only elements present within the particles. In the 2000 series and especially in the Al2024 the AlCu particles are the main source of matrix hardening agents [71]. The stoichiometry between the two elements varied, with the Cu/Al ratio being between 0.15 up to 1.45.

Tensile testing was performed with DIC and strain gauge measurements obtained during the test and revealed a yield strength value of 338MPa at 0.48 % elongation. This is quite a large value for the elongation. It has been reported in literature that usually a 0.2% offset is used for the elongation value at yield point [8, 20, 72, 74]. Yet both the machine read-out (Figure 5.9a) and the strain gauge measurement (figure 5.9b) revealed that the value was correct. A further validation was done by employing a virtual extensometer in the DIC analysis.

145

Figure 5.10 revealed the influence of the reduced cross section on the strain measurements obtained. 2 virtual extensometers were placed on the sample, one running along all the gauge length (74 mm) and the other at the samples' centre (10 mm), and revealed that almost all deformation is taken within a region of 10mm x 10 mm at the centre of the sample. That is also the reason why the global strain taken from the machine were coupled to the ones gained by the strain gauge.

Fatigue testing was performed at 3 different amplitudes at the macroscale: within the elastic region ($0.75\sigma_y$), at the early stages of plastic deformation ($1.02\sigma_y$), and within the plastic region ($1.11\sigma_y$). At low amplitude the area where high strain accumulated is dispersed over a large area, with the tendency to form bands within the material (figure 5-13b). The dispersed strain fields in this case suggest that it is more difficult to locate the region where crack initiation will occur and furthermore which areas are affected and highly strained in the sample and thus in a structural material [14, 26, 27]. The strain accumulation rate is quite small as after 30.000 cycles the strain increase is from 0.004 (initial amplitude of first cycle) to 0.0047 measured with a 10 mm virtual extensometer placed at the samples' centre (17.5% after 30.000 cycles). At mid amplitude (figure 5.13c), the strains highly localise at the centre of the sample and the strain accumulation rate is considerably higher, increasing from 0.007 to 0.015 (more than 100% increase in just 5000 cycles). The high strain fields appear to have formed at an angle close to 45° with respect to the loading direction suggesting the existence of shearing mechanisms in the material. At relatively high amplitude (figure 5.13d), all the plastic strains are highly localised within 10 mm at the centre of the sample, perpendicular to the loading direction, with the strain accumulation rate much higher, increasing from 0.02 to 0.072 (more than 260% increase in just 5000 cycles). Figure 5.14 shows that necking occurred only for the high amplitude cyclic loading (figure 5.14b) with the low and mid amplitude showing no evidence of any form of necking (figure 5.14c and d).

3 more experiments were performed at the meso-scale at the same stress amplitudes: $0.75\sigma_y$, $1.02\sigma_y$, and $1.11\sigma_y$ to investigate the deformation mechanisms at the microstructural level. For all amplitudes the lateral contraction component was found to follow the microstructural features but not the major strain component.

Sample necking was also investigated for all three samples of figure 5.13. A comparison was made for the necking that occurred during tensile testing (figure 5.14a) with the necking that occurred for the same applied strain at the sample centre measured via a virtual extensometer (figure 5.14b). The applied strain in figure 5.14a is 0.065, the same as for figure 5.14b (for the sample cyclically loaded. A virtual extensometer of 10mm was used in both cases. As shown in Fig. 5.14 the amount of necking is much less for the fatigue specimen. This is primarily due to the nature of fatigue. During cyclic loading, the specimen is expected to show less necking and less associated plasticity as damage occurs in a highly localised area(s). During tensile testing the nature of the final fracture is related more to void formation, growth and coalescence (which results in cross sectional reduction); while in fatigue it is the formation of cracks and their corresponding growth that leads to failure. Yet a considerable amount of necking was found also for the specimen in figure 5.14b. This is due to the

fact that the specimen is loaded within the plastic region. The necking component in the other two specimens in figure 5.14c and d was relatively small. Especially the sample loaded within the elastic region shows negligible necking in figure 5.17d, which suggests that most of the strain accumulation occurs via continuum mechanisms.

The strains at the microstructural level were evaluated in section 5.4.3. The major strain component along the loading axis, ε_{yy}, the lateral contraction, ε_{xx}, as well as the shear component, ε_{xy}, were all evaluated for the 3 samples tested. The displacement amplitudes were similar to the ones used in section 5.4.2, one within the elastic region for a stress amplitude of $0.75\sigma_y$, at the early stages of plastic deformation at $1.01\sigma_y$, and within the plastic region $1.11\sigma_y$. Initially the major strain component is discussed here.

In low amplitude fatigue testing, the strain fields along the loading direction were highly non-homogeneous. Direct assessment of the strain map is relatively difficult. Only by creating individual groups or areas with similar strain distributions it becomes relatively easier to understand the strain fields. In figure 5.16, relatively high, mid and low strains appear to be groups within large regions crossing several grains. So the strain fields can be related to the micromechanical behaviour of several neighbouring grains, rather than individual grains [14, 26, 27].

For a mid-strain amplitude, close to the yield point for the material, shear bands form, and govern deformation and damage mechanisms. These bands form close to 45° with respect to the loading direction and cross through several grains. The deformation behaviour in this case is rather macroscopically controlled. At even higher stress amplitudes; i.e. $1.11\sigma_y$, the highest strain values accumulate at the centre of the sample. The highest strains do not localise into shear bands anymore, but strain accumulation occurs in a circular area expanding at the centre of the sample. There is no alteration or shift of the strain patterns during cyclic loading in figure 5.24, suggesting that continuum mechanics approaches and modelling may be used to describe strain and damage accumulation [54]. In this case deformation and damage cannot be fully described by shear bands acting within and across several grains. Void nucleation and evolution is a more adequate method for predicting final failure [75-78].

The major strain component did not follow the microstructural features. Yet for the lateral contraction the strain patterns do follow the grain structure. Grains highly compressed next to grains with low compression were found to exist for all strain amplitudes. The non-homogeneities were enhanced during cyclic loading for all cases; from low to high amplitude cyclic loading. So the material has the tendency at a broad strain spectrum to form long range deformation bands during cyclic loading along the x-direction.

The reason why the x-component follows the microstructural features but the major ε_{yy} component does not, may be explained by simple continuum mechanics. The sample has been rolled, and elongated grains have formed in the sample. If the strain patterns would follow the grains, in the case of 2 neighbouring grains, if one of them would be heavily stretched and the other one compressed, local sample rotation would have been necessary in order to accommodate the occurring

displacements and strains. This is shown schematically in figure 5-28, where the left grain is stretched and the right one compressed. The two black arrowed lines show the amount of sample rotation that is needed to accompany the occurring deformation within the two neighbouring grains. Furthermore, considerable amount of damage would have occurred at the (common) interface between the grains in order to accommodate the occurring strains. So for samples that have large elongated grains, the strain patterns cannot follow the grains, as such an effect would require sample rotation. Furthermore, plastic deformation occurs via shear strains, and in particular via dislocation movement approximately in a direction 45° with respect to the loading direction. Dislocation slip is not favourable parallel to the loading direction as there is not adequate driving force for dislocation movement [74].
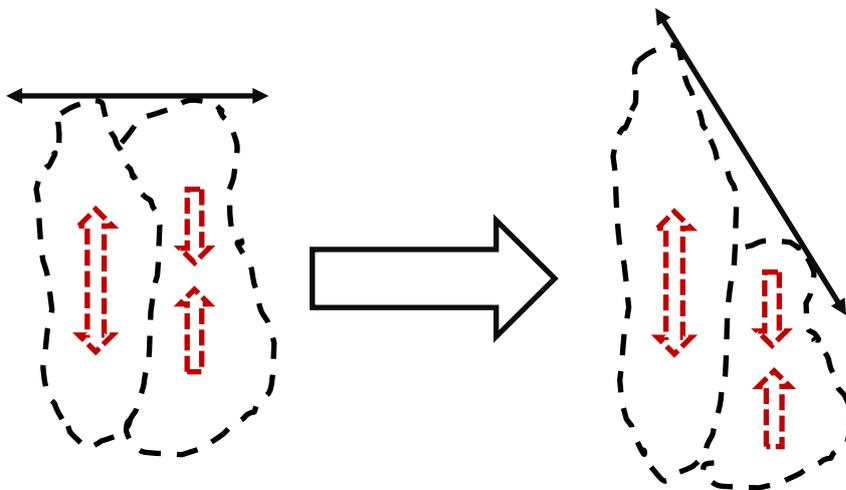
Figure 5-28. Schematic representation of shape changes in two grains for which one of them is under tension and the other under compression.

The shear strain component seemed to follow the microstructural features in some cases. The strain distribution appeared to have a relatively macroscopic behaviour, with the highest absolute strain values being oriented close to 45° with respect to the loading direction. Yet strong non-homogeneities existed even along these 45° orientations. In total the shear strain component had both the characteristics of the ε_{yy} and the ε_{xx} component. It seemed to follow the microstructure, and morphology seemed closer to ε_{xx} component, yet macroscopically the shear strains appeared to be clustered along specific orientations and locations, and seemed to have similar distribution to the ε_{yy} strain component. So the shear strain component is affected by both the lateral contraction component, and also from the normal strain component parallel to the loading direction. This makes sense as in a square unit cell, a loading situation where the two opposite sides are loaded in tension and the other two opposite sides are loaded under compression, equals a pure shear loading configuration for the sample [54, 72]. Yet for the local shear strain distribution a competition between the ε_{yy} and the ε_{xx} component exists. This was not true for the 3rd case (applied stress of 1.11σ_y), in which case there was no correlation in the strain fields between the ε_{xy} and the ε_{yy} component

(figures 5.24 and 5.27). For high amplitude loading, strain accumulation is not affected by shear strains present, and damage nucleation and growth is mainly affected by the major strain component.

5.6. Conclusions

The metallurgy and mechanical behavior of Al2024 T3 was investigated in this chapter by using advanced experimental techniques, such as multiscale DIC, SEM, EBSD and EDS analysis. The material was provided in a slab form and appeared to have large inhomogeneities in the grain size and morphology throughout its thickness, with large columnar/elongated grains present in the slab center and small equiaxed grains at the slab's surface. Al-Cu particles were present in the matrix, with various shapes and sizes, extending from hundreds of nanometers top more than 30µm. Also the chemical composition or Al/Cu ratio was found to vary from 0.15 up to 1.01.

The mechanical properties were evaluated, such as yield point, UTS, and elongation to fracture. A set of fatigue tests was then carried out, for 3 stress amplitudes: within the elastic region, just after the onset of plastic deformation and well within the first stages of plastic deformation. Even though DIC has been available for several years, limited published work can be found on image correlation for samples cyclically loaded, and relating the fatigue performance and strain development with respect to the occurring microstructure. Initially macroscopic 3D-DIC measurements were taken during the test and it was found that while for low and mid amplitudes, macroscopic shear bands form on the sample surface, for high amplitudes, deformation is highly localised at the centre of the sample. Furthermore, considerable amount of necking occurred for the latter loading case, with negligible necking found for the sample loaded within elastic region, and a small amount of necking for the sample loaded just after the yielding. So only within the elastic region, necking can be ignored during cyclic loading.

Meso-scale 2D DIC was also performed at the grain scale, covering a region 10mm x 10mm. For low amplitude, it was found that the strain distribution is clustered in regions of high, low and mid strain magnitudes, signifying that deformation needs to be studied within a region of 3-4 or even more neighbouring grains to yield fruitful results about the strain fields. For mid amplitudes, strong shear bands form on the sample surface while at high amplitudes the strains appear to be highly localised at the centre of the sample, which is in accordance with the observations made above with 3-D DIC. Furthermore, at high amplitudes the strain patterns do not change during cyclic loading, but only the strain values move towards higher values. One fruitful observation for materials with elongated grains-microstructure is that the major strain component does not follow the grain structure and appears to be highly non-homogeneous; while the lateral-contraction strain component does follow the microstructural features. In the next chapter 4-point bending is performed and strain measurements are obtained within the individual grains. The observations made are then connected to the ones made in this chapter. High resolution SEM analysis is also done in Chapter 7 in order to reveal the state of the particles and inclusions in the heavily deformed and undeformed areas.

6

Micromechanical testing

In the previous chapter the material was characterized at 2 different scales: macro and mesoscale. Tension-tension fatigue tests were performed under stress-controlled conditions and revealed the strain development mechanisms across the two different scales. Strain-controlled experiments have been carried out in this chapter at a finer scale in order to investigate strain localisation, FCI and small crack growth.

4 point bending samples were designed, EBSD measurements were carried out over the area of interest to acquire the corresponding grain orientations, followed by in situ displacement-controlled micromechanical testing within an SEM chamber. The local deformation and damage was quantified within individual grains. The EBSD measurements were also used in order to correlate the experimental results with the modelling ones in Chapter 8. In this Chapter, 2 case studies are presented: a low and a mid-amplitude cyclic bending, followed by 2 case studies for samples containing machined holes which were used to study - experimentally - crack initiation and propagation.

6.1.   Low amplitude fatigue testing

The specimen was machined with 50mm length x 7mm width and 4mm thickness. The top surface of the sample was ground and polished down to 0.06 μm Silico, followed by HF etching to reveal the GBs, particles and inclusions. 4-point displacement-controlled micro-bending test was performed with a 2kN Deben vertical bending stage inside a CamScan SEM with a cross head speed of 2mm/min. Initially a static test was performed up to a maximum strain of 0.005 applied to the two left and right edges of the area. The test was interrupted at each 0.2 mm displacement increments, and local displacements and strains were obtained by means of Digital Image Correlation (DIC) as explained in [50]. So the local strains were obtained at maximum displacement - load. Subsequently, displacement controlled cyclic loading was initiated with a frequency of 0.5, from 0 up to maximum displacement. The test was interrupted after the 1st cycle, the 10th cycle, the 100th, 200th, 300th, 400th and 500th cycle, at the maximum displacement applied and images were acquired. The consecutive images were

correlated to the image at the first peak load and hence to the image for the undeformed sample. The micrographs were analysed using the commercial image analysis software, DaVIS 7.0, by LAVision [79] to determine the in-plane displacement field from which plastic strain values were calculated. In the current study, the microstructural features of the material have been directly used as the pattern from which to correlate the images between two successive loading steps. A sensitivity analysis on the interrogation window size was carried out, and a multiscale interrogation window with 16x16 and 32x32 pixels was finally selected in all the experimental results presented in this study. This enables to verify the strain measurements via a multipass algorithm with different interrogation windows. The interrogation window is the square (or any other shape selected by the user) patterns upon which image correlation is performed and in this study contained 16x16 and 32x32 pixels in each image [53]. A low magnification analysis (40x) was pursued in order to acquire the strain fields throughout the whole region shown in figure 6.1, as well as the effect of grain orientation on local deformation and damage. The initial microstructural area selected is shown in Figure 6.1, and corresponds to an area of approximately 5mm x 3.5mm.
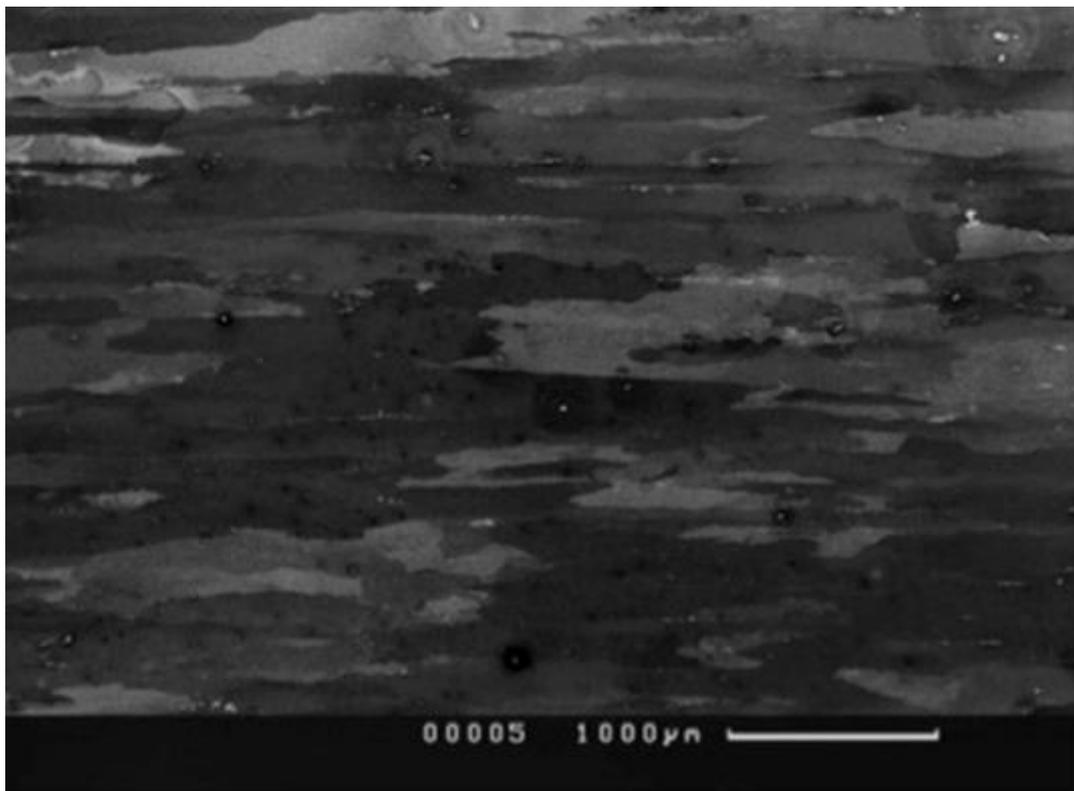
Figure 6-1. SEM image of the region selected for observing in situ strain development within the grains.

Figure 6.2 shows strain localisation in various regions of the area shown in figure 6.1 after few cycles, with bands mainly at 45 degrees with respect to the horizontal loading direction. However various orientations of the bands can be observed with an orientation which depends strongly on the underlying microstructure and orientation of the individual grains. Yet these deformation bands extend further beyond individual grains, and therefore there is evidence of the role of the orientation

of neighbouring grains. This is more pronounced in Figure 6.3a after 500 cycles, where various regions of neighbouring grains show high and low local strain values. Two different stages for metallurgical investigations were then carried out in order to observe the regions of high and low strains and analyse any occurring plastic inhomogeneities and localised damage: a low magnification optically based inspection, followed by a high resolution surface inspection with a FEI Inspect-F SEM.

6.1.1. Macroscopic deformation analysis and damage characterisation

The strain distributions within the whole region of figure 6.1 were obtained which enables to and distinguish between heavily deformed and low deformed grains-regions. Figure 6.3a shows the strain map after 500 cycles, for the fully loaded sample. Highly deformed regions were observed and circled with black dotted lines. There exist high heterogeneities in the microstructure; and this can be attributed to the relatively low applied strains and high anisotropic behavior of the individual grains at low amplitudes. This is in agreement with observations made in reference [26]. To identify the low and highly strained regions, circled areas are drawn (from the author) in figure 6.3a. The black circled regions correspond to highly strained areas and the red circled regions to low strained areas. In figure 6.3b, an optical microscopy image at the same area is shown for comparison. Optical microscopy was used as at this scale it better shows the out of plane deformations and the areas where slip bands have formed. Distinguishing between heavily deformed and undeformed regions is relatively more difficult at this scale; yet several grains appear to have deformed considerably, forming slip bands at various locations. For example the circled area corresponding to region B in figure 6.3a consists of highly deformed grains with the presence of slip bands in Figure 6.3b.

All the locations shown in figure 6.3a were inspected optically. Here only 4 areas are shown: 2 highly strained and 2 low strained areas. Further optical images of the areas shown in figure 6.3a can be found in Appendix. The regions shown in figures 6.4 and 6.5 correspond to the highly strained regions F and B; while regions shown in figures 6.6 and 6.7 correspond to the low strained regions J and L in figure 6.3a. Differential Interference Contrast technique was used for the images of figures 6.4 and 6.5 in order to get sharper images and capture visually the out of plane deformation as well as the occurrence of slip bands. In figure 6.4a the brightly colored grain has undergone significant deformation, while the brown colored grain appears to have deformed uniformly and retained continuity within the matrix. Similar observations for the image of figure 6.4b can be made where significant out of plane deformation and strain localisations can be observed for the brightly colored grain. Plastic deformation was also observed within region B of figure 6.3a. At the central area of figure 6.5, i.e. region b, the grains have deformed plastically, with the formation of ripples-slip bands on the surface.
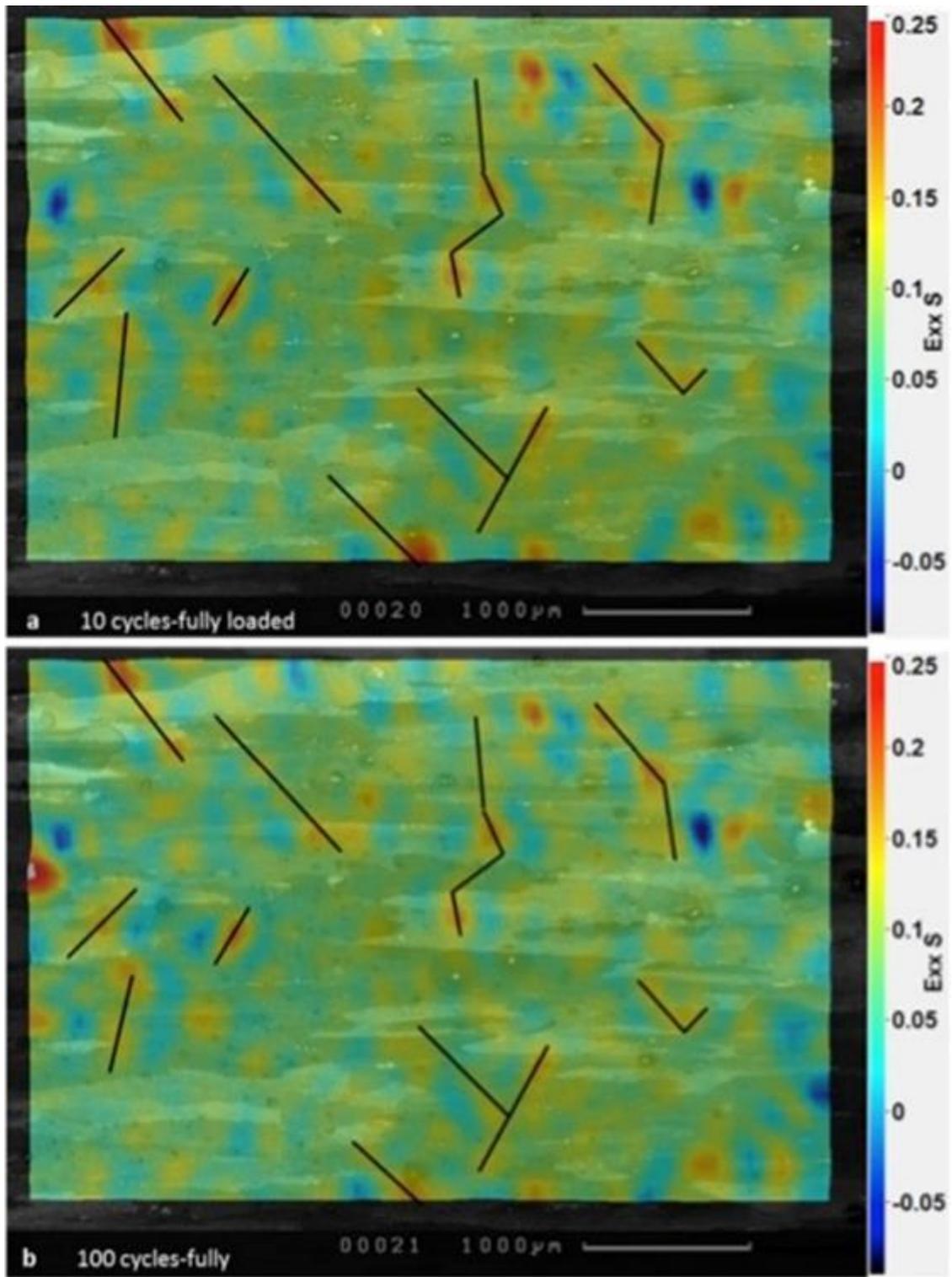
Figure 6-2. a) Strain distribution for the fully loaded sample after a) 10 cycles and b) 100 cycles. No macroscopic strain accumulation was observed.
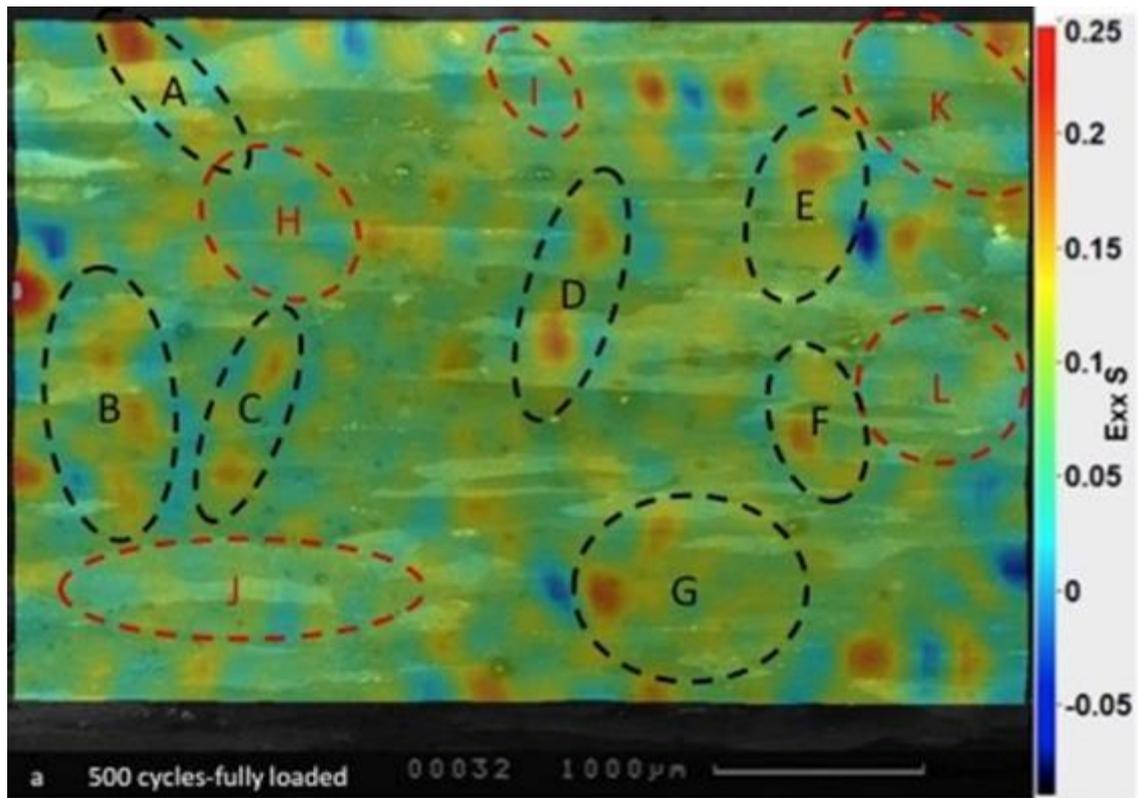
Figure 6-3. a) Strain distribution for the fully loaded sample after 500 cycles, b) optical microscopy image at the same region after 500 cycles (unloaded condition).
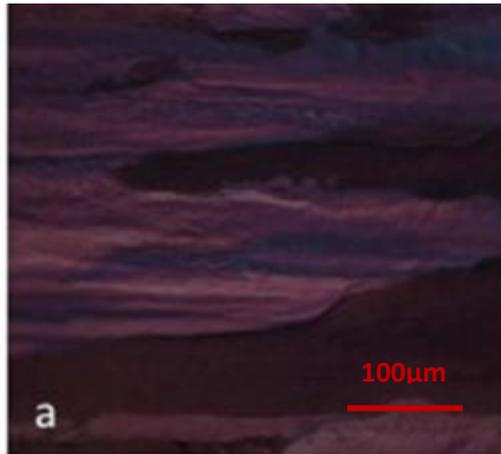
Figure 6-4. High magnification optical microscopy images from area F in Figure 6.3a. a-b) Differential Interference Contrast microscopy technique was used to indicate the presence of out of plane deformation.
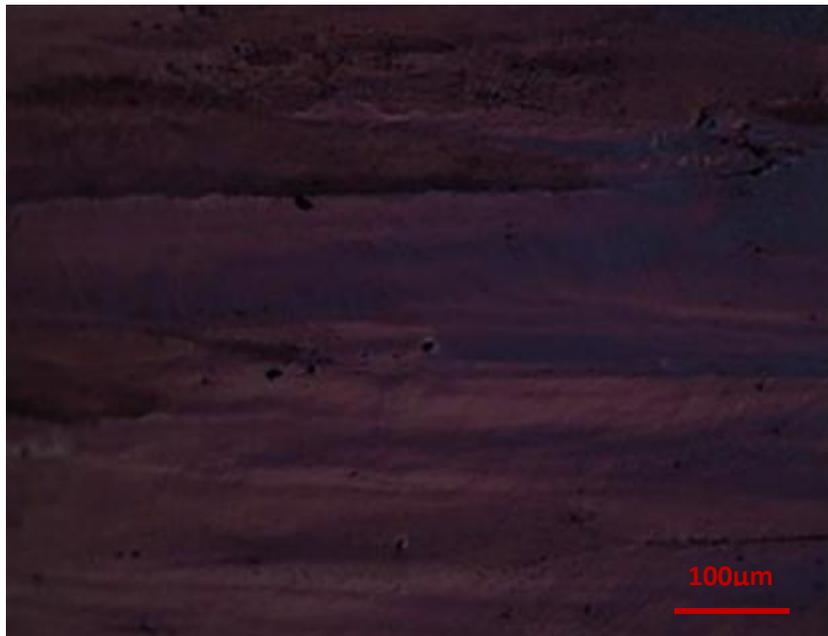
Figure 6-5. High magnification optical microscopy image from area B in Figure 6.3a. Differential Interference Contrast microscopy image indicates the presence of out of plane deformation, and the formation of deformation ripples on the surface.

In contrast Figure 6.6 and 6.7 show areas with minimum or uniform matrix deformation. Figure 6.6 shows 2 optical microscopy images of area J. The image shows the absence of slip bands and any form of localised plasticity. Figure 6.6a uses Differential Interference Contrast to show the absence of any form of out of plane deformation or strain localizations. Similar observations were made for area L in figure 6.7.
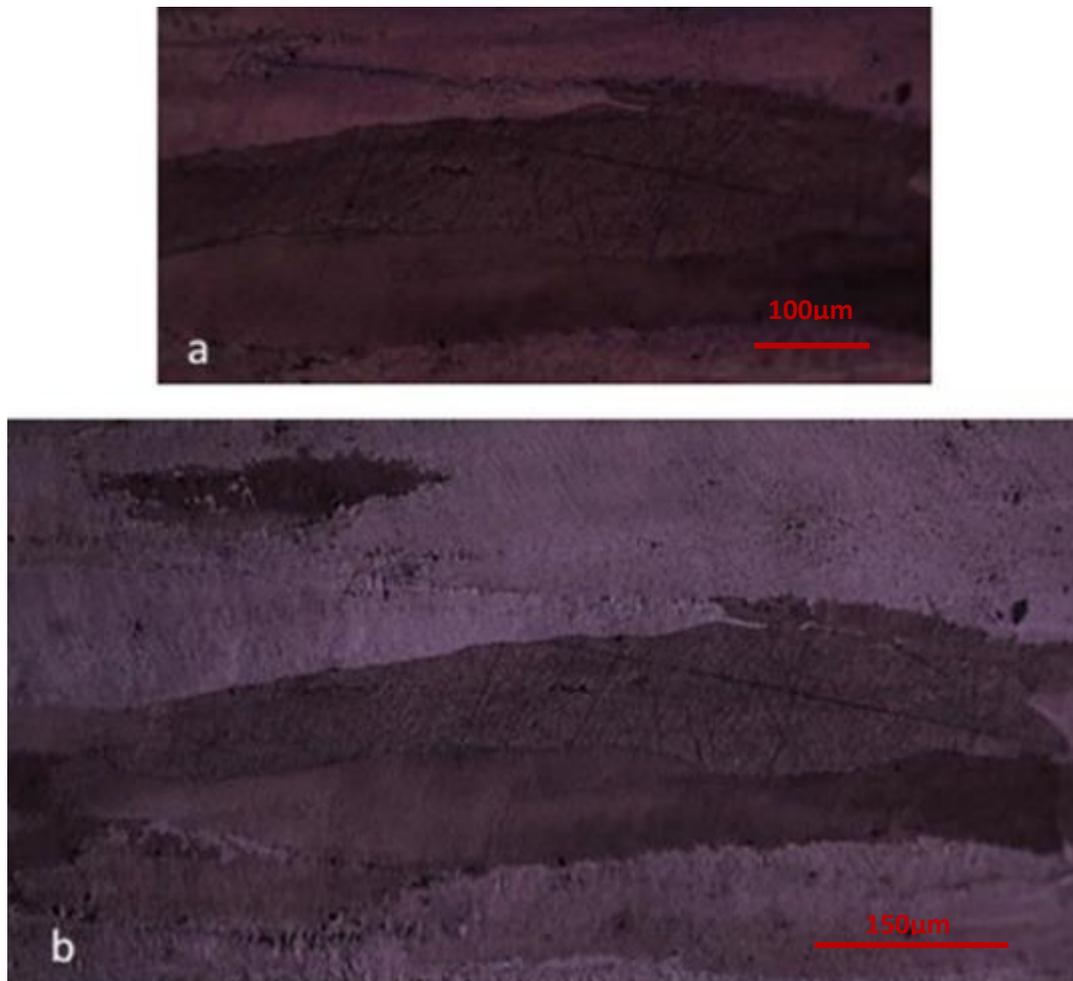
Figure 6-6. High magnification optical microscopy images from area J in Figure 6.3a. a) DIC (Differential Interference Contrast) microscopy image to indicate the presence of negligible out of plane deformation, and b) Optical microscopy image at the same area.
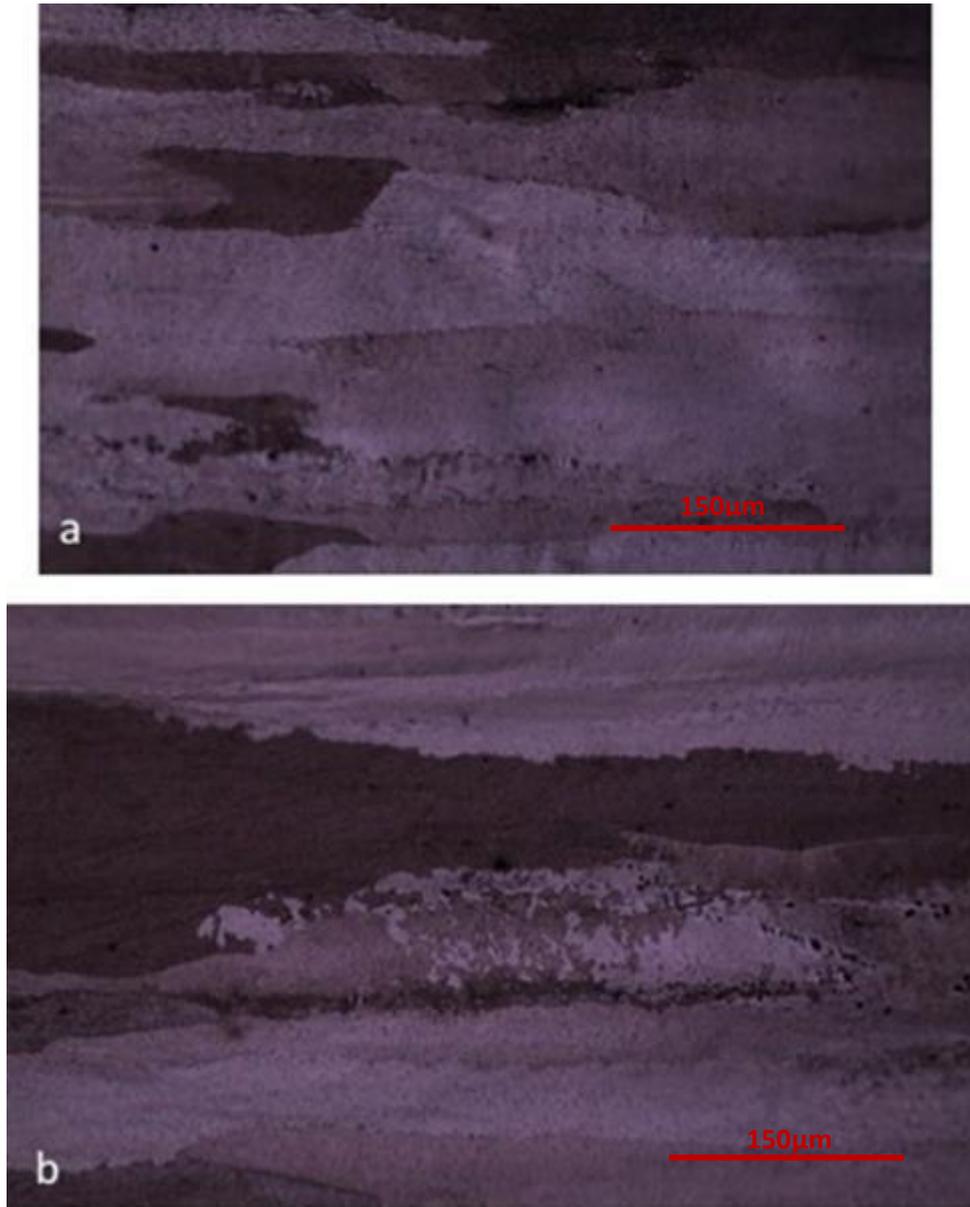
Figure 6-7. High magnification optical microscopy image from area L in Figure 6.3a. Images indicate the absence of slip bands and any significant out of plane deformation.

6.1.2. High resolution deformation and damage characterisation

Following the optically based low magnification analysis shown above, high resolution electron microscopy was used to characterise deformation and damage at smaller scales. It also helps to identify whether the matrix has been extensively stretched. Simply by checking the state of the particles and inclusions within the individual grains, the occurrence of damage by crack or void nucleation is an indicator of plastic deformation within the crystal matrix. Grains that have been extensively deformed, forming slip bands, and localising the plastic strains do initiate damage at their microstructural defects, namely particles. These particles are less deformable with respect to the matrix, and therefore damage nucleation during the first stages of deformation occurs at these sites.

157

Figures 6.8a to g correspond to the high stretched areas of figure 6.3a, while figures 6.8h to l correspond to the low stretched. The first set of SEM images from a to g correspond to highly strained regions, while the second set of SEM images correspond to areas that have been under low strained conditions. A series of SEM images is shown in the corresponding locations as a proof for the occurrence or not of high strains in the selected areas based on the conditions of the particles and inclusions.

Figure 6.8a to g show the occurrence of damage at particles and inclusions, suggesting considerable matrix stretching which cannot be taken by the particles and inclusions. Particles are distinguished from inclusions based on their morphology and type of fracture. Figure 6.8a-g shows that damage at inclusions and particles occurs via different mechanisms. Fracture at particles occurs via a crack formation mechanism, and cracks appear to have rather sharp tips, concentrating high strains in their neighborhood while inclusion damage occurs via interface decohesion, followed by void growth in the matrix; a rather more globular type of damage. Another way of distinguishing between particles and inclusions is that particles usually appear stronger than inclusions and usually stay on the surface during polishing, while inclusions detach from the matrix, and break into pieces during polishing. On the images of figures 6.8a to g, a nomenclature of I, ID and P was used to distinguish between inclusions, interface (or grain boundary) decohesion and particles. The voids formed around inclusions were usually much larger than the cracks formed at particles due to the size of the corresponding particles and the fracture mechanism involved. Voids of as large as 40μm were found as shown in figure 6.8f, while the cracks at particles were no larger than 7μm (figure 6.8a). Figure 6.8c shows void growth at an inclusion site, and the presence of smaller inclusions along GBs. The presence of brittle phases along GBs is usually detrimental and leads to void nucleation along GBs.

The top image in figure 6.8d shows a void generated at the site of the inclusion due to decohesion, while the two lower images show various cracked locations. Many cracks have formed in a cluster of particles, growing either via interface decohesion around the particles or by particle breaking. This observation shows the influence of the spatial distribution of particles/inclusions on damage development. The middle image shows a small particle with thickness less than a micron failed by brittle failure.

In contrast figure 6.10 h-l shows the corresponding regions h-l of figure 6.3a, and shows areas of matrix with no slip bands, minimum out of plane deformation, and particles which have not been damaged. These indications suggest that damage nucleation can only start at particle sites within grain of favourable orientation which have undergone sufficient plastic deformation. Particles at grains within these regions h-l will not contribute to damage nucleation.

c

160
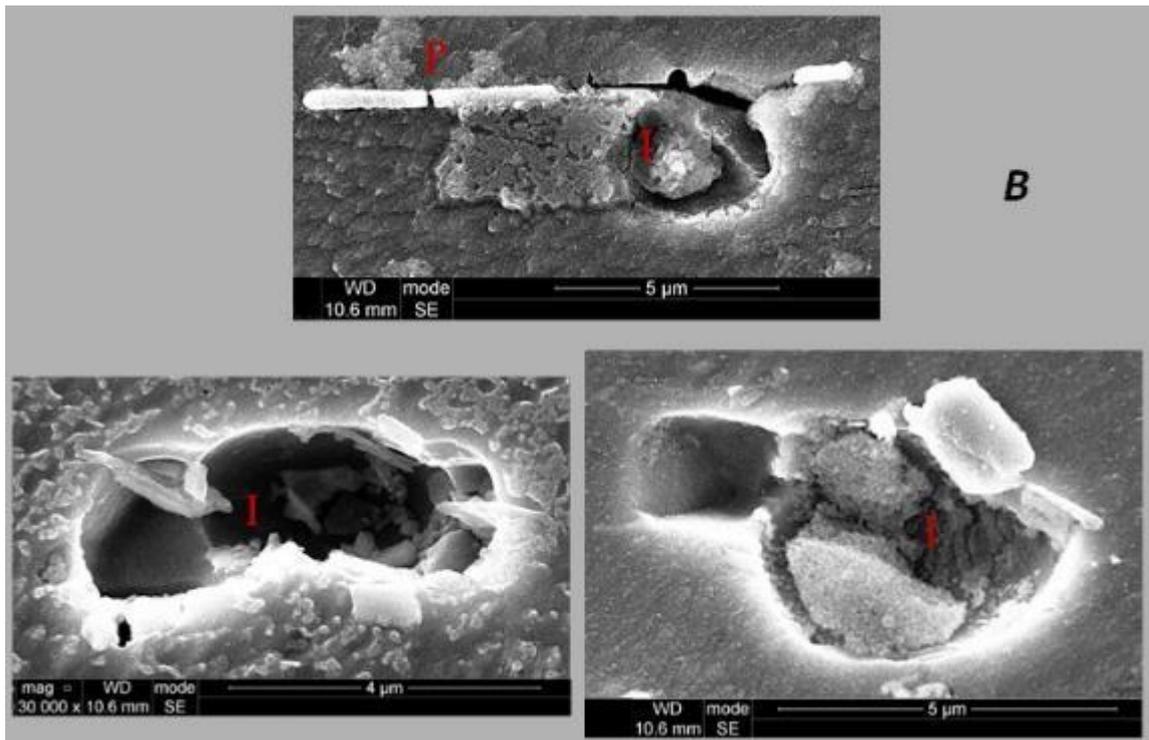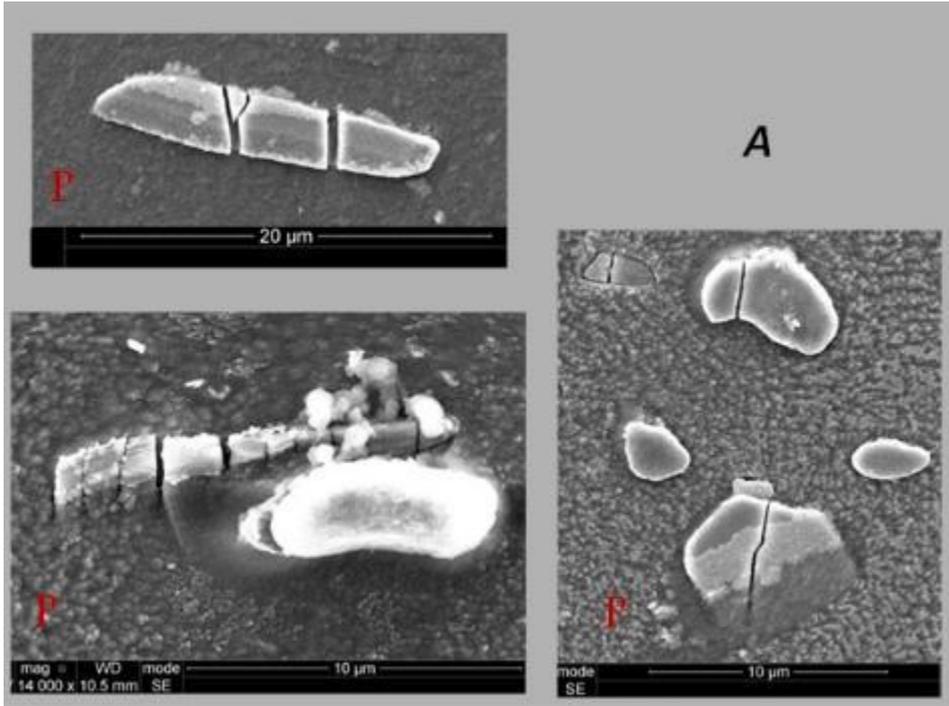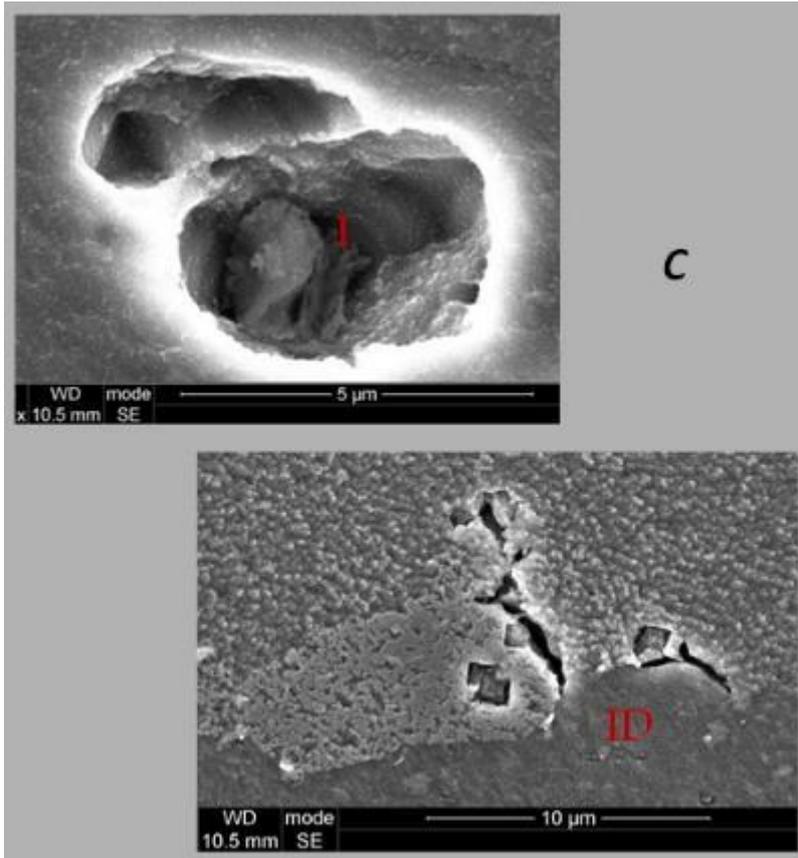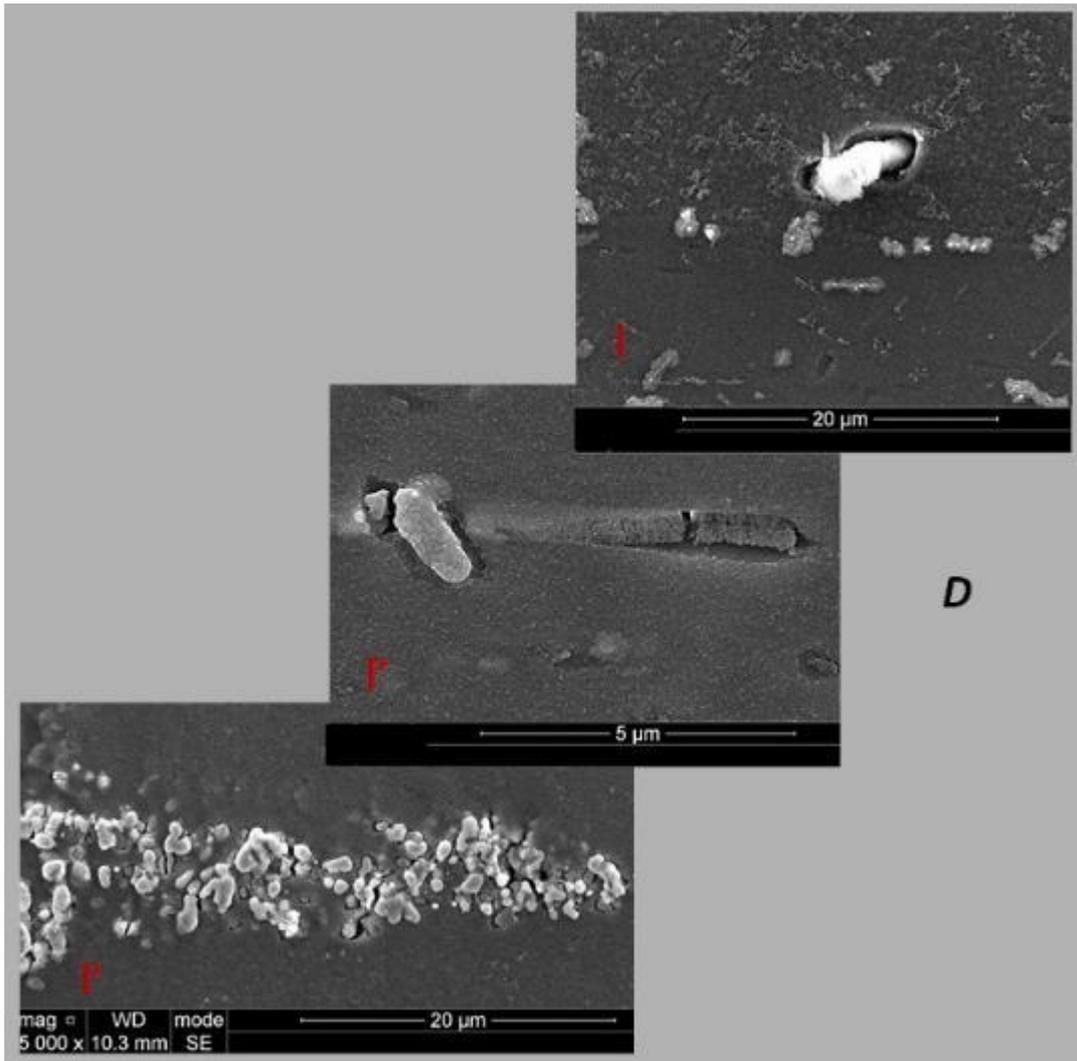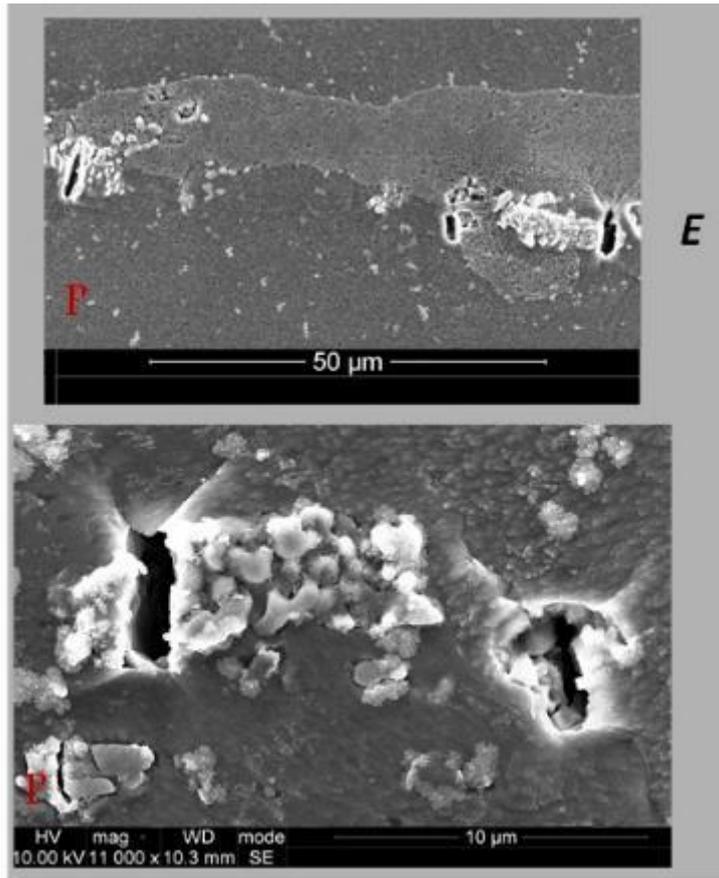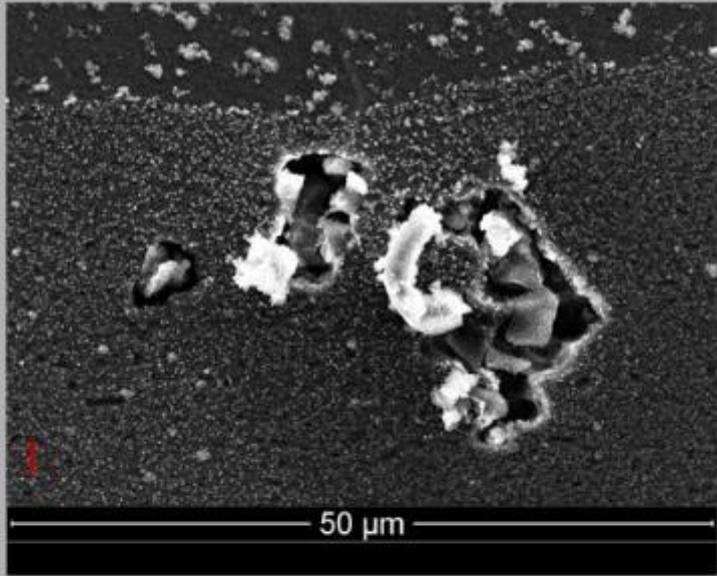
F
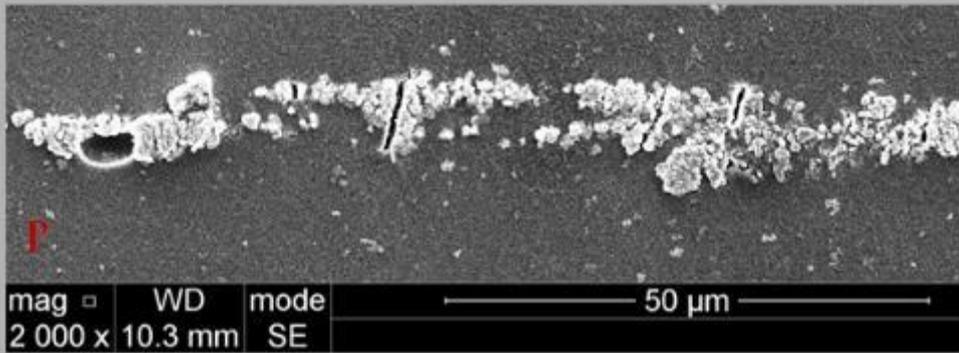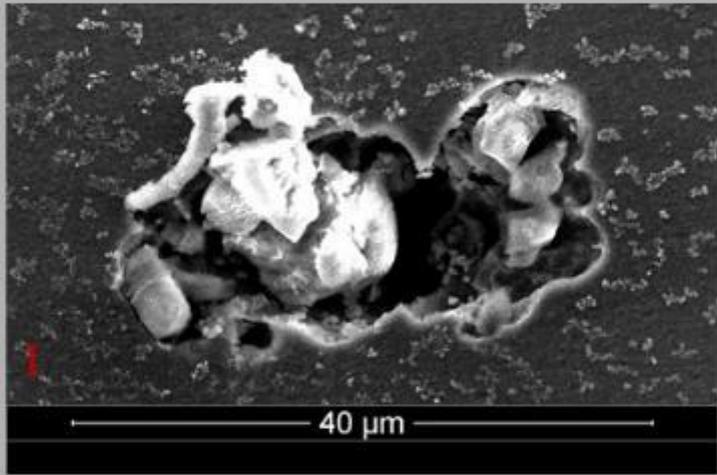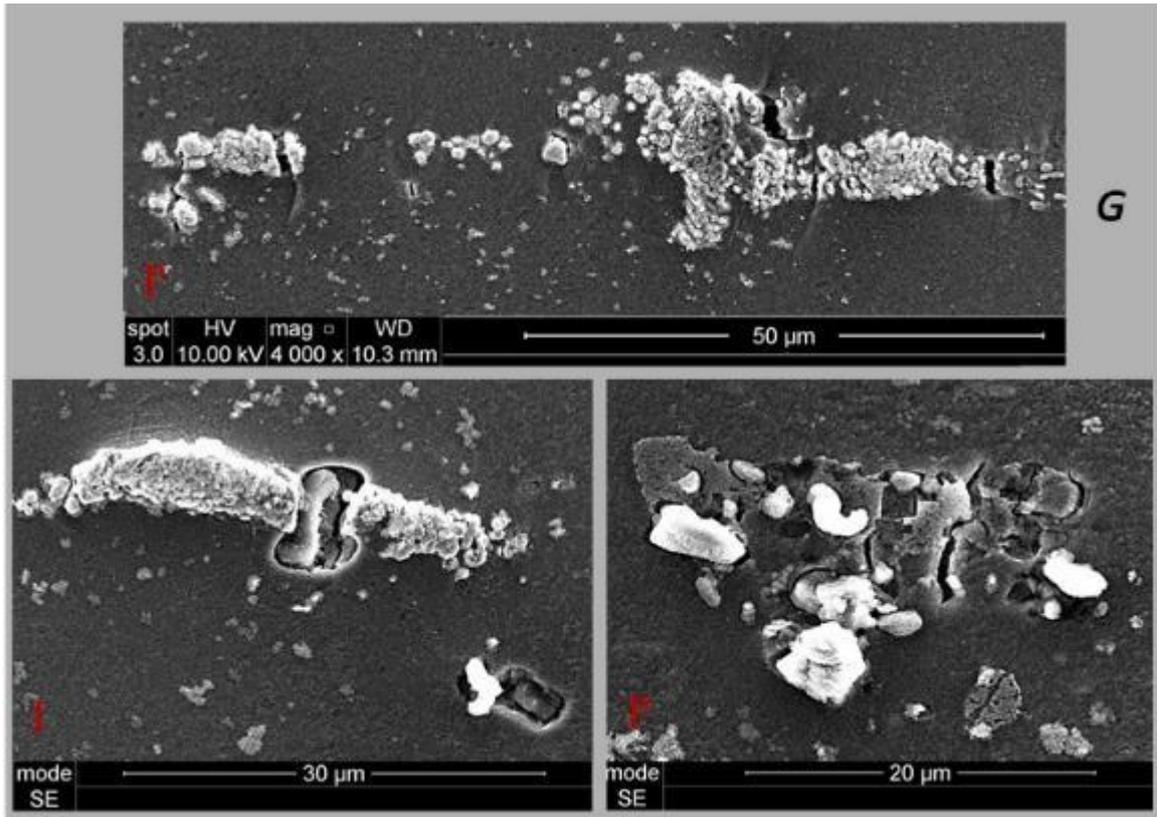
Figure 6-8. a - g) SEM images at the corresponding regions of figure 6.3a. The regions show plastic localisations as well as damage in the neighbourhood of particles and inclusions.

H
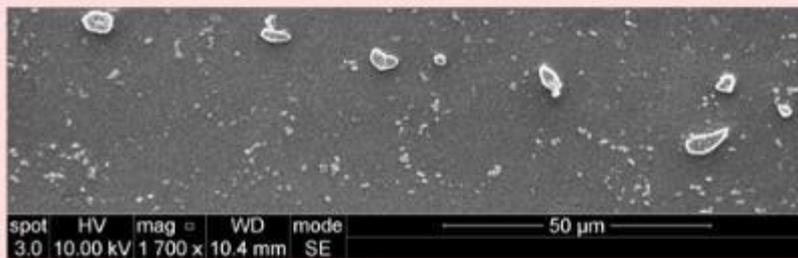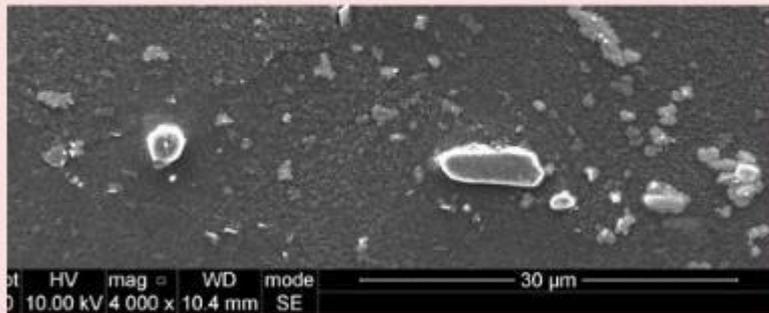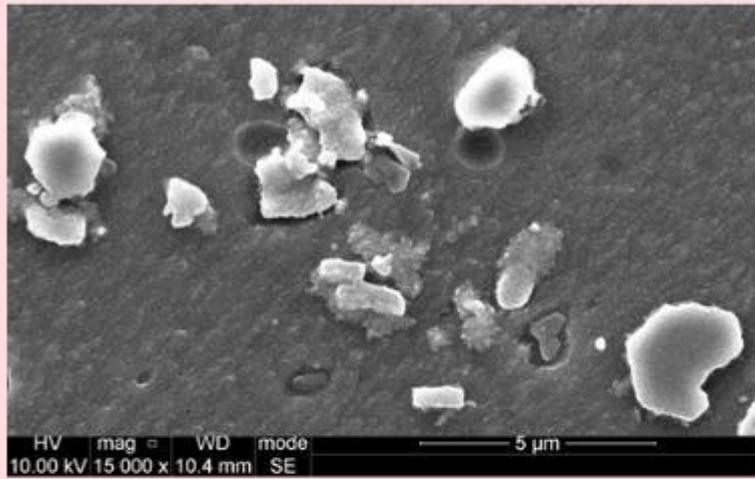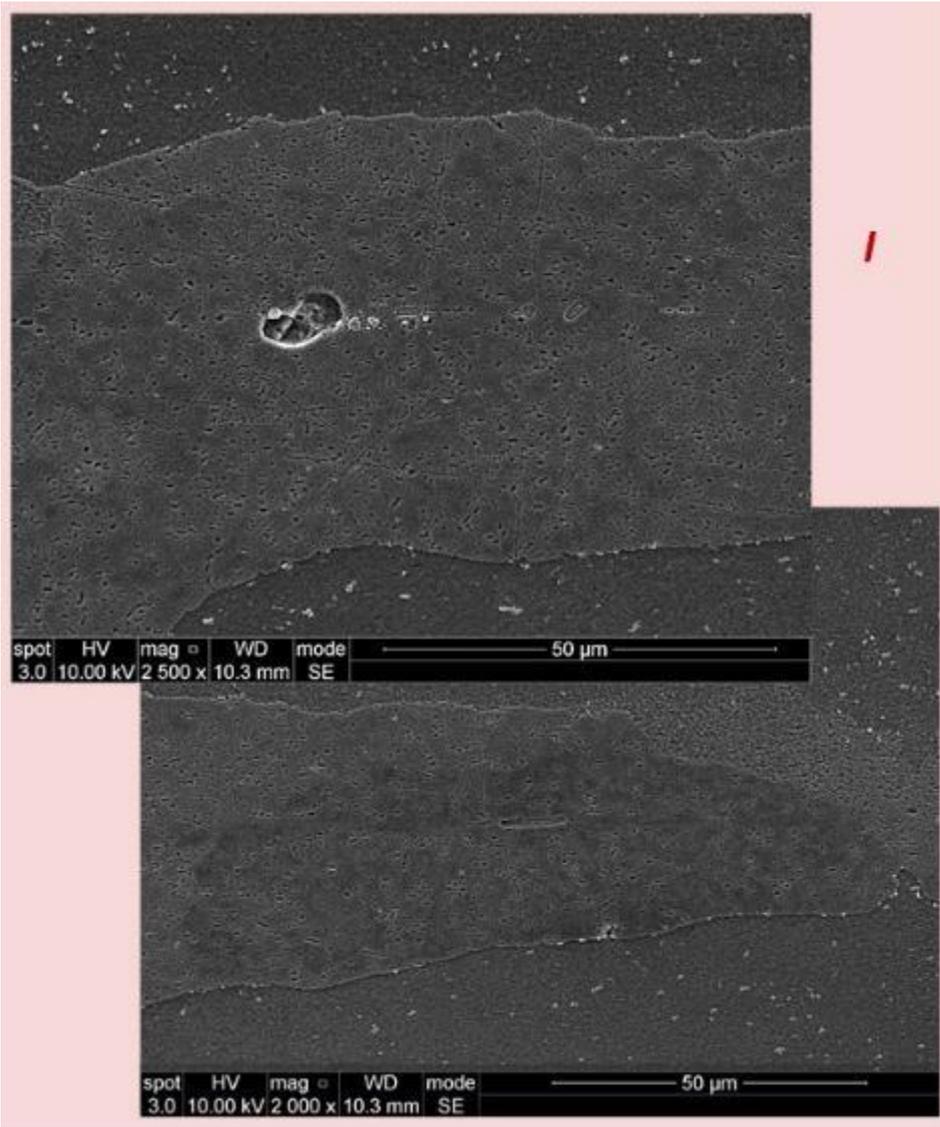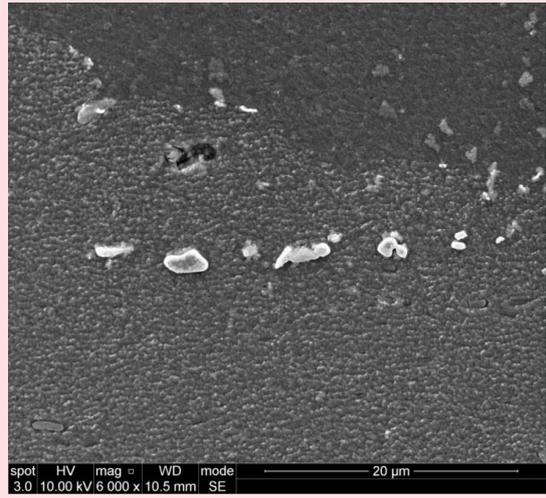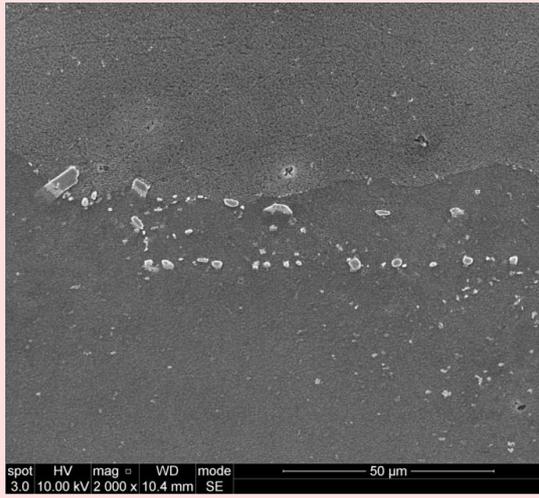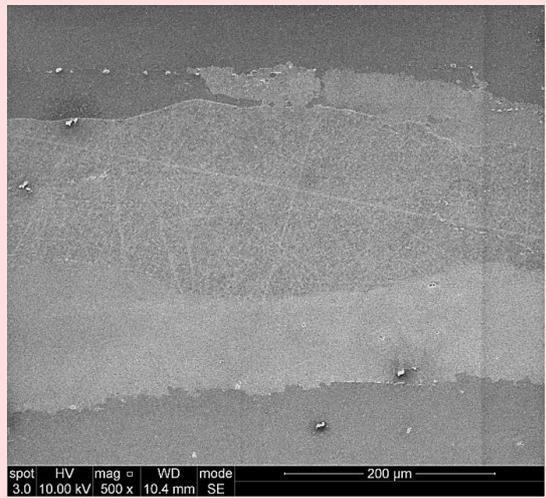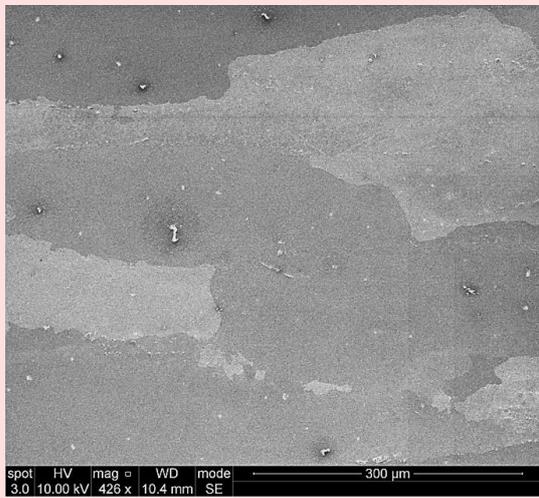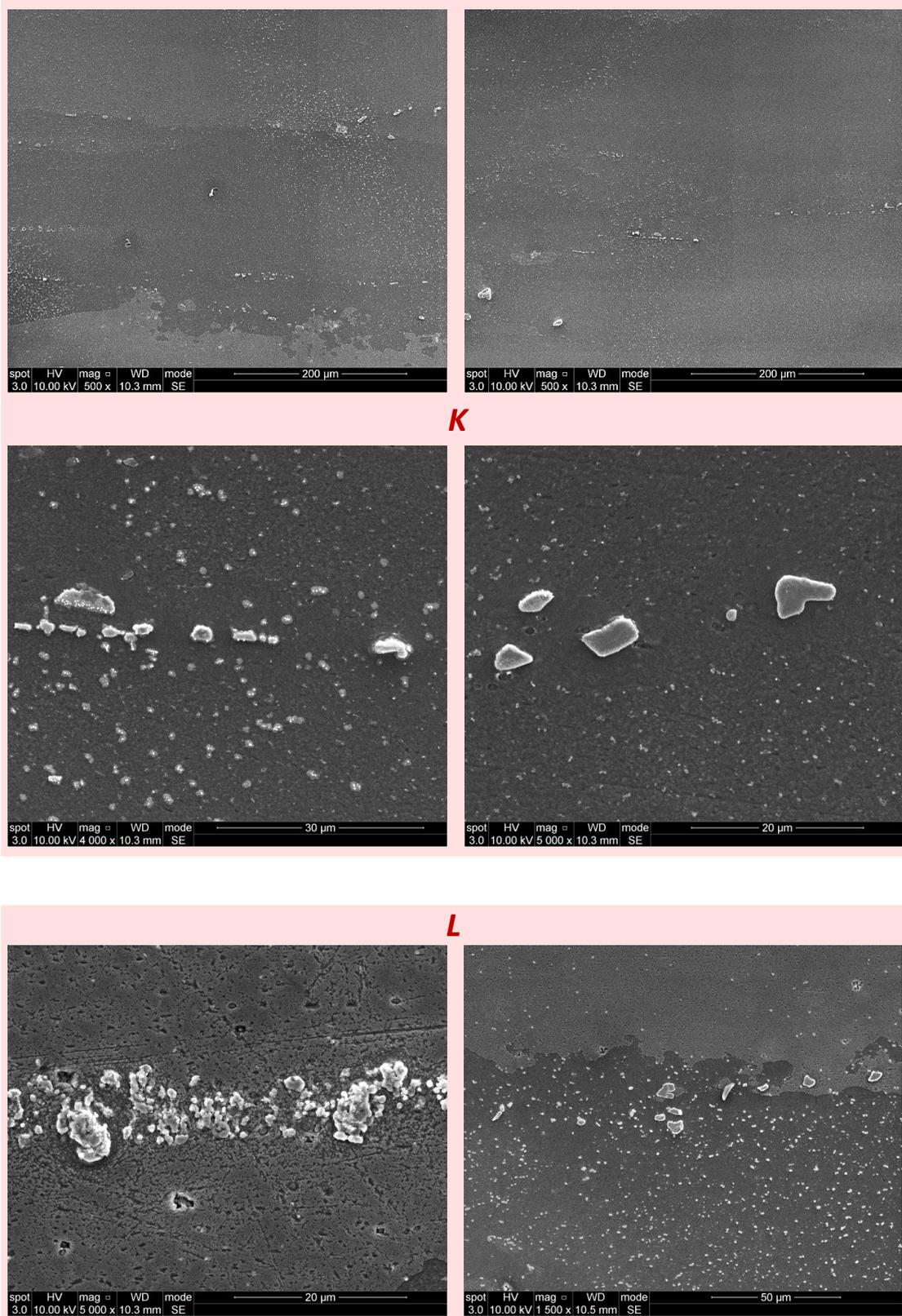
Figure 6-9. h, I, j, k and l) SEM images at the corresponding regions of figure 6.8a. The regions show minimum matrix deformation, absence of plastic localizations, and intact particles.

6.2.   Mid-Amplitude fatigue testing

EBSD measurements were carried out at the central region of the top surface of the 4 point bending sample, region where the maximum displacements-strains are applied during the test. Figure 6.10 shows the map for the Euler angles at the corresponding region, obtained by EBSD, which corresponds to a region of 2.8 x 3.5 mm. Following the EBSD analysis the sample was polished with 0.04 μm Silico to remove any deposited hydrocarbons during the EBSD measurements, followed by HF etching to reveal the GBs, particles and inclusions. The black squared region in figure 6.10b corresponds to the EBSD area of figure 6.10a. The GBs are superimposed from the measurements taken from EBSD.

4-point micro-bending test was performed with a 2kN Deben vertical bending stage inside a CamScan SEM with a cross head speed of 2mm/min. Initially a static test was performed up to a maximum strain of 0.01 applied to the two left and right edges of the area. The test was interrupted at each 0.2 mm displacement increments, and local displacements and strains were obtained by means of Digital Image Correlation (DIC) as explained in [50]. So the local strains were obtained at maximum displacement at the first peak load. Subsequently, displacement controlled cyclic loading was initiated with a frequency of 0.5, from 0 up to maximum displacement. The test was interrupted after the 1st cycle, the 10th cycle, the 100th, 200th and 300th cycle, at the maximum displacement applied and images were acquired. The consecutive images were correlated to the image at the first peak load and hence to the image for the undeformed sample. The micrographs were analysed using the commercial image analysis software, DaVIS 7.0, by LAVision [79] to determine the in-plane displacement field from which plastic strain values were calculated. In the current study, the microstructural features of the material have been directly used as the pattern from which to correlate the images between two successive loading steps. A sensitivity analysis on the interrogation window size was carried out, and a multiscale interrogation window with 16x16 and 32x32 pixels was finally selected in all the experimental results presented in this study. A low magnification analysis (40x) was pursued in order to acquire the strain fields throughout the whole region shown in figure 6.10a, as well as the effect of grain orientation on local deformation and damage.
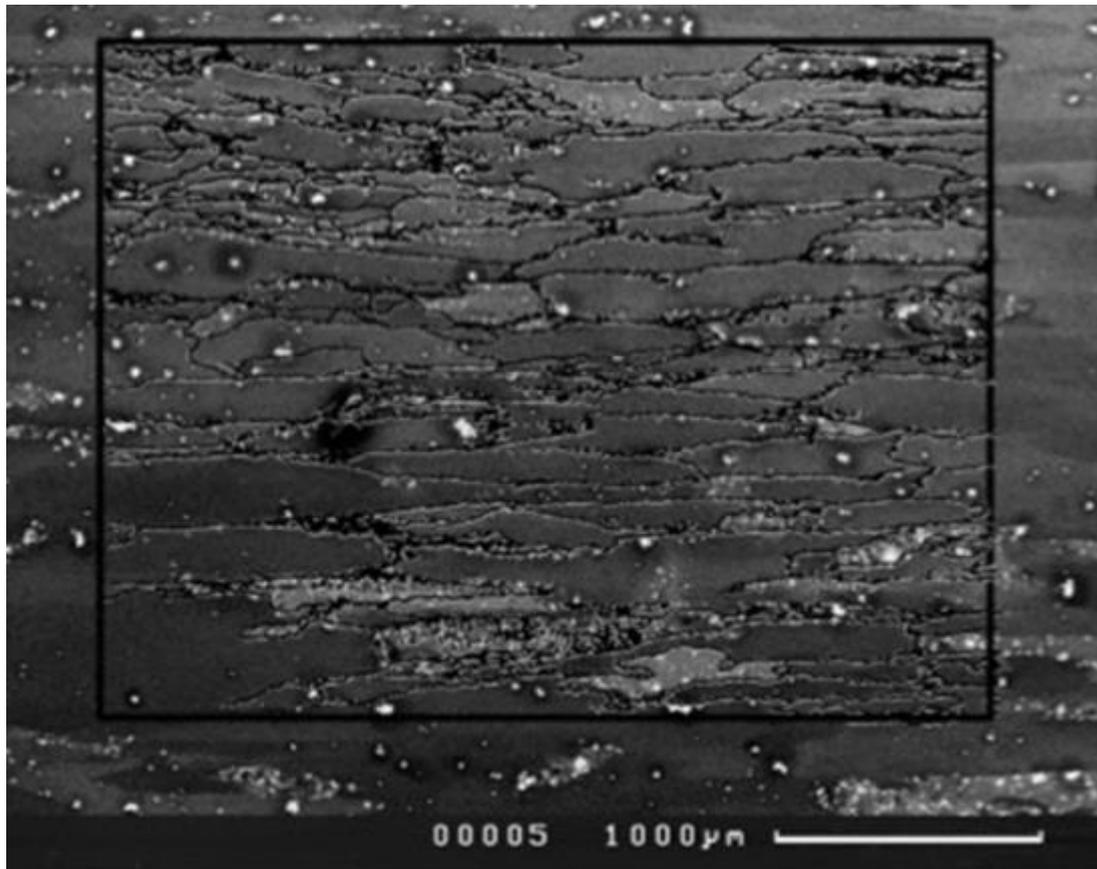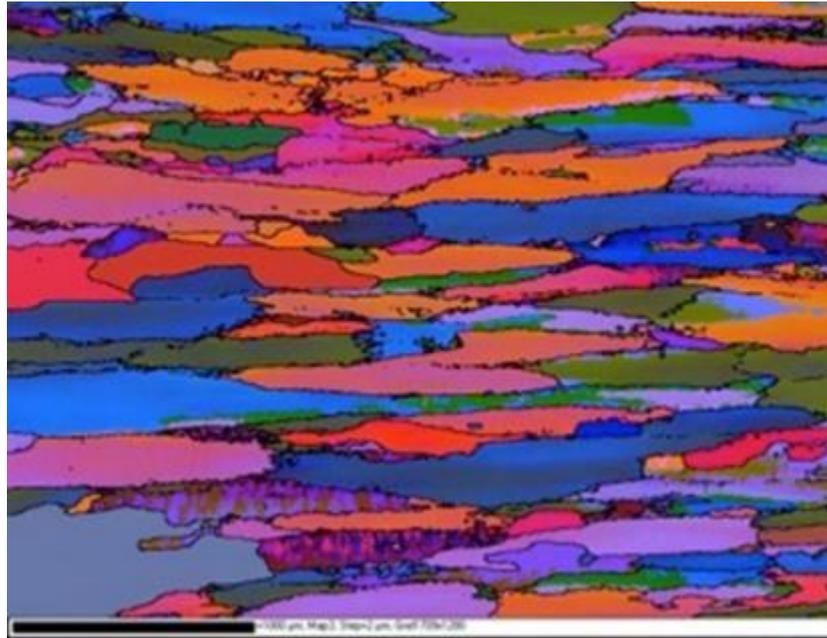
Figure 6-10. a) EBSD measurements at the centre of the top surface of the sample, b) the corresponding etched region.

6.2.1. Macroscopic deformation and damage characterisation

Figure 6.11a shows the strain distribution after 500 cycles for the fully loaded condition for the sample; obtained by means of DIC (LaVision). Similar to previous observations, several shear bands

can be seen within the strain contours overlaid on the microstructure. The labelled grains A-G, correspond to not highly strained areas in figure 6.11a. Figure 6.11b shows an optical microscopy image of the same area, after 500 cycles for the unloaded condition of the sample. The same grains appear to be low strained with no slip bands within their matrix.

6.2.2. High resolution deformation and damage characterisation

Following the macroscopic characterisation, high resolution SEM analysis was pursued within a FEI Inspect-F SEM to metallurgically inspect various regions where low and high strain values were measured by means of DIC. Figure 6.12a shows the EBSD measurements together with the local deformation distribution (obtained by means of DIC) as shown in figure 6.12b. Several locations were selected within the microstructure, based on the strain measurements obtained by means of DIC. The yellow labelled regions of Figure 6.12a, correspond to low strained regions, while the white labelled ones to high strained regions. The same regions are also overlaid on Figure 6.12b.

SEM images were taken at the 3 yellow labelled regions and are shown in figure 6.13. All images (M1-M3) show the absence of cracking and/or slip banding. The matrix appears to have deformed uniformly, with some voids at inclusion sites (M1-M2). Yet no cracking or strain localisations were observed in the neighborhood of these particles (M1-M2). M1-M2 regions correspond to the low-deformed grains (A, B and C) in figure 6.11b, which confirms the observations made by optical microscopy. At the M3 location (region D in figure 6.11b) the particles have not caused any strain localisation and no damage was found. Instead, in the white labelled areas of figure 6.12a, various mechanisms of deformation can be observed and are shown in Figure 6.14. Slip bands are seen in S1, S2 and S3 regions, as shown by the higher magnification images in Figure 6.14. Strain localisations occurred in the neighborhood of the inclusions-particles (L1, L2 and L3 regions), while C1 and C2 show the occurrence of cracking at inclusions-particles due to high strain localisations.
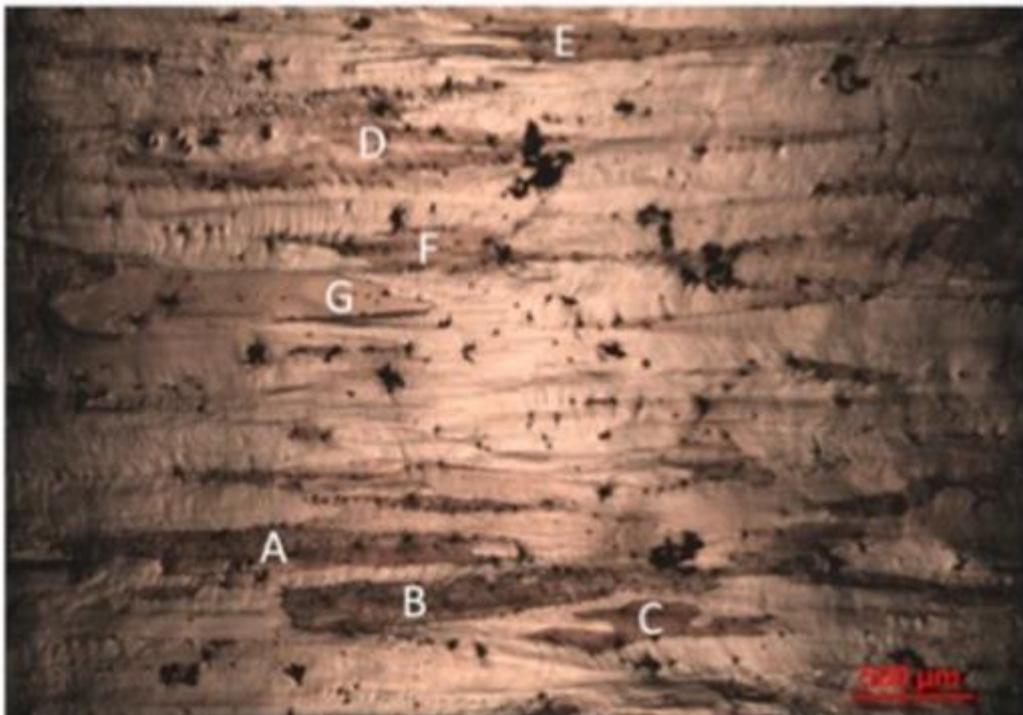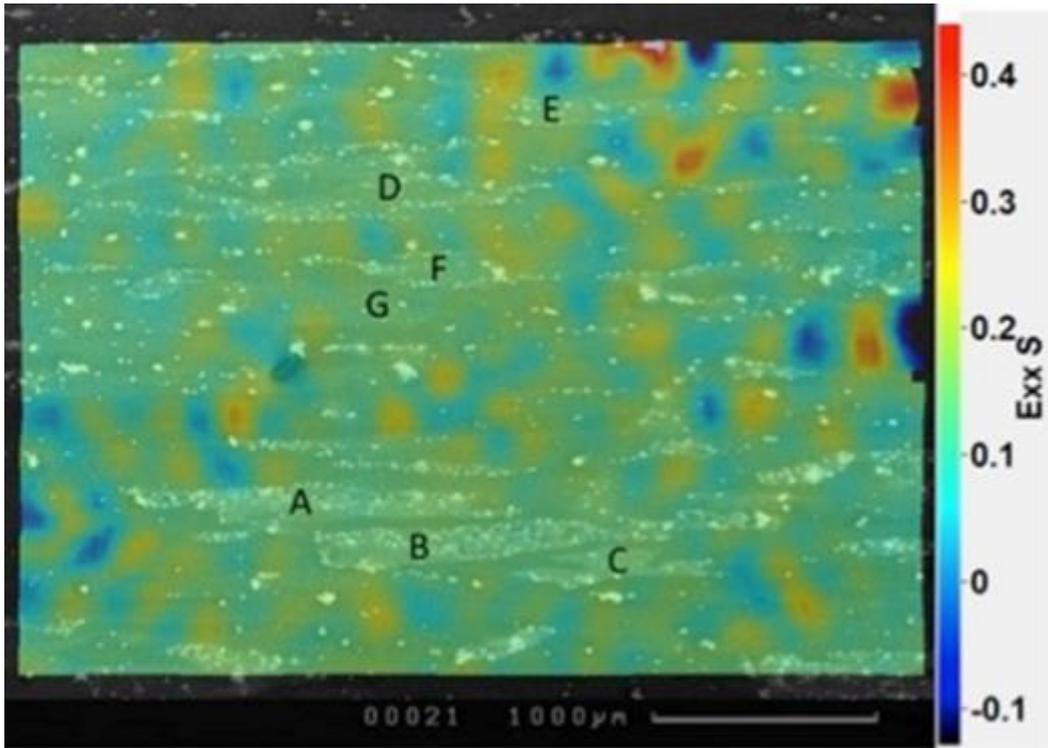
Figure 6-11. a) Strain distribution for the fully loaded sample after 500 cycles, b) optical microscopy image of the same region after 500 cycles (unloaded condition).
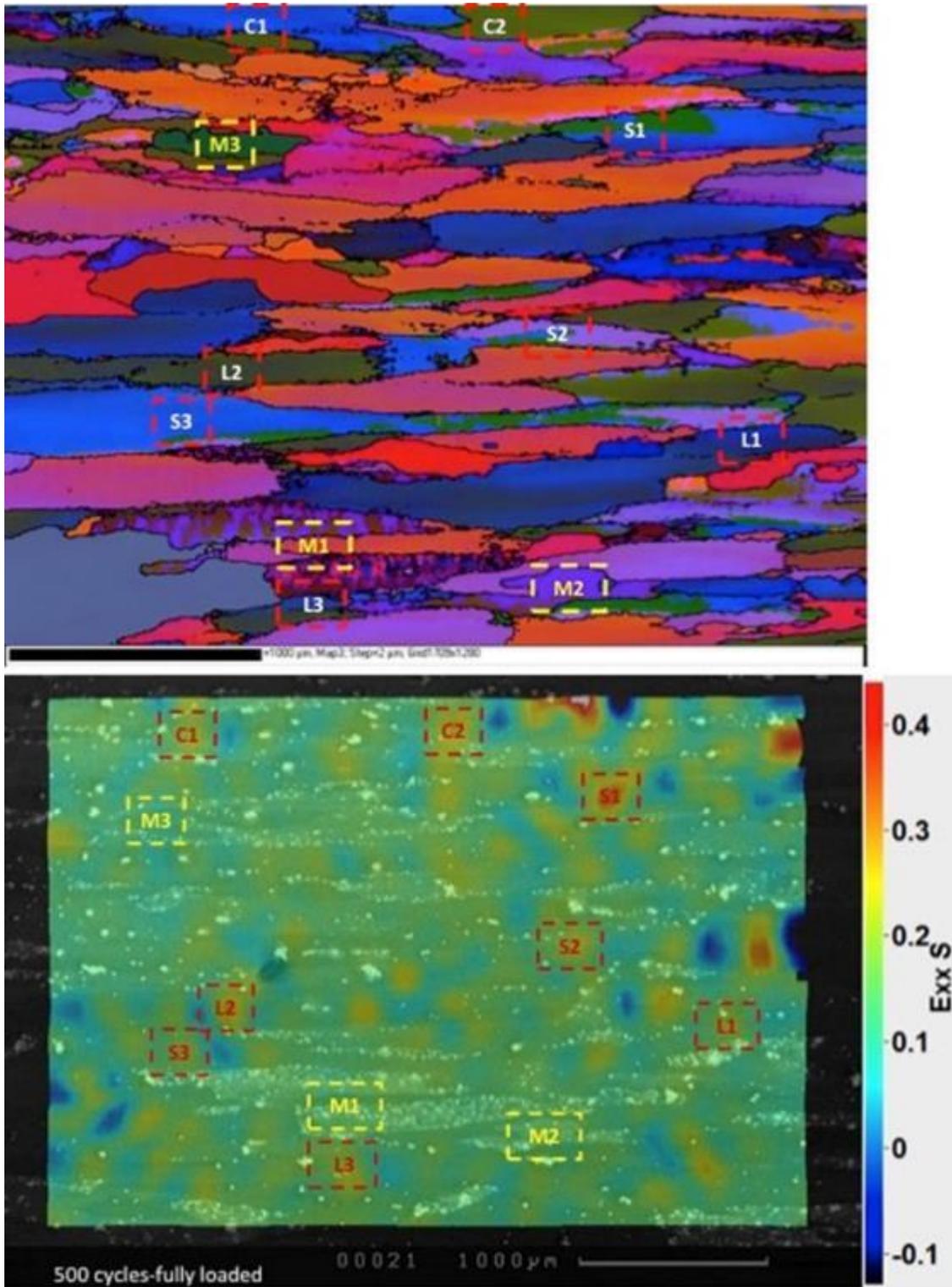
Figure 6-12. a) EBSD measurements and b) strain distributions of the same area after 500 cycles. The boxed areas were inspected with high resolution SEM to check for the occurring microstructural deformation.
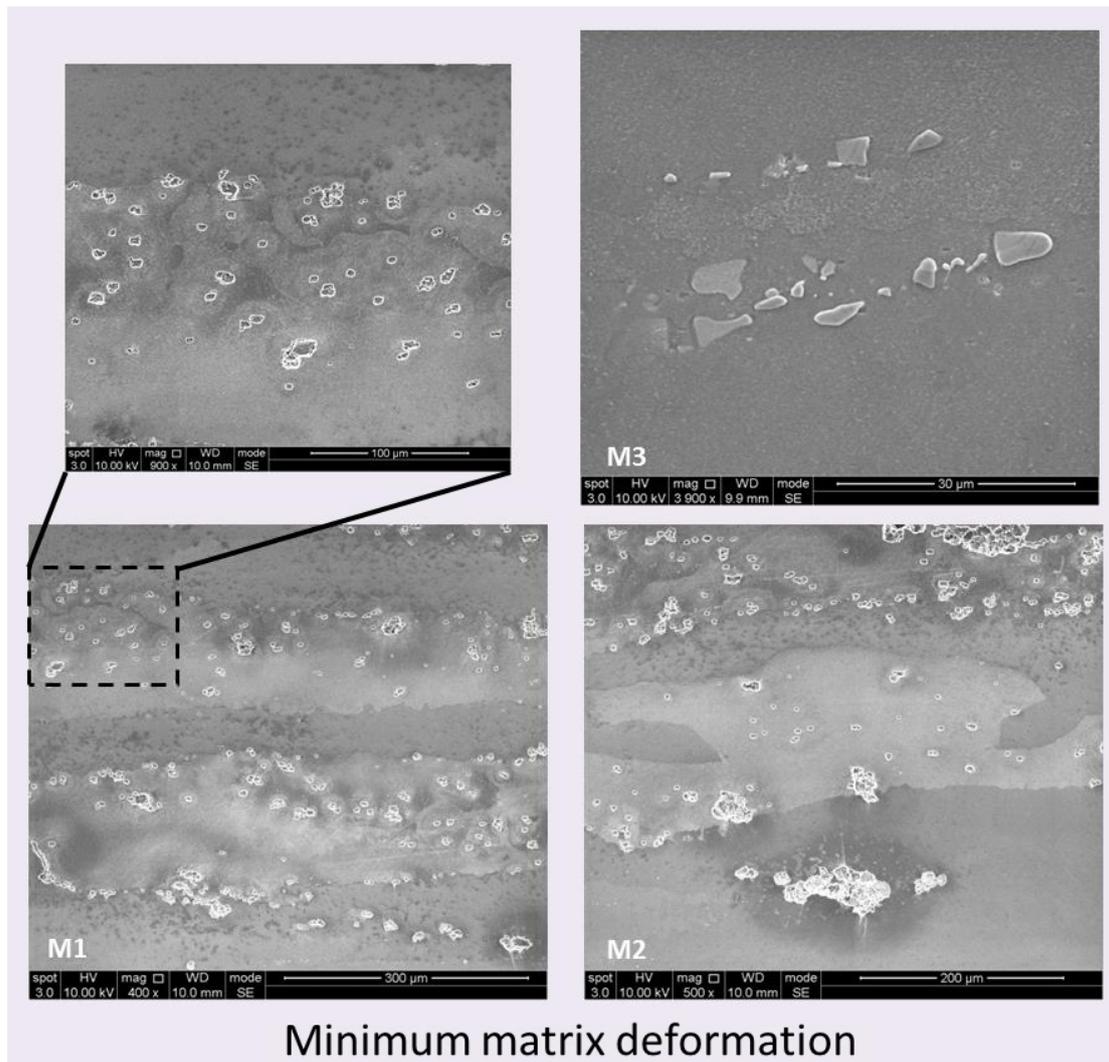
Figure 6-13. Regions where minimum matrix deformation was observed. M1, M2 and M3 correspond to the respective boxed regions in Figure 6.12b

Other mechanisms of damage were also observed such as grain boundary decohesion. This is shown in Figure 6.15, with decohesion at the grain boundaries primarily due to segregation of impurities at the vicinity of the grain boundaries. These voids could also be formed during polishing, and not during fatigue testing. Backscattered images were also taken to verify the presence of impurities at grain boundaries and are shown in Appendix B. Grain boundary sliding was found and is shown in figure 6.16. Grain boundary sliding is highlighted with a red arrow, and this mechanism leads to the formation of strong strain localization, via slip band mechanism along a different direction. The black arrow shows the location of the occurring slip banding in the grain matrix. Network of cracking was found within the clusters of particles in figure 6.17 These cracks formed approximately perpendicular to the loading direction and upon reaching the matrix, they localize stresses and strain upon different directions as shown in the 2 circled regions of Figure 6.17, depending on the active local slip systems of the individual crystals.
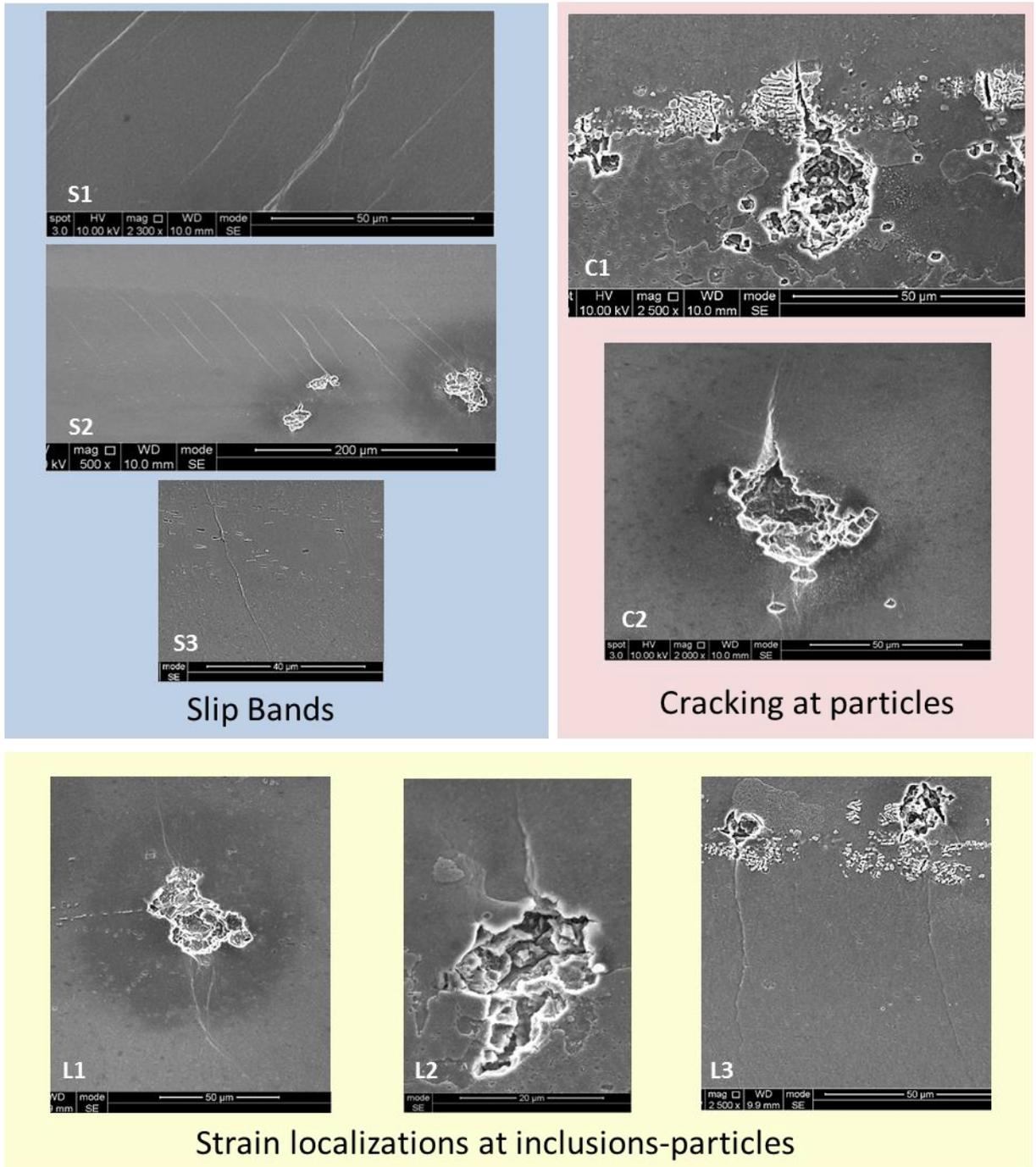
Figure 6-14. Regions where microstructural deformation was observed. S1-S3, C1-C2, and L1-L3 images correspond to the respective boxed areas in Figure 6.12b.

Cracking was observed to occur even at smaller-sized particles, as shown in figure 6.18. Figure 6.18a shows a nano-particle broken perpendicular to the loading direction (horizontal). Figure 6.18b shows a SE and a BSE image at the same location, showing the crack path at two neighbouring particles. Crack path divergence occurs at the interface between the two particles, which suggests that particles do not act similar to inclusions having an isotropic micro-mechanical behaviour, but have some anisotropic character in their micro-mechanical performance, breaking in rather different directions.

175

Yet the crack stops once reaching the matrix, and no strain localisations in the surrounding matrix were observed in all images of Figure 6.18 at the respective crack tips.
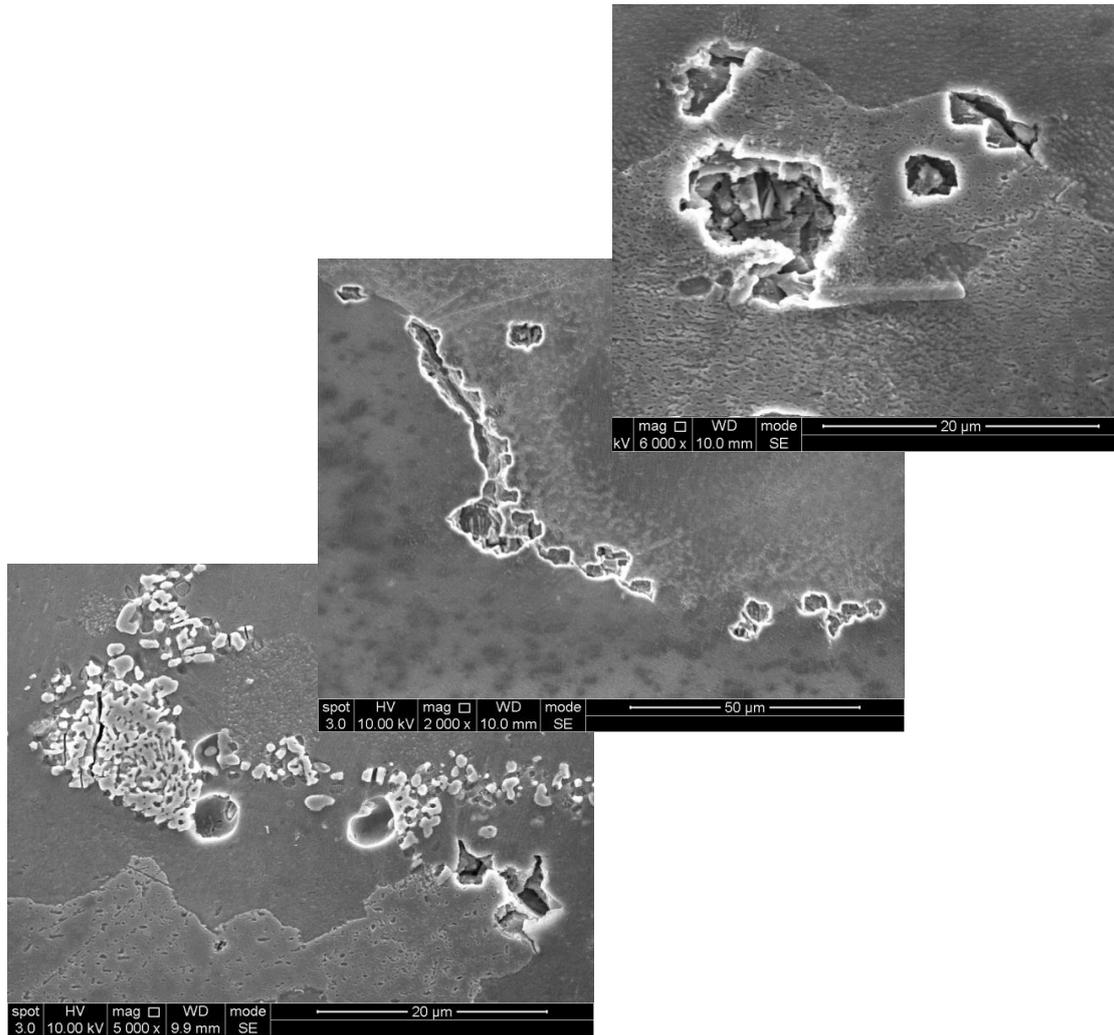
Figure 6-15. Grain boundary decohesions due to segregation of impurities in the vicinity of GBs.
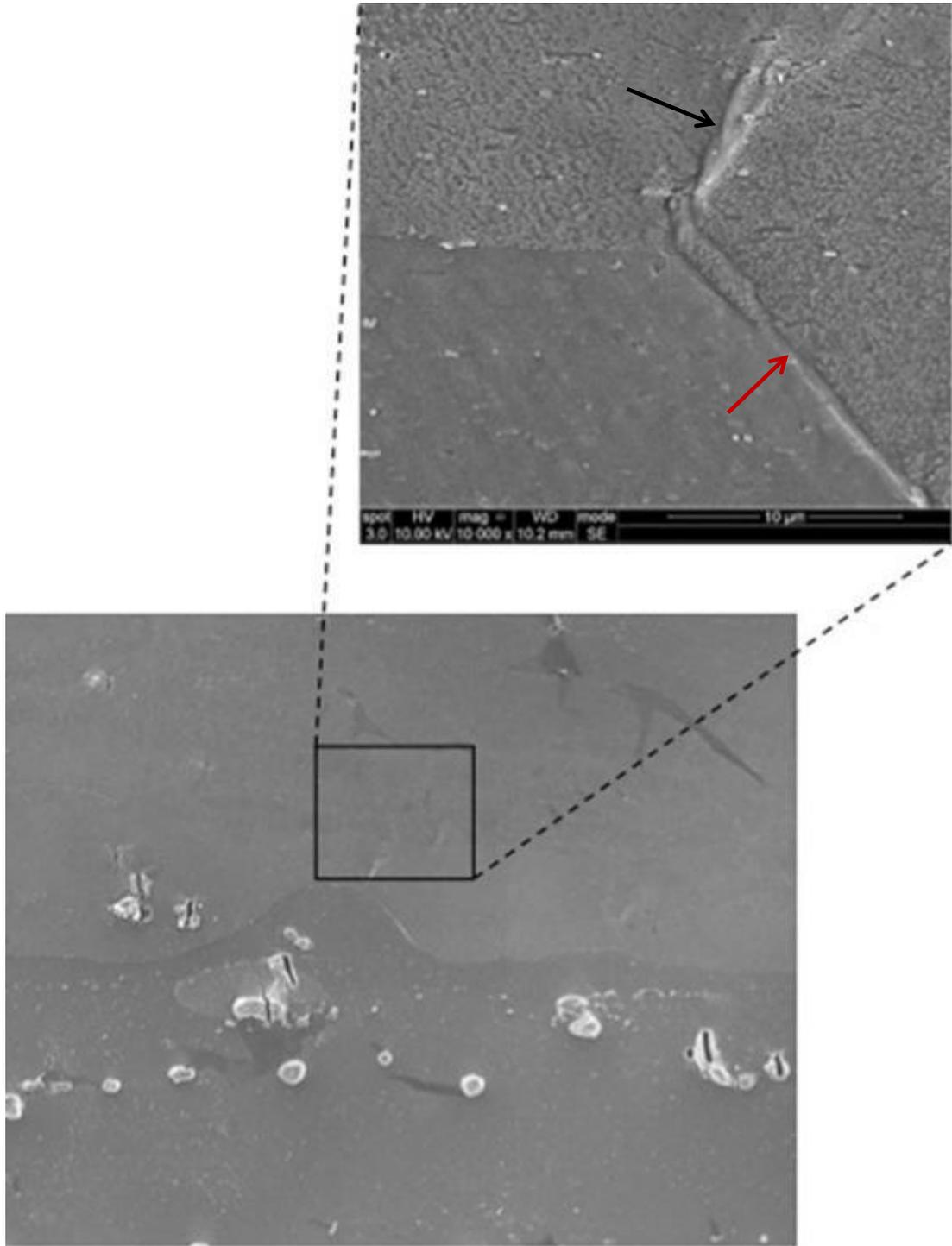
Figure 6-16. Grain boundary sliding and slip band formation in the matrix.
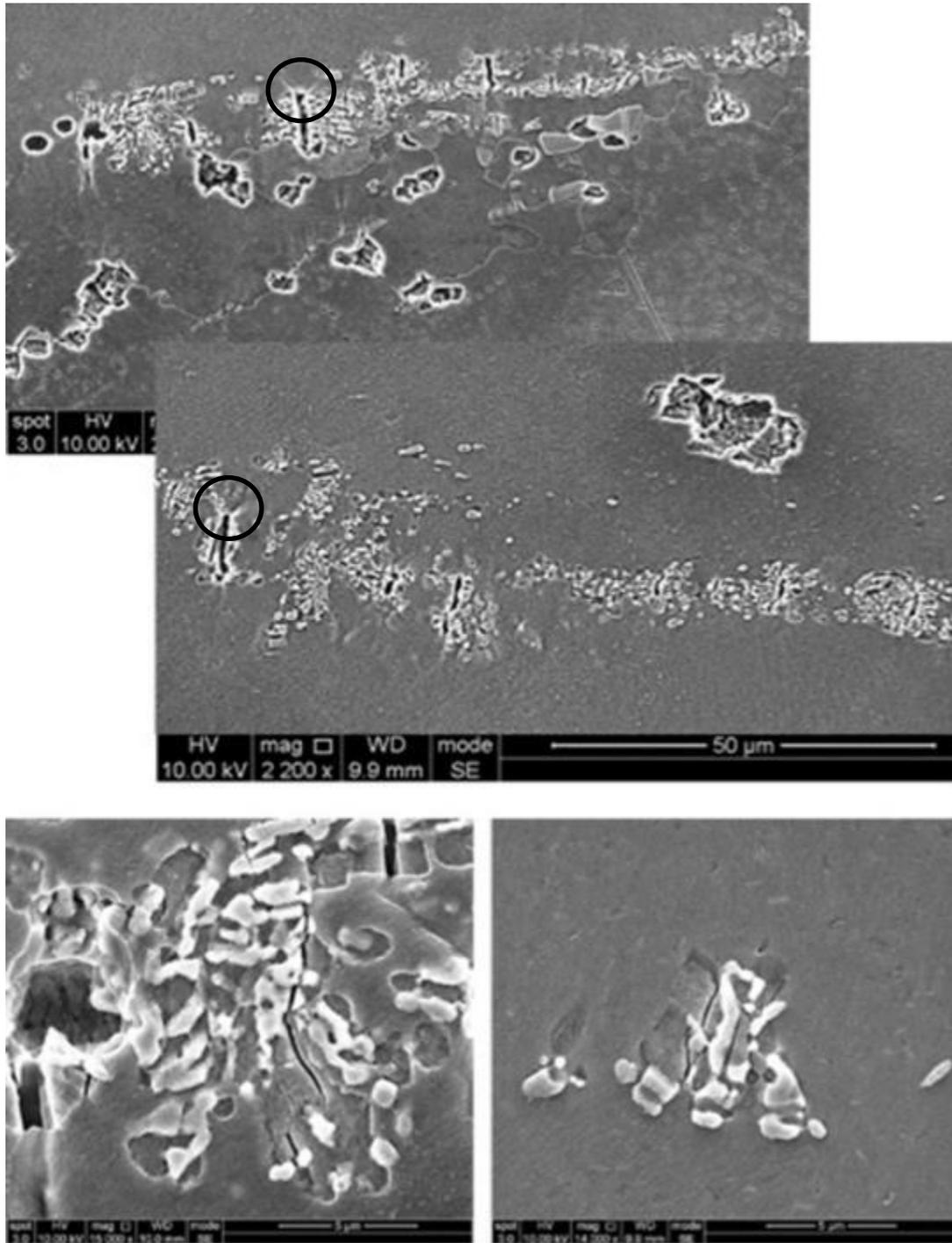
Figure 6-17. Cracks within clusters of particles.
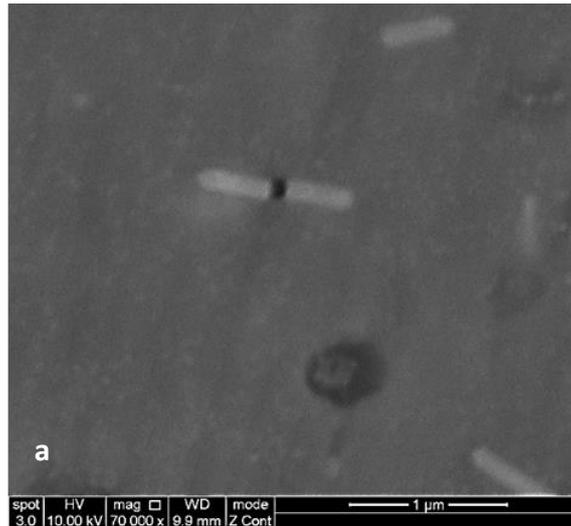
Figure 6-18. Nanoparticles broken, with no strain localizations in the matrix.

6.2.3. Particle Cracking

A case study was selected within the EBSD map of figure 6.12a. This area is shown in Figures 6.19 and 6.20. Figure 6.19 shows low to high magnification images of the same region. The black particles correspond to particles which are aligned between two grains. A high magnification SEM image at the same region is shown in figure 6.20. The grain boundary is drawn with black dotted line to distinguish the geometrical boundary between the two grains. Strain localisations in the particles' neighbourhood are much higher in the grain that lies below the particles, while negligible strain localisations occurs in the grain that lies above them. This effect may be seen in both figures 6.19 and 6.20. The strain localisations are aligned along two different orientations in figure 6.20. These two orientations correspond to the two major slip systems in the corresponding grain. Another key finding is that fatigue cracks at particle sites are not sharp as shown in figures 6.17, 6.18 and 6.20, but as particle cracking occurs, it causes localized necking at the neighbourhood of the crack tip within the grain matrix. This effect can cause local hardening or softening of the material which can affect FCI and

179

small crack growth. For future modeling work it is necessary to take into account these effects and model FCI at particle sites not as sharp cracks present at the particle-matrix interface.
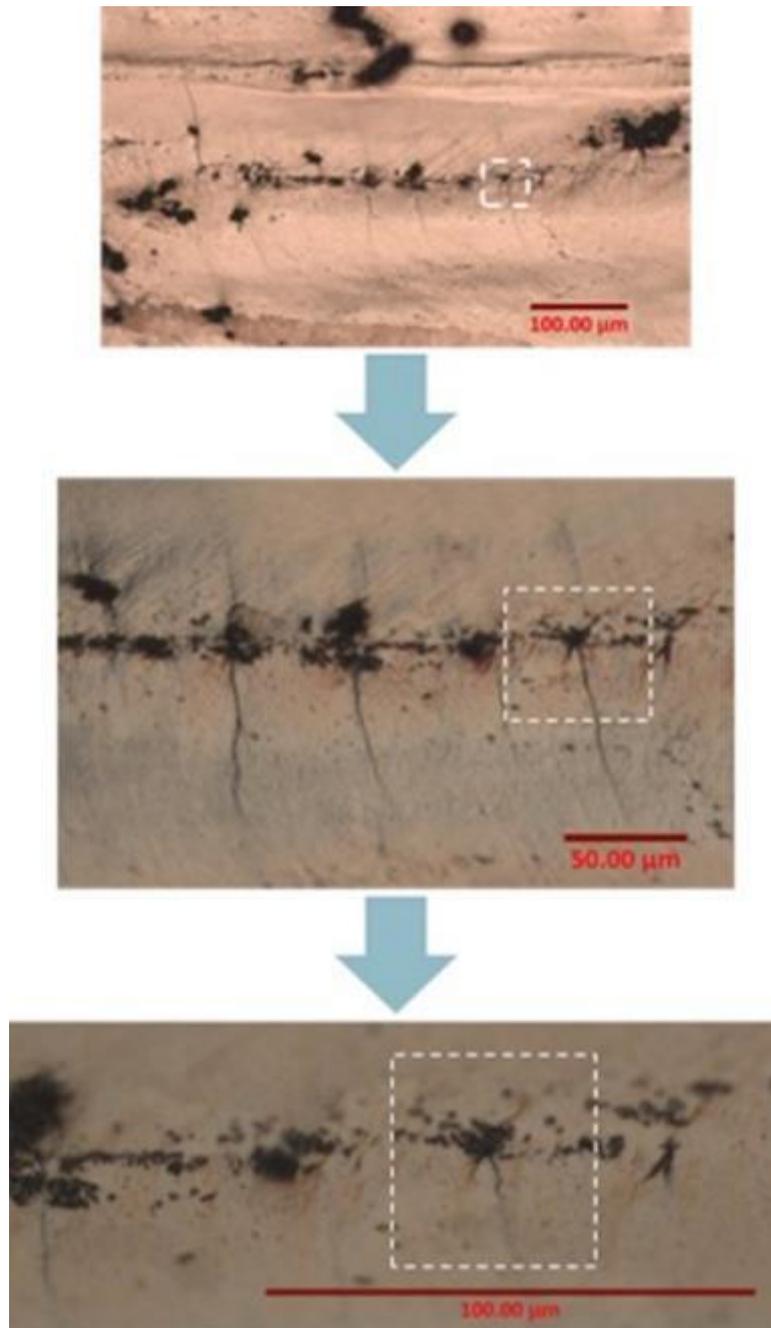
Figure 6-19. Different magnifications of a region where deformation localisations were observed. Strain localisations occurred at the neighborhood of particles lying along a GB.
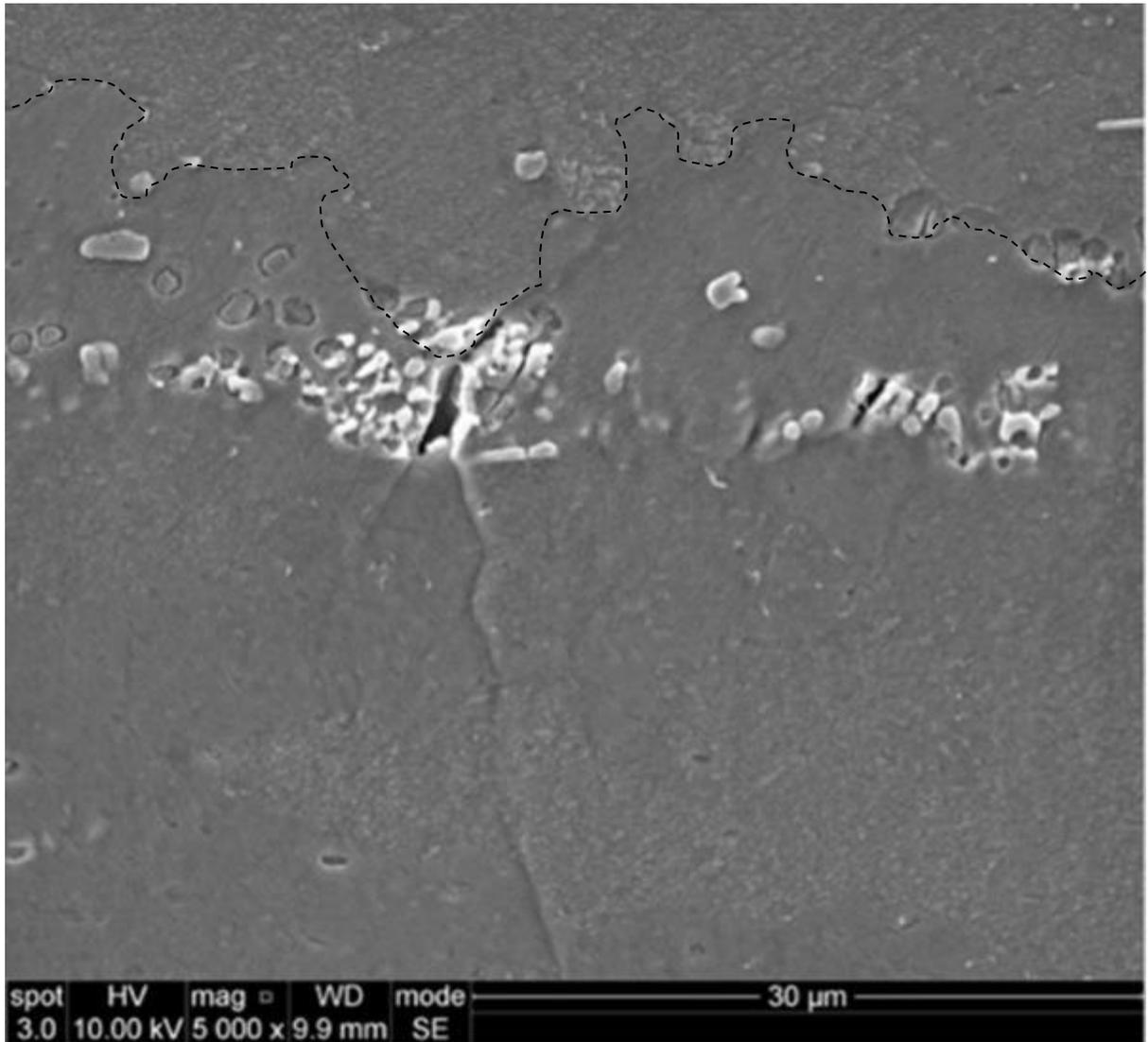
Figure 6-20. High magnification (5000x) image of the same region as in figure 6-19.

6.3. Discussion

4 point bending cyclic loading, under displacement control was done for 2 different amplitudes: low and mid amplitude, and the local displacements and strains were analysed at the top surface. Surprisingly, no significant strain accumulation was found to occur over 500 cycles in the area of interest. This is due to the fact that under stress control, as shown in the previous chapter, the strains increase overall in the corresponding area, while under strain control it is only the accumulation at specific points and small regions that will lead to damage development. Therefore it is a small scale process influenced by local plasticity [15]. The strain patterns for the major strain component did not follow the grains, but only the lateral contraction component did - this is in agreement with the observations made in the previous chapter. Shear bands formed at several locations in the microstructure, such as location A, D, E and B. The bands crossed 2-4 neighbouring grains. Next to these highly deformed areas lied rather undeformed microstructures, suggesting that areas within the same grain can experience high or low deformation depending on the location of the occurring shear

bands. Therefore an individual grain can carry at the same time high and low strains depending on its' neighbouring grains and location.

Differential Interference Contrast microscopy verified the DIC strain maps. It was correctly found that low strained areas show no out of plane deformation, and the matrix appears to be uniformly deformed without any evidence of slip bands. This was in contrast to the heavily deformed areas of figure 6-3, which have significant out of plane deformations and slip bands formed on the top surface.

A systematic analysis was followed to further verify the strain maps of figure 6-3. High resolution SEM analysis was done on the same area in order to make a correlation between the different scales - and to show that highly deformed areas should also show strain localisations and damage at the low scale. Figures 6-8a to g are the corresponding areas of the strain map of figure 6-3. In all the areas the inclusions and particles appeared damaged with severe cracking and void growth mechanisms. GB decohesion was also observed but this phenomenon is related to the presence of segregated particles and impurities at the GB. In contrast, the particles and inclusions in figures 6-8h to l appear undamaged with the matrix showing uniform deformation. This is in contrast with studies which suggest that particle cracking and inclusion void growth is expected to occur even from the first loading cycle independent of the location of the particles with respect to the microstructure (for low amplitude loading) [45, 71]. Here it is found that depending on local orientation, location and neighbouring grains, the particles can be shielded from high displacement fields. This further necessitates the need for more accurate and experimentally validated microstructural models.

For the mid amplitude case study, specific low strained grains were inspected in this case, namely A-E. Especially grain E lies between highly strained areas and yet it appears to be relatively low strained. High resolution SEM analysis shows that no slip bands have formed and the particles and inclusions appeared to be intact. This is in agreement with the observations made in the previous study. Yet in the previous case, differences in the strain fields were observed within the same grains, and the strain fields were analysed within neighbourhoods of grains as these appeared to be more non-homogeneous. This is in agreement with the work in reference [26], where at low amplitude the influence of the neighbouring grains is expected to increase. The strain map in figure 6-12, appears to be more homogeneous. And the grains can be classified into two groups, the low strained 'hard' grains, and the grains that show high non-homogeneities with low and high strain fields even within the same grain. So upon further loading, there exist regions of low and high strained grains; with the strains within the grains appearing highly non-homogeneous. For higher loading conditions, these neighbourhoods tend to 'disappear' and strains highly localize at specific grains. There are many grains that continue to show high non homogeneous strain fields, but some of them show 'hard' grain characteristics. High resolution analysis at the specified areas verified the multiscale process of strain and damage accumulation, with slip bands, crack nucleation and void growth in the highly strained

areas, and uniform matrix deformation with no slip bands or evidence of damage in the low strained grains.

So by connecting these two sections with the observations made in the previous chapter, a linkage between the various length scales can be obtained (micro - meso and macro) and the strain and damage development has been evaluated at various scales. The results have also been verified by high resolution SEM analysis. It was found that at low amplitudes the strains appear highly non homogeneous at the macroscale. Similar were the observations at the mesoscale where regions of high deformation were separated by areas of low strains and the same result was found at the micro-scale in this chapter. Furthermore, SEM analysis showed that in high strained areas the particles and inclusions appear to be damaged, while in low strained areas they appeared to be shielded and undamaged. Therefore strain and damage development is a multi-scale process that affects various microstructural features and their behaviour (shear banding, slip band formation, void growth around inclusions, particle cracking).

6.4. In situ vertical bending test in notched sample

A specimen was machined to a rectangle with 50mm (length) x 7mm (width) x 4mm (thickness) dimensions. A 1mm hole was drilled at the centre of the top surface to localise high stresses and facilitate crack initiation. The sample was mechanical grinded and polished down to 0.06μm (with Silico). Electropolishing was then performed in a solution containing 30% Nitric acid and 70% Methanol, for 13 seconds, at -16° C, 15V and 10mA. EBSD measurements were carried out using a FEI-Sirion SEM, at 20kV and spot size 5 as operating conditions. The step size was 1.5μm, covering approximately a total area of 1.6mm x 3.0mm, as shown in figure 6.21.

Following the EBSD measurements, the specimens were repolished and etched as already described in the previous section 6.3. Micro-mechanical, vertical bending tests were performed using a 2kN Deben testing stage inside a CamScan SEM with a cross head speed of 2mm/min. Initially a static test was performed up to a maximum strain of 0.01 applied to the two left and right edges of the area. The test was interrupted at each 0.2 mm displacement increments, and local displacements and strains were obtained by means of Digital Image Correlation (DIC) as explained in [50]. So the local strains were obtained at maximum displacement at the first peak load. Subsequently, displacement controlled cyclic loading was initiated with a frequency of 0.5, from 0 up to maximum displacement. The test was interrupted after the 1st cycle, the 10th cycle, the 100th, 200th, 300th, 400th and 500th cycle, at the maximum displacement applied and images were acquired. The consecutive images were correlated to the image at the first peak load and hence to the image for the undeformed sample. In the current study, the microstructural features of the material have been directly used as the pattern from which to correlate the images between two successive loading steps. A low magnification analysis (50x) was pursued for this study in order to obtain microstructure representative results and evaluate a relatively large microstructural area with respect to the EBSD map of Figure 6.21. With the current magnification, the 2 areas in-situ observed correspond to the two yellow boxed areas of

Figure 6.21. The 2 corresponding micrographs cover approximately an area of 2.25mm x 1.5mm. The micrographs were analysed using the commercial image analysis software, DaVIS 7.0, by LAVision [79] to determine the in-plane displacement field from which the plastic strain values were calculated. In the current study, the microstructural features of the material have been directly used as the correlating patterns for the images between two successive loading steps. A sensitivity analysis on the interrogation window size was carried out, and a multiscale interrogation window with 16x16 and 32x32 pixels and 25% overlap was finally selected in all the experimental results presented in this study. A multi-pass algorithm (4 passes) [79] with 25% overlap between windows has been used to achieve best correlation results. A displacement accuracy of 0.01 pixels was obtained with a strain resolution of about 0.1% [79]. In the following section the two case studies for the 2 highlighted regions of figure 6.21 are discussed.
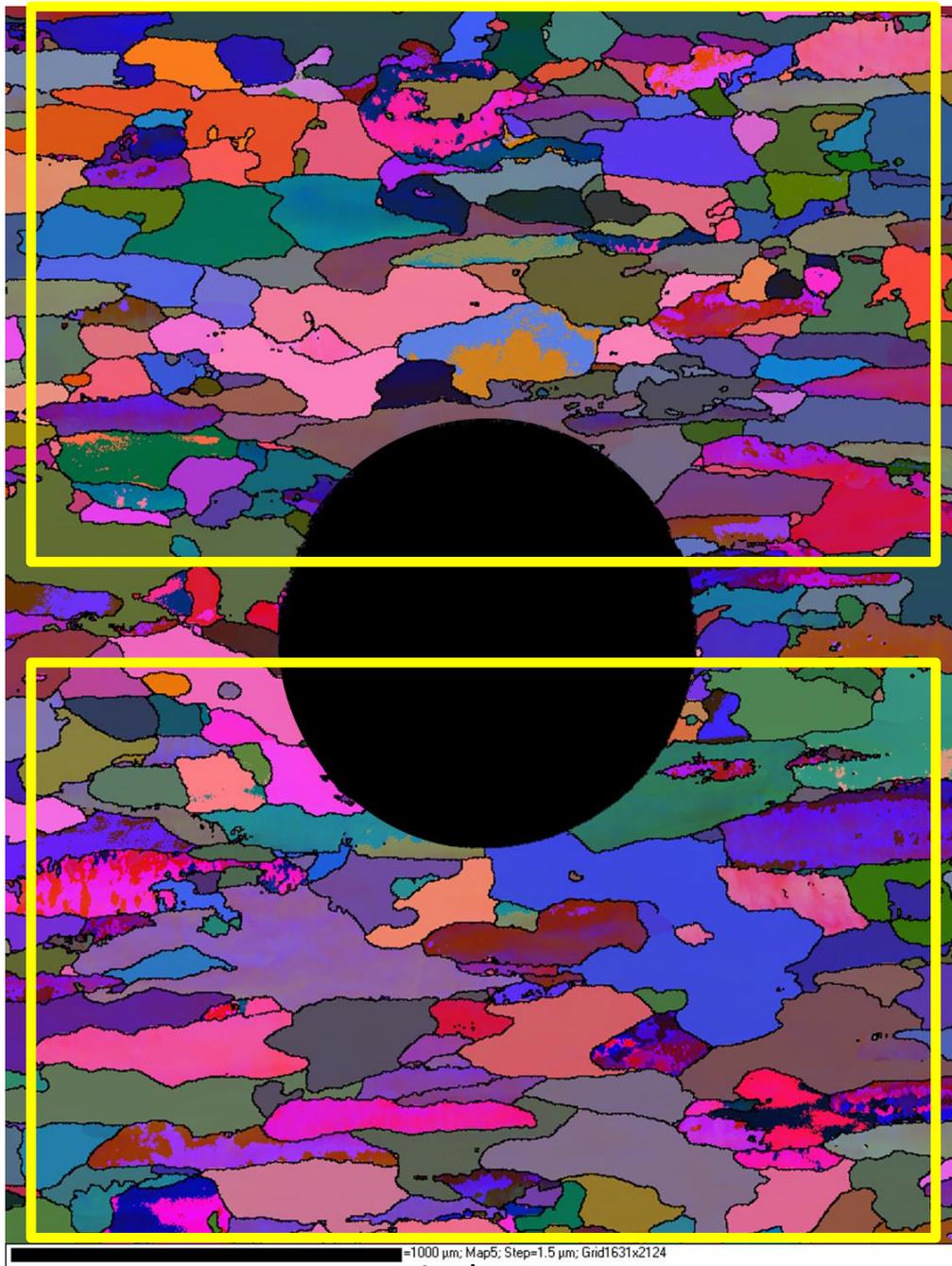
Figure 6-21. EBSD map at the region around the hole. Two highlighted regions were selected and in situ observations were made during micro-bending.

6.4.1. Case study 1

Figure 6.22 shows a SEM image of the upper highlighted region of Figure 6.21. The image corresponds to the unloaded condition for the sample. Individual grains can be seen, yet not all GBs are revealed compared to the EBSD map (figure 6.21). The black lines in figure 6.22 can be ignored as they were created from the evaporation of isopropanol on the sample surface prior to HF etching.
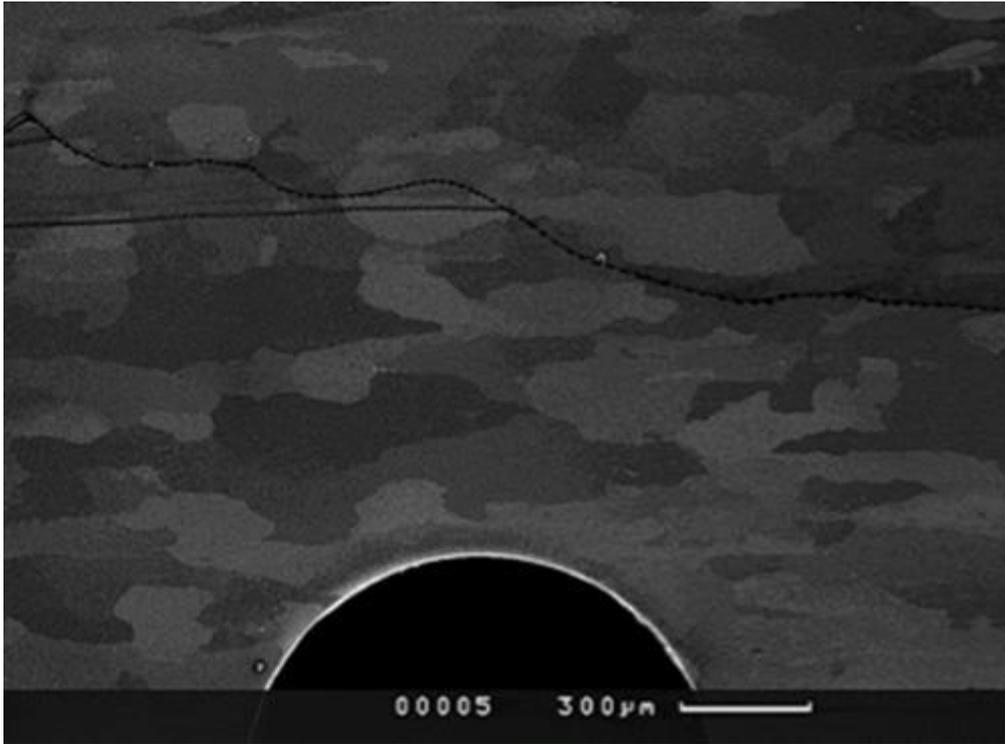
Figure 6-22. SEM image of the region highlighted in figure 6.21.

After just 10 loading cycles, severe slip bands have formed in the red-highlighted grain of figure 6.23a. It is interesting to note that this grain, even though located close to the hole is not at the geometrical edge of the hole. This suggests the strong dependence of texture and grain orientation on the occurring deformation and damage potency. Figure 6.23b, shows the DIC-computed εxx strain for the same region of the microstructure. There is a clear strain localisation ahead of the hole, shown with the white triangle. Even though the highest strain magnitude is at the very edge of the hole, crack initiation does not occur at the corresponding area, and the highest strain localisation occurs away from that point, at the grain highlighted in figure 6.23a. There is no strong overall strain development during cyclic loading through the figures 6-23b, d and f. The strain patterns do not seem to alter or localise in any areas within these figures. The strain maps show the occurrence of high heterogeneities in the microstructure which will be presented in next section. At this stage a detailed microstructural analysis was pursued, to check for the occurrence of damage initiation.

Figure 6.24 shows a detailed view of the highlighted grain in figure 6.23a. It shows the out of plane deformation and the formation of slip bands on the surface. No damage was observed to occur within the grain after the first cycle (figure 6.24a). Yet after 10 cycles, crack initiation occurred as shown in figure 6.24b. After 100 cycles, the crack deflects to a different direction in figure 6.24c (shown with red arrow), which can be related to the plastic fields ahead of the crack tip. If no crack deflection occurred, the crack tip had to go through a largely deformed area with slip bands concentrating close to the GB. By shifting direction, the crack goes through a less deformed region.

Load vector
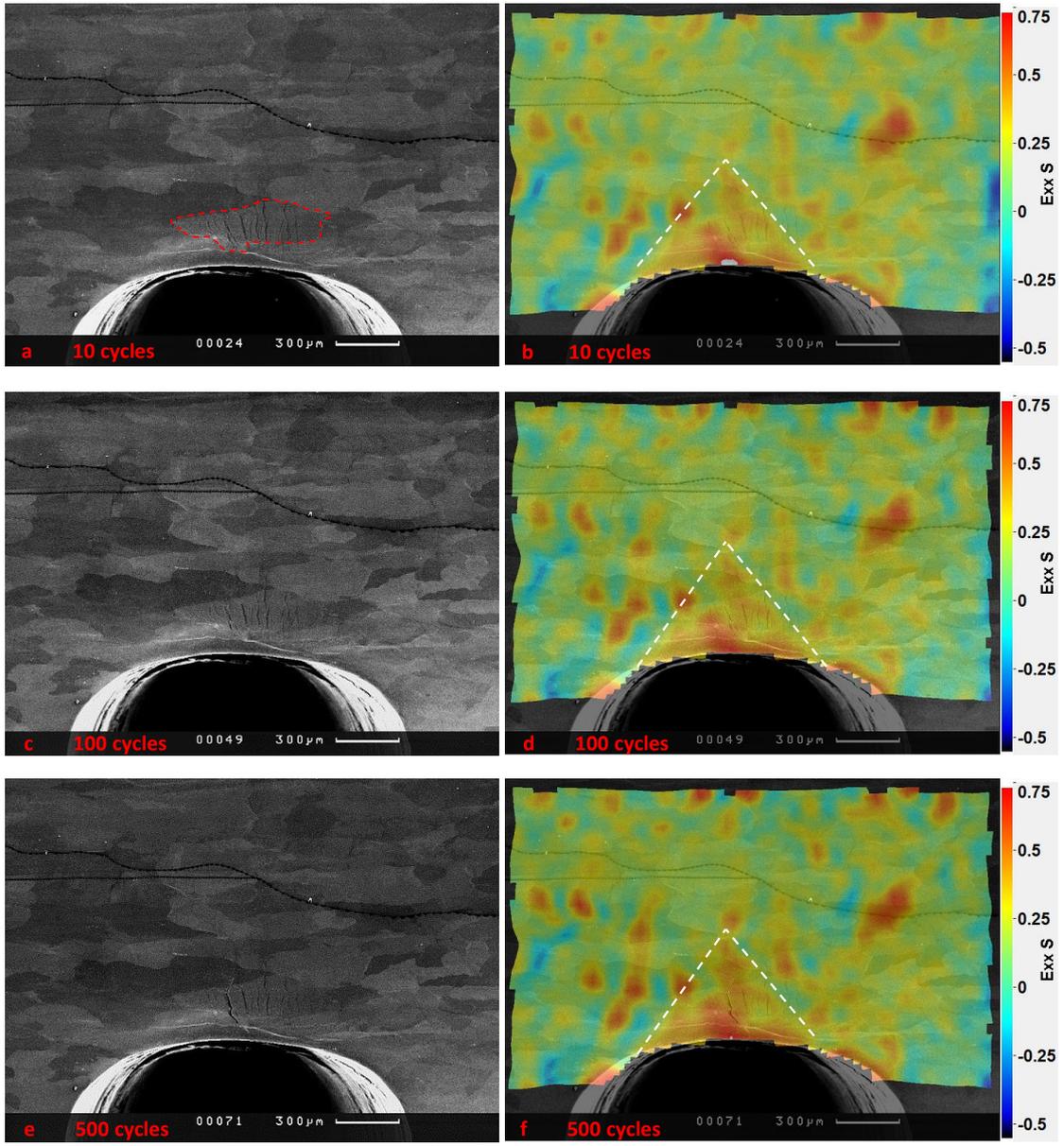
Figure 6-23. SEM images of the same region of the sample as in figure 6.22 for the fully loaded condition of the specimen after: a) 10 cycles, c) 100 cycles and e) 500 cycles. Strain distributions for the fully loaded sample after: b) 10 cycles, d) 100 cycles and f) 500 cycles.
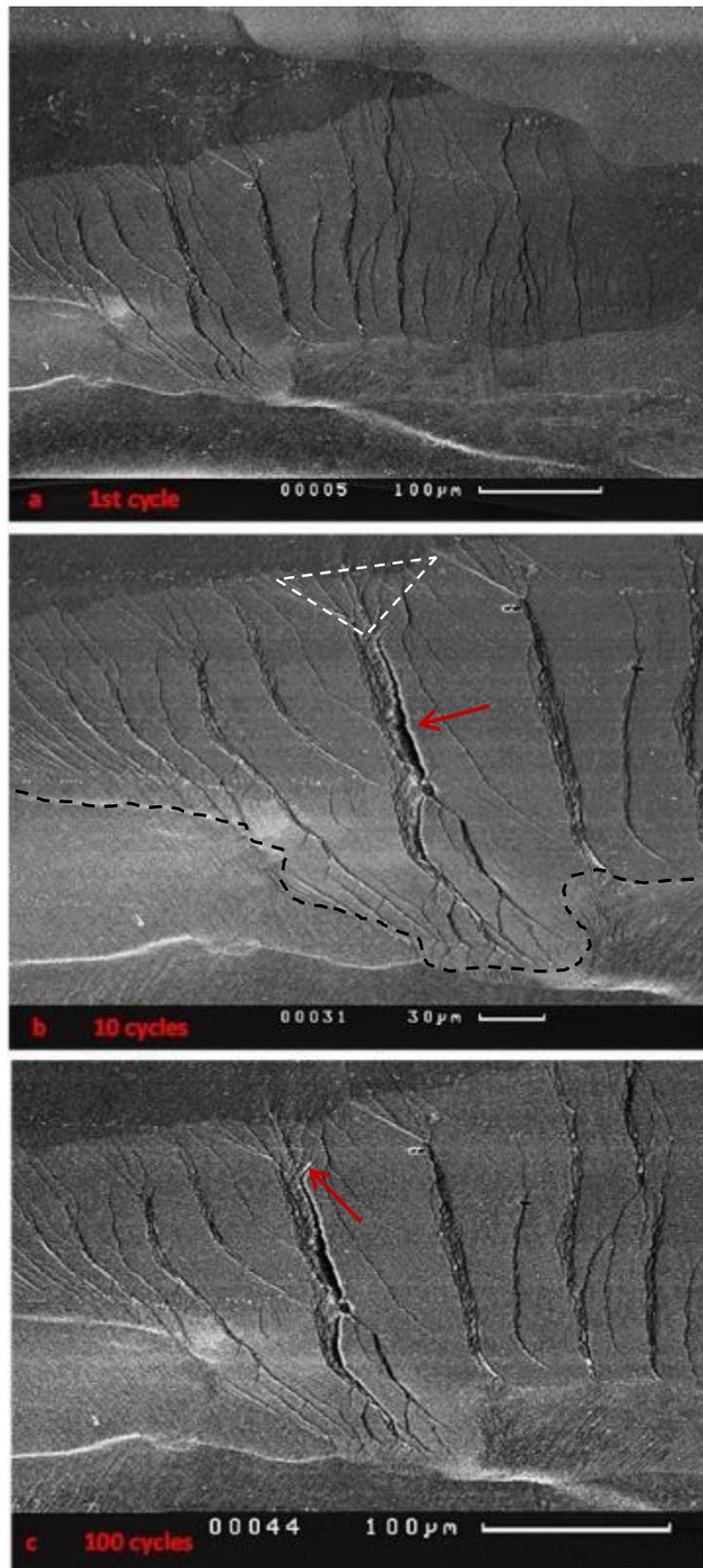
Figure 6-24. SEM images of the highlighted grain of figure 6.23a for the fully loaded condition of the specimen after: a) 1 cycles, b) 10 cycles and c) 100 cycles.

The first crack deflection of figure 6.24c is shown in detail in figure 6.25a. The crack is shown to have a first deflection in order to avoid the largely deformed area A. Area A corresponds to the white triangle

area of figure 6-24b, and corresponds to an area where additional slip systems have been activated close to the GB due to high strain concentrations. Following the first crack deflection, a second and third crack deflection occurs in figure 6.25a, which can be related to the tendency of the crack to pass through less deformed areas. As the initial crack approaches the GB (white dotted line), slip bands accumulate close to the GB, along the specific slip plane highlighted with white arrow (in figure 6.25a). This prevents further movement of dislocations and crack extension, and therefore the crack diverts to a different slip system. A second crack deflection occurs after propagation along the slip system shown with red arrow, followed by a third crack deflection, which sets the crack along the same direction as that of the red arrow (in figure 6.25a). The second crack deflection allows the crack to avoid crossing slip bands orientated perpendicularly to the crack path in the highly deformed region B, where severe slip banding and associated plasticity has occurred. The crack does not change direction upon reaching the GB even though the misorientation angle was quite high (35°), which can be related to the fact that the crack has already deflected upon reaching the GB of the first grain to a direction that favours crack propagation in the next neighbouring grain. The grains are quite large and may be considered to be quite thick below the surface; actually any grains lying below the surface grains can also be picked up the backscattered electron which are diffracted from deeper layers below the surface with respect to the secondary electrons.

For the other crack tip the angles of crack deflection are smaller. This is primarily due to the fact that at the white circled area of figure 6.25a, large plastic deformation has already occurred, with many slip bands having approximately a parallel alignment towards the GB (white dotted line). The shape of the grain is such that it leads to extensive plastic deformation in the white circled area, concentrating a large number of slip bands. The crack is rather restricted from the neighbouring rather parallel slip bands and therefore no crack deflections occur as the crack approaches the GB. After 300 cycles, the crack tip has crossed grain B, entering grain C in figure 6.25b while after 500 cycles, crack opening may be observed within the grain C, with no crack diversion observed as the crack has entered the third grain. The misorientation angle at the two GBs, AB and BC was quite high, approximately 33°, The crack does not deflect upon crossing the GBs, which can be due to the slight crack deflection that already occured within the first grain that favours crack propagation in the grain C. Grain B appears to be quite small in size at the corresponding region to deviate the crack path. Yet severe plastic deformation may be seen to occur at the lower part of the magnified image in figure 6-25b with a secondary crack branching along a different direction. However the main crack continues to propagate along the same direction.

In figure 6.23b, d and f, the highest strains were observed to occur at the edge of the hole. Yet microstructural observations showed that this was not followed by severe damage. Therefore quantifying the strain fields alone is not sufficient to analyse the occurrence of damage nucleation and propagation. The grain at the edge of the hole did extend extensively due to the presence of the geometrical hole, but did not localise the strains and damage.

The much more heavily deformed grain of figure 6.24a, was found to highly localise the strains and lead to crack initiation and propagation. This grain did not carry the highest strain values, yet damage nucleation occurred within this grain. This suggests that the total accumulated slip, or total accumulated strain at a point, is not the critical crack initiation criterion but rather the total accumulated slip along a specific slip plane. Strong slip bands accumulate local strains (ratcheting effect) during cyclic loading and lead to crack nucleation. Damage nucleation and propagation occurred due to slip band formation and local deformation at the scale of less than 2µm (slip band thickness).
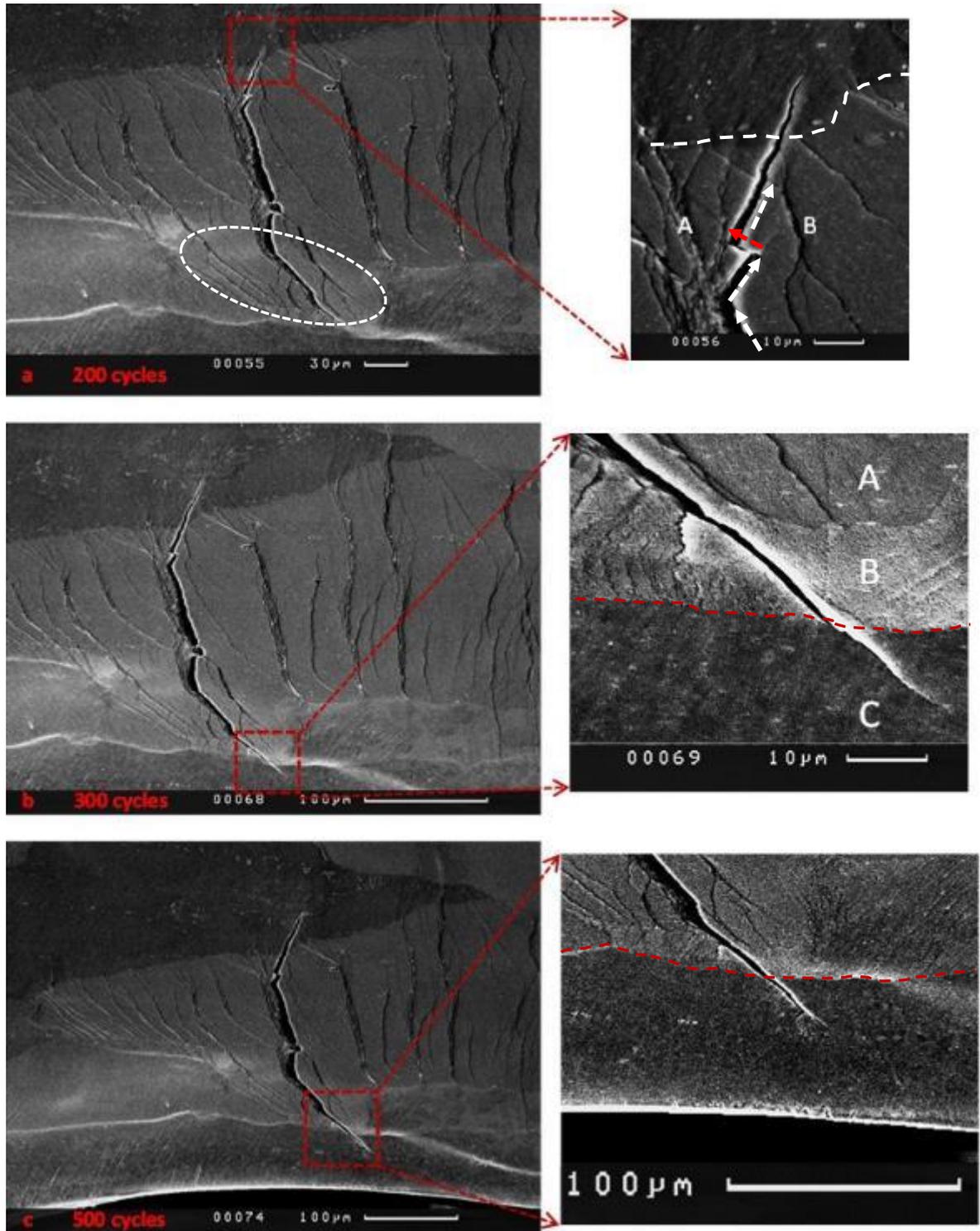
Figure 6-25. SEM images of the highlighted grain of figure 6.23a for the fully loaded condition of the specimen after: a) 200 cycles, b) 300 cycles and c) 500 cycles.

6.4.2. Case study 2

Figure 6.26 shows the SEM image of the lower highlighted region of Figure 6.21. The image corresponds to the unloaded condition for the sample. Individual grains can be seen, yet not all GBs

are revealed compared to the EBSD map (figure 6.21). The black lines can be ignored, and were created from the evaporation of isopropanol on the sample surface prior to HF etching.
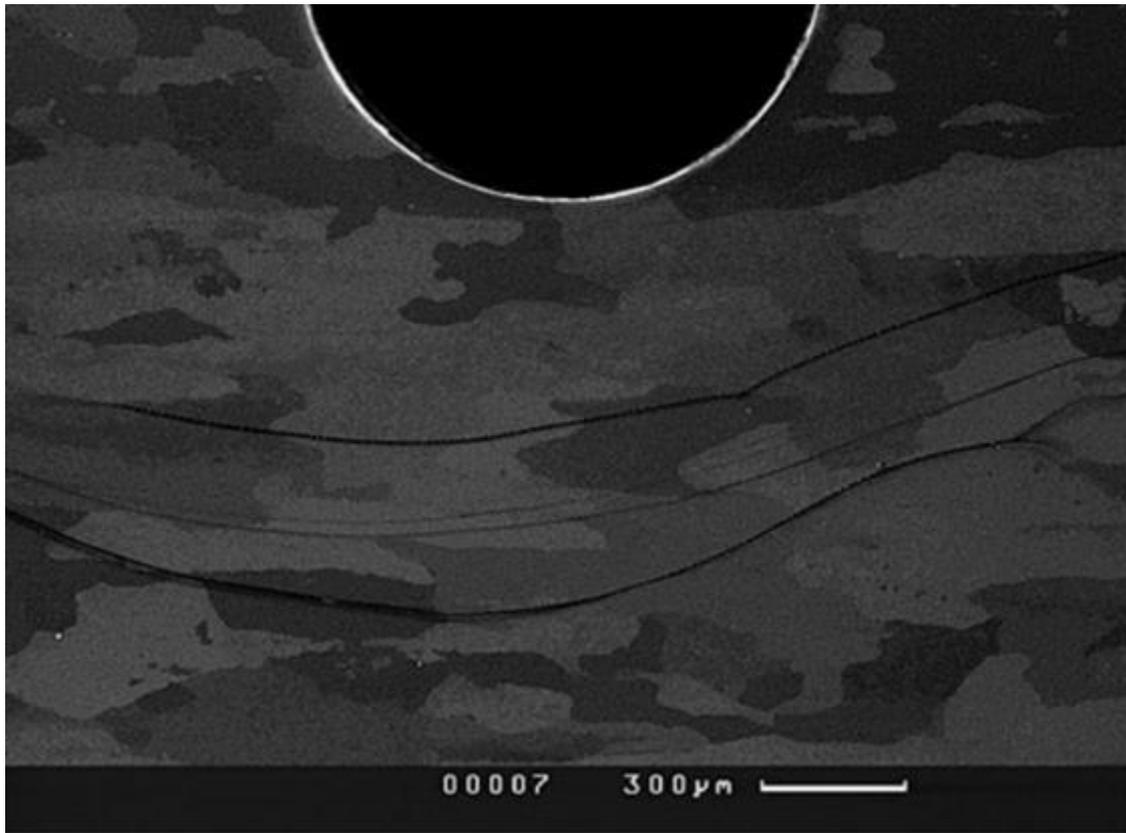
Figure 6-26. SEM image of the bottom region highlighted in figure 6.21.

Figure 6.27 shows the images of the microstructure and the corresponding strain contours at the same areas after 10-100 and 500 cycles. The strains are highly heterogeneous with the highest strains appearing localised again at the edge of the hole, as highlighted by the white triangle. There is no strong overall strain development during cyclic loading through the figures 6-27b, d and f. The strain patterns do not seem to alter or localise in any areas within these figures. Once more there is a critical grain away from the hole with highly localised deformation along slip bands, which is highlighted in figure 6.27a. In this case, the grain is far away from the hole, approximately 450-500µm, and therefore no damage occurs within the grain. In this study, another grain at the edge of the hole forms strong slip bands which lead to damage nucleation and propagation (Figure 6.28). The highest strains in figure 6.27 b, d and f occur at the edge of the hole, and it is at that point that damage nucleation occurs.
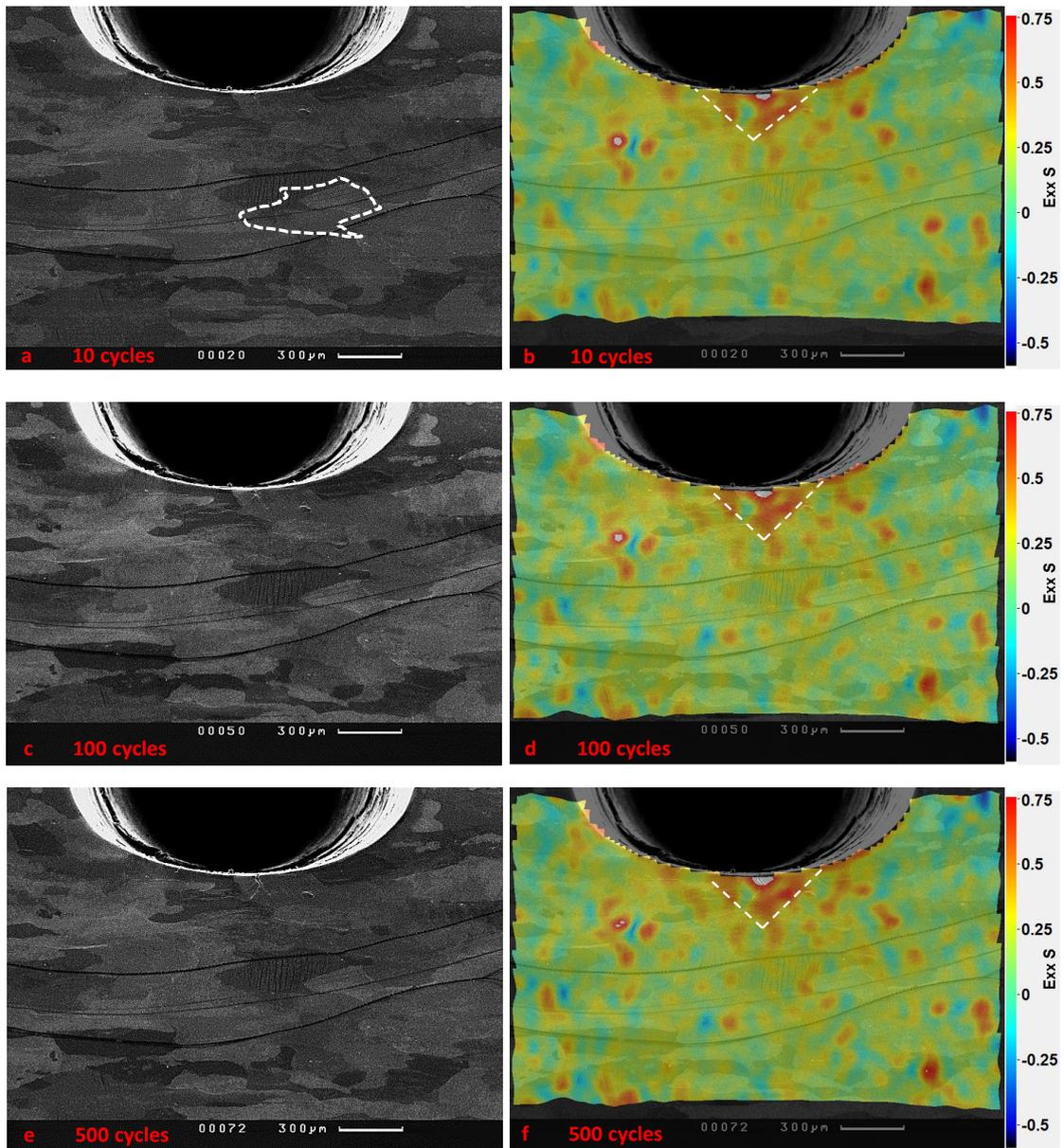
Figure 6-27. SEM images at the same region of the sample with figure 6.26 for the fully loaded condition of the specimen after: a) 10 cycles, c) 100 cycles and e) 500 cycles. Strain distributions for the fully loaded sample after: b) 10 cycles, d) 100 cycles and f) 500 cycles.

The highlighted triangle area in figure 6.27b is shown in figure 6.28. The EBSD map is shown together with low and high magnification SEM images to correlate the occurring localised deformation and damage with the underlying grain structure-shape-orientation and the location of the GBs. In the 2 circled areas, 2 different mechanisms of deformation and damage nucleation are observed. In the white circled area, slip bands form, and crack initiates along the heavily deformed slip bands, while in the black circled area, localised deformation and damage occurs in the neighbourhood of a particle. The corresponding damage development for the 2 sites is different as the mechanisms for damage evolution are different. It is shown below that crack growth along the slip bands, for high amplitude loading, is much higher with respect to crack growth at the particle site, due to the associated high plasticity along the specific slip band which favours crack initiation and propagation.
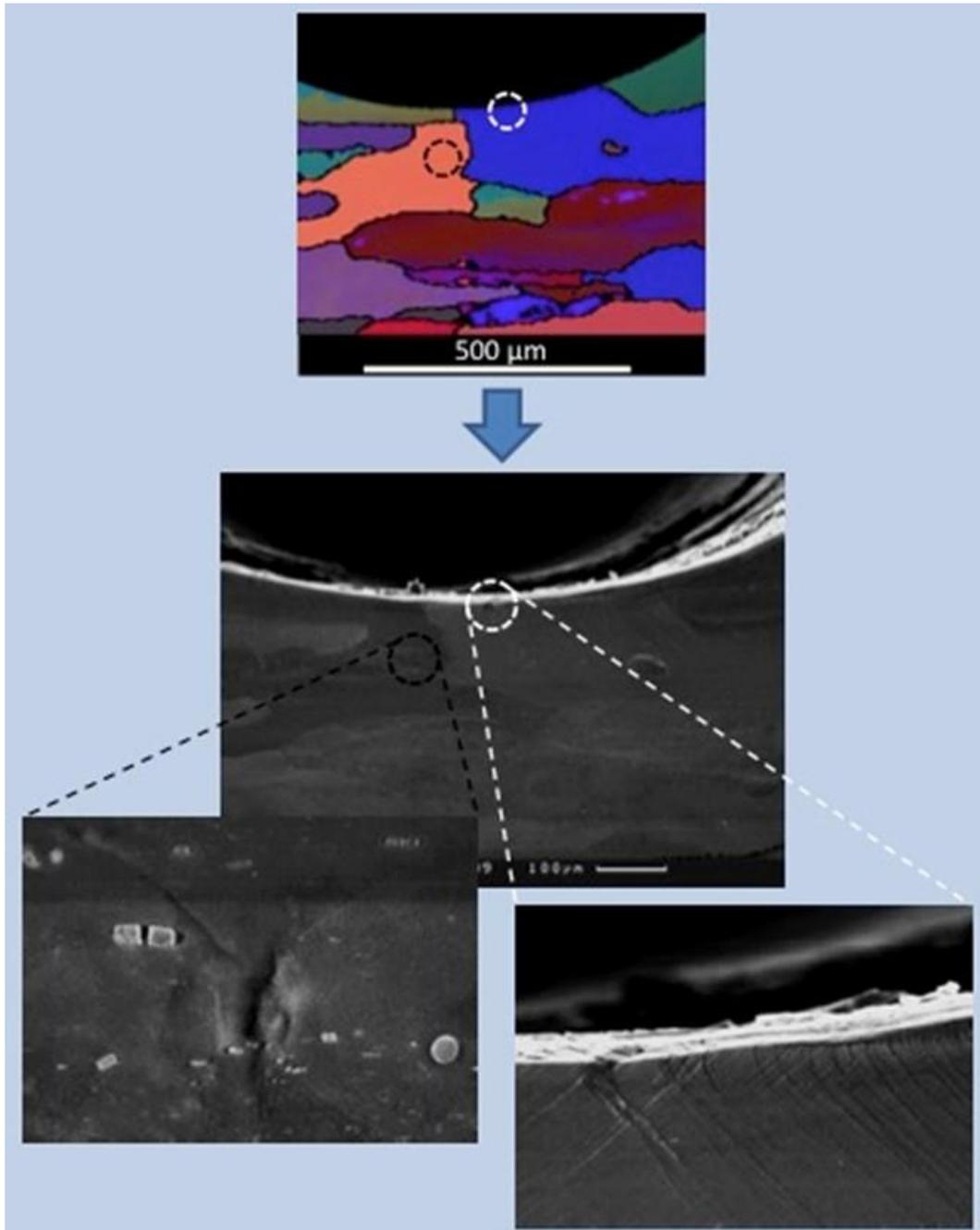
Figure 6-28. EBSD map and SEM images of the triangular region highlighted in figure 6.27b for the fully loaded condition of the specimen after 1 cycle.

a. Damage nucleation at slip bands

The white circled area in figure 6.28 was the most critical in the whole area and therefore images were acquired at different cycles to investigate damage nucleation and growth. Figure 6.29a shows the formation of strong slip bands at the specific location after the 1st peak load (bending test to maximum displacement). After the 1st cycle, at maximum displacement, some voids have formed along the slip band, as shown in the magnified image of figure 6.29b. After only 10 cycles a 22μm crack forms along the slip band at the top surface. The tip of the crack does not appear to be sharp (figure 6.29c). This can be related to the presence of extensive plasticity along the specific slip band.

However after 100 cycles and a small amount of propagation the crack tip looks sharper (figure 6.29d). The growth from 10 cycles to 100 cycles is slower with respect to the initiation stage; i.e. 5.5µm and this can be related to the initial blunt crack tip. Yet the rate of crack growth is still quite fast 6nm/cycle which can be related to the large grain size and the condition of the sample (annealed). At this stage in figure 6-29d the crack is relatively sharp, concentrating high stresses in its neighbourhood.
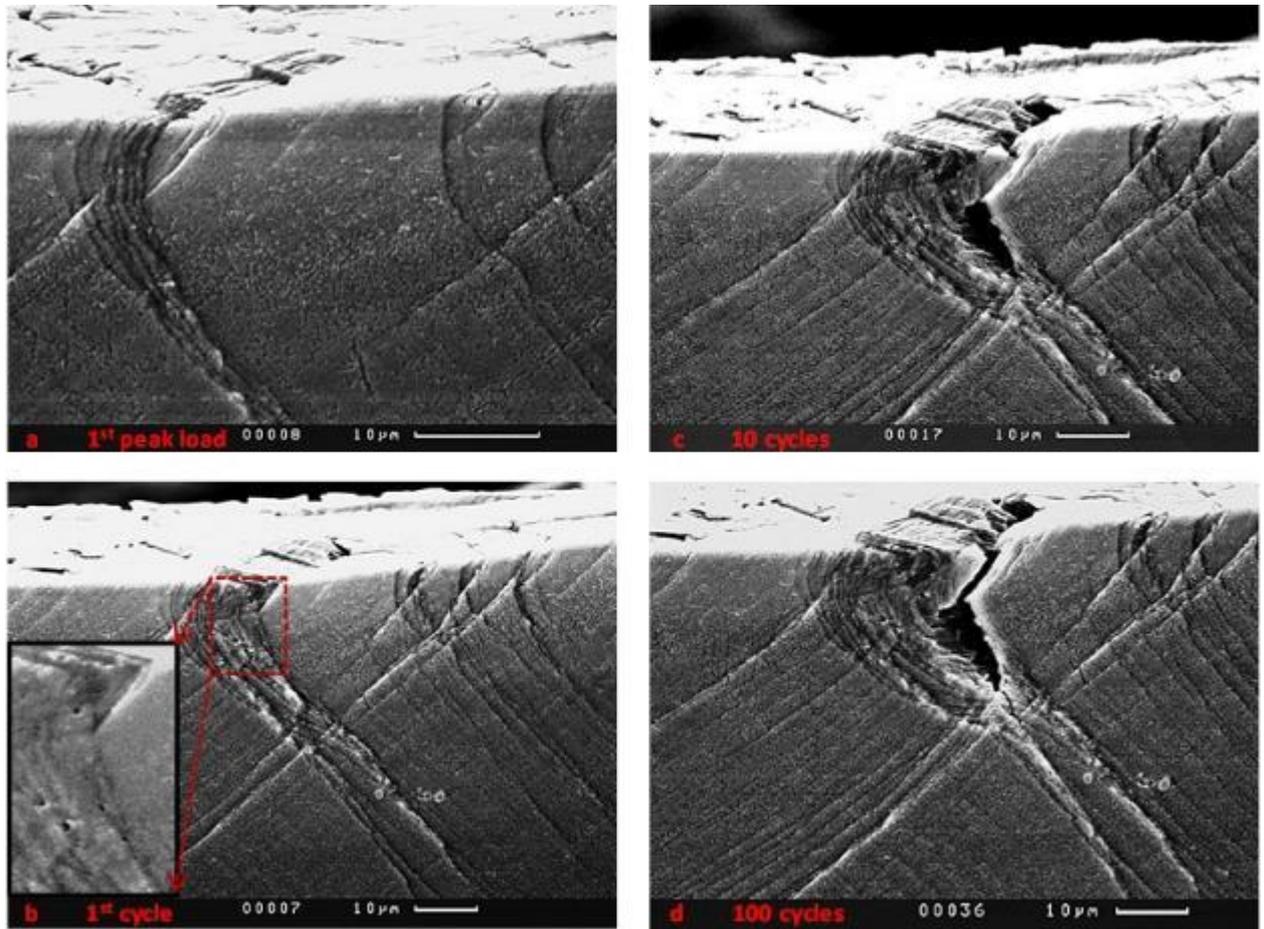
Figure 6-29. SEM images of the white-highlighted region of the EBSD map in figure 6.28 for the fully loaded condition of the specimen after: a) 1st peak load, b) 1 cycle, c) 10 cycles and d) 100 cycles.

From 100 to 200 cycles the crack has grown another 17µm in figure 6.30, accelerating its propagation. After 200 cycles, the crack deflects to a different direction in figure 6.30b and c, gaining a total growth of only 7.5µm after another 100 cycles. The slow rate of propagation can be related to a change of crack path direction, as extra energy is needed to divert the crack. By changing the direction the crack meets the other slip system and moves towards the highly deformed neighbouring grain on the left side, grain A. Crack growth is accelerated, and in only 200 cycles (500 in total), the crack has grown another 80µm approaching the first GB. The reason for crack diversion is primarily due to the fact that for the initial direction the crack would need to go through a uniformly deformed grain which does not show evidence of intense slip bands (see figures 6-39 and 6-40 in the discussion section 6.3.4 for images of this grain, grain B) and therefore acts as barrier to damage propagation, while by diverting

its direction, it can find an easier path through the grain labelled A in figure 6.30d which shows evidence of localised deformation bands (Figure 6-40). It can also be argued that crack deflection results from the presence of what seems to be an inclusion along its path in figure 6-30c. Yet the images in figures 6-39 and 6-40 show extensive slip bands crossing the particle, appearing even after the deformation resistant grain B.
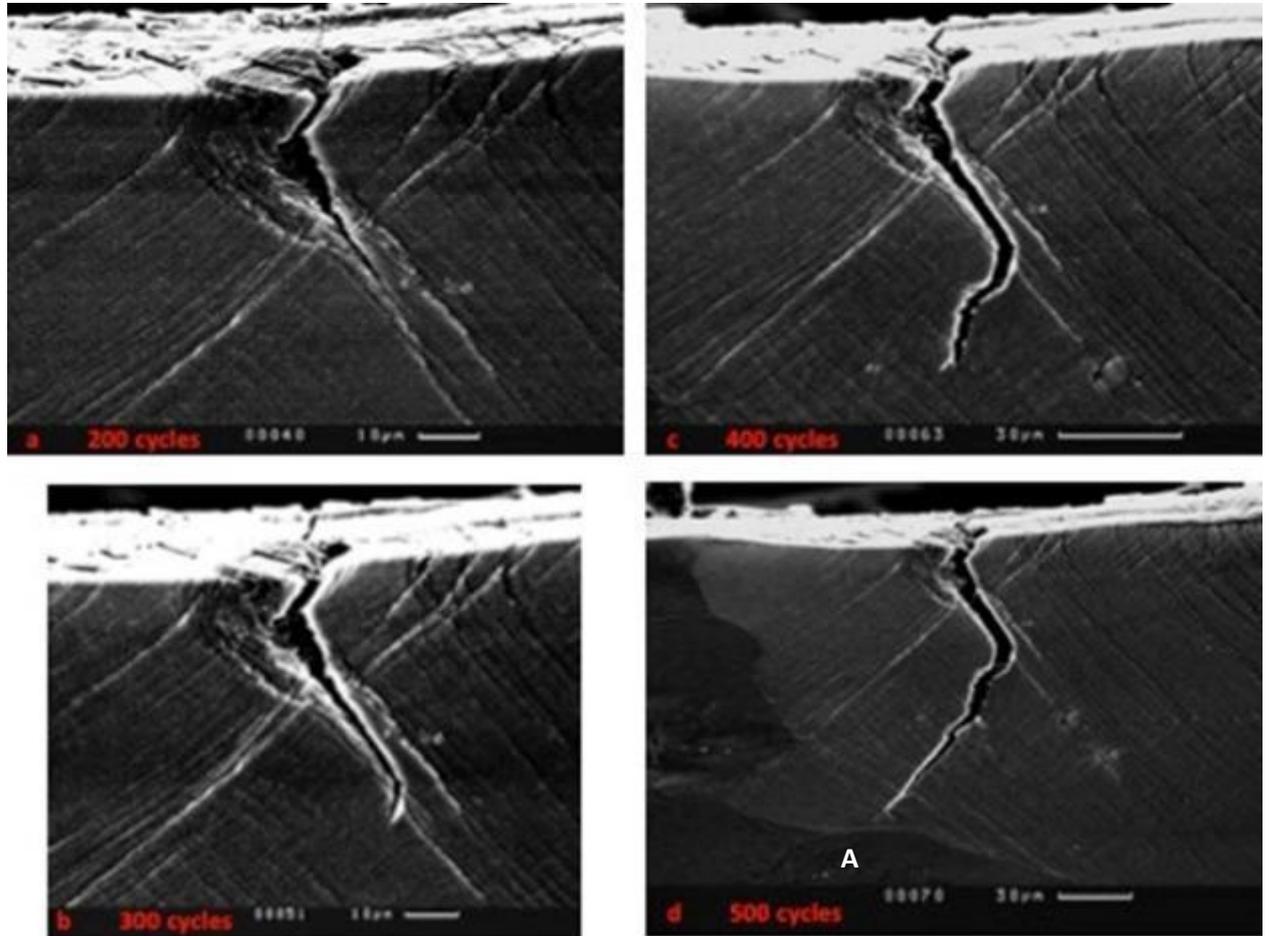
Figure 6-30. SEM images of the white-highlighted region of the EBSD map in figure 6-28 for the fully loaded condition of the specimen after: a) 200 cycles, b) 300 cycles, c) 400 cycles and c) 500 cycles.

b.   *Damage nucleation at particles*

Another mechanism of damage nucleation was also observed along with cracking along slip bands. Cracks were found to form at particle sites (region of the EBSD map in figure 6-28 highlighted by a black circle), and these were observed almost perpendicular to the loading direction. Figure 6.31a-d shows an initial crack of 6μm which has grown to a total length of 16μm after 500 cycles. The crack growth rate was much smaller in this case with respect to the crack in figure 6.30, and this can be related to the different mechanisms that are acting in the propagation of the two cracks. The first crack grows along slip bands, and its growth rate is controlled by the movement of dislocations and the large plasticity that occurs along slip bands through a mode II mechanism, while the 2nd crack grows in a direction perpendicular to the loading direction, through a mode I mechanism. The associated plasticity is much smaller in the latter case, and therefore the growth rate is lower. In this

case the crack does not follow the maximum shear direction, shown by 2 red arrows in figure 6.31c. In general mode I is faster than mode II crack growth. But in this case crack growth is driven by plasticity which occurs favourably at an angle (usually 45°) with respect to the loading axis.
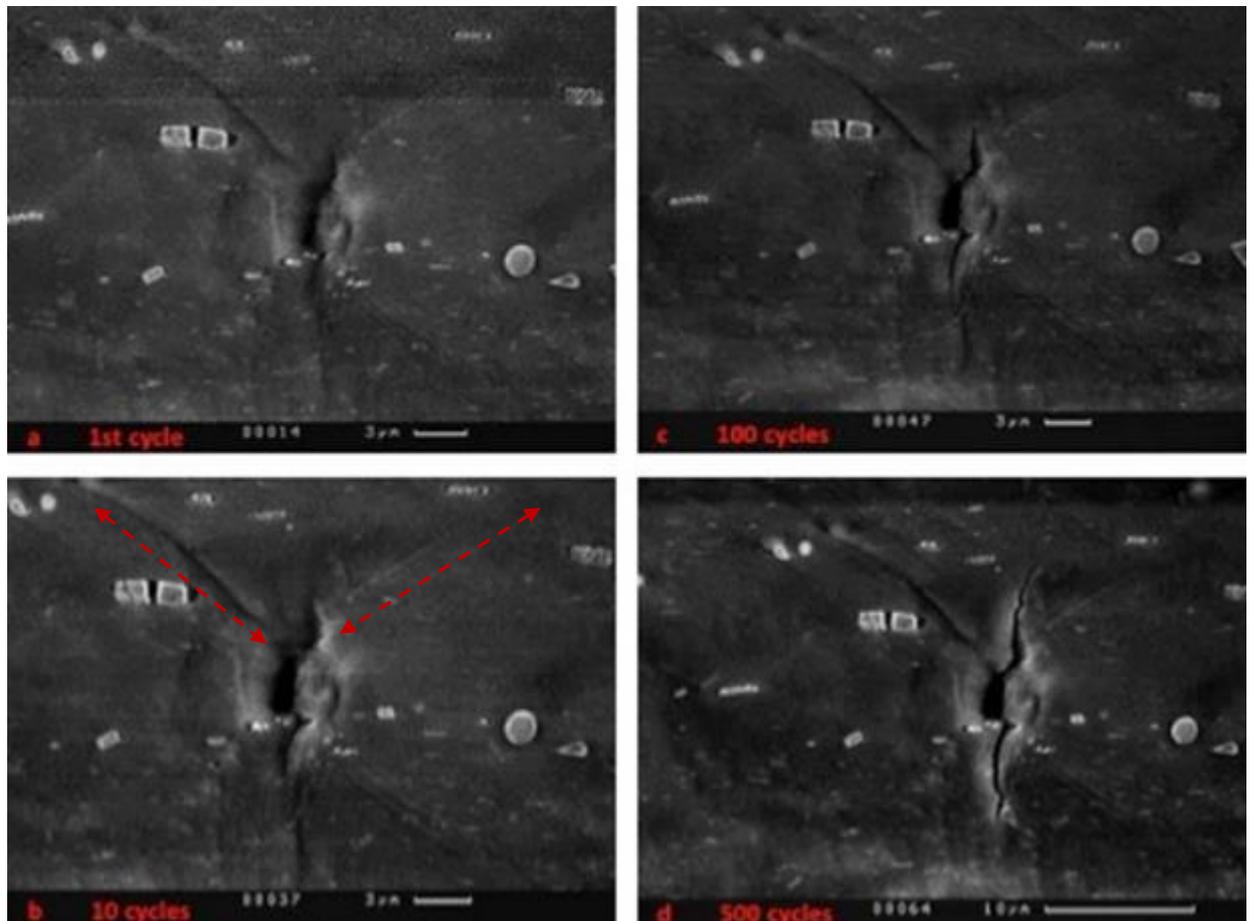
Figure 6-31. SEM images of the region of the EBSD map in figure 6-28 highlighted by a black circle for the fully loaded condition of the specimen after: a) 1 cycle, b) 10 cycles, c) 100 cycles and c) 500 cycles.

To correlate the two scales of cracking, an image was taken with both cracks shown. Figure 6.32 shows the 2 different cracks, and it can be seen that the crack propagating along slip bands is much larger and grows at a much faster rate, even though it was crack nucleating at a particle that first occurred during cyclic loading (at the very first peak load applied). Yet the rates for the two cracks are very different, as the crack along slip bands grows very rapidly due to extensive plasticity that occurs along these slip bands.
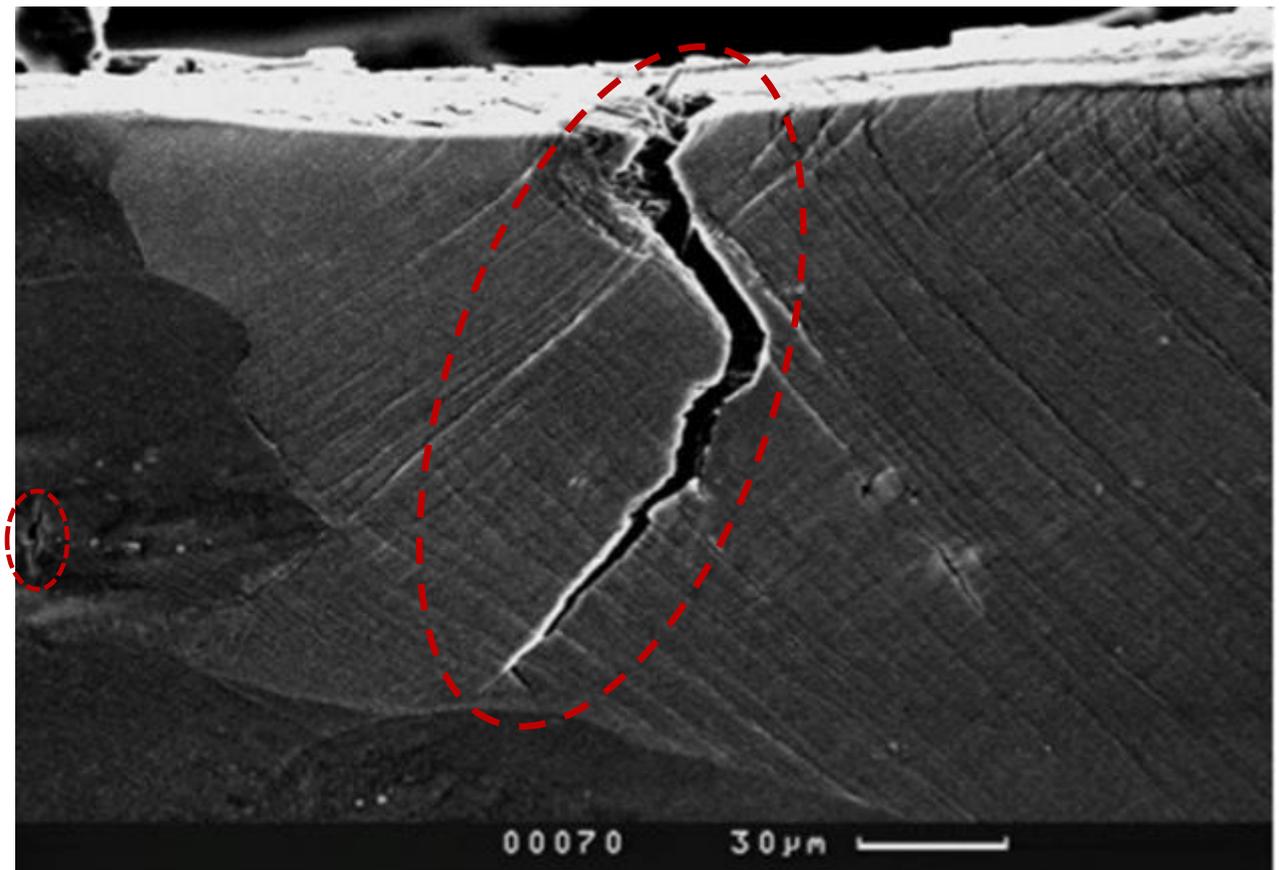
Figure 6-32. SEM images of the region of the EBSD map highlighted by the white and black circles in figure 6-28 for the fully loaded condition of the specimen after 500 cycles.

It was observed in other cases as well, that maximum shear planes, or planes along which slip bands form, ignore the presence of any particles. It was observed in all cases that the direction of crack initiation and propagation at particles was close to a direction perpendicular to the applied load, without following the direction of maximum shear strain.

c.   *Grain with detrimental orientation*

Figure 6.33 shows the highlighted grain of figure 6.27a. This grain had a detrimental crystal orientation and already in the first cycle, strong slip bands have formed on its surface. This grain though is far away from the strongly influenced area around the hole. The grain lies approximately 450-500µm away from the hole edge and 200µm away from the strain influenced area of the triangle drawn in figure 6.27b. The result is that all the plasticity that occurs in the first cycle does not increase/accumulate significantly in the next cycles, and therefore no damage nucleation occurs. The density of slip bands in figure 6.33a and b is the same. This is due to the fact that high strain concentration occurs in the highlighted area of figure 6.27 and all the energy is consumed over a small area around the crack. The corresponding grain is at a distance such that the stress and strain fields of the crack in Fig. 6.27f do not influence the strain fields within this particular grain. If this grain was within the drawn triangle of figure 6.27b, it would have lead probably to crack nucleation similar to the case of figure 6.24 and 6.25.
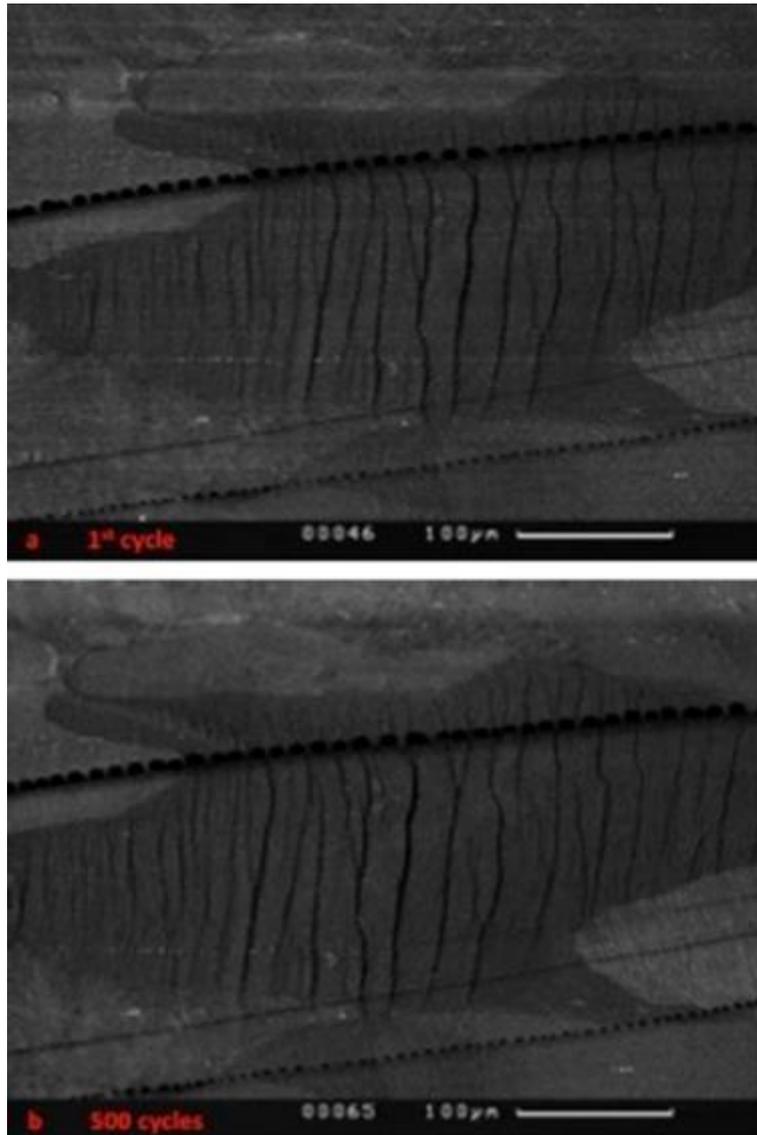
Figure 6-33. SEM images grain highlighted in figure 6-27a for the fully loaded condition of the specimen after: a) 1 cycles and b) 500 cycles.

6.4.3. Detrimental and preferential crystal orientations

In this section a materials design effort is pursued in order to determine the detrimental and beneficial crystal orientations. This helps to design materials with superior fatigue performance. Crystals that have the tendency to localise deformation and damage within specific slip systems and form persistent slip bands may be characterised as 'weak' grains, while crystals with unfavourable orientation for the formation of slip bands, and therefore the localization of damage behave as "strong" crystals.

Initially the full Inverse Pole Figures (IPF) for the EBSD map of figure 6.21 are presented, in order to reveal strong texture components. Figure 6.34 shows the data points of all grains of figure 6.21 within IPF. It is shown, that due to the strong rolling effect, most grains lie on the 001-101 plane with respect to the crystal reference system, and less on the 001-111 plane due to the effect of plastic deformation. In order to better evaluate the population of grains that lie on the 001-101 plane, the

density contours for the population of grains in IPF figure are shown in figure 6.34b. Figure 6.34b shows that there is a considerable amount of grains that lie away from the 001-101 plane which might be prone to damage nucleation, as these grains have resisted plastic deformation during the rolling process.
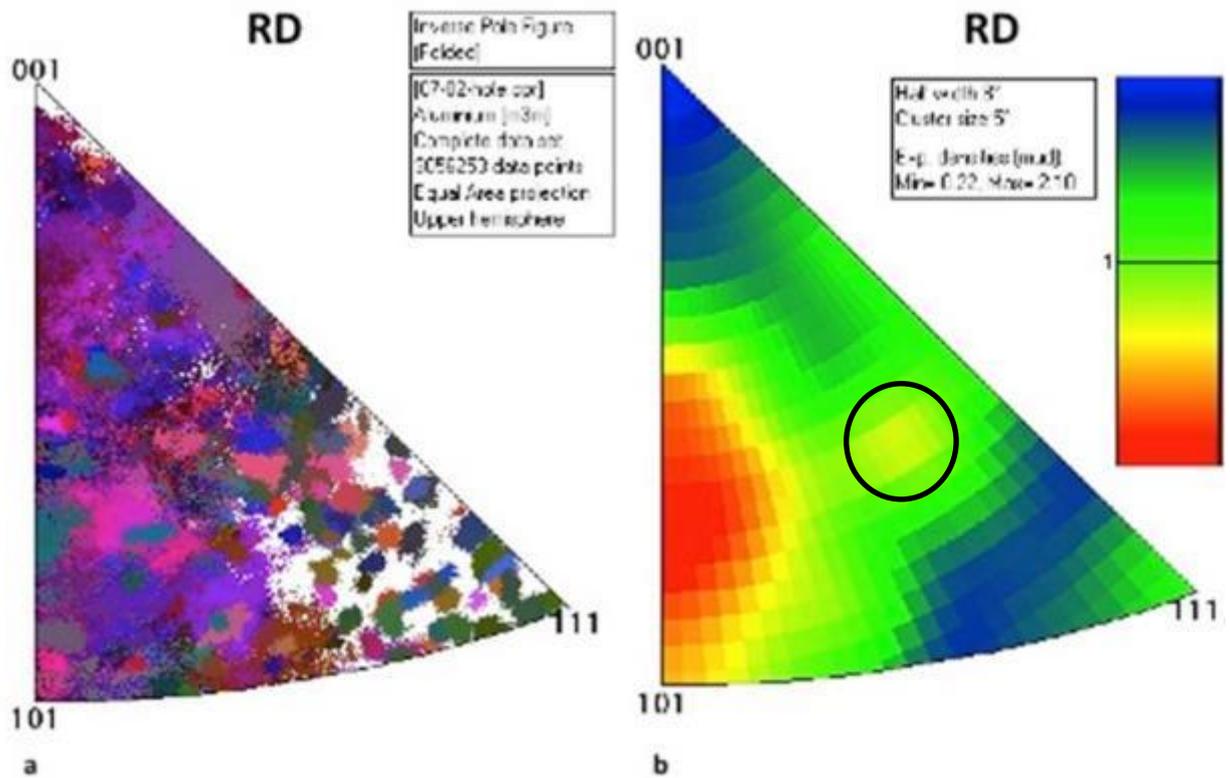
Figure 6-34. Inverse pole figures (IPF) for the EBSD map of figure 6.21 with respect to RD. a) Data points of each grain within the IPF, and b) Density contours showing the effect of rolling.

High resolution SEM analysis was performed with Inspect-F, to fully reveal which crystals are prone to slip band formation, and which ones show uniform plastic deformation. Figure 6.35 shows the grains (high contrast grains) that did not localise plastic deformation, did not form any slip bands and therefore did not contribute to damage nucleation and evolution. Similarly, the highlighted grains of figure 6.36 showed slip banding mechanisms and therefore these grains are detrimental for fatigue crack initiation and are named 'soft' grains.

Figure 6-35. The highlighted grains correspond to 'hard' grains, showing uniform matrix deformation without slip bands observed. Whille the arrowed grain correspond to the grain circled in figure 6-37.

Figure 6-36. Soft grains, with slip bands and non-uniform highly localised plastic deformation.

The highlighted grains of figures 6.35 and 6.36 were selected and the IPF figures were plotted in figure 6.37a and b, respectively. The hard grains lie on the 001-101 plane, while the soft ones on the 001-111 plane. Yet there are two grains shown with arrows whose mechanical behavior is wrongly predicted by IPF maps alone. This effect was attributed to the local texture effects and the orientations of the corresponding neighbouring grains. The data points highlighted with an arrow in

figure 6.37a correspond to the arrowed grain of figure 6.35. This grain lies in a neighbourhood surrounded by 'hard' grains. Furthermore, high misorientations were found with all the corresponding neighbouring grains, therefore restricting plastic flow between the grains. The black arrowed grain in figure 6.37b is close to the 001-101 crystal orientation and yet forms strong slip bands. Yet this grain showed slip bands only in the lower part of the grain, circled in figure 6.36. The misorientations with the neighbouring grains were high, and the 'hard' grain neighbours did not show any slip banding mechanisms. Yet, a sharp corner exists at the grains boundary, which could possibly concentrate stresses and strains. Furthermore, only information from the surface is known, while the grains are 3-dimensional. Below the surface other grains with detrimental orientation may exist at the corresponding highlighted region, highly-straining the grains at the surface. The grain highlighted with an arrow in figure 6.37b showed the strongest slip band formation as explained in Case study 1, and lies very far from the 001-101 orientation.
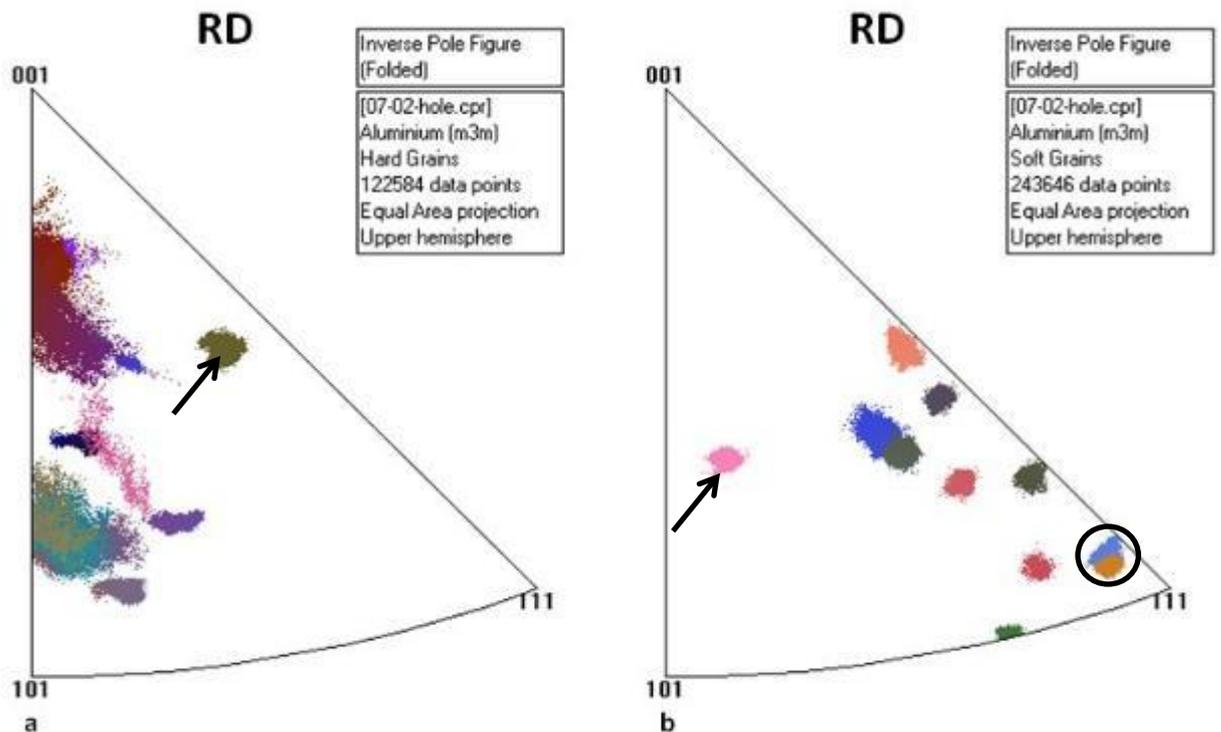
Figure 6-37. Inverse pole figures (IPF) for the highlighted grains of a) figure 6-35 and b) 6-36.

6.4.4. Discussion

4 point bending was performed in an Al2024 T3 rectangular sample, with a 1mm hole drilled at the center of the top surface. The sample was initially grinded and polished. EBSD measurements were taken in the region around the hole to investigate the influence of the local microstructure on fatigue crack initiation and small crack growth. The sample was loaded horizontally, and the two regions above (case study 1) and below (case study 2) the hole were inspected to check for the formation of cracks, and were also used for in situ imaging to facilitate DIC strain measurements.

During cyclic loading, strain localisation occurred close to the drilled-hole region. Figure 6.23 and 6.27 showed that the strains were highly non-homogeneous around the hole. For the specific material type, Al2024, highly strained regions were found to be next to low strained regions, even within the same grains. A triangle of high strain localisation was drawn in figures 6.23 and 6.27 to show the characteristics of strain localisation around the hole. Yet, crack nucleation was found not to occur always at the edge of the hole. Figures 6.24 and 6.29 show that slip band formation was the main mechanism that lead to fatigue crack initiation (for high amplitude loading). A damage prone grain, close to the edge of the hole in figure 6.24, forms strong slip bands, and a crack forms and propagates along the strongly deformed slip bands. Similarly, a damage prone grain, at the edge of the hole in figure 6.29, leads to the formation of strong slip bands at the edge of the hole, and fatigue crack initiation, after just 10 cycles. The mechanism which leads to crack formation is highlighted in figure 6.29b, where small, sub-micron voids form prior to crack initiation. High magnification imaging revealed that the size of these voids was approximately 0.3 to 0.5 µm. It is the accumulation of high numbers of dislocations along the slip bands that leads to sub-micron void formation. Once this void density becomes critical, a crack will form, joining together the aligned voids. The appearance of the crack is relatively sudden, with the crack length already reaching 10 µm, after 10 cycles. This is due to the presence of these voids, which suddenly join up forming a relatively large crack (figure 6.29c). Figure 6.38a shows that fatigue crack initiation is a process involving a large amount of ductility for high amplitude loading. At the location where initiation occurred, elongated voids may be observed together with large out of plane deformation along the extensively deformed slip band. Yet crack propagation is a process with less involved ductility in comparison to crack initiation. FCI involves large three dimensional displacements, while crack propagation was relatively shallow (small out of plane deformations) which is related to the associated strain fields ahead of the crack tip. A larger amount of energy is needed to form a crack, and thus larger amount of plasticity. So the voids appear elongated at the crack nucleation point. The amount of plasticity is much less during crack propagation as shown in the micrograph of figure 6-25a. The crack deviates from the main slip band (strong slip band parallel to the white arrow) and propagates along smaller slip bands as the crack approaches the GB.
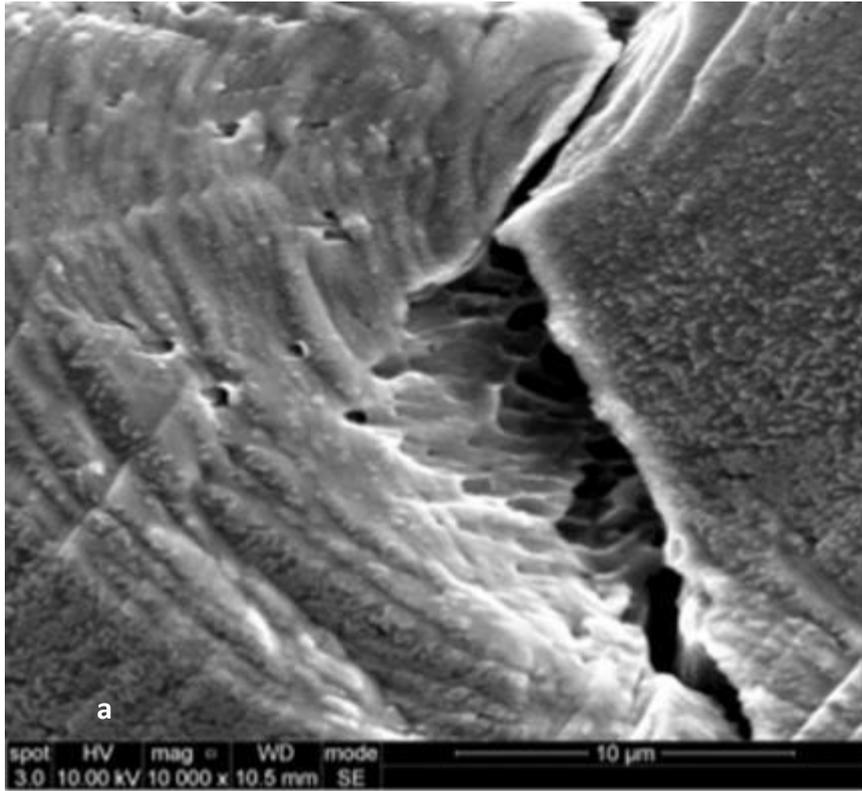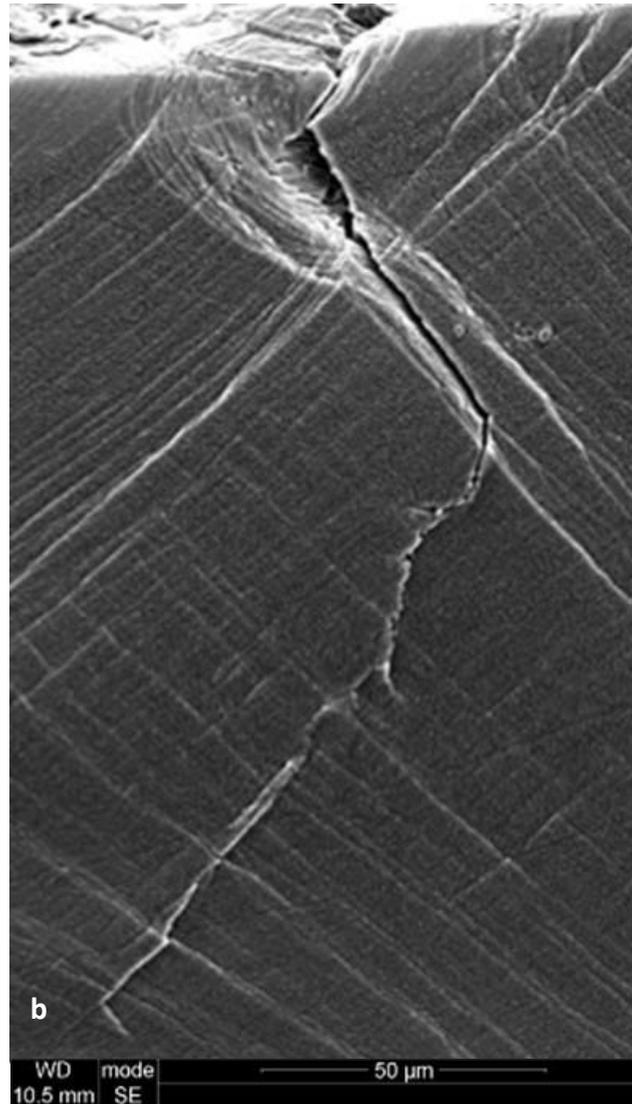
Figure 6-38. a) High magnification imaging at the location where crack initiation occurred, b) Image of the whole cracked area.

After crack formation, the small crack growth characteristics were analysed in detail for the 2 case studies. Crack deflections were observed to occur within the grain where the crack started. In the 1st case study, crack deflection occurred before the crack reached any GB. A triangle area of high plastic deformation and accumulation of slip systems (and dislocations) was found ahead of the crack tip in figure 6.24. The crack deflected from the strongly deformed slip band moving towards a direction out of the heavily deformed triangle in figure 6.24b-c. Strain hardening is expected to occur along the slip band close to the GB. Therefore the crack deflects to different slip systems and directions to avoid crossing highly deformed regions. Several crack deflections occurred in figure 6.25a, in order for the crack to grow towards the grain boundary. These crack deflections delay crack growth. Yet the crack is orientating in a direction that favors crack propagation in the neighbouring grain, and therefore no further crack deflections are needed once the crack has entered the neighbouring grain in figure 6.25a, b and c. In the 2nd case study, the crack formed, as already explained, along a slip system with

highly accumulated plastic deformation (figure 6.29 a, b and c). The grain had two active critical slip systems. However, the crack selects the most critical slip system to initiate. Upon further crack growth, the crack deflects to the secondary slip system. This effect was attributed to the effect of the neighbouring grains. A 'weak' (or damage susceptible) grain lies along the secondary slip system, and therefore facilitates crack growth towards its matrix, as shown in figure 6.40. In contrast a 'hard' (or deformation resistant) grain lies in the path of the first critical slip system which led to crack initiation, and therefore restricts local deformation and further crack growth. A more macroscopic analysis is therefore necessary to assess the crack propagation paths. Figures 6.39 and 6.40 show that the hard grain B lies within an area where strong slip bands and high deformation have occurred in the neighbouring grains. Yet this grain does not show any localised deformation and damage. Therefore, it is stated here that crack deflection within the grain matrix can possibly be influenced by the local texture, and the presence of 'weak' or 'hard' grains. The crack will preferentially grow towards a 'weak' grain, deflecting its direction away from a 'hard' grain. This is further evidenced by the DIC strain maps of figure 6.41a and b. In figure 6.41a, the crack grows through a highly strain region and towards a low strained region, while by deflecting in figure 6.41b the crack propagation remains within highly strained regions.
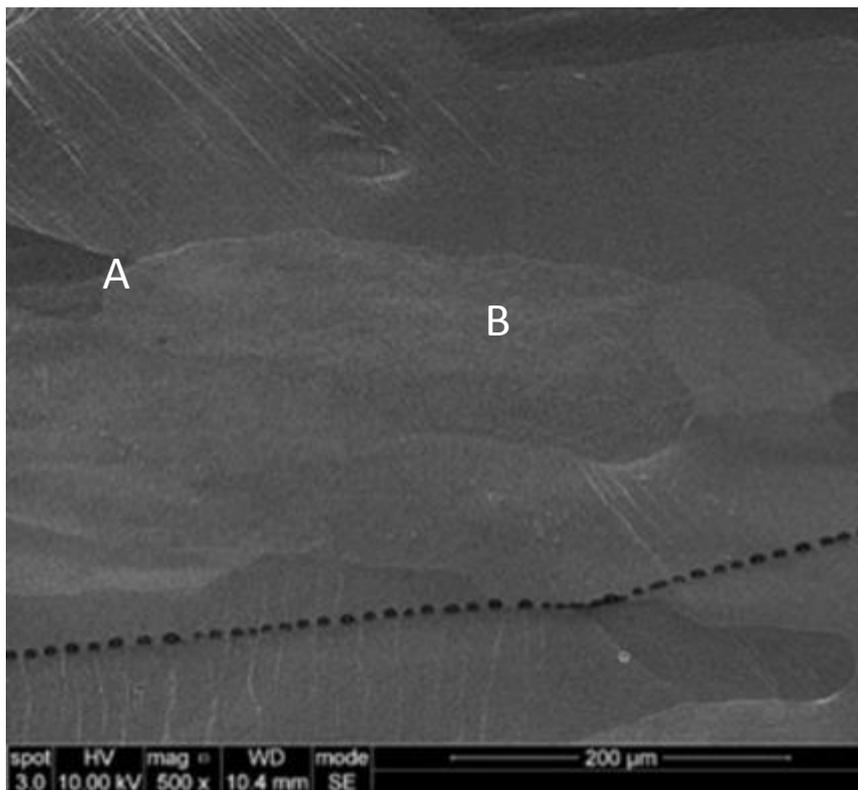
Figure 6-39. 'Hard' grain B in between highly deformed 'weak' grains.
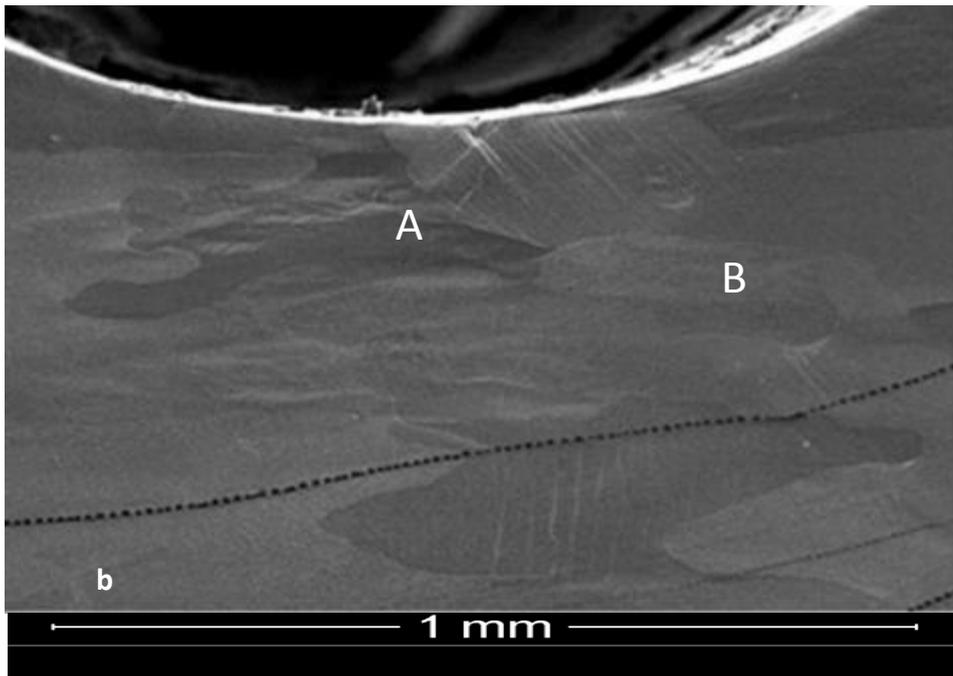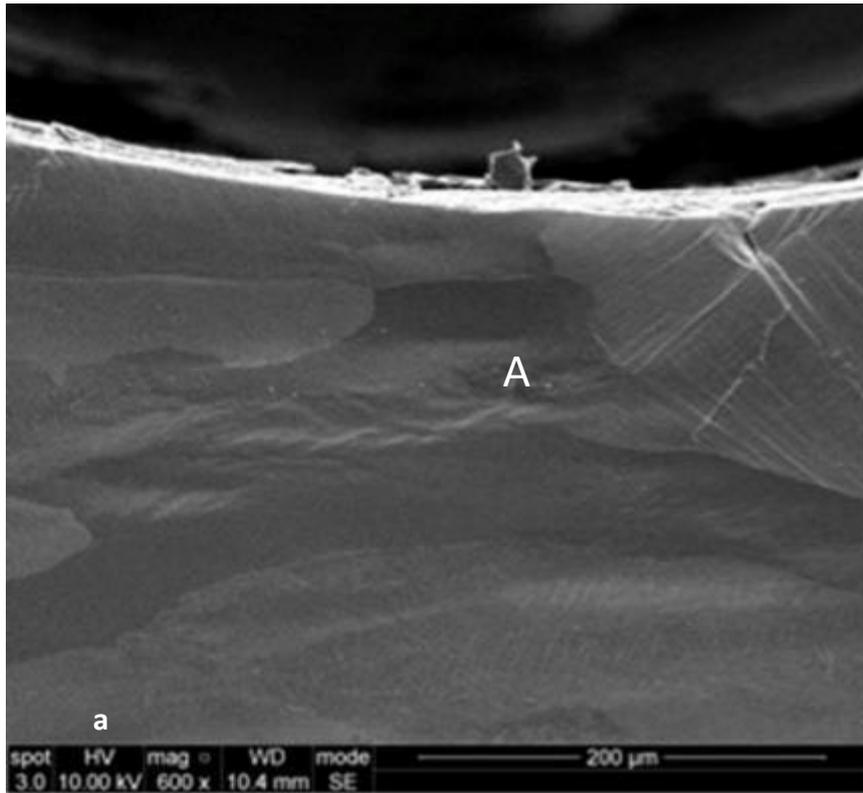
Figure 6-39. a) 'Weak' grain A facilitating a crack path towards its matrix, b) Overview image at the location of cracking, together with grain A and B.
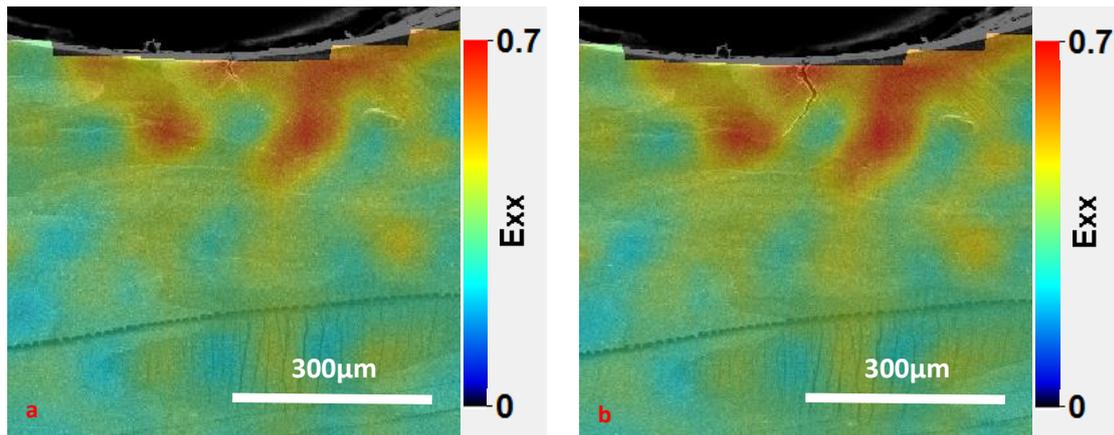
Figure 6-41. DIC strain maps at the region of cracking.

Several FIPs (fatigue indicating parameters) have been suggested in the literature from a modelling point of view [13-15, 26, 45]. Most frequently, the maximum accumulated slip over all the slip systems, the maximum accumulated slip over each slip system, and a local Fatemi-Socie parameter have been used to describe both the fatigue initiation and small crack growth regimes. Yet, there is no published work suggesting which parameter can correctly describe the exact location where fatigue crack initiation will occur in a polycrystal.

One important observation made in this study is that the DIC measured strain is not always an adequate parameter or indicator for the exact location where crack initiation will occur. Figure 6.23 showed that for the 1st case study, the maximum DIC measured strain was at the edge of the hole. Yet, the specific location showed uniform plastic deformation with no slip bands formed. Therefore, the location where the maximum straining occurred did not lead to slip band formation and therefore to crack formation. Instead another grain within the triangle of the highly strained region, forms strong slip bands in figure 6.24 and leads to fatigue crack initiation. In contrast the presence of a 'weak' grain at the edge of the hole in the 2nd case study, localises the highest strains at the edge of the hole. In this case, the location of the highest DIC-measured strain value coincides with the location where crack nucleation occurs. Therefore, the maximum accumulated strain can be an indicator for crack nucleation, but it is not always adequate. It is therefore suggested from this work that a new alternative FIP (fatigue indicator parameter) needs to be introduced, which incorporates both the effect of the total accumulated strain over all slip systems (or the total strain) and the effect of the maximum accumulated slip-strain over each slip system (plasticity along critical slip systems-planes) in order to take into account grain orientation. This is because it is the presence of critical grains, at critical regions (regions of highly localised strains) which will facilitate fatigue crack initiation. Similarly the total accumulated slip over each slip system is not an adequate FIP parameter either. A 'weak' grain in figure 6.33 lies far away from the highly deformed triangle region, and while strong slip bands form just after the 1st cycle, the local stress-strain conditions do not facilitate crack formation. Therefore it is the combination of the two FIP parameters that can correctly and geometrically predict fatigue crack initiation adequately.

A comparison was also made between crack growth from particles and slip band cracking in figure 6.32. Even though crack nucleation at particles occurs earlier with respect to slip band cracking (this can be seen by comparing figure 6.29b and 6.32a), the crack growth rate for slip band cracking is much higher. The crack growth rate for particle cracking in figure 6.32 is approximately 0.032μm/cycle, while in figure 6.32 the slip band crack has an average crack growth rate of 0.3μm/cycle over the course of 500 cycles. Figure 6.32 shows the 2 cracks together; and while the slip band crack has grown to a length of approximately 150μm, the particle crack has just grown to 16μm; approximately one tenth of the crack length due to slip banding. This is due to the associated plasticity involved in the two mechanisms for crack propagation. Slip band mechanisms are associated with high accumulation of plastic deformation along specific orientations, with the generation and movement of a high number of dislocations. It is this high plastic deformation that drives accelerated crack propagation. In contrast, in the neighbourhood of a particle, high inhomogeneities are expected to occur just during the first peak load. As the crack propagates in a direction perpendicular to the loading direction, through a mode I mechanism, the associated plasticity is relatively small. While for slip band cracking, the crack growth rate is controlled by the movement of dislocations and the large associated plasticity that occurs along slip bands through a mode II mechanism.

The micromechanical behavior of individual grains was outlined in the above section. It was shown that specific grains have higher potency for slip band formation and therefore crack initiation. A correlation was established in section 6.3.3 between the observed micromechanical behaviour and the local texture, via EBSD maps and the orientation of the individual grains. It was found that the orientation of the individual grains greatly influences the occurring deformation mechanisms. Figure 6.35 highlights the grains that showed resistance to slip banding and crack initiation mechanisms. These grains were characterized as 'hard' grains, following the nomenclature of reference [13]. Figure 6.37a shows the orientation-data points for the grains of figure 6.35 plotted over the IPF map. Most grains lie along the 001-101 plane, which suggests that the more the rolling of the material or the more the plastic deformation that is given to the material, the 'harder' the grains and the resulting microstructure. Therefore, further rolling of the material yields more data points closer to the 001-101 plane, and therefore superior fatigue performance. Yet it was found that a grain, shown with red arrow in figure 6.35, can be close to the 001-111 orientation plane (shown with red arrow in figure 6.37a), and yet have 'hard' grain characteristics. This effect was related to the local texture effect, and the orientation of the neighbouring grains. It was found that high misorientations (>50^0) for the specific grain was found with all its neighbouring grains, not facilitating the flow of plastic deformation from the neighbouring grains towards the grain matrix of the highlighted grain. Therefore, there is not always a direct correlation between the location of the grain on the IPF map and the tendency for fatigue crack initiation in the corresponding grain. The IPF map can give an indication and a potency for fatigue cracking, yet the orientation of the neighbouring grains needs also to be taken into account for accurate prediction of the occurrence of damage.

Similarly, Figure 6.36 shows the grains which formed strong slip bands, named as 'weak' grains [13]. The location of the corresponding grains on the IPF map is shown in figure 6.37b. The grains lie along the 001-111 orientation plane. The weakest grain is red circled in figure 6.36 and 6.37b. It is therefore suggested that for superior fatigue performance, grains with such orientation should be surely avoided. Once more a grain with orientation far from the 001-111 plane was found and highlighted in figure 6.36. The grain, though, showed strong slip banding characteristics, only in the circled area of figure 6.36. The rest of the matrix in this grain showed uniform plastic deformation characteristics. The exact location where the slip bands formed is shown in figure 6.42a. Slip bands with various orientations were found to occur in the corresponding location probably due to high strain localisations at the corresponding location. The red arrow shows that strong slip bands formed in a rather perpendicular orientation with respect to the slip bands within the black circled region. The high strain patterns shown with red arrow cross the corresponding GB and extend further, as shown with yellow arrow in figure 6.42a. Figure 6.42b shows a lower magnification image of the same region, in order to better visualise the deformation behaviour at the neighbourhood of 3-5 grains. The red arrows show the presence of a deformation band along the 3 neighbouring grains. Therefore it is the effect of a macroscopic deformation band that has led to slip band formation at the lower part of the grain circled in figure 6.36. So, relatively 'hard' grains can be influenced by the applied strain fields, and show 'soft' grain characteristics. Once more a direct correlation between the location of the grain in the IPF map and occurring mechanical behaviour cannot be directly drawn.

Apart from correlating the microstructure with the mechanical performance of the alloy, the importance of this work is that a new FCI criterion has been established that can more accurately predict the location where FCI occurs. This can more accurately inform crystal plasticity based models, and thus lead to more accurate prediction for the total fatigue lifetime of components [14, 15, 18, 20, 27].
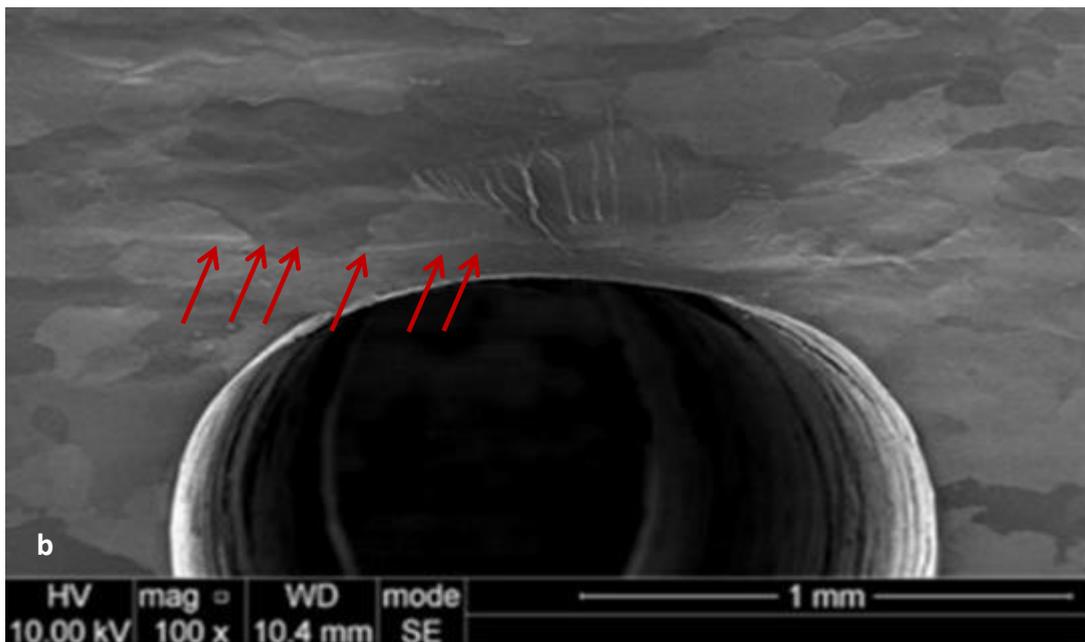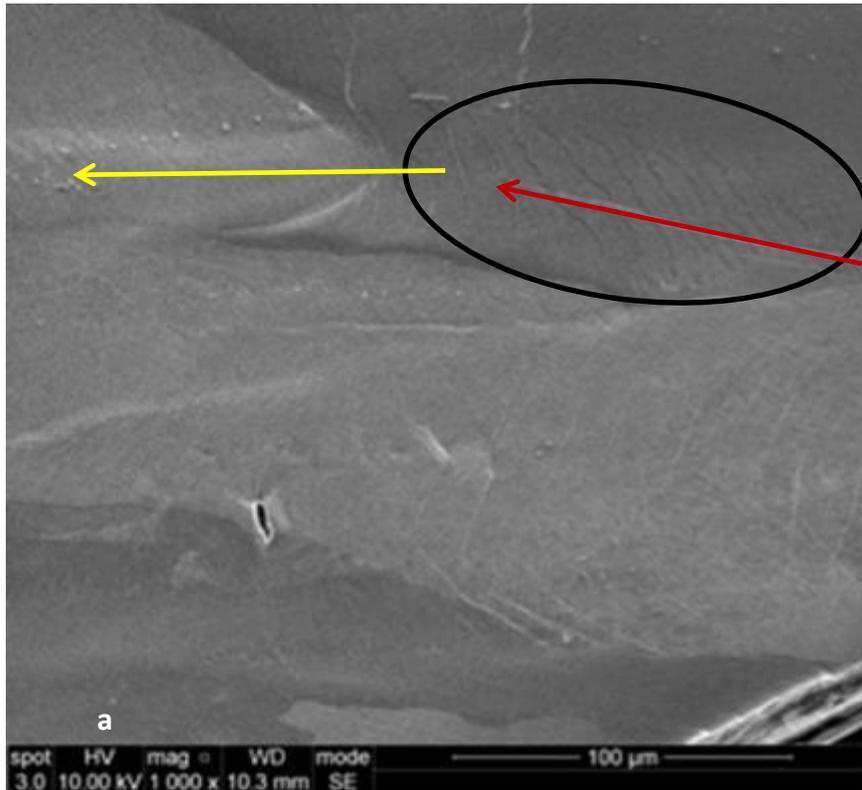
Figure 6-42. a) Sip band formation at the location circled in figure 6-36, b) low magnification imaging at the same area.

6.5. In situ fatigue testing in notched sample (higher magnification)

A specimen was machined to a rectangle 50mm long x 7mm wide x 4mm thick. A hole was drilled at the centre of the top surface to localise high stresses and facilitate crack initiation. The sample was mechanically ground and polished at the top surface down to 0.06µm (with Silico). Electropolishing was then performed in a solution containing 30% Nitric acid and 70% Methanol, for 13 seconds, at -

16° C, 15V and 10mA. EBSD measurements were carried out using a FEI-Sirion SEM, at 20kV and a spot size of 5 for the operating conditions. The step size was smaller with respect to the previous study as the grain size was smaller and in order to get more detailed information close to GBs. The step size was 1.2μm, covering approximately a total area of 1.6mm x 3.0mm, as shown in figure 6.43. Following the EBSD measurements, the specimens were re-polished with Silico for 4 minutes, to remove any Hydrocarbon (HC) deposition, during EBSD-measurement acquisition. Initial experiments revealed that a considerable amount of HC deposition occurred on the surface of the sample at the scanned area (EBSD map-region), which caused SEM imaging problems. Figures of HC deposition are shown in Appendix B. Mechanical polishing with Silico for only 4 minutes was sufficient to remove the HC deposition. The samples were then etched with Keller's reagent (95ml water, 2.5ml Nitric acid, 1.0ml Hydrochloric Acid and 1.5ml Hydrofluoric acid) for approximately 4-5 seconds, to reveal microstructural features such as GBs, precipitates and inclusions.

Micro-mechanical, vertical bending tests were performed using a 2kN Deben testing stage inside a CamScan SEM with a cross head speed of 2mm/min. Initially a static test was performed up to a maximum strain of 0.01 applied to the two left and right edges of the area. The test was interrupted at each 0.2 mm displacement increments to acquire images, and local displacements and strains were obtained by means of Digital Image Correlation (DIC) as explained in [50]. So the local strains were obtained at maximum displacement at the first peak load. Subsequently, displacement controlled cyclic loading was initiated with a frequency of 0.5, from 0 up to maximum displacement. The test was interrupted after the 1st cycle, the 10th cycle, the 100th, 200th, 300th, 400th and 500th, 600th and 700th cycle, at the maximum displacement applied and images were acquired. The consecutive images were correlated to the image at the first peak load and hence to the image for the undeformed sample. In the previous study the global strain field was captured, yet there was no detail on the strain field in the neighborhood of the crack. Furthermore, no information for the strain values could be extracted for crack initiation, and also with respect to crack propagation. The strain distributions were hence insufficient to quantify damage nucleation and propagation, accurately. A higher magnification analysis (100x) was therefore pursued for this study in order to obtain microstructure representative results and also obtain detail on the strain fields for crack initiation and propagation. With the current magnification, the 2 areas selected for in-situ observations correspond to the two yellow boxed areas of Figure 6.43. The 2 corresponding micrographs cover approximately an area of 1.3 mm x 0.8 mm. The micrographs were analysed using the commercial image analysis software, DaVIS 7.0, by LAVision [79] to determine the in-plane displacement field from which plastic strain values were calculated. In the current study, the microstructural features of the material have been directly used as the pattern from which to correlate the images between two successive loading steps. A sensitivity analysis on the interrogation window size was carried out, and a multiscale interrogation window with 16x16 and 32x32 pixels and 25% overlap was finally selected in all the experimental results presented in this study. A multi-pass algorithm (4 passes) [79] with 25% overlap between windows has been used to achieve best correlation results. A displacement accuracy of 0.01

pixels was obtained with a strain resolution of about 0.1% [79]. In the following section two case studies for the 2 highlighted regions of figure 6.43 are discussed.
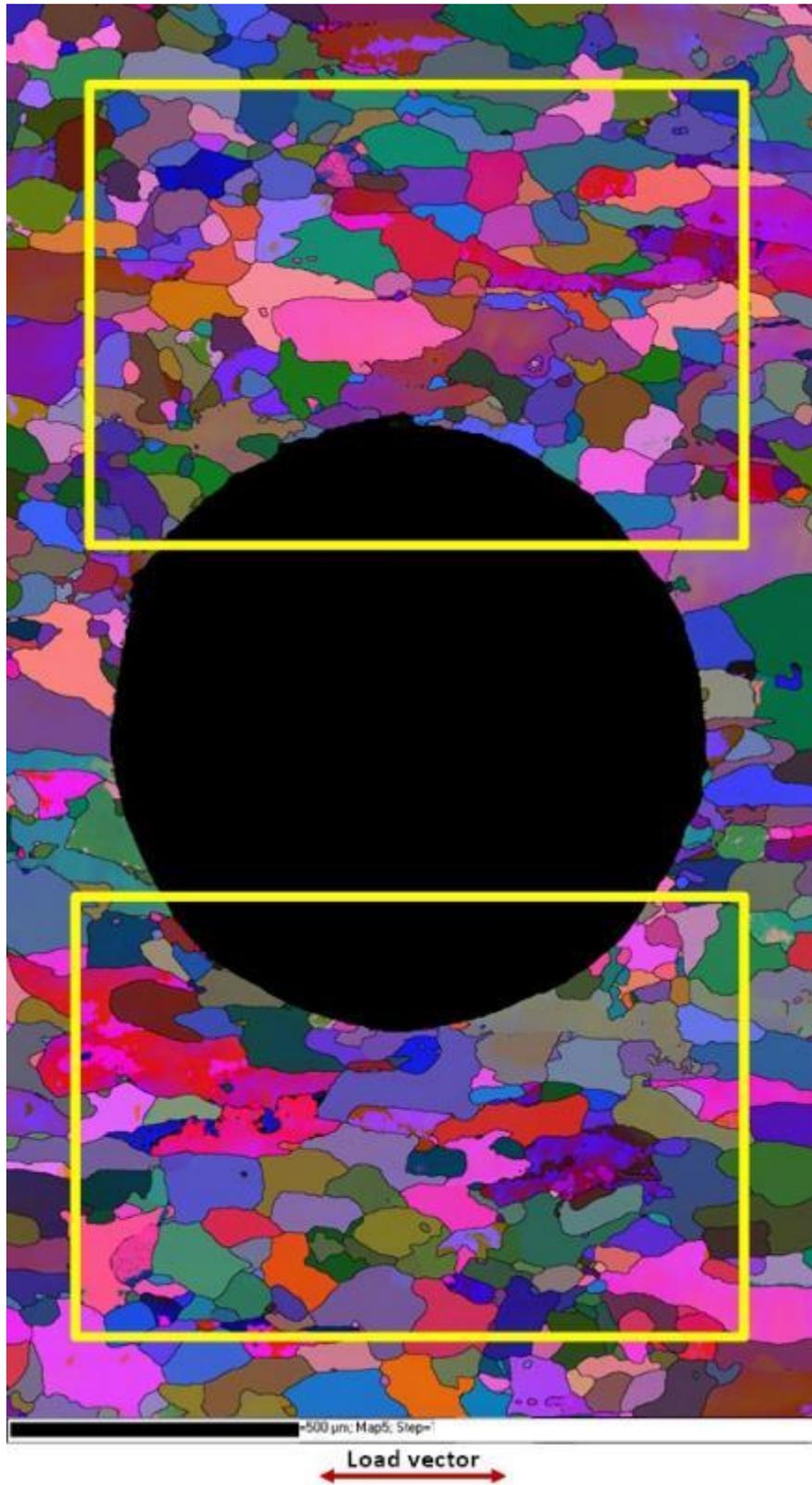
Figure 6-43. EBSD map of the regions around the hole selected for in situ observations during micro-bending.

6.5.1. Case study 1

Figure 6.44 shows the initial SEM image of the upper region highlighted in Figure 6.43, for the unloaded condition for the sample. Individual grains can be seen although not all GBs are revealed compared to the EBSD map (figure 6.43). This highlights the importance and the necessity of EBSD measurements to better quantify the relationship between fatigue crack nucleation and propagation and the underlying microstructure (grains and GBs).
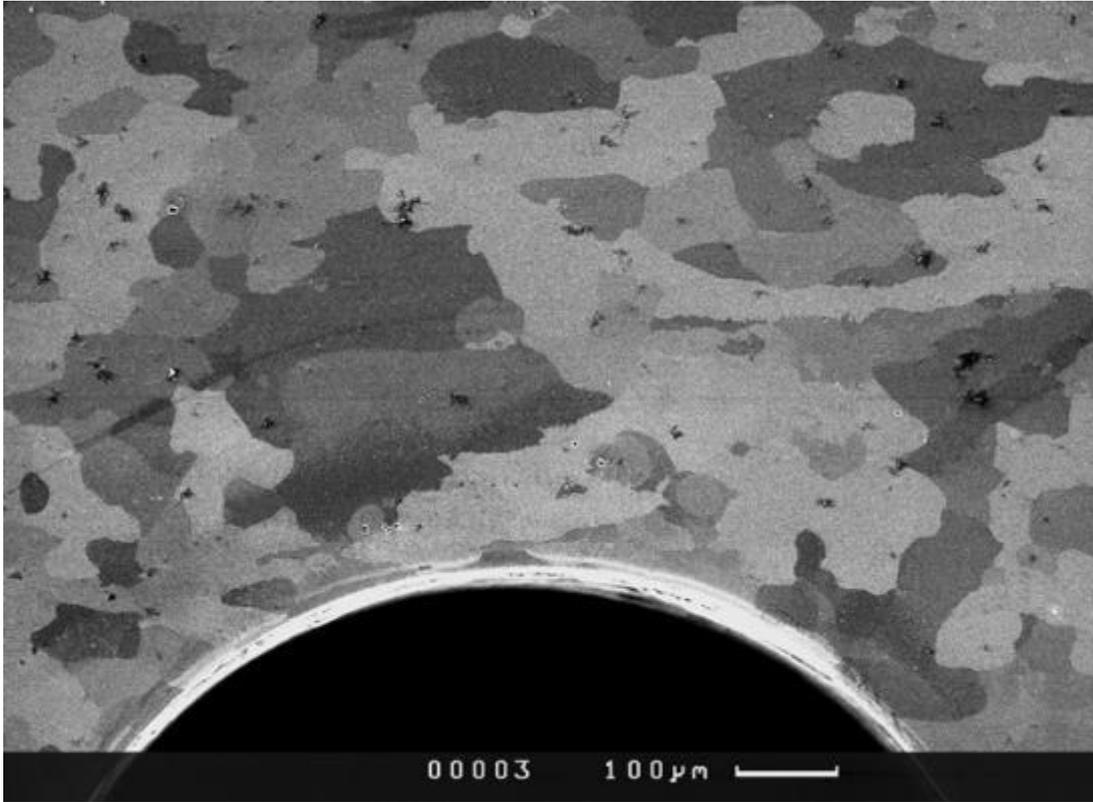
Figure 6-44. SEM image of the region highlighted in figure 6.43.

Figure 6.45 shows the ε_{xx} component along the tensile direction after 1, 100 and 300 cycles at the same area of interest as in figure 6.44 for the fully loaded condition of the sample. It is found that the total accumulated strain component ($\varepsilon_{xx}+\varepsilon_{yy}$ for 2D analysis), has very similar strain fields compared to the ε_{yy} component (see Appendices). Therefore the effect of the ε_{yy} component can be ignored. After 1 cycle, for the fully loaded condition for the sample, three maximum strain locations are found in figure 6.45a, with strain values of 0.50. The black circled regions correspond to areas where crack initiation occurs, while the red circled region corresponds to a highly strained region where no crack initiation-propagation occurs. This observation suggests, as in the previous chapter, that the maximum accumulated strain is not an adequate criterion for crack initiation.

After 100 cycles, 4 regions carry the highest strain values, namely ε_{xx}=0.51, and are highlighted in figure 6.45b. The 3 black-circled regions correspond to regions where crack initiation has occurred; while the red circled area is an area where uniform matrix deformation has prevented strain localisations along specific slip planes and therefore initiation of cracking. This is shown in detail in the next paragraph. After 300 cycles, the highest strains, approximately 0.58 - ignoring the strains

215

occurring at the cracked areas, correspond to the two black circled areas of figure 6.45c, and are both areas where crack propagation occurs. Figure 6.46 shows the strain distributions at 400, 500 and 700 cycles, at the area of interest, and highlights the occurrence of high strain localisation in the neighborhood of the two cracks. The location highlighted by an arrow in figure 6.46b shows the presence of a deformation band along the highlighted direction. The local orientations and the effect of local texture on the deformation band will be analysed later on in section 6.5.4.
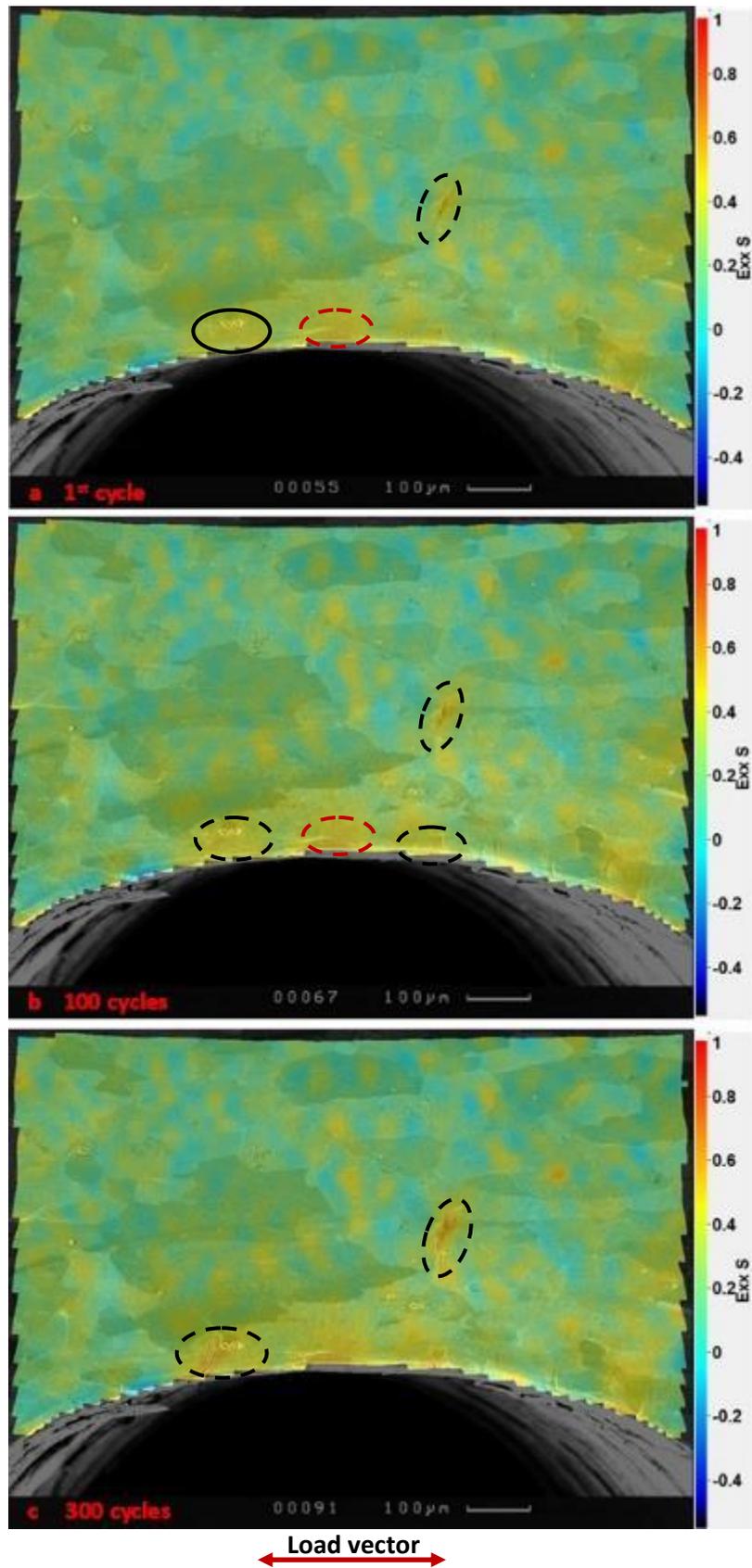
Figure 6-45. Strain distributions for the fully loaded sample after: a) 1, b) 100 and c) 300 cycles. No macroscopic strain accumulation was observed.
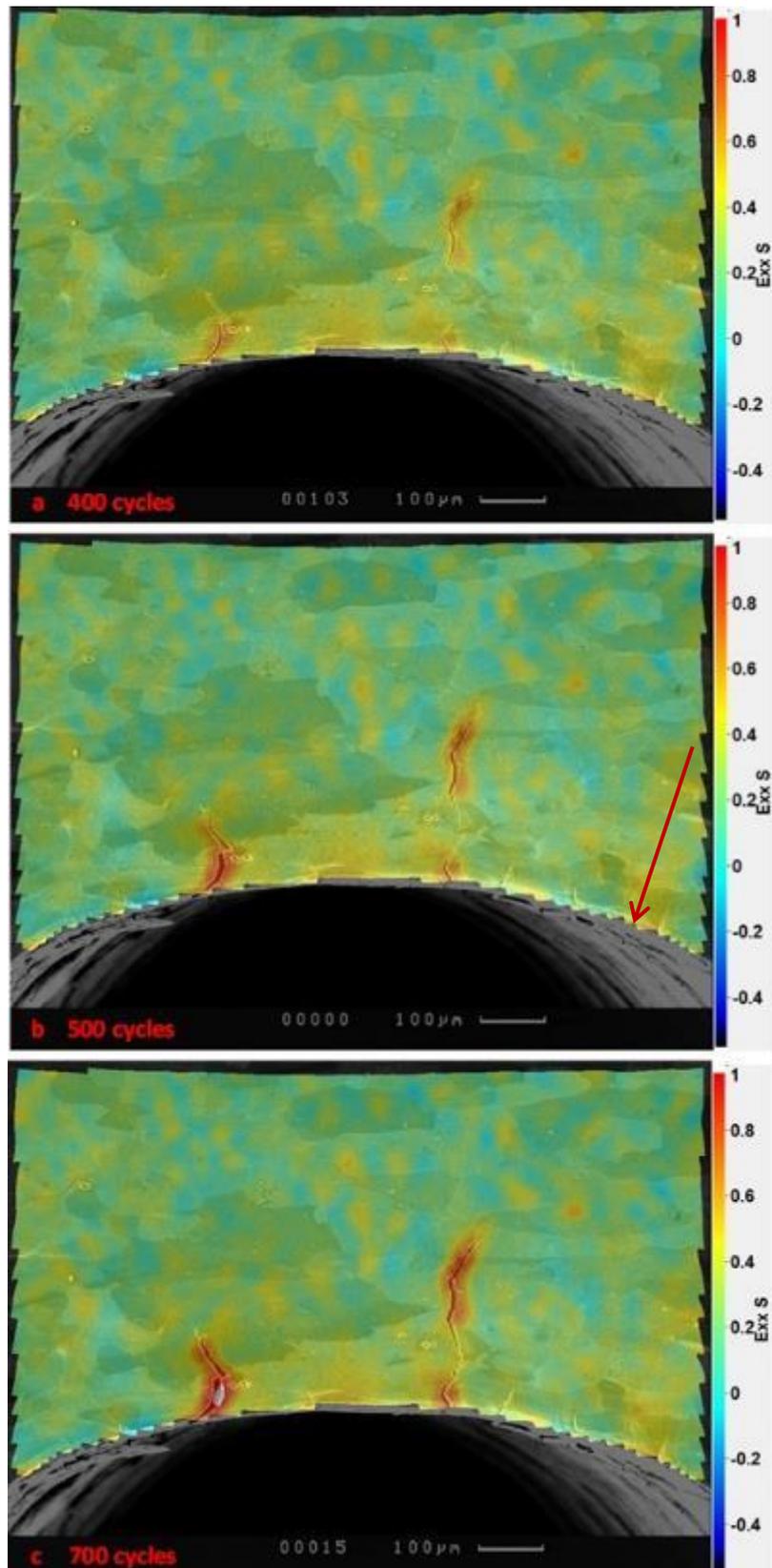
Figure 6-46. Strain distributions for the fully loaded sample after: a) 400, b) 500 and c) 700 cycles.

a)   *Damage nucleation and small crack growth*

Figure 6.47 shows a detailed view of the black (-dotted) circled area of figure 6.45a. Figure 6.47a shows the out of plane deformation and the formation of slip bands on the surface of the corresponding region (near a fourfold point). The EBSD map shows the location where slip banding occurs and is highlighted with a yellow dotted line. No cracking was observed to occur within the corresponding region after the first cycle (figure 6.47a). Yet after 10 cycles, crack initiation occurred as shown in figure 6.47b; the exact location coincides with the yellow dotted line on the EBSD map of figure 6.47a. After 100 cycles, the crack crosses a GB, and then follows the GB path till it reaches one small grain lying on the GB of grain A (arrowed location in EBSD map of figure 6.47c), and deflects towards the matrix of grain A. At 200 cycles, negligible crack propagation has occurred in figure 6.47d with respect to figure 6.47c while the opening of the crack has increased.

The observed slow crack growth is related to the fact that the crack changes directions during crack growth. This can be attributed to two underlying mechanisms. One is the mechanical effect: the crack needs to grow along a direction approximately perpendicular to the loading direction and will significantly affect the local stress and strain fields. Another one is the microstructural effect: the orientation of the slip bands within grain A is not the same with respect to the crack path. The yellow lines of figure 6.47d show that the orientation of the corresponding slip bands rotate upon moving towards the crack. This could be due to the presence of the crack (mechanical effect) or it might be due to the grain shape, local misorientations or even a large grain lying below the surface. The microstructure is three-dimensional, only the surface is observed in this case. Another effect is the presence of misorientations within grain A. Up to 6 degrees local misorientations were found to occur close to the location of the crack and this can be also be the cause for these variations in the orientations of the slip bands in the corresponding grain of figure 6.47c. Another explanation can be that the orientation of the occurring slip bands does not facilitate crack propagation along the initial crack path, as shown in the EBSD map of figure 6.47c.
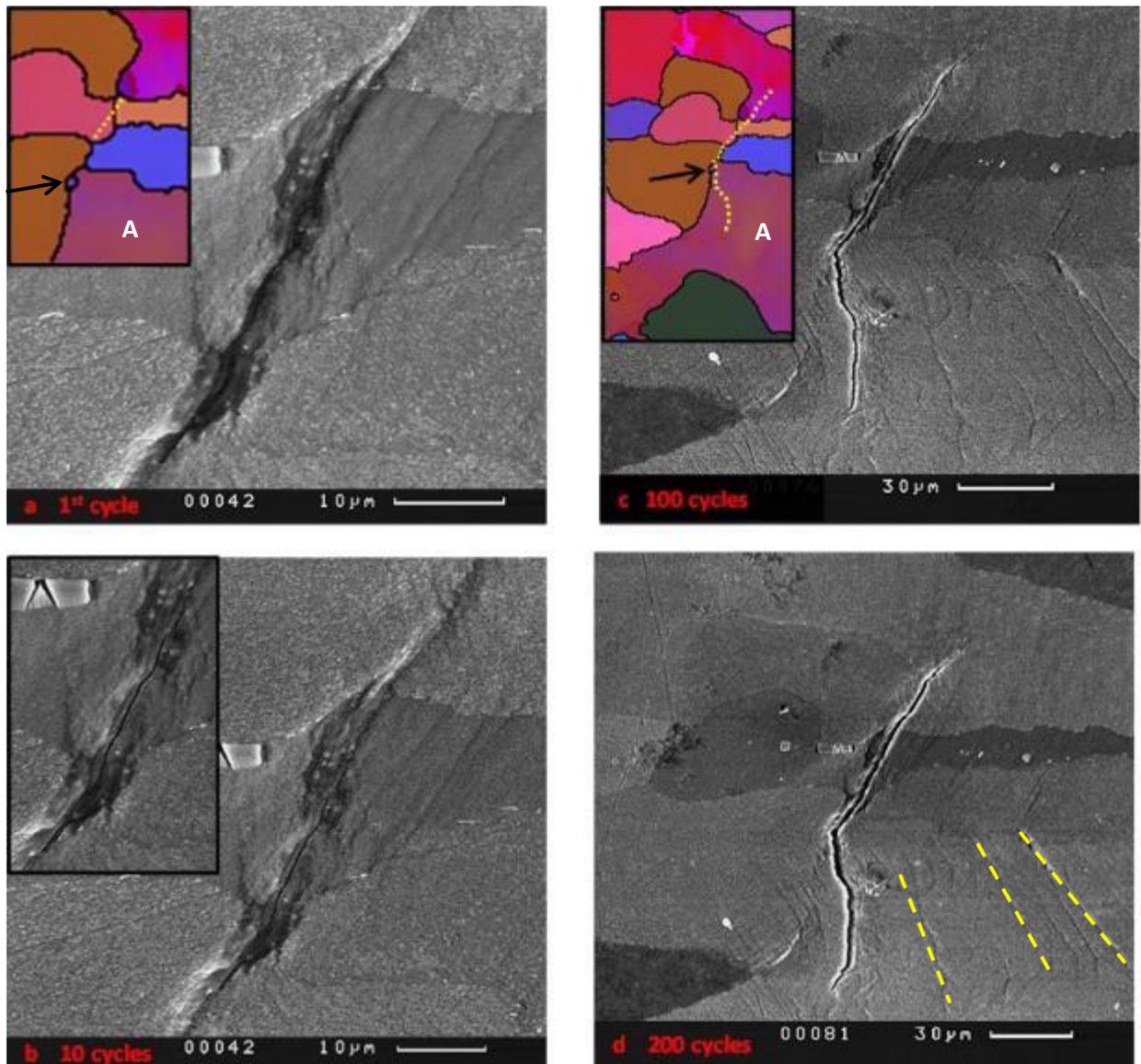
Figure 6-47. SEM images at the black (dotted) circled region of figure 6.45a, for the fully loaded condition of the specimen after: a) 1, b) 10, c) 100 and d) 200 cycles.

After 200 cycles, the crack continues to grow slowly, finding some resistance upon reaching grain B of figure 6.48a. This is due to the high misorientation at the corresponding GB; i.e. 45^0, and the necessity to change the direction of cracking in order to propagate along the critical slip band orientation of grain B. Even though the orientation for the slip bands in the two grains is similar, the crack selects to propagate in a different direction in grain A, not following the slip band direction, but then changes direction upon approaching the GB of grain B, and diverts to a direction parallel to the slip bands of grain B. Figures 6.48a and b show that crack growth slows down upon reaching the GB, but then changes direction before reaching the GB and finds an easy crack path in the neighbouring grain B. Grain B is a 'soft' grain, having slip bands approximately parallel to the slip bands of grain A (it has to be mentioned that the slip bands in grain A had large variations in orientation though). The crack therefore diverts as it was propagating in a non favourable orientation with respect to the observed slip bands, to subsequently follow the path of the slip bands.

The crack path alters close to the proximity of the GB, which can be due to the accumulation of dislocations ahead of the crack tip and close to the GB. The crack therefore changes direction, but this process slows down the crack growth rate. The crack then grows rapidly again within the matrix of grain 'B' as shown in figure 6.48c, which can be due to two reasons: grain 'B' is a soft grain and/or the crack now is at the proximity of the other crack coming towards grain 'B'. This is shown in figure 6.48c, where the crack has progressed rapidly towards the inner part of grain B after 500 cycles. At the same time another crack, C2 crack which started from the edge of the hole and had progressed towards the first crack, namely C1. The details on the crack formation and propagation of crack C2 are shown in next paragraph. Figure 6.49 shows the interaction between the two cracks. The two cracks propagate in opposite direction but on the same line aligned with a critical slip system, in order to meet without the need for further crack deflections. Yet accumulation of plastic deformation occurs in between the two cracks, slowing down the junction of the two cracks. The cracks join only after 700 cycles. Figure 6.49a shows the resistance of the matrix to join the two crack tips.
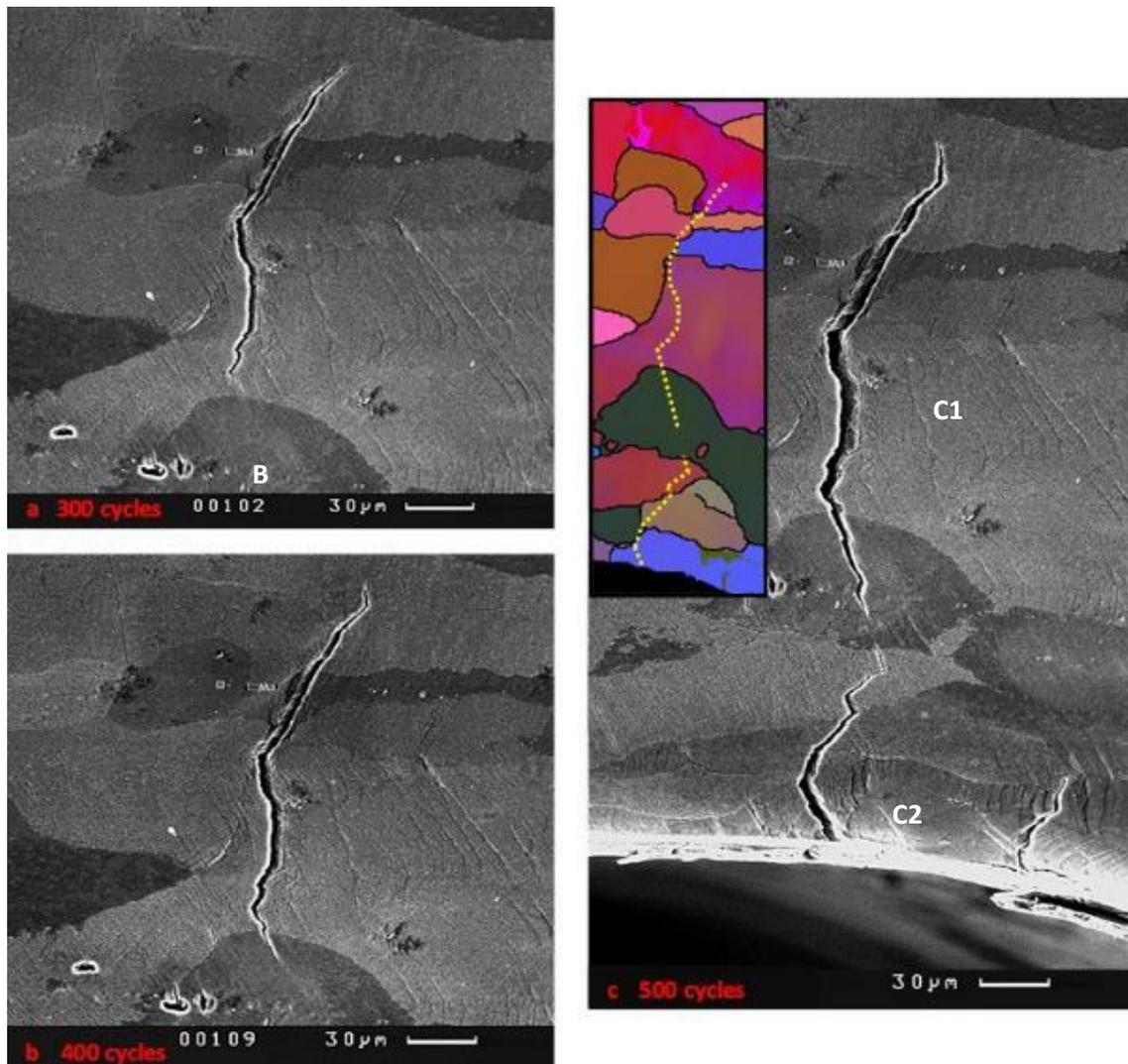
Figure 6-48. SEM images at the black (dotted) circled region of figure 6.45a, for the fully loaded condition of the specimen after: a) 300, b) 400 and c) 500 cycles.

221
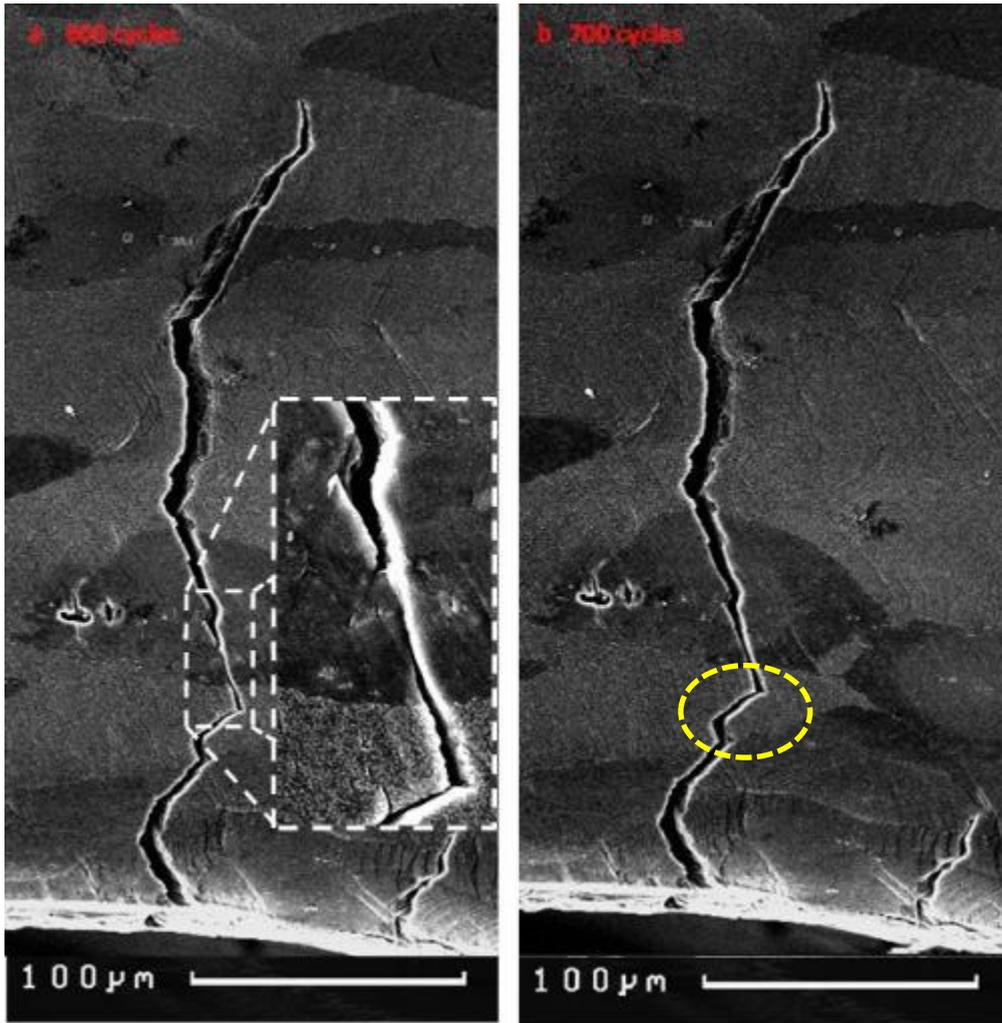
Figure 6-49. SEM images at the black (dotted) circled region of figure 6.45a, for the fully loaded condition of the specimen after: a) 600 and b) 700 cycles. The two crack meet due to the local stress fields.

Figure 6.50 shows the crack formation and propagation of crack C2. As already discussed initiation of C2 crack occurs later with respect to C1 crack. Initiation occurred after the 10th cycle. Crack C1 has reached a crack length of more than 150μm after 100 cycles, whereas crack C2 is only 25μm long; being 4 times smaller. After 200 cycles crack C2 meets grain D, and upon further loading cycles, the crack changes direction for favourable propagation in grain E, as shown in figure 6.50e. Another crack deflection occurs upon reaching grain F. It should be noted that stronger crack deflections, away from the plane of maximum stress occur for the crack C2 with respect to crack C1. This can be related to the size of the two cracks. Crack C1 is much larger and therefore propagates in a more loading-perpendicular direction. While the relatively smaller C2 crack can deflect more easily to reach and join crack C1. After 400 cycles crack C1 is close enough to influence the propagation of crack C2 which then deflects according to the local stress/strain fields between the two cracks. Figures 6.48c and 6.49 show that further strong deflections occur for crack C2 before joining with crack C1. This change of crack paths is circled in yellow in figure 6.49b.
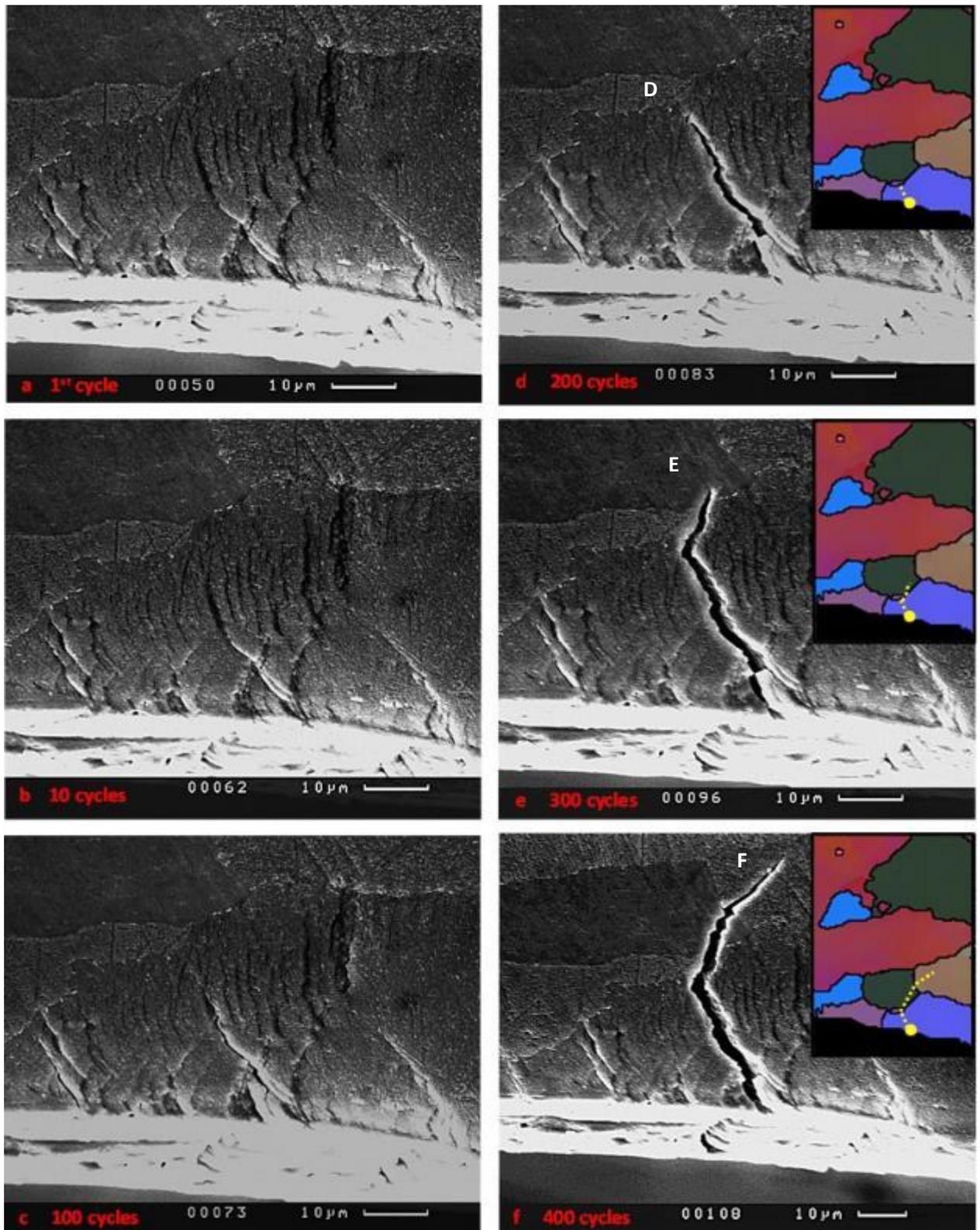
Figure 6-50. SEM images at the location of crack C2, for the fully loaded condition of the specimen after: a) 1, b) 10, c) 100, d) 200, e) 300 and f) 400 cycles.

6.5.2. Case study 2

Figure 6.51 shows a SEM image of the lower region highlighted in Figure 6.43. The image corresponds to the unloaded condition for the sample. It is possible to see the individual grains, yet not all GBs are

revealed compared to the EBSD map of figure 6.43. In contrast to the previous case study, in this instance, the local strain values obtained by means of DIC correctly predict the exact location for crack initiation. The maximum strain measured is highlighted by the black arrow in figure 6.52a, and corresponds to the location where crack initiation occurs just after the first cycle. The local strain value measured is 0.65. The strain fields in figure 6.52a are highly non-homogeneous. Even close to the edge of the hole very high strain values (over 0.5) exist next to strain values of less than 0.1. The red circled regions are areas where the strain values measured by means of DIC are larger than 0.5, while the blue ones correspond to strain values less than 0.1. This result shows the influence of the microstructure and grain orientations on local strain distributions.
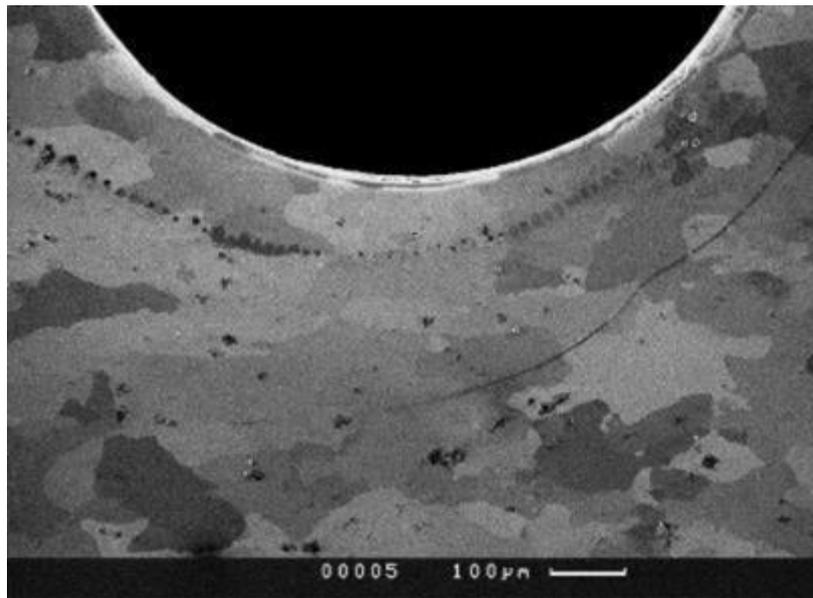
Figure 6-51. SEM image of the region highlighted in figure 6.43.

Following crack initiation after the 1st cycle, small crack growth occurs at the location highlighted by the black arrow in figure 6.52a, and the strain fields appear highly localised at the corresponding location in figure 6.52b, after 100 cycles. Upon further load cycles, i.e. 300 cycles, the strain values slightly decrease in the overall region-map. Ignoring the strain values at the cracked region the average strain values for the DIC maps of figure 6.52b and c respectively decrease from 0.34 to 0.33. This is due to the fact that the highest strain values localise in the cracked region, relaxing the strains in the surrounding regions. Similarly Figure 6.53 shows the strain plots after 400, 500 and 700 cycles at the same area as in figure 6.52. No strain accumulation is observed in the surrounding regions of the crack, with all straining occurring in a very small area in the neighbourhood of the crack. Another observation is that the crack propagates in a rather perpendicular direction with respect to the loading direction (with small crack deflections), and in the neighbourhood of the crack the strain fields are highly non-homogeneous.
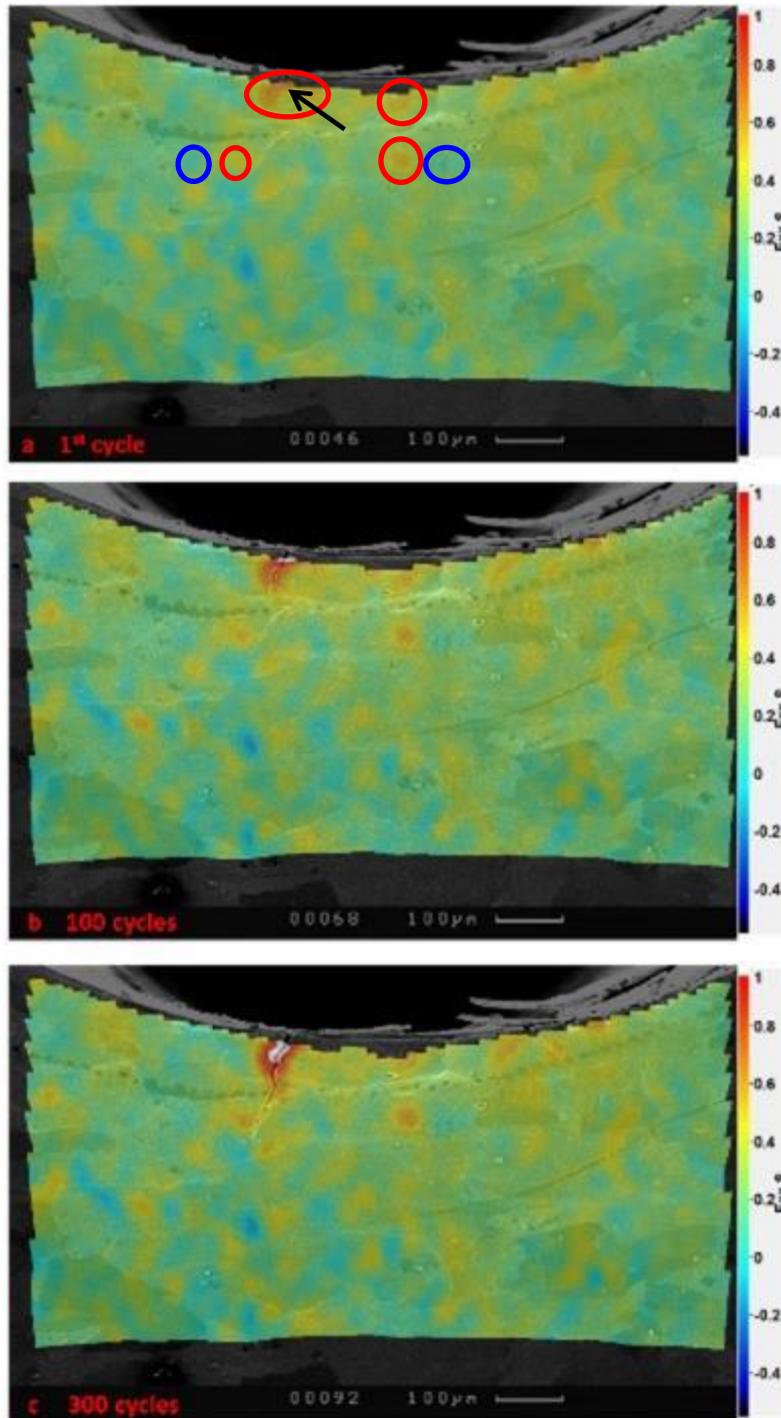
Figure 6-52. Strain distributions for the fully loaded sample after: a) 1, b) 100 and c) 300 cycles.
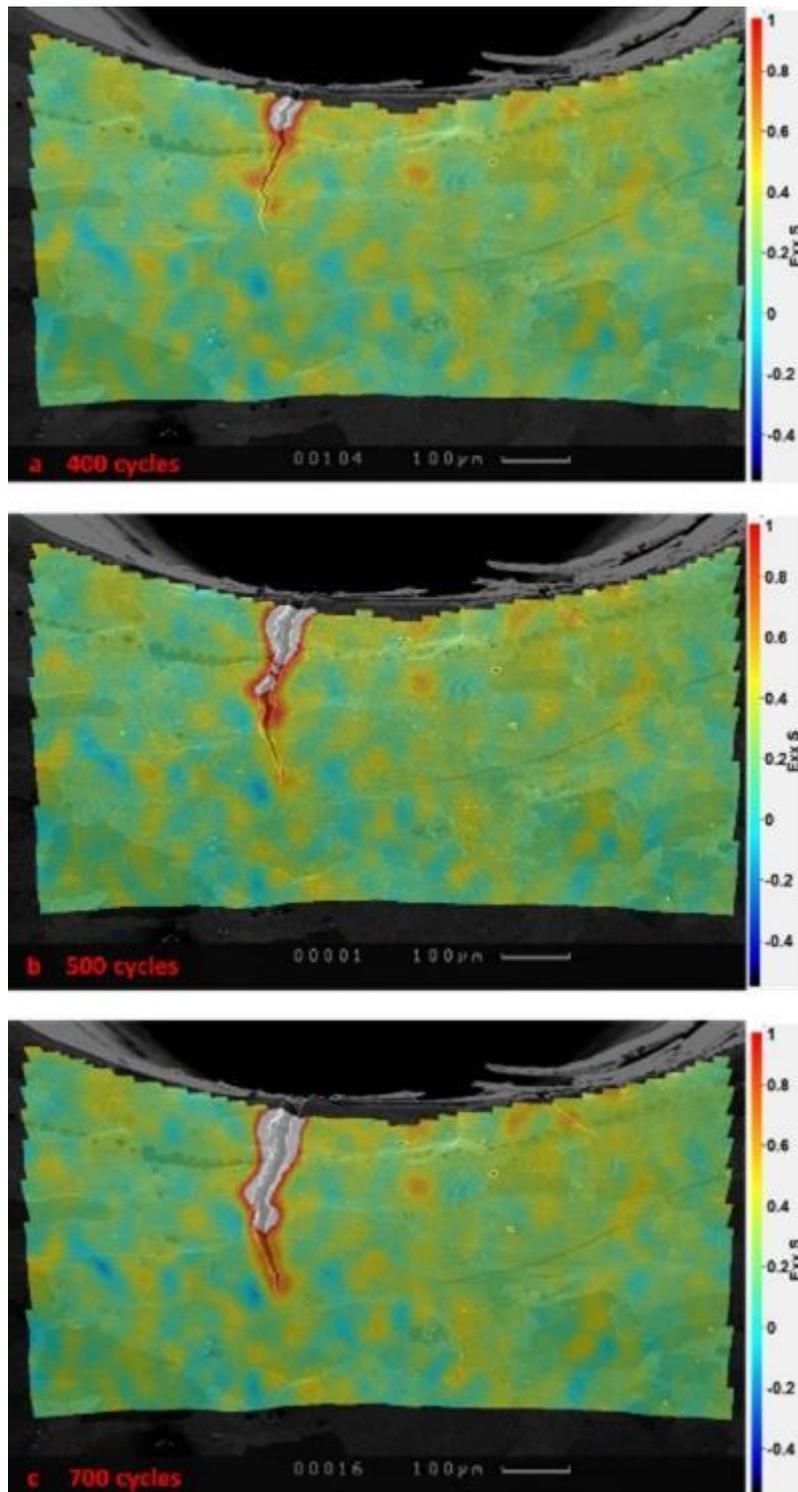
Figure 6-53. Strain distributions for the fully loaded sample after: a) 400, b) 500 and c) 700 cycles.

(a) Damage nucleation and small crack growth

Figure 6.54 shows high magnification images of the region where crack initiation and propagation occurs in the 2nd case study, in order to track the effect of the microstructure - grains on small crack growth; and specifically on the crack path directions. After the first peak load, strong slip bands form at the location highlighted by an arrow in figure 6.54a. This leads to crack initiation just after the first

cycle, as shown in figure 6.54b. The exact location of cracking is shown in the EBSD map of figure 6.54b. Crack propagation continues in the first 10 cycles, and the crack has already crossed two grains as shown in the EBSD map of figure 6.54c.
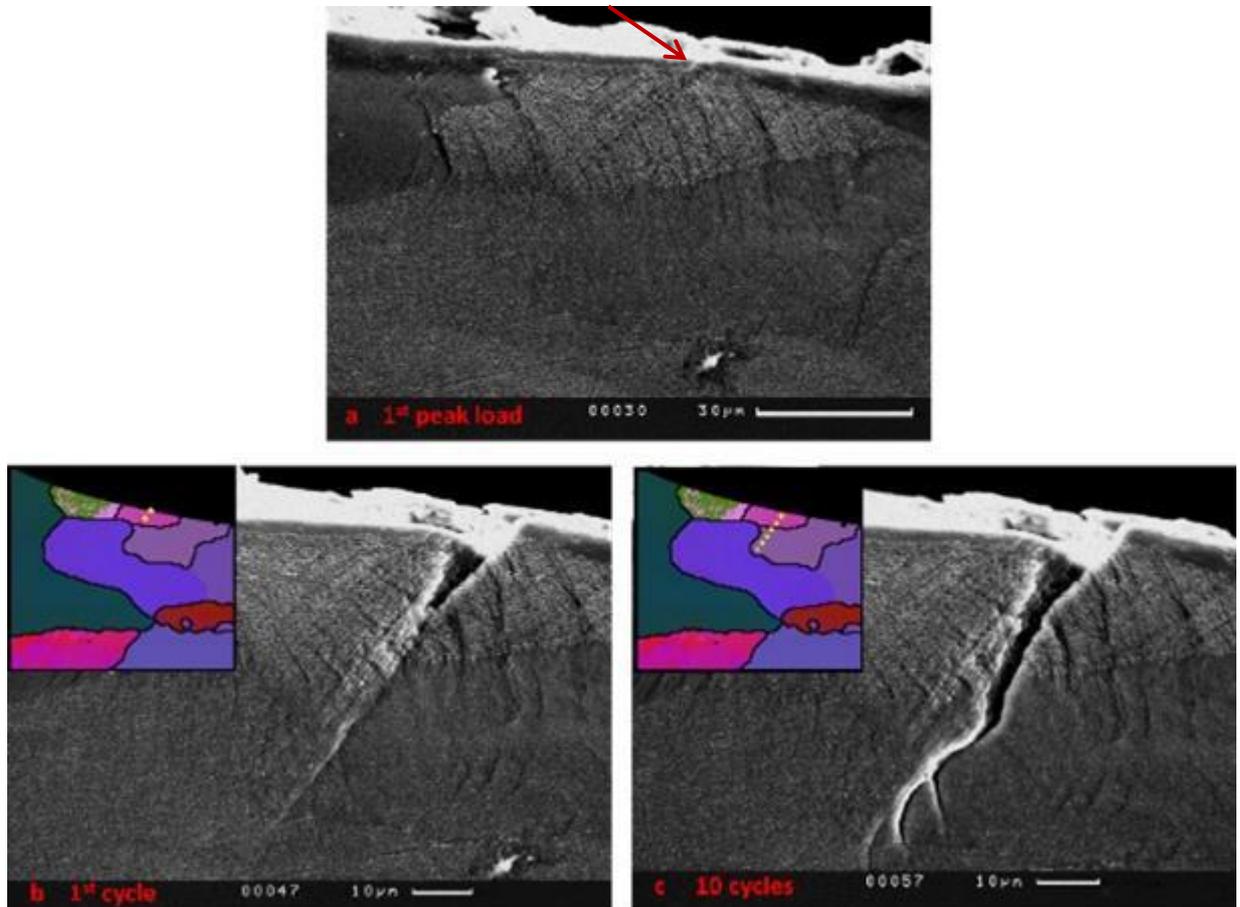
Figure 6-54. SEM images at the black arrowed region of figure 6.52a, for the fully loaded condition of the specimen after: a) 1st peak load, b) 1 cycle and c) 10 cycles.

After 100 cycles, the crack propagates further and now extends over 3 grains, reaching the GB of the 4th grain in figure 6.55a. The EBSD and DIC strain map are also shown in figure 6.55a for comparison. The yellow dotted line on the EBSD map represents the geometry of the crack already formed, while the white dotted line corresponds to the orientation of the occurring slip bands in grain W. Two proposed crack paths are shown on the EBSD map. The path highlighted with the white dotted line corresponds to the slip banding direction while the path highlighted with the red dotted line is the actual crack path after 100 cycles. The crack does not follow the path of the slip bands, but prefers to move in a relatively perpendicular direction. This can be explained by the DIC strain map of figure 6.55a. The black dot corresponds to the tip of the crack in the strain map of figure 6.55a. The crack can either select to follow the slip band direction and move towards the low strained region (white dot), or select to follow the red dotted line and move towards the highly strained area with the red dot; following the path of highly strained regions. Upon reaching the GB of grain A, the crack deflects to a direction following the slip band direction (white dotted line). The crack deflects before reaching

227

the GB, in order to divert its direction towards the highly strained region and grain A, rather than propagating towards the low strained region of grain B. Crack deflection within grain W is also facilitated by the fact that the crack alters direction towards the orientation of the slip bands, assisting further crack growth. The red and white dots show the propagation paths for the two scenarios. It is apparent that propagating towards grain A, is more favourable as a potential crack path. Furthermore, the orientation of the slip bands in grain B (white dotted line on the SEM image figure 6.55b) does not facilitate crack propagation along the current crack path in grain B. The crack would need to grow in a direction rather perpendicular to the slip bands if it was following the red line. Instead it alters direction and follows the path of slip bands in grain W before entering the highly strained grain A.
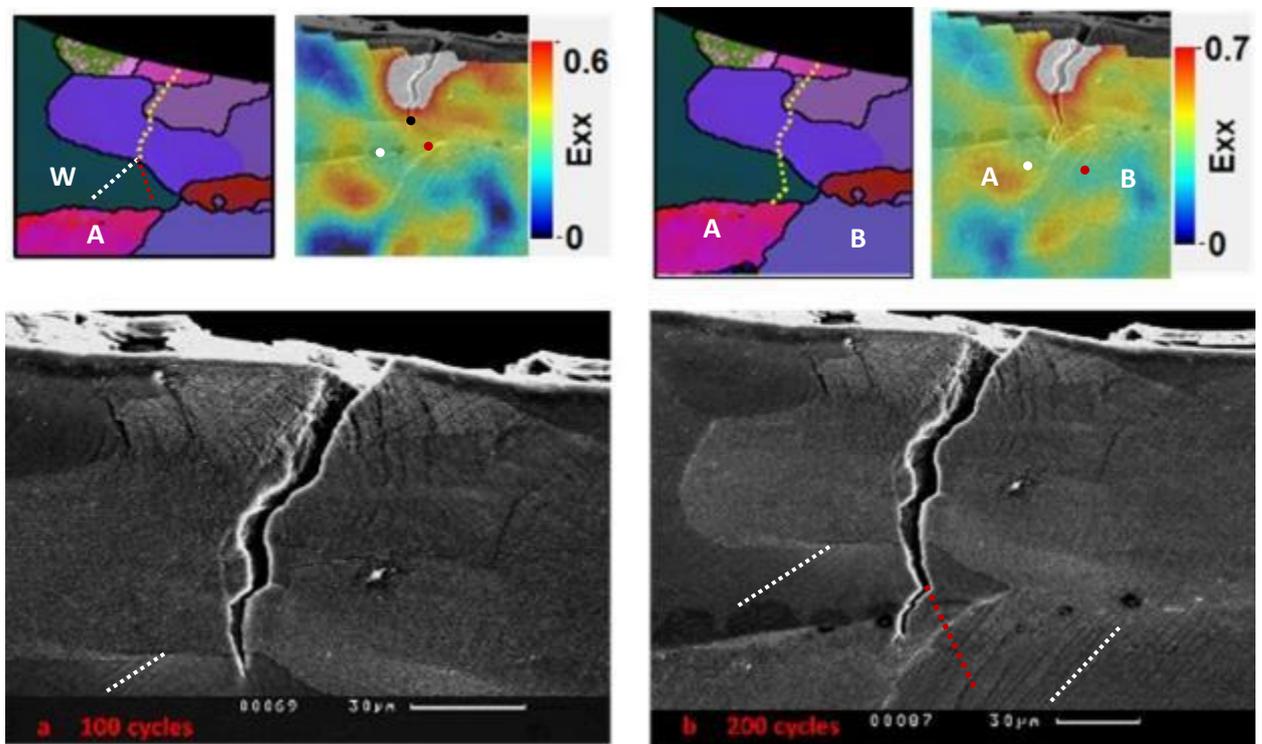
Figure 6-55. SEM images at the black arrowed region of figure 6.52a, for the fully loaded condition of the specimen after: a) 100 cycles and c) 200 cycles.

After 300 cycles, the crack has further propagated and crossed 2 more grains, extending across 6 grains in total. The crack follows the path close to the GBs of the two grains, as shown in figure 6.56b. Upon reaching the GB of the lower grain, it follows the path of the GB and then branches to a direction parallel to the load direction, instead of entering the grain matrix and propagating in a direction perpendicular to the load vector. This can be explained by the related DIC strain map in figure 6.56c. The crack follows the GB and then deflects towards the highly strained area, region D, instead of propagating along the low strained region C.
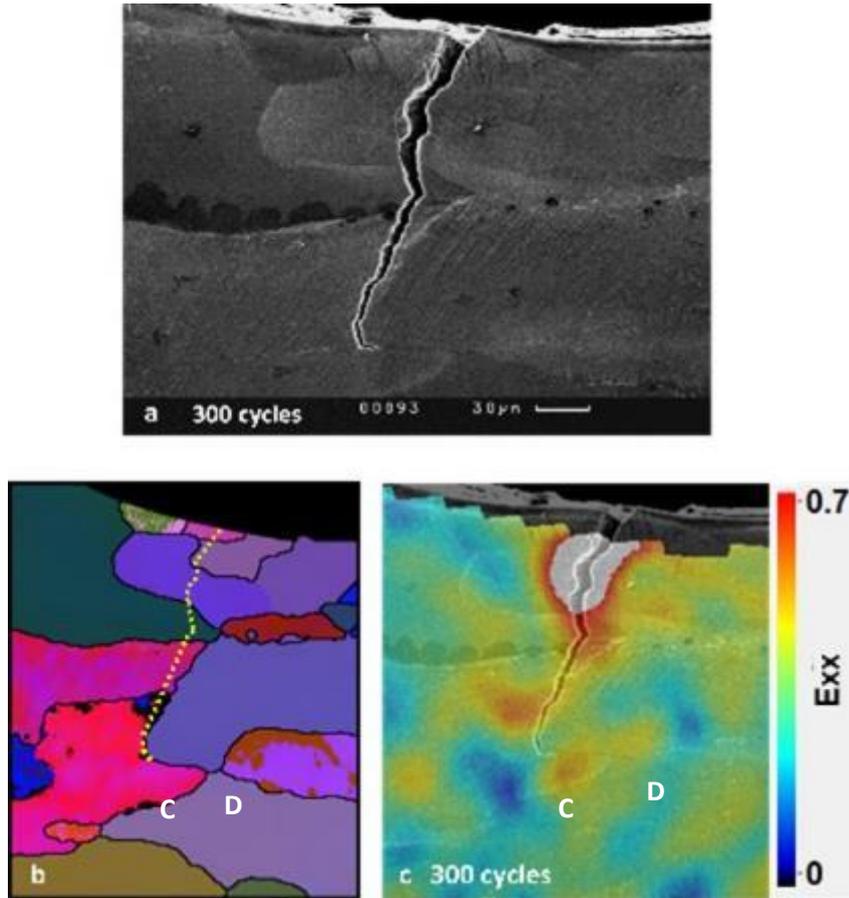
Figure 6-56. a) SEM image after 300 cycles, at maximum displacement, b) EBSD measurements of the corresponding location and c) DIC map at the same region after 300 cycles, at maximum displacement.

After 400 cycles, the crack has advanced within 2 more grains (E & F) in figure 6.57a, extending across 7 grains in total. No signs of slip bands were observed in the two grains, E & F. Yet, the crack followed two straight line segments within the two grains, with small crack deflection occurring at the GB between grain E and F. After 500 cycles, the crack has crossed the 8th grain, grain G, reaching the GB of the highly deformed grain H. Grain H shows high deformation characteristic in both the DIC map of figure 6.57 and figure 6.58b. The crack propagates in grains F and G towards the direction of the highly deformed grain H. Grain H showed strong slip band characteristics. Upon reaching grain H, the crack follows the GB path, growing parallel to the direction of the occurring slip bands in grain H while propagating in a direction perpendicular to the applied load. The full length and geometry of the crack is shown on the EBSD map of figure 6.59. Overall, the crack orientation is perpendicular to the load vector.
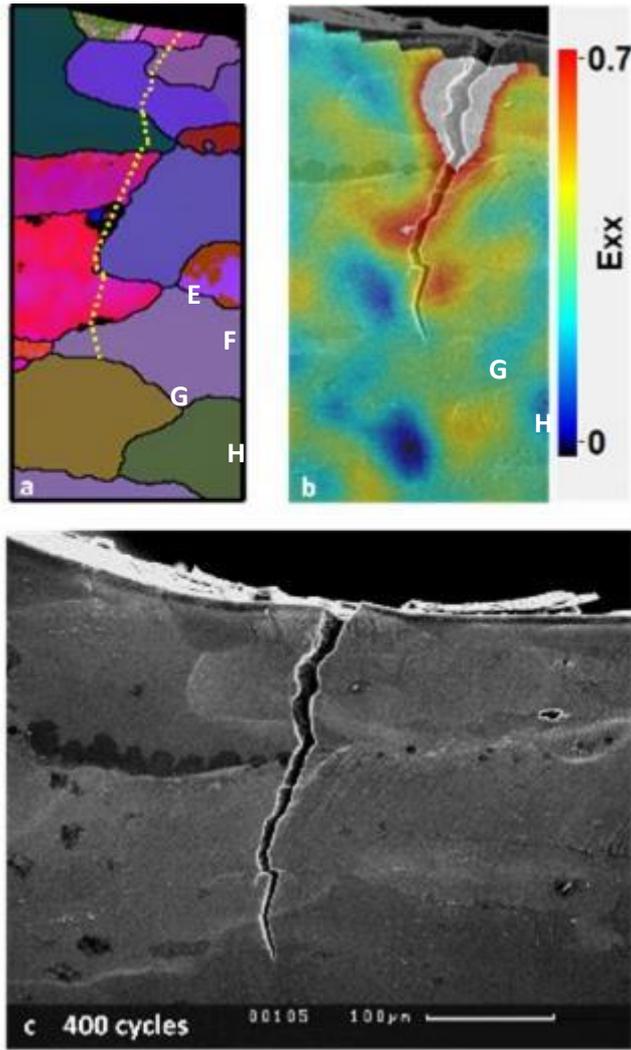
Figure 6-57. a) EBSD map of the undeformed sample with the crack path shown with yellow dotted line, b) DIC strain map at the cracked region, and c) SEM image at the cracked area, for the fully loaded condition of the specimen after 400 cycles.
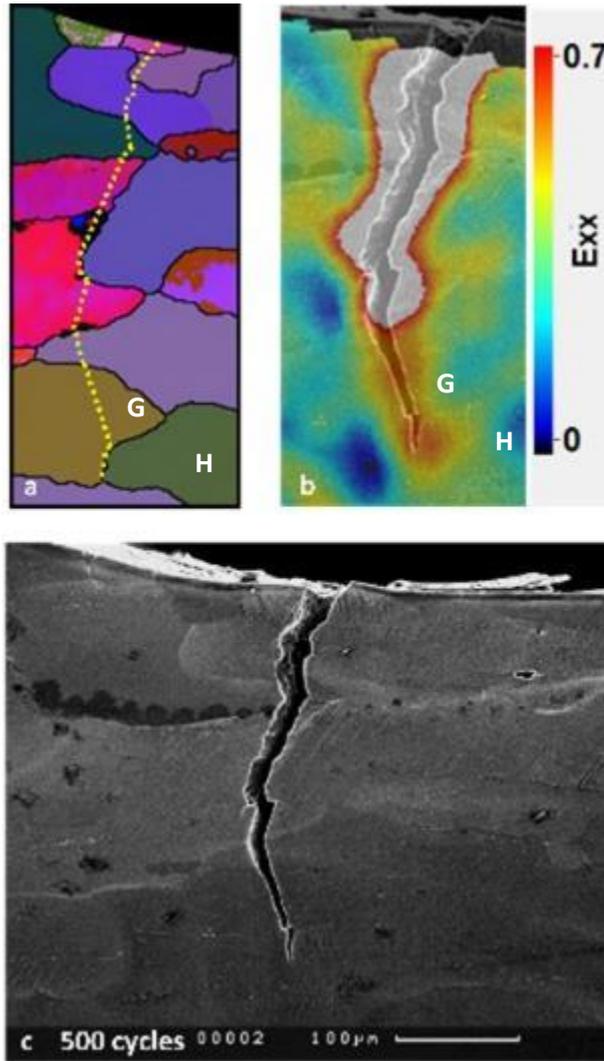
Figure 6-58. a) EBSD map of the undeformed sample with the crack path shown with yellow dotted line, b) DIC strain map at the cracked region, and c) SEM image at the cracked area, for the fully loaded condition of the specimen after 500 cycles.
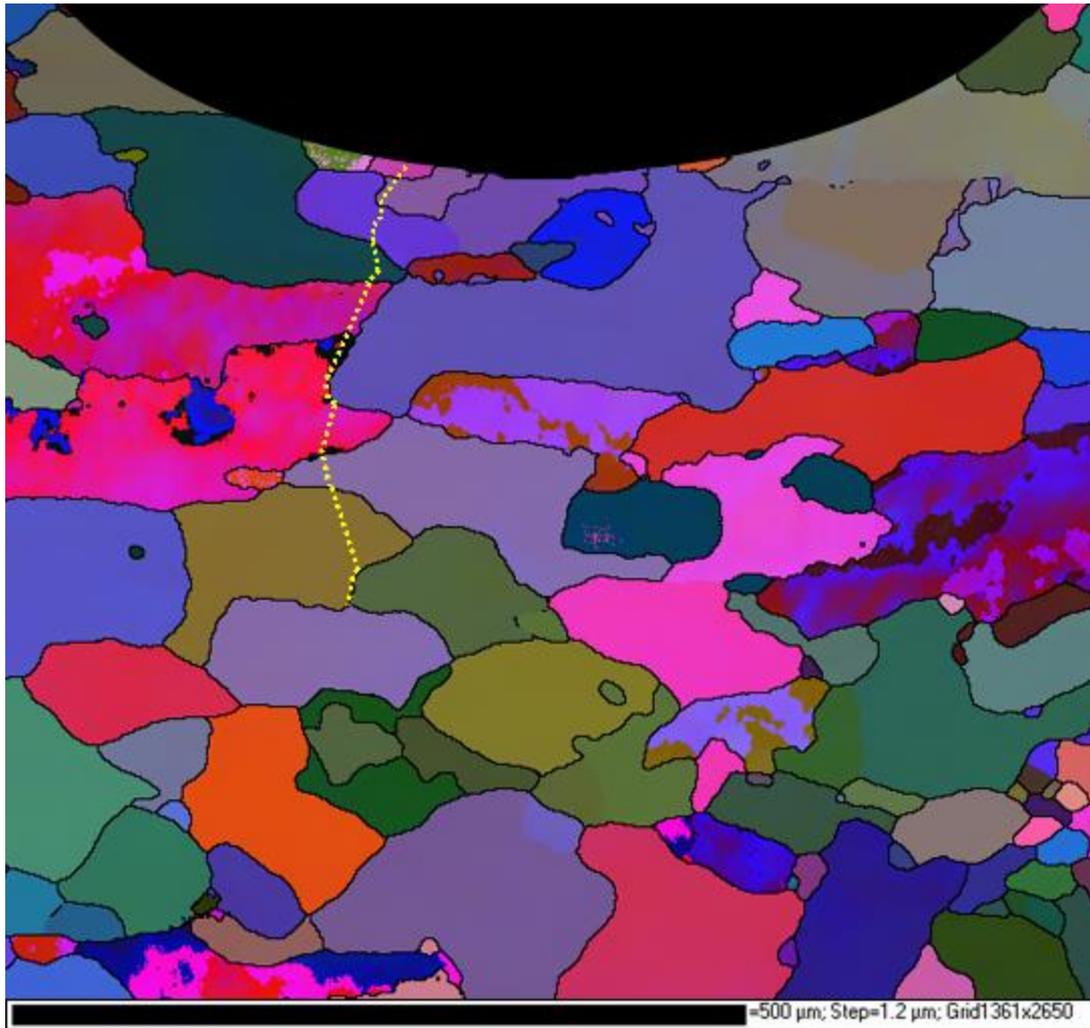
Figure 6-59. EBSD map of the lower part of the map shown in figure 6.43, with the crack path shown with yellow dotted line. The crack corresponds to the failure that occurred after 700 cycles.

6.5.3. Detrimental and preferential crystal orientations

In this section a materials design effort is pursued in order to determine the detrimental and beneficial crystal orientations. This helps to design materials with superior fatigue performance. Crystals that have the tendency to localise deformation and damage within specific slip systems and form persistent slip bands may be characterised as 'weak' grains, while crystals that deform via uniform matrix deformation without forming slip bands, and therefore without localising damage behave as 'strong' crystals.

First, the full Inverse Pole Figures (IPF) for the EBSD map of figure 6.43 are presented, in order to reveal any existing strong texture components in the sample. Figure 6.60 shows the IPF for the individual data points within all grains of figure 6.43. It is shown that, due to the strong rolling effect, most grains lie on the 001-101 plane with respect to the crystal reference system, with only few grains lying on the 001-111 plane, due to the effect of plastic deformation during rolling. In order to better evaluate the population of grains that lie on the 001-101 plane, the density contours for the population of grains in the IPF of figure 6.60a are shown in figure 6.60b. Figure 6.60b shows that there

232

is a considerable amount of grains that lie away from the 001-101 plane, out of the black line drawn in figure 6.60b, which might be prone to damage nucleation, as these grains have not taken up enough plastic deformation during the rolling process.
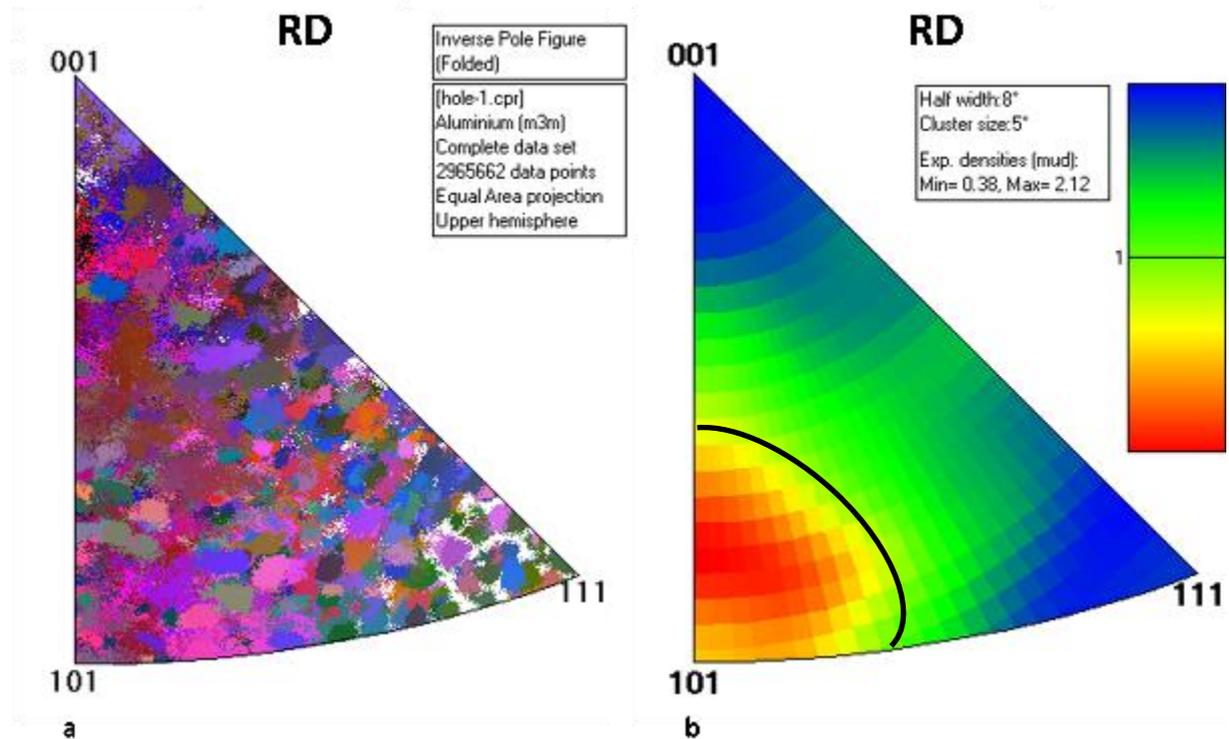
Figure 6-60. Inverse pole figures (IPF) for the EBSD map of figure 6.43 with respect to RD. a) Data points of each grain within the IPF, and b) Density contours showing the effect of rolling.

High resolution SEM analysis was performed with an Inspect-F SEM, to fully reveal which crystals are prone to slip band formation, and which ones show uniform plastic deformation. Grains in the EBSD map of figure 6.43 that showed slip banding mechanisms during fatigue testing were characterised as detrimental and prone to fatigue crack initiation and were named as 'soft' grains. These grains are highlighted in figure 6.61. In contrast, figure 6.62 shows the grains that did not localise plastic deformation and therefore did not contribute, or contributed less, to damage nucleation and evolution. The nomenclature, soft and hard grains was chosen following the reference work of Cheong et al. [13].

The highlighted grains of figures 6.61 and 6.62 were selected and the corresponding IPF figures for these grains are shown in figure 6.63a and b, respectively. The hard grains lie on the 001-101 plane, while the soft ones on the 001-111 plane. Yet there are several grains whose mechanical behavior is not well predicted by means of IPF maps alone. For instance, the two grains shown with red arrows are quite far from the 011-111 plane, and yet form strong slip bands. The slip bands though in the left grain did not appear throughout its matrix but only close to the GB with the neighbouring red arrowed grain.

The circled grains in the IPF figure 6.63a correspond to the grains which formed the strongest slip bands, which are expected to have the lowest mechanical-fatigue resistance. As shown, most soft grains lie within a small region in the IPF map. These grains are also shown with arrows in the EBSD map of figure 6.61.

Figure 6-61. Soft grains, showing non uniform matrix deformation with slip bands observed.

The 'hard' grains were also plotted in the IPF figure which is shown in figure 6.63b. Once more not all grains lie along the 001-101 texture component. Many of the 'hard' grains, influenced by local texture lie closer to orientations that facilitate localised plastic deformation and slip band formation.

Figure 6-62. Hard grains, with no slip bands and uniform plastic deformation.
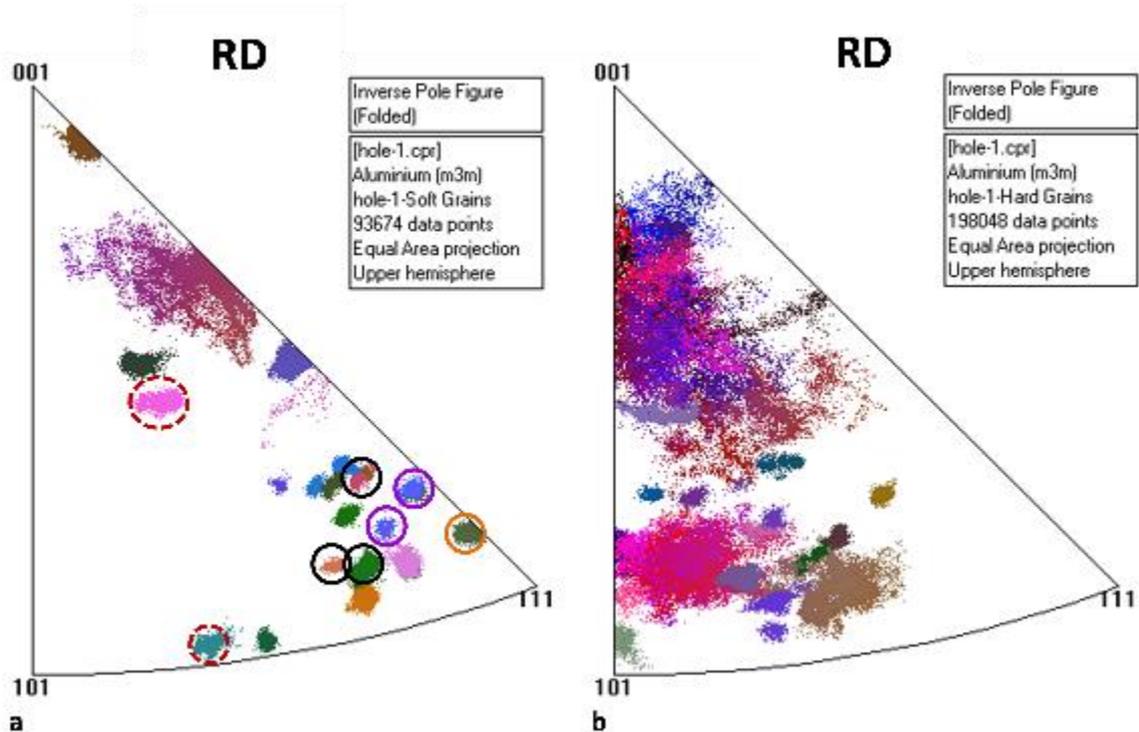
Figure 6-63. Inverse pole figures (IPF) for the highlighted grains of a) figure 6.61 and b) 6.62.

6.5.4. Discussion

Figure 6.45 shows that during cyclic loading, strain localisations occur around the hole edge. Yet the strain are highly non-homogeneous even close to the edge of the hole, with highly strained areas lying next to low strained ones. This is in agreement with the observations made in the previous section 6.4, but also with the results from the tensile fatigue tests in section 6.4.3. In all cases, the strains were highly non-homogeneous even within the same grain. This was also explained in the discussion section 6.5, in figure 6.28, where it was shown that for a material with columnar grains, there cannot be a grain largely elongated next to a compressed grain, as this would necessitate macroscopic sample rotations, or damage development between the grains at the very early stages of deformation.

The highest strain values are exactly at the edge. Yet crack nucleation does not necessarily occur at the edge of the hole, as shown in figure 6.45c. Furthermore, the DIC measured strain is not always an adequate parameter and indicator for the exact location where crack initiation occurs (similar observations were also found in section 6.3). Figure 6.45a shows 3 locations where maximum strain values were measured prior to FCI. Yet only the black circled locations are areas where cracking occurs in figure 6.45b-c while the red circled areas did not reveal any underlying cracking mechanism. The red circled area showed uniform plastic deformation without any visible slip bands formed.

In contrast to the observations made in Figure 6.45, the presence of a 'weak' grain at the edge of the hole in figure 6.52a, localises the highest strains at the edge of the hole, and at this case coincides

with the location where crack nucleation occurs. Figure 6.47a and b shows that slip band formation is the main mechanism that leads to crack initiation. Two neighbouring grains (with similar orientation, and low misorientation angle: 15^0), damage prone and close to the edge of the hole, form strong slip bands, and a crack forms after 10 cycles and propagates along the slip band planes. Similarly, a damage prone grain, at the edge of the hole in figure 6.50, leads to the formation of strong slip bands at the edge of the hole, and subsequent crack initiation, after 100 cycles. Similarly, slip bands form after the first peak load in figure 6.54a and leads to crack initiation in figure 6.54b, after just 1 cycle. The appearance of the crack is sudden in all cases, and this was related to the mechanism described in section 6.3.4. Voids form along the slip bands, and upon cyclic loading the density of voids increases, till reaching a critical value upon which they coalesce forming a relatively large (with respect to the size of the voids) micro-crack.

Several FIPs (fatigue indicating parameters) have been suggested in the literature from a modelling point of view [13, 14, 26, 45, 80]. Most frequently, the maximum accumulated slip over all the slip systems, the maximum accumulated slip over each slip system, and a local Fatemi - Socie parameter have been used to describe both the fatigue initiation and small crack growth regimes. Yet, there is limited published work suggesting which parameter is best fitted for correctly describing the exact location where fatigue crack initiation occurs in a polycrystal with direct observations made by using in-situ imaging techniques during the fatigue test. In reference [14] a single FIP is introduced based on maximum accumulated slip over all the slip systems, however in later studies all the parameters have been investigated for FCI. And furthermore the same parameters have been used for the small crack growth regime [18, 20, 26, 32, 41, 45, 81]. In a more recent study, in situ fatigue testing was performed on a 4-point bending set-up, and the FCI and small crack growth regimes were evaluated under HCF conditions [15]. Yet a rather sharp notch was created on the sample, in order to restrict FCI in a small area. FEM analysis was used to predict the exact location within the grain where FCI occurs. The modeling results were compared to the experimental ones, and fruitful results and observations were made. But FCI in this case was restricted within a small region, thus the model might not be able to correctly predict the exact location where FCI occurs in a large region containing several grains loaded under the same macroscopic BCs (same amplitude of displacements). In the current study a rather large hole was employed, which can allow FCI in a relatively large region containing 32 grains for both case studies (8 grains along the edge of the hole x 4 grains towards the rest of the sample); for 2 samples loaded under LCF conditions. Within this region, in any of the grains, FCI can happen due to the high strain localisations and due to the presence of the hole. Yet it was found that the local strain, or maximum accumulated strain (or maximum strain at each point) is not always adequate as an indicator for crack nucleation. In the first case study, the maximum measured strain did not lead to crack initiation at the red circled area of figure 6.45a. It is therefore suggested that an alternative FIP is needed, which incorporates two parameters: the locally applied high strain which is the total accumulated strain at each point and the maximum accumulated slip along the specific critical slip

systems (which is related to the formation of slip bands within 'soft' grains). This new parameter accounts for both the presence of critical grains (with detrimental orientation that leads to the formation of strong slip bands), and the presence of these grains within critical regions (regions of highly localised strains) that will facilitate FCI. Therefore it is the presence of critical grains which form strong slip bands, within highly strained areas that will lead to FCI.

Crack propagation does not always follow the direction of the slip bands. In figure 6.47d the crack grows in a rather perpendicular direction with respect to the loading direction, rather than following the direction of the slip bands highlighted with a yellow line, which suggest that the critical slip planes are no longer the critical parameters for small crack growth. Yet figures 6.48a and b show that the crack deflects before reaching grain B, and follows an orientation parallel to the slip bands of grain B. Therefore the total accumulated slip over each slip system is not always an adequate FIP parameter that can predict the paths for the small crack growth regime; this has been also found to be true in ferritic steels [79]

Another important observation was made in figure 6.48, where crack deflections were found to occur before reaching the corresponding GBs and not exactly at the GBs. Similar observations were made in figure 6.50, where the crack deflects before reaching the GB of grain D in figures 6.50d and e. This is in contrast with several published work on modeling crack paths, where in all cases the paths are modeled to change orientation exactly at the GB [28, 81].

Figure 6.50 shows that the crack grows in a zig-zag form -after reaching the GB of grain F-, switching between two approximately perpendicular directions – corresponding to two different slip planes. This was also observed in Section 6.4, where the crack switched from the main crack path to a rather perpendicular direction. Therefore crack deflections can also occur within a grain, further complicating the modeling of the small crack growth regime.

The small crack growth regime can be better analysed in the 2nd case study, where the crack after 700 cycles has crossed 8 grains. Figure 6.57a shows that the crack can also divert from the direction of the local slip bands, in order to reach the locally high-strained 'soft' region of grain H, and avoid neighbouring, low strained rather 'hard' regions. Similarly, the DIC map of figure 6.56b shows that the crack follows the path of a GB in order to divert towards a highly strained area instead of following the orientation of the slip bands in grain 'E' as shown in the SEM image of figures 6.56c. Therefore once the crack forms, the crack can follow the highly strained areas rather than the critical slip systems. This observation suggests that the total accumulated slip over all slip systems or total accumulated strain is a more accurate FIP with respect to the accumulated slip over individual slip systems. Therefore the former criterion is a better FIP for the small crack growth regime.

Upon reaching the grain in figure 6.58, the crack grows along the GB, in a direction parallel to the slip bands of grain H. Therefore a crack, upon reaching a highly strained grain, with slip bands formed

perpendicular to the loading direction can also select to follow the path of the GB. Therefore taking into account the mechanical behaviour of GBs is vital for more accurate crystal plasticity simulations [65].

In general in the literature the transition of a crack from Stage I to Stage II is not well established, and more importantly the transition between nucleation, small crack growth and macroscopic crack propagation [2, 3]. In this study it is suggested that as soon as the crack nucleates it behaves already relatively macroscopically even within the first grain (nucleation stage). In the previous section 6.4, it was shown that even within the first grain, the crack can switch between the two main slip systems in order to grow along a direction that facilitates crack growth. Figure 6.47 shows that the crack with 2 grains can be affected by the loading direction and grow relatively perpendicular to the loading direction, while figure 6.55 shows that a crack with a size of 4 grains, can switch between 2 main slip systems depending on the local strain fields. Figure 6.56 shows that a relatively large crack, extending over 6 grains can follow a GB affected by the local strain fields. In conclusion, as soon as a crack nucleates its propogation is strongly affected by both the local stress fields (figure 6.47) and more importantly the local strain fields (6.55 and 6.56) as well as the microstructure (local orientations).

Figure 6.61 highlights the grains that localised plastic deformation by forming strong slip bands, and are characterised as 'weak' grains following the nomenclature of reference [13]. The location of the corresponding grains on the IPF map is shown in figure 6.63a. The grains lie along the 001-111 orientation plane. It is therefore suggested that for superior fatigue performance, grains with such orientation should be avoided by improved rolling/manufacturing processes. There are two grains in figure 6.63a with orientation far from the 001-111 plane which are circled with red broken lines. These grains showed strong slip banding characteristics and are highlighted with broken arrows in figure 6.61. The pink-coloured grain in figure 6.61 showed strong plastic localisations throughout its matrix while the jade-coloured grain (mixture between green and blue colour) showed strong slip bands only close to the GB with the neighbouring pink coloured grain. Both grains are shown in figure 6.64. The pink coloured grain can be characterised as 'weak' grain and is named B, while the neighbouring grain, grain A, only localises deformation close to the GB, with the rest of the grain showing uniform plastic deformation with no slip bands in figure 6.64. The misorientation relationship between the two grains was obtained and a high angle GB with a misorientation of 51 degrees was found between the two grains. The two grains lie far away on the IPF map, which suggests that they might have incompatible modes of deformation. Therefore a strong strain gradient should be expected close to the GB which can also be seen in figure 6.64 as the rest of the matrix of grain A shows no slip banding characteristics. The high misorientation might also be the reason for the presence of strong slip bands in grain A close to the GB with grain B. It has to be pointed out that grain B lies along the deformation band in figure 6.46b. The deformation band highlighted with a red arrow appears in all images in figures 6.45 and 6.46. The presence of this deformation band is not fully understood. It could be due to both a mechanical effect (effect of the hole), or a microstructure

effect. The mechanical effect should be negligible as such band was not observed at similar locations in the other experimental work (sections 6.3 and 6.4). With respect to the microstructure, the grains at the corresponding location have high misorientations at the corresponding GBs and are far apart on the IPF map. Figure 6.65 though shows that all the highlighted grains lie relatively far from the 001-101 plane, which does not facilitate the formation of slip bands within the highlighted region of figure 6.65a.
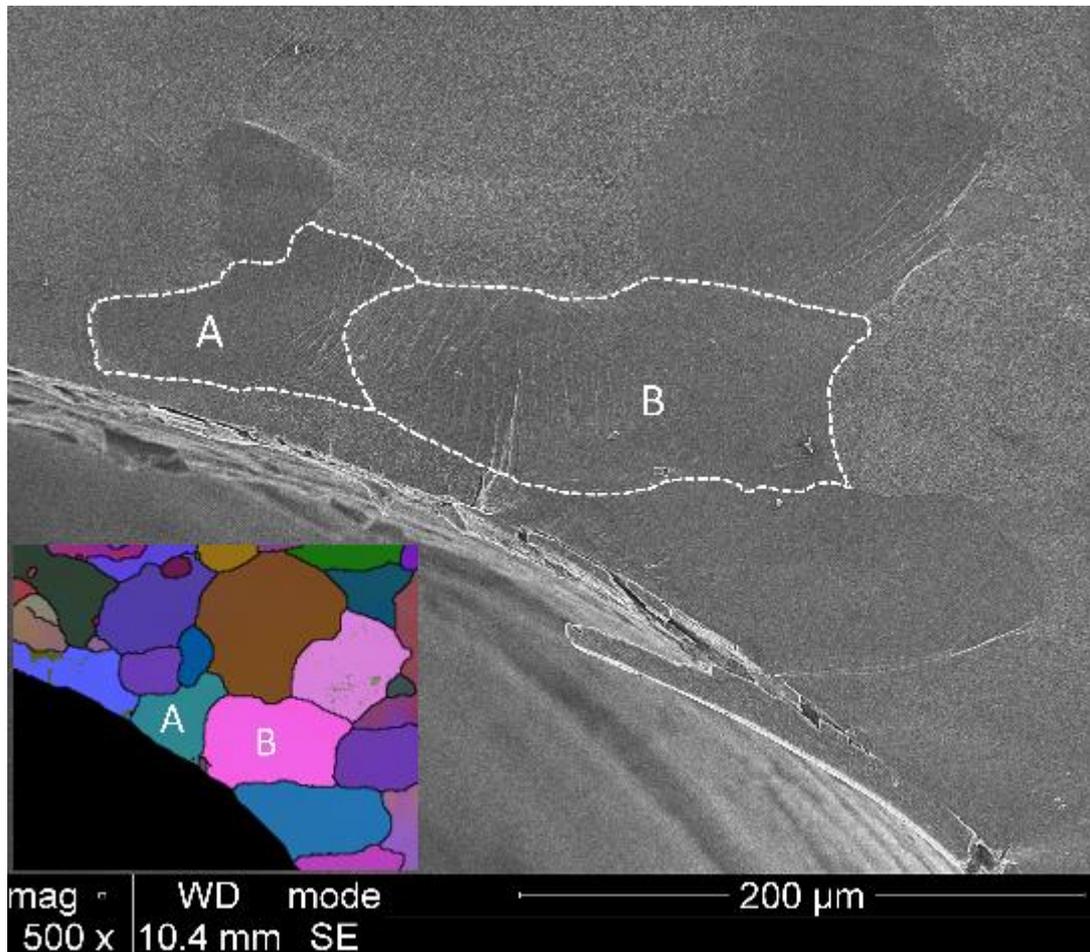
Figure 6-64. Two grains close to the edge of the hole showing strong slip banding mechanisms.

Figure 6.62 highlights the grains that showed resistance to slip banding and crack initiation mechanisms and are characterised as 'hard' grains, following the nomenclature of reference [13]. Figure 6.63b shows the orientation-data points for the highlighted grains of figure 6.62 plotted over the IPF map. Most grains lie along the 001-101 plane, which suggests that the higher the deformation during the rolling process the 'harder' the grains are in the resulting microstructure and lower the potency for slip band formation at the early stages of plastic deformation. Therefore, further rolling applied to the material should yield more data points closer to the 001-101 plane, and therefore superior fatigue performance. Yet, several hard grains orientations lie far from the 001-101 plane, suggesting that the influence of local texture is stronger than the influence of the individual grains separately. Therefore grains characterised as 'soft' with respect to their corresponding location on the

IPF map can have a 'hard' grain characteristics in terms of their mechanical behaviour and the potency to form slip bands and fatigue cracks.

Therefore, there is not always a direct correlation between the location of the grain on the IPF map and the tendency for fatigue crack initiation in the corresponding grain. The IPF map can give an indication of the potency for fatigue cracking, yet the orientation of the neighbouring grains needs also to be considered to better predict the occurrence of damage.
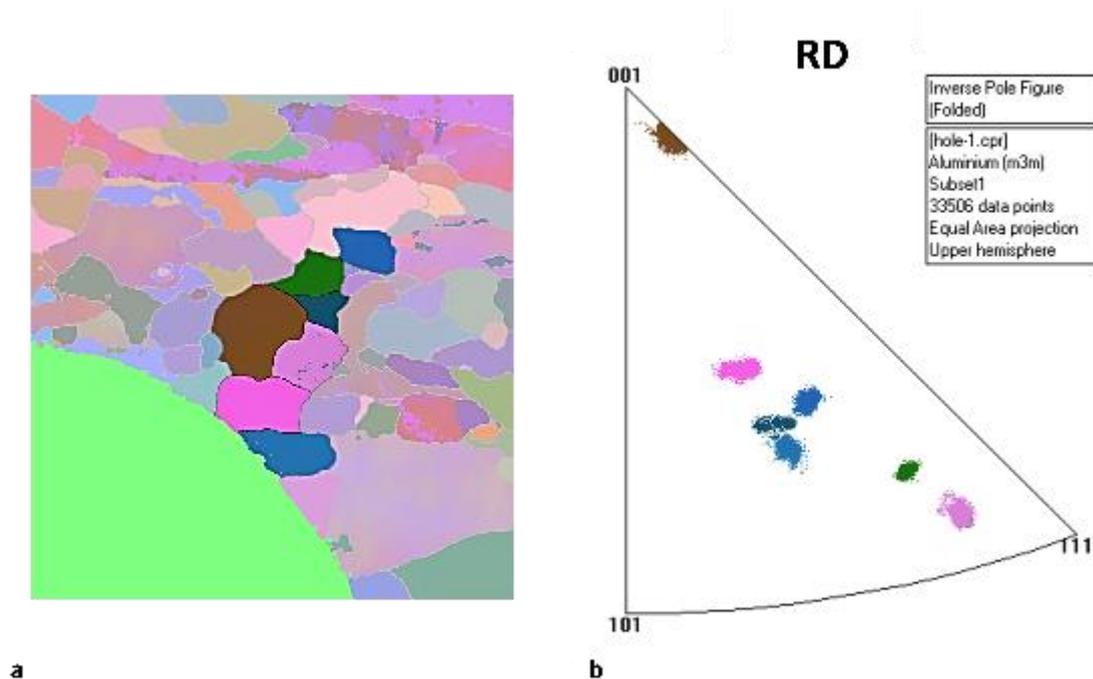
Figure 6-65. Texture components at the location where the deformation band formed in figures 6.45 and 6.46.

6.5.5. Conclusions

In situ mechanical (4 point bending cyclic fatigue) testing within a CamScan SEM chamber was performed for low and mid-amplitude. Similarly to the observations made during tensile fatigue testing in the previous chapter, the strains appeared to be clustered within the regions of several grains. Neighborhoods of highly strained grains were observed, close to areas of low strained grains. Optical microscopy inspections revealed large out of plane deformations and slip bands in the highly strained regions and negligible out of plane deformation in the low strained areas.

Fractured particles and voids around inclusions were observed in the highly strained areas with high strain localisations within the matrix adjacent to the particles and inclusions while in the low strained areas the particles and inclusion areas appeared to be intact in most cases. Therefore the strain fields and strain localisations were evaluated at three different scales: macroscale (DIC measurements), mesoscale (optical microscopy) and microscale (SEM inspections) and a direct correlation and good agreement was established between the corresponding observations. Strain distributions at the grain level strongly affect the occurring phenomena within the neighbourhood of a particle or inclusion.

Two 4 point bending tests were done with the 1mm central hole sample geometry. In both studies it was found that the formation of strong slip bands within 'weak' grains that lie within highly deformed areas leads to FCI. This result led to the introduction of a new FCI criterion that incorporates two parameters: the total accumulated slip at each point (over all slip systems) and the total accumulated slip over each slip system (the slip system that accumulates the highest shear strains). Once the crack formed even within the first grain, it could deflect from the major slip system-band due to the applied local stress- (and more importantly) strain fields. Crack deflections occurred due to various occurring phenomena. Cracks deflected when getting close to the GB to avoid the heavily deformed areas close to the GB and ahead of the crack tip. Cracks deflected within the grain matrix in order to propagate towards a heavily deformed grain and avoid a relatively 'hard' neighboring grain. The cracks also followed the GBs in order to move towards highly deformed area within the same grain. All these occurring phenomena tha drive crack deflection suggest that modeling the small crack growth regime is far more complicated and scientifically challenging compared to modeling FCI.

Texture evaluation via the inverse pole figures, revealed as a general trend that the heavily rolled grains appear to be 'hard' grains resisting slip band formation, while the grains close to the 001-111 orientation behave as 'weak' ones with the tendency to form strong slip bands and micro-cracks. However, a direct relationship between grain orientation and slip band formation or cracking cannot always be established, showing that the influence of neighboring grains on plastic accumulation of individual grains needs also to be evaluated. Therefore analysis on individual grains cannot always yield comprehensive understanding of the local deformation patterns.

Multiscale Modelling of fatigue

The aim of the modeling work is to gain experimental insight from the results of Chapter 5 and 6 and provide useful information for the parameters of the crystal plasticity model developed. A comparison was made for the macroscopic stress-strain behaviour for both monotonic, and cyclic fully reversed and positive amplitude loading conditions. A new FCI criterion was introduced, while the FCI lifetime was predicted and compared to the total fatigue lifetime of the sample (experimentally observed). The influence of particles was also introduced in order to incorporate the interaction between crystal lattice and the particles. A Multiscale approach was used in order to model realistic structural components.

7.1. Single crystal plasticity modelling

The UMAT code is based on the formulations of Huang et al [19], with modifications made on the incorporation of the Euler angles and kinematic hardening (for cyclic hardening effects) within the original code, as described in Chapter 4. The code has been first verified by comparing model predictions with experimental results on copper single crystals. In 1975, Takeuchi et al. measured experimentally the tensile response of copper single crystals for different crystal orientations and for different temperature conditions [82], which showed the strong influence of the crystal orientation on the corresponding mechanical properties. His results were used in order to validate Huang et al UMAT code [19]. The parameters for the constitutive equations were taken from [18, 20, 56, 57], where further details can be found. A small discrepancy between the experimental and modeling results exist in figure 7.1.

To outline the basic differences between a crystalline slip-hardening model and a simple elasto-plastic model, a simple geometry with a hole in the middle was created, and the meshed part is shown in figure 7.2. An aluminium elasto-plastic material with mechanical behaviour described later on by the stress-strain curve of figure 7.5 from the tensile experiment, and an aluminium single crystal with material properties shown in Table 7.1 were considered. For the elasto-plastic material, the existence of the hole leads to stress concentrations around the neighbourhood of the hole, and plasticity is highly localised on the sides of the hole (figure 7.3a). For the case of a single crystal with a hole in the middle, the results show significant differences. Figure 7.3b shows a single crystal oriented parallel to the global system; i.e. (1 0 0) - (0 1 0) orientation. Significant deformation occurs, leading to large

plastic zones extending throughout the whole width of the specimen. Plasticity is constrained to follow the paths at 45° with respect to the loading direction.

Moreover in the single-crystal plasticity model, the total deformation of the body is more pronounced. It can be seen from Figure 7.3b zones of high deformation separated by zones of negligible deformation; while for the elasto-plastic material the gradients of deformation are smoother. Apart from a very small area of high localisation (shear lips), plasticity is more uniformly distributed. The influence of crystal orientation can be seen in figure 7.3c. The deformed body with global orientations (1 0 0) - (0 1 0) corresponds to a single crystal with orientation: [1 1 1] - (1 1 2). In this case the slip systems are not orientated favourably at 45° with respect to the loading direction. Therefore slip and therefore hardening is more difficult given this orientation. The plasticity zone is much smaller and the formation of shear zones is restricted.
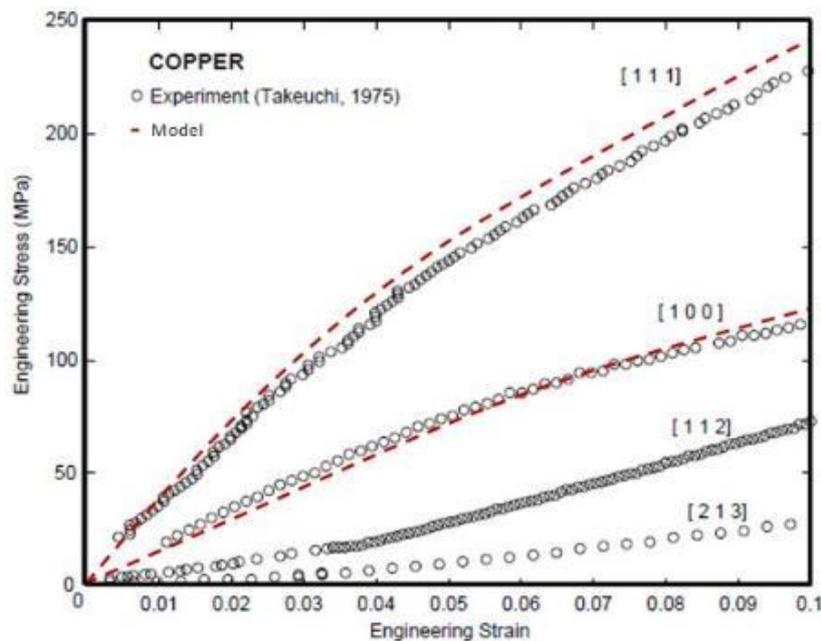
Figure 7-1. The influence of orientation for a Copper single crystal on the stress-strain curve. The open circles correspond to the experimental results; and the red lines obtained by using the UMAT code.
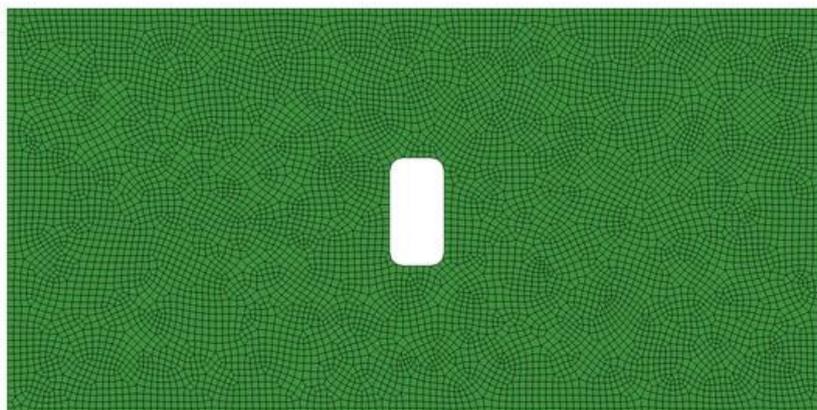
Figure 7-2. Meshed part.
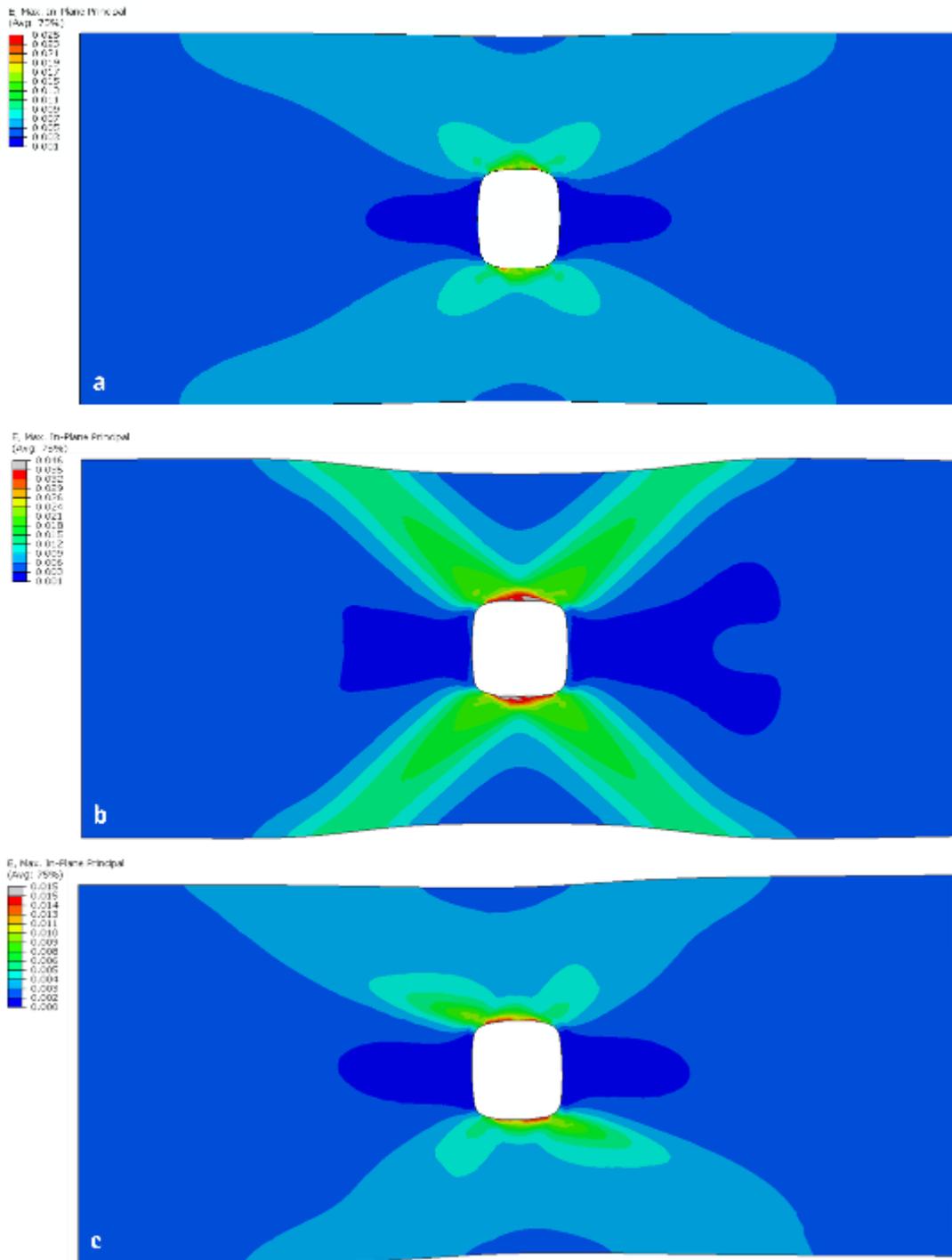
Figure 7- 3. a) Deformed body for an elasto-plastic material; the contours show the maximum in plane principal strain, b) Deformed body by using crystal plasticity on an aluminium single crystal; the contours show the maximum in plane principal strain; the local orientation of the crystal is parallel to the global orientation of the specimen, c) Deformed body by using crystal plasticity on an aluminium single crystal; the contours show the maximum in plane principal strain; the local orientation of the crystal is [1 1 1] - (1 1 2) while the global orientation of the specimen correspond to (1 0 0) - (0 1 0).

7.2. Polycrystal plasticity for Al2024

7.2.1. Material Parameter identification

The material investigated in this research project is Al2024. The relevant material parameters were obtained based on [18, 20, 56, 57] and by performing a parametric study to correlate the

experimental results with the modelling ones (see figure 7.5). The material parameters used for the crystal plasticity model are shown in Table 7.1. A homogenisation study was pursued and it was found that 80 crystals are reasonably adequate to yield the macroscopic response for the artificially created microstructure. The grain orientation was given within a Fortran subroutine. For each grain, three random number generators were employed to assign each grain with the corresponding orientation given by three Euler angles. Therefore an RVE of 80 Voronoi polygons was created and meshed as shown in figures 7.4a and b. Aluminium has a FCC structure, and has 12 slip systems, all lying on the (111) plane; as shown in Table 7.2.

Elastic moduli (GPa)							
C_{1111}	C_{1122}	C_{2222}	C_{1133}	C_{2233}	C_{3333}	C_{1112}	C_{2212}
112	59.5	114	59	57.5	114	1.67	-0.574
C_{3312}	C_{1212}	C_{1113}	C_{2213}	C_{3313}	C_{1213}	C_{1313}	C_{1223}
-1.09	26.7	1.25	-0.125	-1.12	-1.92	26.2	-0.125
C_{2223}	C_{3323}	C_{1123}	C_{1323}	C_{2323}			
1.86	0.068	-1.92	-1.09	24.7			
Hardening exponent & Hardening coefficient							
$\dot{\gamma}_0$				n			
0.001 sec^{-1}				10			
Self & Latent Hardening							
h_0		τ_s	τ_0		q		q_1
37		100	82.5		1		1

Table 7-1. Material parameters for Al2024 [18, 20, 56, 57].

Nr	Slip plane	Slip direction
1	(1 1 1)	[0 -1 1]
2	(1 1 1)	[1 0 -1]
3	(1 1 1)	[-1 1 0]
4	(-1 1 1)	[1 0 1]
5	(-1 1 1)	[1 1 0]
6	(-1 1 1)	[0 -1 1]
7	(1 -1 1)	[0 1 1]
8	(1 -1 1)	[1 1 0]
9	(1 -1 1)	[1 0 -1]
10	(1 1 -1)	[0 1 1]
11	(1 1 -1)	[1 0 1]
12	(1 1 -1)	[-1 1 0]
Number of slip systems	**12**	

Aluminium: FCC	
12 slips systems	(111) family planes

Table 7-2. Slip systems in aluminium polycrystals.
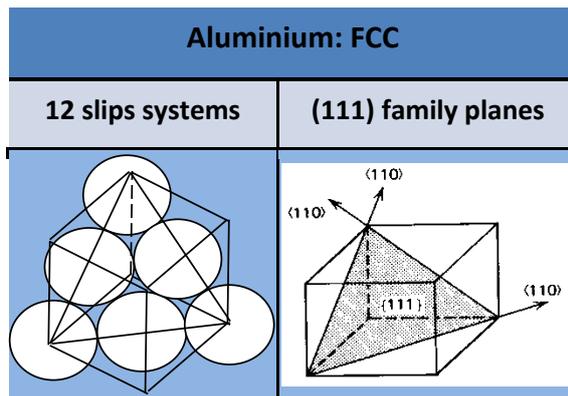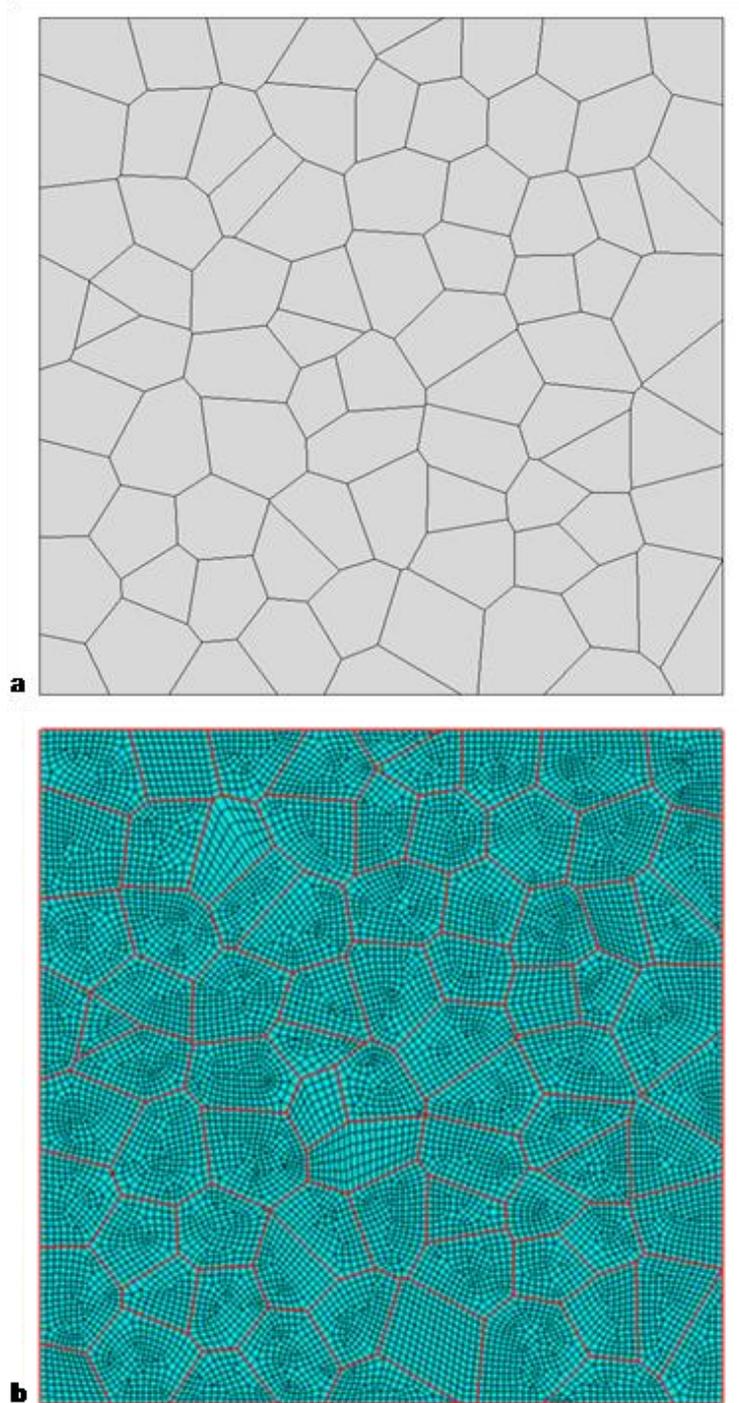
Figure 7-4. a) The created geometry for the 2-D RVE, and b) the meshed part.

7.2.2. BCs, Homogenisation & Mesh sensitivity

A mesh sensitivity study was pursued. 4-node plane strain quadrilateral elements (CPE4) were employed in all cases. A python code was developed in order to optimize the mesh size (computational time versus homogenized stress-strain fields). The stress strain fields were homogenized over the whole area (all integration points). A mesh size with an edge size of 0.1 micron was finally selected for this analysis; approximately 100 seeds on each side of the RVE (the seeds are markers that indicate the mesh density). The meshed part can be seen in figure 7.4b.The bottom edge

of the polycrystal was gripped in the y-direction, the left-edge was gripped in the x-direction, and a constant displacement was applied at the right edge (displacement=0.01); with the top edge left free. Periodic boundary conditions were also applied to this RVE via Abaqus CAE (interface), but similar results were obtained for the macroscopic response. An optimization python code was written which minimises the squares of differences between the experimental values and modeling ones. The fitted values for the hardening parameters (h_0, τ_s and τ_0) of Asaro's hardening rule (equation 7.1) were obtained and are shown in Table 7.1:

$$h_{\alpha\alpha} = h(\gamma) = h_o \cdot \sec h^2 \left| \frac{h_o}{\tau_s - \tau_o} \right| \qquad (7.1)$$

h_0, τ_s and τ_0 were found to be 37, 100 and 82.5, respectively. As shown in figure 7.5, a rather good agreement between the experiment and the modelling results was obtained. The fitted curve is shown alongside 2 other cases which yielded slightly larger deviations from the experimentally observed curve.
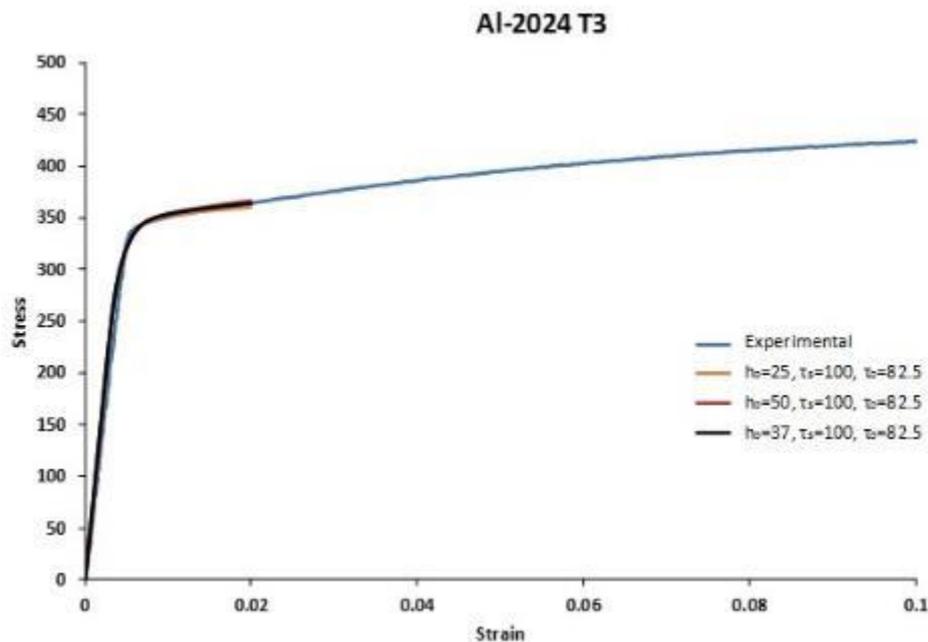
Figure 7-5. Comparison between modelling and experimental results for Al2024 for strain up to 0.02.

A numerical procedure was developed to identify both the slip systems which accommodate high shear strains, and the combination of slip systems that are acting in the 2D RVE polycrystal of figure 7.4a leading to major plastic deformation. The process is shown in Figure 7.6, and the results are shown in Table 7.3. Initially the accumulated slip in each node was stored for each of the slip systems. The shear strain values for all the nodes within each grain were added for each of the slip systems separately. In each grain, the slip systems were sorted in descending order, from maximum strain to minimum. So, the first four slip systems with major shear strain accumulation are stored for each grain in descending order (from the slip system that carries the highest shear strain value down to the fourth highest-one). Finally the number of times these combinations of slip systems appear in the

polycrystal are counted and listed. Table 7.3 shows the combinations of critical slip systems that appear in the deformed RVE of 80 grains in figure 7.4a. The 1st and 2nd slip systems in Table 7.3 were found to carry strain values one order of magnitude larger than those for 3rd of 4th slip systems in Table 7.3. 92.5% of the total deformation is due to 3 combinations of 4 slip systems; namely 1-4-9-10, 2-6-7-11 and 3-5-8-12. Most combinations of slip systems are inactive, and some have a very small effect (1st, 2nd, 3rd, 4th, 6th, and 7th row in Table 7.3). The slip systems accumulating the highest shear strains- plastic deformation were the 1st, 2nd and 3rd, with the most critical one being the 3rd one. The most critical combination of slip systems was the 3-5-8-12.
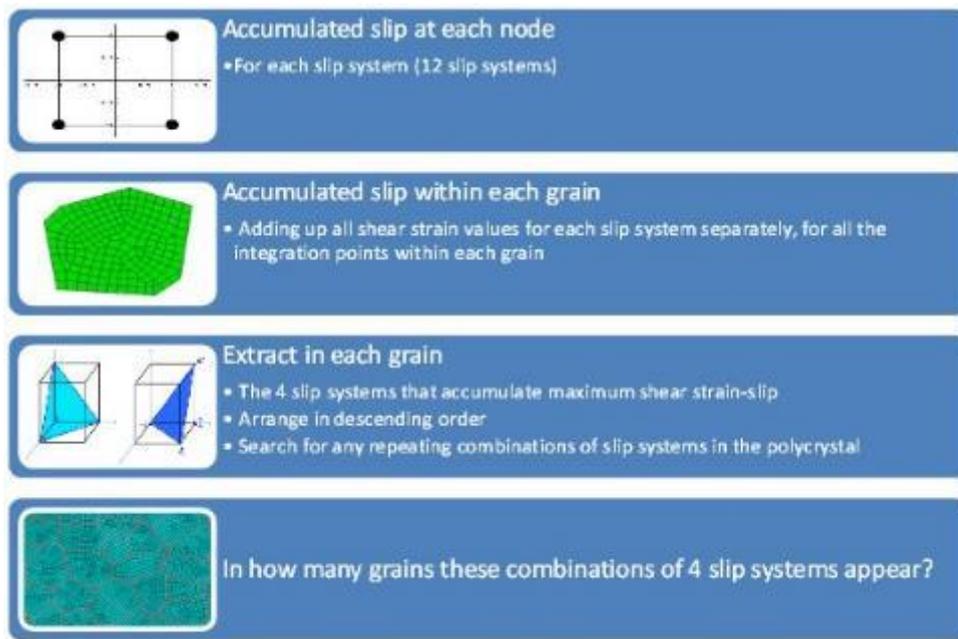
Figure 7-6. Process for identifying the slip systems with maximum shear strain values within the 2D RVE polycrystal of figure 7.5a.

Table 7-3. Critical slip systems for the RVE of figure 7.5

Combinations of critical slip systems (the critical slip systems appear to group in 4)				*In how many grains appear these slip systems?*
1st crit. slip system	2nd crit. slip system	3rd crit. slip system	4th crit. slip system	Nr of grains
1	2	6	11	1
1	2	10	11	1
1	3	4	9	1
1	3	5	8	1
1	**4**	**9**	**10**	**28**
2	4	6	11	1
2	5	8	11	1
2	**6**	**7**	**11**	**16**

3	5	8	12	30

7.3. Modelling Fatigue for Al2024 T3 with crystal plasticity

In this section the kinematic hardening laws applied in the UMAT code originally developed by Huang et al [19] are described, and a comparison is made with the experimentally obtained stress-strain curves. A brief description of the available FCI and small crack growth criteria used in the literature is then presented in the 2nd section (7.4.2).

7.3.1. Kinematic hardening

Metallic materials show different hardening response in monotonic and cyclic loading conditions. In fully reversed loading systems, after a certain amount of forward plastic deformation, the material may yield at lower stress levels in compression than in tension; this phenomenon is called Bauschinger effect [8]. Even in the case of positive amplitude cyclic loading, kinematic hardening effects should be taken into account. The Armstrong-Frederick hardening rule was considered in this study, given by equation 8.2:

$$\dot{\chi}^{(\alpha)} = b\dot{\gamma}^{(a)} - r\chi^{(\alpha)}\left|\dot{\gamma}^{(a)}\right|$$

(7.2)

The parameters b and r were defined by strain-controlled, fully reversed cyclic fatigue experiments up to a strain amplitude of 0.02. Further details about the procedure for obtaining the two parameters can be found in [18, 20]. Values of -24 and 1 were used for b and r. The two curves, the experimentally obtained stabilised curve and the simulation curve are shown in figure 7.7. A rather good agreement was obtained for the simulated polycrystal of figure 7.4a.
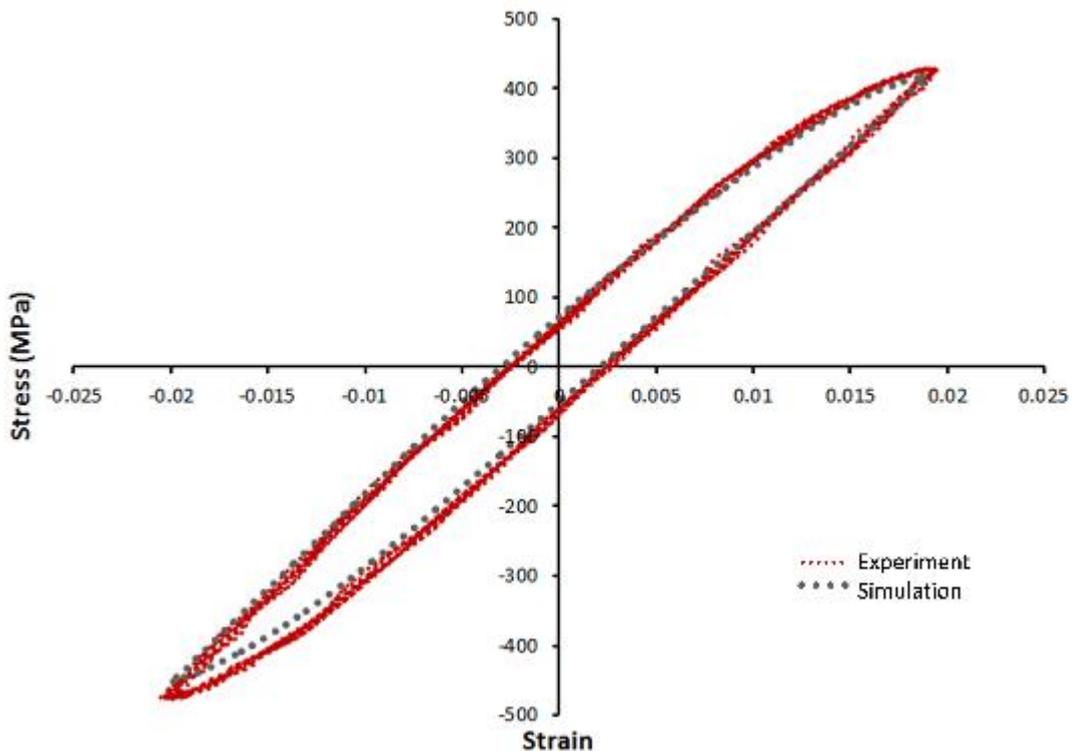
Figure 7-7. Comparison between the experimentally obtained stabilised stress-strain curve and the simulated one for R=-1 and strain amplitude of 0.02.

Cyclic fatigue simulation up to a strain amplitude of 0.01 was applied to the 2D RVE of figure 7.4a, with R=0. Figure 7.8 shows 2 points in neighbouring grains where at one point, Point A, strain accumulation occurs, while at Point B cyclic (strain) softening occurs. Figure 7.9 shows the accumulation of plastic strain within the 12 individual slip systems, during the first 10 cycles at point A of figure 7.8. The 3rd slip system is the major slip system accumulating high shear strains- plastic slip. Apart from the first 3 slip systems (1st, 2nd, and 3rd), the rest of the slip systems remain relatively inactive, without any noticed shear strain accumulation.
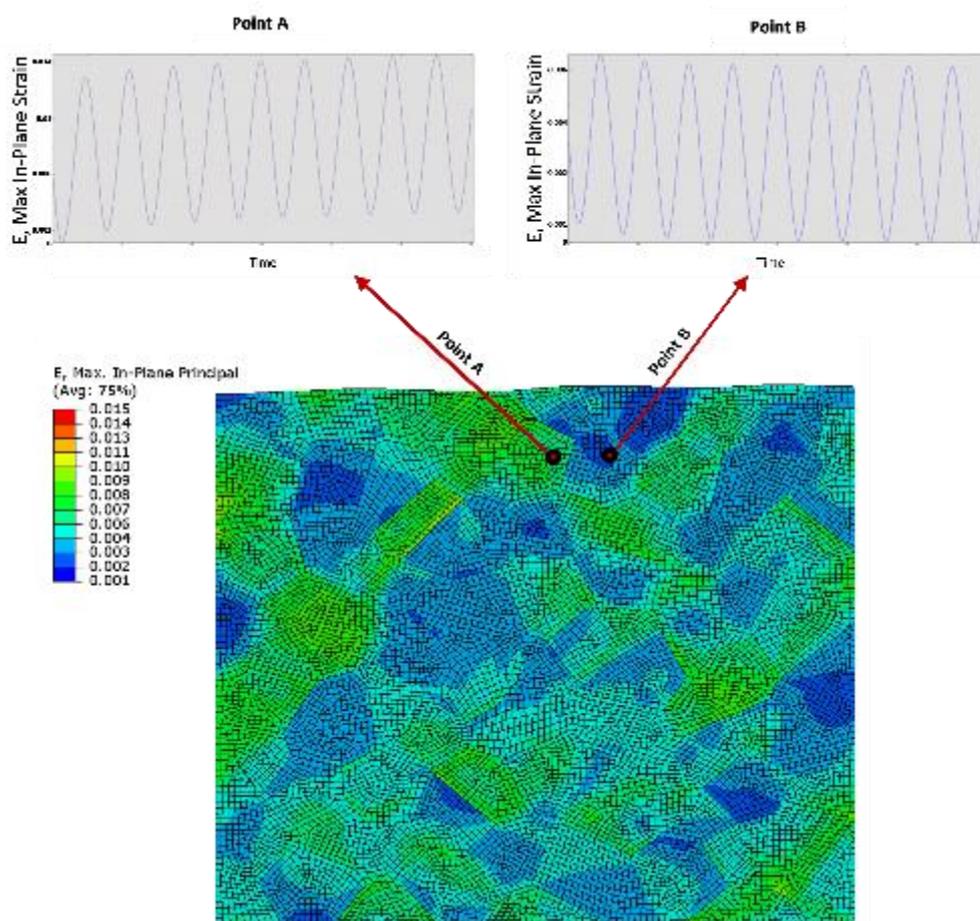
Figure 7-8. Maximum in plane strain deformation for the RVE of figure 7.5, under cyclic loading conditions, at maximum displacement and after 10 cycles. The two points show the corresponding hardening and softening that occurs at the highlighted points (A & B).
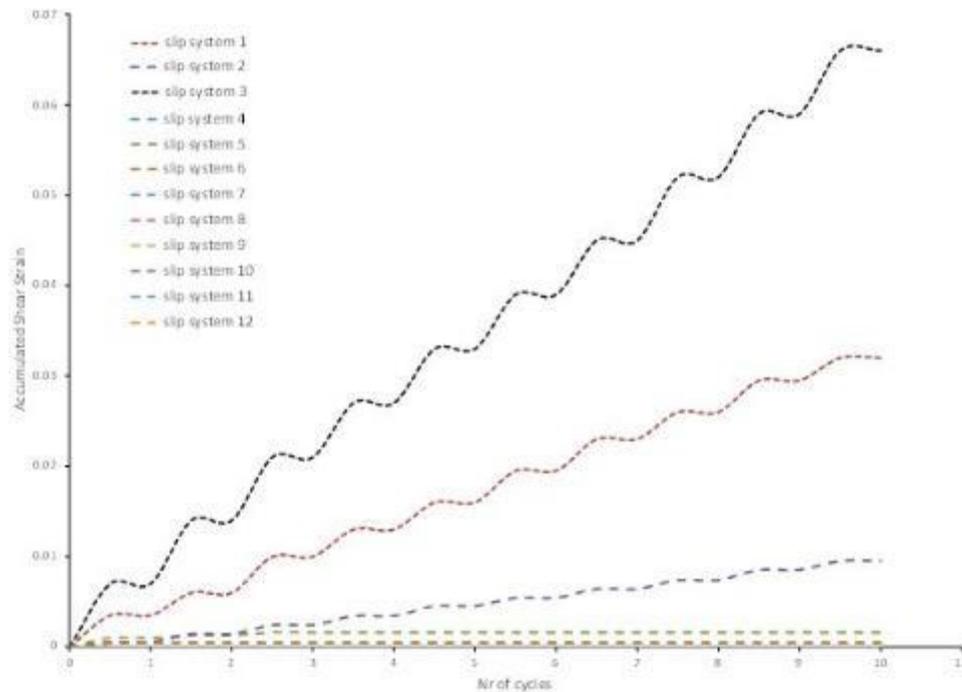
Figure 7-9. Accumulated shear strain for each slip system against the number of cycles at location A in figure 7.8.

7.3.2. Fatigue Crack initiation and small crack growth criteria

Being able to apply the most appropriate damage initiation and propagation criteria represents the heart of fatigue modelling. The phenomena that occur and lead to crack initiation are highly localised. Dislocation dipoles, interface decohesion, triple points and other microstructural features can lead to the formation of a crack. The propagation of a small crack depends on the resistance and strength of the matrix to crack growth. Furthermore, depending on the location of the crack, whether it sits close or far away from a GB, crack acceleration or deceleration may occur. Particles embedded in the matrix may act either as easy bridges for further cracking - by increasing the stress concentrations ahead of the crack tip, or as crack growth obstacles by forcing the crack to create a new crack tip in the crystal matrix as the particle is broken, and therefore delay further crack propagation in the matrix. As a result factors affecting local damage can be very complex and therefore a universal damage criterion must be able to predict fatigue crack development for all the different microstructural cases.

Cheong et al used an energy based approach and defined the local energy dissipated in terms of plastic work, which served as an indicator for FCI [13]. Manonukul and Dunne used a very simple crack initiation criterion which is based on the critical accumulated slip [14]. Shenoy et al made a thorough study and utilised 5 Fatigue Indicator Parameters in order to be able to identify their ability to indicate fatigue crack initiation and small crack growth: accumulated plastic slip per cycle (P_{cyc}), impingement of slip due to pile-ups (P_r), critical accumulated plastic slip which leads to crack initiation (p_{crit}), Fatemi-Socie parameters (P_{FS}) which describes the local loading conditions upon small crack growth, and the maximum range of cyclic shear strain (P_{mps}) when the normal stresses to a small crack are zero [26]. Similarly to Shenoy et al. who found very good agreement with the experimental results, Hochhalter et al used 5 Nucleation metrics to describe the crack initiation and small crack growth phenomena:

252

the maximum accumulated slip over each slip system (Nucleation metric D1), the maximum accumulated slip over each slip plane (D2), the maximum accumulated slip over all slip systems (D3), the maximum energy dissipated on a slip plane (D4) and a modified Fatemi-Socie criterion (D5) which takes into account the tensile stress normal to the crack and the shear strain range acting along the crack [45]. Table 7.4 shows the different fatigue parameters for the 4 papers outlined above.

K.-S. Cheong, M. J Smillie & D.M Knowles	$$E_{\mathrm{p}} = \int \boldsymbol{\sigma} : \mathbf{L}^{\mathrm{P}} \, \mathrm{d}t, \quad \mathbf{L}^{\mathrm{P}} = \dot{\mathbf{F}}^{\mathrm{P}} \mathbf{F}^{\mathrm{p}-1}$$
A. Manonukul and F. Dunne	$$p_{\mathrm{cyc}} N_{\mathrm{f}} = p_{\mathrm{crit}}$$
D. L. McDowell, J. Zhang & M. Shenoy	$$P_{\mathrm{cyc}} = \int_{\mathrm{cyc}} \sqrt{\frac{2}{3}} \dot{p} \, \mathrm{d}t = \int_{\mathrm{cyc}} \sqrt{\frac{2}{3} \mathbf{D}^{\mathrm{P}} : \mathbf{D}^{\mathrm{P}}} \, \mathrm{d}t$$ $$P_{\mathrm{cyc}} N_{\mathrm{inc}} = p_{\mathrm{crit}}$$ $$P_{\mathrm{r}} = \max \left(\int_{\mathrm{cycle}} \dot{\varepsilon}_{ij}^{\mathrm{p}} \, n_i \, t_j \, \mathrm{d}t \right)$$ $$P_{\mathrm{FS}} = \frac{\Delta \gamma_{\mathrm{max}}^{\mathrm{P}}}{2} \left[1 + k^* \frac{\sigma_{\mathrm{n}}^{\mathrm{max}}}{\sigma_{\mathrm{y}}} \right]$$ $$P_{\mathrm{mps}} = \frac{\Delta \gamma_{\mathrm{max}}^{\mathrm{P}}}{2}$$
J. D. Hochhalter, D. J. Littlewood, R. J. Christ Jr, M. G. Veilleux, J. E. Bozek, A. M. Maniatty & A. R. Ingraffea	$$\Gamma^{\alpha} = \int_0^t |\dot{\gamma}^{\alpha}| \, \mathrm{d}t$$ $$D_1 = \max_{\alpha} \Gamma^{\alpha}$$ $$D_3 = \Gamma = \sum_{\alpha=0}^{N_s} \Gamma^{\alpha}$$ $$D_4 = \max_p \int_0^t \sum_{\alpha=0}^{N_d} \left| \dot{\gamma}_p^{\alpha} \tau_p^{\alpha} \right| \, dt$$ $$D_5 = \max_p \int_0^t \sum_{\alpha=0}^{N_d} |\dot{\gamma}_p^{\alpha}| \left(1 + k \frac{\langle \sigma_n^p \rangle}{g_o} \right) \, dt$$

Table 7-4. Fatigue parameters for indicating damage initiation and small crack growth.

7.3.3. Modelling FCI and small crack growth (FIP analysis)

The concepts outlined in chapter 5 were used in order to model polycrystals. The Voronoi technique was used to introduce a user-defined number of grains into the modelling geometry, while user-specified crystal orientations were applied. A 2-dimensional RVE geometry, containing a 1mm hole, was generated and is shown in figure 7.10. The total number of grains was 1200. In section 6.4, the EBSD map contained 1441 grains in a rectangular area of 5.18 mm^2. In this case a smaller area was selected, simulating the 2 DIC areas, covering a rectangular area of 4.31 mm^2. The same number of grains was used in this study, but the shape of the grains was not accounted for. In section 6.4 the grains were elongated due to the rolling process, while here the grains have a polygonal, rather equiaxed shape as shown in figure 7.10. The grain orientations of the RVE were random numbers selected from the sets of Euler angles obtained from the EBSD map of figure 6.45 (and shown in 6.62b) in order to represent the same overall texture as in figure 6-34b. Meshing of the geometry was done with 4-node bi-linear plane strain quadrilateral elements. 1% strain was applied to the two left and right edges (an average of 1% strain was applied in the case study of section 6.4 and 6.5), while the bottom side was clamped in the y-direction.

Following the concepts presented in Table 7.4, and the observations made in sections 6.3 and 6.4, an additional FIP parameter is introduced here, namely D^*. Using the notation by Hochhalter et al [45] the D1 metric was employed, which represents the maximum accumulated slip over each slip system, and the D3 metric, which is the total accumulated slip over all slip systems. The new D^* is a combination of the two metrics:

$$D^* = \sqrt[(2\alpha+\beta)]{D1^{2\alpha} \cdot D3^{\beta}} \qquad\qquad (7.3)$$

For this study α and β are 1. In this criterion a combination of D1 and D3 metrics was employed as it is the presence of critical grains (that lead to strong slip bands) within regions with high strains that leads to FCI. In areas where high strains are observed it will be preferentially the critical grains (that facilitate strong slip banding mechanisms) that will initiate cracks, and that is the reason why an exponent of 2 is used for D1 metric, while an exponent of 1 is used for D3 metric. The D3 metric is also important, as it was found that critical grains outside critically loaded areas formed slip bands but did not lead eventually to FCI (section 6.3.2), as the applied stresses and strains were not high enough to facilitate FCI. This signifies the importance of both parameters: D1 and D3. The $(2\alpha + \beta)$ root is used in order to obtain similar scale with respect to D1 and D3 metric, but is not necessary in the relationship. More experiments are necessary in the future to validate the importance and the competition between the two parameters, namely D1 and D3. Furthermore, there could be an influence of the material investigated, Al2024 on the values for the two exponents. Different polycrystals, such as Nickel superalloys or Ti alloys or steels might yield different dependence between the two metrics.
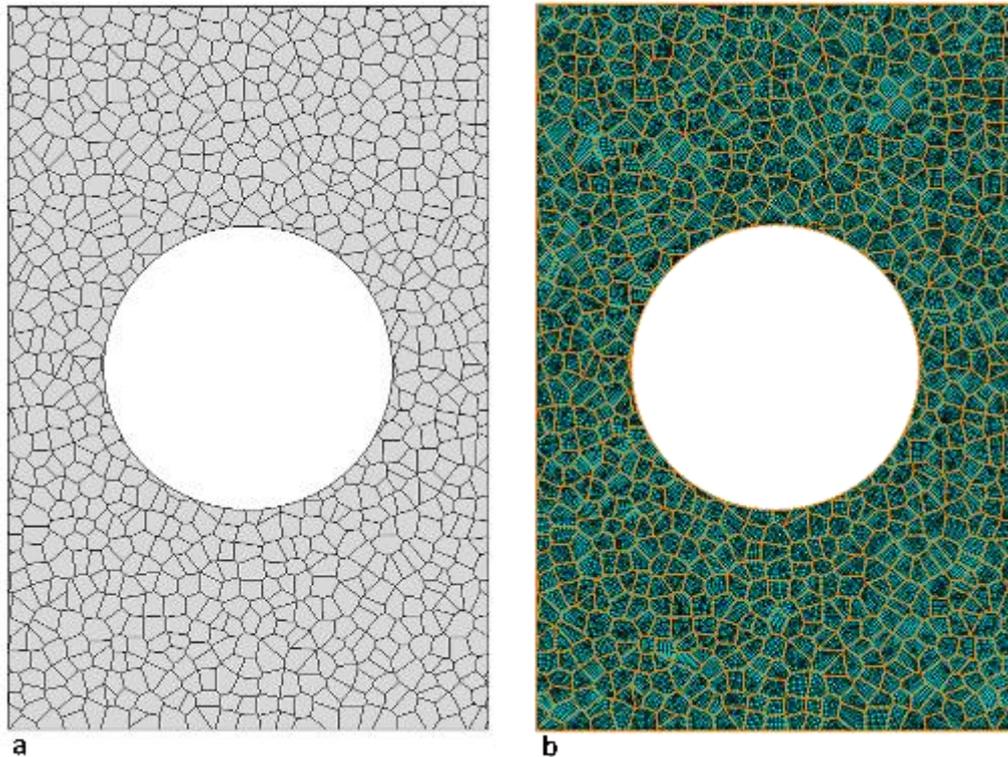
Figure 7-10. a) The geometry used in Abaqus modeller. The Voronoi grains had random orientations, while grain boundaries were modelled explicitly, b) Meshed part.

Figure 7.11a shows the total accumulated slip over all slip systems, the D3 metric, after 1 cycle at maximum displacement. The total accumulated slip is highly non homogeneous. Shear bands have formed, extending from the edge of the hole at 45° towards the rest of the material. The highest strain localisations occur at the edge of the hole. The maximum value for D3 is 0.057 and therefore a criterion based on D3 predicts failure at the edge of the hole. Similar observation can be made at the lower semi-circle of the hole, with the highest shear strain values found at the edge; i.e. 0.047. Figure 7.11b shows the newly introduced FIP, D^*. The shear bands are still observed in the D* strain distribution. Yet the strains appear to be even more non -homogeneous in comparison with figure 7.11a, showing an increased influence of the individual grains. The highest values for D^* are found to occur close to the edge of the hole but not exactly at the edge of the hole, as shown by the strain contours in figure 7.11b. Similar observations can be made for the lower semi-circle of the hole, where the highest D* values are also observed to occur not exactly at the edge of the hole. Figure 7.12 shows the locations predicted to fail by using the metric D3; i.e. total accumulated slip over all sip systems. The grains predicted to initiate cracks are coloured in grey and both correspond to locations at the edge of the hole. By using the newly introduced FIP, D*, the FCI locations (highlighted in red) are not located at the edge of the hole. Furthermore for the upper semi-circle of the hole, the two corresponding locations are relatively far away, which means that the two metrics, D3 and D*, can lead to a very different prediction of the FCI process. For the lower part of the hole, the 2 corresponding areas are in neighbouring grains. Yet the exact location is not the same.

255
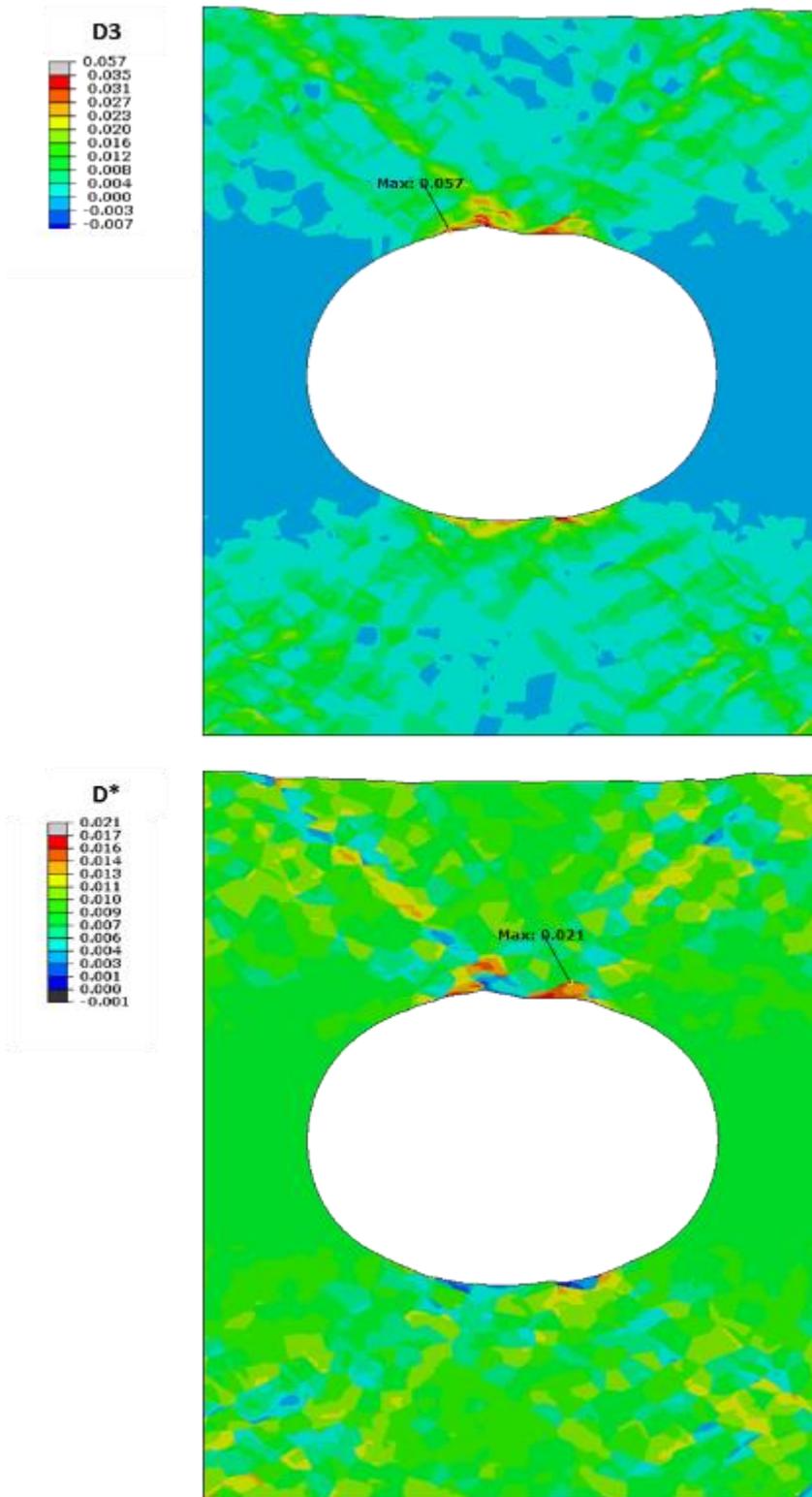
Figure 7-11. Deformed microstructure after 1 cycle for an applied strain of 0.01. a) The contours show the variations of the: a) D3 metric and b) the FIP introduced.
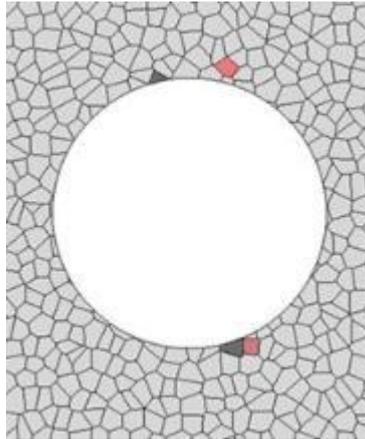
Figure 7-12. Predicted location for damage initiation by using the D3 metric (grey grains), and by using the FIP criterion (light red coloured grains).

The critical slip systems were evaluated for the deformed geometry shown in figure 7.11a; but only for the grains that were plastically deformed; a strain cut-off value was used in order to eliminate the grains aligned along the hole, which were under low stress-strain conditions. Three combinations of slip systems were the most active ones (1-4-9-10, 2-6-7-11 and 3-5-8-12), covering a total of 83% of the microstructural tessellation, as shown in Table 7.5. The total amount of plastic deformation due to the 3 major combinations of slip systems was smaller in comparison to Table 7.3; this was due to the fact that the strains were highly localised at the edge of the hole, with the rest of the simulation domain being under low strained conditions. Under low deformation, the most critical slip systems are not rather active yet, and the differences from the contribution of other slip systems are smaller. The most critical slip system was the 3rd one, with the most critical combination of slip systems being 3-5-8-12, similar to the observations made in Table 7.3.

Table 7-5. Critical slip systems and the number of grains these appear for the RVE of figure 7.9.

Combinations of critical slip systems (the critical slip systems appear to group in 4)				*In how many grains appear these slip systems?*
1st crit. slip system	2nd crit. slip system	3rd crit. slip system	4th crit. slip system	Nr of grains
1	2	10	11	27
1	4	9	10	132
1	5	8	10	15
2	3	5	11	2
2	4	6	7	1
2	5	8	11	10
2	6	7	11	146
3	4	9	12	17
3	5	6	7	1

3	5	8	12	263
3	6	7	12	11
4	6	7	9	26

7.4. Modelling Interactions

At low amplitude loading, it was shown in Chapter 6 that the influence of the particles becomes increasingly important, not macroscopically in terms of stress-strain curve, but micro-mechanically. Strain concentrations around the neighbourhood of particles and inclusions lead to damage nucleation. Inclusions cracking and interface decohesion was observed. While decohesion leads to void growth, cracking leads to high strain concentrations in the crystal matrix and subsequent crack growth within the matrix. In the case of the particles, cracking occurred in all cases. Particle cracking leads to high strain concentrations at the neighbourhood of the particles, as it was shown in figure 6.23. The most deteriorating cracking conditions at particle sites were observed to occur within particle clusters. This was attributed to the particle size and configuration effect. And it was also observed that these clusters behaved rather like a solid body, or specifically like a large particle. The size of these clusters appeared to extend more than 1 mm along the rolling direction (figure 5.4). Yet the important geometrical feature is the particle length along the direction perpendicular to the rolling direction (ND direction-loading direction). It was found that the average 'thickness' of the particle clusters was 20μm. The particles were within the grains, not crossing any GBs. A 2D RVE with 80 grains and 140 particles was created and is shown in figure 7.9a. In this geometry the size of the particles was 20μm. The shape was circular. Therefore the modeling geometry does not actually represent accurately either the size or shape of real particles - but it is actually a geometry representing the most important feature of the particles. 4-node plane strain quadrilateral elements (CPE4) were employed. A mesh size with an edge size of 0.01 was selected for this analysis; approximately 100 seeds on each side of the RVE, yielding a 100x100 mesh distribution for the edges. The meshed part is shown in figure 7.13b. The following boundary conditions were used for the geometry: the bottom edge of the polycrystal was constrained in the y-direction, the left-edge was constrained in the x-direction, and a 0.03 strain was applied at the right edge; with the top edge left free. An applied strain of 0.03 that lies within the elasticity region for Al2024 T3 was selected in order to model the behaviour of particles; as these become more important at low amplitude loading conditions. 10 fatigue cycles were modelled in this section.
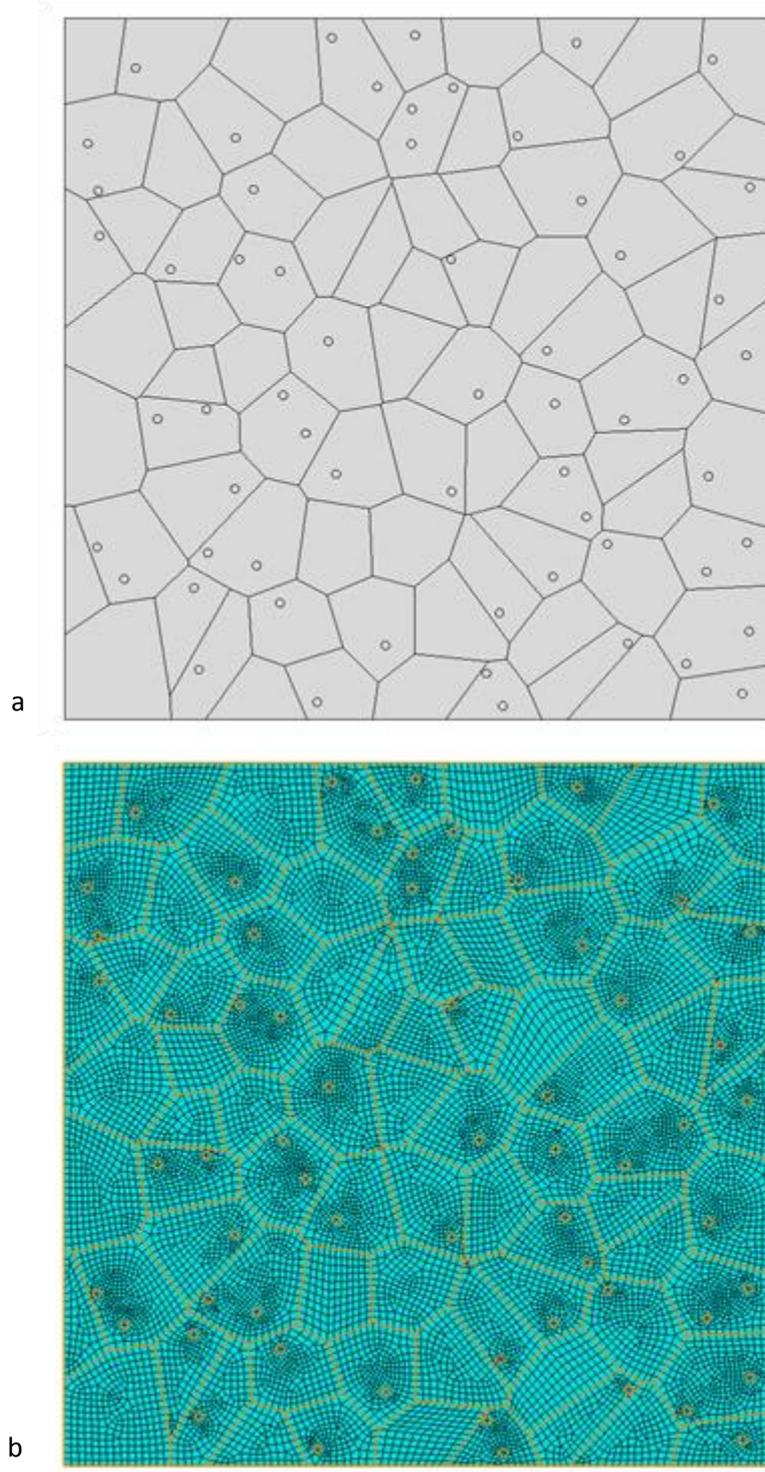
Figure 7-13. a) Polycrystal geometry created containing a user-defined distribution of particles. b) Meshed part

7.4.1. Elasto-plastic continuum matrix with 2ⁿᵈ phase particles

Instead of using crystal plasticity modelling, a continuum elasto-plastic formulation was employed. The mechanical behaviour for the matrix was obtained simply by using the macroscopic stress-strain curve of figure 5.9a up to the UTS point. The results for the maximum in plane principal strain are shown in figure 7.14. The model correctly predicts the location of high strain localisation at the neighbourhood of the particles. Yet it was observed in Chapter 6, that not all particles are strained in

259

equal proportions. Depending on the orientation of the grains, some grains appear to have 'hard' characteristics, and shield the particles and inclusions from damage development, while other grains form strong slip bands or stretch to large proportions. In the latter case, particle cracking occurred and high strain localisations at the neighbouring matrix were observed. This necessitates the use of crystal plasticity concepts to accurately predict the location where damage nucleates.
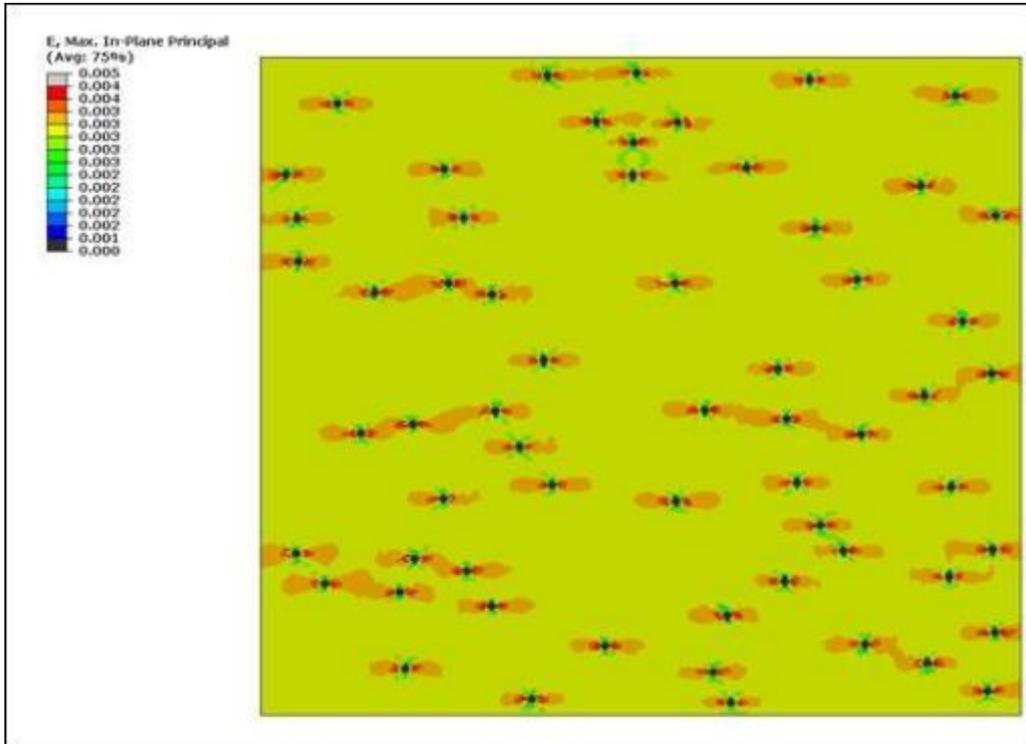
Figure 7-14. Deformed body after a 3% displacement. The contours show the variations of Von Mises stresses.

7.4.2. Polycrystal plasticity with particles (2D)

In this section crystal plasticity was applied for the grains of figure 7.13a. The meshed geometry was the same as the one shown in figure 7.13b. Figure 7.15a shows the maximum accumulated slip over the most critical slip system at each integration point, and figure 7.15b shows the total accumulated slip over all slip systems; both after 10 cycles and for the fully loaded condition of the geometry. Both figures show that the plastic strains are highly non-homogeneous. While there are areas- grains which are under low strained condition, it can be seen that the particles tend to localise high strains. This justifies also the observation that in some of the low strained grains observed experimentally, cracked particles could also be found. For the high strained crystals, the particles localise strains with values as high as 0.014, well within the plastic region, and therefore are expected to fail and initiate damage within the matrix.

A comparison between figure 7.14 and 7.15a shows that less interaction between the particles occurs for the latter case. Plastic deformation in the neighbourhood of the particles for the crystal plasticity case looks more constrained. The two figures 7.15a and b show similar strain patterns. The scale (0.000 up to 0.003) for the total accumulated slip over the most critical slip system (D1 max) shows that from the total accumulated slip over all the slip systems, which has a scale between 0.004 up to

0.014, most plastic deformation is due to the major slip system. Therefore, most of the plastic deformation is not due to only one major slip system. This slip system is not the same for all grains but depends on the orientation of the individual grains. Figure 7.15c shows the newly introduced FIP, D*, discussed in section 7.4.3. The scale expectedly is different with respect to figure 7.15b, as the FIP does not represent an actual strain value or metric. Yet the strain distribution looks similar to figure 7.15a and b. Table 7.6 shows the most critical slip systems responsible for plastic deformation in figure 7.15a. Most of the plastic deformation is due to the 1st, 2nd and 3rd slip systems. But many combinations of slip systems were active in this case, 7 in total, accounting for a total deformation of 92.5%. The most critical slip system was the 3-5-8-12 similarly to Tables 7.3 and 7.4. Yet in this case most of the plastic deformation is due to the activation of multiple slip systems.

a

b
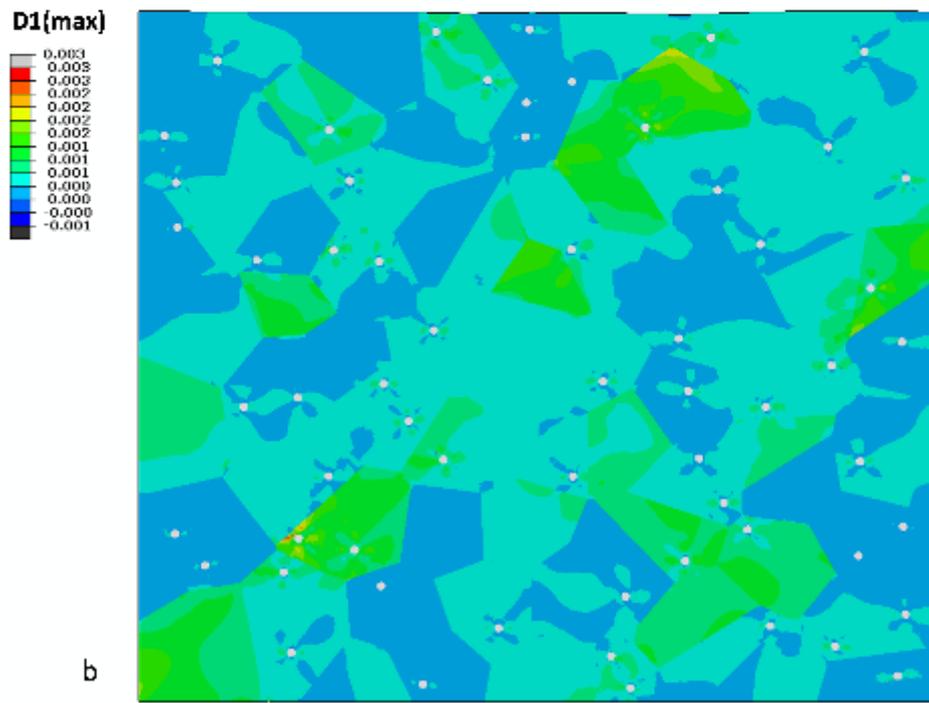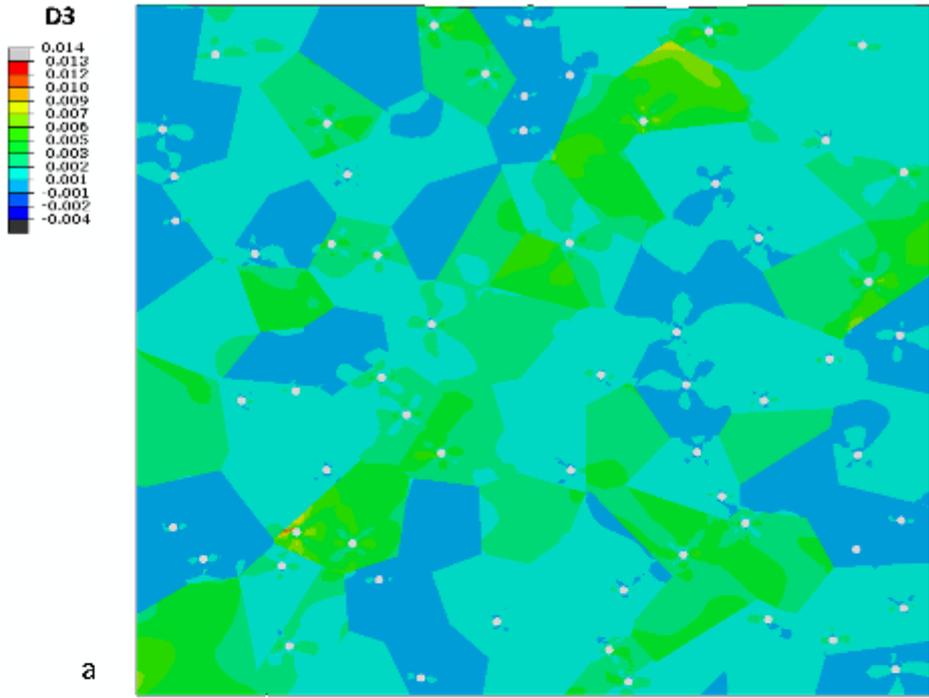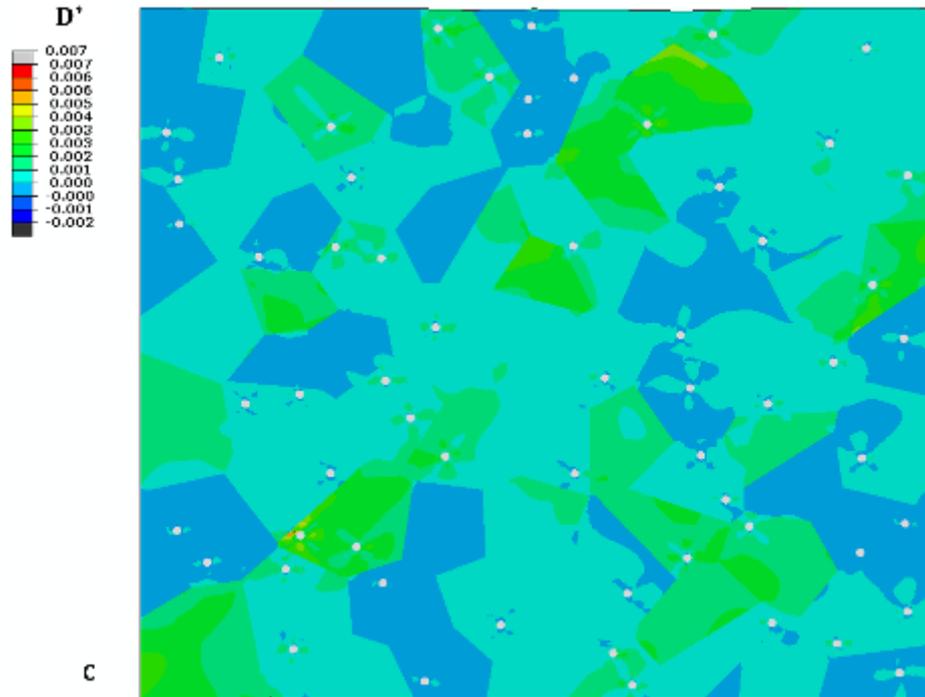
Figure 7-15. The strain contours for a) D3, b) D1(max), and c) D* metrics.

Table 7-6. Critical slip systems and the number of grains these appear for the RVE of figure 7.9.

Combinations of critical slip systems (the critical slip systems appear to group in 4)				In how many grains appear these slip systems?
1st crit. slip system	2nd crit. slip system	3rd crit. slip system	4th crit. slip system	Nr of grains
1	2	10	11	6
1	4	9	10	10
2	5	8	10	3
2	5	8	11	6
2	6	7	11	11
3	4	9	12	9
3	5	8	12	25
3	6	7	12	3
4	6	7	9	7

7.5. FCI & Total Fatigue Lifetime

The purpose of this study was not concentrated on evaluating the S-N curves for a broad spectrum of stress-strain values, but rather to focus on nucleation and small crack growth conditions. Yet it is crucial to be able to model the total fatigue lifetime of a component-specimen. 9 tests were done up to final failure for 3 strain amplitudes: 0.003 (elasticity region), 0.007 and 0.03. The first experiment

represent the HCF conditions and the two latter the LCF. The experimental results are shown in figure 7.16 with (**x**) symbols.

From a modelling perspective, the kinematic formulations (Armstrong-Frederick hardening rule) described in section 7.4.1 were applied within a crystal plasticity UMAT code developed by Huang et al [19]. Crack initiation occurred in the model once the value of D3 reached a critical value. A critical plastic strain value of 0.52 was used, determined from the strain observations made in Sections 6.4 and 6.5, where strain measurements were obtained in situ during crack initiation and propagation for four individual case studies. In more detail, the strain values measured before crack initiation were found to be 0.50, 0.52, 0.52 and 0.53. The red points correspond to the FCI predicted values. As shown for the case of HCF, the importance of FCI period becomes increasingly important as it represents a higher proportion of the total life time. The modelling work of this section made use of the facilities of Iceberg High Performance Computing Cluster at Sheffield University to minimize the computational times.
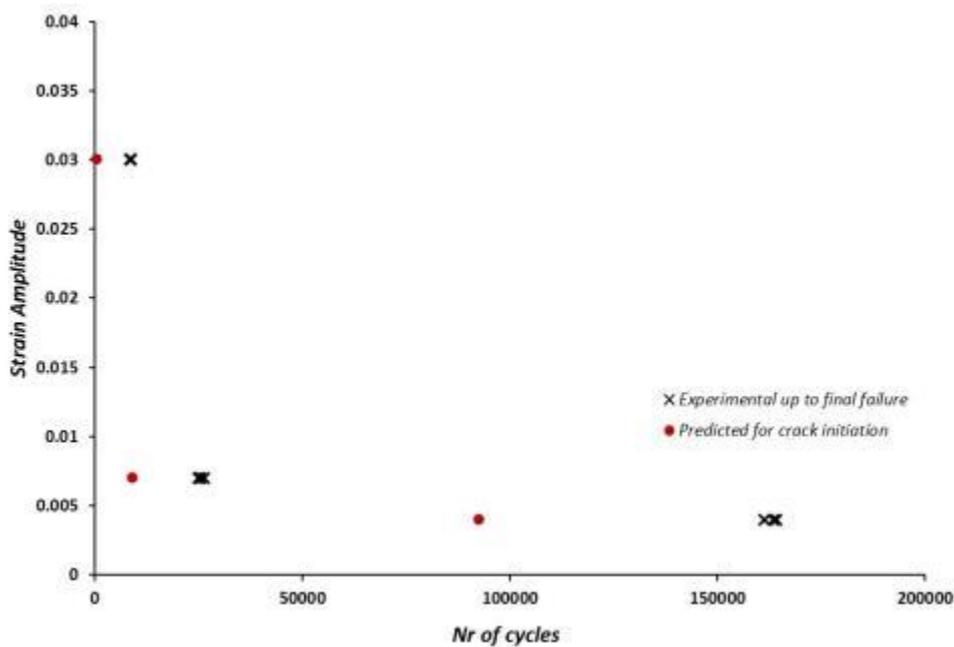
Figure 7-16. S-N curve for the material studies. Comparison between the total fatigue lifetime experimental results (number of cycles up to failure) and the modelling predicted values for the FCI period (number of cycles up to the point where FCI occurs).

7.6. Discussion

Single crystal validation is necessary to check the accuracy of the original crystal plasticity model developed by Huang et al [19]. A lot of published experimental work is available, so validating single crystal plasticity is relatively easy. A single crystal with a rectangular hole in the middle was created, and the stress-strain fields were evaluated for the case of an elasto-plastic material and a single crystal. The plastic zone was much larger in the latter case at critical locations and dependent on crystal orientation. Rotating the crystal in figure 7.3 leads to much different strain fields with respect to figure 7.2c. The crystal plasticity code was then applied to Al2024 polycrystals. The elastic constants were taken from [18, 20, 56, 57], while the parameters for Asaro's hardening rule were

optimised by evaluating the global stress-strain curve with respect to the experimentally measured one for an 80 grain RVE (figures 7.5 and 7.6). The most critical combinations of slip systems were also evaluated. It was found that 3 combinations of slip systems were responsible for almost 92.5% of the total deformation.

Modelling of the fatigue behaviour of Al2024 was then pursued, with assigning the proper kinematic hardening parameters that enable the modelling of both tensile testing as well as cyclic fatigue (tension-tension, tension-compression). The kinematic hardening rule was applied at the microscale, in order to model cyclic hardening and softening at specific locations in the microstructure. It was observed in Chapter 5 and 6, that specific locations were accumulating progressively more strains showing a softening behaviour. Focus was then given on FCI, and on the corresponding FCI criteria that are available on literature. An additional FCI parameter was introduced, D*, in order to be able to more accurately predict the location were FCI occurs in the experimental results reported in Chapter 6. A geometry similar to the one tested in Section 6.4 was created with the crystals being generated with the Voronoi technique. The highest strains were found to occur at the edge of the hole. Yet with the new criterion it is possible to model FCI that may not occur at the location of maximum deformation at the edge of the hole, simply by accounting for both the highest strains and the critical grain orientations that may be found in critically strained locations. The combinations of critical slip systems were evaluated for the whole geometry, and it was found that 3 combinations of slip systems account for a total deformation of 83%; considerably less than the case of the RVE of figure 7.5. This is due to the high strain localisation at the edge of the hole (activating only the most active slip systems), with the rest of the geometry being strained to a lower extent and therefore activating more slip systems. The low-strained cyclic loading conditions (within the elasticity region) were also modelled together with the effect of particles on strain distributions by using both a classic elasto-plastic formulation as well as crystal plasticity for an RVE of 80 grains. By using crystal plasticity it is possible to more accurately predict strain localisation and therefore FCI. It was found that low strained grains shield the particles from cracking, while highly strained grains tend to localise very high strains at the interface of the particles with the crystal matrix, therefore leading to cracking. This represents a more accurate modelling approach agreeing with the experimental observations of section 6.1. The combinations of critical slip systems were also evaluated for the RVE containing both grains and particles, and it was found that 7 combinations were responsible for a total of 92.5% of the total deformation. More combinations were active in this case with respect to the other two case studies: RVE with the hole (Section 7.3.3) and homogenised RVE (Section 7.2). This is due to the low strain amplitude which activates more slip systems and not just the most critical ones. In all cases it was found that the most critical combination of slip systems was the 3-5-8-12, with the 3rd slip system being the most critical one. The 3rd and 4th slip systems were (always) found to be one order of magnitude smaller, yet they are incorporated in the analysis as it has been observed that during crack propagation (section 6.3 and 6.4), crack deflections occur at various orientations which means that more than 2 slip systems can be activated at the crack tip. The small crack growth regime was not

modelled in this work, as it was observed in section 6.4 that crack paths are very complex. Both transgranular and intergranular crack growth situations were observed, with the crack deflecting also within the same grain. Small crack growth is a multiscale problem governed by two processes: the microscale strain fields involving 2-4 neighbouring grains and the nanoscale phenomena occurring at the crack tip (such as dislocation nucleation and propagation). But there is a strong interaction between the two. More experiments are necessary to properly inform new modelling strategies, realistically modelling crack propagation at the microstructural level [80]. The total fatigue lifetime of the specimen-RVE was evaluated.

7.6.1. Multiscale approach

The concept of RVEs and in general assigning the microstructural mechanical properties to the corresponding features (grains, inclusions, precipitates etc.) is restricted to the micro-scale. Yet these features do exist in large structures, and the possibility to model structures such as an airplane wing or a suspension of a car part, incorporating such information (microstructural information at the microscale) is computationally extremely demanding, and several weeks or months might be needed to run just a single model. The solution is to use a Multiscale approach, and move out of the small scale and model large components-specimens. The Multiscale approach is a very efficient way to connect the different length scales, by connecting the macroscopic boundary conditions (loads or displacements) to the stresses and strains at the micro-scale. In figure 7.17, the RVE is modelled with a very fine mesh by using crystal plasticity modelling, while the overall specimen is modelled with a coarse mesh, as a continuum elasto-plastic material. By using a simpler model (elasto-plastic) with a coarser mesh, the computational times reduce significantly. Figure 7.18 shows that the Multiscale approach is versatile and can be easily applied also to real structures like the rib of an airplane wing. In this way it is possible to apply more realistic boundary conditions to the microscale; and obtain information for crack initiation, crack resistance and growth during in-service conditions.

The only problem with the Multiscale approach is that the user is already predefining the critical location, where damage nucleation is expected to occur – the corresponding region where the RVE is employed.

A python code was developed which runs initially the material as fully elasto-plastic, and obtains the location(s) where the maximum stresses and strains occur at the first peak load. At the critical locations RVEs are introduced and the part is re-meshed. Then a 2nd step is created where the part is loaded under cyclic fatigue. In this way it is possible to model more realistic problems as discussed already. Yet this methodology may not be correct when applied for low amplitude fatigue loading, as it is relatively more difficult to locate the highly strained areas.

Crystal Plasticity formulations

Elasto-plastic material
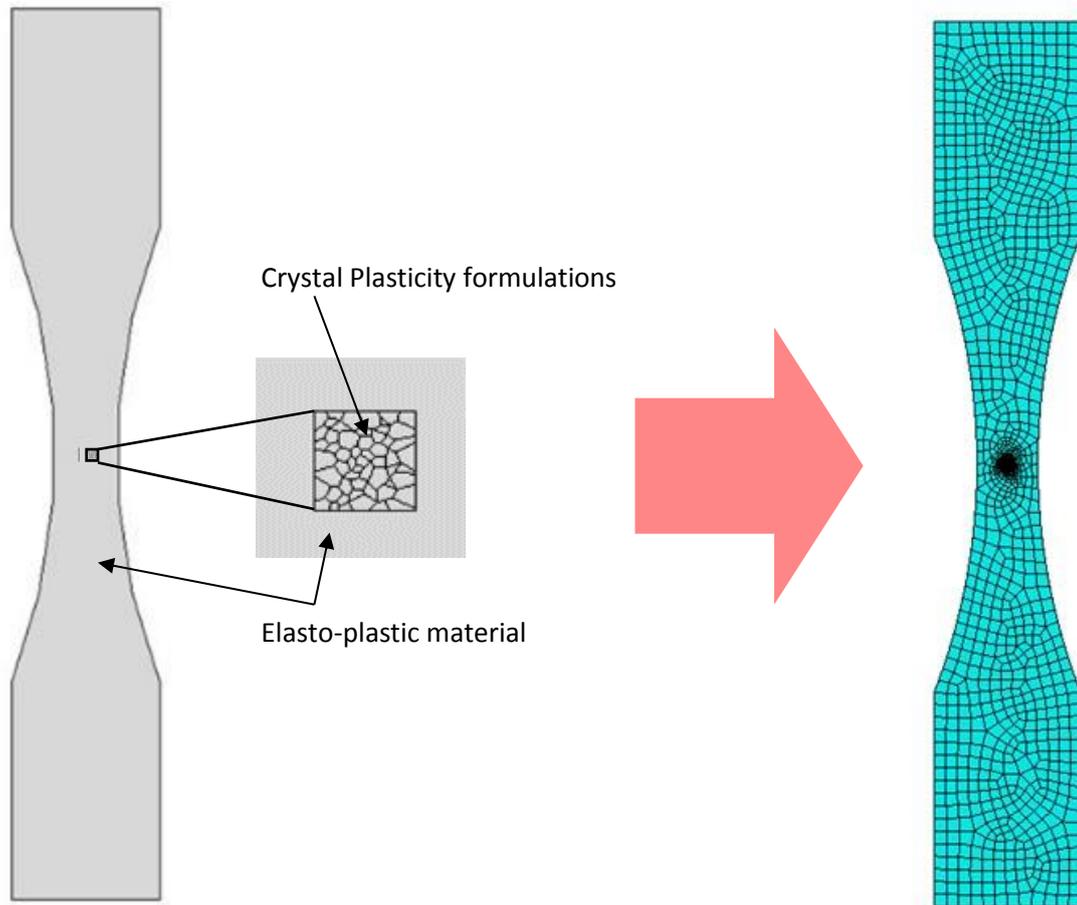
Figure 7-17. Multiscale approach for a tensile specimen
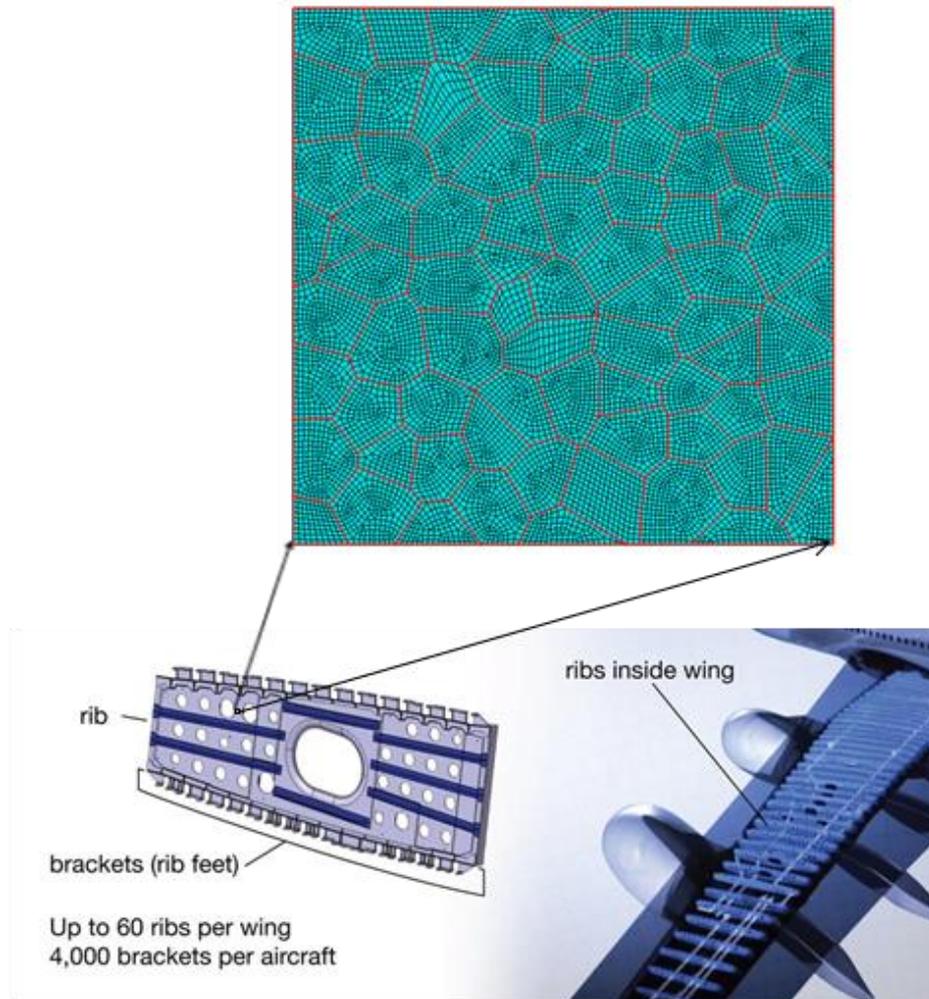
Figure 7-18. Multiscale approach for a more complex geometry.

7.7. Conclusions

Crystal plasticity was used to model macroscopic stress-strain behavior, as well as fatigue performance. By using 2D RVE with generated polycrystals it is feasible to model FCI potency in Al2024. By introducing a new FIP, D* it was possible to more accurately locate the region where damage is expected to occur at high amplitude cyclic loading. Polycrystals with particles-incorporated were also generated to model low amplitude fatigue and account for the effect and the interaction between the crystalline matrix and the particles embedded into it. The strain fields at the area of the particles were not quantitatively examined. Yet the model accounts for the interaction between the crystals and the particles. Areas of low strained matrix were found to be acting as a shield to the particles preventing them from fracture, while highly strained grains were expected to locate damage at particle sites. The model predicted that FCI represents a large part of the total fatigue lifetime of the RVE for low mid and high strain amplitudes. Finally it is possible to introduce the RVE at critical locations in a structure, and thus see the effect of the microstructure on the local stress-strain fields and damage evolution.

<div style="text-align: right;">8</div>

Conclusions and Future Recommendations

The main objective of this work was to develop a multi-scale study on FCI by combining a new experimental procedure (in-situ vertical fatigue bending tests with DIC) and crystal plasticity FE modelling. The mechanical performance of Al2024 T3 was evaluated by using a multiscale DIC approach at the macro-, meso- and microscale and a correlation was obtained between the corresponding scales.

At low amplitudes, strains are highly non-homogeneous (observed by macroscale DIC), the low and high strains tend to concentrate at clusters of grains (observed by mesoscale DIC) rather than in individual grains or large areas, and this is related to the fact that the 'critical' slip systems are not yet dominating the deformation and more slip systems take part in polycrystalline deformation. In this case the influence of particles and inclusions is also important. Cracks tend to initiate at these imperfections, but mostly within highly deformed grains, which was observed experimentally (by DIC as well as by metallurgical inspections) and predicted also in the crystal plasticity model.

At mid amplitudes, shear bands form, within which slip bands have formed along several grains (found by metallurgical inspections). Within these highly strained regions, particles and inclusions are damaged but do not lead to matrix cracking. Instead within these highly strained regions, a critical grain(s) with detrimental orientation will hold strong slip bands which upon cyclic loading will initiate a crack.

Finally at high amplitude loading, the highest strains were observed to localise at the centre of the sample, with the strains appearing rather homogeneous, minimising the effect of the microstructure.

Two in situ vertical tests were performed within a SEM chamber to further investigate FCI at mid amplitudes. It was found that strong slip bands are the major source for FCI. It is the presence of **'weak' grains** with detrimental orientation in **highly strained areas** that leads to FCI. Both conditions are necessary to nucleate a crack. Small crack growth was investigated. It was found that a crack does not necessarily follow the major slip bands within a grain but can follow a path towards highly strained areas. A crack may also deflect within the grain matrix to avoid dislocation pile up close to GBs and avoid a neighbouring 'hard' grain. Finally the crack can also follow the GB path to avoid low strained areas or grow parallel to high strained areas. These observations suggest that modeling the

small crack growth regime can be relatively difficult. And furthermore using the same FIP parameters for FCI and small crack growth leads to severe simplifications.

The pole figures revealed that there is a strong influence between texture and fatigue performance. Grains oriented far away from the rolling direction had a strong tendency to form strong slip bands and potentially act as FCI locations. Yet direct investigation on individual grains does not yield confident results. The influence of the local microstructure and neighboring grains was found to play a major role (on FCI) as grains with orientations far from the characterised 'weak' orientations in the IPF were found to form strong slip bands depending on the micro-mechanical performance of the surrounding grains.

The novelty of the current work can be summarized into the introduction of a new FCI criterion validated by experimental results, the insight brought on the small crack growth regime, the connection obtained for the strain distributions at the corresponding different length scales, and the relationship gained between material design and mechanical performance.

Future recommendations

The future recommendations are summarized in the following bullets points:

- ✓ Perform DIC at various strain amplitudes and see the rate of strain accumulation for each case. For this case image capture should be performed more frequently in order to capture the variation in strain accumulation throughout the lifetime of the specimen-component

- ✓ Perform low amplitude bending tests and see the mechanisms for crack propagation from particle sites.

- ✓ Use Cellular Automaton and incorporate within specific-randomly distributed elements particles to gain faster computational times. Use a strain criterion obtained from the experiments, which splits the critical(s) element(s) into cells. Within one of the cells a particle or more are embedded. In this way particle-matrix interactions are modeled only at critical locations-grains.

- ✓ Perform more bending tests with other materials as well, to check for the FCI and propagation criteria that are available. And whether new criteria must be introduced. If possible high resolution EBSD maps at the crack tips if possible would be very useful in order to gain information on the kinetics of crack growth, the influence of dislocation, local slip bands as well as macroscopic strain fields within the region of 2-3 grains.

- ✓ Analyse thoroughly the influence of local microstructure, by obtaining the strain fields within the grains by high-resolution SEM. Two techniques can be used to more accurately predict the strains within less than 1 micron step: a) micro-grid technique, and b) particle deposition methods within a FIB-SEM. By analysing the strain fields within this scale it will be possible to investigate the influence of the neighboring grains.

References

1. *http://www.theguardian.com/business/2012/feb/08/a380-superjumbo-checks-wing-cracks#* .

2. Miller, K.J., *Metal Fatigue—Past, Current and Future.* Proceedings of the Institution of Mechanical Engineers, Part C: Journal of Mechanical Engineering Science, 1991. **205**(5): p. 291-304.

3. Miller, K.J., *THE TWO THRESHOLDS OF FATIGUE BEHAVIOUR.* Fatigue & Fracture of Engineering Materials & Structures, 1993. **16**(9): p. 931-939.

4. Stroh, *A theory of the Fracture of Metals.* Advances in Physics, 1957. **6**(24): p. 418-465.

5. J. Man, K.O., C. Blochwitz, J. Polak, Acta Materialia, 2002. **50**: p. 3767-3780.

6. Holdsworth, *Optimisation of the methodologies to predict crack initiation and early growth in components under complex creep-fatigue loading.* Synthesis Report, 1997.

7. Brinckmann, S. and E. Van der Giessen, *A fatigue crack initiation model incorporating discrete dislocation plasticity and surface roughness.* International Journal of Fracture, 2007. **148**(2): p. 155-167.

8. Suresh, S. *Fatigue of Materials*. 1998; Available from: http://public.eblib.com/EBLPublic/PublicView.do?ptiID=1103761.

9. Chaboche, J.L., *Constitutive equations for cyclic plasticity and cyclic viscoplasticity.* International Journal of Plasticity, 1989. **5**(3): p. 247-302.

10. Brückner-Foit, A. and X. Huang, *Numerical simulation of micro-crack initiation of martensitic steel under fatigue loading.* International Journal of Fatigue, 2006. **28**(9): p. 963-971.

11. Huang, X., et al., *Simplified three-dimensional model for fatigue crack initiation.* Engineering Fracture Mechanics, 2007. **74**(18): p. 2981-2991.

12. Kramberger, J., et al., *Extension of the Tanaka–Mura model for fatigue crack initiation in thermally cut martensitic steels.* Engineering Fracture Mechanics, 2010. **77**(11): p. 2040-2050.

13. Cheong, K.-S., M.J. Smillie, and D.M. Knowles, *Predicting fatigue crack initiation through image-based micromechanical modeling.* Acta Materialia, 2007. **55**(5): p. 1757-1768.

14. Manonukul, A. and F.P.E. Dunne, *High– and low–cycle fatigue crack initiation using polycrystal plasticity.* Proceedings of the Royal Society of London. Series A: Mathematical, Physical and Engineering Sciences, 2004. **460**(2047): p. 1881-1903.

15. Sweeney, C.A., et al., *The role of elastic anisotropy, length scale and crystallographic slip in fatigue crack nucleation.* Journal of the Mechanics and Physics of Solids, 2013. **61**(5): p. 1224-1240.

16. Dunne, F.P.E., D. Rugg, and A. Walker, *Lengthscale-dependent, elastically anisotropic, physically-based hcp crystal plasticity: Application to cold-dwell fatigue in Ti alloys.* International Journal of Plasticity, 2007. **23**(6): p. 1061-1083.

17. *ABAQUS, Version 6.9. Hibbitt Karlsson and Sorensen, Inc., Providence, RI; 2009.*

18. Luo, C. and A. Chattopadhyay, *Prediction of fatigue crack initial stage based on a multiscale damage criterion.* International Journal of Fatigue, 2011. **33**(3): p. 403-413.

19. Huang, Y., *"A user-material subroutine incorporating single crystal plasticity in the ABAQUS finite element program, Mech Report 178".* Division of Engineering and Applied Sciences, Harvard University, Cambridge, Massachusetts.

20. Luo, C. *Multiscale Modeling & Virtual Sensing for Structural Health Monitoring*. 2011; Available from: http://hdl.handle.net/2286/7ozpxe85egh.

21. Luo, C., et al., *Fatigue Damage Prediction in Metallic Materials Based on Multiscale Modeling.* AIAA Journal, 2009. **47**(11): p. 2567-2576.

22. Ding, F., T. Zhao, and Y. Jiang, *A study of fatigue crack growth with changing loading direction.* Engineering Fracture Mechanics, 2007. **74**(13): p. 2014-2029.

23. Jiang, *A fatigue criterion for general multiaxial loading.* Fatigue & Fracture of Engineering Materials & Structures, 2000. **23**(1): p. 19-32.

24. Kalnaus, S. and Y. Jiang, *Fatigue life prediction of copper single crystals using a critical plane approach.* Engineering Fracture Mechanics, 2006. **73**(6): p. 684-696.

25. Garruchet, S., et al., *An empirical method to determine the free surface energy of solids at different deformations and temperature regimes: An application to Al.* Surface Science, 2005. **586**(1–3): p. 15-24.

26. Shenoy, M., J. Zhang, and D.L. McDowell, *Estimating fatigue sensitivity to polycrystalline Ni-base superalloy microstructures using a computational approach.* Fatigue & Fracture of Engineering Materials & Structures, 2007. **30**(10): p. 889-904.

27. Przybyla, C.P. and D.L. McDowell, *Microstructure-sensitive extreme value probabilities for high cycle fatigue of Ni-base superalloy IN100.* International Journal of Plasticity, 2010. **26**(3): p. 372-394.

28. Lin, B., L.G. Zhao, and J. Tong, *A crystal plasticity study of cyclic constitutive behaviour, crack-tip deformation and crack-growth path for a polycrystalline nickel-based superalloy.* Engineering Fracture Mechanics, 2011. **78**(10): p. 2174-2192.

29. Bishop, J.F.W. and R. Hill, *XLVI. A theory of the plastic distortion of a polycrystalline aggregate under combined stresses.* The London, Edinburgh, and Dublin Philosophical Magazine and Journal of Science, 1951. **42**(327): p. 414-427.

30. Zhan, Z.L. and J. Tong, *A study of cyclic plasticity and viscoplasticity in a new nickel-based superalloy using unified constitutive equations. Part I: Evaluation and determination of material parameters.* Mechanics of Materials, 2007. **39**(1): p. 64-72.

31. Zhao, L.G. and J. Tong, *A viscoplastic study of crack-tip deformation and crack growth in a nickel-based superalloy at elevated temperature.* Journal of the Mechanics and Physics of Solids, 2008. **56**(12): p. 3363-3378.

32. Simonovski, I. and L. Cizelj, *The influence of grains' crystallographic orientations on advancing short crack.* International Journal of Fatigue, 2007. **29**(9–11): p. 2005-2014.

33. Riesch-Oppermann, H., *Generation of 2D random Poisson–Voronoi mosaics as framework for micromechanical modeling of polycrystalline materials-algorithm and subroutines description. .* Technical Report, FZKA 6325, Forschungszentrum Karlsruhe, 1999.

34. Mineur, M., P. Villechaise, and J. Mendez, *Influence of the crystalline texture on the fatigue behavior of a 316L austenitic stainless steel.* Materials Science and Engineering: A, 2000. **286**(2): p. 257-268.

35. Weyer, S., et al., *Automatic finite element meshing of planar Voronoi tessellations.* Engineering Fracture Mechanics, 2002. **69**(8): p. 945-958.

36. Kovac, M.C.L., *Influence of microstructure of development of large deformations in reactor pressure vessel steel : dissertation = Vpliv mikrostrukture na razvoj velikih deformacij jekla reaktorske tlacne posode : disertacija*. 2004, Ljubljana: [M. Kovac].

37. Bennett, V.P. and D.L. McDowell, *Crack tip displacements of microstructurally small surface cracks in single phase ductile polycrystals.* Engineering Fracture Mechanics, 2003. **70**(2): p. 185-207.

38. Potirniche, G.P. and S.R. Daniewicz, *Analysis of crack tip plasticity for microstructurally small cracks using crystal plasticity theory.* Engineering Fracture Mechanics, 2003. **70**(13): p. 1623-1643.

39. Simonovski, I., *Mechanisms for thermal fatigue initiation and crack propagation in NPP components : final report*. 2005, S.l.: s.n.].

40.   I. Simonovski, K.-F.N., L. Cizelj *Material properties calibration for 316L steel using polycrystalline model. In: .* ICONE 13: proceedings of the 13th international conference on nuclear engineering. Beijing, 2005.

41.   Simonovski, I., K.-F. Nilsson, and L. Cizelj, *Crack tip displacements of microstructurally small cracks in 316L steel and their dependence on crystallographic orientations of grains.* Fatigue & Fracture of Engineering Materials & Structures, 2007. **30**(6): p. 463-478.

42.   Lillbacka, R., E. Johnson, and M. Ekh, *A model for short crack propagation in polycrystalline materials.* Engineering Fracture Mechanics, 2006. **73**(2): p. 223-232.

43.   Prasannavenkatesan, R., et al., *3D modeling of subsurface fatigue crack nucleation potency of primary inclusions in heat treated and shot peened martensitic gear steels.* International Journal of Fatigue, 2009. **31**(7): p. 1176-1189.

44.   Bozek, J.E., et al., *A geometric approach to modeling microstructurally small fatigue crack formation: I. Probabilistic simulation of constituent particle cracking in AA 7075-T651.* Modelling and Simulation in Materials Science and Engineering, 2008. **16**(6): p. 065007.

45.   Hochhalter, J.D., et al., *A geometric approach to modeling microstructurally small fatigue crack formation: II. Physically based modeling of microstructure-dependent slip localization and actuation of the crack nucleation mechanism in AA 7075-T651.* Modelling and Simulation in Materials Science and Engineering, 2010. **18**(4): p. 045004.

46.   Hochhalter, J.D., et al., *A geometric approach to modeling microstructurally small fatigue crack formation: III. Development of a semi-empirical model for nucleation.* Modelling and Simulation in Materials Science and Engineering, 2011. **19**(3): p. 035008.

47.   Schreier, H.O.J.-J.S.M.A. *Image Correlation for Shape, Motion and Deformation Measurements Basic Concepts,Theory and Applications*. 2009; Available from: http://dx.doi.org/10.1007/978-0-387-78747-3.

48.   Zafar, A., *Digital Image Correlation.* CEE 498KUC Experimental Methods in Structures and Materials.

49.   Berfield, T.A., et al., *Fluorescent image correlation for nanoscale deformation measurements.* Small, 2006. **2**(5): p. 631-5.

50.   Ghadbeigi, H., et al., *Local plastic strain evolution in a high strength dual-phase steel.* Materials Science and Engineering: A, 2010. **527**(18–19): p. 5026-5032.

51.   Kang, J., et al., *Digital image correlation studies for microscopic strain distribution and damage in dual phase steels.* Scripta Materialia, 2007. **56**(11): p. 999-1002.

52.   Ososkov, Y., et al., *In-situ measurement of local strain partitioning in a commercial dual-phase steel.* International Journal of Materials Research, 2007. **98**(8): p. 664-673.

53.   Ghadbeigi, H., C. Pinna, and S. Celotto, *Quantitative Strain Analysis of the Large Deformation at the Scale of Microstructure: Comparison between Digital Image Correlation and Microgrid Techniques.* Experimental Mechanics, 2012. **52**(9): p. 1483-1492.

54.   Asaro, R., *Mechanics of Solids and Materials.* V. Lubarda, 2011.(ISBN: 9780521166119).

55.   Taylor, G.I., *The Mechanism of Plastic Deformation of Crystals. Part I. Theoretical.* Proceedings of the Royal Society of London. Series A, 1934. **145**(855): p. 362-387.

56.   Asaro, R.J., *Crystal Plasticity.* Journal of Applied Mechanics, 1983. **50**(4b): p. 921-934.

57.   Asaro, R.J. and J.R. Rice, *Strain localization in ductile single crystals.* Journal of the Mechanics and Physics of Solids, 1977. **25**(5): p. 309-338.

58. Asaro, R.J.B.U.M.S.P., *Micromechanics of crystals and polycrystals*. 1982, Providence, R.I.: Division of Engineering, Brown University.

59. Hill, R., *Generalized constitutive relations for incremental deformation of metal crystals by multislip.* Journal of the Mechanics and Physics of Solids, 1966. **14**(2): p. 95-102.

60. Hill, R. and J.R. Rice, *Constitutive analysis of elastic-plastic crystals at arbitrary strain.* Journal of the Mechanics and Physics of Solids, 1972. **20**(6): p. 401-413.

61. Peirce, D., R.J. Asaro, and A. Needleman, *An analysis of nonuniform and localized deformation in ductile single crystals.* Acta Metallurgica, 1982. **30**(6): p. 1087-1119.

62. Peirce, D., *Analysis of nonuniform deformation in ductile single crystals.* Ph.D. Thesis (1st Edn) Brown University, 1982.

63. Liu, C., *Dislocation-Based Crystal Plasticity Finite Element Modelling of Polycrystalline Material Deformation.* PhD thesis. UCLA, 2006.

64. Peirce, D., C.F. Shih, and A. Needleman, *A tangent modulus method for rate dependent solids.* Computers & Structures, 1984. **18**(5): p. 875-887.

65. Roters, F., et al., *Overview of constitutive laws, kinematics, homogenization and multiscale methods in crystal plasticity finite-element modeling: Theory, experiments, applications.* Acta Materialia, 2010. **58**(4): p. 1152-1211.

66. *Transactions on Computational Science IX; Special Issue on Voronoi Diagrams in Science and Engineering. 978-3-642-16007-3.*

67. *Matlab, 2010a. The Mathworks Inc. Natick. Massachusetts.*

68. Randle, V.E.O., *Introduction to texture analysis : macrotexture, microtexture and orientation mapping*. 2000, Amsterdam, The Netherlands: Gordon & Breach.

69. *http://neon.materials.cmu.edu/rollett/rollett.html.*

70. Kocks, U.F.T.C.N.W.H.-R., *Texture and anisotropy : preferred orientations in polycrystals and their effect on materials properties*. 1998, Cambridge, U.K.; New York: Cambridge University Press.

71. *http://eurocodes.jrc.ec.europa.eu/.*

72. Hertzberg, R.W., *Deformation and Fracture Mechanics of Engineering Materials.* ISBN-13: 978-0471012146, 4th Edition.

73. D. A. Porter, K.E.E., and M. Y. Sherif, *Phase Transformations in Metals and Alloys.* (Boca Raton FL: CRC Press 2009).

74. Bacon, H., *Introduction to dislocations.* 4th Edition, 2001.

75. A.L., G., *Continuum Theory of Ductile Rupture by Void Nucleation and Growth: Part I Yield Criteria and Flow Rules for Porous Ductile Media. Journal of Engineering Materials and Technology.* 1977a. **99**: p. 2-15.

76. Rice, J.R.a.T.D.M., *On the ductile Enlargement of Voids in Triaxial Stress Fields.* Journal of the Mechanics and Physics of Solids, (17): p. 201-217.

77. Rousselier, G., *Ductile fracture models and their potential in local approach of fracture.* Nuclear Engineering and Design, 1987. **105**(1): p. 97-111.

78. Tvergaard, V., *Influence of voids on shear band instabilities under plane strain conditions.* International Journal of Fracture, 1981. **17**(4): p. 389-407.

79. Efthymiadis, P., *Multiscale Expreimentation and Modeling of fatigue crack development in aluminium alloy Al2024.* University of Sheffield, 2014.

80. McDowell, D.L. and F.P.E. Dunne, *Microstructure-sensitive computational modeling of fatigue crack formation.* International Journal of Fatigue, 2010. **32**(9): p. 1521-1542.

81. Simonovski, I., K.-F. Nilsson, and L. Cizelj, *The influence of crystallographic orientation on crack tip displacements of microstructurally small, kinked crack crossing the grain boundary.* Computational Materials Science, 2007. **39**(4): p. 817-828.

82. Takeuchi, T., *Work Hardening of Copper Single Crystals with Multiple Glide Orientations.* Transactions of the Japan Institute of Metals, 1975. **16**(10): p. 629-640.

Appendices

Figure A1 shows images of a grain that shows resistance to slip banding mechanisms, and therefore diverts the direction of the crack, in order for the crack to find an easy passage through grain A of figure A2.
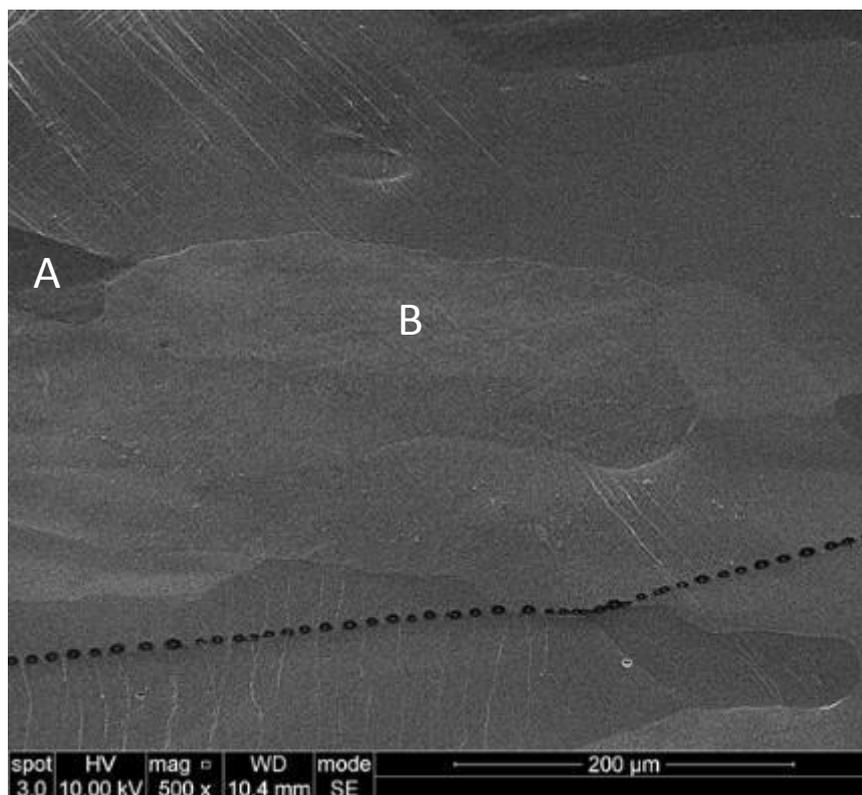
Figure A1. A hard grain in between highly deformed 'weak' grains.
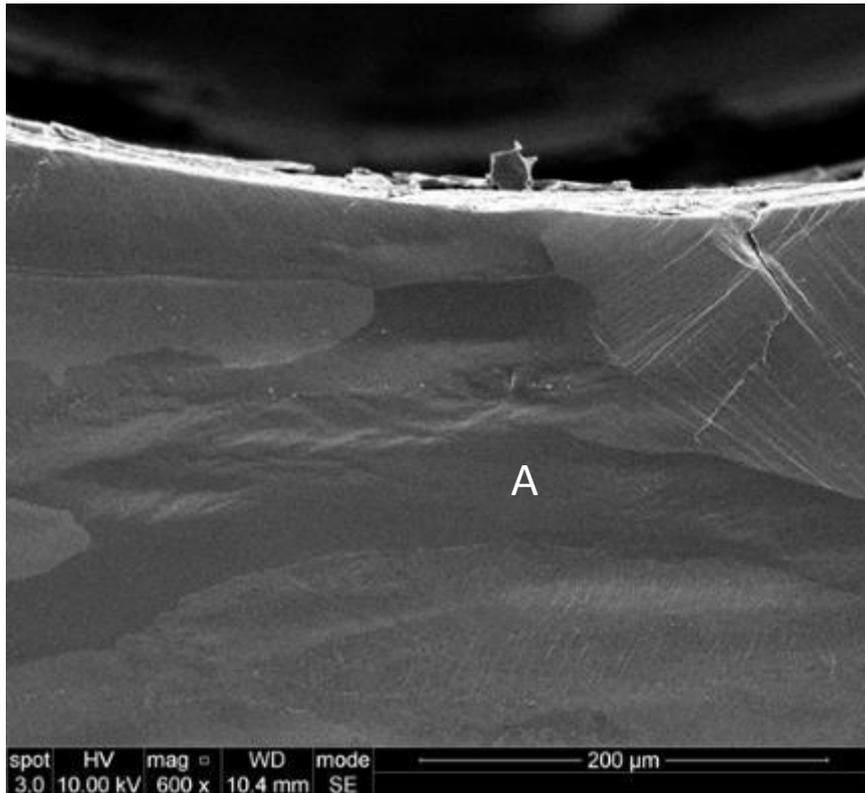
Figure A2. A 'weak' grain deflecting the crack towards its' matrix.
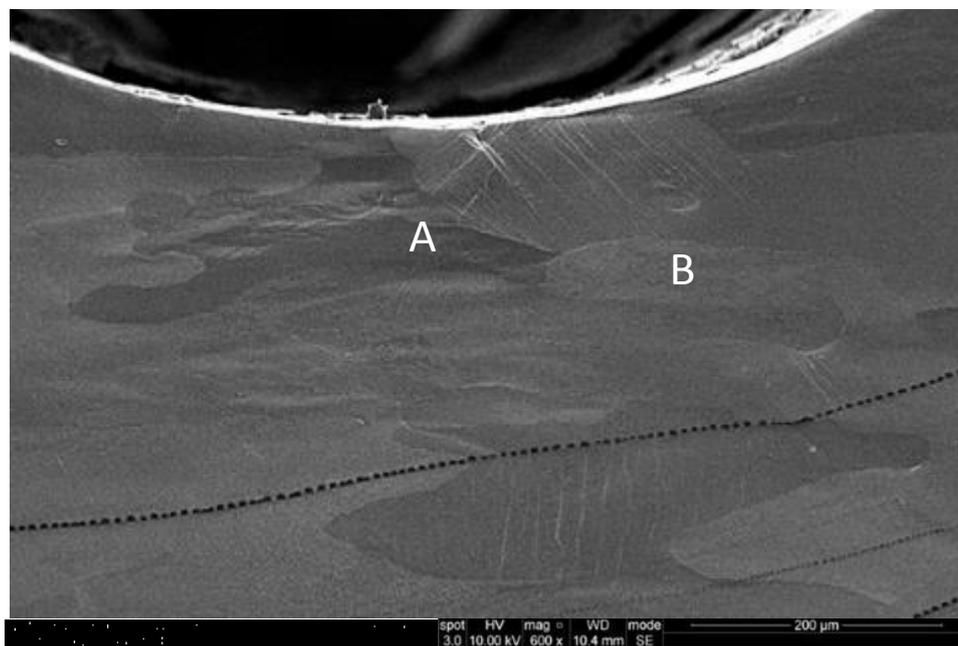
Figure A3. Overview image at the location of cracking, together with grain A and B

B
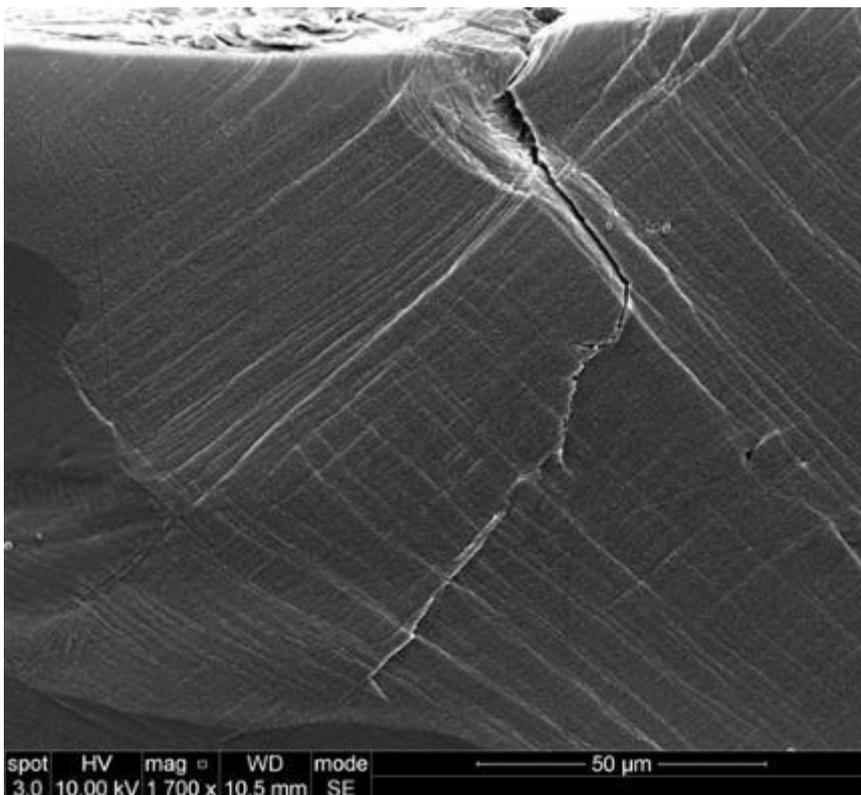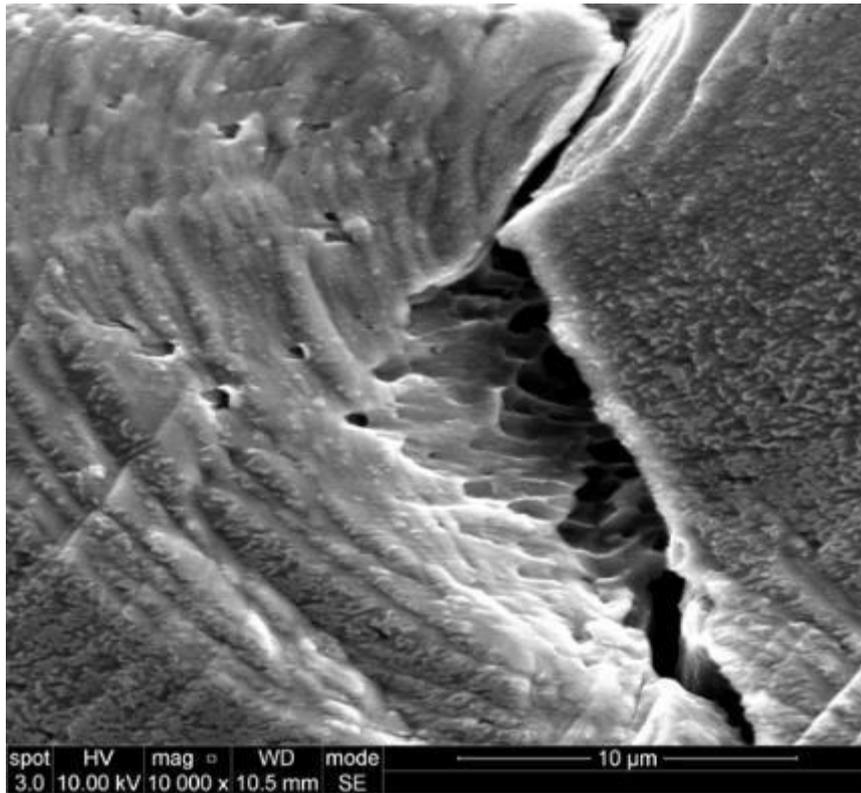
HC deposition

HC deposition was observed to occur during EBSD acquisition. Figures A1 and A3 shows the effect of HC deposition in SEM imaging.

Figure B1. HC deposition. Imaging at the location were EBSD measurements were previously taken, for the after etched condition for the sample.
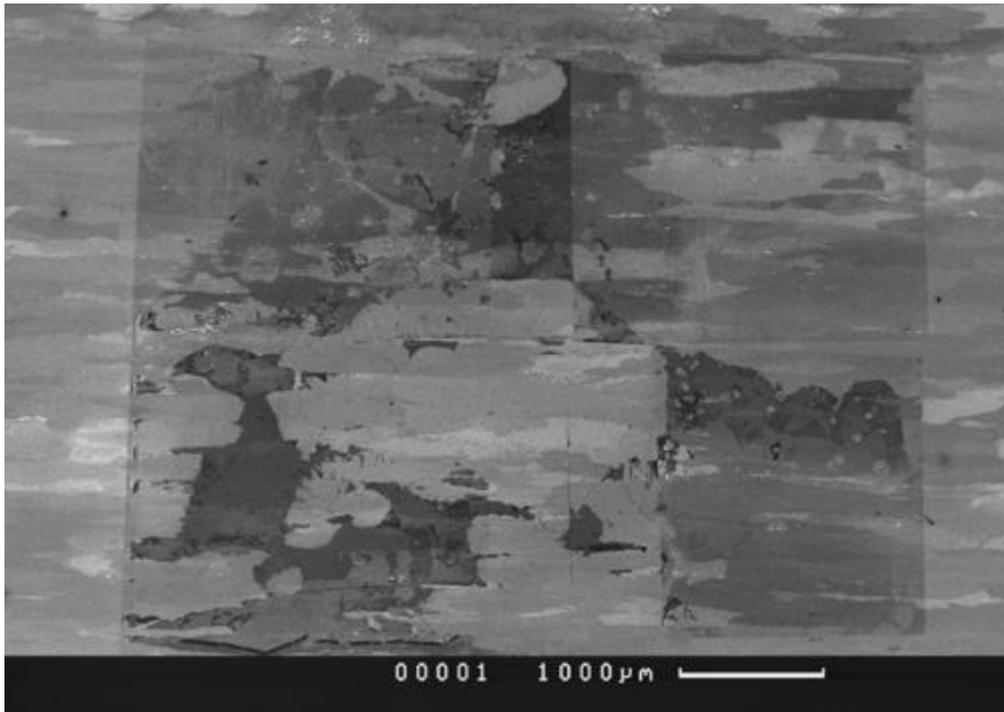
Figure B2. HC deposition. Imaging at the location were EBSD measurements were taken, for the after etched condition for the sample.